REVIEW OF THE VKI DOCTORAL RESEARCH

2018 - 2019



von Karman Institute for Fluid Dynamics

Front cover: The figure's background displays a post-treated frame from high speed camera recordings of the plasma jet oscillations in the Inductively Coupled Plasma wind tunnel Plasmatron of VKI. Numerical investigations of the plasma stability features link these oscillations to the concept of absolute instability. The nature of the instabilities can be established by plotting contours of the perturbation's growthrate σ in the complex wave-number (α_r;α_i) plane: According to the Briggs and Bers criterion, the instability is either convective or absolute depending on the sign of the growth-rate where the contours from a saddle point: σ_0.
For $\sigma_0 > 0$, the instability is absolute, and as illustrated on the (x; t) graph, these instabilities allow self-sustained perturbations to grow both upstream and downstream of their source in the aftermath of a localized impulse.
Picture of Simon Demange

©2019 by the von Karman Institute for Fluid Dynamics
Waterloosesteenweg 72, B-1640 Sint-Genesius-Rode
To order: https://www.vki.ac.be

ISBN 978-2-87516-149-9

D/2019/0238/718, T. Magin, Editor-in-Chief

The contents of this book are the property of the von Karman Institute for Fluid Dynamics. No part of this book may be reproduced or distributed in any form of by any means, or stored in a database or retrieval system, without the prior written permission from the Publisher.

PREFACE

The tenth symposium on the doctoral research of the von Karman Institute for Fluid Dynamics took place during the period March 11 to 13, 2019. The doctoral students present the progress of their research work carried out in the three departments: Aeronautics and Aerospace, Environmental and Applied Fluid Dynamics, Turbomachinery and Propulsion. The first year students have presented a poster on their research plans and some preliminary results, while the most advanced students have proposed a presentation followed by a session of questions.

This event was attended by the faculty of the von Karman Institute, as well as by colleagues from universities and industrial partners. The Symposium is open to external attendees free of charge. In addition to the presentations of the PhD candidates, we had the pleasure to welcome three prominent keynote lecturers who open each day the Symposium:

- Dr. Laurent Gicquel, CERFACS, France, *"The application of LES techniques for turbomachinery flows,"*
- Prof. Paolo Di Marco, Università di Pisa, Italy, "*Changing game rules: experimentation with fluids in microgravity,"*
- Prof. Beverley McKeon, Caltech, USA, "*Systems analysis of wall turbulence: Characterizing natural and synthetic self-sustaining and self-similar processes."*

This year, the best presentation award has been attributed to Simon Demange for his research on "Absolute Instability in Plasma Jet" We would like to congratulate him on this achievement. The illustrated cover art of these proceedings is based on his research results. The best poster presentation has been attributed to Cem Berk Şenel for a work on "Generalized scale-adaptive 3D planetary boundary layer model based on LES for the Earth's and Mars atmospheres" and to Andrea Fagnani for his work on "Comprehensive characterization of the aerothermomechanical response of space debris to atmospheric entry plasmas."

This proceedings volume contains 44 papers, which are divided into the following topics: Liquid Metal and Industrial Flows, Environmental Flows and Safety, Aeroacoustics, Liquid and Solid Propulsion, Aerothermochemistry, Aerothermodynamics, Rarefied and Plasma Flows, Turbine & Compressor Aerodynamics and Heat Transfer, Shape Optimization.

We would like to emphasize that this publication serves as a tool for communication and aims to enhance exchange between the doctoral candidates, the faculty and external attendees. The annual publication of their results in proceedings is of crucial importance to the VKI research providing a thorough review of the different activities within the three departments.

As such, the doctoral candidate students play a key role in strengthening the expertise in experimental research, computational methods, and physical modelling. In addition to basic research, works carried out at the von Karman Institute often leads to implementation of real life industrial applications critical to the fluid dynamics community.

Andrea Attavino Francisco Torres Herrador Phd Representatives	Thierry Magin Professor	Christelle Debeer Organizer / Editor

The contribution of all VKI members who helped with this event is deeply acknowledged in particular the faculty, library and printing office staff.

TABLE OF CONTENTS

Editorial notes i

Table of contents iii

LIQUID METAL AND INDUSTRIAL FLOWS

Andrea ATTAVINO 3
Numerical Investigation of the Effect of Buoyancy Forces on the Deflagration of Hydrogen in the Thai Facility

Adriana ENACHE 13
Analytical and Experimental Investigation of Icing Phenomena on Wind Turbine Blades

Zoe JARDON (First year PhD student) 23
Numerical and Experimental Validation of a Reliable Crack Localization System for 3D Printed Metallic Components based on the eSHM Methodology

Maxim VAN CAPPELEN 25
Modeling Particle Trajectory Crossing in Poly-Dispersed Particle-Laden Flows, a Quadrature based Approach

Agustín VILLA ORTIZ 37
Large Eddy Simulations on a Natural Convection Boundary Layer at Prandtl Numbers 0.71 And 0.025

ENVIRONMENTAL FLOWS AND SAFETY

Nicolas COUDOU 51
Effects of the Fidelity Level on the Numerical Reproduction of the Wake Meandering Phenomenon

Charline FOUCHIER 61
Scaled Model of the Pollutant Dispersion Driven by a Condensed-Phase Explosion in an Urban Environment

Sara PORCHETTA 69
A Coupled Atmosphere-Wave Model: an Investigation of the Influence of the Wind-wave Alignment on the Vertical Wind Profile

Cem Berk ŞENEL (First year PhD student) 83
Generalized Scale-Adaptive 3D Planetary Boundary Layer Model based on LES for the Earth's and Mars Atmospheres

Nishio YOSHIYUKI 85
CBRN Dispersion Modeling in the Atmosphere

AEROACOUSTICS

Joachim DOMINIQUE 97
Towards Quieter Fans : Multi-port Eduction of Installation Effects in Small Axial Fan System

Riccardo ZAMPONI 109
Investigation of Turbulence-Surface Interaction Noise Mechanism and their Reduction using Porous Materials

Alessandro ZARRI 121
Low-Order Aeroacoustic Prediction of Low-Speed Axial Fan Noise

LIQUID AND SOLID PROPULSION

Claudia ESPOSITO 133
Experimental Study of Cavitating Flow and Fluid Hammer in Cryogenic Conditions

Dominico FIORINI (First year PhD student).....143
Gas-Liquid Interface Dynamics in Non-isothermal Sloshing: Experimental Analysis and Simplified Modeling

Ali Can ISPIR (First year PhD student).....145
Multi-dimensional Design and Optimization of a Hypersonic Propulsion System

Maria Teresa SCELZO 147
Numerical Simulations of a Slurry Flow in Horizontal and Vertical Pipes: Effect of Forces Modelling

AEROTHERMOCHEMISTRY

Joffrey COHEUR.....159
Bayesian Parameter Inference for PICA Devolatilization Pyrolysis at High Heating Rates

Anabel DEL VAL BENITEZ 171
Towards a Systematic Framework for the Design of Experiments: Application to Catalytic Phenomena in Plasma Wind Tunnels

Bruno Ricardo DIAS BARROS.....185
Ablation Modelling for the Simulation of the Atmospheric Entry of Meteors

Andrea FAGNANI (First year PhD student).....195
Comprehensive Characterization of the Aerothermomechanical Response of Space Debris to Atmospheric Entry Plasmas

David HENNEAUX (First year PhD student) 197
Development of High-Fidelity Numerical Methods for the Simulation of the Aerothermal Ablation of Space Debris during Atmospheric Entry

Francisco TORRES HERRADOR.....199
Pyrolysis Modeling for Aerospace Applications

Ray VANDENHOECK 207
Massively Parallel and Robust High-Order Methods for Transitional Hypersonic Flow Modelling on Unstructured Grids

Ludovico ZANUS.....221
Nonlinear Parabolized Stability Analysis of Chemically Reacting Boundary-Layers

AEROTHERMODYNAMICS

Florian DAVIN 235
Laminar to Turbulent Transition Prediction in Hypersonic Flows with Neural Networks Committee

Zdeňek ILICH.....245
Review of the VKI Longshot Hypersonic Tunnel Operation for Martian Entries

Iván PADILLA MONTERO.....263
Analysis of the Stability of a Flat Plate High-speed Boundary Layer with Discrete Roughness

RAREFIED AND PLASMA FLOWS

Federico BARISELLI.....279
Elastic and Ionisation Cross Sections for DSMC Simulations of Metallic Vapours in Meteor Hyperthermal Environments

Firas BEN AMEUR (First year PhD student).....289
Development of High-Order Adaptive Algorithms for Simulating Magnetic Reconnection Processes with Uncertainty Quantification

Stefano BOCCELLI.....291
Modeling of Rarefied and Ionized Flows for Electric Space Propulsion

Simon DEMANGE.....299
Absolute Instability in Plasma Jet

Vincent Fitzgerald GIANGASPERO (First year PhD student).....309
Modeling Strategy for Blackout Analysis of Re-Entry Phases in Space Exploration Missions

Quentin WARGNIER.....311
Transport Properties in Multicomponent Two-Temperature Magnetized Plasmas: Application to the Sun Atmosphere

TURBINE & COMPRESSOR AERODYNAMICS & HEAT TRANSFER

Cédric BABIN (First year PhD student).....327
Impact of Shrouded Stator Cavity Flow on Axial Compressor Performances

Elissavet BOUFIDI.....329
An Uncertainty Estimation Method for Turbulence Statistics

Matteo BURIGANA (First year PhD student).....343
Turbine Endwall Contouring and Blade Tip Optimization with Experimental Validation at Engine-Like Conditions

Tânia Sofia CAÇÃO FERREIRA.....345
On the Influence of High Turbulence on the Convective Heat Flux on the High-Pressure Turbine Vane LS89

Bogdan Cezar CERNAT.....357
Near-Tip Heat Transfer Mechanisms in an Unshrouded Turbine Equipped with Advanced Blade Tip Geometries

SHAPE OPTIMIZATION

Tom DE BRUYN (First year PhD student).....375
Aero-Elastic Tailoring of Composite Turbomachinery Blades through Gradient-Based Optimization

Arnaud CHÂTEL 377
Multipoint Optimization of an Axial Turbine Cascade using a Hybrid Algorithm

Maria FARUOLI 391
A Topological Adjoint Method for the Optimization of Stirling Engine Regenerators

Giacomo ALESSI 401
Trained RANS by Means of an Adjoint Method403

Alberto RACCA 407
Turbocharger Design and Optimization by Adjoint Method Coupled with CHT Analysis

LIQUID METAL AND INDUSTRIAL FLOWS

Numerical Investigation of the Effect of Buoyancy Forces on the Deflagration of Hydrogen in the Thai Facility

Andrea Attavino

Environmental and Applied Fluid Dynamics Department, von Karman Institute for Fluid Dynamics, Belgium, andrea.attavino@vki.ac.be

Supervisor: Philippe Planquart and Jean-Marie Buchlin

Research Manager, Environmental and Applied Fluid Dynamics Department, von Karman Institute for Fluid Dynamics, Belgium, philippe.planquart@vki.ac.be

Full Professor, Environmental and Applied Fluid Dynamics Department, von Karman Institute for Fluid Dynamics, Belgium, buchlin@vki.ac.be

University Supervisor: Alessandro Parente

Associate Professor, Aero-Thermo-Mechanics Department, Université Libre de Bruxelles, Belgium, alessandro.parente@ulb.ac.be

Abstract

Accumulation of hydrogen in the building of a nuclear reactor, during a severe accident, can lead to a deflagration event, resulting in high dynamic pressure loads which could threaten the containment structures and the operability of technical equipment. Hydrogen is usually released in the building alongside a large amount of steam. The presence of steam, which acts as a diluent, and the absence of a strong initial flow field in the building, makes deflagration event relatively slow. In this case the propagation of the flame front is mostly controlled by the self-wrinkling of the flame and by buoyancy forces. For this work, CFD computations of hydrogen deflagration in a closed compartment have been performed, with the aim of studying the effect of buoyancy forces on the flame front propagation. The cases considered are the experiments HD-22 and HD-23 performed in the THAI facility in the framework of the OECD/NEA THAI project [1]. In the experiments the facility has been filled with a mixture of air, hydrogen and steam. The igniter is located either in upper or lower area of the facility, resulting in a different direction of the flame propagation in the two tests. The numerical calculations have been performed using the open source software OpenFOAM. The flame front propagation has been described using the model developed by Weller derived by means of a conditional averaging technique on the transport equations [2]. Different turbulence models have been tested and the effect of turbulence production/destruction by the buoyancy force has been studied. Comparison between the computed temperature and pressure evolution with experimental results will be presented.

Keywords: Hydrogen combustion, Hydrogen deflagration, Computational fluid dynamics, Severe accidents

1. Introduction

During a severe nuclear accident, a large amount of hydrogen can be produced in the core of a light water nuclear reactor. To decrease the pressure in the reactor core, the produced hydrogen has to be released in the atmosphere of the containment building, alongside a large amount of steam. As the released gases accumulates in the building, the concentration of hydrogen may exceed the flammability limit. The presence of a combustible mixture in the building represents a serious threat to the integrity of the containment. For this reason, hydrogen mitigation systems must be installed, and the building should be designed to be able to withstand a deflagration event.

The most important parameters that must be considered for preventing the breaching of the containment are the thermal and pressure loads caused by the combustion. These parameters are strongly dependent on

the concentration profile of hydrogen and steam in the building, the geometry and the materials of the wall, in case the heat transfer is not negligible. Moreover, the presence of a flow field and turbulence in the building, due to a ventilation system or natural convection, can influence the combustion process, leading to flame acceleration and, in the worst case, transition of the deflagration to the detonation regime, with a consequent increase in the over pressure achieved.

The estimation of the thermal and pressure loads requires knowledge of the thermochemical properties of the combustible mixture that forms in the containment building. Those parameters can be divided in two categories, the equilibrium parameters, which depends only on the energetics of the mixture, and nonequilibrium parameters, which depends on the chemical kinetics and transport rates [3]. As described by Sherman [4], the first category of parameters can be used to estimate the result of a deflagration that happens in simple configurations, such the combustion of a premixed gas in single compartments with negligible heat transfer. Among those parameters the most relevant ones are the flammability limits and the Adiabatic Isochoric Complete Combustion Pressure. The flammability limits are defined as the critical composition of the fuel-air-inert diluent mixture beyond which the mixture cannot sustain steady flame propagation. This parameter depends on the initial thermophysical state of the mixture [5], as well as the direction of the flame propagation due to buoyancy effects [6]. This parameter can be computed to high accuracy using data from thermodynamic tables [7].

However, in many practical cases it is not possible to use the aforementioned assumptions. When the concentration of hydrogen is close to the flammability limit, the deflagration process is particularly slow, the convective and radiative heat transfer to the structures becomes relevant, and the combustion process is strongly influenced by buoyancy forces and turbulence. The description of the combustion phenomenon becomes more complex and simple correlations cannot predict accurately the magnitude of the thermal and pressure loads. For this reason, Computational Fluid Dynamics and Lumped Parameters codes can be of great aid in the hydrogen analysis of the containments and safety systems of nuclear reactors. However, due to the small dimension of the reacting layer of a propagating flame even CFD codes are not capable of fully describe the combustion event. Many features of the flame, such as the wrinkling due to turbulence and hydrodynamic instabilities, particularly important for lean hydrogen mixtures, have to be modelled. For that reason, extensive validation of CFD is a prerequisite, to improve the reliability of their results.

In this paper results of CFD simulations of hydrogen deflagration test, performed in the THAI test facility, will be shown. The aim of the work is to validate the models that have been implemented in the CFD code OpenFOAM and show how the propagating direction of the flame and the presence of steam in the combustible mixture affects the pressure peak of a deflagration event in a large scale facility.

2. Governing Equations

A complete description of the combustion phenomena is extremely computationally expensive because of the high amount of equations that have to be solved and the small dimension of the flame front, compared to the dimension of a large-scale facility. In order to reduce the computational cost of combustion simulations Weller et al. [8] developed a new model in which the laminar-flamelet approach is used with conditional averaging to create a set of equations that can be used to describe the complex combustion phenomenon.

The governing equations are conditionally averaged by multiplying by an indicator function I, which is 0 in the burnt zone and 1 in the unburned one, and by applying conventional averaging technique, density weighted or otherwise. The form of the averaged continuity and momentum transport equations are the same as the canonical Favre averaged equations. They are then coupled with the energy transport equation for the burned and unburned mixture. The last equation to be solved is the transport of the density weighted regress variable $\tilde{b}$, defined as:

$$\tilde{b} = \frac{\tilde{f} - f_b}{f_u - f_b}. \tag{1}$$

Where $\tilde{f}$ is the density weighted fuel mass fraction and the subscripts u and b denote respectively the unburned and burned mixture. Following this approach, a generic property of the fluid ϕ can be expressed as:

$$\phi = \tilde{b}\phi_u + \left(1 - \tilde{b}\right)\phi_b. \tag{2}$$

The transport equation for $\tilde{b}$ yields:

$$\frac{\delta\bar{\rho}\tilde{b}}{\delta t} + \nabla\left(\bar{\rho}\tilde{\mathbf{U}}\tilde{b}\right) - \nabla\left(\rho\mathcal{D}\nabla\tilde{b}\right) = -\bar{\rho}_u S_l \Xi \left|\nabla\tilde{b}\right|. \tag{3}$$

Where $\bar{\rho}$ is the averaged density, $\tilde{\mathbf{U}}$ the density average velocity, $\mathcal{D}$ the turbulent diffusion coefficient,

$\bar{\rho}_u$ the averaged unburnt density, S_l the laminar flame speed and Ξ the flame wrinkling factor. The term on the right-hand side of the equation represent the evolution of the flame due to the chemical reactions, and it includes all the parameters that affects the combustion process. The laminar flame S_l speed is computed using a correlation derived by Bentaib et al. [9]:

$$S_l(\phi, \psi, T, p) = \alpha(\phi) \cdot \beta(\psi) \cdot \left(\frac{T}{T_{ref}}\right)^{2.2} \cdot \left(\frac{p}{p_{ref}}\right)^{-0.5}. \quad (4)$$

$$\alpha(\phi) = 1.44\phi^2 + 1.7\phi - 0.29.$$

$$\beta(\phi) = (1 - \psi)^4.$$

Where ϕ is the equivalence ratio of the hydrogen-air mixture, ψ the molar fraction of the diluent, T_u the temperature of the unburned gas, p the pressure, $p_{ref} = 10^5\ Pa$ and $T_{ref} = 298\ K$.
The flame wrinkling Ξ function, appearing in the r.h.s. of equation (3) represents the ratio between the average flame area per unit of volume in the cell, over the average flame area projected onto the mean propagation direction in the cell. To compute this function Weller proposes to solve a transport equation, where the terms representing the generation and removal of surface area are only linked to the turbulent quantities of the flow. However, in the case considered in this study there is absence of flow and turbulence at the beginning of the test, and the flame propagation is mostly controlled by self-wrinkling. For this reason, we used a model proposed by Molkov [10], which uses a modified version of the Yakhot equation [11] yelding:

$$\Xi = \Xi_K \cdot \Xi_f \cdot \Xi_{lp} \cdot \Xi_t. \quad (5)$$

The four terms on the r.h.s. of equation (6) are representative of the different mechanism whereby flame surface area is generated. Ξ_K is the wrinkling factor due to the turbulence generated by the flame front itself. This parameter increases gradually with the distance the flame has travelled from its ignition point, to mimic the transition from the laminar regime to the fully developed turbulent flame:

$$\Xi_K = 1 + (1 - \Xi_K^{MAX})\left(1 - exp\left(-\frac{R}{R_0}\right)\right). \quad (6)$$

Where R is the distance from the ignition ignition point, R_0 a reference distance set equal to 1 m and Ξ_K^{MAX} the maximum value of the self-wrinkling which can be calculated as [12]:

$$\Xi_K^{MAX} = \frac{E_i - 1}{\sqrt{3}}. \quad (7)$$

Where E_i is the expansion coefficient of the combustion products.

Ξ_f is the wrinkling factor due to the fractal evolution of the flame front, it is assumed that this term has an effect only after transition to the turbulent self similar regime:

$$\Xi_f = \begin{cases} 1 & \text{if } R < R_0 \\ \left(\frac{R}{R_0}\right)^{D-2} & \text{if } R \geq R_0 \end{cases}. \quad (8)$$

The value of the fractal dimension D has been set equal to 7/3 in agreement with experimental evidence [13].

Ξ_{lp} is the enhancement of turbulent burning velocity due to the leading point mechanism, which is linked to the negative Markstein length of lean hydrogen flames. The high diffusivity of hydrogen increase the flame speed in the cusps that are formed due to instabilities effect, leading in an increase in area of the flame wrinkles. It is assumed that the leading point coefficient increases linearly with the distance R until it reaches its maximum value $\Xi_{lp}^{MAX} = 2.4$:

$$\Xi_{lp} = \begin{cases} 1 + (1 - \Xi_{lp}^{MAX})\left(\frac{R}{R_0}\right) & \text{if } R < R_0 \\ \Xi_{lp}^{MAX} & \text{if } R \geq R_0 \end{cases}. \quad (9)$$

The last term Ξ_t is the flame wrinkling generated due to the turbulence in the flow. Since there is no initial flow field this and the turbulence fluctuation u' is really small, a simple algebraic relation has been used:

$$\Xi_t = 1 + 0.62\left(\frac{u'}{S_l}\right). \quad (10)$$

The model has been implemented in the opensource CFD platform OpenFOAM.

3. The THAI test facility and experiments

The model has been tested against experiments of hydrogen deflagration in the test facility THAI (Thermal hydraulics, Hydrogen, Aerosols, and Iodine), which is a containment test facility located at Eschborn, Germany. As shown in Fig. 1, the main component of the facility is a 60 m^3 stainless steel vessel,

9.2 m high, and 3.2 m in diameter, and the outer wall is insulated by a 120-mm rock-wool layer. The container is equipped with three independent oil jackets to control the wall temperature during the tests and to precondition the atmosphere inside the facility.

Thanks to its modular structure and the presence of appropriate feeding/generation devices for different gases, experimental configuration and operating conditions typical of those for PWR or BWR can be produced in the THAI vessel.

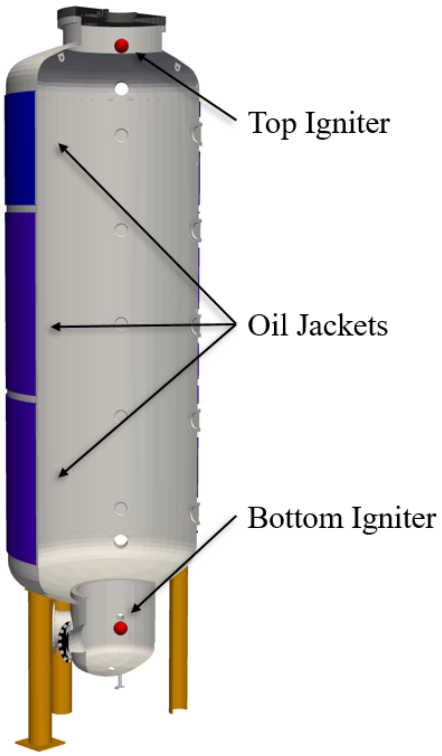

Figure 1: Schematic of the THAI test facility.

In the framework of the OECD-NEA THAI-1 project [14], a series of tests has been performed to investigate the deflagration of hydrogen-air-steam mixture, under the conditions that can be found in a containment of a nuclear reactor during a severe accident. Among those tests, four of them have been selected to be simulated in this study.

In the first two tests, HD-15 and HD-16, the facility has been filled with a mixture composed of only hydrogen and air. The pressure and temperature in the facilities, prior to ignition, has been set respectively to 1.5 bar and 90 . A recirculation fan has been used to homogenize the atmosphere inside the facility. In the HD-15 test the deflagration is started by the igniter positioned in the bottom part of the vessel, while in the HD-16 test the top igniter has been used. The tests HD-22 and HD-23, are analogous to the previous one except that the mixture has been diluted with steam. A summary of the test conditions is shown in Table 1.

Table 1: Summary of the computational grids used in the CFD simulations

Test	Vol. H_2	Direction	Vol. H_2O
HD-15	10	$\uparrow\uparrow$	0
HD-16	12	$\downarrow\downarrow$	0
HD-22	10	$\uparrow\uparrow$	25
HD-23	12	$\downarrow\downarrow$	25

During the tests 43 fast sheathed thermocouples were installed at 13 different elevations to monitor the flame front propagation and the temperature during the combustion, while 4 fast pressure transducers (strain gauge type) were used to monitor the transient deflagration pressure.

4. Simulations Setup

The combustion models are implemented in the solver XiFoam, which has been modified to take into account the effect of flame self-acceleration, not considered in the original model. Three unstructured axisymmetric meshes have been generated using the meshing utility snappyHexMesh. The computational grids have a uniform cell size in the whole domain, with an exception for the wall and the area around the igniter, where the mesh is finer, as shown in Fig. 2.

The reactants and products composition have been set according to the specification of each test, and completeness of the combustion process has been assumed. The initial temperature and pressure have been set equal to 90 $^{\circ}C$ and 1.5 bar for all the tests. The atmosphere has been considered at rest. The system of averaged equations is closed with the k-SST turbulence model, the initial value of the turbulent fluctuation u' has been set equal to 10^{-2} m/s and the dissipation rate has been set in order to obtain a value of the turbulent viscosity lower than the molecular one, as suggested in the test report [15]. All the variable have been discretized using a second order upwind scheme, while the turbulent kinetic energy k and the dissipation rate ω have been discretized with a first order upwind scheme. Concerning the temporal discretization, the first order Euler scheme have

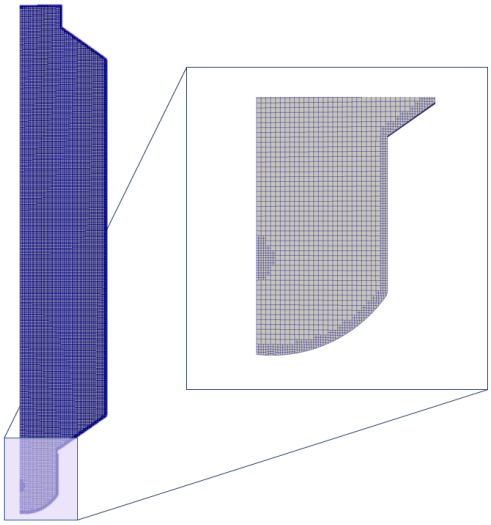

Figure 2: Mesh of the THAI facility for the simulation of the test HD-15.

been used. Radiation has been considered in the solution of the energy equation. The emissivity of the gas has been computed using the weighted sum of gray gases model [15], while the radiative transport has been modelled using the P1 radiation model.

The boundary of the domain is composed of a single wall. A no slip boundary condition has been applied to the velocity field, while wall functions have been used for the turbulence equations. The wall, of the THAI facility is made of a 22 *mm* tick steel structure. Compared to the energy released during the combustion the thermal inertia of the structure is relatively high. If the heat released during the deflagration would be evenly distributed over the whole metal structure, its temperature would increase of only 3 *K* degrees. For this reason, the boundary condition for the energy equation has been set to a constant value, equal to the initial one. This assumption leads to an error in the later stages of the simulation, when the inner part of the metal structure starts to heat up and the convective and radiative heat transfer to the walls should reduce.

5. Results

The ignition in the simulation has been started at time $t = 0$ *s*, however, it is described in the experimental report that the ignition of the mixture does not happen at the exact time of the igniter activation. For this reason, all the results shown in this section have been shifted in order to match the beginning of the calculations with the ignition time of the experiments. Moreover, the igniter, which operates at a frequency of 1 *Hz*, is kept active for several seconds during the tests. In the simulation the ignition is modelled as a sink term in the regress variable equation, in agreement with the experiment description, and this sink was kept active during the first 2 seconds of simulation.

Table 2: Cases used for testing the performance of the combustion model.

Test	N Cells	Cell Size [*cm*]	CPUh
Mesh 1	1598	10	80
Mesh 2	6113	5	178
Mesh 2	22479	1.5	732

5.1. HD-15 Test

For the test HD-15 three simulations have been performed using the three different grids, characterized by a different cell size. The pressure transients obtained in the different simulations are shown in Figure 3 and they are compared with the experimental results.

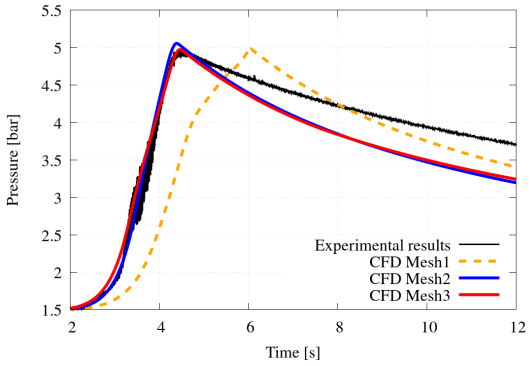

Figure 3: Comparison between the results obtained with numerical computations on the three different grids and the experimental results of the test HD-15.

The dashed orange line represents the pressure computed using the coarsest mesh. The other two simulations, performed with the more refined grids, yields similar results, however, the pressure peak computed with the intermediate mesh is slightly overestimated. The small difference between the second and third simulation is a consequence of the small influence that the flow field has on the flame propagation. The absence of an initial flow field makes the turbulence

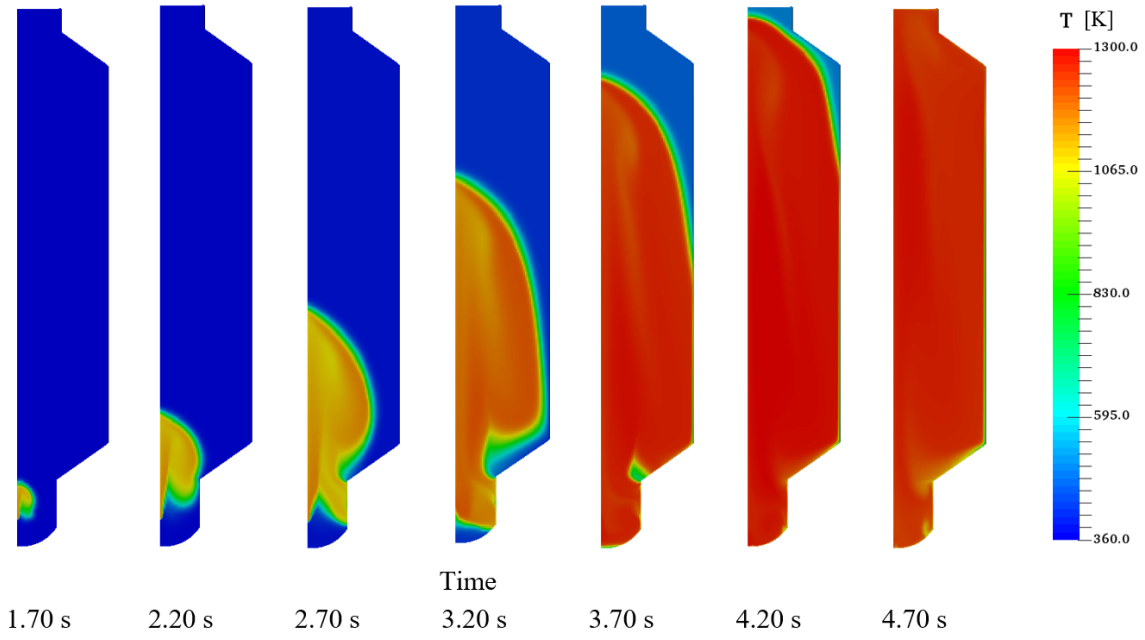

Figure 4: Temporal evolution of the temperature profile during the test HD-15.

level at the beginning of the test really small and then the combustion process is mostly controlled by the self acceleration mechanisms described in equations (6)-(9), which depend only on the distance from the ignition point and the gradient of the regress variable itself, as shown in equation (3). The only effect due to the flow is the presence of the buoyancy force which enhances the flame speed by pushing upward the burned gases, like a bubble of light gas surrounded by a heavier medium.

The first mesh however was too coarse, and the numerical error on the gradient of the regress variable becomes too high when the flame travels outside of the more refined ignition area. It was not possible then, to capture the correct evolution of the flame front during the deflagration.

All the simulations have been running on a 16 core AMD Ryzen processor. As it can be seen in Table 2 the computational time is relatively small for the first 2 simulations, while it drastically rises for the last simulation. The calculations for the other tests have been performed using the intermediate grid, due to the short computational time required and the small difference with the results obtained with the finer mesh.

Figure 4 shows the evolution of the temperature field during the simulation of the test. In the initial time steps the flames assumes the shape of a mushroom cloud, after a short time the flame evolves into an elongated shape. For most of the combustion time the hot gases are not in contact with the cold walls of the facility.

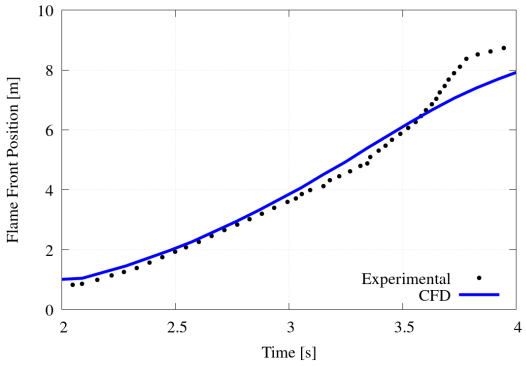

Figure 5: Comparison between the measured position of the flame front and the simulated one for the test HD-15.

This effect, combined with the relatively short combustion time results in a correct prediction of the peak pressure, even though the temperature of the wall is kept constant in the simulation and therefore the heat transfer is overestimated in the second part of the simulation. The temperature signal recorded by the thermocouples has been used to calculate the position of the flame front in the center line of the facility. Fig-

ure 5 shows the comparison between the experimental curve represented by the black dots and the computed one represented by the blue curve. The curves agree well except in the very last half second. This difference is due to a distortion of the flame near the top flange of the facility which is not observed in the numerical calculations that have been performed using an axisymmetric domain. Overall the numerical and experimental results agree well, proving that the flame wrinkling model shown in section 2 is well suited to compute a deflagration process that happens in a single compartment.

5.2. HD-16 Test

Differently from the previous test, the flame in the experiment HD-16 propagates in the downward direction. In this case the buoyancy force is directed in the opposite direction than the flame propagation. When the mixture is ignited, the initial flame bubble is pushed upward against the ceiling of the facility. It then starts propagation downward, assuming a flat shape as can be seen in Figure 6. During most of the test the hot burned gases are in contact with the cold wall. For this reason, the peak pressure is underestimated as shown in Figure 7a, while the flame propagates at the correct speed, compared to the measurements, shown in Figure 7b. The peak pressure and temperatures are overall higher than the one observed during the test HD-15, this is due to the higher concentration of hydrogen in the mixture. In this case the wrinkling model is again capable of predicting the correct propagation of the flame, the flame speed and time at which the combustion is ended is well predicted. The error on the pressure peak computed shows the importance of applying a correct boundary condition for the temperature, not yet implemented in the current version of the solver.

5.3. HD-22 HD-23 Tests

In the tests HD-22 and HD-23 steam was added to the initial mixture. The steam concentration has been kept equal to 25% and for the whole duration of the test the partial pressure of the steam is lower than the saturation pressure.

The presence of steam raises the concentration of diluents in the mixture, which was previously only composed of Nitrogen, but since the hydrogen concentration is kept constant the overall equivalence ratio of the combustible mixture increases, resulting in a value of the flame speed computed trough equation (4) which is around 40% lower than the values computed for the previous tests. As a result, the combustion process is slower than the tests conducted without steam, as it is shown in Figure 8 (c)-(d). In the case of the flame propagating in the upward direction this slowing effect is damped by the buoyancy force acting on the raising flame bubble. For this reason, and because of the elongated shape of upward propagating flames, the pressure peaks of tests HD-15 and HD-22 are comparable, while the highest pressure measured and computed for the test HD-23 is considerably lower than the one of the HD-16 test, as it is shown in figure 8 (a)-(b). In the latest case the hot gases transfer energy to the walls for a considerably longer time during the combustion event. On the other side, the heat transfer during the second part of the test, after the combustion has ended, is lower due to the lower temperature of the burned gases. In these cases, a larger discrepancy is observed between the pressure evolution and the tracked flame front position. A possible reason could be that the parameters used, such as the fractal dimension in equation (8) and the wrinkling of the flame due to the leading point in equation (9), are not suited for simulations of mixture with high fractions of steam as a diluent.

6. Conclusion and Future Work

It has been shown that the model implemented in OpenFOAM, is capable of describing the deflagration of a hydrogen-air mixture. The pressure transient and the position of the flame front agrees well with the experimental results. A large discrepancy in the results occur after the end of the deflagration due to the boundary condition for the temperature, which have been set uniform and equal to the initial value for all the duration of the simulation. In the future a 1D conjugate heat transfer model will be added to the solver, to resolve properly the heat transfer to the metal structure of the THAI vessel.
When steam is added to the mixture however a large difference in the results of the numerical calculations and the experimental one can be observed. Additional work is necessary to adapt the models to the presence of a diluent.

Acknowledgments

We thank BelV for sponsoring this work, and the OECD-NEA for providing the experimental database.

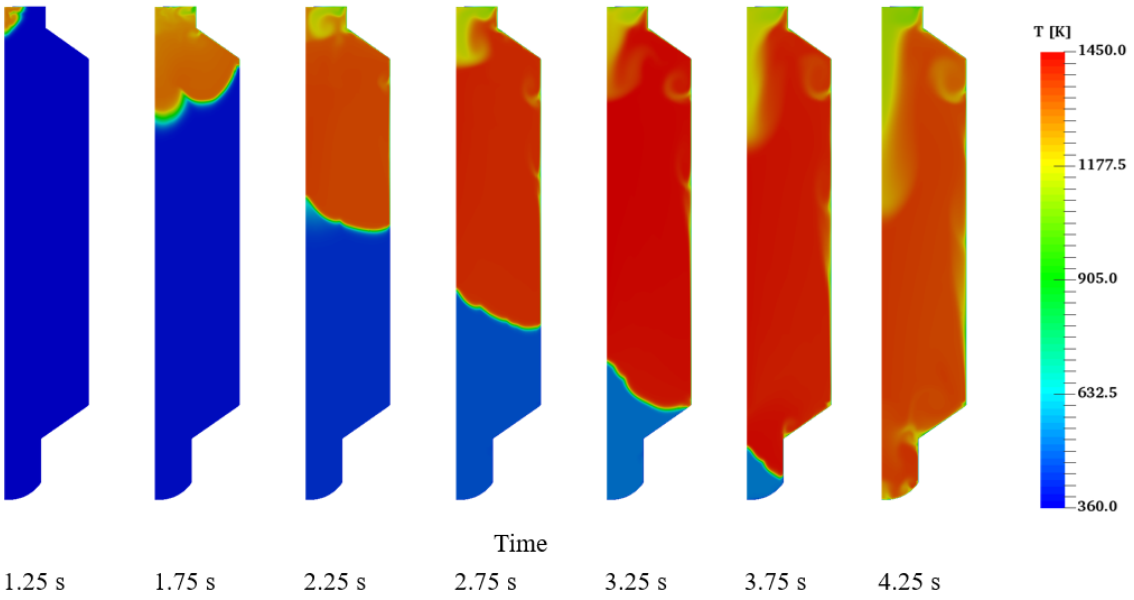

Figure 6: Temporal evolution of the temperature profile during the test HD-16.

References

[1] S. Gupta, Experimental investigations relevant for Hydrogen and Fission Product issues raised by the Fukushima accident, Nuclear Engineering and Technology 47 (2015) 11–25.

[2] H. Weller, The development of a New Flame Area Combustion Model Using Conditional Averaging, Pr, Department of Mechanical Engineering, Imperial College of Science Technology and Medicine March (1993).

[3] J.H.S. Lee, M. Berman, Hydrogen Combustion and Its Application to Nuclear reactor Safety , Advances in Heat Transfer 29 (1997) 59–127.

[4] M.P. Sherman, Hydrogen Combustion in Nuclear Power Plant Accidents and Associated Containment Loads, Nuclear Engineering and Design 82 (1984) 13–24.

[5] H. F. Coward, G. W. Jones, Limits of Flammability of Gases and Vapors, Tech. rep., United States printing Office (1952).

[6] D.W. Stamps, M. Berman, High-Temperature Hydrogen Combustion in Reactor Safety Applications, Nuclear Science and Engineering 109 (1991) 39–48.

[7] D. R. Stull, H. Prophet, JANAF Thermochemical Tables (second edition), Tech. rep., United States printing Office (1952).

[8] H.G. Weller, G. Tabor, A.D. Gosman, C. Fureby, Application of a flame-wrinkling les combustion model to a turbulent mixing layer, Symposium (International) on Combustion 27 (1998) 899–907.

[9] A., Bentaib, A. Bleyer, N. Meynet, N. Chaumeix, B. Schramm, M. Hhne, P. Kostka, M. Movahed, S. Worapittayaporn, T. Brhler, H. Seok-Kang, M. Povilaitis, I. Kljenak, P. Sathiah, SARNET hydrogen deflagration benchmarks: Main outcomes and conclusions, Annals of Nuclear Energy 74 (2014) 143–152.

[10] V. Molkov, Fundamentals of Hydrogen Safety Engineering II, www.bookboon.com, 2012.

[11] V. Yakhot, Propagation Velocity of Turbulent Premixed Flames, Combustion Science and Technology 60 (1988) 191–214.

[12] B. Karlovits, D.W. Denniston, F.E. Wells, Investigation of turbulent flames, Journal of Chemical Physics 19 (1951) 541–547.

[13] H. Kobayashi, H. Kawazoe, Flame instability effects on the smallest wrinkling scale and burning velocity of high-pressure turbulent premixed flames, Proceedings of the Combustion Institute 28 (2000) 375–382.

[14] OECD/NEA THAI Project Final Report - Hydrogen and Fission Product issues relevant for containment safety assessment under severe accident conditions, Tech. rep., NEA/CSNI/R (2007).

[15] T.F. Smith, Z.F. Shen, Evaluation of Coefficients for the Weighted Sum of Gray Gases Model, Journal of Heat Transfer 104.

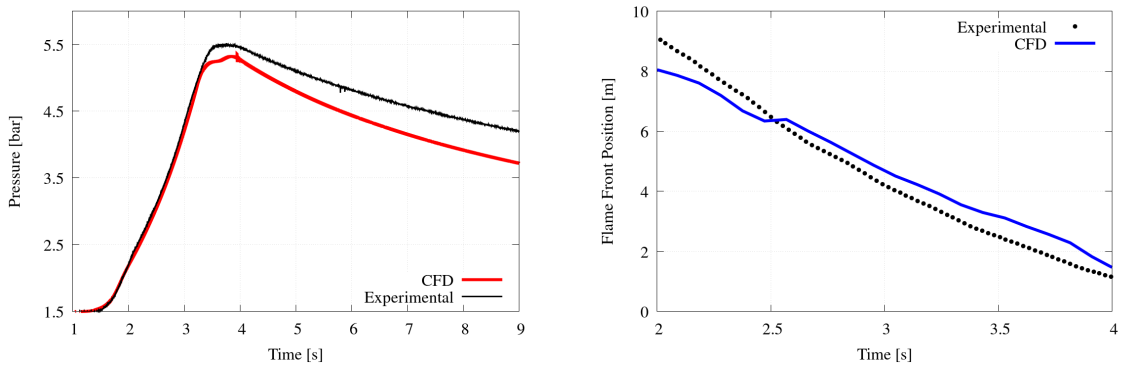

(a) (b)

Figure 7: Pressure history of test HD-16 (a) and position of the flame front on the center line of the THAI facility during the test HD-16 (b).

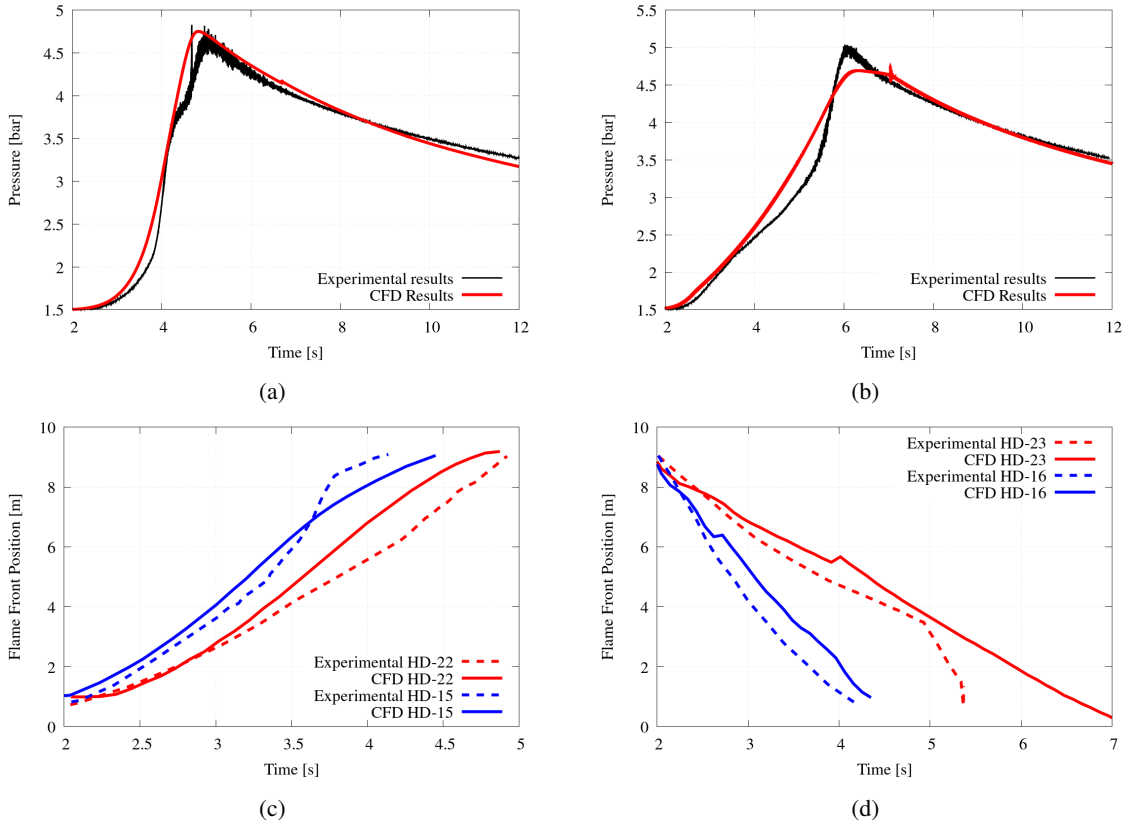

(a) (b)

(c) (d)

Figure 8: . Pressure history of tests HD-22 (a) and HD-23 (b). Comparison between the flame front position during the tests performed without steam (blue lines) and the one containing steam in the mixture (red lines), for upward (c) and downward (d) propagating flames.

Analytical and Experimental Investigation of Icing Phenomena on Wind Turbine Blades

Adriana Enache

Environmental and Applied Fluid Dynamics Department, von Karman Institute for Fluid Dynamics, Belgium, adriana.enache@vki.ac.be

Supervisor: Jeroen van Beeck

Dean of the Faculty, Professor and Head of Department, Environmental and Applied Fluid Dynamics Department, von Karman Institute for Fluid Dynamics, Belgium, vanbeeck@vki.ac.be

University Supervisor: Gérard Degrez

Professor, Aero-Thermo-Mechanics (Fluid Mechanics), Université Libre de Bruxelles, Belgium, Gerard.Degrez@ulb.ac.be

Abstract

The existing electro-thermal de-icing systems (ETIPS) used for aviation need adaptation to wind engineering applications to eliminate the wind turbine icing risks. To answer the demand, this research proposes the development of an analytical tool, by studying ETIPS's main limitations. In this paper, the ice shedding phenomenon is investigated using numerical and experimental means. A one-dimensional phase change model is developed and used to simulate the de-icing system. Moreover, an experimental campaign conducted in the VKI Icing wind tunnel (CWT-1) shows several ice detachment mechanisms. Coupled numerical and experimental results are used to determine the most important ice shedding parameters.

Keywords: de-icing, ice shedding, icing wind tunnel, phase change modeling, heat transfer, wind turbines

1. Introduction

In cold climate regions, the wind energy production is annually decreased up to 25% by operating the wind turbines in icing conditions [1]. For a wide range of low temperatures, the super-cooled water droplets present in atmosphere freeze at their impact with the turbine blades. Different ice accretion regimes form [2] and degrade the aerodynamic blade properties, increasing the energy losses [3] [4]. Moreover, in some cases the production stops because the turbine icing generates unbalanced forces acting on the rotor and important safety hazards due to ice shedding [5] [6].

Ice mitigation systems designed for aeronautic applications by Sonaca could be used to reduce these negative effects, although they imply high additional costs and decrease the wind turbine capacity. The use of these techniques is limited for wind energy production applications by the occurrence of ice shedding and run-back ice phenomena, both imposing safety and efficiency issues.

This research project proposes the development of an analytical tool to optimize an electro-thermal de-icing systems [7] for wind turbine applications. Analytical models are elaborated and validated based on experimental campaigns developed in the VKI's icing wind tunnel. The studied physical phenomena are triggered by the activation of a de-icing system, where the applied heating produces a phase change at blade's surface [8]. The water layer evolution decreases ice adhesion and under the dynamical forces produced by wind's action two phenomena are possible: the ice slides and refreezes downstream of the heated area, resulting in run-back ice phenomenon, or it detaches from the substrate, leading to ice shedding.

Considering these physical mechanisms, the analytical tool developed for this study is divided into a thermal part, which addresses the phase change, and a dynamical part which predicts the ice sliding or detachment. Using these two modules, the code is designed to determine the run-back ice sliding distance and the minimum heating power needed to be applied

for a safe ice shedding.

The present paper focuses on the physical mechanism of the ice shedding phenomenon, which imposes multiple engineering problems for several industries. The study is conducted using both experimental and numerical methods, the final aim being the development of a shedding model.

The ice shedding phenomenon's effects and the studied de-icing systems are shortly described in Section 2. A brief introduction on the mathematical problem of melting, together with different modeling approaches are presented in Section 3. The developed numerical model is detailed in Section 4 and in Section 7 the solver is used to compute the water layer thickness for the ice shedding experiments presented in Section 5. Experimental results and observations over the ice shedding mechanism are reported in Section 6. Section 8 concludes the presented work and summarizes the on-going activities, proposing further research steps.

2. Ice shedding literature survey

The ice shedding impacts multiple fields as aviation, electrical power transmission and wind energy production.

For aviation, the detached ice pieces are dangerous due to the important damage they cause downstream on the airplane's structure [9]. As an example, ice shed into propeller's blades provokes engine mechanical failure [10]. This is one reason why the allowed ice dimensions are strictly controlled.

In the case of power transmission lines, the ice shedding represents a safety hazard for nearby inhabitants [11] [12]. The ice removal under the wind's action generates dynamic effects in the physical network, changing the phase-to-phase and phase-to-tower spacing, generating flash-overs. The increased dynamical loads could generate cascading towers failure, the power transmission being stopped [13].

The ice shedding has a big impact on the on-shore wind energy production. It generates safety hazards for the nearby inhabitants [14], [6], transportation and neighboring constructions due to big chunks of ice thrown at large distances (ice throw distance being proportional with structure's height)[15]. Ice throw and risk assessment models [16], [17] are intensively developed for the wind energy industry, but in several countries legislation prohibits the production during icing events [1], which provokes important power losses.

Moreover, the ice shedding phenomenon is one of the most important drawbacks of the increasingly used electro-thermal de-icing systems first presented in [7]. Depicted in Fig.1, the technique is based on a series of resistive elements activated in a cyclic manner which are used to detach and remove the ice from wing's profile. It has a good ice-removal efficiency, being suited for heavy icing events and uses less energy than its anti-icing version [18].

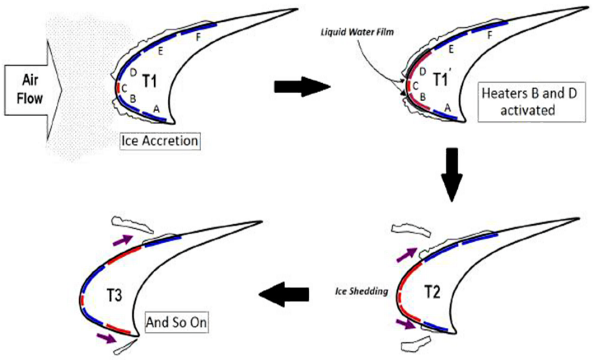

Figure 1: Schematic of a electro-thermal ice protection system - de-icing cycle [8]

These systems are already used in the aeronautical field but they need adaptation for wind energy applications due to different flow conditions and shedding safety regulations.

Previous numerical works on electro-thermal de-icing systems used for aeronautical applications have studied the generated ice shedding mechanism [19], [20], [8]. Thermal and mechanical models developed in [8] investigate the ice cracking mechanism and show the importance of phase change at the blade-ice interface. Moreover, a shedding criterion is defined as the percentage of wetted area over the total ice-blade contact area.

3. Phase change modeling

An initial step towards modeling the ice shedding is the development of a transient phase change model. Melting or solidification of a material, is known in literature as the Stefan problem [21].

The Stefan problem is a specific case of boundary value problem for partial differential equations, in which one of the boundaries is moving due to the phase change evolution. As shown in Fig.2, one has to solve two heat equations, one for liquid and one for

the solid phase. A third equation given by an energy balance at the interface is solved to retrieve the phase boundaries. This equation relates the liquid front velocity with the material's latent heat of fusion.

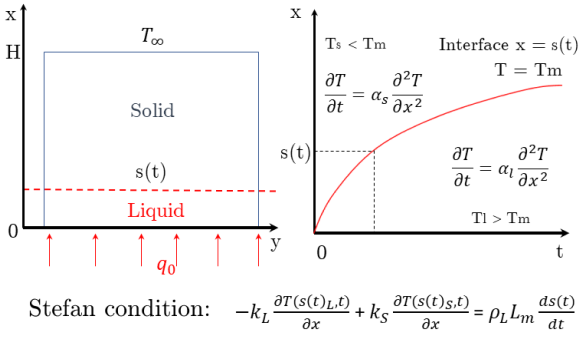

Figure 2: Description of melting phenomenon.

Figure 2 shows a detailed description of the melting phenomenon, where the left side schematic presents the evolution of liquid-solid interface position in time $s(t)$, as a heat flux q_0 is applied at bottom of the ice domain, which is surrounded by air at atmospheric temperature T_∞ below melting temperature T_m. In the right side, the mathematical formulation of melting in a de-icing system is presented. Two heat equations in the solid and liquid phases, signalized by the l, s subscripts, respectively, which use the thermal diffusivity, α, are completed by an energy balance at the interface (Stefan condition). The latter relates the melting front velocity, $\frac{ds(t)}{dt}$ to the latent heat of fusion, L_m and the heat transferred over the interface. Liquid phase density ρ_L and thermal conductivity of liquid and solid phases $k_{L,S}$, are considered.

3.1. Literature survey phase change modeling

The phase change phenomenon was intensively studied in literature during the years [22], [23], [24]. Analytical solutions exist for very simplified theoretical cases, limited to the use of pure phase change materials and one dimensional domains. A melting analytical solution presented in [21] is used as validation for the current numerical code.

Two main numerical approaches are used to study the phase change phenomenon for industrial applications: *front tracking* and *fixed grid methods*.

The first ones explicitly track the moving interface using the Stefan condition. They impose either a fixed spatial step Δx and adapt the time step Δt to capture always the interface position in a spatial node, or impose a fixed Δt and use different spatial steps for the two phases [24]. These methods are used for simplified Stefan problems and require increased computational resources.

The second ones, the fixed grid methods are suitable for more complex industrial problems. Also called *enthalpy methods*, they solve one equation for the entire phase change domain, including liquid and solid phases, avoiding an explicit interface tracking. The physical limits of each phase and the melted front position are automatically retrieved from the computed enthalpy values.

The fixed grid methods split in three major phase change models: a pure ethalpy model, a heat capacity method and a temperature-transforming model. Their main difference is the thermal treatment of the phase change. A pure enthalpy method assumes an isothermal phase change, which generates a strong enthalpy jump at the melting temperature. Under the assumption of a sharp liquid interface, the algorithm encounters difficulties tracking the melting front while it travels inside a spacial cell, generating the so-called interface 'staircase aspect' [22].

The equivalent heat capacity method assumes that the phase change material can absorb or release heat keeping its temperature constant at the melting point. This means its heat capacity at the melting temperature is infinite. The method assumes a non-isothermal phase change, which occurs in a temperature interval. For pure substances with a well-defined melting point, a very narrow interval should be defined. The method is simple to implement, but difficult to tune, being very sensitive to the selection of time step and phase change temperature interval, generating unphysical interface oscillations [23].

The temperature-transforming model [23] combines the advantages of both previous presented models. It assumes a non-isothermal phase change, defining a mushy region in which the solid and liquid phase co-exist. The enthalpy evolution in function of the phase change material can be observed in Fig. 3.

The enthalpy evolves linearly in the mushy region, the interface being captured without spurious non-physical oscillations.

A modified version of the temperature transforming model is used for the numerical study presented in this paper. The model is further detailed in the following section.

4. Modified temperature-transforming model

Based on the temperature-transforming model presented in [23], a one-dimensional phase change model

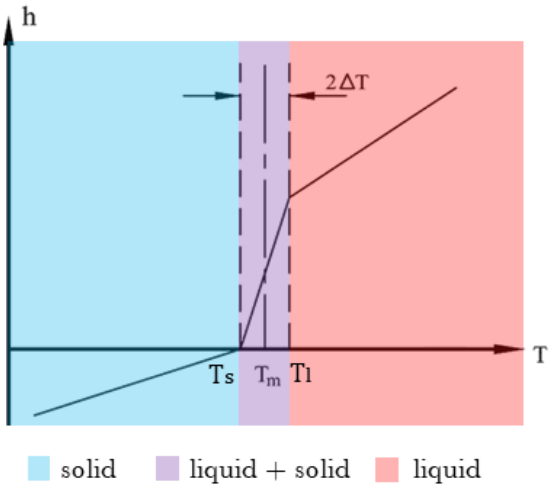

Figure 3: Mathematical formulation of melting in a de-icing system [23]

was developed in Matlab.

A finite difference implementation is used with a second order spatial discretization in space and an explicit time marching. The numerical scheme's stability is ensured adjusting the time step in function of a maxim CFL number of 0.5.

To retrieve the phase change evolution in time, an enthalpy formulation of the one-dimensional heat equation is used as presented in [23].

The model takes into account the specific and sensible heat variations with temperature and assumes a non-isothermal phase change, the melting taking place over a certain temperature interval. In this $2\Delta T$ interval, as shown in Fig.3, a mushy region is defined as a mixture of liquid-solid phases. Here, an average liquid-solid specific heat is defined and half of the latent heat of melting is considered to be absorbed. As water is a pure substance characterized by an isothermal phase change, a very narrow temperature interval of $\Delta T = 0.025°C$ was chosen to define the mushy area, as previously used in [25].

The solver computes enthalpy values using imposed temperature dependent boundary conditions (both Dirichlet and Neumann boundary conditions can be applied). For this reason, the enthalpy formulation was inverted to obtain temperature profile in length of the domain at every time step. Together with temperatures, all thermal properties are retrieved and used as initial condition for computing the next time steps.

The temperature-transforming model was modified by implementing a different thermal conductivity computation [26], using a linear interpolation of the thermal resistance inside the mushy region. To define the thermal resistances, a liquid fraction computation based on the difference between each node's temperature and the phase change thermal interval limits (T_s– solidus temperature, T_l - liquidus temperature in Fig.3) is used [27].

4.1. Model Validation

The modified temperature transforming phase change model was developed to observe numerically the water layer thickness evolution as it was difficult to determine it experimentally.

The interface is located, at every time step, where the nodal enthalpy corresponds to the enthalpy range of the mushy region.

The obtained results are compared with the analytical solution for the Stefan problem presented in [21]. Validation is obtained in terms of both temperature profile in the two phases and ice-water interface position in time.

The analytical test case studies the melting of a one-dimensional semi-infinite ice slit subjected at one of its limits to a constant temperature boundary condition and insulated at the other end (adiabatic). Initially the ice block is at a temperature below the melting point, with no liquid phase in the initial time step.

The solution assumes an isothermal phase change, the sharp liquid interface position being expressed by Eq. 1, where λ is solution of the transcendental equation presented in [21] and it is determined using a Newton iterative method.

$$S(t) = 2\lambda\sqrt{\alpha_l t} \tag{1}$$

The physical properties considered for each phase are presented in Table 1. The numerical parameters, initial and boundary conditions of the validation test case are presented in Table 2.

Table 1: Phase physical properties

Phase	K [W/mK]	c [J/kgK]	ρ [kg/m^3]
Ice	2.1	2060	1000
Water	0.6	4185	1000

To evaluate the numerical discretization influence over the solution, a grid independence study was performed. From Fig. 4 it can be observed that the increased spatial resolution doesn't influences much the

Table 2: Conditions and numerical parameters

Initial Conditions	Boundary Conditions	Numerical Parameters
D_{Ice} = 0.5 m	T_{bottom} = 293 K	CFL number = 0.45
T_{Ice} = 263 K	q_{top} = 0 W/m	ΔT = 0.025°

results in terms of temperature, the numerical solution being overlapped with the analytical one for most of the cases. Figure 5 shows the influence of spatial discretization over the liquid-solid interface evolution. It can be observed that with increased resolution the results are significantly improved.

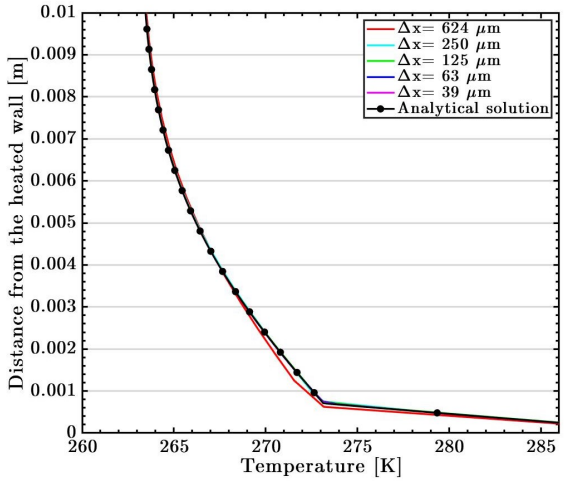

Figure 4: Validation of temperature profiles

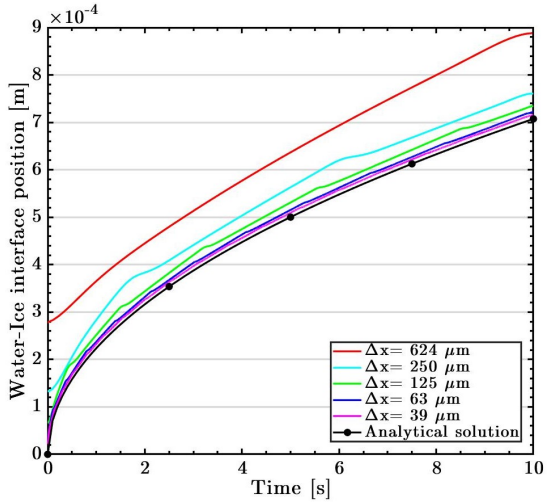

Figure 5: Validation of water-ice interface position

Finally, despite the different assumptions over the thermal phase change interval, the numerical model is validated against the analytical solution. The validation was performed for several temperature boundary conditions.

5. Experimental Ice Shedding

5.1. The VKI Icing wind tunnel (CWT-1) facility

The experimental campaign was conducted in the VKI Icing wind tunnel (CWT-1). The facility is a closed circuit wind tunnel able to operate in a thermal range of 0 to -40 °C, with maximal flow velocity of 70 m/s. A facility sketch can be seen in Fig.6. Built

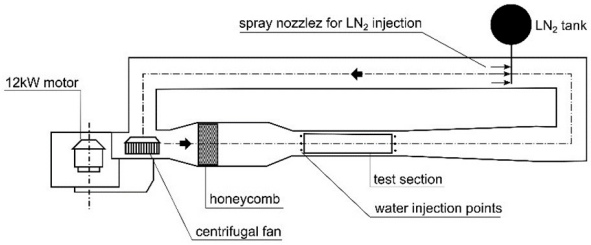

Figure 6: Schematic of the icing wind tunnel (CTW-1) facility

out of wood and epoxy-fiberglass composite, and internally insulated by polystyrene foam covered with an epoxy layer, the wind tunnel is refrigerated by the injection of liquid nitrogen through 6 spray nozzles in the return circuit.

A centrifugal fan driven by an inverter-controlled 12 kW DC motor is used to generate the flow which is settled down using a honeycomb. The wind tunnel has a 1.6 m long transparent test section, with a 0.1x0.3 m cross section. It is made of double glazed windows which allows the use of optical measurements. The wind tunnel is equipped with two type K thermocouples to register the inside temperature and wall mounted pressure taps in the settling chamber and at the beginning of the test section to retrieve the air speed.

5.2. Experimental procedure

The experimental procedure is composed by visualizations and shedding time measurements in a simplified configuration of ice models frozen on flat plates equipped with embedded resistive elements provided by Sonaca. A schematic of the experiments is presented in Fig. 7 a.

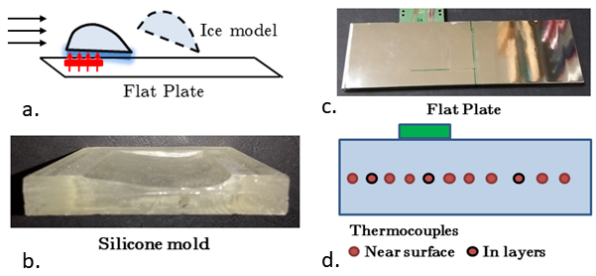

Figure 7: Ice shedding experiment - a. experiment schematic, b. ice model silicone mold, c. embedded resistive element flat plate (Sonaca), d. flat plate embedded thermocouples

An ice shape silicone mold (Fig. 7b) is vertically attached to the flat plate (Fig. 7c) and filled with distilled water. A special care is given to the air bubbles removal and the flat plate-mold assembly is placed in the freezer.

After the ice model is completely frozen, the silicone mold is detached and the flat plate is placed inside the pre-cooled wind tunnel. The embedded thermocouples presented in Fig. 7d, are used to check the flat plate temperature at the beginning and during experiments. The in-depth mounted thermocouples measurements are used to compute the heat flux on one of the flat plate's side.

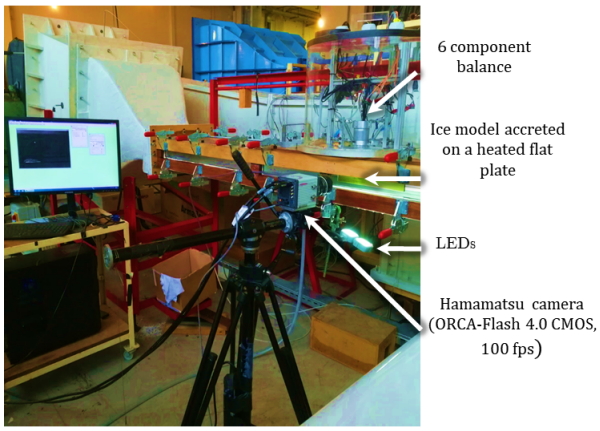

Figure 8: Ice shedding experimental test section

The experimental test set-up is depicted in Fig.8. The flat plate with the accreted ice models are vertically placed inside the wind tunnel. A six component balance is used to obtain qualitative information about aerodynamic loads. The flow field is illuminated using two arrays of LED's and a rolling shutter high frequency CMOS Hamamatsu camera (ORCA-Flash 4.0) is used to record the ice shedding phenomenon at a frame rate of 100 fps.

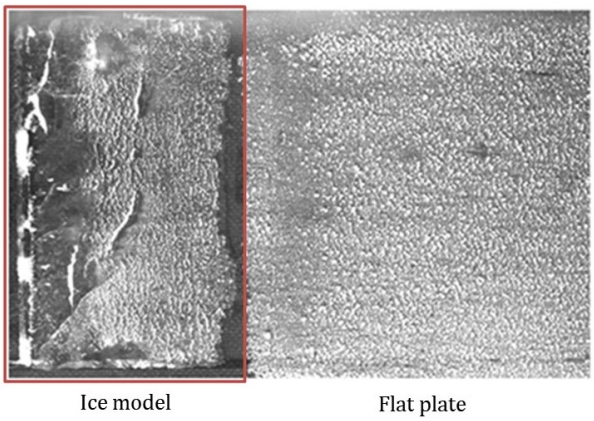

Figure 9: Exemplary image of an ice shedding experiment - heated region marked in red

The shedding time is retrieved from the videos. An exemplary image of an ice shedding experiment is shown in Fig. 9. The test begins with the electro-thermal de-icing system switched off, with the ice in thermal equilibrium with interior of the icing wind tunnel. The de-icing system is activated and the camera starts recording. The ice block is heated from below, the heated area being signalized by the red rectangular. A water layer starts to form and it evolves until the shedding occurs.

6. Experimental Results

A parametric study over the influence of several parameters on the ice shedding process has been performed. The varied parameters were the icing wind tunnel temperature (between 243 K and 268 K), the applied heat flux and the flat plate surface roughness.

6.1. Ice shedding mechanisms

During the experimental campaign, two different shedding mechanisms were observed: sliding and cracking, both followed by shedding.

For a lower surface roughness and higher wind tunnel temperatures a water layer starts evolving when the de-icing is activated. The water layer evolves both in width and height, but it remains trapped under the ice block. At a certain moment, on top of it the ice block loses the adhesion to plate's surface and it starts sliding downstream under the wind's action. From this movement after a period it detaches and is shed away.

For a higher surface roughness and lower wind tunnel temperatures, the ice starts melting and water forms at the activation of de-icing system. Under the wind shear action, rivulets are formed downstream the ice block. in this case, water escapes from under the ice, but the ice block remains attached. After a while cracks develop inside the ice block and at one moment the entire block cracks, detaches and it is shed by the wind. Usually small pieces of ice remain attached to the plate when this shedding mechanism occurs.

6.2. Influence of studied parameters over shedding time

Influence of the main tested parameters over the ice shedding time is presented in this section.

In Fig.10 the influence of the icing wind tunnel temperature T_{IWT}, over the shedding time t_{IS}, is illustrated. As expected, a linear relation links the two parameters. With increasing wind tunnel temperature the shedding time decreases as less time is needed to melt the necessary amount of water in order to detach the ice block.

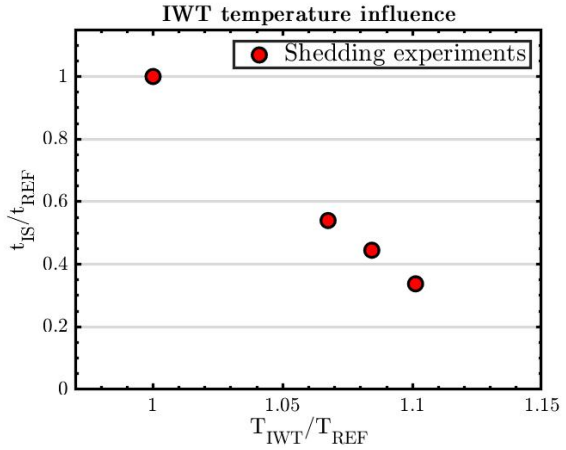

Figure 10: Non-dimensional icing wind tunnel temperature influence over the shedding time

Moreover, as shown in Fig.11, the shedding time decreases as the applied heating power increases, which it was expected as higher provided power results in a higher melting rate and a quicker detachment.

On the other hand, the influence of surface roughness R_{IS}, over the ice shedding time remains an important open question as an interesting non-monotonic behavior is observed in Fig.12. From the available measurements it appears that for low roughnesses the

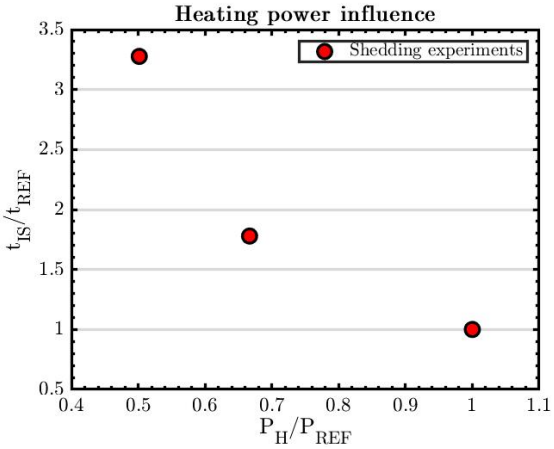

Figure 11: Non-dimensional applied heating power influence over the shedding time

ice shedding time decreases with increasing roughness. However, for the measurement point in the higher range, the shedding time increases again, therefore, one can not draw any conclusion.

A further experimental investigation at medium roughness would be useful to draw a conclusion on the influence of this parameter.

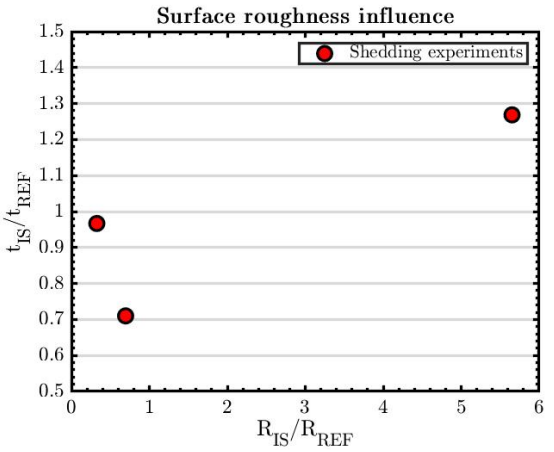

Figure 12: Non-dimensional roughness influence over the shedding time

7. Coupled Numerical and Experimental Results

The numerical investigation over the water layer evolution and its impact on the ice shedding phenomenon is presented. Starting from the hypothesis of an existing threshold wetted surface stated in previous studies [8], the one dimensional phase change

model was used to compute the water layer thickness evolution in time, from the de-icing system activation until the moment of shedding.

The ice shedding moment was experimentally determined inside the VKIs Icing wind tunnel facility presented in Section 5. The experimental settings have been applied as boundary conditions in the numerical model and the melting was developed until the moment of shedding. The water layer thickness was computed using a spatial cell size Δx of 15 μm and a time step of 100 μs.

The three different heat fluxes used in experiments were numerically tested. For the highest heat flux applied, four temperatures of the icing wind tunnel were investigated, varying in a range of 243 to 268 K. For the medium and low heat fluxes only the lower temperatures were tested.

It is important to mention that the ice and wind tunnel flow were at the same temperature in the moment of testing, so an adiabatic condition was numerically imposed at top of the ice block. An approximate 70% wind speed of the maximum tunnel speed was imposed for all the tests, keeping constant dynamic conditions. All these parameters were chosen to isolate the effect of water layer evolution over the ice shedding.

Fig.13 shows the interface progression in time, for the same applied heating power, but starting from different wind tunnel temperatures. The thermal inertia effect can be observed in the delayed occurrence of the liquid layer.

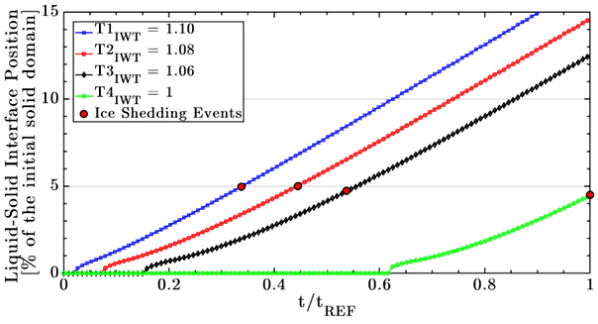

Figure 13: Computed water-ice interface position at the experimental shedding time for the highest applied heat flux for different icing wind tunnel temperatures

For the highest heat flux experiments, the ice shedding occurred at the instant in which the computed water layer thickness was between 4 to 5% of the initial ice domain. As the wind speed, the blade roughness and the ice shape are kept constant for all cases, the experiment's dynamics should not change. It would be expected that ice shedding occurs around the same water layer percentage also for the lower heating powers applied.

Fig.14 presents the water layer thickness results for all tested cases.

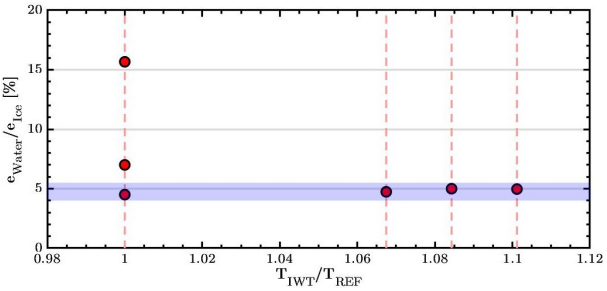

Figure 14: Computed water-ice interface position at the experimental shedding time for all the applied heat fluxes at different icing wind tunnel temperatures

It can be observed that considering only the highest heat flux cases, a threshold of 4-5.5% water layer thickness could be defined as a shedding criterion in the studied configuration. But also it can be observed that decreasing the applied heat flux, the water layer percentage at the moment of shedding increases to 7 and 15% of the ice domain. Under the assumption of constant dynamic conditions, these two cases could be seen as outliers which are out of range due to some unexplained changes during experiments (for example 2D effects or unexpected heat losses).

An extended experimental campaign for lower applied heat fluxes at higher wind tunnel temperatures would be necessary to clarify this phenomenon.

8. Conclusions

The ice shedding phenomenon is studied both experimentally and numerically. The experiments confirmed that thickness of the melted layer is one of the most important parameters influencing the ice shedding mechanism. In this paper:

- A new one dimensional phase change model was developed and validated against the analytical solution of the Stefan problem;
- The numerical model was used to compute the water layer thickness for the experimentally determined shedding time and a 5% water layer detachment threshold was found for majority of the studied cases;

- Both ice sliding and ice cracking shedding mechanisms had been observed during the experimental campaign;
- From experiments, the influence of several tested parameters over the shedding time is determined. The shedding time increases with increasing temperature and decreasing applied heating power. The roughness influence could not be clearly determined, due to a non-monotonic observed behavior.

As further consideration, the one dimensional phase change model should be experimentally validated in a simplified configuration. This is a progressing activity in one Research Master project.

An ongoing work is the algorithm optimization for the two dimensional phase change model and the beginning of a dynamic model for the ice shedding phenomenon, by taking into account the water layer thickness and the ice sliding velocity.

Regarding the experimental investigation, a future work should address an extended ice shedding campaign to verify the 5% water layer threshold for the ice detachment for lower values of applied heat fluxes.

Also, an improved experimental investigation of the roughness influence over the shedding time should be performed.

Acknowledgments

The author gratefully acknowledge the Belgian FNRS for their support with a FRIA grant, and the Sonaca Group, for supporting the experiments and for the permission to publish the material presented.

References

[1] R. Bredesen, R. Cattin, N.-E. Clausen, N. Davis, P. Jordanes, Z. Khadiri-Yazami, R. Klintstrm, A. Krenn, V. Lehtomki, G. Ronsten, M. Wadham-Gagnon, H. Wickman, Expert group study on recommended practices. Wind energy projects in cold climates, TR 13-2nd edition, International Energy Agency (IEA) Wind (2017).

[2] M.-L. Pervier, Mechanics of ice detachement applied to turbomachinery, Ph.D. thesis, Cranfield University (2012).

[3] C. Hochart and G. Fortin and J. Perron and A. Ilinca, Wind Turbine Performance under Icing Conditions, Wind Energy Journal 11 (2008) 319–333.

[4] A. Lacroix and J.F. Manwell, Wind Energy: cold weather issues, University of Massachusetts at Amherst Renewable Energy Research Laboratory.

[5] E. Bossanyi and C. Morgan and H. Seifert, Assessment of safety risks arising from wind turbine icing, no. Boreas IV, Hetta, Finland, 1998.

[6] H. Xue and H. Khawaja, Review of the phenomenon of Ice shedding from wind turbine blades, The International Journal of Multiphysics 10 (3) (2016) 265–276.

[7] C. d'Etude du Givrage, Rapport du 19 Mai 1938, Bulletin des Services Techniques 85, Publication Scientifiques et Techniques du Ministere de l'Air (1939).

[8] L. Bennani, Modelisation bidimensionnelle de systemes electrothermiques de protection contre le givre, Ph.D. thesis, Universite de Toulouse (2014).

[9] M. Papadakis and H.W. Yeong and I.G. Suares, Simulation of ice shedding from a bussiness jet aircraft, no. 45th AIAA Aerospace Science Meeting and Exhibit, Reno, Nev, USA, 2007.

[10] J. Jacob, Experimental and computational aerodynamic analysis of ice fragments shed from aircraft surface, Ph.D. thesis, Wichita State University (2005).

[11] M. Eskiandarian, Ice shedding from overhead electrical lines by mechanical breaking, Ph.D. thesis, Universite du Quebec (2005).

[12] M. Koosher, Ice shedding from cables and conductors - a cracking model of atmospheric ice, Ph.D. thesis, Universite du Quebec (2007).

[13] A. Jamaleddine, G. McClure, J. Rousselet, R. Beauchemin, Simulation of ice-shedding on electrical transmission lines using Adina, Computers and Structures 47 (4/5) (1993) 523–536.

[14] C. Morgan and E. Bossanyi, Wind turbine icing and public safety-a quantifiable risk?, Bengt Tammelin Kristiina Sntti.

[15] L. Battisti, Wind turbines in cold climates: Icing impacts and mitigation systems, Springer, 2015.

[16] H. Beaugendre and F. Morency and F. Gallizio and S. Laurens, Computation of Ice Shedding Trajectories using cartesian grids, penalization, and level sets, Modelling and Simulation in Engineering 2011 (3).

[17] H. Seifert, A. Westerhellweg, and J. Krning, Risk analysis of ice throw from wind turbines, Boreas 6 (9).

[18] O. Fakorede, Z. Feger, H. Ibrahim, A. Ilinca, J. Perron, C. Masson, Ice protection systems for wind turbines in cold climate: characteristics, comparisons and analysis, Renewable and Sustainable Energy Reviews 65 (2016) 662–675.

[19] A. D. Yaslik, K. J. De Witt, T. G. KEITH and W. Boronow, Three-dimensional simulation of electrothermal deicing systems, Journal of Aircraft 29 (6) (1992) 523–536.

[20] R. Henry, Development of an electrothermal de-icing/anti-icing model, no. 30th Aerospace Sciences Meeting and Exibit, Reno, NV, 1992.

[21] B. Åarler, Stefans work on solid-liquid phase changes, Engineering Analysis with Boundary Elements 16 (2) (1995) 83–92.

[22] V. Alexiades, A. D. Solomon, Mathematical modeling of melting and freezing processes, Hemisphere Publ., Washington, 1993.

[23] A. Faghri, Y. Zhang, Transport phenomena in multiphase systems, Elsevier, 2006.

[24] H. Hu and S.A. Argyropoulos, Mathematical modelling of solidification and melting: a review, Modelling and Simulation in Materials Science and Engineering 4 (4) (1996) 371–396.

[25] M. Sugawara, Y. Komatsu and H. Beer, Melting of ice stuck on cylinders placed horizontally in a water flowing duct, Heat Mass Transfer 52 (4) (2015) 693–700.

[26] R. Chauvin, Un modele unifie pour les phenomenes de givrage en aeronautique et les systemes de protections thermique, Ph.D. thesis, Universite de Toulouse (2015).

[27] V. Voller and C. Prakash, A fixed grid numerical modelling methodology for convection-diffusion mushy region phase-

change problems, Journal of Heat and Mass Transfer 30 (8) (1987) 1709–1719.

Numerical and Experimental Validation of a Reliable Crack Localization System for 3D Printed Metallic Components based on the eSHM Methodology

Zoé Jardon

Environmental and Applied Fluid Dynamics Department, von Karman Institute for Fluid Dynamics, Belgium, zoe.jardon@vki.ac.be

Supervisor: Jeroen van Beeck

Dean of the Faculty, Professor and Head of Department, Environmental and Applied Fluid Dynamics Department, von Karman Institute for Fluid Dynamics, Belgium, vanbeeck@vki.ac.be

University Supervisor: Patrick Guillaume

Professor and Head of Department, Mechanical Engineering, Acoustics and Vibration Research Group, Vrije Universiteit Brussel, Belgium, patrick.guillaume@vub.be

Abstract

There is an industrial enthusiasm in a wide range of sectors for the metal additive manufacturing (AM) processes, more commonly known as 3D metal printing. 3D printing is a promising technology with maximum design freedom. Building layer by layer, the technique prints components with highly complex geometries from almost any digital model. This creates interesting opportunities in a wide range of applications but also induces an important structural drawback. The 3D printed components exhibit poor fatigue performances and contain residual stresses due to the high temperature gradients during the printing process. The in-situ monitoring of residual stresses during additive manufacturing is a relatively unexplored subject, although it is a main source of component deformation and cracking. A critical element in aeronautics non-destructive testing is the detection of the presence of a crack before it reaches a critical size. Similar important issues retarded the introduction of lightweight composite materials in aeronautics. The effective Structural Health Monitoring (eSHM) system, patented by the Vrije Universiteit Brussel, fully exploits the flexibility offered by the 3D printing process by integrating a smart structural health monitoring technology inside the 3D-printed metallic components with additive manufacturing techniques. The system is used to localize fatigue cracks and relies on the propagation of pressure waves with constant propagation speed through circular capillaries embedded in the structure. The nature of these waves, and therefore their propagation speed, seem to be determinant for the accuracy of the crack localization system. To achieve a better physical understanding of the nature of the propagating waves through the capillaries, computational fluid dynamics simulations are performed and compared to experimental results obtained with a self-built test setup. The presence of propagating shock waves is observed in the simulations and experiments, as well as a complex reflection mechanism around the leak location. Shock waves show the characteristic of not propagating at a constant velocity. This property complicates the actual localization system. To solve this, the constant velocity assumption should be replaced with the effective velocity evolution to increase the localization accuracy. The amplitude of the shock wave is attenuated with propagating distance, which proves that the effect of friction plays an important role and can, in turn, influence the localization system.

Keywords: structural health monitoring; additive manufacturing; crack localization; shock wave propagation; acoustic pressure wave; computational fluid dynamics

Modeling Particle Trajectory Crossing in Poly-Dispersed Particle-Laden Flows, a Quadrature based Approach

Maxim Van Cappellen

Environmental and Applied Fluid Dynamics Department, von Karman Institute for Fluid Dynamics, Belgium, maxim.van.cappellen@vki.ac.be

Supervisor: Delphine Laboureur

Assistant Professor, Environmental and Applied Fluid Dynamics Department, von Karman Institute for Fluid Dynamics, Belgium, delphine.laboureur@vki.ac.be

University Supervisor: Maria Rosaria Vetrano

Associate Professor, Faculty of Engineering Science, Katholieke Universiteit Leuven, Belgium, rosaria.vetrano@kuleuven.be

Abstract

In this paper the conditional quadrature method of moment (CQMOM) is tested for poly-dispersed poly-kinetic particle-laden flows. The CQMOM is evaluated on a one-dimensional case involving particle trajectory crossing of a poly-sized population of particles, showing promising results. This case study allowed the identification of some important research questions still to be resolved in order to create an Eulerian model for kinetic flows involving poly-dispersed particles.

Keywords: Poly-dispersed, poly-kinetic, particle-laden flows, particle trajectory crossing, method of moments, QBMM, CQMOM

1. Introduction

Particle-laden turbulent flows are frequently encountered in the industries. Application can range from fluidized beds, stirring tank reactors to even rocket engines. The dynamic behavior of particles suspended in a carrier flow can be very complex and difficult to predict using conventional experiment based engineering techniques. This is certainly true in industrial scaled applications. Due to recent advances in computing power and multiphase modeling techniques, numerical methods are becoming the preferred tool for research and development for industrial multiphase problems. The current framework of multiphase models describing particle-laden flows can be categorized based on their level of complexity, illustrated in fig. 1. At a microscopic level, particle-laden flows are completely determined by the transport equation of the multi-particle-fluid joint probability density function (describing the evolution of a particulate phase suspended in a fluid) when coupled with the Navier-Stokes equation [1; 2]. The number of independent variables is however too large for industrial applications. For engineering purposes reduction of the degrees of freedom in the microscale physics is needed that results in a macroscale description of the physics. Two types of model reduction approaches can be identified: models that use volume/ensemble averaging and models that start from the mesoscale kinetic equations, the mesoscopic models (fig. 1). As the former is rather outdated, it will not

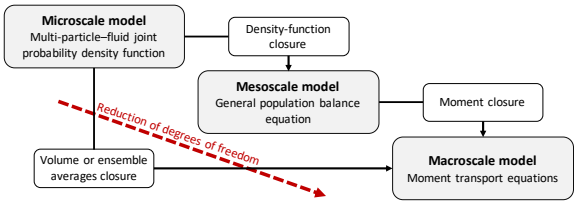

Figure 1: Stairs of model reduction for particle-laden flows.

be discussed. The mesoscale formulation is obtained by integrating the microscopic governing equations over the complete ensemble of particles. This results in a single-particle kinetic equation, called the general population balance equation (GPBE) [3]. Some well-known example are the Williams spray equation [3] and the Boltzmann equation [4]. The main two simulation approaches that start from the GPBE are the (Eulerian) moment closure models and the Euler-Lagrangian models.

Moment closure models use an averaging procedure to find the moments of the number density function (NDF) appearing in the GPBE. This leads to a set of moment transport equation that describe the dynamics of the system on a macroscopic scale. The moments approach has a wide variety of possible formulations, which can be categorized by their applicability in different particle-laden flow regimes. These regimes are defined by the particle Stokes number St_p and particle volume fraction α_p (see fig. 2). The simplest moment models are found at very low St_p, here the so called dusty gas equations are applicable. This is a single fluid model including a density transport equation. At slightly higher St_p the particles will advect at a different rate compared to the fluid. The local particle velocity will converge exponentially fast to an equilibrium and becomes only a function of particle size and the velocity of the surrounding fluid. Here the equilibrium Euler model can be applied [7]. This technique allows to capture important phenomena, such as preferential particle accumulation and turbophoresis. At still higher Stokes number ($\mathrm{St}_p < 1$) the equilibrium assumption is no longer valid and separate

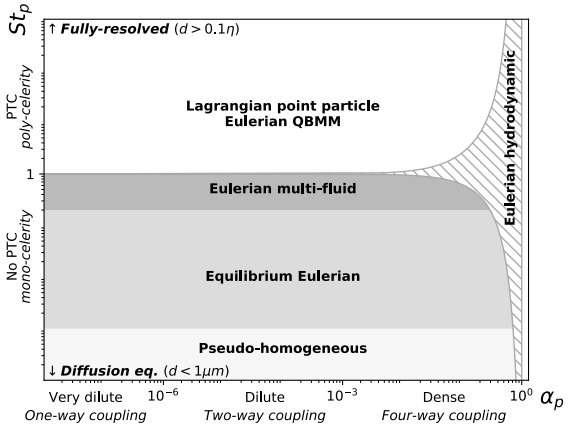

Figure 2: Modeling approaches for turbulent multiphase flow based on particle Stokes number St_p and particle volume fraction α_p. [5; 6; 1]

transport equations for the particulate phase have to be solved. In this approach both the continuous flow and the dispersed entities are treated as interpenetrating fluids. Hence the name multi-fluid model. In the limit of dilute to dense flows particle-particle interaction will start to dominate the evolution of the particle velocity distribution function and an additional collision model need to be added to the transport equations. For very dense flows the GPBE is no longer valid, due to sustained particle-particle contact [8; 2]. In this case a simplified hydrodynamic closure can be used [9], where the particlulate phase behaves like a compressible fluid. The aforementioned models all assume that $\mathrm{St}_p < 1$, which approximates the particle velocity distribution to be uni-modal or monokinetic. When St_p is larger than one, the particle velocity distribution function can become multi-modal (*a.k.a particle poly-celerity*). A multi-modal velocity distribution can cause particle trajectory crossing (PTC) and neglecting this behavior will result in non-physical delta-shocks. These are locations where all the crossing particles accumulate [10].

Until now, high Stokes number flows are being simulated by Eulerian-Lagrangian solvers, which directly solve the GPBE [11; 12]. From a physical point of view this method can cope with a wide range of flow regimes. However, there are two major practical flaws: the computational time increases with increasing number of particles and two-way coupling with the continuous phase is not guaranteed to produce grid converged solutions due to statistical noise [5; 2; 11]. Clearly these issues are problematic for industrial scaled problems. The modeling framework is even more complicated as, in fig. 2, St_p and α_p are local variables and can not always be generalized for the entire system. Making model selection a difficult task. The optimal multiphase solver, for large-scale turbulent solid-liquid flow, should be applicable over a large range of Stokes numbers and concentrations up to the hydrodynamic limit, while being computational affordable. In the last decade a new class of Eulerian models has emerged, called quadrature based moment methods (QBMM) [13]. The QBMM have the ability to approximate multivariate populations while still operating in an Eulerian framework. Several QBMM based on different moment-inversion algorithms have been proposed in the literature, such as the tensor-product method [14], conditional quadrature method of moments (CQMOM) [15], anisotropic Gaussian method (AG)[16] and most recently the hyperbolic conditional quadrature method of moments (HyCQMOM) [17]. These models have demonstrated the

ability to simulate the dynamics of mono-dispersed high Stokes flows. The most noticeable findings are: QBMM can reproduce PTC, they have a solution close to Euler-Lagrangian methods [16], they can compute denser cases with particle collisions [14] and, unlike the Euler-Lagrangian methods, QBMM are free from statistical noise in strongly coupled cases [2].

The purpose of this paper is to evaluate if these quadrature methods are well suited to model poly-dispersed poly-kinetic particle laden flows. This is performed by testing the conditional quadrature method of moments (CQMOM) on a simple free transport kinetic equation in one dimension. This simple case study enables us to identify the strength and weaknesses of the quadrature framework and allows to asses the future research topics that need to be addressed to construct a robust numerical model for poly-dispersed poly-kinetic particle laden flows.

2. The kinetic equation and PTC

In this paper the kinetic equation describing free transport of poly-dispersed poly-kinetic particles in the infinite Knudsen number limit is studied, given by

$$\partial_t f + \partial_x \cdot (vf) = 0, \tag{1}$$

with $f = f(t, x, \xi, v)$ the joint size-velocity number density function, with ξ the size of the particles and v the velocity in one dimension. In the infinite Knudsen number limit, the spatial density of particles is very dilute and no collisions are bound occur. This means that the path traveled by different particles can cross unhindered, also known as particle trajectory crossing (PTC). As mentioned in the introduction, PTC behavior is an important physical occurrence which is closely linked to the particle Stokes number St_p and the volume fraction α_p. At low $\mathrm{St}_p < 1$ the particle inertia has little influence on the path of the particles. Which implies that two or more particles in close vicinity of each other will move in similar directions and thus have parallel paths. When the inertia of the particles is significant compared to the force exerted by the flow, the path history of the particle will have a significant influence on the future path of the particles. Thus reducing spatial correlation and causing neighboring particles to be able cross paths. Since this phenomena is missing in the conventional Eulerian multiphase solvers, it is a perfect measure to test the ability of the QBMM to model poly-dispersed poly-kinetic particles laden flows. The remainder of the paper is structured as followed: first we breakdown the framework needed to close the moment equation for multi-variable number density functions, followed by the numerical discretization of the transport equations. Hereafter the one-dimensional model is tested and the effect of the finite volume method is discussed. In the final section future topics of research are briefly discussed by demonstrating their importance.

3. Quadrature Based Model

3.1. Conditional quadrature moments method

In conditional quadrature moments methods, the joint number density function is transformed into:

$$f(\xi, v) = f(\xi|v)f(v) \tag{2}$$

making use of the Kolmogorov definition for statistical dependent variables. The power moments of $f(\xi, v)$ are then given by:

$$M_{k,l} = \int_0^{+\infty} \int_{-\infty}^{+\infty} f(\xi|v)f(v)\xi^k v^l dv d\xi \tag{3}$$

The number density function $f(v)$ is approximated by a discrete N_v-point distribution in the form of a weighted sum of Dirac delta functions.

$$f(v) \cong \sum_{\alpha=1}^{N_v} w_\alpha \delta(v - v_\alpha) \tag{4}$$

where w_α and v_α are called respectively the weights and abscissas. By using the sampling property of the delta function, the power moments become:

$$M_{k,l} = \sum_{\alpha=1}^{N_v} w_\alpha v_\alpha^l \int_{-\infty}^{+\infty} f(\xi|v_\alpha)\xi^k d\xi. \tag{5}$$

Without loss of generality it can be assumed that the zero-order moment of $f(\xi|v_\alpha)$ is equal to one and hence forward we make use of the notation

$$\langle \xi^k \rangle(v_\alpha) = \int_{-\infty}^{+\infty} f(\xi|v_\alpha)\xi^k d\xi \tag{6}$$

for the conditional moments of order k. This results in the following non-linear system of equations for the weights and abscissas

$$M_{0,l} = \sum_{\alpha=1}^{N_v} w_\alpha v_\alpha^l. \tag{7}$$

Which is equivalent to the classic QMOM [18] approximation of the pure power moments $M_{0,l}$ for $l =$

$0, \cdots, 2N_v - 1$, since by definition $\langle \xi^O \rangle(v_\alpha) = 1$. The weights and abscissas can be found by using the Wheeler algorithm [19]. The conditional moments $\langle \xi^k \rangle(v_\alpha)$ can now be found by solving the linear system:

$$M_{k,l} = \sum_{\alpha=1}^{N_v} w_\alpha v_\alpha^l \langle \xi^k \rangle(v_\alpha) \tag{8}$$

Which is equivalent to

$$\begin{bmatrix} w_1 v_1^0 & \cdots & w_{N_v} v_{N_v}^0 \\ \vdots & \ddots & \vdots \\ w_1 v_1^{N_v-1} & \cdots & w_{N_v} v_{N_v}^{N_v-1} \end{bmatrix} \begin{bmatrix} \langle \xi^1 \rangle(v_1) & \cdots & \langle \xi^{2N_\xi-1} \rangle(v_1) \\ \vdots & \ddots & \vdots \\ \langle \xi^1 \rangle(v_{N_v}) & \cdots & \langle \xi^{2N_\xi-1} \rangle(v_{N_v}) \end{bmatrix} = \begin{bmatrix} M_{1,0} & \cdots & M_{2N_\xi-1,0} \\ \vdots & \ddots & \vdots \\ M_{1,N_v-1} & \cdots & M_{2N_\xi-1,N_v-1} \end{bmatrix} \tag{9}$$

where N_ξ is the highest quadrature order that can be used to reconstruct the conditional densities $f(\xi|v_\alpha)$. Thus for each $\alpha = 1, \cdots, N_v$, the conditional momentsets $\{\langle \xi^1 \rangle(v_\alpha), \cdots, \langle \xi^{2N_\xi-1} \rangle(v_\alpha)\}$ found by solving the linear system in eq. (9) can be used to compute the N_v-quadratures

$$\langle \xi^k \rangle(v_\alpha) = \sum_{\beta=1}^{N_\xi} \rho_{\alpha\beta} \xi_{\alpha\beta}^k \tag{10}$$

using again the Wheeler algorithm. Here $\rho_{\alpha\beta}$ and $\xi_{\alpha\beta}$ are called the conditional weights and abscissa of the N_ξ-point approximation of $f(\xi|v_\alpha)$. The final quadrature representation of the pure power moments results in

$$M_{k,l} = \sum_{\alpha=1}^{N_v} \sum_{\beta=1}^{N_\xi} w_\alpha \rho_{\alpha\beta} v_\alpha^l \xi_{\alpha\beta}^k \tag{11}$$

3.2. Kinetic based finite volume method

Applying the power moment transformation to the kinetic equation in eq. (1) yields

$$\partial_t M_{k,l} + \partial_x M_{k,l+1} = 0 \tag{12}$$

By applying the conditional quadrature closure defined in eq. (11), the system of equations in eq. (12) is closed if the $N_v(2N_\xi - 1)$ pure moments of the moment matrix

$$\begin{bmatrix} M_{0,0} & \cdots & M_{0,N_v-1} & \cdots & M_{0,2N_V-1} \\ \vdots & \ddots & \vdots & & \\ M_{2N_\xi-1,0} & \cdots & M_{2N_\xi-1,N_v-1} & & \end{bmatrix}. \tag{13}$$

are known. Meaning that $N_v(2N_\xi - 1)$ transport equations have to be solved, for the moments in eq. (13). This can be performed by the finite volume method. However, great care must be taken when choosing the time integration method and the schemes for reconstructing the fluxes at the cell interfaces. The main problem with using QBMM for kinetic equations is the (loss of) realizability of the moment set. Indeed if a moment set becomes unrealizable (*a.k.a a corrupt moment set*), the moment inversion algorithm will yield non-physical weights and abscissa or even produce no solution at all. Furthermore will the advection term in eq. (12) corrupt neighboring cells if the fluxes are computed from a corrupt moment set. This issue will be explained later on.

The finite volume method starts by volume-averaging on a uniform grid with spacing Δx and using a single-stage Euler explicit time-integration, gives the updated moment set at time $(m+1)\Delta t$:

$$(M_{k,l})_i^{m+1} = (M_{k,l})_i^m - \frac{\Delta t}{\Delta x}\left[(M_{k,l+1})_{i+1/2}^m - (M_{k,l+1})_{i-1/2}^m\right] \tag{14}$$

The preferred method for flux reconstruction on the cell interfaces for QBMM is to use kinetic based finite volume methods (KBFVM). The basic principle of KBFVM is to split the fluxes in eq. (14) between particles moving upstream and downstream by defining two new moment sets [15; 20]:

$$M_{k,l}^+ = \sum_{\alpha=1}^{N_v} \sum_{\beta=1}^{N_\xi} w_\alpha \rho_{\alpha\beta} \max(0, v_\alpha) v_\alpha^{l-1} \xi_{\alpha\beta}^k \tag{15}$$

and

$$M_{k,l}^- = \sum_{\alpha=1}^{N_v} \sum_{\beta=1}^{N_\xi} w_\alpha \rho_{\alpha\beta} \min(0, v_\alpha) v_\alpha^{l-1} \xi_{\alpha\beta}^k \tag{16}$$

and by definition $M_{k,l} = M_{k,l}^+ + M_{k,l}^-$. Inserting these new moments into eq. (14) and introducing an effective number density function $h_i(\xi, v)$, the updated moment can be written as $(M_{k,l})_i^{m+1} = \int h_i v^l \xi^k dv d\xi$. The effective number density function $h_i(\xi, v)$ is thus equivalent to

$$h_i = f_i - \lambda v^+ f_{i+1/2,l} - \lambda v^- f_{i+1/2,r} + \lambda v^+ f_{i-1/2,l} + \lambda v^- f_{i-1/2,r} \tag{17}$$

where $\lambda = \Delta t/\Delta x$ and the time step superscript m is omitted for readability. The subscripts l and r denote the value of the interface, approaching from respectively the left and right side of the cell (*i.e. upstream and downstream*). As stated before, standard finite volume schemes do not ensure that the updated moment sets will be realizable. Dejardins *et al.* [10] figured that when a finite volume scheme can be proven

to produce a positive h_i, the scheme will produce realizable moment sets. Following this principle Vikas *et al.* [20] proved that when a single-stage Euler explicit time integration is used with 1-st order reconstruction of the abscissas and arbitrary order reconstruction of the weights, the non-negativity of h_i can always be ensured with an explicit constraint on the time step. It must be noted that this theorem does not include the possibility of having additional passive internal variables in the NDF. However it can easily be shown that the same principle is valid for any number of internal variables as long as all the reconstructed abscissas are 1-st order in space. To our knowledge, the question if higher-order reconstruction of passive internal abscissas can be ensured to produce realizable moments has not yet been addressed in the literature.

Following the idea of Vikas *et al.* the effective reconstructed NDF becomes:

$$h_i = \sum_{\alpha=1}^{N_v}\sum_{\beta=1}^{N_\xi}(Z_{\alpha\beta,i} - \lambda v^+ Z_{\alpha\beta,i+1/2,l} + \lambda v^- Z_{\alpha\beta,i-1/2,r}) \\ \delta(\xi - \xi_{\alpha\beta,i})\delta(v - v_{\alpha,i}) + \epsilon^+ \tag{18}$$

Here the non-negative third and fourth terms of eq. (17) are grouped by ϵ^+ and $Z_{\alpha\beta} = w_\alpha \rho_{\alpha\beta}$. The positiveness of h_i can thus be ensured if the first term between brackets is positive for all velocity abscissas,. This produced the following restriction on the time step:

$$\Delta t \leq \\ \min_{\forall \alpha,\beta}\left(\frac{Z_{\alpha\beta,i}\Delta x}{\max(0, v_{\alpha,i})Z_{\alpha\beta,i+1/2,l} - \min(0, v_{\alpha,i})Z_{\alpha\beta,i-1/2,r}}\right) \tag{19}$$

Here we demonstrate that for any order of spatial flux reconstruction of the weights and first order reconstruction of all the abscissas, an explicit time-step constrained can be found that ensures a realizable updated moment set. One can notice that this time-step (eq. (19)) is not strictly the largest possible realizable time step, because the magnitude of the term ϵ^+ will also have a positive influence on the non-negativity of h_i. Though, mathematically deriving a constrained for the maximum realizable time step is still an open question in literature.

4. Results

In this section the algorithm previously described will be tested for both mono-sized PTC and polydispersed PTC. The quadrature order for both the velocity and size distribution is fixed to $N_\xi = N_v = 2$. This is done to have a more in-depth understanding of the way the abscissas and weights behave as an analytic solution to this moment inversion algorithm can be derived.

4.1. Monodispersed particle crossing

In the first test case, we consider two particle same-sized packets crossing. The initial moments are computed from the two-node distribution seen in fig. 3. This is the identical test case found in the work of Chalons *et al.* [21], except that we have added the particle size as an internal variable. The particles at the left of $x = 0.5$ will move at constant velocity to the right and the particles at the right move in the opposite direction. This can be seen in the initial conditions of the velocity abscissas v_1 and v_2 (fig. 3). Note that both velocity abscissas are identical, which is actually a special case in quadrature moment methods. Because this means that a one-point distributions is represented by a two-node distribution, where the total number of particles is distributed over the two weights $w_1 = w_2 = M_{0,0}/2$. This special case is called the frontier of moment space [21] and will be discussed in section 5.1. The initial moments for this test case are given in fig. 4. The simulation is performed on a uniform grid between 0 and 1 with 200 grid points and the CFL $= \lambda/|v_{max}|$ was set to 1. The weights at the interface are reconstructed using a first order upwind scheme (eq. (20)).

$$w_{\alpha,i+1/2,l} = w_{\alpha,i-1/2,r} = w_{\alpha,i} \tag{20}$$

At $t = 0.1$ the particle packets overlap and form a mixing zone where the mean velocity is zero ($M_{0,1}$) and the two velocity abscissas are of opposite sign (figs. 5 and 6). If only a one-node quadrature was employed (like in classic Eulerian multiphase solvers), the velocity abscissa would be equal to $M_{0,1}/M_{0,1}$, which is zero in the mixing zone and would cause the particle to accumulate at $x = 0.5$. This phenomena is called a δ-shock and is exactly the problem what the QBMM try to overcome. At $t = 0.4$ (figs. 7 and 8) we see that the two groups of particles have successfully crossed and exactly match the analytic solution (dotted line). Finally we see that during the simulation the particle size has not been altered and is passively transported by the velocity abscissas.

4.2. Polydispersed particle crossing

In the next test case the weights and abscissas are initialized according to fig. 9. The velocity abscissas and weights are here initialized identical to

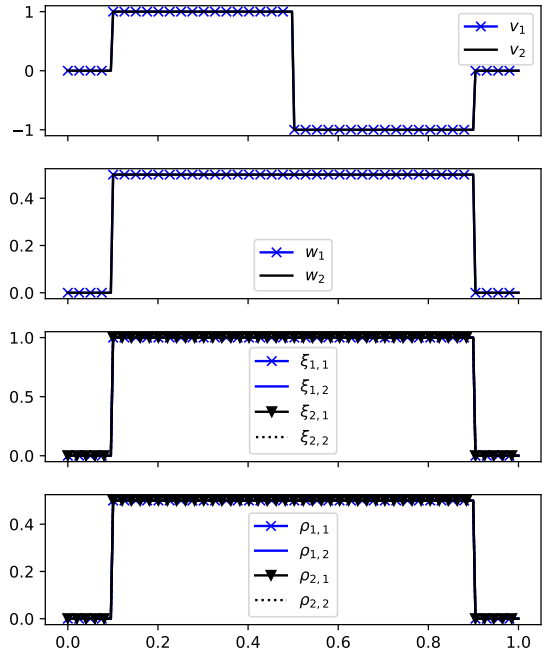

Figure 3: Initial weights and abscissas for the monodispersed particle crossing test case.

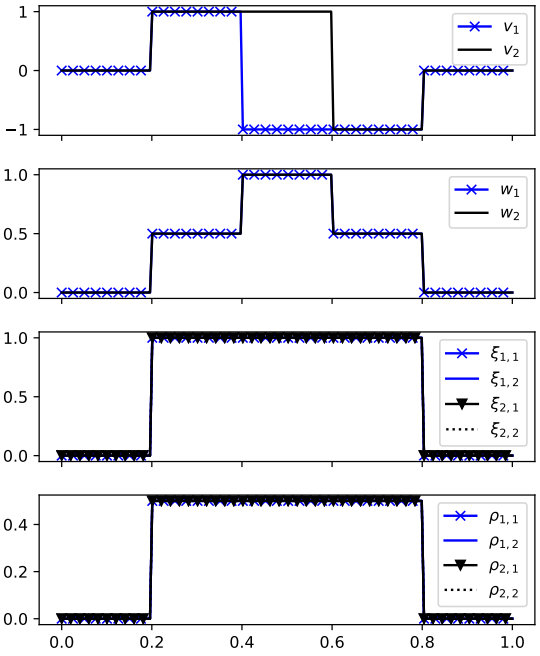

Figure 5: Weights and abscissas for the monodispersed particle crossing test case at $t = 0.1$.

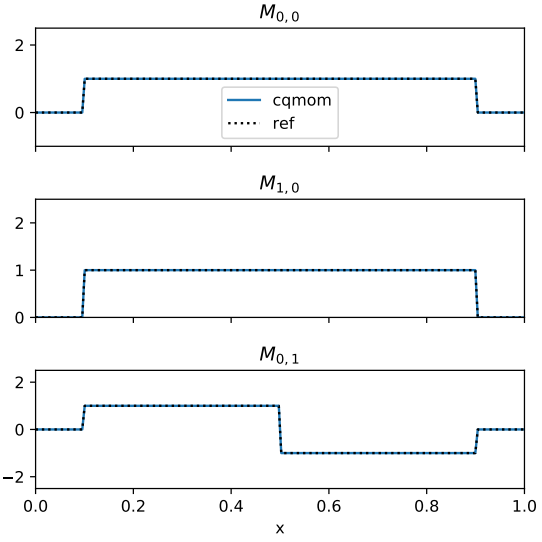

Figure 4: Initial moments for the monodispersed particle crossing test case.

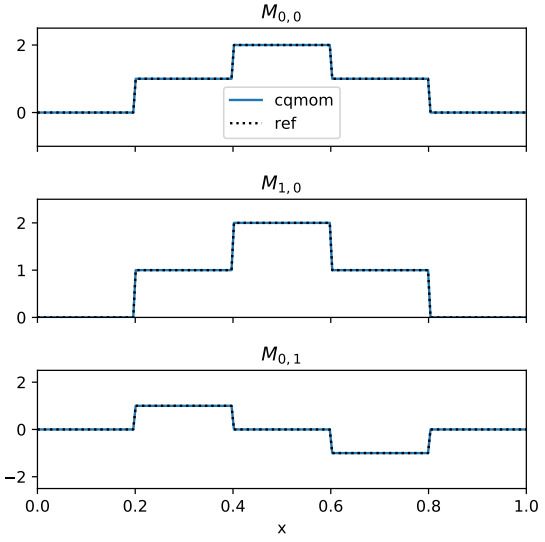

Figure 6: Moments for the monodispersed particle crossing test case at $t = 0.1$.

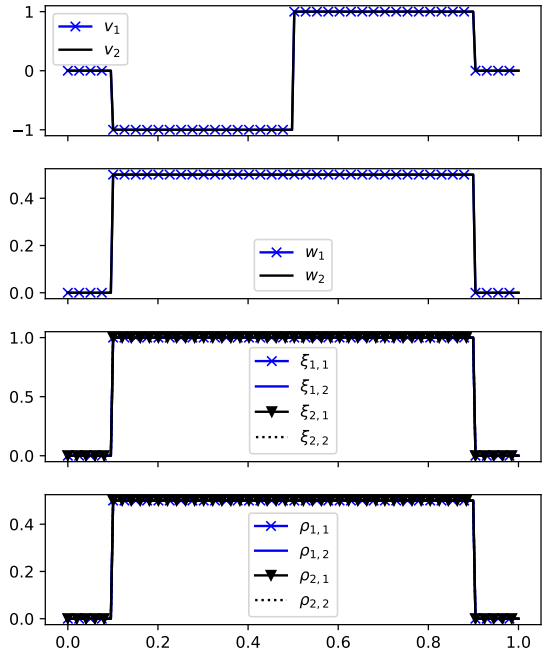

Figure 7: Weights and abscissas for the monodispersed particle crossing test case at $t = 0.4$.

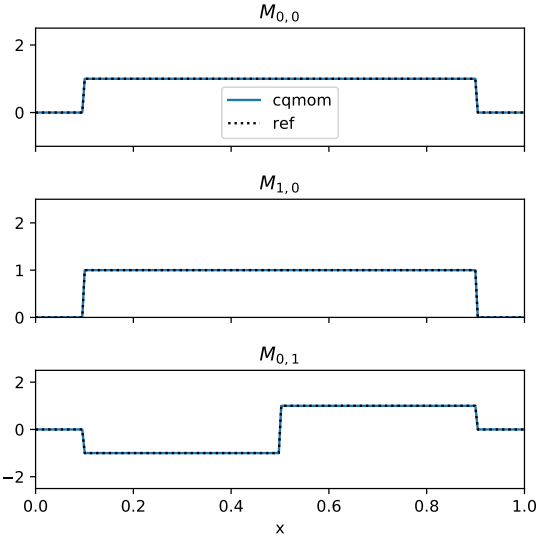

Figure 8: Moments for the monodispersed particle crossing test case at $t = 0.4$.

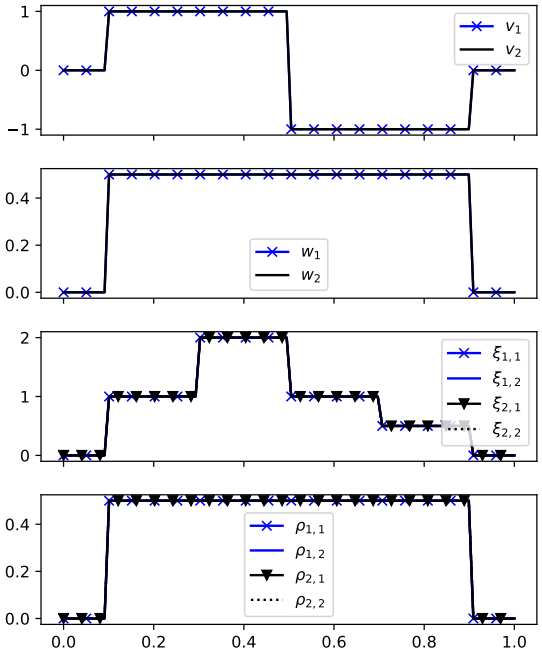

Figure 9: Initial weights and abscissas for the polydispersed particle crossing test case.

the previous test case but now the size abscissas are poly-dispersed. In fig. 11 to fig. 14 the evolution of the quadrature nodes and corresponding moments is given. Like in the previous test case the particles cross without any numerical interference and exactly reproduce the analytic solution. So here we demonstrate how the CQMOM can be used to model poly-dispersed poly-kinetic particles in an Eulerian framework.

4.3. Numerical diffusion

In the previous cases the CFL number was fixed to one while the velocity abscissas where equal to 1 or -1. This causes the weights and abscissas from one numerical cell to be fully transported to the neighboring cell. In such a case the solution does not exhibit any numerical diffusion and the analytic solution is exaclty reproduced. If the CFL number is lower than one numerical diffusion, which is typically large for 1st-order reconstructions of the fluxes, will decrease the accuracy of the solution. The primary solution to this loss off accuracy is to employ higher order schemes for the reconstruction of the weights. Using higher order schemes for the abscissas is not possible as the solution can not be ensured to be realizable, as was discussed in section 3.2. Here a second order scheme

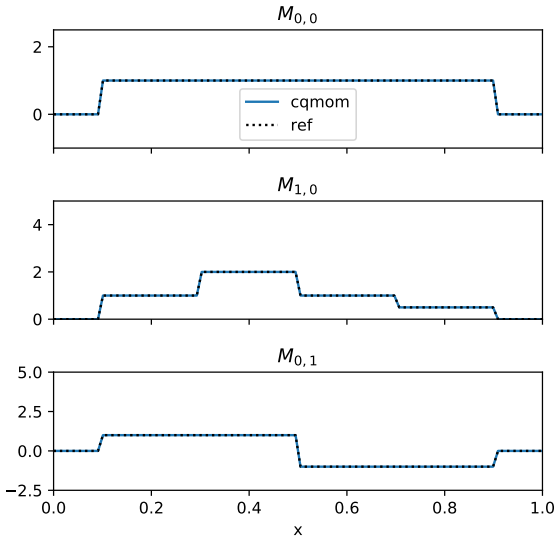

Figure 10: Initial moments for the polydispersed particle crossing test case.

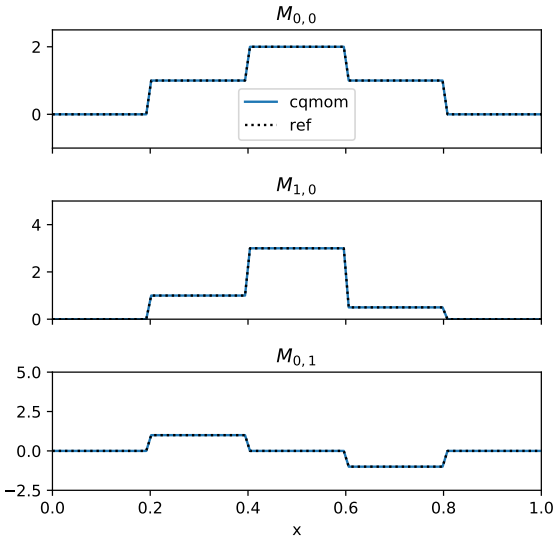

Figure 12: Moments for the polydispersed particle crossing test case at $t = 0.1$.

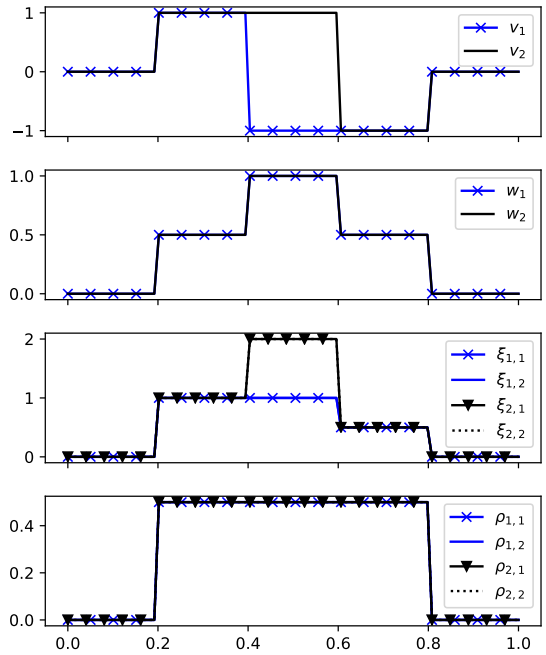

Figure 11: Weights and abscissas for the polydispersed particle crossing test case at $t = 0.1$.

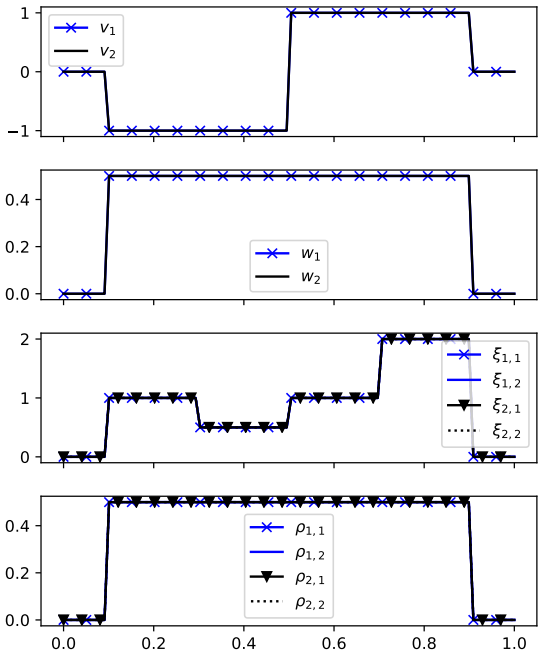

Figure 13: Weights and abscissas for the polydispersed particle crossing test case at $t = 0.4$.

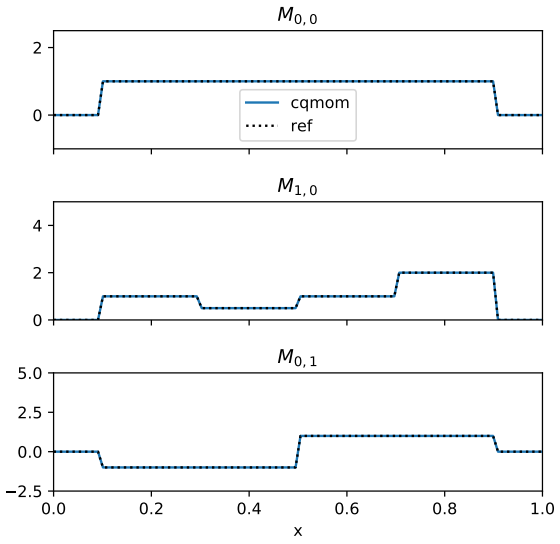

Figure 14: Moments for the polydispersed particle crossing test case at $t = 0.4$.

is tested for the weights, using a minmod limiter for the slopes [1]. This numerical setup is called a quasi-second order scheme as only the weights use higher order reconstruction [20]. This scheme is given by

$$\begin{aligned} w_{\alpha,i+1/2,l} &= w_{\alpha,i} + \frac{1}{2} S_{a,i} \\ w_{\alpha,i-1/2,r} &= w_{\alpha,i} - \frac{1}{2} S_{a,i} \end{aligned} \tag{21}$$

with

$$S_{a,i} = \text{minmod}(w_{\alpha,i+1} - w_{\alpha,i}, w_{\alpha,i} - w_{\alpha,i-1}) \tag{22}$$

and the midmod slope limiter

$$\text{minmod}(a,b) = \begin{cases} a & \text{if } |a| < |b| \;\&\; ab > 0 \\ b & \text{if } |a| > |b| \;\&\; ab > 0 \\ 0 & \text{if } \quad ab < 0 \end{cases} \tag{23}$$

The influence of the numerical diffusion and the order of the scheme is given in figs. 15 and 16 with the same initial data as in fig. 10. It is clear that at CFL<1 the solution is spread out due to the numerical diffusion. When employing the quasi-second order scheme the model can more accurately compute the discontinuous solution. Note that for this test case it is absolutely necessary to use a slope limiter because without, the fluxes would go to infinity due to the discontinuities.

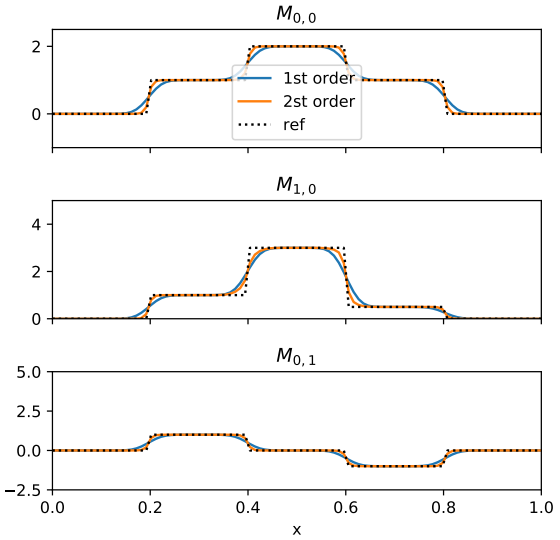

Figure 15: Influence of numerical diffusion: Moments for the polydispersed particle crossing test case at $t = 0.1$ with CFL = 0.5.

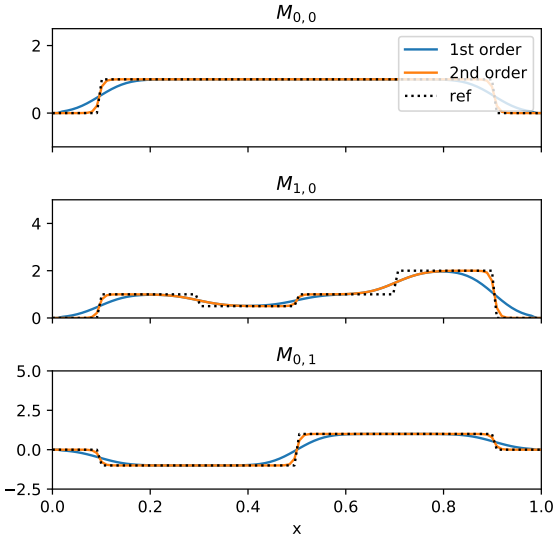

Figure 16: Influence of numerical diffusion: Moments for the polydispersed particle crossing test case at $t = 0.4$ with CFL = 0.5.

5. Future research topics

In this section we identify the research topics that still need to be examined in order to fully control the numerical stability and accuracy of the model.

5.1. Behavior at the frontier of moment space

In order to explain the concept of the frontier moment space, we examine the two-node quadrature for a mono-dispersed particle distribution in one dimension. In this case the kinetic equation is expressed in function of the number density $f(v) = \rho_1\delta(v - v_1) + \rho_2\delta(v - v_2)$. By definition the moment set $\mathbf{M} = [m_0, m_1, m_2, m_3]^t$ is said to be inside the convex moment space Ω if $m_0 > 0$ and $m_0m_2 - m_1^2 > 0$. In this case the abscissas will be distinct $v_1 \neq v_2$ with $\rho_1, \rho_2 \in \mathbb{R}_0^+$. The frontier of moment space is reached when $m_0m_2 - m_1^2 = 0$ with $m_0 > 0$. In this case $v_1 = v_2$ and all the higher order moments can be written in terms of m_0 and m_1. The kinetic equation can thus be solved using a one-node quadrature. However, when the solution moves from inside moment-space towards the frontier, problems can arise. This is analytically proven in the work of Chalons *et al.* [21], where they demonstrate that when $e = m_0m_2 - m_1^2$ approaches zero, three distinct cases can occur based on the value of $q = (m_3m_0^2 - m_1) - 3m_1(m_0m_2 - m_1^2)$, namely

$$\lim_{e\to 0^+} \rho_2 = \begin{cases} m_0 & \text{if } q > 0 \\ 0 & \text{if } q < 0 \\ \frac{m_0}{2} & \text{if } q = 0 \end{cases} \tag{24}$$

$$\lim_{e\to 0^+} \rho_1 = \begin{cases} 0 & \text{if } q > 0 \\ m_0 & \text{if } q < 0 \\ \frac{m_0}{2} & \text{if } q = 0 \end{cases} \tag{25}$$

$$\lim_{e\to 0^+} v_2 = \begin{cases} \frac{m_1}{m_0} & \text{if } q > 0 \\ -\infty & \text{if } q < 0 \\ \frac{m_1}{m_0} & \text{if } q = 0 \end{cases} \tag{26}$$

$$\lim_{e\to 0^+} v_1 = \begin{cases} +\infty & \text{if } q > 0 \\ \frac{m_1}{m_0} & \text{if } q < 0 \\ \frac{m_1}{m_0} & \text{if } q = 0 \end{cases} \tag{27}$$

In other words, when the solution approaches the frontier of moment space with a non-zero q, one of the abscissas will grow indefinitely with a very small weight. From a numerical point of view we can clearly see that this behavior can be problematic and should be controlled.

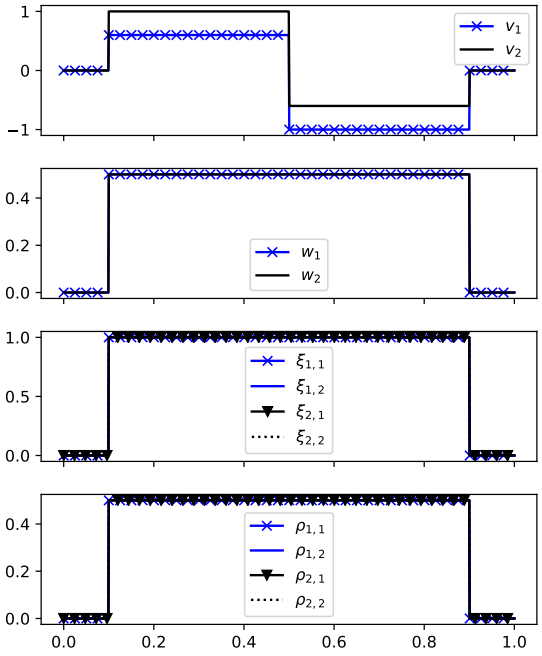

Figure 17: Initial weights and abscissas for monodispersed PTC, four particle packets crossing.

5.2. Hyperbolic CQMOM

Chalons *et al.* [21] also demonstrated that the system of equations in eqs. (11) and (12) is weakly hyperbolic. This means that when more PTCs take place than the number of nodes in the quadrature, small δ-shock appear in the solution. For example, we simulate the free transport (eq. (1)) using the initial data in fig. 17. In this case initially there are in total four packets of particles with a distinct velocity. When these packets collide in the center, two δ-shocks are observed in the weights of the velocity abscissas and thus also in the moments. This is shown in fig. 18. This could be resolved by using a higher order quadrature, which in turn means that more higher order moments have to be transported in the model. Recently, Fox *et al.* [17] proposed a solution to the weak hyperbolic nature of the CQMOM closure, called the Hyperbolic CQMOM. In this new closure algorithm the quadratures in the moment transport equations are calculated from the central moments with a hyperbolicity constrained on the highest order central moment, forcing the system to be hyperbolic. Furthermore, does this closure require less moments than those in eq. (13), making this method a promising alternative to the CQMOM.

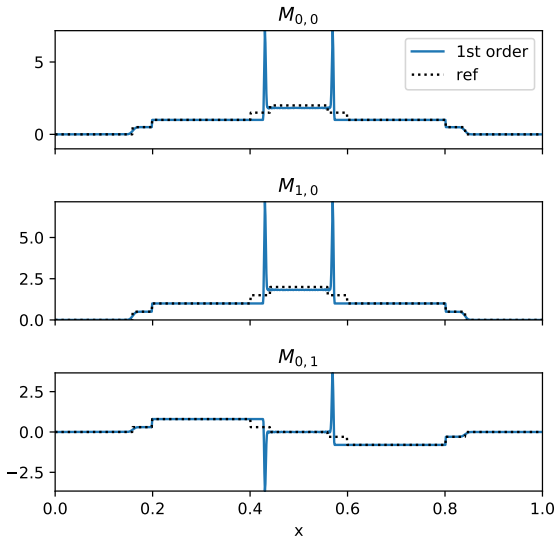

Figure 18: Moments for monodispersed PTC with four particle packets crossing, at t = 0.1.

5.3. Influence of the conditioning variable

In eq. (2) we choose to condition the joint size-velocity NDF on the velocity coordinate, this corresponds to one permutation of the CQMOM [1]. It is of course equally valid to condition on the size coordinate. This will result in another set of weights and abscissas, which also provides a valid reconstruction of the NDF. The question which permutation is the better choice has not yet been answered in literature. Marchisio and Fox [1] suggest to put the size variable at the beginning of the conditioning, in order to correctly predict the fluxes of ξ. However no mathematical or numerical evidence is provide to make a definite conclusion on this matter.

6. Conclusion

In this paper we investigate the quality of the CQMOM closure for simulating free transport of poly-dispersed poly-kinetic particle-laden flows. The particle-laden flow regime of interest is a infinite Knudsen number flow with $\mathrm{St}_p > 1$. In this regime particle trajectory crossing is bound to occur. PTC is known to create nonphysical δ-shocks in the results of classical Eulerian multiphase models for particulate flows. In recent years, QBMM have shown to be a powerful Eulerian closure, which can operate in this particular regime, assuming mono-sized particles [13; 2; 17; 15; 10; 16]. In this work we apply the CQMOM algorithm to deal with the poly-dispersed variant, which is (more) frequently encountered in industrial mixing problems. Our results show that the CQMOM can accurately reproduce free-transport of poly-dispersed particles and can in general resolve the issue of PTC. However, there are still some issues that need to be investigated. First, there is the behavior of the closure at the frontier of moment-space. Secondly, it is shown that δ-shocks can still appear in the solution if the number of PTCs is higher than the order of the (velocity) quadrature. And lastly, the question of which permutation of the CQMOM is the better choice has still to be resolved.

Acknowledgments

This work is funded by the PhD fellowship Strategic Basic Research of the Research Foundation-Flanders (FWO), as part of the project (1S C61 19N).

References

[1] D. L. Marchisio, R. O. Fox, Computational Models for Polydisperse Particulate and Multiphase Systems Providing, Cambridge Series in Chemical Engineering, 2013.
[2] R. O. Fox, Large-Eddy-Simulation Tools for Multiphase Flows, Annual Review of Fluid Mechanics 44 (1) (2012) 47–76.
[3] F. A. Williams, Spray combustion and atomization, Physics of Fluids 1 (6) (1958) 541–545.
[4] C. Cercignani, The Boltzmann equation and its applications, Vol. 67, 1988.
[5] S. Balachandar, A scaling analysis for point-particle approaches to turbulent multiphase flows, International Journal of Multiphase Flow 35 (9) (2009) 801–810.
[6] F. Laurent, A. Vié, C. Chalons, R. O. Fox, M. Massot, A hierarchy of Eulerian models for trajectory crossing in particle-laden turbulent flows over a wide range of Stokes numbers, Proceedings of the Summer Program 2012 - Center for Turbulence Research (2012) 193–204.
[7] J. Ferry, S. Balachandar, A fast Eulerian method for disperse two-phase flow, International Journal of Multiphase Flow 27 (7) (2001) 1199–1226.
[8] Y. Forterre, O. Pouliquen, Flows of Dense Granular Media, Annual Review of Fluid Mechanics 40 (1) (2008) 1–24.
[9] H. Struchtrup, Macroscopic Transport Equations for Rarefied Gas Flows Approximation, Springer Berlin Heidelberg, 2005.
[10] O. Desjardins, R. O. Fox, P. Villedieu, A quadrature-based moment method for dilute fluid-particle flows, Journal of Computational Physics 227 (4) (2008) 2514–2539.
[11] I. Ayranci, S. M. Kresta, J. J. Derksen, Experiments and simulations on bidisperse solids suspension in a mixing tank, Chemical Engineering and Technology 36 (11) (2013) 1957–1967.
[12] B. Blais, F. Bertrand, CFD-DEM investigation of viscous solidliquid mixing: Impact of particle properties and mixer characteristics, Chemical Engineering Research and Design 118 (2014) (2017) 270–285.

[13] R. O. Fox, F. Laurent, M. Massot, Numerical simulation of spray coalescence in an Eulerian framework: Direct quadrature method of moments and multi-fluid method, Journal of Computational Physics 227 (6) (2008) 3058–3088.
[14] A. Passalacqua, J. E. Galvin, P. Vedula, C. M. Hrenya, R. O. Fox, A quadrature-based kinetic model for dilute non-isothermal granular flows, Communications in Computational Physics 10 (1) (2011) 216–252.
[15] C. Yuan, R. Fox, Conditional quadrature method of moments for kinetic equations, Journal of Computational Physics 230 (22) (2011) 8216–8246.
[16] A. Vié, F. Doisneau, M. Massot, A. Vié, F. Doisneau, M. Massot, A. Gaussian, A. Vi, On the anisotropic gaussian velocity closure for inertial- particle laden flows, Communications in Computational Physics 17 (2015) 1–46.
[17] R. O. Fox, F. Laurent, A. Vié, Conditional hyperbolic quadrature method of moments for kinetic equations, Journal of Computational Physics 365 (2018) 269–293.
[18] R. McGraw, Description of Aerosol Dynamics by the Quadrature Method of Moments, Aerosol Science and Technology 27 (2) (1997) 255–265.
[19] J. C.Wheeler, Modified moments and guassian quadrature, Rock mountain journal of mathematics 4 (2) (1974) 287–296.
[20] V. Vikas, Z. J. Wang, A. Passalacqua, R. O. Fox, Realizable high-order finite-volume schemes for quadrature-based moment methods, Journal of Computational Physics 230 (13) (2011) 5328–5352.
[21] C. Chalons, D. Kah, M. Massot, Beyond pressureless gas dynamics: Quadrature-based velocity moment models, Communications in Mathematical Sciences 10 (4) (2012) 1241–1272.

Large Eddy Simulations on a Natural Convection Boundary Layer at Prandtl numbers 0.71 and 0.025

Agustín Villa Ortiz

Environmental and Applied Fluid Dynamics Department, von Karman Institute for Fluid Dynamics, Belgium, villaortiz@vki.ac.be

Supervisor: Jean-Marie Buchlin

Full Professor, Environmental and Applied Fluid Dynamics Department, von Karman Institute for Fluid Dynamics, Belgium, buchlin@vki.ac.be

University Supervisor: Tony Arts

Professor, Institute of Mechanics, Materials and Civil Engineering (IMMC), Université Catholique de Louvain, Belgium, arts@vki.ac.be

Abstract

The development of Generation IV nuclear reactors involves the research of liquid metal coolants, considered as appropriate coolant agents due to their high heat transfer properties, lowering the hazard of nuclear energy. Liquid metals are characterized by a very low Prandtl number (between $0.006 - 0.025$). The design of new reactors consists of a numerical modelling phase, where computational fluid dynamics handles the momentum and heat transfer between the core and heat exchangers, and the thermal hydraulic phenomena that occur during the reactor operation. Several scenarios must be considered to ensure a proper reactor design. Two of them are the maintenance scenario or the loss-of-flow, where there are no devices pumping the liquid metal inside the reactor. A natural circulation loop establishes inside the reactor, and as a part of the passive cooling design, the evaluation of this loop is crucial to avoid undesired fluid stratification or thermal stresses. To do so, designers are normally supported by numerical approaches, where the relevant physics within the reactor must be included. Considering the nuclear reactor thermal hydraulics, RANS simulations are chosen to model the reactor. However, the actual status of turbulence RANS modelling in the particular case of low Prandtl numbers presents deficiencies that compromise the accuracy of the reactor simulation and therefore, the nuclear reactor design. In the present article, Large Eddy Simulations over a natural convection boundary layer at $Pr = 0.025$ are presented and described, in order to assess and validate RANS thermal models. Turbulence is triggered in these simulations by adding a perturbation in the boundary layer. The used numerical approach is validated in a Large Eddy Simulation at $Pr = 0.71$, where heat transfer, friction coefficient and mean and turbulent flow fields are compared with literature. Once turbulence is reached in the Pr=0.025 boundary layer, flow characteristics as Nusselt number, skin friction coefficient and turbulent profiles are calculated and compared with the Pr=0.71 simulation.

Keywords: natural convection, low prandtl number, turbulent boundary layer, large eddy simulation, OpenFOAM

1. Introduction

The energy demand of society is increasing continuously. Petroleum and gas as main raw energy sources cannot support this growth. Moreover, their environmental impact pushes towards an energy production with reduced pollution levels, specially in terms of CO2 footprint. As currently renewable energy is unable to supply the needs of humanity, nuclear reactors play an important role in electricity production.

During 2017, nuclear energy provided the 10.3% of the worldwide electricity, and the 25.2% inside the European Union [1]. However, the events of the Fukushima Daiichi accident have provoked a decay of interest in nuclear energy in near-term. Despite this problematic, the nuclear energy long-term perspectives are positive, due to the zero CO2 footprint, and the increasing energy demand [2].

The nuclear industry learns from the past, and nowadays the Generation IV nuclear power plants goals include the increase of safety during operation and in case of anomalies or accidents. Generation IV reactors consider heavy liquid metals as coolant agents [3]. Their thermal and neutronic properties ensure a good heat removal from the core, and a better control during the operation phase. In case of accidental (loss of coolant flow) or maintenance scenarios, where the pumps may fail, the fluid is not driven by external forces any more. The difference of temperatures within the reactor will induce a natural convection mechanism, where the liquid metal is driven by buoyancy forces. Phenomena such as temperature stratification or increase of thermal stresses in critical locations would cause undesired damage to the reactor integrity, thus compromising the reactor's safety. The correct understanding and quantification of heat transfer mechanisms in this flow regime are of great importance.

Within the European Union, diverse groups are concerned about the design of Generation IV reactors. Before the construction of such nuclear power plants, smaller research reactors are in phase design. Currently four demonstration reactors are nowadays in design and development in Europe. One of them is the MYRRHA (Multi-purpose hYbrid Research Reactor for High-tech Application) reactor [4; 5]. It is an accelerator driven system, able to operate in sub-critical and critical mode. MYRRHA uses a lead bismuth eutectic alloy (LBE) to remove the produced heat during the nuclear reaction.

During the design phase of the MYRRHA reactor, the thermal hydraulics of liquid metals is needed to be characterized. European projects such as the FP7 THINS, and the Horizon 2020 MYRTE and SESAME targets the better understanding of liquid metals thermal hydraulics. As the opaque nature of liquid metals restricts the measurement resolution, an effort has been done in high fidelity numerical simulations to obtain a better knowledge of liquid metal turbulent momentum and heat transfer.

In fluid mechanics, one of the main characteristic of liquid metals is their low Prandtl number value. The Prandtl number is defined as the ratio between the kinematic viscosity ν and the thermal diffusivity α:

$$Pr = \frac{\nu}{\alpha} \tag{1}$$

This dimensionless number relates the diffusion rate of momentum and thermal energy. In liquid metals varies between $0.1 - 0.001$. It implies that the thermal diffusion is much faster than the momentum one. It is observed that the thickness of thermal boundary layers are affected by the Prandtl number. Low Prandtl numbers leads to thick temperature boundary layers in comparison with the velocity ones, and viceversa.

Direct Numerical Simulations and Large Eddy Simulations at low Prandtl numbers have been performed for some prototype configurations, such channel flows [6; 7], non conventional walled flows [8; 9; 10], impinging jets, mixing layers [11], and backward facing steps [12; 13].

The previous cases cover the forced and mixed convection flow regime. The fluid is driven by external forces, strong enough to restrict the thermal effects in the flow. Except the case of Rayleigh Benard cells [14], the author is not aware of pure natural convection flows in high fidelity simulations. A huge effort has been done in forced convection and a good understanding of low Prandtl number fluids has been collected, however the natural convection scenarios that one faces in a nuclear reactor still need to be studied. As equal as it has been done in the forced convection regime, an increase of numerical simulations in natural convection would benefit the knowledge of liquid metals, and improve the design of facilities using them.

In the present article, LES of turbulent natural convection boundary layers (TNCBL) is presented. Two Prandtl numbers, $Pr = 0.71$ and 0.025 are considered. The first one corresponds to air as working fluid, while the second one to LBE. Transition is triggered in both simulations to ensure reaching the turbulent regime. A comparison in function of the Prandtl number is carried out, in terms of heat transfer, wall shear stress, velocity, temperature and turbulent fluctuations.

2. Numerical methodology

2.1. Governing equations discretization

In Large Eddy Simulations, the Navier-Stokes equations are filtered in space. Only the large motion scales are resolved, while the small ones are modelled. For a natural convection flow, buoyancy forces are taken into account in the system of equations. Considering constant fluid properties, the filtered incom-

pressible Navier Stokes equations are written as:

$$\frac{\partial U_j}{\partial x_j} = 0 \tag{2}$$

$$\frac{\partial U_i}{\partial t} + \frac{\partial U_i U_j}{\partial x_j} = -\frac{\partial P}{\partial x_i} + \nu \frac{\partial^2 U_i}{\partial x_j^2} - \frac{\partial \tau_{ij}}{\partial x_j} + g_i \left(1 - \beta \left(T - T_{ref}\right)\right) \tag{3}$$

$$\frac{\partial T}{\partial t} + \frac{\partial U_j T}{\partial x_j} = \alpha \frac{\partial^2 T}{\partial x_j^2} - \frac{\partial \pi_j}{\partial x_j} \tag{4}$$

where P is the reduced pressure $P = p/\rho$, and $g_i\,(1 - \beta \Delta T)$ is the buoyant source modelled by using the Boussinesq approximation [15; 16]. The temperature difference is defined as $\Delta T = T - T_{ref}$.

The filtering process introduces two new terms in Eqs. (3) and (4): the sub-grid stress tensor τ_{ij} and the sub-grid heat flux π_j, allowing the closure of the filtered Navier Stokes equations. In the present work, they are modelled based in the simple gradient hypothesis of Boussinesq. The sub-grid tensor is then defined as:

$$\tau_{ij} = -2\nu_{sgs} S_{ij} \tag{5}$$

being ν_{sgs} the sub-grid viscosity, and S_{ij} the filtered gradient tensor:

$$S_{ij} = \frac{1}{2}\left(\frac{\partial U_i}{\partial x_j} + \frac{\partial U_j}{\partial x_i}\right) \tag{6}$$

In the present investigation, the WALE model [17] is used to compute ν_{sgs}.

The sub-grid heat flux is defined in a similar form:

$$\pi_j = -\alpha_{sgs} \frac{\partial T}{\partial x_j} \tag{7}$$

where α_{sgs} is the sub-grid thermal diffusivity. Analogously to Eq. (1), the sub-grid Prandtl number is defined as:

$$Pr_{sgs} = \frac{\nu_{sgs}}{\alpha_{sgs}} \tag{8}$$

In most of the LES literature, a value $Pr_{sgs} = 0.4 - 0.5$ is recommended. In the present work, the value $Pr_{sgs} = 0.5$ is adopted during the simulations of TNCBL at $Pr = 0.71$. In the case of $Pr = 0.025$ simulations, no sub-grid model for π_j is employed. This last choice is based on the mesh criteria by Grötzbach [18]. When decreasing the Prandtl number, the thermal structures become larger than the momentum ones, so if the mesh is capable to resolve most of the momentum, no thermal sub-grid model is needed since the thermal field is completely resolved.

The open source code OpenFOAM v5.0 has been used to perform the calculations [19]. The PISO algorithm has been used to couple pressure and velocity fields. The equations are discretized following the finite volume method. An implicit backward, unbounded second order scheme has been used in the time derivatives, while a second order central differencing is applied in the spatial derivatives.

2.2. *Boundary and initial conditions*

A general sketch of the TNCBL simulations is presented in Fig. 1. It is divided in two blocks in the y direction: the one in contact with the wall, and the other in contact with the bottom boundary. They both share the inlet boundary, and the spanwise patches. The spanwise patches are considered periodic boundaries. The inlet boundary has a time depending flux:

$$\phi = \frac{\sum_j A_j \phi_j}{\sum_i A_i} \tag{9}$$

applied uniformly in all its extension, ensuring continuity. The index j indicates the $j - th$ outlet face, while $i - th$ does the same in the inlet patch. A is the face area and ϕ is the flux passing through it. The wall is heated at a temperature T_h, while the fluid enters at the inlet with T_c. No-slip conditions are applied on the wall. On the outlet, a zero gradient condition is applied for all the variables except the velocity, that is defined as an advective boundary condition.

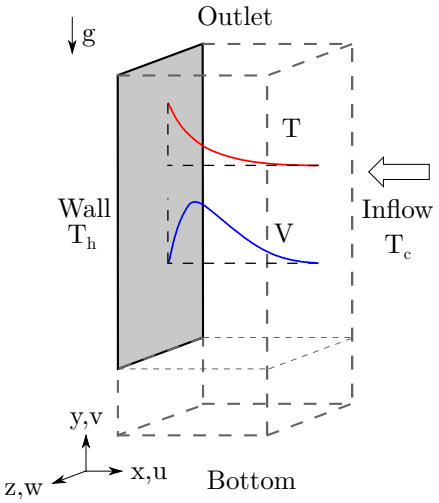

Figure 1: Computational domain of TNCBL simulations.

In the bottom block, slip conditions are applied in the patch below the wall and in the bottom boundary. The fluid is then forced to enter into the domain only through the inlet.

The flow is initialized with a laminar profile for velocity and temperature, inspired by the calculations of [20].

2.3. Transition triggering technique

The use of a triggering technique is highly recommended to promote the flow to turbulence ([21]). The proposed method consists in the excitation of the natural frequency of the boundary layer simulation. The flow fluctuations at that frequency get amplified, and introduce enough disturbances in the flow to turn it turbulent. Sayadi [22] introduced this methodology in forced convection boundary layers with satisfactory results. In this study, a velocity perturbation is introduced in the wall, at a location y_p. The velocity fluctuation is introduced in the direction normal to the wall as:

$$u_w = \begin{cases} \mathcal{U}\psi(y_s)\sin(2\pi f_n t) & \text{if } y_i < y < y_p \\ \mathcal{U}\psi(y_e)\cos(2\pi f_n t) & \text{if } y_p < y < y_f \end{cases} \tag{10}$$

$$y_i = y_p - \lambda \tag{11}$$

$$y_f = y_p + \lambda \tag{12}$$

$$\psi(y) = 15.1875y^5 - 35.4375y^4 + 20.25y^3 \tag{13}$$

$$y_e = \frac{y - y_i}{y_p - y_i} \tag{14}$$

$$y_f = \frac{y_f - y}{y_f - y_p} \tag{15}$$

being $\mathcal{U}$ and f_n the amplitude and frequency of the oscillation. The perturbation is applied in the range $y_i - y_f$, which is centered in y_p. Out of this range, no slip condition is applied.

3. Results and discussion

3.1. Simulation configuration

Following the described numerical methodology, four different LES of a TNCBL are presented in this Section. Two fluids with Prandtl numbers of 0.71 and 0.025 are considered, and the previous transition technique has been used to promote turbulence as soon as possible. The proposed simulations are presented in Table 1. The lengths L_i^* are computed as $L_i^* = L_i/L_b$, where $L_b = \left(\nu^2/(g\beta\Delta T)\right)^{1/3}$ $[m]$.

To perform an appropriate comparison, the maximum Rayleigh number $Ra = 2.9 \cdot 10^{11}$ is required in all the simulations. Due to the two different Prandtl number values, the length of the $Pr = 0.025$ boundary layers is larger in order to accomplish this Rayleigh number condition. Two different regions are considered in the computational domain: the one that contains the heated plate, and the slip one located in the bottom. For both regions, the mesh in the x direction increases exponentially, and ensures a first grid point of $x_1^* = 0.001$. An uniform cell distribution is applied in the y and z directions.

For both Prandtl numbers, one simulation was performed with and without a transition control technique. When applied, the perturbations parameters are given in Table 2. Frequency is expressed as $f_n^* = f_n * t_b$, where $t_b = \left(\nu/(g\beta\Delta T)^2\right)^{1/3}$ $[s]$. Similarly, the velocity amplitude is expressed as $A^* = A/u_b$, where $u_b = (g\beta\Delta T\nu)^{1/3}$ $[m/s]$.

3.2. Comparison of NCTBL of Pr=0.71 and Pr=0.025

Once the simulations has reached the statistical steady state, they are averaged in time and along the spanwise direction. The Nusselt number relates the heat transfer by conduction in the wall and the one by convection within the fluid. Its expression is:

$$Nu = \frac{q_w y}{\kappa \Delta T} = \frac{hy}{\kappa} \tag{16}$$

where q_w is the wall heat flux at a location y in the plate, and κ the thermal conductivity. The wall heat flux and the reference temperature difference are grouped in the convective heat transfer coefficient h. The representation of the Nusselt number for all the simulations is shown in Fig. 2. The two linear trends in the left and the right indicate the Nusselt number evolution in the laminar and turbulent regions. At intermediate values of Rayleigh, transition occurs. Comparing Air1 with Air2, and LBE1 with LBE2 shows that the transition takes place significantly earlier when turbulence is triggered by the applied transition technique. It allows to study the turbulent region for an extended range. If no transition control is applied, the boundary layer turns to turbulence around $Ra = 2 \cdot 10^{10} - 9 \cdot 10^{10}$ for both Prandtl numbers. As it is observed, the transition location decreases one approximately order of magnitude in terms of Rayleigh number. It really helps to compare the present Air1 and Air2 simulations against the experimental data and correlations denoted in Fig. 2.

Case	Pr	Gr	Ra	$L_x^* \times \left(L_y^* + L_{y,s}^*\right) \times L_z^*$	$N_x \times \left(N_y + N_{y,s}\right) \times N_z$	Perturbation
Air 1	0.71	$4.10 \cdot 10^{11}$	$2.9 \cdot 10^{11}$	$3920 \times (7430 + 1486) \times 930$	$100 \times (512 + 102) \times 128$	No
Air 2	0.71	$4.10 \cdot 10^{11}$	$2.9 \cdot 10^{11}$	$3920 \times (7430 + 1486) \times 930$	$100 \times (512 + 102) \times 128$	Table 2
LBE 1	0.025	$1.16 \cdot 10^{13}$	$2.9 \cdot 10^{11}$	$3920 \times (22668 + 1486) \times 930$	$100 \times (1562 + 102) \times 128$	No
LBE 2	0.025	$1.16 \cdot 10^{13}$	$2.9 \cdot 10^{11}$	$3920 \times (22668 + 1486) \times 930$	$100 \times (1562 + 102) \times 128$	Table 2

Table 1: Information of cases: name, Prandtl, Grashof, Rayleigh numbers, dimensions of the heated plate and number of cells on the different directions.

Case	y_p^*	λ^*	f_n^*	$\mathcal{U}^*$
Air 2	215	18.34	$7.342 \cdot 10^{-2}$	1.367
LBE 2	215	85	$5.160 \cdot 10^{-2}$	8.749

Table 2: Information of applied perturbations: location in the wall and length amplitude on it, frequency and velocity fluctuation.

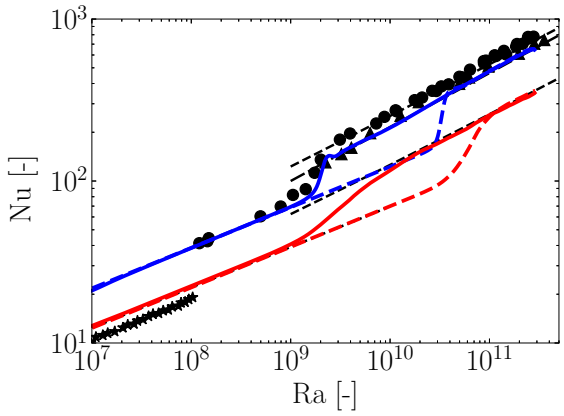

Figure 2: Nusselt number for cases Air1 (blue dash), Air2 (blue solid), LBE1 (red dash), LBE2 (red solid) compared with the experiments of Saunders [23] (▲), Tsuji [24] (•), Sparrow's analytical solution [25] (dots), Bayley's [26] (black dotted dash) and Churchill's correlations [27] (dash), and experiments of Humphreys [28] (⋆).

One can see that the laminar regime is well captured by both simulations with $Pr = 0.71$. The triggering technique allows Air2 to get close to the experimental transition of Tsuji [24]. However, the Nusselt number values obtained in the turbulent regime are slightly underestimated when comparing Air1 and Air2 against Tsuji's data. The simulations provide a good agreement when comparing with the experiments of Saunders [23] and the correlation of Bayley [26]. In the case of the low Prandtl number simulations, a good agreement is found with the analytical solution of Sparrow [25]. Evermore, the experiments of Humphreys [28] are close to the numerical results. This reference data, obtained in a vertical channel flow with isothermal walls for mercury ($Pr = 0.023$), yields still in the laminar region. Regarding the turbulent region, simulations collapses with the turbulent correlation of Churchill [27]. Although the lack of experiments is needed to have a proper validation of the presented heat transfer ratios, the existing solutions and correlations increase the confidence on the present simulations. They can be considered as a good reference data and used in the assessment of further investigations.

It is observed that the Nusselt number magnitude decreases with the Prandtl number. Indeed, the laminar Nusselt prediction is 1.75 times lower in the case of $Pr = 0.025$. This ratio increases in the turbulent region to $1.8 - 2$. An explanation can be found when considering the convective heat transfer coefficient h. This parameter is expressed in terms of the Stanton number:

$$St = \frac{h}{\rho C_p u_b} \tag{17}$$

whose evolution for the precedent cases is shown in Fig. 3. The Stanton number identifies the ratio between the heat transferred into the fluid and its thermal capacity. It is evident that LBE cases have a higher Stanton number, thus it collects easily the thermal energy from the wall. The immediate effect is that the

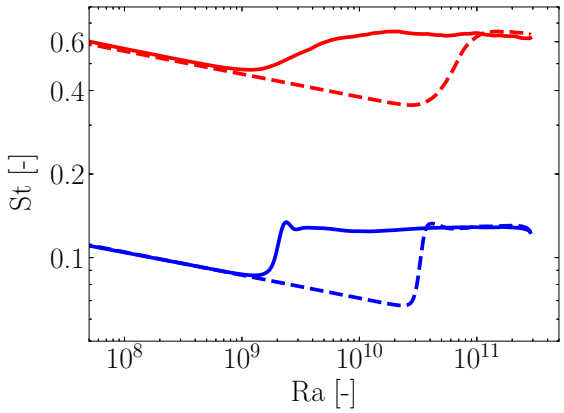

Figure 3: Stanton number for cases Air1 (blue dash), Air2 (blue solid), LBE1 (red dash) and LBE2 (red solid).

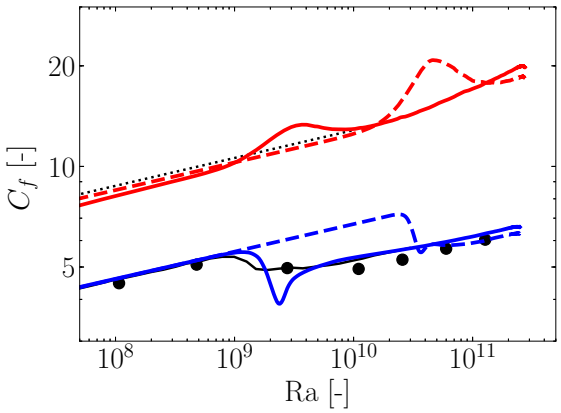

Figure 4: Skin friction coefficient for cases Air1 (blue dash), Air2 (blue solid), LBE1 (red dash), LBE2 (red solid) compared with the experiments of Tsuji [24] (•), LES of Nakao [29] (black solid) and Sparrow's analytical solution [25] (dots).

thermal effects develops further to the wall in the LBE case than in the air one. Temperature gradients in the case of low Prandtl numbers are then less steep, affecting directly to the Nusselt number prediction. The opposite case is found for the air simulations: strong gradients are expected close to the wall. When considering the Nusselt number in terms of wall heat flux and thermal conductivity ()$\kappa_{LBE} = 10.72\ W/m\ K$ and $\kappa_{air} = 0.02624\ W/m\ K$), the existing temperature gradient is linked to the differences in the thermal fluid properties. Such difference of magnitude in the thermal conductivity is the responsible for the observed Nusselt distribution.

The skin friction coefficient is presented in Fig. 4. Its is defined as:

$$C_f = \frac{\|\tau_w\|}{\frac{1}{2}\rho u_b^2} \tag{18}$$

where τ_w is the wall shear stress. In Fig. 4 the skin friction coefficient is presented for the four different simulations. At low Rayleigh numbers, the laminar region is found where the skin friction coefficient follows a linear trend. There, both Air and LBE simulations follow adequately the reference databases. The C_f rise is interrupted by the transitional regime. Cases of Air1 and Air2 show an abrupt decrease when turning turbulent, while for the cases with $Pr = 0.025$, a local maximum is observed. After reaching a peak value, the skin friction coefficient increases linearly. This behaviour is the one of the turbulent region, at high Rayleigh values.

An increment is found on the skin friction coefficient when decreasing the Prandtl number. The wall shear stress is significantly higher for the LBE cases. In the laminar region, a factor 1.84 is found between the $Pr = 0.025$ and 0.71 predictions, while in the turbulent one this ratio varies between $2.4 - 3.1$. An explanation is found when the buoyancy forces are compared in function of the Prandtl number. According to the Boussinesq approximation of Eq. (3), the buoyant forces depend on the temperature field. High temperature differences will ensure a strong buoyant phenomenon. Observing the instantaneous velocity and temperature fields of Air2 in Figs. 5 and 6, and comparing against the ones of LBE2 of Figs. 7 and 8, shows that the boundary layer is larger in the low Prandtl number flow. The difference in size ensures a bigger high temperature region in the cases of LBE1 and LBE2. The buoyant forces are then stronger for $Pr = 0.025$ than $Pr = 0.71$. The increase of the driving force results in a velocity increase. Then, close to the wall, the viscous forces balance the buoyant ones close to the wall, and it results in an increment of the wall shear stress.

The instantaneous velocity and temperature fields for the Air2 case are presented in Figs. 5 and 6. The thermal and momentum boundary layers are very thin in the laminar region. When transition appears after $Ra = 10^9$, fluctuations in velocity and temperature appear. Then, the boundary layer increases its size rapidly. A similar behaviour is found for the case LBE2 in Figs. 7 and 8. In this low Prandtl number case, the velocity magnitude increases due to the stronger buoyant forces. The fluctuations between

$10^8 < Ra < 10^9$ that lead the flow into the turbulent state are larger in this case than at $Pr = 0.71$

From this point, only Air2 and LBE2 simulations are compared, as they present a larger turbulent region than Air1 and LBE1. The database of Tsuji [24] has been employed to compare the results of Air2. Air1 and Air2 have a better agreement in terms of Nusselt number with [23; 26], however these references do not provide information about the velocity and temperature boundary layer.

Figure 9 presents the dimensionless streamwise velocity $\langle V \rangle^+$, referred in wall units:

$$\langle V \rangle^+ = \frac{\langle V \rangle}{u_\tau} \tag{19}$$

$$u_\tau = \sqrt{\frac{\tau_w}{\rho}} \tag{20}$$

where u_τ is the friction velocity. The distance with the wall is expressed as:

$$x^+ = \frac{x u_\tau}{\nu} \tag{21}$$

The velocity profiles in Fig. 9 corresponds to the laminar region, characterized by a sharp peak. An internal linear inner sublayer $\langle V \rangle^+ = x^+$ is found in both Prandtl number simulations until approximately $x^+ \approx 5$. The simulation at low Prandtl number has a thicker boundary layer, and velocity is larger in comparison with the air case. The $Pr = 0.71$ case is in good agreement with the measurements of Tsuji.

In the turbulent region, the velocity fields behave as shown in Fig. 10. The linear sublayer is also present in the turbulent regime, but several differences are clearly visible. The first one is that the velocity magnitude increases. Then, the sharp profile of Fig. 9 disappears, and the velocity peak becomes slightly flat. The boundary layer thickness increases respect to the laminar profile. Again, the air simulation reproduces accurately the experiments of Tsuji.

The temperature is also evaluated referring to the wall properties:

$$\langle T \rangle^+ = \frac{T - T_h}{T_\tau} \tag{22}$$

$$T_\tau = \frac{q_w}{\rho C_p u_\tau} \tag{23}$$

where T_τ is the friction temperature, and C_p is the specific heat of the fluid. The laminar temperature profile is presented in Fig. 11. The linear sublayer extends until $Pr \cdot x^+ \approx 8$ in the $Pr = 0.71$ case and $Pr \cdot x^+ \approx 2$ for $Pr = 0.025$. A good prediction is retrieved by the simulation with $Pr = 0.71$ in the laminar region compared against the experiments of Tsuji [24]. The temperature magnitude is significantly reduced in the LBE simulation, compared to the air one. When considering the turbulent prediction, the LES is not able to capture properly the temperature field for the air case. The differences in the Nusselt number prediction between the experiments of Tsuji and the present LES are responsible of this mismatch in the temperature prediction. After the linear sublayer, a logarithmic region is observed for air in the range $Pr \cdot x^+ = 100 - 1000$, and $60 - 80$ for $Pr = 0.025$.

The resolved velocity fluctuations in the streamwise direction $\langle v'v' \rangle^{1/2^+}$ are considered in Fig. 13. It is expressed dividing the fluctuations by the friction velocity of Eq. (20). The air simulation has a good agreement with the experimental data. Between $x^+ = 1-10$, the velocity fluctuations increases rapidly, and after they increase at a lower rate until its maximum value reached in $x^+ = 400$. Then, fluctuations go to zero when approaching the end of the boundary layer. In the case of the LBE boundary layer, the fluctuations appear closer to the wall. The maximum velocity fluctuation is reached at $x^+ = 10$. Differently from the case with $Pr = 0.71$, a second slightly maximum is found in $x^+ = 1000$. Then, fluctuations decrease until the end of the boundary layer. Both the fluctuating and the mean velocities are larger for lower Prandtl numbers.

The resolved thermal fluctuations $\langle T'T' \rangle^{1/2^+}$ decrease with the Prandtl number, as one can see in Fig. 14. The friction temperature was used to compute its dimensionless form. As for the mean temperature profile, in the turbulent region the fluctuations are overpredicted at $Pr = 0.71$. Nevertheless, the location of the maximum $\langle T'T' \rangle^{1/2^+}$value is well predicted in $Prx^+ = 12.8$. It corresponds to the region between the linear and logarithmic sublayers. Fluctuations tend to zero as they approach the end of the boundary layer. The LBE maximum value is reached around $Prx^+ = 5.4$. Fluctuations are weaker in this last case. Indeed, the thermal scales are larger when compared with the $Pr = 0.71$ case, resulting in smaller fluctuations.

The resolved Reynolds stress component $\langle u'v' \rangle^+$is presented in Fig. 15. Experiments and simulations have the same profile shape for $Pr = 0.71$. Close to the wall, the stress is negligible, but then, negative $\langle u'v' \rangle^+$values are observed. The stress increases in magnitude, and reaches its maximum value at $x^+ = 380$. After $\langle u'v' \rangle^+$ decreases until the end of the boundary layer. The LBE stress magnitude is larger

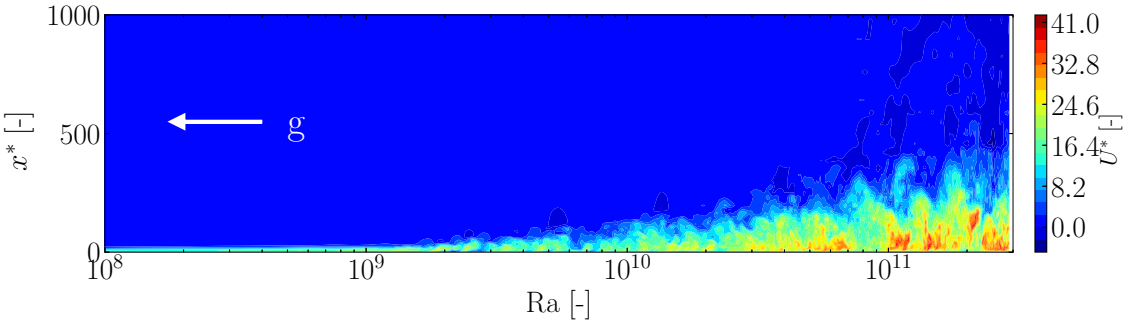

Figure 5: Instantaneous velocity field for Air2, Pr = 0.71.

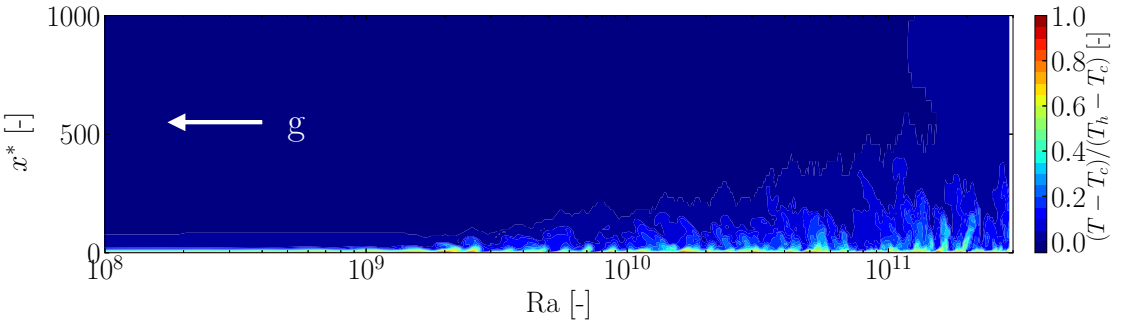

Figure 6: Instantaneous temperature field for Air2, Pr = 0.71.

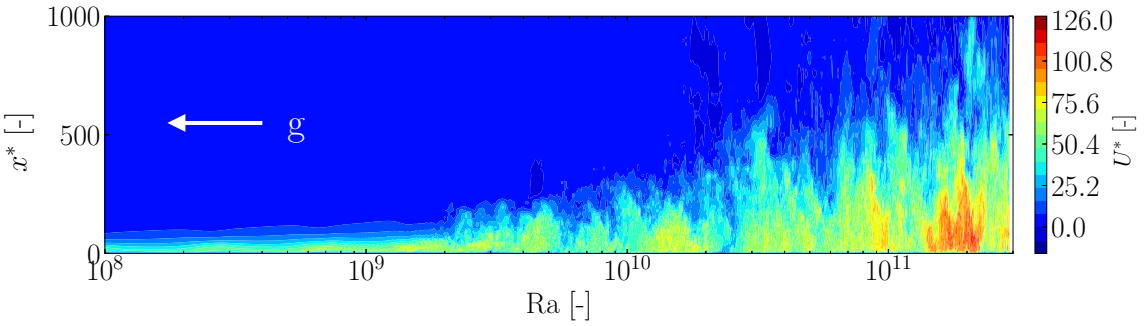

Figure 7: Instantaneous velocity field for LBE2, Pr = 0.025.

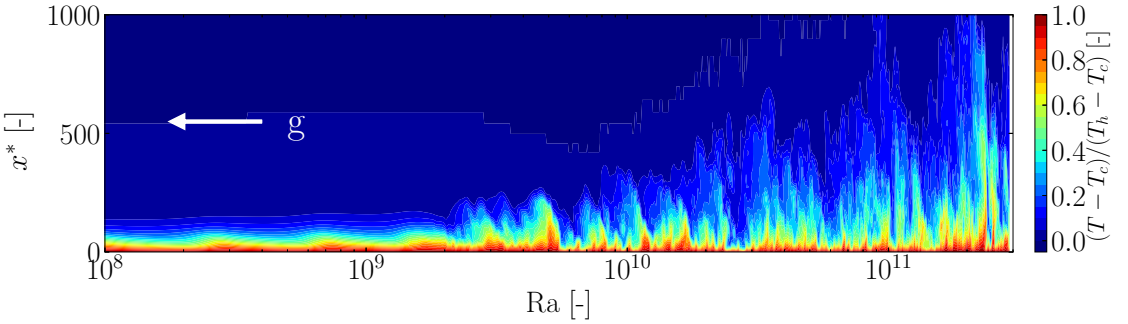

Figure 8: Instantaneous temperature field for LBE2, Pr = 0.025.

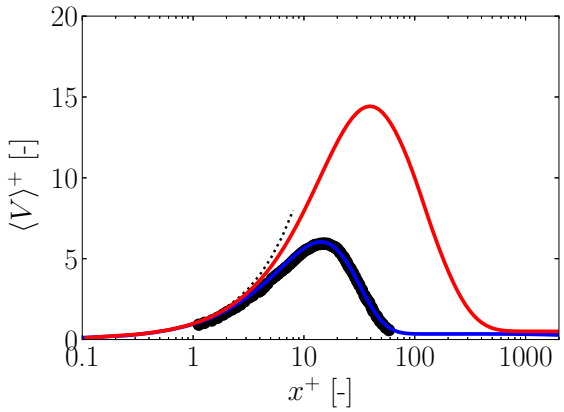

Figure 9: Velocity profile $\langle V \rangle^+$ for Air2 (blue), LBE2 (red) and experiments of Tsuji [24] (•), at $Ra = 1.08 \cdot 10^8$.

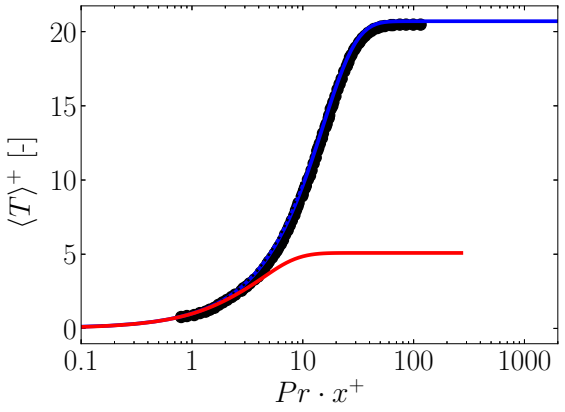

Figure 11: Temperature profile $\langle T \rangle^+$ for Air2 (blue), LBE2 (red) and experiments of Tsuji [24] (•), at $Ra = 1.08 \cdot 10^8$.

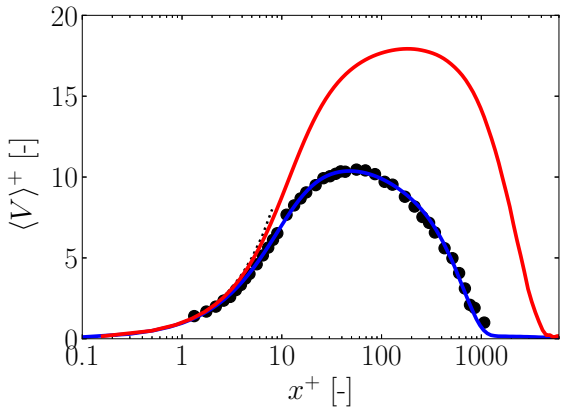

Figure 10: Velocity profile $\langle V \rangle^+$ for Air2 (blue), LBE2 (red) and experiments of Tsuji [24] (•), at $Ra = 1.28 \cdot 10^{11}$.

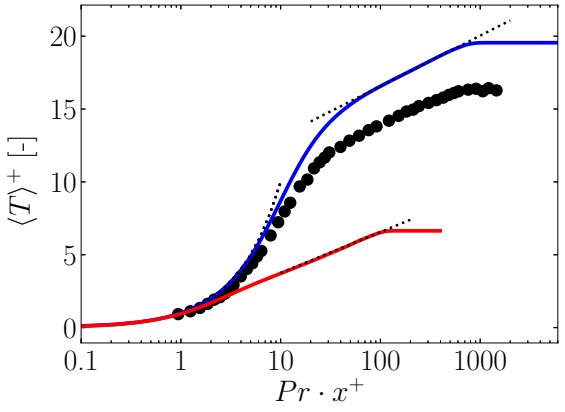

Figure 12: Temperature profile $\langle T \rangle^+$ for Air2 (blue), LBE2 (red) and experiments of Tsuji [24] (•), at $Ra = 1.28 \cdot 10^{11}$.

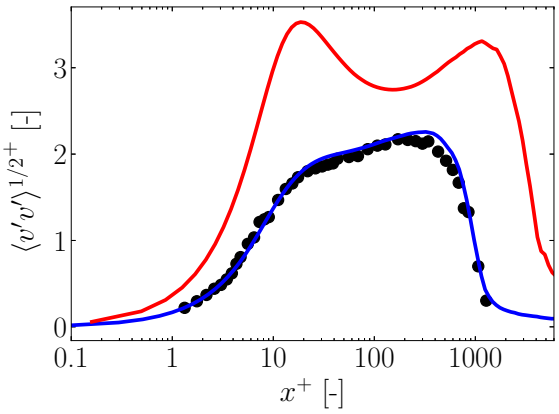

Figure 13: Velocity fluctuations profile $\langle v'v' \rangle^{1/2^+}$ for Air2 (blue), LBE2 (red) and experiments of Tsuji [24] (•), at $Ra = 1.28 \cdot 10^{11}$.

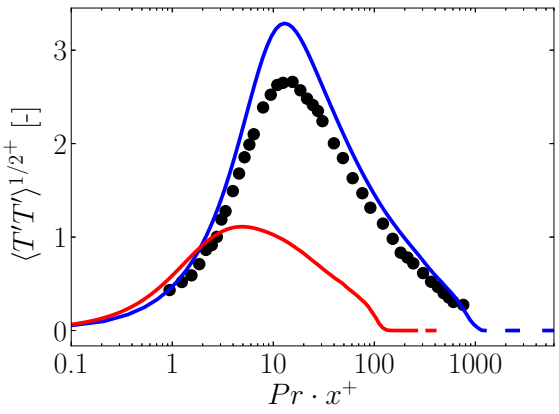

Figure 14: Temperature fluctuations profile $\langle T'T' \rangle^{1/2^+}$ for Air2 (blue), LBE2 (red) and experiments of Tsuji [24] (•), at $Ra = 1.28 \cdot 10^{11}$.

than the air case, and its maximum is reached at $x^+ = 1400$. The minimum and maximum locations are then delayed in space as the Prandtl number decreases.

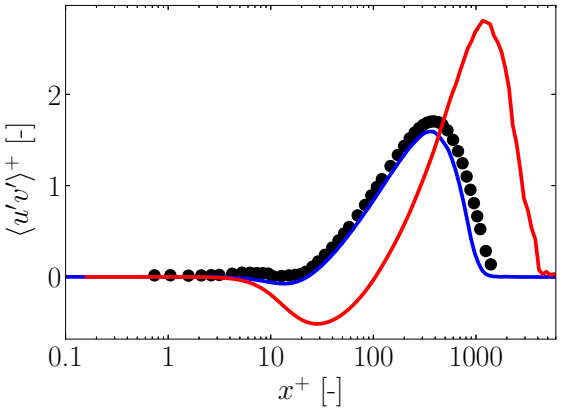

Figure 15: Reynolds stress profile $\langle u'v' \rangle^+$ for Air2 (blue), LBE2 (red) and experiments of Tsuji [24] (•), at $Ra = 1.52 \cdot 10^{11}$.

The resolved heat fluxes are also studied. The normalwise component $\langle u'T' \rangle^+$in Fig. 16 shows that its magnitude decreases with the Prandtl number. Also, the flux profile develops later in terms of the distance with the wall x^+. The LBE heat flux $\langle u'T' \rangle^+$has a comparable magnitude with the one of air, slightly lower. The larger thermal conductivity of LBE redistributes efficiently the injected heat, decreasing the temperature gradients. The same is found in the streamwise

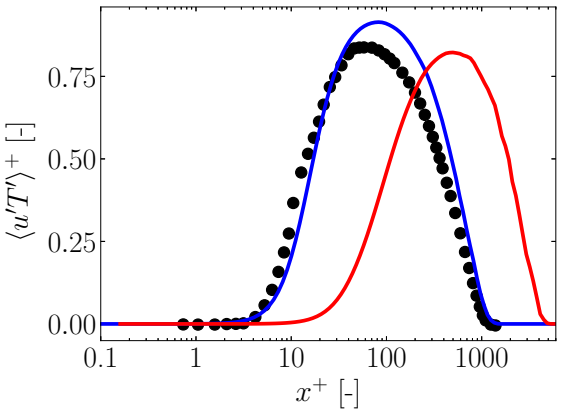

Figure 16: Normalwise turbulent heat flux profile $\langle u'T' \rangle^+$ for Air2 (blue), LBE2 (red) and experiments of Tsuji [24] (•), at $Ra = 1.28 \cdot 10^{11}$.

turbulent heat flux $\langle v'T' \rangle^+$shown in Fig. 17. In this

case, negative values of $\langle v'T' \rangle^+$are found, as for the stresses $\langle u'v' \rangle^+$. In this case, the difference in the heat flux value are more evident than in the heat flux component $\langle u'T' \rangle^+$. For both turbulent heat flux compo-

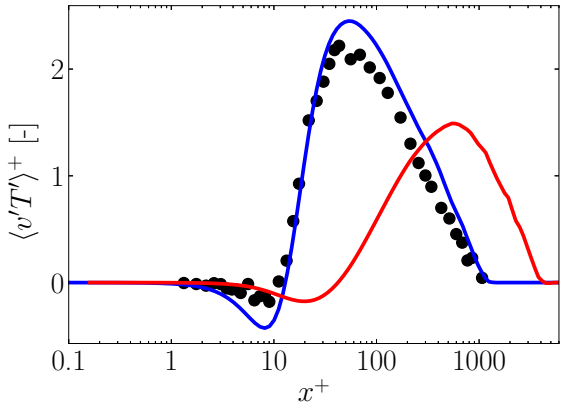

Figure 17: Streamwise turbulent heat flux profile $\langle v'T' \rangle^+$ for Air2 (blue), LBE2 (red) and experiments of Tsuji [24] (•), at $Ra = 1.28 \cdot 10^{11}$.

nents, the simulations are in good agreement with the experiments of Tsuji in case of $Pr = 0.71$.

4. Conclusions

In this investigation, turbulent natural convection boundary layers have been studied by means of Large Eddy Simulations. A triggering technique has been used with the objective of promote turbulence as early as possible. Two Prandtl numbers (0.71 and 0.025) have been used to carry out the simulations.

Results have shown that the Nusselt number value is drastically affected by the Prandtl number value. A low Prandtl number decreases the Nusselt number value, and increases the skin friction coefficient magnitude. The boundary layer thickness enlarges when considering low Prandtl numbers. Due to the existing buoyancy forces, the velocity magnitude increases, in both mean and fluctuating velocity components. Temperature gradients decrease in the case of $Pr = 0.025$, since the thermal structures increase in size, and they are much slower. This provokes very low temperature fluctuations. The turbulent heat flux is comparable for both Prandtl numbers 0.71 and 0.025, being the last one slightly lower.

Acknowledgments

The present work has been partially funded by the European SESAME Horizon 2020 project (grant agreement n° 654935).

References

[1] International Energy Agency, Worldwide energy outlook: Scenarions, https://www.iea.org/weo/ (2017 (accessed November 30, 2018)).

[2] OECD Nuclear Energy Agency, Technology Roadmap: Nuclear Energy, OECD Nuclear Energy Agency, 2015.

[3] OECD, Handbook on Lead-bismuth Eutectic Alloy and Lead Properties, Materials Compatibility, Thermal-hydraulics and Technologies, OECD Nuclear Energy Agency, 2015.

[4] MYRRHA Project http://myrrha.sckcen.be/ (2019).

[5] F. Roelofs, K. Van Tichelen, M. Tarantino, European thermal-hydraulic progress for sodium and lead fast reactors, in: 17th International Topical Meeting on Nuclear Reactor Thermal Hydraulics, NURETH 2017, 2017.

[6] I. Tiselj, L. Cizelj, Dns of turbulent channel flow with conjugate heat transfer at prandtl number 0.01, Nuclear Engineering and Design 253 (2012) 153 – 160, sI : CFD4NRS-3. doi:https://doi.org/10.1016/j.nucengdes.2012.08.008.
URL http://www.sciencedirect.com/science/article/pii/S0029549312004396

[7] I. Tiselj, Tracking of large-scale structures in turbulent channel with direct numerical simulation of low prandtl number passive scalar, Physics of Fluids 26 (2014) 125111. doi:10.1063/1.4905018.

[8] O. Errico, E. Stalio, Direct numerical simulation of low-prandtl number turbulent convection above a wavy wall, Nuclear Engineering and Design 290 (2015) 87 – 98, thermal-Hydraulics of Innovative Nuclear Systems. doi:https://doi.org/10.1016/j.nucengdes.2014.12.005.
URL http://www.sciencedirect.com/science/article/pii/S0029549314006530

[9] D. Angeli, E. Stalio, M. A. Corticelli, G. S. Barozzi, A fast algorithm for direct numerical simulation of natural convection flows in arbitrarily-shaped periodic domains, Journal of Physics: Conference Series 655 (1) (2015) 012054.
URL http://stacks.iop.org/1742-6596/655/i=1/a=012054

[10] D. Angeli, A. Cimarelli, A. Fregni, A. Shams, F. Roelofs, E. Stalio, Numerical simulation of mixing buoyant jets: Preliminary studies, in: 17th International Topical Meeting on Nuclear Reactor Thermal Hydraulics, NURETH 2017, 2017.

[11] M. Duponcheel, Y. Bartosiewicz, Low prandtl turbulent heat transfer in unconfined or wall-bounded configurations: Dns of a mixing layer and of an impinging jet, in: 17th International Topical Meeting on Nuclear Reactor Thermal Hydraulics, NURETH 2017, 2017.

[12] J. Oder, I. Tiselj, Direct numerical simulations of sodium flow over a backward facing step, in: 17th International Topical Meeting on Nuclear Reactor Thermal Hydraulics, NURETH 2017, 2017.

[13] S. Buckingham, Prandtl number effects in abruptly separated flows: LES and experiments on an unconfined backward facing step, PhD Thesis, Université catholique de Louvain, Louvain-la-Neuve, Belgium (2018).

[14] I. Otic, G. Grötzbach, Dns based analysis and modeling of the turbulent heat transfer by natural convection in liquid lead-bismuth, in: ASME 2005 Summer Heat Transfer Conference collocated with the ASME 2005 Pacific Rim Technical Conference and Exhibition on Integration and Packaging of MEMS, NEMS, and Electronic Systems, American Society of Mechanical Engineers, 2005, pp. 985–990.

[15] J. Boussinesq, Theorie analytique de la Chaleur, Gauthier-Villars, 1903.
URL https://books.google.be/books?id=O08NmgEACAAJ

[16] E. Spiegel, G. Veronis, On the Boussinesq Approximation for a Compressible Fluid., Astrophysical Journal 131 (1960) 442. doi:10.1086/146849.

[17] F. Nicoud, F. Ducros, Subgrid-scale stress modelling based on the square of the velocity gradient tensor, Flow, Turbulence and Combustion 62 (3) (1999) 183–200. doi:10.1023/A:1009995426001.
URL https://doi.org/10.1023/A:1009995426001

[18] G. Grötzbach, Revisiting the resolution requirements for turbulence simulations in nuclear heat transfer, Nuclear Engineering and Design 241 (11) (2011) 4379 – 4390, 13th International Topical Meeting on Nuclear Reactor Thermal Hydraulics (NURETH-13). doi:https://doi.org/10.1016/j.nucengdes.2010.12.027.
URL http://www.sciencedirect.com/science/article/pii/S0029549311000744

[19] The OpenFOAM Foundation, OpenFOAM v5 User Guide, https://cfd.direct/openfoam/user-guide (2019).

[20] M. Bachiri, A. Bouabdallah, An analytic investigation of the steady-state natural convection boundary layer flow on a vertical plate for a wide range of prandtl numbers, Heat Transfer Engineering 31 (7) (2010) 608–616.

[21] A. Villa Ortiz, L. Koloszar, P. Planquart, J. M. Buchlin, S. Keijers, Large Eddy Simulation of a turbulent natural convection boundary layer on a vertical plate at a low Prandtl number, in: 17th International Topical Meeting on Nuclear Reactor Thermal Hydraulics, NURETH 2017, 2017.

[22] T. Sayadi, C. W. Hamman, P. Moin, Direct numerical simulation of complete h-type and k-type transitions with implications for the dynamics of turbulent boundary layers, Journal of Fluid Mechanics 724 (2013) 480509. doi:10.1017/jfm.2013.142.

[23] O. Saunders, The effect of pressure upon natural convection in air, Proceedings of the Royal Society of London A: Mathematical, Physical and Engineering Sciences 157 (891) (1936) 278–291. arXiv:http://rspa.royalsocietypublishing.org/content/157/891/278.full.pdf, doi:10.1098/rspa.1936.0194.
URL http://rspa.royalsocietypublishing.org/content/157/891/278

[24] T. Tsuji, Y. Nagano, Characteristics of a turbulent natural convection boundary layer along a vertical flat plate, International Journal of Heat and Mass Transfer 31 (8) (1988) 1723–1734.

[25] E. M. Sparrow, J. L. Gregg, Details of exact low Prandtl number boundary-layer solutions for forced and for free convection, Tech. rep., NASA Lewis Research Center (1959).

[26] F. J. Bayley, An analysis of turbulent free-convection heat-transfer, Proceedings of the Institution of Mechanical Engineers 169 (1) (1955) 361–370. arXiv:https://doi.org/10.1243/PIME_PROC_1955_169_049_02, doi:10.1243/PIME_PROC_1955_169_049_02.
URL https://doi.org/10.1243/PIME_PROC_1955_169_049_02

[27] S. W. Churchill, H. H. Chu, Correlating equations for laminar and turbulent free convection from a vertical plate, International Journal of Heat and Mass Transfer 18 (11) (1975) 1323 – 1329. doi:https://doi.org/10.1016/0017-9310(75)90243-4.
URL http://www.sciencedirect.com/science/article/pii/0017931075902434

[28] H. W. W., W. J. R., Natural convection with mercury in a uniformly heated vertical channel during unstable laminar and transitional flow, AIChE Journal 21 (2) (1975) 268–274. arXiv:https://onlinelibrary.wiley.com/doi/pdf/10.1002/aic.690210207, doi:10.1002/aic.690210207.
URL https://onlinelibrary.wiley.com/doi/abs/10.1002/aic.690210207

[29] K. Nakao, Y. Hattori, H. Suto, Numerical investigation of a spatially developing turbulent natural convection boundary layer along a vertical heated plate, International Journal of Heat and Fluid Flow 63.

ENVIRONMENTAL FLOWS AND SAFETY

Effects of the Fidelity Level on the Numerical Reproduction of the Wake Meandering Phenomenon

Nicolas Coudou

Environmental and Applied Fluid Dynamics department, von Karman Institute for Fluid Dynamics, Belgium, nicolas.coudou@vki.ac.be

Supervisor: Jeroen van Beeck

Dean of the Faculty, Professor and Head of Department, Environmental and Applied Fluid Dynamics department, von Karman Institute for Fluid Dynamics, Belgium, vanbeeck@vki.ac.be

University Supervisor: Laurent Bricteux

Professor, Fluids-Machines unit, Université de Mons, Belgium, Laurent.bricteux@umons.ac.be

University Supervisor: Philippe Chatelain

Professor, Institute of mechanics, materials and civil engineering, Université catholique de Louvain, Belgium, Philippe.chatelain@uclouvain.be

Abstract

We aim to verify that a modeling approach affordable at wind farm scale, in this case a fourth-order finite differences code combined with a rotating actuator disk, provides equivalent results in terms of wake meandering compared to a method with a higher fidelity level, i.e. a Vortex Particle-Mesh method combined with immersed lifting lines.

Keywords: wind turbine, wake meandering, large eddy simulation, vortex particle-mesh method

1. Introduction

Wind turbine wake meandering is a critical issue in wind farms as this oscillatory motion of the wakes increases fatigue loads on downstream machines and impacts their power production. The first step to study this phenomenon is to detect the wake centerline. Several methods for tracking the wake centerline of an isolated wind turbine subject to a uniform inflow and a synthetic turbulent inflow were proposed in [1]. The simulations were performed with a state-of-the-art Vortex Particle-Mesh (VPM) method combined with immersed lifting lines. The most robust technique was then deployed inside a fourth-order finite differences (FD) code combined with rotating actuator disks (AD) to track the wakes of the machines at wind farm scale. The robustness of this technique is here improved by means of an advection model to limit the search of the wake centroid to an area around its expected position.

The aim of the work presented in this paper is to verify that a modeling approach affordable at wind farm scale, in this case the FD code combined with rotating actuator disks, provides equivalent results in terms of wake centerline position compared to a higher level of fidelity, i.e. the VPM method combined with immersed lifting lines. To answer this question, we compare the wake centerlines obtained by both approaches for an isolated 5MW NREL wind turbine subject to several synthetic turbulent inflows. The comparison is quantified through the study of the wake position signal in terms of amplitude, wavelength and frequency.

2. Wake centerline tracking algorithm

Among the algorithms tested in Coudou et al. [1], the most robust technique to perform run-time tracking of the wake centroid in a cross-flow plane located

downwind of a machine subject to a turbulent inflow is based on the convolution

$$(y_c, z_c) = \text{argmax}\,(p * f_G) \tag{1}$$

between the available power density in the flow

$$p(y,z) = \frac{1}{2} u_x |\mathbf{u}|^2 \tag{2}$$

and a Gaussian masking function

$$f_G(y,z) = A \exp\left(-\left(\frac{(y-\mu_y)^2}{2\sigma_y^2} + \frac{(z-\mu_z)^2}{2\sigma_z^2}\right)\right) \tag{3}$$

with $A = -1$, $\mu_{y,z} = 0$, and $\sigma_{y,z} = 0.5D$. Note that $\sigma_{y,z}$ can be adapted automatically in space and time during the simulation through the implementation of a method based on Laplacian computation [1]. As it does not impact the wake centroid location, $\sigma_{y,z}$ was kept constant for this study to make easier the comparison between the two approaches tested.

Physically, this convolution method relies on the computation of the wind power inside a disk (with a Gaussian weighting) located in a cross-flow plane and with a diameter equal to the rotor diameter D. This disk center position can be shifted in $y-$ and $z-$directions; the wake center corresponds to the disk position for which the available power is minimum [2].

Finally, by tracking the wake centroid in several downwind cross-flow planes, the wake centerline can be obtained.

3. Numerical tools

3.1. Vortex Particle-Mesh (VPM) method

The Vortex Particle-Mesh method [3; 4; 5; 6] relies on the discretization of the velocity ($\mathbf{u}$)-vorticity ($\boldsymbol{\omega} = \nabla \times \mathbf{u}$) formulation of the incompressible Navier-Stokes equations in a Lagragian form. In this method, the vorticity field is discretized with particles which are used solely for the advection treatment, thereby avoiding dispersion errors and waiving classical time stability constraints (CFL number). The use of a mesh along with the particles in the VPM method offers several advantages. The mesh enables the treatment of the Lagrangian distortion through the periodic regularization onto the grid of the particles set [6]. In addition, the mesh handles the computationally intensive tasks : the evaluation of differential operators and the use of fast Poisson solvers for the computation of velocity. Both discretisations communicate through high order interpolation.

This method is able to solve complex turbulent flows at high Reynolds number by using a LES approximation with a Regularized Variational Multiscale (RVM) subgrid-scale model [7] designed as an eddy viscosity model acting only on the small scales.

3.1.1. Blade modeling through immersed lifting lines

The generation of vorticity along the rotor blades is accounted for through immersed lifting lines. Under the assumption of slender blades, a blade can be approximated as a concentrated bound vortex going through the quarter-chord line, and treat the flow around the airfoil in a section as essentially two-dimensional. For a steady flow, the lift per unit span $\mathbf{L}$ and the bound circulation $\boldsymbol{\Gamma}(r,t)$ are then related by the Kutta-Joukowski theorem

$$\mathbf{L} = \rho \mathbf{V}_{rel} \times \boldsymbol{\Gamma} \tag{4}$$

where ρ is the air density and $\mathbf{V}_{rel} = \mathbf{u} - \mathbf{u}_{blade}$ is the velocity relative to the blade. The lift can also be obtained from the relative velocity and the airfoil lift behavior, through its C_L coefficient –either static or in a dynamic stall model; this allows to compute the bound circulation $\boldsymbol{\Gamma}(r,t)$ as well as the shed vortex sheet from the solenoidal property of $\boldsymbol{\omega}$.

3.1.2. Turbulent inflow

A turbulent velocity field $\mathbf{u}'$ is synthesized through Mann's algorithm [8]. In order to carry the turbulence into the domain through the inflow plane, this turbulent velocity field is translated into a set of vorticity particles, more adequate for the Lagrangian method used. Note that because of the unbounded conditions in the $y-$ and $z-$directions, this initially periodic velocity field is made compact through a smooth clipping along its edges.

3.1.3. Numerical setup

The simulations are performed for an isolated NREL offshore 5-MW baseline wind turbine [9] operating at its optimum Tip-Speed Ratio $TSR = 7.55$. Only the blades of the machine are modeled using immersed lifting lines. The spatial resolution is such that 32 points are used to model each blade. The computational domain initially extends over $14D \times 4D \times 4D$; the domain is unbounded in $y-$ and $z-$directions. Based on the spatial resolution of the blades, it leads to an initial grid with approximately 59 million nodes ($\Delta x = \Delta y = \Delta z \simeq 1.97$m). The wind turbine rotor is

located $3D$ after the inlet and is subject to several turbulent inflows synthesized through Mann's algorithm [8] in a $26D \times 4D \times 4D$ box. The inflow velocity is $U_\infty = 9\ \mathrm{ms}^{-1}$ in the $x-$direction and the turbulence intensities tested are $TI = u'/U_\infty = 6\%, 10\%$ and 15%.

3.2. Fourth-order finite differences (FD) code

The VPM approach is well suited for high-fidelity and high-resolution simulations of an isolated wind turbine. However, it becomes unaffordable for simulations at wind farm scale for which another approach is required : LES on coarse meshes, performed using a fourth-order finite difference (FD) code [10]. In this code, instantaneous velocities are imposed at the inlet boundary and a convective boundary condition is applied at the outflow. Periodic boundary conditions are imposed in the spanwise direction and no-through flow is enforced at the top.

3.2.1. Blades modeling through advanced actuator disk

The wind turbines are modeled with advanced AD, which account for thrust and torque effects; these disks also use the local prevailing velocities at every point of the AD for the computation of the aerodynamic loads [11; 12]. The model has been supplemented with a tip-loss correction based on a local estimation of the effective upstream velocity at every point of the AD [12].

3.2.2. Turbulent inflow

As for the VPM approach, several turbulent velocity fields $\mathbf{u}'$ are synthesized through Mann's algorithm [8].

3.2.3. Numerical setup

Again, we consider the NREL-5MW machine at the same operating conditions. Only the blades of the machine are modeled using an advanced actuator disk. The domain size is $14D \times 9D \times 9D$ in order to be as close as possible to the unbounded conditions used in the VPM method. In order to evaluate whether the FD code could be a suitable tool to study wake meandering at wind farm scale, the resolution is kept to a typical resolution used for a wind farm : 16 points per rotor diameter ($\Delta x = \Delta y = \Delta z \simeq 7.88$m). The AD is located at $3D$ from the inlet and the inflow conditions are the same as the ones used for the VPM method.

4. Results

Figure 1 shows the wake centerlines, superimposed on snapshots of the velocity magnitude, obtained by the VPM method (solid line) and with the FD code (dash-dot line) in a horizontal plane at hub height for inflow turbulence intensities of $TI = 6\%$, $TI = 10\%$, and $TI = 15\%$. As it can be observed, the wake centerlines obtained clearly follow the wake motion. Qualitatively, there is a good agreement between the wake centerlines obtained by the two approaches up to five rotor diameters downstream the machine. Beyond this distance, the wake centerline obtained by the FD code starts to drift away from the one obtained by the VPM method, especially as the inflow turbulence level increases.

In the next paragraphs, we aim to compare quantitatively the wake centerlines obtained by the two approaches. The statistics are computed from the data of 67 rotor revolutions, i.e. approx. 28 convective times ($t^* = \frac{D}{U_\infty}$). These data are represented on Fig. 2 in a dimensionless manner as a function of space and time for the three inflow turbulence intensities tested. As it can be observed, the wake centerline motions obtained by the two approaches are similar in shape but vary in amplitude.

The envelopes of the wake centerlines (Fig. 3) show that the maximum deviation in time, as a function of space, of the wake centerline obtained by the FD code is larger that the one obtained by the VPM method, especially as the inflow turbulence intensity is larger. The analysis of the probability to find the wake centerline inside bins of $D/8$ shows that the wake centerline distribution obtained by the FD code is wider compared to the one obtained by the VPM code (Fig. 4).

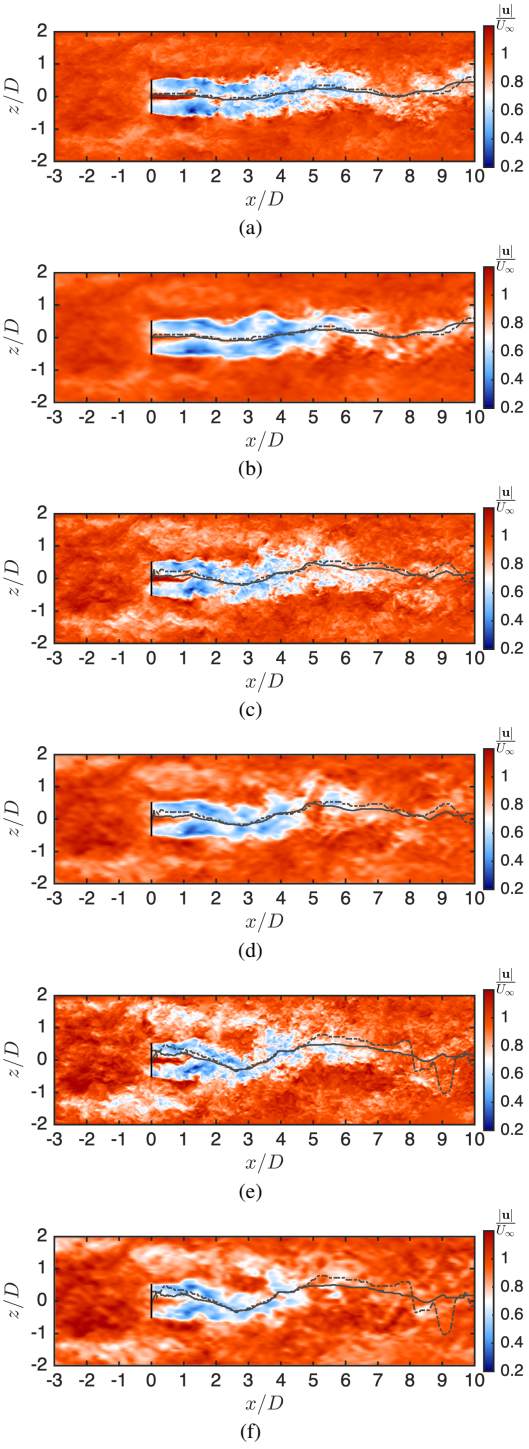

Figure 1: Snapshots in a horizontal plane at hub height of the velocity magnitude obtained by the VPM method ((a)-(c)-(e)) and the FD code ((b)-(d)-(f)). The wake centerlines obtained by VPM method (solid line) and with FD code (dash-dot line) are superimposed for several inflow turbulence intensities: TI = 6% ((a)-(b)), TI = 10% ((c)-(d)), and TI = 15% ((e)-(f))

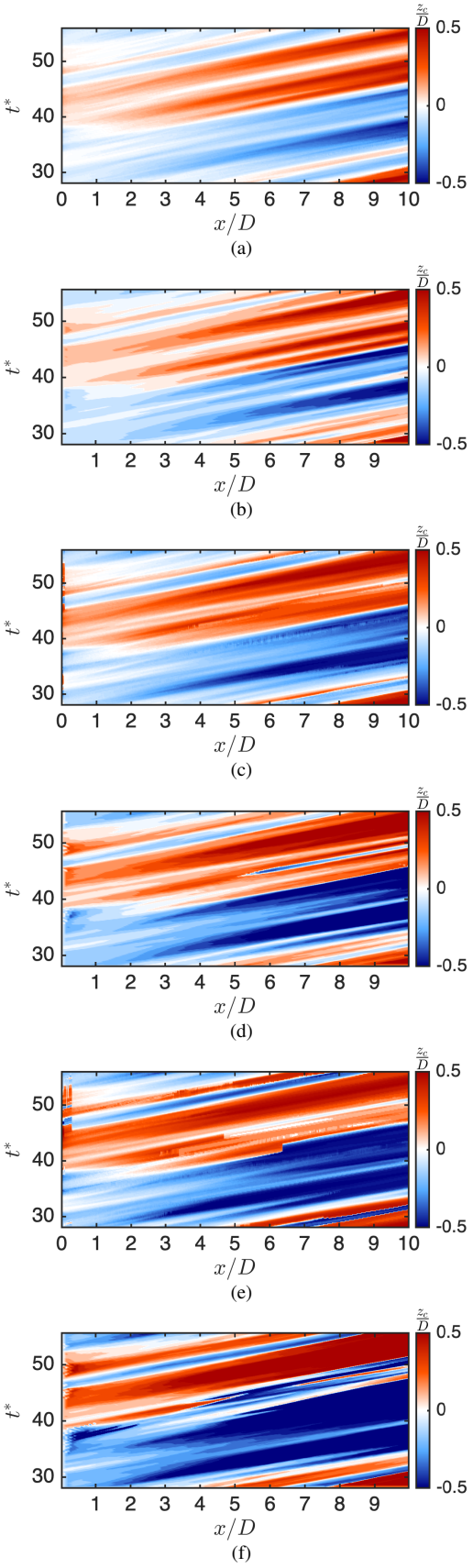

Figure 2: Dimensionless horizontal motion of the wake centerline as a function of space and time obtained by the VPM method ((a)-(c)-(e)) and the FD code ((b)-(d)-(f)) for several inflow turbulence intensities : TI = 6% ((a)-(b)), TI = 10% ((c)-(d)), and TI = 15% ((e)-(f))

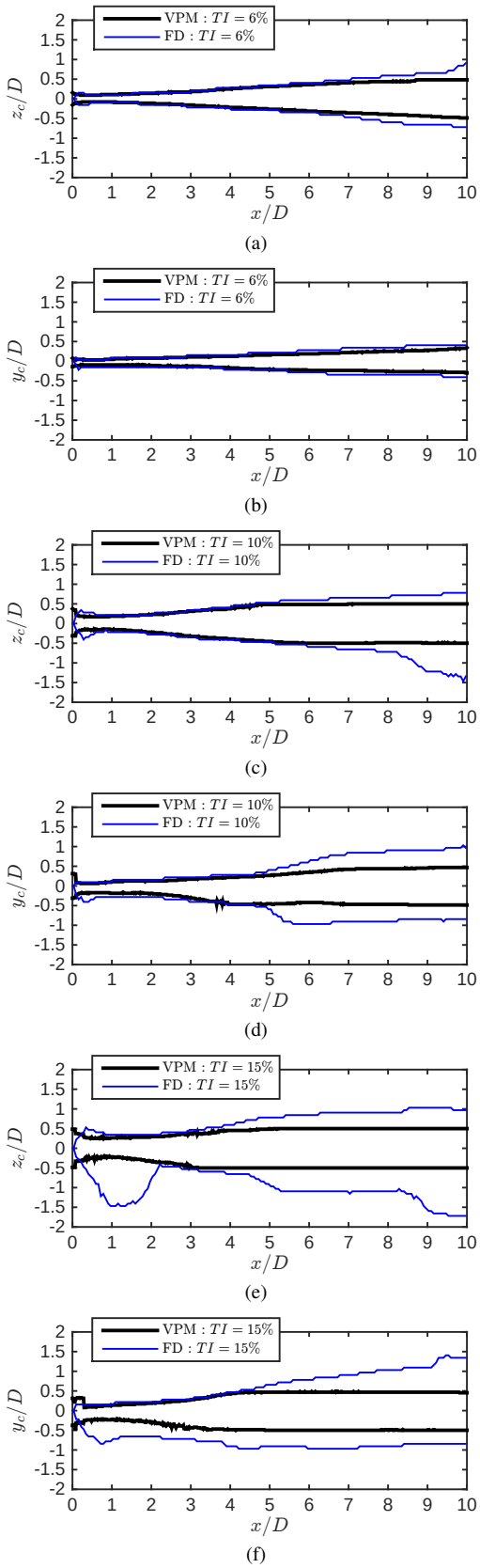

Figure 3: Dimensionless envelopes of wake centerlines obtained by the VPM method (thick black line) and the FD code (thin blue line) in a horizontal ($z-x$) and in a vertical ($y-x$) plane for several inflow turbulence intensities : TI = 6% ((a)-(b)), TI = 10% ((c)-(d)), and TI = 15% ((e)-(f))

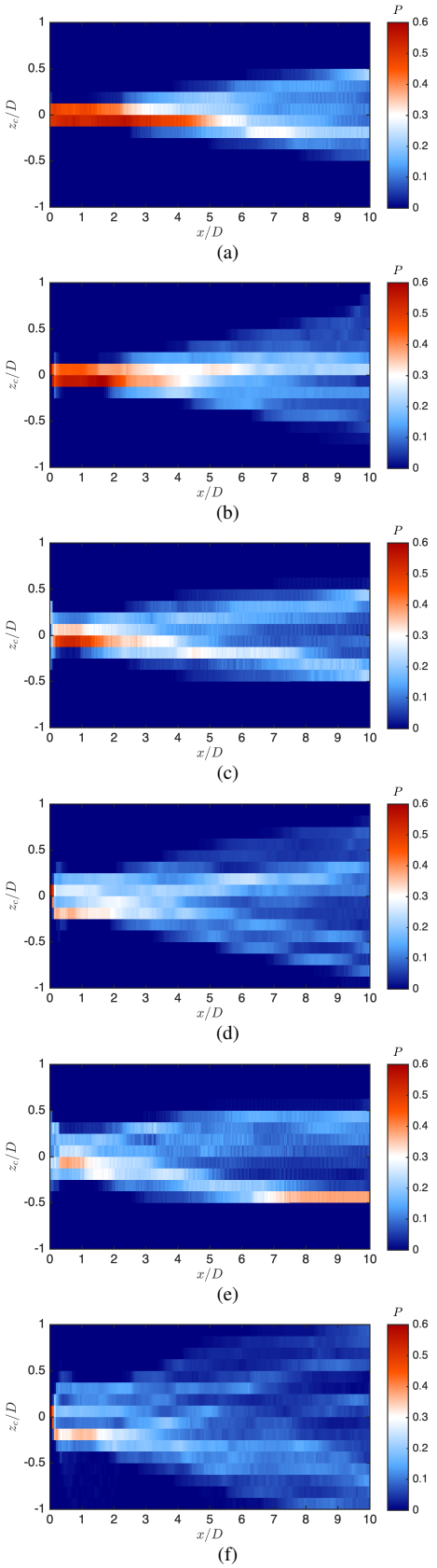

Figure 4: Probability of finding a wake centerline at a certain location in a horizontal plane at hub height in the wind turbine wake, obtained by the VPM method ((a)-(c)-(e)) and the FD code ((b)-(d)-(f)) for several inflow turbulence intensities : TI = 6% ((a)-(b)), TI = 10% ((c)-(d)), and TI = 15% ((e)-(f))

In addition, a quantitative analysis of the wake centerline characteristics was performed on the basis of the work of Foti et al. [13]. In the following results, the amplitude of wake meandering is computed as half the cross-wind distance between consecutive maximum-minimum while the wavelength is computed as the streamwise distance between two consecutive maxima or minima. The downstream position of these quantities was set to the intermediate position of the two points involved in the computation. The quantities were then binned, with respect to the downwind distance from the rotor, into half-diameter bins and the mean values were computed. The wake oscillations are captured in a horizontal plane at hub height and in a vertical plane passing through the hub. Note that for the sake of clarity, downwind distances ranging from $0D$ to $10D$ are presented in Fig. 5 and 6, even if the exploitable part of the graphs is for $3 \lesssim x/D \lesssim 7$ because of the method used to determine the amplitude and wavelength of the oscillations.

Figures 5(a),(b) show the mean amplitude of the wake oscillations as a function of space. This amplitude increases with the distance downwind from the rotor and with the inflow turbulence level. Furthermore, the linear growth of the meandering amplitude with respect to the downwind distance from the rotor is highlighted on Fig. 5(c),(d), where the amplitude is normalized by the downstream distance. Indeed, the profiles are fairly constant in the central part of Fig. 5(c),(d). One can observe that the mean amplitude of the oscillations obtained by the VPM and FD methods are in good agreement for $TI = 6\%$ and $TI = 10\%$ and that the FD method leads to a larger amplitude overall. In terms of mean wavelength of the oscillations, they are spread over $3D$ and $4.5D$ (Fig. 6).

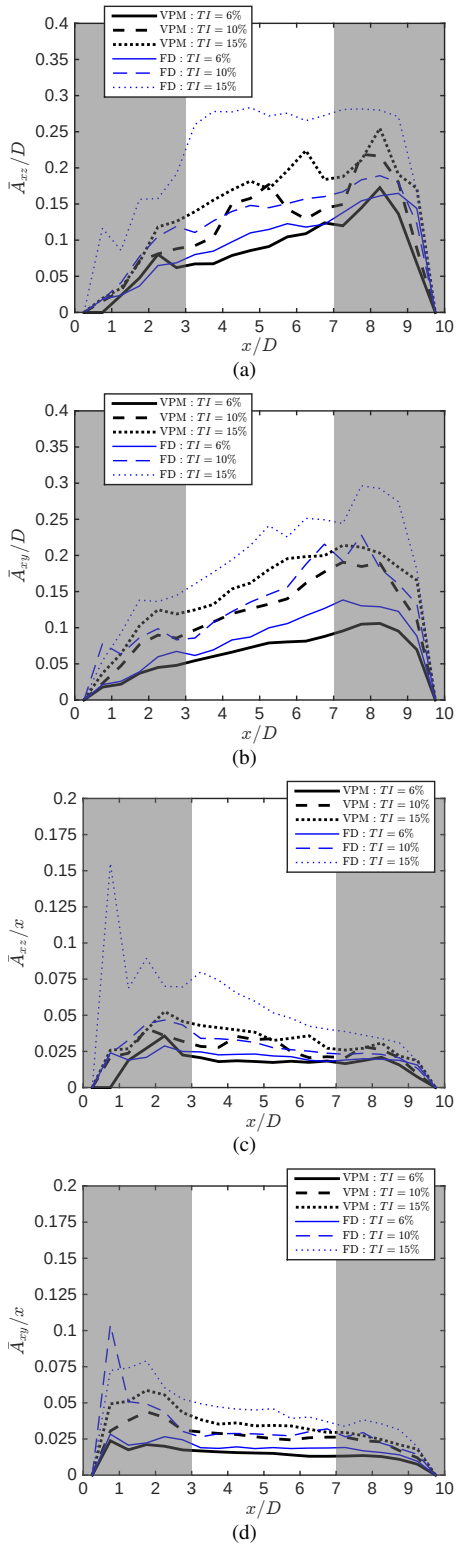

Figure 5: Mean binned wake centerlines amplitudes ($\bar{A}$) obtained by the VPM method (thick black line) and the FD code (thin blue line), in a horizontal ($z-x$) and in a vertical ($y-x$) plane, normalized by the rotor diameter ((a)-(b)) and by the downwind distance from the rotor ((c)-(d)), for several inflow turbulence intensities : $TI = 6\%$, $TI = 10\%$, and $TI = 15\%$; note that the exploitable part of the graphs ranges between $3 \lesssim x/D \lesssim 7$ because of the method used to determine the amplitude and wavelength of the oscillations

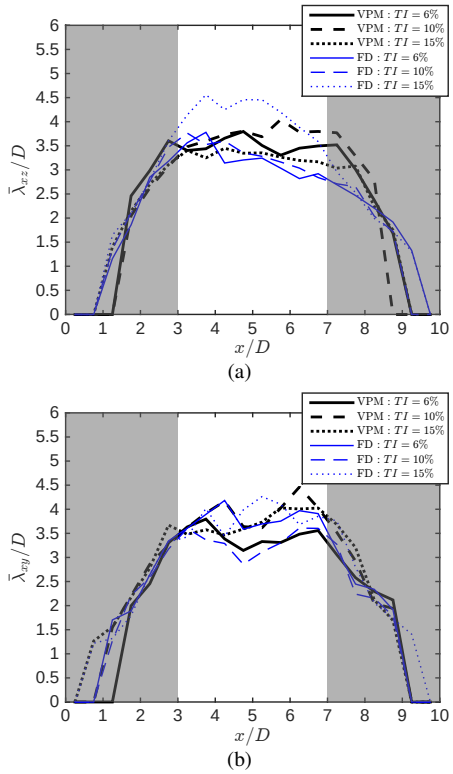

Figure 6: Mean binned wake centerlines wavelengths (λ) obtained by the VPM method (thick black line) and the FD code (thin blue line), in a horizontal ($z-x$) and in a vertical ($y-x$) plane, normalized by the rotor diameter ((a)-(b)) for several inflow turbulence intensities : $TI = 6\%$, $TI = 10\%$, and $TI = 15\%$; note that the exploitable part of the graphs ranges between $3 \lesssim x/D \lesssim 7$ because of the method used to determine the amplitude and wavelength of the oscillations

Moreover, a spectral analysis was performed on the wake centerlines. Fig. 7 shows the average power spectrum density (PSD) multiplied by the frequency (f). Note that the first low frequency peak at Strouhal number $St = fD/U_\infty = 0.036$ ($f = 0.0026$ Hz) corresponds to the length of the Hanning window used in the Fast Fourier Transform. The other low frequency peaks correspond to the wake meandering frequencies : $St = 0.11 - 0.14$ ($f = 0.008 - 0.01$ Hz).

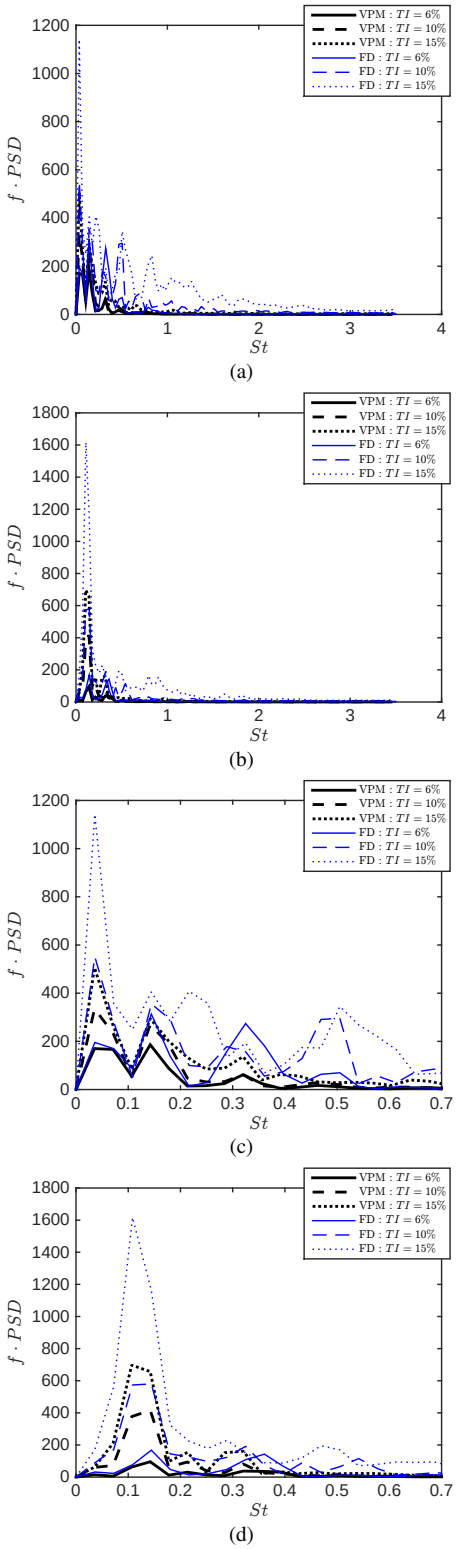

Figure 7: Power spectral density of the wake centerlines fluctuations acquired at hub height ((a)-(c)) and in the vertical symmetry plane ((b)-(d)) for several inflow turbulence intensities: $TI = 6\%$, $TI = 10\%$, and $TI = 15\%$; ((c)-(d)) are a zoom of ((a)-(b)) in St range of interest

Finally, a spectral analysis (Fig. 8) was performed to characterize the inflow from the streamwise velocity fluctuations acquired at hub height at the location ($x/D = -1$; $z/D = 0$). For the three turbulent inflows used in the simulations, the power spectral density multiplied by the frequency f reveals peaks at $St = 0.14$ ($f = 0.01$ Hz).

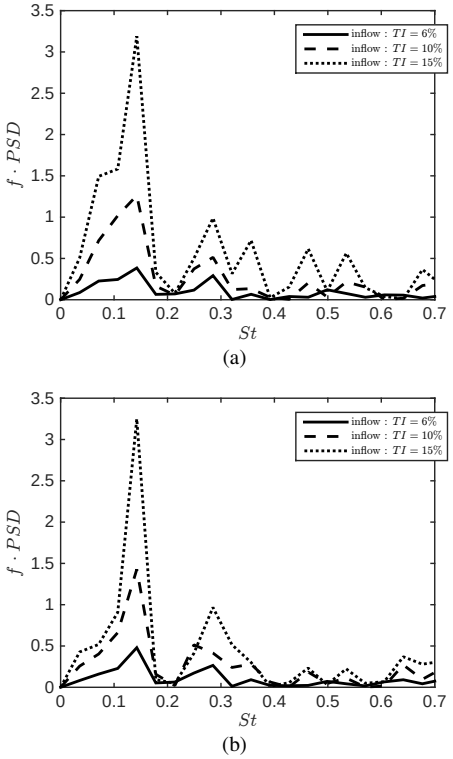

Figure 8: Power spectral density of the streamwise velocity fluctuations acquired at hub height at ($x/D = -1$; $y/D = 0$; $z/D = 0$) in the VPM simulations (a) and the FD simulations (b) for several inflow turbulence intensities: $TI = 6\%$, $TI = 10\%$, and $TI = 15\%$

5. Conclusions and perspectives

The aim of this work was to verify that a modeling approach affordable at wind farm scale, in this case a fourth-order FD code combined with an advanced rotating actuator disk, provides equivalent results in terms of wake meandering compared to a method with a higher fidelity level, i.e. a VPM combined with immersed lifting lines.

A direct comparison of the wake centerlines reveals a good match between the two approaches up to five rotor diameters downwind of the rotor. Beyond that distance, the wake centerline obtained by the FD code starts to drift away from the one obtained by the VPM method, especially as the inflow turbulence level increases. Concerning the amplitude and wavelength of the wake meandering, the FD code leads to larger amplitudes than the VPM code while there is not a clear trend for the wavelength. Furthermore, it was observed that the amplitude of the wake oscillations increases with the distance from the rotor and with the inflow turbulence level. A spectral analysis performed on the wake centerlines reveal two main frequencies for wake meandering: $St = 0.11$ and $St = 0.14$, which is in agreement with the literature for wake meandering: $0.1 < St < 0.3$ [14; 15; 16; 17; 18; 19] . A spectral analysis of the inflow reveals that these frequencies are contained in the inflow.

The next steps will be to improve the robustness of the tracking method for the wind farm simulation tool (the FD code) in order to study wakes interaction and merging with the view to perform wind farm control. A track that will be investigated to improve the robustness of the method is the use of a Kalman filter blending measurements with the predictions of a simple wake advection model.

Acknowledgments

Nicolas Coudou is funded by the *Fonds pour la Formation à la Recherche dans l'Industrie et dans l'Agriculture (FRIA)*, Belgium. The simulations used computational resources made available on the Tier-1 supercomputer of the Fédération Wallonie-Bruxelles, infrastructure funded by the Walloon Region under the Grant Agreement No. 1117545

References

[1] N. Coudou, M. Moens, Y. Marichal, J. van Beeck, L. Bricteux, P. Chatelain, Development of wake meandering detection algorithms and their application to large eddy simulations of

an isolated wind turbine and a wind farm, Journal of Physics: Conference Series 1037 (7) (2018) 072024.
URL http://stacks.iop.org/1742-6596/1037/i=7/a=072024

[2] L. Vollmer, G. Steinfeld, D. Heinemann, M. Kühn, Estimating the wake deflection downstream of a wind turbine in different atmospheric stabilities: an LES study, Wind Energy Science 1 (2) (2016) 129–141.

[3] P. Chatelain, A. Curioni, M. Bergdorf, D. Rossinelli, W. Andreoni, P. Koumoutsakos, Billion vortex particle direct numerical simulations of aircraft wakes 197 (13) (2008) 1296–1304.

[4] P. Chatelain, S. Backaert, G. Winckelmans, S. Kern, Large eddy simulation of wind turbine wakes, in: W. Rodi (Ed.), Proceedings of The 9th International Symposium on Engineering Turbulence Modelling and Measurements (ETMM-9), June 6–8, 2012, Thessaloniki, Greece, Vol. 91 of Flow, Turbulence and Combustion, ERCOFTAC, Springer, 2013, pp. 587–605. doi:10.1007/s10494-013-9474-8.

[5] S. Backaert, P. Chatelain, G. Winckelmans, Vortex particle-mesh with immersed lifting lines for aerospace and wind engineering, in: J. H. Walther (Ed.), Symposium on Particle Methods in Fluid Dynamics, October 15-17 2012, DTU Copenhagen, Vol. 18 of Procedia IUTAM, IUTAM, 2015, pp. 1–7. doi:10.1016/j.piutam.2015.11.001.

[6] G. Winckelmans, Vortex methods, in: E. Stein, R. De Borst, T. J. Hughes (Eds.), Encyclopedia of Computational Mechanics, Vol. 3, John Wiley and Sons, 2004.

[7] H. Jeanmart, G. Winckelmans, Investigation of eddy-viscosity models modified using discrete filters: A simplified "regularized variational multiscale model" and an "enhanced field model" 19 (5) (2007) 055110. doi:10.1063/1.2728935.

[8] J. Mann, Wind field simulation, Probabilistic Engineering Mechanics 13 (4) (1998) 269–282.
URL http://www.sciencedirect.com/science/article/pii/S0266892097000362

[9] J. Jonkman, S. Butterfield, W. Musial, G. Scott, Definition of a 5-mw reference wind turbine for offshore system development, Tech. Rep. NREL/TP-500-38060, National Renewable Energy Laboratory (NREL) (February 2009).

[10] M. Duponcheel, L. Bricteux, M. Manconi, G. Winckelmans, Y. Bartosiewicz, Assessment of RANS and improved near-wall modeling for forced convection at low Prandtl numbers based on LES up to $Re_\tau = 2000$, International Journal of Heat and Mass Transfer 75 (2014) 470–482.

[11] M. Moens, M. Duponcheel, G. Winckelmans, P. Chatelain, Les of wind farm response to transient scenarios using a high fidelity actuator disk model, Journal of Physics: Conference Series 753 (2016) 032053.

[12] M. Moens, M. Duponcheel, G. Winckelmans, P. Chatelain, An actuator disk method with tip-loss correction based on local effective upstream velocities, Wind EnergyAccepted for publication.

[13] D. Foti, X. Yang, F. Sotiropoulos, Similarity of wake meandering for different wind turbine designs for different scales, Journal of Fluid Mechanics 842 (2018) 525. doi:10.1017/jfm.2018.9.

[14] D. Medici, P. H. Alfredsson, Measurements on a wind turbine wake: 3D effects and bluff body vortex shedding, Wind Energy 9 (3) (2006) 219–236.

[15] D. Medici, P. H. Alfredsson, Measurements behind model wind turbines: further evidence of wake meandering, Wind Energy 11 (2) (2008) 211–217.

[16] E. Barlas, S. Buckingham, J. van Beeck, Roughness Effects on Wind-Turbine Wake Dynamics in a Boundary-Layer Wind Tunnel, Boundary-Layer Meteorol 158 (1) (2016) 27–42.

[17] V. L. Okulov, I. V. Naumov, R. F. Mikkelsen, I. K. Kabardin, J. N. Sørensen, A regular strouhal number for large-scale instability in the far wake of a rotor, J Fluid Mech 747 (2014) 369–380.

[18] K. B. Howard, A. Singh, F. Sotiropoulos, M. Guala, On the statistics of wind turbine wake meandering: An experimental investigation, Phys Fluids 27 (7).

[19] N. Coudou, S. Buckingham, L. Bricteux, J. van Beeck, Experimental study on the wake meandering within a scale model wind farm subject to a wind-tunnel flow simulating an atmospheric boundary layer, Boundary-Layer Meteorology 167 (1) (2018) 77–98. doi:10.1007/s10546-017-0320-8.
URL https://doi.org/10.1007/s10546-017-0320-8

Scaled Model of the Pollutant Dispersion Driven by a Condensed-Phase Explosion in an Urban Environment

Charline Fouchier

Environmental and Applied Fluid Dynamics, von Karman Institute for Fluid Dynamics, Belgium, charline.fouchier@vki.ac.be

Supervisors: Jean-Marie Buchlin and Delphine Laboureur

Full Professor, Environmental and applied fluid dynamics, von Karman Institute for Fluid Dynamics, Belgium, buchlin@vki.ac.be

Assistant Professor, Environmental and applied fluid dynamics, von Karman Institute for Fluid Dynamics, Belgium, delphine.laboureur@vki.ac.be

University Supervisor: Alessandro Parente

Professor, Aero-Thermo-Mechanical Department, Université Libre de Bruxelles, Belgium, alparent@ulb.ac.be

Abstract

The propagation of a blast induced by a condensed-phase explosion as well as the atmospheric dispersion in an urban or industrial environment are well documented in the literature. However, there is a lack of knowledge about the dispersion triggered by rapid and short phenomena such as an explosion. This knowledge is essential to develop accurate tools to simulate the dispersion after an explosion inside a complex environment.

The global objective of the project is the investigation of pollutant dispersion driven by a condensed-phase explosion in an urban environment. Investigations have been conducted inside the subsonic wind tunnel L1-b at the von Karman Institute (Belgium). A condensed-phase explosion leading to the dispersion of solid particles is experimentally simulated in free field under a controlled urban atmospheric boundary layer. Two gram-scale explosives are studied: a RP80 and a RP83 exploding-bridge-wire detonators. Two micro-talc powders with different diameters are used to simulate the pollutant dispersion. The atmospheric boundary layer representative to an urban environment is reproduced in the wind tunnel by placing roughness elements of an appropriate size. The pollutant dispersion and the overpressures caused by the explosion are measured through a fast response optical measurement technique and fast response pressure sensors. The main challenge of the study is the adaptation of the existing measurement technique of dispersion to fast phenomena visualizations.

The velocity of the particles inside the cloud are obtained through a Large Scale Particle-Image-Velocimetry analysis. This technique is first analyzed on fictive displacements. Then, it is applied on experimental images leading to velocity maps of the dispersion. Two kind of visualization are investigated and compared: one obtained with a powerful light source and one with a laser sheet.

Keywords: latex, template, ...

1. Introduction

Explosion, whether accidental or not, is a major concern in the security and safety fields. Examples of tragedies caused by explosions along with dangerous chemical dispersion are numerous. Improvement of security and safety is driven by a better understanding of the phenomenon. An explosion generates a pressure wave, called blast wave. If a pollutant is released together with the explosion, both the dispersion of the pollutant and the blast wave will be affected. To predict the pollutant dispersion after an explosion in a complex environment, it is necessary to understand the propagation of the blast wave and its effect on the plume dispersion.

Numerical models have been developed in attempt to simulate the plume dispersion after an explosion.

A model based on the Large Eddy simulations (LES) approach has been used to simulate the Oslo bombing in 2011 [1]. The dispersion and deposition of particles following the detonation have been calculated using both an Eulerian and a Lagrangian model, based on the spherical particle sizes smaller than 20 μm with a high density (1000kg.m-3), assuming a no particle-particle interaction. To couple the cloud dynamics and chemical transformations, the numerical model called ADORA has been recently developed by N. Moussa et al. [2]. This model provides the time evolution of toxic emissions and their dispersion in the atmosphere after a fire or an explosion by solving the conservation of mass, momentum, energy and species equations in an integral formulation.

To ensure an accurate and reliable prediction of the plume dispersion after an explosion, it is necessary to couple the modeling with strong empirical data. The rapid dispersion of inert spherical steel particles [3] [4], glass bubbles [5] or liquid [6] after a detonation has been investigated using a high speed camera coupled with pressure sensors. The dispersion turned out to depend on the pollutant characteristics (solid or liquid) and the geometry of the explosive charge. The particle image velocimetry technique (PIV) has been applied to obtain the velocity field of the metallic particles after the detonation [7].

However, the existing studies focus on the near-field effects of the explosion, few milliseconds after the detonation. An effort still has to be made to improve the experimental data base on the dispersion of the plume under an atmospheric boundary layer (ABL). Moreover, explosions in laboratory scale with controlled atmospheric conditions are not familiar. This knowledge is essential to develop accurate tools in order to simulate the dispersion after an explosion inside a complex environment.

The global objective of the present research is the investigation of pollutant dispersion driven by a condensed-phase explosion in an urban environment. Detonators are used to disperse talc powder. The present paper summarizes the experimental set-up used and the characteristics of the explosives in free field. A condensed phase explosion surrounded by a pollutant (solid particles) is then experimentally simulated in free-field under an urban ABL through a scale of 1:200. Flows visualizations and large scale particle image velocimetry (LS-PIV) are conducted to investigate the velocity fields of the dispersion.

2. Materials and Methods

2.1. Experimental Set-up

The experimental set-up has been designed to conduct non-destructive studies of air-blast in free field and in urban configurations under a controlled atmospheric boundary layer. Experiments have been performed inside the subsonic wind tunnel L1-b at the von Karman Institute. It is 2 m high, 3 m wide and 15 m long with a roughened floor to allow the growth of a turbulent boundary layer similar in nature to the lower part of the neutral atmospheric boundary layer. The test section ceiling is flexible and continuously adjustable to achieve control of the longitudinal pressure gradient. Flow velocity can be varied between 2 and 50 m/s. An urban atmospheric boundary layer is developed inside the wind tunnel through plastic cups fixed on the floor. The dimensions of the roughness elements have been defined by B. Conan [8] to obtain an atmospheric boundary layer typical to an urban environment at a 1:200 reduced scaled. Tests are conducted on a 2.8 m diameter circular wood table. Figure 1 left illustrates the test table inside the wind tunnel.

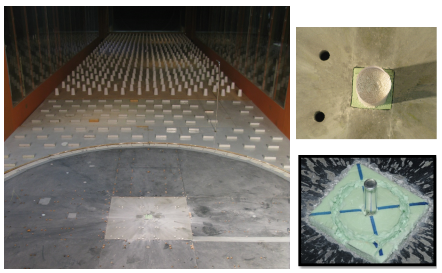

Figure 1: Left: Experimental wood test table, 2.8 m diameter, inside a wind tunnel. The roughness elements create turbulence to develop an urban boundary layer at a 1:200 reduced scale. Right bottom: Solid foam support with a RP83 detonator. A groove has been performed to place properly the paper cylinder around the explosive. Right top: Paper cylinder filled with talc powder

The setup has been designed to conduct non-destructive studies of 3 dimensional free field air blast propagation. For each test, the explosive is placed at the center of the circular test table. A metal plate of 55 x 55 cm replaces the wood in the middle of the table to protect it against the explosion. The effect of the explosive source is investigated through two kinds of exploding-bridge-wire detonators: RP80 and RP83, distributed by RISI. The TNT equivalents of the two explosives have been experimentally estimated at 0.136 g and 1.31 g respectively for the RP80-EBW and the RP83-EBW. The detonators are acti-

vated using a FM150 firing module and a FD201 firing system. More details about the detonators used can be found in [9].

The dispersion is simulated using talc powder of two different diameters, distributed by Imerys. The talc is an inert powder that will not react after the explosion. The first powder, called JetFine 1, or light powder, has a diameter of 1 μm and a loose density of 0.10 g/cm^3. The second powder, called Mistron 200, or heavy powder, has a diameter of 7.8 μm and a loose density of 0.44 g/cm^3. Table 1 summarizes the characteristics of the powders used. The two talc powders have different response time and are expected to be affected by the explosion in a different way. The powder is maintained around the explosive by a paper cylinder. A circular groove is performed on the solid foam support to maintain the cylinder and assure that the talc is homogeneously distributed around the explosive.Pictures given in Figure 1 top and bottom right show the detonator inside the talc powder kept by a paper cylinder and the groove inside the support.

Name	Diameter	Loose bulk density	Density	Response Time
Heavy Powder	7.8 μm	0.44 g/cm^3	2.78 g/cm^3	0.51 ms
Light Powder	1 μm	0.10 g/cm^3	2.78 g/cm^3	0.0084 ms

Table 1: Characteristics of the talc powders used

The repeatability of the tests is systematically checked by measuring the pressure generated by the explosion using PCB 116 pressure sensors set flush to the surface of the test table. The sensors are held by elastics to disconnect them from the test table. This system has been designed and tested to reduce the effect of the table vibrations on the blast measurement. The pressure variation is recorded with a sample frequency of 8 MHz, using a NI PXIe 7962R system with an acquisition module NI-5751. The sample size is equal to 40x10^6 points per channel, which represents 5 seconds of acquisition.

A Phantom V7.1 high speed camera (HSC) is used to acquire the images of the dispersion. The camera is set on the side of the wind tunnel to have a front view of the dispersion or on the top to obtain a top view. Two different illumination methods are used. The first one, which will be called "Global Visualization", consists in illuminating the flow using a powerful light source set on the side of the flow. The dispersion is acquired at 10869 Hz (f0) with an exposure time of 60 μs. The second one, called here "Planar Visualization", consists in illuminating the flow with a 10 W continuous laser sheet, produced by an optical set-up coupling divergent and convergent lenses and acquires at 2000 Hz with an exposure time of 500 μs. The dispersion is investigated through Flow Visualization and Large Scale Particle Image Velocimetry (LS-PIV) [10]. Three wind speeds are investigated: 0 m/s, 3 m/s and 5 m/s.

2.2. *Repeatability of the tests*

The blast wave generated by a detonation is characteristic of each explosive. Tests have been conducted without and with talc around the detonators to investigate the effect of the powder on the pressure wave. Figure 2 gives the blast pressure signals obtained with a RP80 detonator, measured at 350 mm from the center of the explosion without powder around the explosive, with the light powder and with the heavy powder. An equal volume of powder (67 cm^3) is used, which represents 10 g for the light powder and 28 g for the heavy powder. It has been estimated that 28 g of heavy powder were reducing the total energy of the detonation by 70 %; while 10 g of light powder reduce the energy by 30 %.

As the powder affects the blast characteristics, the homogeneity of the distribution of the powder around the explosive before the explosion can be investigated using the pressure sensors: if the powder is equally distributed, the blast propagation should be hemispherical, as it is without powder. Figure 3 gives an example of a case where the powder was not well distributed around the explosion. The four pressure signals, C3, C6, C7, and C2 generated by a RP83 detonator, have been measured at 750 mm around the explosive. These blasts are not equal, highlighting a non hemispherical propagation of the blast. The geometry of the explosion is controlled systematically in this way to enssure the repeatability between tests.

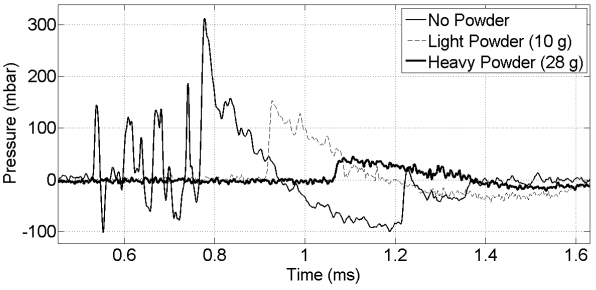

Figure 2: Effect of the talc powder on the blast wave generated by the explosion of a RP80, signal at 350 mm from the explosion, 200 kHz filtered

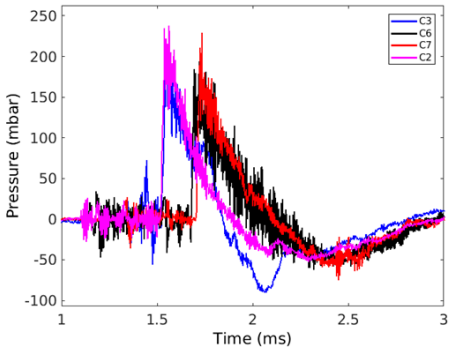

Figure 3: Example of powder not well distributed around the explosive: RP83 detonator pressure signals at 750 mm around the explosion, 200 kHz filtered

2.3. Contour of the dispersion

The contour of the dispersion is obtained via grey-scale image processing, based on Matlab tools [11]. Figure 4 shows the images resulting from the post-processing, step by step. Image A is the initial image. Image B is the image where the background has been removed and the contrast increased to make the processing easier. Image C is the image binarized by a threshold of 0.15. This threshold has been chosen arbitrarily and represent the best value to obtain a contour, taking into account the luminosity of the images and the variation of powder concentration regarding the time. Image D is the contour obtained, after a smoothing of the border to remove the solid projectiles that should not be taken into account and applying the edge detection function from Matlab.

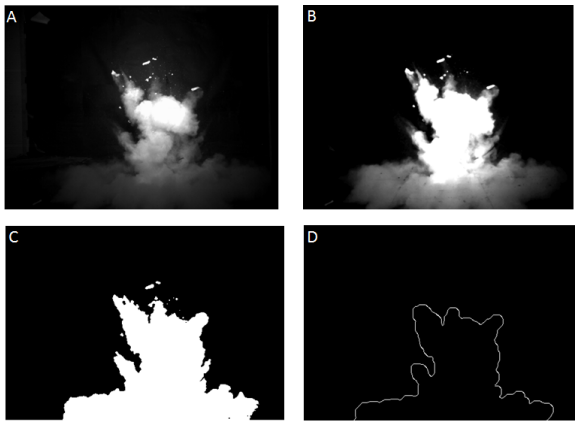

Figure 4: Post-processing of the flow visualization images to obtain the contour of the cloud. A: initial image. B: Background removed and contrast increased. C: Binarization by threshold (0.15) and crop of the image. D: Border smoothing and edge detection

3. Investigation on the LS-PIV technique

LS-PIV is based on the same principles than the standard PIV. However, as the studied structures in the flow are different, the correlation matrices are also different. Figure 5 shows the two types of correlation matrices. While the correlation peak of the PIV correlation matrix is well defined and can be extrapolated as a gaussian, the peak of LS-PIV is larger. A study has been performed to understand how to detect properly the correlation peak, what is the optimal displacement according to the resolution of the study, what is the minimum displacement that can be studied, and what is the effect of the different structures in the flow. PIVLab [12], a free access code available on Matlab[11], is used for the investigation.

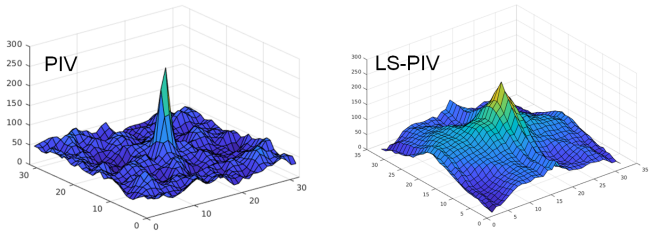

Figure 5: Correlation matrices

3.1. Parametric analysis on fictive displacements

In order to investigate the LS-PIV technique, the translation of a grey scale image, given in Figure 6, has been studied. This image is translated 16 px to the right. LS-PIV is applied to this couple of images created in order to retrieve the displacement. Two methods are used to solve the cross-correlation function: the direct cross correlation method DCC, which estimates the correlation matrix in the spatial domain, and the discrete fourier transform (DFT), which estimate the correlation matrix in the frequency domain. For both methods, an overlap of the interrogation window of 50 % is applied. For the DFT, two steps are done for a given interrogation window size. First, the displacement is obtained in the center of the window. The information obtained from the windows overlapping is used to estimate the displacement at several pixels in the interrogation zone through bi-linear interpolation. The interrogation area is therefore deformed via bi-linear interpolation according to the displacement obtained during the first step of the analysis. The second step consists in correlating the original interrogation window with the deformed zone. These steps allow

to reduce the loss of information due to the displacement of structures in the flow. More details about the methods can be found in[12] [13].



Figure 6: Original image

Table 2 gives the averaged displacement (Da) obtained, as well as the sound to noise ratio (SN) for interrogation window sizes of 32 px, 64 px, 128 px et 256 px. The image displacement of 16 px represents respectively 50%, 25%,12.6% et 6.2 % of the interrogation window size. The SN ratio has been obtained dividing the first correlation peak by the second. The DCC method provides more accurate results for small windows. However, when the size of the window increases, this method overestimates the displacement and the DFT method gives results closer to the theory. The disadvantage of the DCC method is its high computational cost, especially for large windows. The DFT method is therefore preferred.

		DCC		DFT	
Window	% Displacement	Da	SN	Da	SN
32 px	50%	13.19 px	3.89	7.9 px	1.14
64 px	25 %	17.18 px	2.87	12.8 px	1.636
128 px	12.5%	18.36 px	2.48	14.3 px	2.04
256 px	6.2 %	18.97 px	2.39	15.38 px	2.42
3 refinement steps	-	-		15.9 px	9.1

Table 2: Averaged displacement and SN ratio obtained via DCC and DFT for different interrogation window sizes

The quality of the results depends directly on the interrogation window size. The grey image displacement has been investigated with the DFT method using different window sizes. Velocity maps obtained during the analysis are given in Figure 7. The accuracy of the results increases with the window size. Although it is advised to analyze a maximal displacement lower than 1/4 of the interrogation window for PIV analysis [13], it appears that for the LS-PIV, the window should be around 16 times larger than the displacement to obtain good quality results.

A refinement technique is usually used to improve the results. This technique consists in conducting the analysis on a large interrogation window (256 px) and

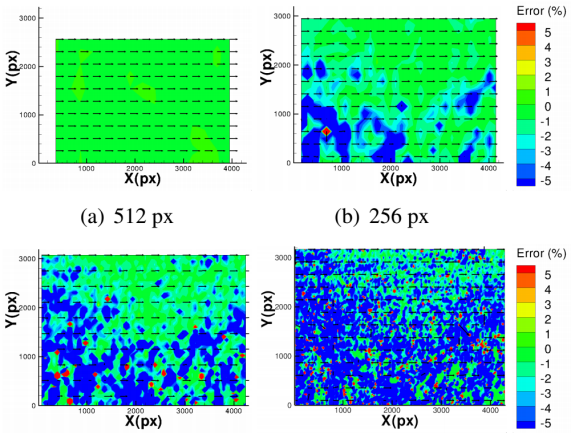

(a) 512 px (b) 256 px

(d) 128 px (e) 64 px

Figure 7: Velocity map from the DFT method applied on a window of 512 px (a), 256 px (b), 128 px (c) and 64 px (d) - displacement of 16 px

refine the analysis to smaller windows (128 px, 64 px, and 32 px). This method in several steps makes the analysis faster and improves the results. Velocity maps obtained with a refinement of one step and three steps are proposed in Figure 8. Refining the analysis improves the accuracy of the results.

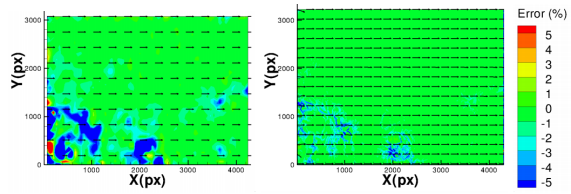

(a) One step refinement (b) Three steps refinement

Figure 8: Velocity map from the DFT method applied on a window of 256 px refined in one step to 128 px (a) and in three steps to 32 px (b) - displacement of 16 px

Finally, results can be improved by enhancing the contrast of the studied structures in the flow. This can be done with different filters. Figure 9 gives an image processed with a Contrast Limitd Adaptive Histogram Equalization Filter (CLAHE ([12]) and the velocity map resulting from a DFT analysis with a window of 256 px, refined in 3 steps to 32 px. These setting represent the optimal configuration for the studied displacement.

LS-PIV has been applied to experimental images, given in Figure 10, which have been shifted up of 4 px. For the sake of clarity, the background has been removed on the presented images.

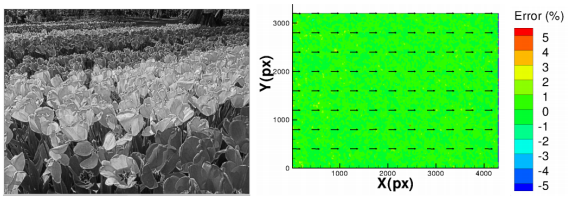

(a) image filtered (b) Three steps refinement

Figure 9: Image filtered with CLAHE (a) and velocity map from the DFT method applied on a window of 256 px refined in three steps to 32 px (b) - displacement of 16 px

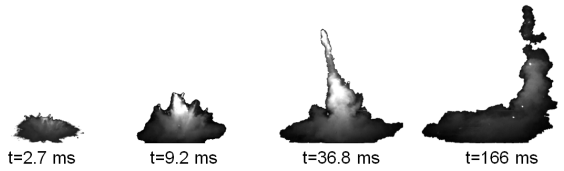

Figure 10: Images taken from the dispersion of talc driven by a RP80-EBW detonator under a wind of 5 m/s

Different methods to detect the correlation peak have been tested on the experimental images with an interrogation window of 64 px refined in 3 steps to 8 px:

- a one dimensional Gaussian fit subpixel peak finding method. This technique, often used for PIV analysis, uses the vertical and horizontal pixels directly adjacent to the maximum peak of the correlation matrix in order to evaluate the subpixel coordinates of the peak.

- a two dimensional Gaussian fit subpixel peak finding method. By using a two-dimensional Gaussian function, the techniques is more suitable for elliptical shapes.

- a centroid method. A matlab function has been tested to extrapolate the correlation matrix in order to detect the supixel position of the peak.

- a pixel method. This method takes the maximum of the correlation matrix.

- a pixel method on up-sampled images. An attempt has been made to improve the accuracy of the analysis by up-sampling the image.

The error made on the mean displacement by the tested methods is given in Figure 11 for the four experimental images. For the kind of images tested, the one dimensional Gaussian method gives the most accurate results.

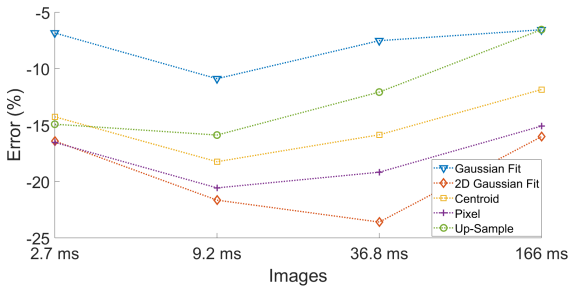

Figure 11: Methods to detect the correlation peak

3.2. *Parametric study on the dispersion driven by an explosion*

A parametric study has been conducted on the experimental dispersion of 10 g of heavy powder driven by the explosion of a RP80-EBW detonator under a calm atmosphere with a Global Visualization. The objectives of the investigation is the selection of the optimal interrogation window size and separation time between two images.

The quality of the results directly depends on the analyzed displacement and the interrogation window size. If the displacement is lower than a given limit, the results are overestimated. This limit depends on the size of the interrogation window. Figure 12 gives the variation with time of the mean velocity of the dispersion under a calm atmosphere for three window sizes. In the given example, the mean velocity is estimated through the mean value of the velocity magnitude (Equation 1). Another way to study the mean velocity would be to estimate the mean value of the horizontal component of the velocity and the mean value of the vertical component (Equation 2). However, this last method decreases the effect of the noise of the analysis while the mean value of the velocity magnitude increases it.

$$\overline{Vmagnitude} = \frac{1}{n}\sum_{i=1}^{n}(\sqrt{(Vxi^2 + Vyi^2)}) \quad (1)$$

$$\overline{Vmean} = \sqrt{(\frac{1}{n}\sum_{i=1}^{n} Vxi)^2 + (\frac{1}{n}\sum_{i=1}^{n} Vyi)^2} \quad (2)$$

where n is the number of vectors and Vx and Vy the horizontal and vertical components of the velocity.

In theory, the mean velocity should converge to 0. In practice, the null value is never reached due to the limits of the LS-PIV analysis. Limits for windows of 64 px, 128 px and 256 px can be found in Table 3.

The limit decreases when the size of the first interrogation window increases. For an analysis using an initial window size of 64 px, the mean velocity converges to 0.1 px and the deviation starts at 0.2 px while the mean velocity obtained with a window of 128 px converges to 0.025 px and starts to deviate at 0.05 px.

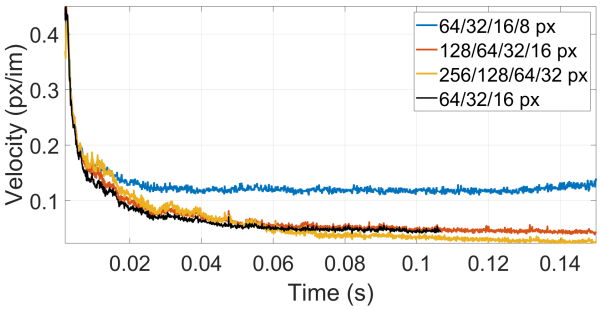

Figure 12: Limit of the analysis according to the window size for an acquisition of 10869Hz (f0)

Final Window Size	8 px	16 px	32 px
Minimum	0.1 px	0.05 px	0.025 px
Threshold	0.2 px	0.1 px	0.05 px

Table 3: Limits of the LSPIV for 3 final interrogation window sizes

A way to solve small displacements while keeping a good resolution is to increase the separation time between two images. This solution has been chosen to obtain the velocity of the studied dispersion. A window of 64 px, refined in 3 steps to 8 px with an overlap of 50 % is used to solve the dispersion. Up to 46 ms after the explosion, the dispersion is analyzed with a frequency of 5000 Hz (f0/2). After this time, the frequency is increased to 2000 Hz (f0/5). Before 2.7 ms, the cloud is too small and compact to be studied by LS-PIV and the velocity of the plume is obtained via a contour analysis. Figure 13(solid line) gives the variation of the mean velocity as a function of time under two atmospheric conditions. A good connection between the two studied frequencies can be observed, justifying the choice of these frequencies.

4. Results

This section gives results about the velocity of a talc dispersion driven by a RP80-EBW under different atmospheric conditions. LS-PIV has been applied using an interrogation window of 64 px, refined in 3 steps to 8 px, with an overlap of 50%. Before 2.7 ms, a frequency of 5000 Hz is used ; after this time, a frequency of 2000 Hz is used.

4.1. Comparison of the two flow visualizations

LS-PIV has been applied for the two kinds of flow visualizations (global and planar) for a dispersion of 10 g of heavy powder under a calm atmosphere.

Figure 13 gives the variation of the mean velocity (estimated using the Equation 1 for the two types of visualization. Before 2.7 ms, the dispersion is too small to be analyzed via LS-PIV so the mean velocity is given as a contour expansion mean velocity. Results of the contour expansion velocity can be found in Figure 14. A good overlap is observed after 20 ms. Before, the Global Visualization involves an underestimated value of the velocity and a Planar Visualization should be privileged. A good overlap is also observed between the contour expansion velocity and the Planar Visualization at the first moments of the dispersion.

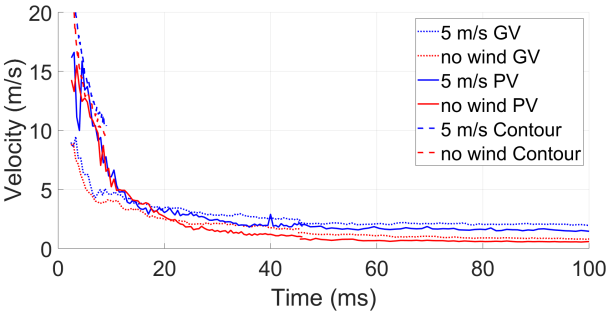

Figure 13: LS-PIV applied on the Global Visualization (GV) and the Planar Visualization (PV) for the dispersion driven by a RP806EBW under two atmospheric conditions

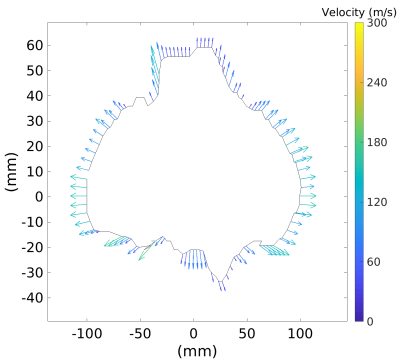

Figure 14: Contour expansion velocity under a calm atmosphere (RP80, 28 g)

4.2. *Effect of the wind on the dispersion*

The velocity profiles at 40 ms and 180 ms after the explosion, obtained via LS-PIV, are proposed in Figure 15. The averaged horizontal component of the velocity is represented by solid lines while the vertical component is given by dashed lines. The averaged vertical dispersion is similar for the three wind velocities, highlighting the fact that the wind does not have a major effect on the vertical dispersion. Contrarily, the horizontal velocity increases with the height similarly to the wind velocity profile of the atmospheric boundary layer applied. Under a calm atmosphere, the symmetrical dispersion leads to a null horizontal averaged velocity.

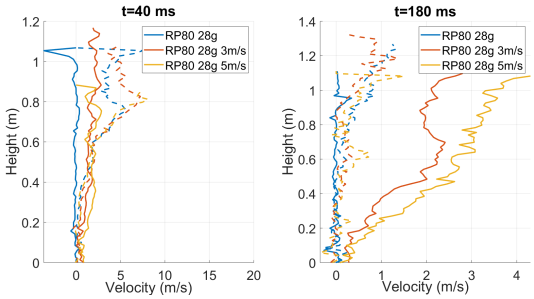

Figure 15: Velocity profiles of the dispersion under 3 atmospheric conditions, RP80 (dashed line: vertical component of the velocity, solid line: horizontal component of the velocity)

5. Conclusion and perspectives

The dispersion by explosive under an atmospheric boundary layer is investigated inside a subsonic wind tunnel. The velocity of the particles are obtained via Large-Scale Particle Image Velocimetry. A parametric study has been conduced on the optical method. First of all, fictive displacements have been analyzed on a grey-scale image and experimental images. Different techniques to detect the peak of the correlation matrix have been compared and an optimal displacement range has been selected. LS-PIV has been therefore applied on experimental images to obtain the velocity map of the dispersion. A global visualization and a planar one have been compared. After 20 ms, LS-PIV results are similar for the two types of visualization. Before this time, the velocity is underestimated via the global visualization. The planar visualization shows good overlap with expansion velocity at the first milliseconds of the dispersion.

Acknowledgments

This work has been conducted in the context of collaboration with the Direction des applications militaires (DAM) of the Centre d'Etudes de Gramat (CEG), from the Commissariat à l'énergie atomique et aux énergies alternatives (CEA).

References

[1] E. Wingstedt, H. Fossum, B. Reif, Simulation of bomb residue deposition following the oslo bombing, July 22 2011, FFI Rapport 2012/01836, ISBN 978-82-464-2176-6.

[2] N. Moussa, V. Devarakonda, Prediction of toxic emissions from chemical fire and explosion, Fire safety science-proceedings of the eleventh international symposium. pp. 1457-1468. DOI:10.308/IAFSS.FSS.11-1457.

[3] F. Zhang, D. Frost, P. Thibault, S. Murray, Explosive dispersal of solid particles, Shock Waves, January 2001, Volume 10, Issue 6, pp 431-443.

[4] D. Frost, C. Ornthanalai, Z. Zarei, V. Tanguay, F. Zhang, Particle momentum effects from the detonation of heterogeneous explosives, Journal of applied physics 101, 113529 (2007). DOI:10.1063/1.2743912.

[5] C. Sturtzer, Etude des mécanismes de dispersion par choc et des régimes de combustions de nuages de particules d'aluminium, ISAE-ENSMA-Poitier, 2014.

[6] L. Li, X. Ren, X. Lu, X. Yan, On the characteristics of liquid explosive dispersing flow, World academy of science, engineering and technology 70 2010, pp 606-610.

[7] C. Jenkins, R. Ripley, C. Wu, Y. Horie, K. Powers, W. Wilson, Explosively driven particle fields imaged using a high speed framing camera and particle image velocimetry, Internation journal of multiphase flow, Volume 51, May 2013, pp 73-86.

[8] B. Conan, Wind resource accessment in complex terrain by wind tunnel modelling, Ph.D. thesis, Université d'Orléans, 2012.

[9] C. Fouchier, D. Laboureur, L. Youinou, E. Lapebie, J. Buchlin, Experimental investigation of blast wave propagation in an urban environment, Journal of Loss Prevention in the Process Industries 49 (2017) 248 – 265. doi:https://doi.org/10.1016/j.jlp.2017.06.021.

[10] I. Fujita, M. Muste, A. Kruger, Large-scale particle image velocimetry for flow analysis in hydraulic engineering application, Journal of hydraulic research, 1998, 36:3, 397-414, DOI:10.1080/00221689809498626.

[11] C. Thompson, L. Shure, Image processing toolbox: For use with matlab, [user's guide]. MathWorks, 1995.

[12] W. Thielicke, E. Stamhuis, Pivlab towards user-friendly, affordable and accurate digital particle image velocimetry in matlab, Journal of Open Research Software, 2: e30, DOI: http://dx.doi.org/10.5334/jors.bl.

[13] M. Raffel, C. Willert, S. Wereley, J. Kompenhans, Particle Image Velocimetry, Springer, second edition, 2007.

A Coupled Atmosphere-Wave Model: an Investigation of the Influence of the Wind-Wave Alignment on the Vertical Wind Profile

Sara Porchetta

Environmental and Applied Fluid Dynamics Department, von Karman Institute for Fluid Dynamics, Belgium, sara.porchetta@vki.ac.be

Supervisor: Jeroen van Beeck

Dean of the Faculty, Professor and Head of Department, Environmental and Applied Fluid Dynamics Department, von Karman Institute for Fluid Dynamics, Belgium, vanbeeck@vki.ac.be

University Supervisor: Nicole van Lipzig

Professor, Department of Earth and Environmental Sciences, KULeuven, Belgium, nicole.vanlipzig@kuleuven.be

Abstract

Offshore wind-wave interactions can be studied by coupled mesoscale models due to an increase in computational power and the collaboration between different research expertise groups. In this research the Coupled-Ocean-Atmosphere-Wave-Sediment Transport (COAWST) model is employed to study the wind-wave interaction at the air-sea interface. More specifically, atmosphere only and atmosphere-wave models with different roughness length parameterizations are investigated. Special attention will be paid to a new roughness length parameterization which includes the effect of the alignment between the wind and wave direction. The effect of different roughness length parameterizations and different (coupled) models on the vertical wind profile are studied. A better representation of the vertical wind profile will help the offshore wind industry.

Keywords: COAWST, wind-wave interaction, roughness length parameterization

1. Introduction

Coupled models are more often being employed within the latest years due to an increase in computational power and the collaboration between different research expertise groups. As such, the Coupled-Atmosphere-Ocean-Wave-Sediment-Transport (COAWST) model [1], among other coupled models, was developed. Coupled models help to investigate the interaction between the separate models, which is essential for different kind of applications. These applications range from coastal erosion studies (wave-sediment model) important for tidal studies [2], to artic sea ice loss studies (ocean-atmosphere model) [3] or sea surface temperature studies during typhoons (ocean-wave-tide model) [4].

In this study, however, the focus lies on the interaction between the atmosphere and the waves. Different studies were performed by this type of coupled models, for example [5] investigated if coupling an atmospheric and wave model improved the prediction of the wave height and surface winds. Improving the wind estimations is of major importance for the offshore wind energy industry. A little improvement in the estimation of the winds would result in a better estimation of the power output for offshore wind turbines, this because the power is related to the velocity cube. A better representation of the power output would not only help with the scheduling of routine and maintenance works but also with the wind farm layout and the allocation of new offshore wind farms. These aspects become more important as the offshore wind industry felt an enormous growth in the last decennia and is believed to grow and exceed a market size of $60 billion USD by 2024. This growth is caused by higher winds offshore compared to onshore and related less societal constraints together with an expansion of (coastal) populations and thus a higher energy demand [6].

In order to correctly represent winds offshore, the

exchanges of momentum between the atmosphere and the sea surface should be modelled to such a degree that enables an accurate estimation of these winds. Particular for the sea surface is that it changes in time and space, and this should thus be represented by the models. The exchange of momentum from the wave model to the atmospheric model in COAWST is depicted by imposing a shear stress, which is dependent on the drag coefficient. Moreover, the drag coefficient itself is a function of the roughness length z_0. Different parameterizations of the roughness length exist in literature. Most atmospheric models include the Charnock roughness length parameterization [7], however, in time more elaborated roughness length parameterizations taking into account wave parameters were developed. These parameterizations are especially interesting for coupled models as the interaction between the two models can be improved by passing information from one model to the other. To mention a few, [8] developed a roughness length parameterization including wave age, [9] included wave steepness, and [10] included the effect of sea spray etc.

Over time multiple studies were conducted investigating the effect of the coupling between an atmospheric model and wave model using different roughness length parameterizations. [11] coupled simulations including the Charnock roughness length parameterization showed that young waves increased the roughness length and therefore decreased the ten-meter wind velocity. Later, [12] tested the differences between the roughness length of [13] and [14] which model the Charnock coefficient based on wave state parameters instead of a constant value. Their research reports that including a modified roughness length parameterization enhance the estimation of surface variables, however they also conclude that it only has little effect on the synoptic-scale of storms. Analysis by [15] revealed that coupled models show a notable improvement to wave heights when compared to buoy measurements.

Interestingly, the influence of the alignment between the wind and wave direction, in coupled atmosphere-wave models has scarcely been examined or discussed. Even though there is a substantial body of literature on this subject, both numerically and experimentally. [16] provided support based on Large Eddy Simulations (LES) that swell waves aligned to the wind have a lower drag compared to opposed swell waves. In line with these findings [17] observed a similar behavior based on Reynolds-Averaging Navier-Stokes (RANS) equations. Multiple measurements campaigns also noted that the shear stress on the wavy sea surface is not necessarily aligned with the wind direction [18; 19; 20].

This mechanism of misalignment between the wind and wave direction has been taken into account by [21] in a new roughness length parameterization. This approach yields to support current findings in literature which can be implemented in coupled models which follow a roughness length implementation. The present study investigates if this new roughness length parameterization improves the COAWST model, with specific attention to the offshore wind speed estimations. Such an improvement would benefit the offshore wind industry through different aforementioned aspects.

2. Model description and set-up

The Coupled-Ocean-Atmosphere-Waves-Sediment Transport (COAWST) model [1] consists of four separate models which are coupled by the Model Coupling Toolkit (MCT). COAWST is an open source code which can be used in different configurations. In this study only the coupling between the atmospheric model and the wave model will be employed to investigate the offshore wind. The atmospheric model used is the Weather Research and Forecasting (WRF) model [22], while the wave model is the Simulating WAves Nearshore (SWAN) model [23]. The fields exchanged between these models are on one hand the wind speed from WRF as a forcing to SWAN and on the other hand the wave height and wave length from SWAN to WRF. Different grids for the different models are feasible, this is made possible by the Spherical Coordinate Remapping Interpolation Package (SCRIP) [24], which computes the interpolation weights between the different grids. The simulations are performed over the North Sea, as measurements of the Forschungsplattformen in Nord- un Ostee Nr. 1 (FINO1) are used for validation.

2.1. Atmospheric model

The atmospheric model, WRF, of the coupled simulations has been developed at the National Centre for Atmospheric Research (NCAR). It solves the non-hydrostatic compressible Euler equations based on a finite difference discretisation [22]. Additionally, parameterizations schemes are implemented to describe the sub grid scale processes like turbulent dissipation rates, microphysics, radiation etc. Important for this study especially are the surface layer schemes, which

calculate the friction velocity and the exchange coefficients and subsequently impose the surface fluxes over the water surfaces. A different approach is used for land surfaces where the surface fluxes are calculated by the land surface schemes. Either on land or over the sea surface, these fluxes serve as a lower boundary for the planetary boundary layer schemes, these latter take into account the sub grid scale turbulent fluxes in the vertical direction.

The physical parameterization used for the simulations in this study are the Thompson microphysics scheme [25], the long and short wave Rapid Radiative Transfer Model for GCMs [26], the Kain-Fritsch cumulus scheme [27] only for the largest domain, and the NOAH land surface scheme [28]. Because the surface layer scheme is a boundary for the planetary boundary layer schemes these schemes have to be imposed accordingly. The roughness length parameterization of [8], [9] and [29] taking into account wave parameters are implemented in the Mellor-Yamada Nakanishi Ninno (MYNN) planetary boundary layer scheme [30] and the associated surface layer scheme. Consequently, to investigate the wind-wave interaction, these MYNN schemes are used in the current research.

The computational domain is situated around the FINO1 measurement mast location, positioned in the North Sea and covering a large part of Europe (Fig. 1). Three one-way coupled nested domains with a horizontal grid resolution of 27 km, 9 km and 3 km for the outer, middle and inner domain respectively are being employed. The vertical resolution consists of 53 vertical eta levels, close to the surface the grid spacing is 2 m while it reaches 2 km at the upper part of the domain. This stretched vertical gird approach ensures a better representation of the lower part of the boundary layer. All the simulations cover a ten-day time period starting from December 9th till December 19th 2010, where the first day is considered as spin-up and will be excluded from the results. The year 2010 is examined as high resolution measurements and measurements at different altitudes are available. The simulations are initialized and forced 6 hourly at the boundaries by the ERA-Interim reanalysis data set made available by the European Centre for Medium-Range Weather Forecast [31].

2.2. *Wave model*

The wave model, SWAN, solves the spectral density evolution equation especially designed for shallow water, nevertheless it can be used for deep water. The frequency ranges from 0.04 Hz to 1 Hz and is

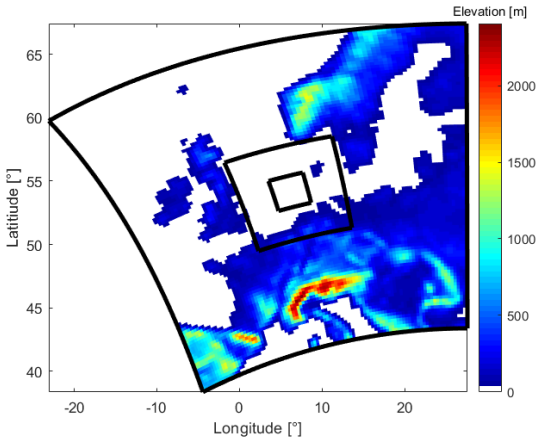

Figure 1: WRF computational configuration, consisting out 3 nested domains with a horizontal resolution of 27 km, 9km and 3 km from the outer domain to the inner most domain. The color bar shows the elevation over a part of Europe.

divided into 25 frequency bins, in addition 36 directional bins are considered. The model includes processes like shoaling, refraction, defraction, non linear wave-wave interactions, wave breaking and bottom dissipation. The wave model runs in the third-generation mode, which allows wave growth by wind, quadruplet and tried interactions as well as wave dissipation by whitecapping and breaking. Breaking is taken into account with a proportionality coefficient of one and a breaker index of 0.73. The expression of [32] is activated for the bottom friction, while for the whitecapping and the linear growth of waves due to the wind the model of [33] is selected. For the wave model two nested grids are employed (Fig. 2), including a larger grid with 100 grid points in each direction, covering a region including part of the Baltic Sea, the North Sea and part of the North Atlantic Ocean. The smaller grid, with 173x142 grid points, is centred around the FINO1 mast location, and covering a large part of the North Sea. On the lateral boundaries 13 tidal constituents (M2, S2, N2, K2, K1, O1, P1, Q1, Mf, Mm, M4, Ms4, Mn4) are employed based on the OSU Tidal Prediction Software (OTPS) code [34].

2.3. *Modelling the wind-wave interaction*

In this study we address the investigation of the model parameterization of the momentum exchange between the atmosphere and the wave surface. The total shear stress, τ, a combination of the turbulent, wave and viscous stress is imposed as a lower boundary condition to the atmospheric model. This shear

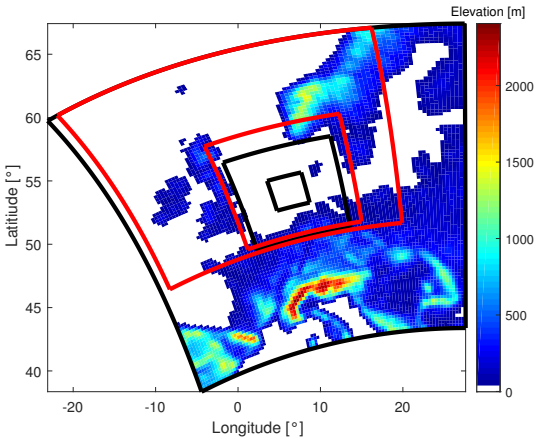

Figure 2: WRF computational configuration (black) and SWAN computational configuration (red), consisting out 2 nested domains with 100x100 and 173x142 grid points respectively. The color bar shows the elevation over a part of Europe.

stressed is modelled based on a roughness length z_0. Different roughness length parameterizations are available in the COAWST model. Like most numerical mesoscale models the roughness length over the sea surface is mostly described based on the Charnock parameterization [7] (Eq. 1). In this equation, α, is the Charnock coefficient, u_*, the friction velocity and g the gravitational constant.

$$z_0 = \alpha \frac{u_*^2}{g} \tag{1}$$

The Charnock coefficient in the COAWST model is set to 0.016 which corresponds to rapidly rising seas. A substantial body of literature investigated this coefficient and suggest that it should be function of wave parameters [35], and also suggest to take the water depth into account [36]. In time, multiple new roughness length parameterizations have been proposed, all with a different focus. The roughness length parameterization of [8] taking into account the inverse wave age (u_*/c_p) and multiple offshore conditions of pure wind-sea, rough-flow over deep water is shown by Eq. 2. Here, H_s, is the significant wave height and, c_p, the wave phase speed at the peak of the energy spectrum.

$$\frac{z_0}{H_s} = 3.35 \left(\frac{u_*}{c_p} \right)^{3.4} \tag{2}$$

This roughness length includes the effect of fetch and duration which is of importance for offshore conditions, and ensures an increased roughness length for young waves compared to old waves. Young waves are defined by a inverse wave age smaller than 0.05, while wave ages larger than 0.05 correspond to old waves. It is used in [37] to study the fully coupled model for the Caspian Sea. Moreover, [38] also studied the effect of different roughness length parameterization concerning a hurricane study of hurricans Ida and Nor'Ida. This study noticed that the coupled model improved the performance of the estimations, in particular the wind intensities and wave height, when compared to the stand alone modules.

Recently, [21], proposed a new roughness length parameterization (Eq. 3) accounting for wind-wave (mis)alignment. In this equation, θ, is expressed in radians and is the difference of the wind direction and the peak wave direction of the waves. Based on offshore measurements they concluded that an increased roughness length is present for misaligned wind-wave directions, and that this effect is more pronounced for old waves.

$$\frac{z_0}{H_s} = 20 \cdot cos\,(0.45\theta) \left(\frac{u_*}{c_p} \right)^{3.8 \cdot cos(-0.32\theta)} \tag{3}$$

The study mention above is the first one including the effect of misalignment in a bulk roughness length parameterization which works for various planetary boundary layer schemes. Although, this is the first bulk parameterization counting for wind-wave alignment, [39] examined a directional coupling for hurricane applications. Considerable attention in this paper went to the estimation of the two component wave stress from third generation wave models. Up to now they were not able to present the small wave numbers, which are essential in high wind conditions of hurricanes. This study focuses on a correct implementation of the small wave numbers in a two dimensional stress parameterization. To conclude, particularly little attention has been paid to research examining the comparison of models whether or not including the (mis)alignment effect on the vertical wind profile. Therefore, in this paper, the role of the (mis)alignment on the vertical wind profile is examined based on coupled numerical mesoscale atmospheric-wave models.

2.4. Set of experiments

In order to investigate the influence of the coupled model and the different roughness length parameterizations on the vertical wind profile multiple simulations are performed. The first simulation (S1) is an atmospheric model only, including the Charnock roughness length parameterization (Eq. 1). Furthermore, two atmosphere-wave coupled simulation

are performed, one including the roughness length parameterization of [8] (Eq. 2) (S2) and one with [21] roughness length parameterization (Eq. 3) (S3). The latter roughness length parameterization has been implemented in the COAWST model as it was not present yet. To accomplish this implementation and extra field has to be exchanged between the two models, namely the wave direction, with the purpose of calculating the difference between the wind and wave direction. An overview of these different simulations is presented in Table 1.

Table 1: Overview simulations

Simulation	Atmospheric Model	Wave Model	Roughness Length Parameterization
S1	✓		[7]
S2	✓	✓	[8]
S3	✓	✓	[21]

2.5. Study period and data availability

The different simulations are analyzed and compared during the period of December 9th to December 19th, 2010. The first 24 hours are used as spin up and are therefore excluded from the results in the next section. Measurements of the FINO1 mast are used to validate the simulations. The measurement tower is located in the North Sea, 45 km of the German coast. At this location atmospheric measurements together with wave measurements are being documented. To conduct a comparison study of the roughness length parameterization and their effect on the vertical profile, this measurement mast will serve perfectly for this purpose, as it contains measurements up to 100 m above sea level, at 8 different altitudes. Cup anemometers measure the velocity at 30, 40, 50, 60, 70, 80, 90 and 100 m, while the wind direction is measured at 30, 50, 70 and 90 m. Moreover, additional low response measurements, such as temperature, air humidity, pressure and precipitation are present at this location. The water depth, at the location of the measurement mast, is approximately 30 m deep, and at close vicinity of the mast a Datawell/MKIII bouy measures the significant wave height, peak wave direction and (peak) wave period.

3. Results and discussion

The time series of the velocity and wind direction at 30 m, the peak wave direction and the difference between the wind and peak wave direction are shown in Fig. 4. The wind velocity and wind direction are compared to the FINO1 measurements. Overall a good agreement between the different models and the measurements can be observed. At time step 47 and 60 a larger discrepancy is present, which can be caused by a weather front passing, resulting in a sharp velocity gradient. Both the wind and the waves travel from the North most of the time, except for the last three days. For these days, there can be noticed that the wind is traveling from the South, while the waves come from their fetch unlimited region in the North. The wind and wave direction are thus opposed, which in most cases correspond to a lower velocity of wind blowing from land.



Figure 3: FINO1 measurement mast.

However, from Fig. 4, it is not clear how to interpret which model performs best for the chosen time period. For this reason the simulated and observed (FINO1) wind speeds are temporally averaged for different altitudes and compared in (Fig. 5). From the vertical profiles, there can be observed that all three models, do fall in the range of one standard deviation of the mean FINO1 observations. In more detail, it appears that S3 has an improved performance in the lower part of the boundary layer, while this is not completely clear above 50 m.

After calculating the root mean square error (RMSE) at the different altitudes (Fig. 6), it is clear that S3 performs best at all altitudes, followed by S1 and finally S2. It is not completely clear why the uncoupled model S1 performs better than S2. Further investigation by a coupled simulation including the Charnock parameterization might improve our un-

derstanding. We can separate the RMSE calculations based on the alignment, where aligned corresponds to a difference between the wind and wave direction of less than 60°, perpendicular corresponds to differences between 60°-120° and opposed to differences of more than 120°. The results of this classification are shown in Fig. 7. The figure shows that the RMSE decreases more for opposed and perpendicular cases compared to aligned. The differences between the models is also more pronounced for non aligned cases. For the S3 simulation the RMSE decreases when the misalignment increases, while this is not the case for S2 and S3. This improvement of opposed cases might be caused by the new roughness length parameterization of [21], which takes into account the effect of an increase of roughness length for an increase in misalignment. To include the difference in propagation of wind and wave direction in the roughness length parameterizatioin has a positive effect on the estimation of the vertical wind profile.

Despite the fact that S3 has the lowest RMSE, the differences between the models are small. Statistical tests indicate that the results from the roughness length parameterization of [21] (S3) are not significantly different from the results of the roughness length parameterization of [8] (S2) (p-value 0.23), while the results of (S3) and (S2) are significantly different from (S1) (p-value 0.002). For this reason, we are investigating a simulation of one year.

The overall performance of the different simulations based on different scoring criteria (RMSE, absolute total bias, Spearman correlation coefficient) at different altitudes is shown in Table 2. All three different scoring criteria confirm S3 to be the best performing model compared to the other models. It's improved performance is more pronounced at the lower altitudes, however, this is still existent at the higher altitudes. The models S1 and S2 perform similarly good. A little improvement on the velocity estimations could indicate a large improvement on the power estimations.

In Fig. 8 the velocity field for the three different models (S1-S3) is shown for three different situations. First for an aligned situation, second for an opposed one and last the mean field over the ten day simulation. Higher wind velocities are present for the aligned situation compared to the opposed situation. Moreover, the model S1 obtains the lowest velocities while S2 obtains the highest velocities. This can be linked to the roughness length parameterizations, the roughness length corresponding to the velocity fields shown in Fig. 8, are shown in Fig. 9. As such, S1 models the highest roughness length, while S2 models it the lowest, resulting in the lowest and highest mean wind velocities respectively. In order to investigate the difference between the two models, a further investigation of the wave age could improve our understanding. The difference between the roughness length, and thus the velocity, between model S2 and S3 can be described based on the difference in the wind and wave direction. In Fig. 10 the difference between the wind and wave direction of an aligned situation is shown. There can be noticed that for the FINO1 location the wind-wave direction is indeed aligned, which results in similar roughness lengths and wind speeds. However, to the West of Ireland a strong misalignment between the wind and waves can be observed, resulting in a higher roughness length for S3 compared to S2. In Fig. 11 the difference between the wind and wave direction of an opposed situation is shown. To the South of Ireland and at the FINO1 location, a strong misalignment results in higher roughness lengths and thus lower velocities.

There are thus indications that different roughness length parameterizations, can influence the velocity field at hub height. Moreover, the parameterization taking into account wave age and wind-wave misalignment [21], indicates to have the best performance. Hence, a longer study period is needed in or-

Table 2: Model evaluation

		S1	S2	S3
RMSE	30m	2.28	2.38	2.10
	40m	2.26	2.42	2.13
	50m	2.31	2.41	2.14
	60m	2.27	2.45	2.15
	70m	2.28	2.45	2.17
	80m	2.35	2.49	2.21
	90m	2.35	2.51	2.23
BIAS	30m	413	452	395
	40m	408	458	400
	50m	422	453	399
	60m	423	465	408
	70m	427	476	418
	80m	431	486	426
	90m	436	496	434
	100m	441	504	441
Spearman correlation	30m	0.83	0.83	0.85
	40m	0.83	0.83	0.86
	50m	0.84	0.84	0.87
	60m	0.85	0.85	0.87
	70m	0.85	0.85	0.87
	80m	0.85	0.85	0.87
	90m	0.85	0.86	0.88
	100m	0.86	0.86	0.88

der to conclude this. In addition an offline coupling should be performed to investigate the effect of the two way coupling. In a further study, this type of bulk roughness length parameterization can be compared to a model employing a two-dimensional stress [39]. An important remark is that the numerical mesoscale model used in this study, similar to many other models, assume the validity of the Monin-Obukhov Similarity Theory (MOST). This topic is under debate and should be considered in further studies.

4. Conclusions

This study investigated the effect of three different roughness length parameterizations on the vertical wind profile. Three simulations were performed, first a simulation including the roughness length parameterization of Charnock [7], second a simulation including the roughness length parameterization of [8] and last a simulation including the roughness length parameterization of [21]. The latter two models were a coupled atmosphere-wave model, while the former was an atmosphere only model. The roughness length of [21] is a recent proposed parameterization taking a reduced roughness length for an increase in misalignment between the wind and wave direction into account. The results of the simulationz were compared to FINO1 measurements. From this comparison multiple main conclusion could be formed. First, all three models are able to represent the atmospheric conditions for the 10 day period. Second, comparing the vertical wind all the models lie not further than one standard deviation from the mean observations. For low altitudes the model including the roughness length parameterization of [21] seems to perform the best. This is confirmed by three model evaluation criteria (RMSE, absolute total BIAS, and Spearmann correlation), which concluded that the more advanced roughness length parameterization ([21]) has an improved performance compared to the other models and this is not only restricted to the lower altitudes. Moreover, the improvement of the estimation of the velocity is more pronounced for misaligned cases compared to aligned case, where the model differences are less. Further investigation of a coupled wind-wave model including the Charnock roughness length parameterization [7], a offline coupled model, models with different roughness length parameterizations and the investigation of the wave age could improve our understanding in this complex phenomena at the air-sea interface.

Acknowledgments

This research was funded by FWO-SB.

References

[1] J.C., Warner, B., Amstrong, R., He, and J.B. Zambon, Development of a coupled ocean-atmosphere-wave-sediment transport (COAWST) Modelling system, Ocean. Model. 35 (2010) 230–244.

[2] A.J. Bever, ad M. MacWilliams, Simulating sediment transport processes in San Pablo Bay using coupled hydrodynamic, wave, and sediment transport models., Marine Geology 345 (2013) 235–252.

[3] C., Deser, R.A., Tomas, and L., Sun, The role of ocean-atmosphere coupling in the zonal-mean atmospheric response to artic sea ice loss., Journal of Climate 28 (2015) 2168–2186.

[4] I.-J., Moon, Impact of a coupled ocean wave-tide-circulation system on coastal modeling., Ocean. Model. 119 (2005) 397–407.

[5] K., Wahle, J., Stavena, W., Koch, L., Fenoglio-Marc, H.T.M., Ho-Hagemann, and E.V., Stanev, En atmosphere-wave regional coupled model: improving predictions of wave heights and surface winds in the southern North Sea., Ocean Sci. 13 (2017) 289–301.

[6] S., Keivanpour, A., Ramudhin, and D.A., Kadi, The sustainable worldwide offshore wind energy potential: a systematic review., Journal of Renewable and Sustainable Energy 9 (2017) 065902.

[7] H., Charnock, Wind stress on a water surface., Q.J. Roy. Meteor. Soc. 81 (1955) 639–640.

[8] W.M., Drennan, H.C., Graber, D., Hauser, and C. Quentin, On the wave age dependence of wind stress over pure wind seas., J. Geophys. Res. 108 (2003) 8065(C3).

[9] P., Taylor, and M., Yelland, The dependence of sea surface roughness on the height ad steepness of the waves., J. Phys. Oceanogr. 31(2) (2001) 572–590.

[10] B., Liu, H., Liu, L., Xie, C., Guan, and D., Zao, A coupled atmosphere-wave-ocean modeling system: simulation of the intensity of an idealized tropical cyclone., Mon. Weather Rev. 139 (2011) 132–152.

[11] J.D., Doyle, Coupled ocean wave/atmosphere mesoscale model simulation for cyclogenesis., Tellus A 47 (1995) 766–788.

[12] S., Desjardins, J., Mailhot, and R., Lalbeharry, Examination of the impact of a coupled atmospheric ocean wave system. Part I: Atmospheric Aspects., J. Phys. Oceanogr. 30 (2000) 385–401.

[13] S.D., Smith, R.J., Anderson, W.A., Oost, C., Kraan, N., Maat, J., De Cosmo, K.B., Katsaros, K.L., Davidson, K., Bumke, L., Hasse, and H.M., Chadwick, Sea surface wind stress and drag coefficients: the HEXOS results., Bound.-Layer Meteorol. 60 (1992) 109–142.

[14] P.A.E.M., Janssen, Wave-induced stress and the drag of air flow over sea waves., J. Phys. Oceanogr. 19 (1989) 745–754.

[15] R., Lalbeharry, J., Mailhot, S., Desjardins, and L., Wilson, Examination of the impact of a coupled atmospheric and ocean wave system. Part II: ocean wave aspects., J. Phys. Oceanogr. 30 (2000) 402–415.

[16] P.P., Sullivan, J.B., Edson, T., Hristov, and J.C., McWilliamns, Large-eddy simulations and observation of atmospheric boundary layers above nonequilibrium surface waves., J. Atmos. Sci. 65 (2008) 1225–1245.

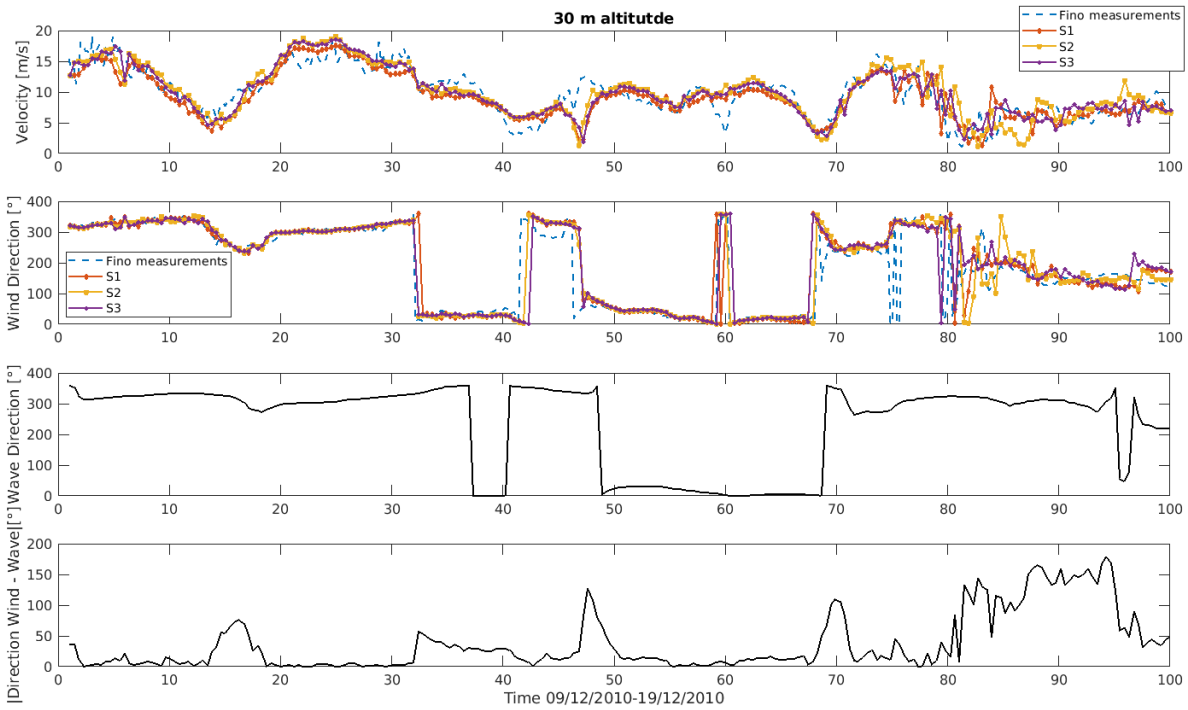

Figure 4: From top to bottom. First, a time series of the velocity at 30 m for the three different simulations compared to the measurement mast. Second, the time series of the wind direction at 30 m compared for the three simulations with the measurements. Third, the peak wave direction over time. Lastly, the difference in wind direction and peak wave direction over time. See Table 1 for legend.

[17] S.M., Kalvig, E., Manger, and R., Kverneland, A method for wave dirven wind simulations with CFD, no. Energy Procedia, Deepwind, 35, 148-156, Norway, 2013.

[18] A.A., Grachev, C.W., Fairall, J.E., Hare, J.B., Edson, and S.D., Miller, Wind stress vector over ocean waves., J. Phys. Oceanogr. 33 (2003) 2408–2429.

[19] K.F., Rieder, and J.A., Smith, Removing wave effects from the wind stress vector., J. Geophys. Res. 103 (1998) 1363–1347.

[20] Q., Li, E., Bou-Zeid, N., Vercauteren, and M., Parlange, Signatures of air-wave interactions over a large lake., Bound.-Layer Meteorol. 167 (2018) 445–468.

[21] S., Porchetta, O., Temel, D., Munoz-Esparza, J., Reuder, J., Monbaliu, J., van Beeck, and N., van Lipzig, A new rougnhness length parameterization accounting for wind-wave (mis) alignment., Atmos. Chem. Phys. Discuss. in review.

[22] W., Skamarock, J., Klemp, J., Dudhia, D., Gill, D., Barker, M., Duda, X., Huang, W., Wang, and J., Powers, A description of the advanced research WRF version 3, Tech. rep., National Center for Atmospheric Research Note NCAR/TN-475+STR, Boulder, Colorado (2008).

[23] N., Booij, R.C., Ris, and L.H., Holthuijsen, A third-generation wave model for coastal regions. Part I: Model description and validation., Journal of Geophysical Research 104(C4) (1999) 7649–7666.

[24] J. P.W., A users guide for SCRIP: A spherical coordinate remapping and interpolation package, v1.4, Tech. rep., Los Alamos National Laboratory (1997).

[25] G., Thompson, P.R., Field, R.M., Rasmussen, and W.D., Hall, Explicit forecasts of winter precipitation using an improved bulk microphysics scheme. Part II: Implementation of a new snow parameterization., Mon. Wea. Rev. 136 (2008) 5095–5115.

[26] M.J., Iacono, J.S., Delamere, E.J., Mlawer, M.W., Shephard, S.A., clough, and W.D., Collins, Radiative forcing by long lived greenhouse gases: calculations with the AER radiative transfer models., J. Geophys. Res. 113 (2008) D13103.

[27] J.S., Kain, The Kain-Fritsch convective parameterization: An update., J Appl. Meteor. 43 (2004) 170–181.

[28] M., Tewari, F., Chen, W., Wang, J., Dudhia, M.A., LeMone, K., Mitchell, M., Ek, G., Gayno, J., Wegeil, and R.H., Cuenca, Implementation and verification of the unified NOAH land surface model in the WRF model, no. 20th conference on weather analysis and forecasting/16th conference on numerical weather prediction, 2004.

[29] W.A., Oost, G.J., Komen, C.M.J., Jacobs, and C. van Oort, New evidence for a relation between wind stress and wave age from measurements during ASGAMAGE., Bound. Lay. Meteorol. 103(3) (2002) 409–438.

[30] M., Nakanishi, and H., Niino, An improved Mellor-Yamada level 3 model: its numerical stability and application to a regional prediction of advecting fog., Bound. Lay. Meteorol. 119 (2006) 397–407.

[31] European Centre for Medium-Range Weather Forecasts., ERA-Interim Project. , no. Research Data Archive at the National Center for Atmospheric Research, Computational and Information Systems Laboratory., Accessed 7-02-2019.

[32] O.S., Madsen, Y.-K., Poon, and H.C., Gaber, Spectral wave attenuation by bottom friction., Coastal Engineering 34 (1988) 492–504.

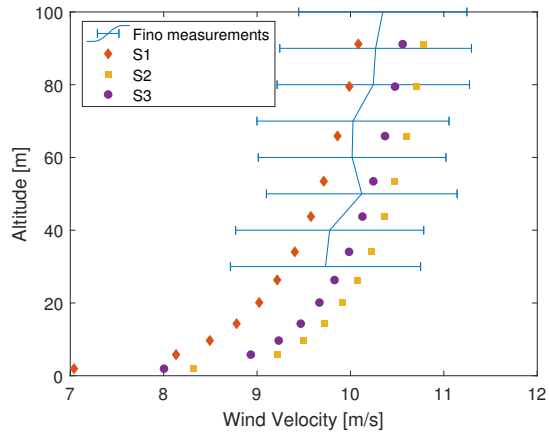

Figure 5: Mean vertical velocity profile of the three different simulations compared to the FINO1 measurements. See Table 1 for legend.

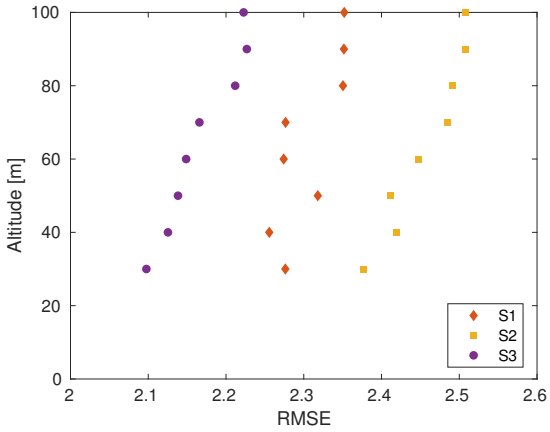

Figure 6: The average root mean square error of the three different simulations at 8 different altitudes. See Table 1 for legend.

[33] G.J., Komen, S., Hasselmann, and K., Hasselmann, On the existence of a fully developed windsea spectrum., Journal of Physical Oceanography 14 (1984) 1271–1285.

[34] G.D., Egbert, and S.Y., Erofeeva, Efficient inverse modeling of barotropic ocean tides., Journal of Atmospheric and Oceanic Technology 19.2 (2002) 183–204.

[35] N., Maat, C., Kraan, and W.A., Oost, The Roughness of wind waves., Bound.-Layer Meteorol. 54 (1991) 89–103.

[36] P.A., Jimenez, and J., Dudhia, On the need to modify the sea surface roughness formulation over shallow waters., J. Appl. Meteorol. Climatol. 57 (2018) 1101–1110.

[37] N., Bruneau, and R., Toumi, A fully coupled atmosphere-ocan-wave model of the Caspian Sea., Ocean Model. 107 (2016) 97–111.

[38] M., Olabarrieta, J.C., Warner, B., Amstrong, J.B., Zambon, and R. , He, Ocean-atmosphere dynamics during Hurricane Ida and Nor'Ida: An applicatioin of the coupled ocean-atmosphere-wave-sediment transport (COAWST) modeling system., Ocean Model. 43-44 (2012) 112–137.

[39] S.S., Chen, W., Zhao, and M.A., Donelan, Directional wind-wave coupling in fully coupled atmosphere-wave-ocean models: results from CBLAST-hurricane., Journal of the Atmospheric Sciences 70 (2013) 3198–3215.

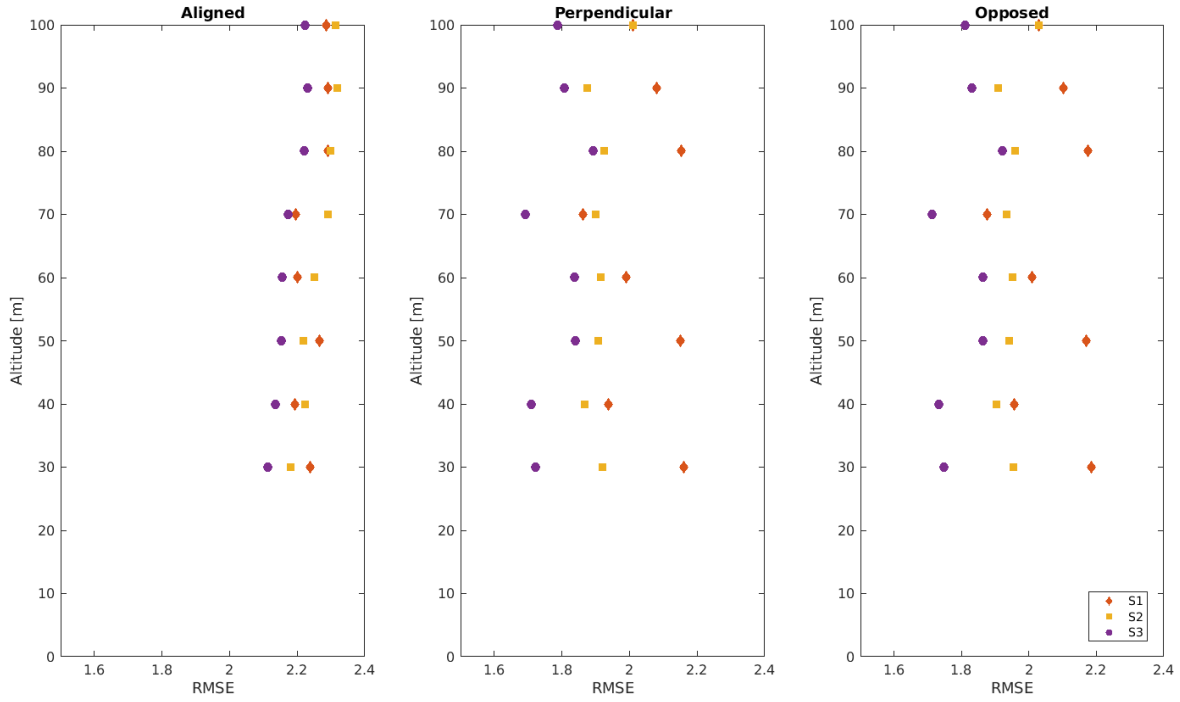

Figure 7: The average root mean square error of the three different simulations at 8 different altitudes and for three different categories, aligned, perpendicular and opposed. See Table 1 for legend.

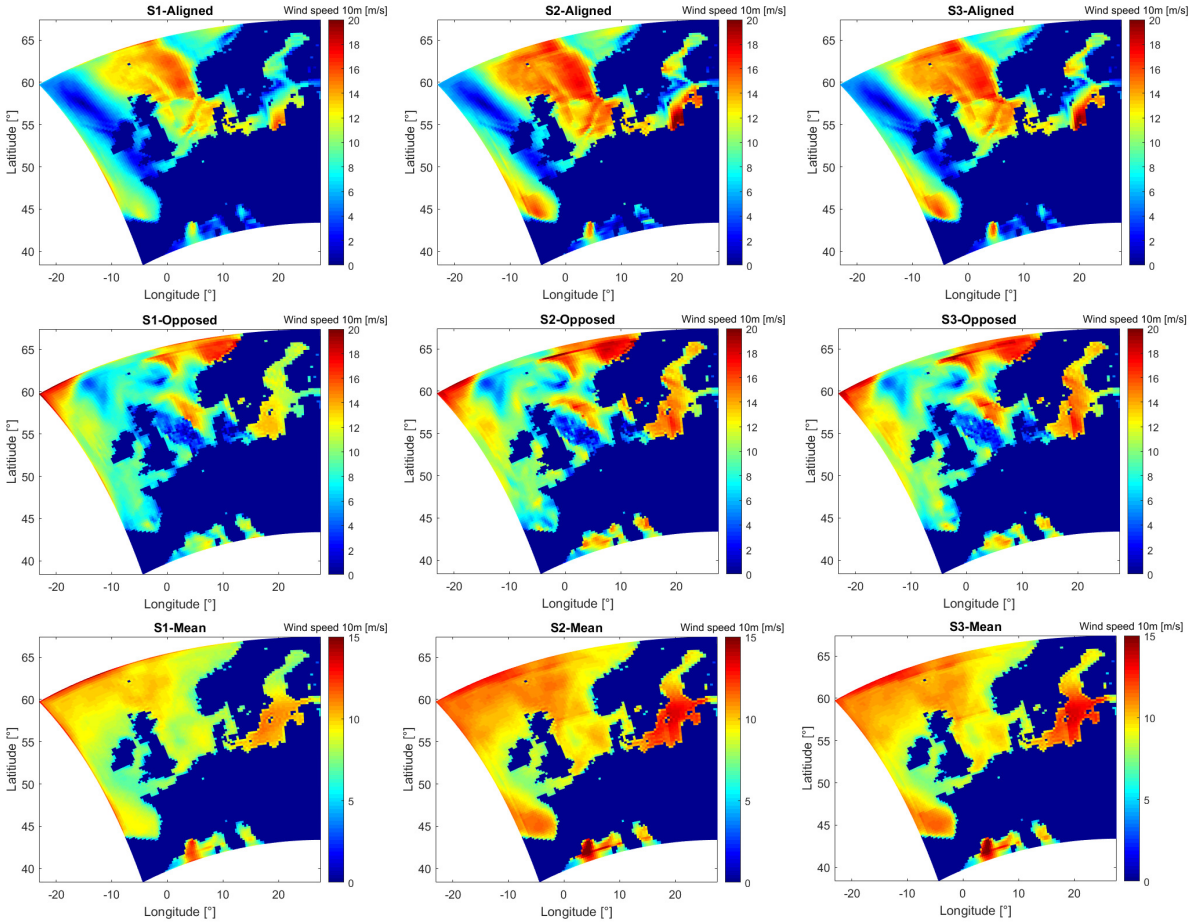

Figure 8: The velocity field for aligned (top), opposed (middle) and mean field (bottom) for the three different models S1 (left), S2 (middle) and S3 (right). See Table 1 for the differences between simulations.

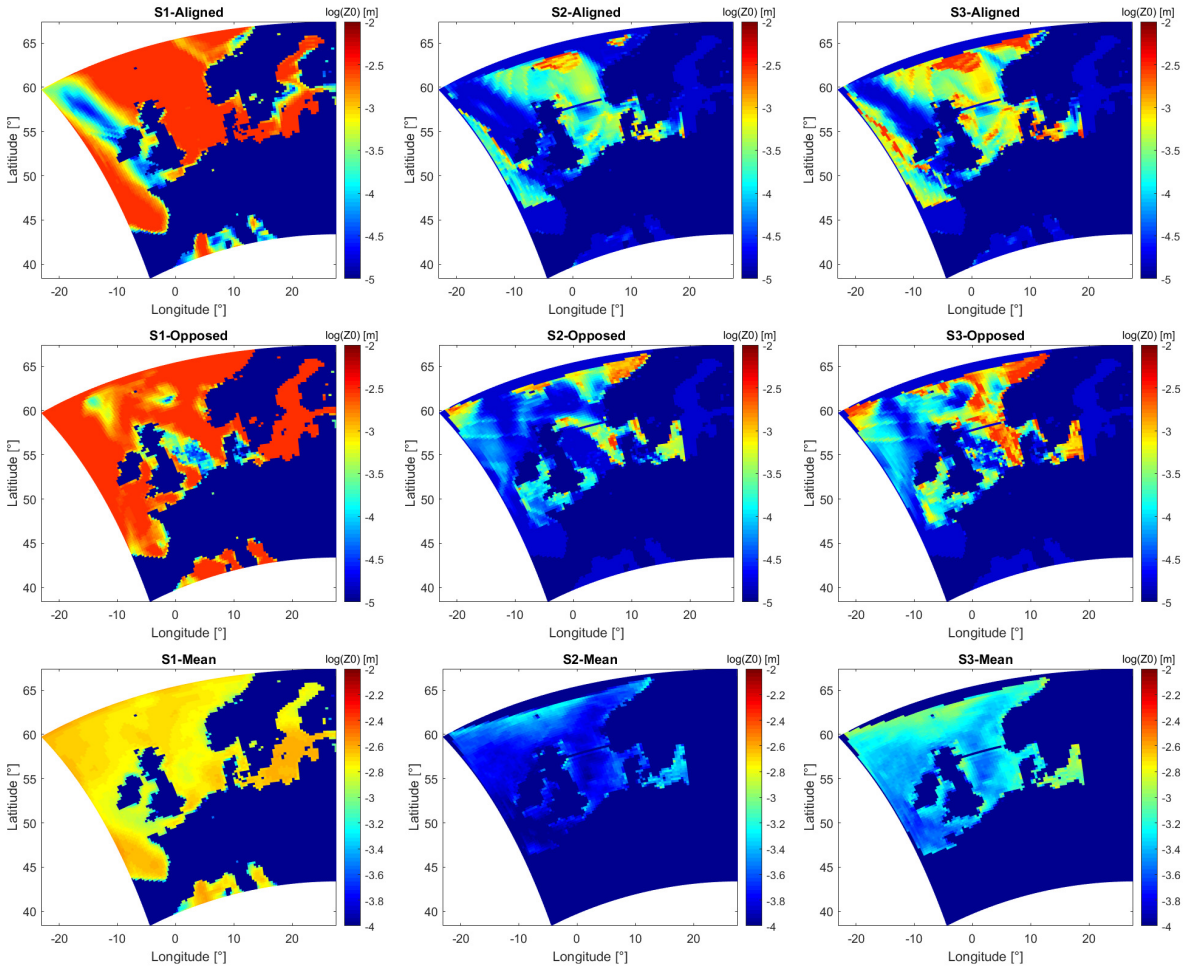

Figure 9: The roughness length field for aligned (top), opposed (middle) and mean field (bottom) for the three different models S1 (left), S2 (middle) and S3 (right). See Table 1 for the differences between simulations.

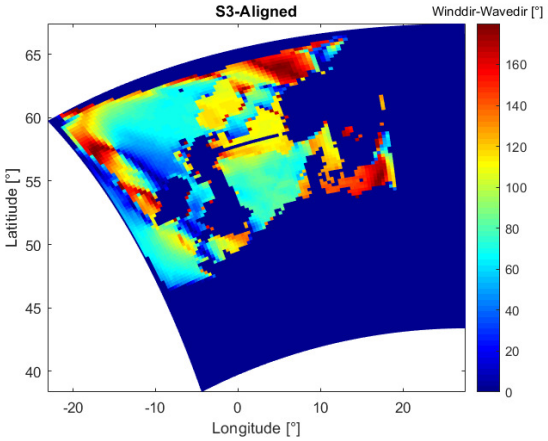

Figure 10: Difference between the wind direction and the peak wave direction for an aligned situation for model S3. See Table 1 for S3 set up.

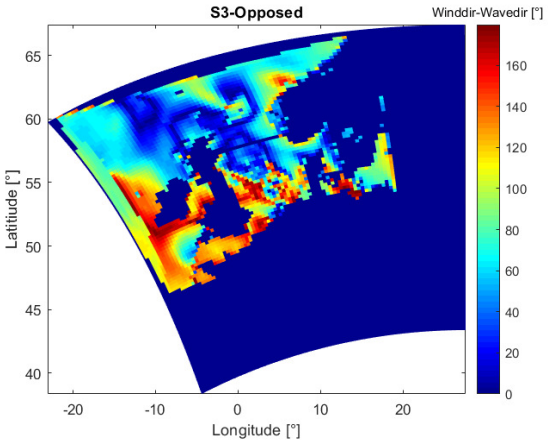

Figure 11: Difference between the wind direction and the peak wave direction for an opposed situation for model S3. See Table 1 for S3 set up.

Generalized Scale-Adaptive 3D Planetary Boundary Layer Model based on LES for the Earth's and Mars Atmospheres

Cem Berk Senel

Environmental and Applied Fluid Dynamics Department, von Karman Institute for Fluid Dynamics, Belgium, cem.berk.senel@vki.ac.be

Supervisor: Jeroen van Beeck

Dean of the Faculty, Professor and Head of Department, Environmental and Applied Fluid Dynamics Department, von Karman Institute for Fluid Dynamics, Belgium, vanbeeck@vki.ac.be

University Supervisor: Alessandro Parente

Professor, Aero-Thermo-Mechanics Department, Université Libre de Bruxelles, Belgium, Alessandro.Parente@ulb.ac.be

Abstract

The planetary boundary layer is located in the lowest part of the troposphere, involving complex turbulent structures induced by the solar radiation. In recent years, there is a growing interest to understand the characteristics of PBL turbulence from wind engineering assessments towards planetary missions. There is therefore a strong need for a highly accurate representation of the PBL physics closely linked with the advances in PBL modeling. As far as the validity range is concerned, large-eddy simulation (LES) models are valid for microscales (i.e. horizontal grid space, $\Delta_{LES} < 100\ m$). At the LES limit, grid spacing is much lower than the size of energy-containing eddies (i.e. $\Delta_{LES} << \mathcal{L}$), so that energetic large scales are *explicitly resolved* while dissipative small scales are modeled by three-dimensional LES subgrid-scale (SGS) models. On the other hand, mesoscale models are valid for more regional domains with coarser grid resolutions (i.e. $\Delta_{meso} > 1\ km$). Since $\Delta_{meso} >> \mathcal{L}$ at the mesoscale limit, all the turbulence becomes subgrid and *implicitly modeled* by one-dimensional mesoscale SGS models. These so-called 1D PBL models can only represent the 1D-turbulence by neglecting all the horizontal turbulent fluxes and derivatives. Between these two asymptotic limits, i.e. terra-incognita zone, both approaches are no longer valid, considering they are originally designed for their own limits. So far, there is no conclusive theory on how to model turbulence in this transition zone. In this context, the overarching goal is to develop a generalized scale-adaptive 3D PBL model that will fill the gap between the broad range of scales encountered in PBL modelling. This scale bridging model will work in a generalized framework as 3D LES mode at LES limit, as 3D mesoscale mode at mesoscale limit while as 3D terra-incognita mode across the TI zone. The proposed model will initially be tested for the Earths PBL over BLLAST campaign in southern France. Then it will be tested for the Martian PBL, over the landing site of ExoMars2020 mission by ESA. This final stage will be conducted in collaboration with the Royal Observatory of Belgium.

Keywords: Planetary boundary layer, turbulence, LES, terra-incognita modeling, Earth's and Mars atmosphere.

CBRN Dispersion Modeling in the Atmosphere

Yoshiyuki Nishio

Department of Mechanics, Royal Military Academy (RMA), Belgium, yoshiyuki.nishio@rma.ac.be

Supervisor: Jeroen van Beeck

Dean of the Faculty, Professor and Head of Department, Environmental and Applied Fluid Dynamics Department, von Karman Institute for Fluid Dynamics, Belgium, vanbeeck@vki.ac.be

University Supervisors: Bart Janssens and Karim Limam

Associate Professor, Department of Mechanics, Royal Military Academy (RMA), Belgium, bart.janssens@rmi.ac.be

Professor, LaSie, Université de La Rochelle (ULR), France, klimam01@univ-lr.fr

Abstract

In the context of a Chemical, Biological, Radiological and Nuclear (CBRN) application for the Belgian Defense, the aim of the current work is to propose a DNS model, derived from the code developed in the thesis of Janssens, B. to predict the dispersion of particles in the atmosphere. The code uses FEM for both the fluid and the dispersed solid phase.

In this article, we focus on applying the fluid model to the thermally neutral Atmospheric Boundary Layer (ABL) , thus assuming the turbulence is predominantly generated mechanically due to wind shear. To represent this ABL, a neutral pressure-driven (i. e. constant pressure gradient) boundary layer with symmetry condition at the top, periodicity in the stream-/span-wise directions and impermeability in combination with Schumanns wall-stress boundary conditions at the bottom is considered. For the latter, the wall-stress is being related to the wall parallel velocity components at the first grid points.

In the literature, this method is usually described for a Finite Difference Method (FDM), but we adapted it for use with the Finite Element Method (FEM). The adaptation in finite element code is not trivial but could be beneficial when using tetrahedral meshes (allowing automatic and complex model meshing). Indeed, in FEM, the type of element has less impact on the accuracy of the results and can improve its accuracy by use of higher order polynomials.

The basic implementation of the boundary condition was validated in 2D but couldn't be confirmed in 3D due to oscillations introduced by the numerical method.

One of the observed symptoms is an increasing velocity with the number of timesteps. To counter this behavior, a limiter was developed. The limiter modifies the driving force, taking into account the reference velocity and the previously computed velocities. The latter does work as expected but the velocity profile remains far from the expected logarithmic profile.

We suspect that the stabilization currently used in our finite element method is insufficient to damp the oscillations in this high Reynolds number flow, so we intend to amend it using the techniques from the Variational Multiscale Method, which provides a combined framework for stabilization and turbulence modeling.

Keywords: ABL, CFD, FEM, LES, Multiphase Flow, Turbulent Flow

Nomenclature

A	[m^2]	area
$B_1(\cdot,\cdot)$	bilinear form	
$B_2(\cdot,\cdot,\cdot)$	trilinear form	
F	[N]	force
N	[-]	number of steps
N_i	[-]	shape function
U, V	[m/s]	velocity vectors
V	[m^3]	volume
Δt	[s]	timestep
Γ	[m^2]	contour of the domain
Ω	[m^3]	space domain
α	[$kg/m^3\ s^2$]	negative constant
β	[kg/m^3 s]	negative constant
ϵ	[-]	parameters
κ	[-]	von Karman constant (≈ 0.4)
$\mathcal{V}$	[-]	test and weighting function spaces
$\nabla^s u$	$= (\nabla u + (\nabla u)^T)/2$	
ν	[m^2/s]	kinematic viscosity
ρ	[kg/m^3]	density
τ_w	[Pa]	shear stress at the wall
$\tau_{PS,SU,BU}$	[s]	time scales
$\tau_{M,C}$	momentum and continuity stabilization operators	
f	[N/kg]	body force
h	[m]	height of the model
n	[m]	normal vector
$r_{M,C}$	momentum and continuity local coarse-scale residual	
t	[s]	time
u	[m/s]	velocity
u, v, w, q	[m/s]	velocity components
u_{tau}	[m/s]	friction velocity
x_s	[m]	surface points
y	[m]	vertical distance from the wall

Acronyms

ABL	atmospheric boundary layer
BU	bulk
CBRN	chemical, biological, radiological and nuclear
CFL	CourantFriedrichsLewy condition := $\frac{u\Delta t}{\Delta x}$
NURBS	non-uniform rational b-spline
PG	Petrov–Galerkin
PS	pressure stabilized
SU	streamline upwind
VMS	variational multiscale theory

Superscripts and Subscripts

Ω	space domain
G	Galerkin term
h	mesh parameter
m, c	momentum, continuity
MS	multiscale term
PS, SU, BU	parameter of PSPG/SUPG/BULK stabilization
Q	space-time domain
T	transpose of

1. Introduction

With regard to CBRN applications, being able to predict the propagation direction of a gas can be very useful for both the attacker and the defender. The former could use the information to find the optimal position to arm the diffusion source. The latter will have a clear idea on the area of contamination and how it could evolve. For both cases, the weather forecast and the topography of the considered area are key parameters.



Figure 1: Gas dispersion's experiment (source: [1])

In 2014, a DNS model for fluids laden with small particles was developed in the thesis of Janssens, B. [2]. The model, using FEM for both the fluid and the dispersed phase, was validated by reference and experimental CFD case studies (e. g. "Turbulent channel flow" case, "Taylor-Green vortex flow" case and "Turbulence-induced coalescence in aerosols" case).

Furthermore, thanks to the significant improvement in computing resources the last decades, CFD codes increased their simulations capabilities, in terms of model dimensions, processing time and resolution. As a consequence, it becomes more realistic to study, jointly, smaller turbulent scales and meso-scales effects.

Consequently to these validations and to the computing resources' improvement, the aim of the proposed CFD model is to predict the dispersion of particles in the atmosphere, for an area on the order of the hectometer, taking into account detailed geometries of the topography. However, the atmosphere's

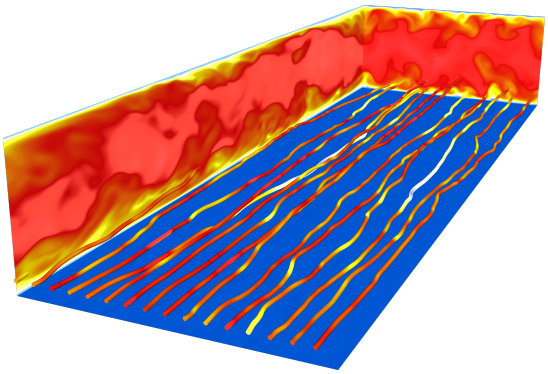

Figure 2: Turbulent channel flow (source: [2])

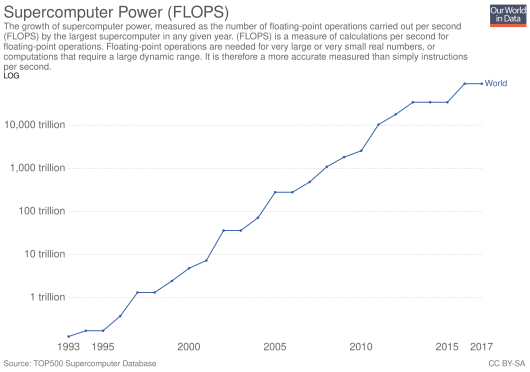

Figure 3: Supercomputer power in FLOPS (source: [3])

representation is not straightforward and needs to be implemented first.

In this work, the primary step is to design a one-phase model representing correctly a thermally neutral ABL.

2. Theory

2.1. Atmospheric Boundary Layer (ABL)

The ABL has a thickness varying from 500m to 2km above the surface of the earth (see Fig. 4).

This boundary layer is influenced mechanically by the shear stresses due to the surface roughness (e. g. buildings, trees, etc.) and thermally by solar radiation mainly during daytime.

When the wind is strong enough to overcome the thermal influence, the ABL is defined as neutral. In this work, a neutral ABL will be considered to reduce the system to pure convection.

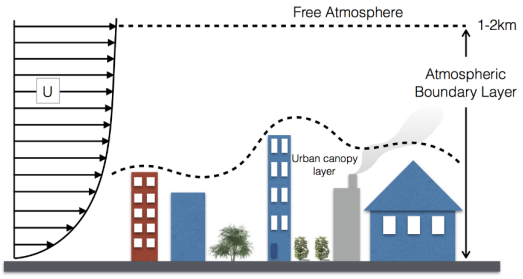

Figure 4: Urban ABL sketch (source: [4])

2.2. Finite Element Methods (FEM)

2.2.1. FEM vs other methods

Finite Difference Methods (FDM) were historically used in CFD computations. In FDM, the differential equations representing the physics of the subject, are studied in their discrete forms and derived into algebraic equations, using Taylor's series expansions. FDM is easier to implement than other methods.

When Finite Volume Methods (FVM) appeared, it allowed the study of flows around complex geometries although achieving the required mesh quality can be challenging.

Finite Element Methods (FEM) have their roots in structural analysis. In FEM, the idea is that the solution is approximated using interpolation and weighted functions. These are then integrated over the domain. FEM have gained interest in CFD thanks to the creation of higher order elements, allowing to increase the resolution at a limited cost according to [5]. FEM is also less sensitive to irregularities in the grid, making it easier to generate an unstructured mesh automatically, without sacrificing accuracy.

The methodology proposed in this work was first developed for a Finite Difference Method (FDM) in [6] and was adapted to FEM in the current work.

2.2.2. Navier-Stokes in FEM

The model that is being implemented is based on the first two Navier-Stokes transport equations. These can be written following [2]:

$$\nabla \cdot u = 0$$

$$\frac{\partial u}{\partial t} + (u \cdot \nabla)u + \frac{u(\nabla \cdot u)}{2} + \nabla p - \nu \nabla^2 u = 0 \qquad (1)$$

Discretized with a stabilized FEM, these can be re-written, following [7], in the integral forms:

$$\int_\Omega (N_i + \tau_{SU}(\vec{u}\cdot\nabla N_i))\vec{R}_m d\Omega + \int_\Omega \tau_{BU}\nabla N_i R_c d\Omega = 0$$
$$\int_\Omega N_i R_c d\Omega + \int_\Omega \tau_{PS}\nabla N_i \cdot \vec{R}_m d\Omega = 0 \tag{2}$$

where one can refer to [2] for details of the discretization.

2.2.3. *Wall boundary condition*

To avoid requiring many elements near the wall (i. e. high velocity gradient and small turbulence scale), using the first node above the wall allows the computation to smoothly converge while keeping a value that follows a local law-of-the-wall formulation.

Because in FEM we use an unstructured grid where all quantities are computed on the nodes, there is no concept of a first cell layer. For this reason, we started the mesh at a height y_{wall} from the wall, where y_{wall} plays the role of first cell height. A representation is given below:

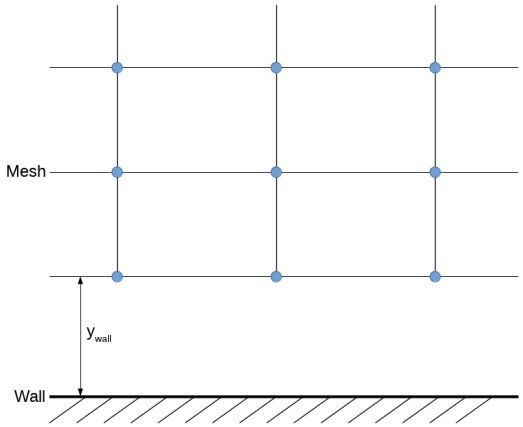

Figure 5: 1st nodes above the wall

2.2.4. *ABL implementation*

Since most of the literature and code in CFD is written for FDM and FVM, a FDM implementation of the ABL, proposed in [6], was chosen. This work proposed a Large Eddy Simulation (LES) modeling (i. e. CFD simulation including the most energetic turbulences) with non penetration at the wall and Schumann's wall model (i. e. where the wall-stress is being related to the wall parallel velocity components at the first grid points). This expression is derived from [8], an improved local law-of-the-wall formulation:

$$\tau_w = -\left[\frac{\kappa}{\ln(y_{wall}/y_0)}\right]^2 \left(\bar{u}_1^2 + \bar{u}_2^2\right) \tag{3}$$

with τ_w the shear stress at the wall. This formulation is used in LES of a high-Reynolds number boundary layer, where the viscous sublayer is not resolved. Notice that:

$$\tau_{w_i} = \nu\frac{\partial u_i}{\partial x_j}n_j \quad \rightarrow \quad \frac{\partial u_i}{\partial x_j}n_j = \frac{\tau_{w_i}}{\nu} \tag{4}$$

and that the natural Robin boundary condition is:

$$\epsilon u + \frac{\partial u}{\partial n} = 0 \quad \rightarrow \quad \frac{\partial u}{\partial n} = -\epsilon u \tag{5}$$

Knowing that $\tau_w = f(u)$ (Eq. (3)), the Robin condition (Eq. (5)) leads to an expression where the wall model appears in the system matrix, represented using the FEM shape functions N as follows:

$$\int_\Gamma \frac{1}{\nu}\left(\frac{\kappa}{\log\frac{y_{wall}}{y_0}}\right)^2 |u| N^T(u)N(u)|\bar{n}|d\Gamma = 0 \tag{6}$$

3. Application of the model

The specificity related to ABL being explained, a computational domain, following the setup proposed by [6], has been set up. This is a basic rectangular domain with dimensions (height: 1200 m, length: 6 x 1200 m, width: 4 x 1200 m for 3D model), meshed with first-order hexahedras. The considered fluid is air (density: $\rho = 1.2\,\mathrm{kg/m^3}$, dynamic viscosity: $\mu = 1.8\times10^{-5}$ Pa s). Below, a sketch of the mesh:

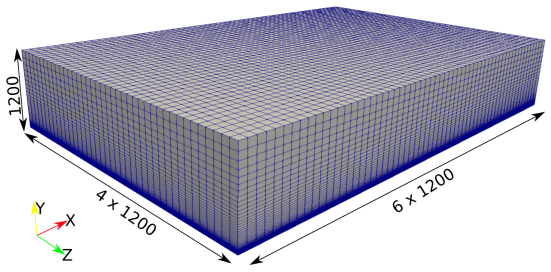

Figure 6: Sketch of the ABL mesh

The used mesh sizes are 64 x 64 x 64 and 64 x 128 x 64.

3.1. Initial and boundary conditions

3.1.1. Boundary conditions

Boundary conditions give the numerical model its physical meaning. Therefore, they have to be consistent. In this model, periodicity was applied to the front, end (and sides for 3D) of the model. In other words, the input is connected to the output, the left side to the right side.
A symmetry condition was applied to the top (i. e. the topside should be far enough, not to influence the domain of interest). For the bottom, the vertical velocity was set to 0 (impermeability) and combined with the Schumann's [9] wall-stress boundary conditions presented in section 2.2.4.

3.1.2. Initial conditions

Eventually, to accelerate the convergence, an initial condition was set, equal to a logarithmic profile:

$$u_x^{inlet} = \left(\frac{u_\tau}{\kappa}\right)\log\left(\frac{y + y_{wall}}{y_0}\right) \tag{7}$$

The reference velocity is 4 m/s at a height of 200 m. A timestep of 0.1 s was taken (0.05 s sec in 3D) to ensure stability and convergence of the simulation (i. e. a CFL below 0.2 in this case).

3.1.3. Body force

Eventually, the model and its boundaries being defined, a body force f was set to keep the ABL at constant speed. This body force can be found by requiring equilibrium between the force F_f and the force F_w induced by the wall shear stress:

$$\begin{aligned} F_f = fV\rho \quad \& \quad F_w = A_w\tau_w \\ if \quad F_f = F_w \quad \rightarrow \quad f = \frac{\tau_w}{\rho h} \end{aligned} \tag{8}$$

and

$$u_\tau = \sqrt{\frac{\tau_w}{\rho}} \quad \rightarrow \quad f = \frac{u_\tau^2}{h} \tag{9}$$

with h the height of the model.

Expressed in terms of speed on the first node, derived from Eq. (3):

$$u_\tau = \frac{\kappa u_{ref}}{\ln((y_{ref} + y_{wall})/y_0)} \tag{10}$$

3.1.4. Limiter implementation

In 3 dimensions with an unsteady viscous flow, the body force is first computed thanks to the requested velocity and subsequently iteratively updated using a feedback scheme which compare the velocity from the computed flow to the requested velocity [10].
This method facilitates the flow convergence and stabilizes the velocity profile.

The adapted body force has following pattern:

$$f(x_s, t) = \alpha \int_0^t u(x_s, t')dt' + \beta u(x_s, t) \tag{11}$$

where a large α coefficient will result in a fast response and a large β coefficient in a greater damping. Eventually, the time integral can be approximated by a Riemann sum:

$$\int_0^t u(x_s, t')dt' \approx \sum_{j=1}^{N} u(x_s, j)\Delta t \tag{12}$$

where N is the number of steps and Δt is the size of the timestep.

4. Results

In a first stage, there will be a qualitative analysis in 2D, where we use a laminar flow to confirm that the velocity at the first node is correct, to verify the implementation of the Schumann boundary condition.

In a second stage, the 3rd dimension will be added (to enable horizontal turbulence generation) to allow the execution of the LES. The latter drastically boosted the number of elements and computation time. Moreover, the energy contained in the model was continuously rising, resulting in an increasing velocity profile. The limiter described in 3.1.4 was used to counter this behavior.

4.1. Qualitative analysis

4.2. Sensitivity to the mesh-wall distance

As mentioned in section 2.2.3, there is an offset between the physical wall and the mesh. If the boundary condition is implemented correctly, the velocity at the first node as a function of this offset should follow the theoretical logarithmic profile. Figure 7 confirms that this is indeed the case. One can see the analytic value from Eq. (10) is nearly equal to the value computed by the simulation, on the 1st node. This confirms that our translation of Schumann's model to FEM is correctly implemented.

4.3. 3D results

4.3.1. Limiter impact

Figure 8 shows the behavior of a simple limiter, where u_{ref} is set at the reference height, the body force

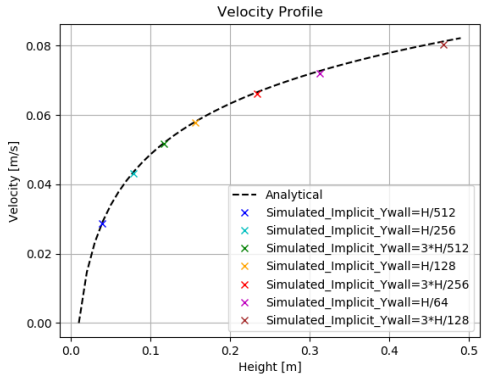

Figure 7: Velocity on the 1st node $[m/s]$ vs 1st node's height [m]

f is initialized and then computed for each timestep with a correction $corr = \left(\frac{u_{ref} - u_{mean}}{||u_{ref}||}\right)$.

For the sake of illustration, the velocity is plotted, in one probe located at the reference height, where it should be equal to the value specified by the model constraints. When the velocity computed at reference

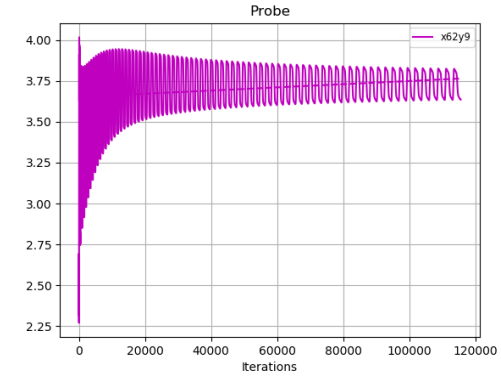

Figure 8: 1st trivial implementation of a limiter

height exceeds the requested value, the body force counter balances it, not taking the previous timesteps into account (no feedback loop). As a consequence, the computed velocity tries to return to the requested value but with an opposite derivative, without damping. Figure 8 shows the saw teeth behavior of the first implementation.

Figure 9 shows the feedback scheme result for the 3 probes located at low- (1/20 of the height), mid- (9/20) en top- (19/20) locations of the model. In this plot, the velocities are rapidly changing and also damping efficiently when reaching the specified velocity.

When looking to the body force in figure 10, it is

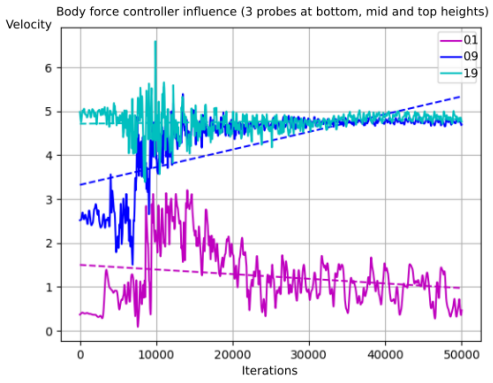

Figure 9: Limiter implementation with feedback scheme: Velocities at 3 different heights

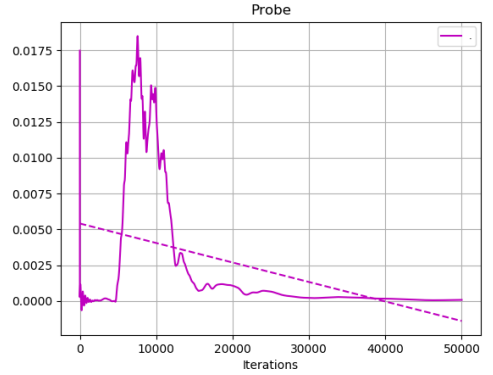

Figure 10: Limiter implementation with feedback scheme: body force value in the whole domain

observed that the intensity is high in the first steps, allowing a fast alteration of the physical properties of the model and then, decreasing rapidly with the number of iterations, consequence of the limiter, enforcing a reduction and damping of the body force intensity. The body force computed analytically is equal to 3.584×10^{-3} N/kg while the converged numerical value is 3.077×10^{-4} N/kg. The factor 10 here is due to the use of the limiter, but this means that the shear stress is a lot lower than expected, so it indicates a serious problem with the solution. In the considered case, α was set to -1 and β to -0.2.

4.3.2. Velocity profile

The resulting velocity profile, given by figure 11, reaches convergence after 50k iterations on 128 processors.

It can be seen that the statistical average of all horizontal points on the domain, gives a velocity profile

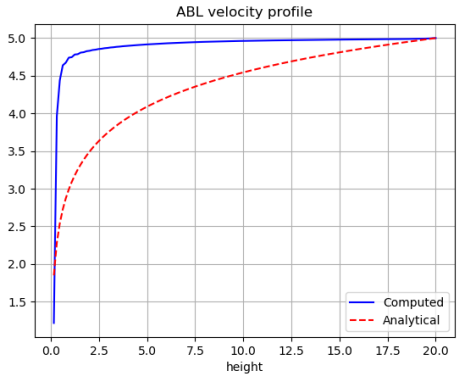

Figure 11: Statistically computed velocity profile vs analytically

that does not correspond to the analytical profile (i. e. logarithmic shape). This error could be explained by oscillations of the numerical model as illustrated, for a not yet converged simulation, in figure 12.

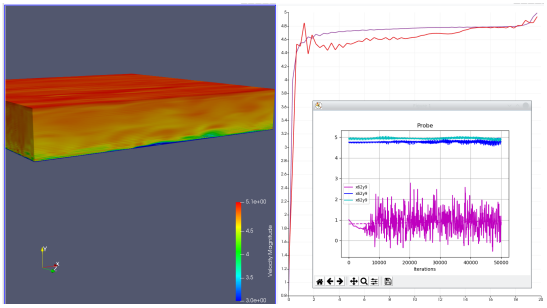

Figure 12: Spurious oscillations visible on the instantaneous contour and plot on a line

To counter this behavior, we will look for an alternative method to stabilize the equations.

5. Discussions

5.1. The variational multiscale theory of turbulence

5.1.1. Initiation

The Variational MultiScale (VMS) concepts for LES were introduced in [11] and the development in [12] proposes an efficient version for NURBS and classical finite elements that is, in every respect, the motivation to develop it in the following sections.

The first idea is to avoid the traditional filtered equations, source of difficulties (e. g. in-homogeneous non-commutative filters necessary for wall bounded flows), by use of the variational projections (developed in [12]).

The second idea is to confine the 'modeling' to the fine-scale equations so that the numerical consistency in the coarse-scale equations is retained, facilitating the numerical method's convergence. In the traditional approach, the convergence rate is limited due to the 'artificial' viscosity effects in the fully resolved scales (e. g. Smagorinsky-type models), introducing the turbulent dissipation and de facto, inducing a consistency error.

Note concerning 'modeling': For a spectral case, the coarse-scale space consists of all Fourier modes beneath a supposed sufficiently large cut-off wave number and containing most of the energy. Small-scale space represents the rest. The coarse-scale space has a finite dimension inducing a finite system whereas the fine-scale space has an infinite dimension that has to be approximated. Therefore the 'modeling'.

To conclude this first section and to confirm the interest, Farhat and Koobus [13] have implemented a finite element/volume code for an unstructured mesh and compressible flow that was successfully applied to complex test cases, avoiding the use of eddy viscosities while allowing to capture all scales consistently and therefore demonstrating the competitiveness with traditional LES methods.

5.1.2. Navier-Stokes vs VMS formulation

Before diving into the VMS in FEM, a slightly different formulation (compared to Eqs. (1)) of the incompressible Navier-Stokes equations will be proposed to ease the equivalence with the variational formulation. The former can be expressed as:

$$\frac{\partial u}{\partial t} + \nabla \cdot (u \otimes u) + \nabla p = \nu \Delta u + f \tag{13}$$

$$\nabla \cdot u = 0 \tag{14}$$

$$u = 0 \tag{15}$$

$$u(0^+) = u(0^-) \tag{16}$$

where Eq. (13) is the momentum balance, Eq. (14) the continuity, Eq. (15) the no-slip boundary condition and Eq. (16) the initial condition.

The variational formulation, as described in [12], is stated as follow:

Find $U \in \mathcal{V}$, where $\mathcal{V}$ is both the test solution and the weighting function spaces, such that $\forall W = \{w, q\} \in \mathcal{V}$:

$$B(W, U) = B_1(W, U) + B_2(W, U, U) = L(W) \tag{17}$$

with

$$B_1(W,U) = (w(T^-),u(T^-))_\Omega - \left(\frac{\partial w}{\partial t},u\right) + (q,\nabla\cdot u)_Q - (\nabla\cdot w,p)_Q + (\nabla^s w, 2\nu\nabla^s u)_Q \quad (18)$$

$$B_2(W,U,V) = -(\nabla w, u\otimes v)_Q \quad (19)$$

$$L(W) = (w,f)_Q + (w(0^+),u(0^-))_\Omega \quad (20)$$

where $V = \{v,\cdot\}$, $\nabla^s u = (\nabla u + (\nabla u)^T)/2$, Q is the space-time domain defined as $Q = \Omega\times]0,T[\subset \mathbb{R}^3\times\mathbb{R}^+$ with Ω, the space domain and T, the time domain. $B_1(\cdot,\cdot)$ and $B_2(\cdot,\cdot,\cdot)$ are respectively the bilinear and trilinear forms.

In its Euler-Lagrange form, it can be rewritten as:

$$0 = \left(w, \frac{\partial u}{\partial t} + \nabla\cdot(u\otimes u) + \nabla p - \nabla\cdot 2\nu\nabla^s u - f\right)_Q + (q,\nabla\cdot u)_Q + (w(0^+),u(0^+)-u(0^-))_\Omega \quad (21)$$

Eq. (21) implies satisfaction of Eqs. (13), (14), (16) while Eq. (15) is included in the considered space. Thus, it can be established that the variational formulation is equivalent to the incompressible Navier-Stokes equations. In practice, the time domain is sliced into smaller slabs Q_n, making the system more suitable for numerical schemes while remaining an *exact* formulation.

The next step will be to show how the variational multiscale formulation can be seen as an evolution of the stabilized formulations used until now in present work.

5.1.3. Multiscale implementation

The *unique* space decomposition between coarse- (exact) and fine- (approximation) scales is accomplished by using a projector $\mathbb{P} : \mathcal{V} \to \overline{\mathcal{V}}$ in such a way that

$$\mathcal{V} = \overline{\mathcal{V}} \oplus \mathcal{V}' \quad (22)$$

where $\overline{\mathcal{V}}$ and $\mathcal{V}'$ are respectively the coarse- and the fine-scale subspace, allowing the coarse-scale to approximate all scales by

$$\overline{U} = \overline{\mathbb{P}}U \Rightarrow U' = U - \overline{\mathbb{P}}U \quad (23)$$

and similarly for the weighting function W allowing to decompose the original variational equation Eq. (17) into a coupled coarse- / fine-scale equations:

$$B(\overline{W},\overline{U}+U') = L(\overline{W}) \quad (24)$$

or when translated to the elements scale, after some iterations:

$$B^{MS}(W^h,U^h) = L^{MS}(W^h) \quad (25)$$

with MS-superscript for multiscale and h- for a mesh parameter.

In Eq. 25:

$$B^{MS}(W^h,U^h) = B^G(W^h,U^h) + (u^h\cdot\nabla w^h + \nabla q^h, \tau_M r_M(u^h,p^h))_\Omega + (\nabla\cdot w^h, \tau_C r_C(u^h))_\Omega + (u^h\cdot(\nabla w^h)^T, \tau_M r_M(u^h,p^h))_\Omega - (\nabla w^h, \tau_M r_M(u^h,p^h)\otimes\tau_M r_M(u^h,p^h))_\Omega \quad (26)$$

with

$$B^G(W^h,U^h) = \left(w^h,\frac{\partial u^h}{\partial t}\right)_\Omega - (\nabla w^h, u^h\otimes u^h)_\Omega - (\nabla\cdot w^h,p^h)_\Omega + (q^h,\nabla\cdot u^h)_\Omega + (\nabla^s w^h, 2\nu\nabla^s u^h)_\Omega \quad (27)$$

and

$$L^{MS}(W^h) = (w^h,f)_\Omega \quad (28)$$

In Eq. (26), on the right-hand side, the Galerkin term is followed by the two classical stabilization terms (with $\tau_{\{M,C\}}$ being resp. the momentum and continuity stabilization operators and $r_{\{M,C\}}$, their resp. local coarse-scale residuals). The last two terms are specific to the variational multiscale method and complete the formulation with a second cross-stress and the Reynolds-stress.

In this sense, the variational multiscale methods are usually considered as the more general formulation of the classical stabilized methods (e. g. SUPG).

This is the reason why this method is currently being implemented in this work. Hopefully, it will produce results not altered by numerical oscillations and therefore, generating the expected ABL profile.

6. Conclusions

In this work, to model a multiphase flow for CBRN applications, the first step was to attempt to simulate a neutral ABL so that dispersion in the atmosphere could be possible. This was implemented using FEM and the implementation of Schumann's wall model was verified in a 2D test case.

The 3D simulation with direct simulation of the turbulence revealed oscillations that lead to an incorrect mean velocity profile. The first correction that was implemented was the limiter. It was demonstrated that it does what it was implemented for. To correct the model, we will implement a variational multiscale method, which should offer better stabilization and remove the oscillations.

Eventually, when the 3D model will be completely consistent, a 2nd phase (i.e. particles) will be added to provide a detailed distribution on the released particles, taking into account the multiphase behavior.

7. Acknowledgments

This study is promoted by the Royal Military Academy (RMA), in cotutelle with the Université de La Rochelle (ULR) and the von Karman Institute for Fluid Dynamics (VKI). The author is thankful to these three institutions to give him the opportunity to work on this subject.

References

[1] Top 10 cbrn (chemical, biological, radiological and nuclear) survival tips, http://www.cbrneportal.com/top-10-cbrn-chemical-biological-radiological-and-nuclear-survival-tips/, accessed: 2017-03-16.

[2] B. Janssens, Numerical modeling and experimental investigation of fine particle coagulation and dispersion in dilute flows, Ph.D. thesis, Université de La Rochelle (2014).

[3] Supercomputer power (flops), https://ourworldindata.org/grapher/supercomputer-power-flops, accessed: 2019-01-21.

[4] C. García Sánchez, Quantifying inflow uncertainties for cfd simulations of dispersion in the atmospheric boundary layer, Ph.D. thesis, University of Antwerp (2017).

[5] T. Hughes, T. Tezduyar, Finite element methods for first-order hyperbolic systems with particular emphasis on the compressible euler equations, Computer Methods in Applied Mechanics and Engineering 45 (1984) 217–284.

[6] J. P. Goit, Optimal control of energy extraction in large-eddy simulation of windfarms, Ph.D. thesis, KU Leuven (2015).

[7] T. Bányai, D. V. Abeele, H. Deconinck, A fast fully-coupled solution algorithm for the unsteady incompressible navier-stokes equations, in: Conference on Modelling Fluid Flow (CMFF06). Budapest, Hungary, 2006, p. 00.

[8] E. Bou-Zeid, C. Meneveau, M. Parlange, A scale-dependent lagrangian dynamic model for large eddy simulation of complex turbulent flows, Physics of fluids 17 (2) (2005) 025105.

[9] U. Schumann, Subgrid scale model for finite difference simulations of turbulent flows in plane channels and annuli, Journal of computational physics 18 (4) (1975) 376–404.

[10] D. Goldstein, R. Handler, L. Sirovich, Modeling a no-slip flow boundary with an external force field, Journal of Computational Physics 105 (2) (1993) 354–366.

[11] T. J. Hughes, L. Mazzei, K. E. Jansen, Large Eddy Simulation and the variational multiscale method, Computing and Visualization in Science 3 (1-2) (2000) 47–59. doi:10.1007/s007910050051.

[12] Y. Bazilevs, V. Calo, J. Cottrell, T. Hughes, A. Reali, G. Scovazzi, Variational multiscale residual-based turbulence modeling for large eddy simulation of incompressible flows, Computer Methods in Applied Mechanics and Engineering 197 (1-4) (2007) 173–201.

[13] C. Farhat, B. Koobus, Finite volume discretization on unstructured meshes of the multiscale formulation of large eddy simulations, in: Proceedings of the Fifth World Congress on Computational Mechanics (WCCM V), Vienna University of Technology, Austria, 2002, p. 00.

AEROACOUSTICS

Towards Quieter Fans : Multi-Port Eduction of Installation Effects in Small Axial Fan System

Joachim Dominique

Environmental and Applied Fluid Dynamics Department, von Karman Institute for Fluid Dynamics, Belgium, joachim.dominique@vki.ac.be

Supervisor: Christophe Schram

Full Professor, Environmental and Applied Fluid Dynamics Department, von Karman Institute for Fluid Dynamics, Belgium, christophe.schram@vki.ac.be

University Supervisor: Wim Desmet

Professor, Production Engineering, Machine Design and Automation (PMA) Section, KU Leuven, Belgium, wim.desmet@kuleuven.be

Abstract

In HVAC or domestic appliance applications, industrial fan noise is usually characterized under uniform inflow profile. However, those ideal conditions are rarely met when the fan is installed in its final product. The fan is often in the wake of an obstacle or after a bend, which causes non-uniform ingested flow. Under those distorted inflow condition, the fan noise signature changes causing an increase in noise power level. This paper presents a multi-port eduction technique to investigate those installation effects in a compact axial fan situated in a circular duct. The noise emitted by the fan was compared to independent measurements performed using the ISO-5136 method to highlight the benefits of the multi-port technique regarding the elimination of the spectral features caused by the reflections of the acoustic wave on the duct terminations. Installation effects generated by circumferential and turbulence flow distortions were produced using wooden grids. The influence of those grids on the scattering coefficients of the tested module led to an analysis of the changes in acoustic power radiated by the fan under those non-uniform ingested flows.

Keywords: Induct acoustic measurements, multi-port, ducted fan noise, installation effects

1. Introduction

Rising concerns on the health impact of environmental noise has led to stronger regulations and market demands applying to small air moving devices used in domestic appliances, heating, air-conditioning and cooling (HVAC) systems, etc. To comply with those new regulations and market expectations, the involved industrial actors thrive to improve fan acoustic design. This has increased the need for a better understanding of aeroacoustic mechanisms, in particular of the interactions taking place between the components of compact ducted systems. An important objective thereto, is to devise more efficient noise reduction techniques based on a more accurate characterization of so-called aerodynamic and acoustic installation effects.

Along the design stage, the noise emitted by the fan is usually predicted and qualified with a fairly uniform and steady inflow profile, even though such conditions are rarely met in the final product due to integration constraints. The ingestion by the machine of non-uniform and/or turbulent inflow usually induces the production of extraneous tonal and broadband noise, whose reduction adds expensive experimental prototyping time and costs to the design cycle. Those installation effects are the focus of the research presented below.

Installation effects are threefold. Firstly, the non-uniformity of the flow ingested by the fan and its turbulence affect the unsteady rotating forces acting on the blades, which are the dominant sources of noise for fans with low tip Mach number [1]. Secondly, the installation of a fan within a circuit can also bring the

fan to off-design operation, which affects its aerodynamic performance [2]. Finally, the acoustic radiation efficiency of the encapsulating duct terminations affects the propagation of noise towards the exterior, which is a purely acoustical propagation effect [3].

Given the complexity of the problem at stake, the investigation of installation effects relies heavily on experiments. Indeed, the modelling of the unsteady forces acting on the rotor blades depends on many parameters. This makes the design of a quiet system by means of aeroacoustic simulations a difficult, expensive and time-consuming task, especially as confined flows with complex geometries are involved [4]. However, in-duct acoustic measurements also raise some issues, such as the superposition of the acoustic field emitted by the fan with the field that is reflected by the duct terminations and the contamination of the microphones readings by the turbulent boundary layer (TBL) pressure fluctuations.

A well-established technique to minimize the influence of those scattering and TBL fluctuations effects is the multi-port methodology [5] introduced by Lavrentjev in 1996 [6]. This approach is an extension of the two-port method to higher order modes [7; 8]. Implementing arrays of microphone and loudspeaker, it describes the acoustic field as a superposition of a finite number of acoustic modes, that are analytically known for simple enough duct cross-section geometries, mainly circular and annular. The technique permits to discriminate between aerodynamic and acoustic pressure fluctuations and provides the acoustic field emitted by the source free from duct scattering and TBL pressure fluctuations.

Recent studies [9; 10] showed the potential of the multi-port technique for the investigation of installation effects in aircraft Environmental Control Systems and automotive fans. This study addresses the noise generated by a compact axial fan having characteristics comparable to those of models used in some systems developed by Dyson Ltd, when subjected to a non-uniform and turbulent inflow. A specific challenge here is the application of the multi-port methodology up to the second azimuthal mode for a fan of smaller dimension than the test section. Grids are used upstream of the fan to condition the flow and force the fan to operate in non-uniform inflow conditions. The influence of those off-design conditions on the scattering, noise and aerodynamic performances of the fan is measured to provide a more accurate insight on the influence of installation effects and assess the validity of such investigations.

2. Facility

The experimental setup is shown in Figure 1. The test rig, located in the ALCOVES aeroacoustic facility of the von Karman Institute, consists of a duct of 0.15m diameter including two arrays of 12 loudspeakers and 13 Bruel & Kjaer microphones on both sides of the fan. A smaller diameter duct and two convergent-divergent modules were designed to fit the 0.1 m-diameter fan to the test rig. The grids generating the inflow distortion are installed upstream of the fan, within the 0.1 m-diameter section, at a distance of two diameters from the rotor blades leading edge plane. In this work three different obstructions are investigated: named ”Fractal”, ”Grid” and ”Half”, and are shown in Figure 1.

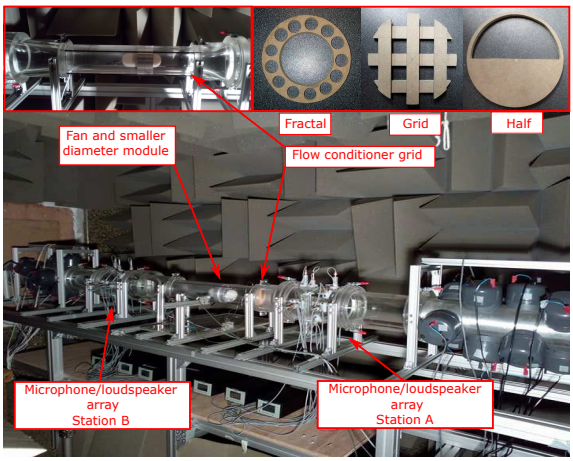

Figure 1: Experimental facility of the von Karman Institute and the Dyson Ltd fan.

This test rig is dedicated to the application of the multi-port method, and hosts all the necessary equipment to this end, besides the microphone and loudspeaker arrays: a specific interface for the acquisition of the signals by high-bandwidth acquisition systems and the generation of synthetic signals driving the loudspeakers. In addition, to permit the measurement of the aerodynamic performance, a Kiel probe is installed at the outlet of the duct.

3. Multi-port methodology

3.1. Duct acoustics

Duct have a specific way of propagating sounds since their confined environment acts as acoustic waveguide. Solving the Helmholtz equation for the acoustic propagation in a straight duct shows that, at

a given angular frequency ω, the acoustic field is a superposition of modes which shape depends on the cross-section of the duct [11]. For a circular cross-section with radius R and in absence of mean flow, we have the solution expressed in a cylindrical coordinate system as:

$$p(r,\theta,z) = \sum_{m=-\infty}^{\infty}\sum_{\mu=0}^{\infty} U_{m\mu}(r)\left(p^{+}_{m\mu}\, e^{-ik_{m\mu}z} + p^{-}_{m\mu}\, e^{ik_{m\mu}z}\right) e^{-im\theta} \quad (1)$$

where $p^{+}_{m\mu}$ and $p^{-}_{m\mu}$ are the amplitudes of the right- and left-propagating modes, respectively (assuming the convention $a(t) = a\, e^{i\omega t}$), with (azimuthal, radial) order (m,μ). The first modes are shown in Figure 2.

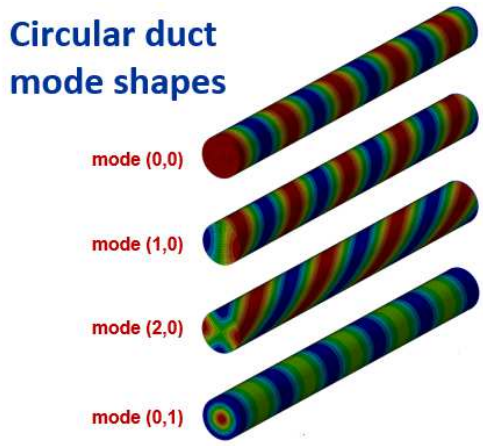

Figure 2: Examples of circular duct mode shapes, from top to bottom: planar mode, first azimuthal mode, second azimuthal mode, first radial mode [12].

The radial dependence of each mode is given by

$$U_{m\mu}(r) = N_{m\mu}\, J_m(\alpha_{m\mu} r) \quad (2)$$

and

$$N_{m\mu} = \left(\frac{1}{2}\left(1 - \frac{m^2}{\alpha^2_{m\mu}}\right) J_m(\alpha_{m\mu})^2\right)^{-1/2}$$

is a normalization coefficient [11]. In (2), J_m denotes the Bessel function of the first kind and order m, $\alpha_{m\mu}$ is the μth non trivial zero of the derivative of $J_m(\alpha_{m\mu} r)$ ensuring the hard-wall boundary condition at $r = R$. Finally, the wavenumber $k_{m\mu} = \sqrt{\omega^2 - \alpha^2_{m\mu}}$ is defined such that $\Re(k_{m\mu}) \geq 0$ and $\Im(k_{m\mu}) \leq 0$. In what follows, the so-called cut-off or evanescent modes for which $\alpha^2_{m\mu} > \omega^2$ such that the wavenumber $k_{m\mu}$ is purely imaginary, are not retained in the summation, leading to a finite summation in (1). The modal cut-on frequencies are given by the relation $f_{m\mu} = \frac{\alpha_{m\mu} c_0 \sqrt{1-M^2}}{2\pi R}$ and are shown in Table 1 for two different duct radii present in the test rig (the plane wave mode being always propagative).

Modes cut-on	$(m,\mu) = (0,0)$	$(m,\mu) = (\pm 1, 0)$
$R = 0.075$ m	0 Hz	1327 Hz
$R = 0.05$ m	0 Hz	2010 Hz
Modes cut-on	$(m,\mu) = (\pm 2, 0)$	$(m,\mu) = (0,1)$
$R = 0.075$ m	2200 Hz	2763 Hz
$R = 0.05$ m	3335 Hz	4183 Hz

Table 1: First cut-on frequencies for the 0.15 m- and 0.1 m-diameter duct elements present in the test rig.

If a mean and uniform flow is present, the axial wave number is split into left- and right-propagative wavenumbers:

$$k^{\pm}_{m\mu} = \frac{\omega}{c_0} \frac{\sqrt{1 - (\alpha_{mn} c_0/(\omega R))^2 (1 - M^2)} \mp M}{1 - M^2} \quad (3)$$

which has the effect that additional acoustic modes might be cut-on when the flow rate increases [13]. The microphones station used for this modal decomposition are situated upstream of the grid distortion (Station A) and sufficiently downstream the fan exhaust (station B) to comply with the assumption of uniform flow profile in Equation (1). Indeed, at those locations, the flow should be fairly uniform expect for the influence of the boundary layer whose effect should be negligible given the low Mach number considered in this application.

3.2. Acoustic multi-ports

Considering N cut-on modes, Equation (1) has $2N$ unknowns. Therefore, $2N$ microphone measurements provide a closed set of equations that permits the experimental retrieval of the amplitudes for the left- and right-going waves for each of the N modes $p^{+}_{m\mu}$ and $p^{-}_{m\mu}$. For analysis frequencies below the first cut-on frequency, only the plane wave is propagative ($N = 1$) and considering two microphones placed at different axial positions noted 1 and 2, this system of equations can be written as:

$$\underbrace{\begin{bmatrix} p_1 \\ p_2 \end{bmatrix}}_{\mathbf{P}} = \underbrace{\begin{bmatrix} e^{-ik^{+}_{0,0}z_1} U_{0,0}(r_1) & e^{ik^{-}_{0,0}z_1} U_{0,0}(r_1) \\ e^{-ik^{+}_{0,0}z_2} U_{0,0}(r_2) & e^{ik^{-}_{0,0}z_2} U_{0,0}(r_2) \end{bmatrix}}_{\mathbf{J}} \underbrace{\begin{bmatrix} p^{+}_{0,0} \\ p^{-}_{0,0} \end{bmatrix}}_{\mathbf{P}^{\pm}}$$

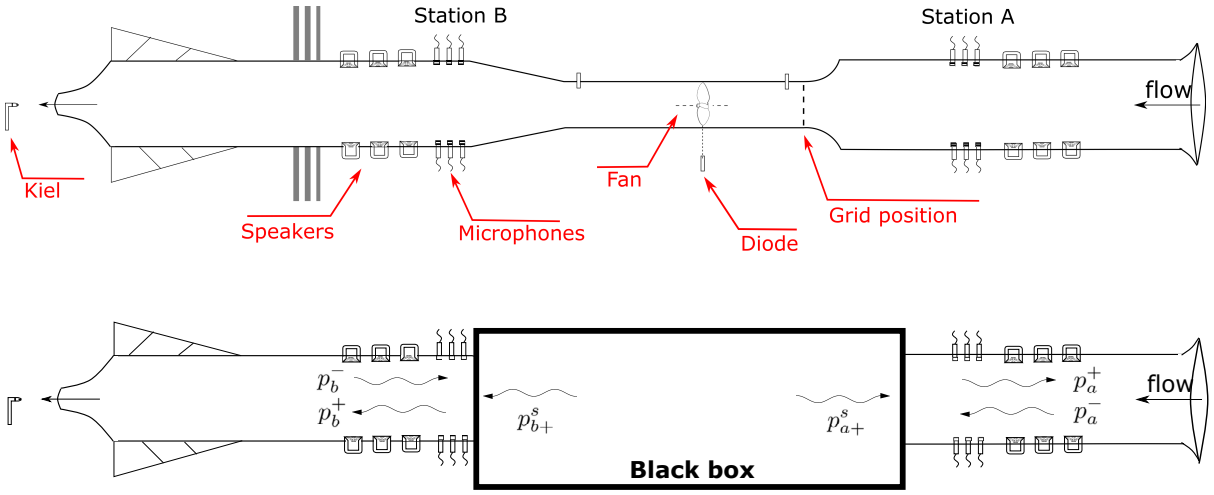

Figure 3: Schematic of the multi-ports method.

where in practice the microphones are connected to sensing ports at the wall of the duct such that $r_1 = r_2 = R$. The above equation can be rewritten as

$$\mathbf{P} = \mathbf{J}\mathbf{P}^{\pm} . \tag{4}$$

When investigating higher frequencies, additional modes become propagative and the size of the $\mathbf{J}$ matrix in Equation (4) increases to $[2N \times 2N]$. Extra microphones are then required.

mic	Δx	θ	mic	Δx	θ
1 and 14	0	0	7 and 20	0.07	90
2 and 15	0	90	8 and 21	0.07	180
3 and 16	0	270	9 and 22	0.07	270
4 and 17	0	315	10 and 23	0.11	0
5 and 18	0.4	45/135	11 and 24	0.11	90
6 and 19	0.7	0	12 and 25	0.11	180
			13 and 26	0.11	270

Table 2: Microphones positions at station A (1 to 13) and station B (14 to 26) in meter (Δx) and degree (θ)

The quality of the microphones placement for the modal decomposition can be evaluated using the condition number of the $\mathbf{J}$ matrix. The condition number is equal to one when the microphones give independent readings and tends to infinity otherwise. For the present investigation, the position of the 13 microphones used at each microphone stations is given in Table 2. Theoretically, There are enough microphones to reach the first radial mode, but Figure 4 shows that their positioning prevent accurate measurements above the third cut-on frequency as the condition number tend toward infinity for $f > f_{0,1}$. It can be also be seen that the transition between propagation modes at the cut-on frequency corresponds to another singularity. However this singularity is caused by a very low axial propagation phase velocity that tends to zero at those frequencies and therefore does not depend on the the position of the microphones.

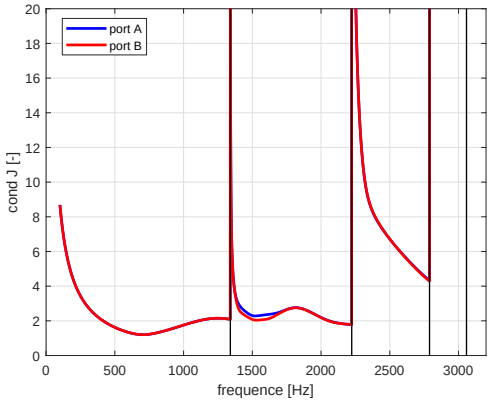

Figure 4: Evolution of the $\mathbf{J}$ matrix condition number. The vertical lines represent the cut-on frequencies of the large duct

The multi-port technique uses this modal description of the acoustic field to provide a 'black box' analysis of a ducted component, by means of arrays of microphones located upstream and downstream of that component, at axial stations noted A and B in Figure 3. It can be seen that due to duct terminations, and taking again the case of plane wave propagation as an example, the wave going away from the source at station A, called p_a^+, can be seen as the superposition of

three components:

- the acoustic wave emitted by the source: p^s_{a+},
- the reflected part of the wave going towards the source in A: $\rho_a p^-_a$,
- the transmitted part of the wave going through the source from B: $\tau_a p^-_b$,

where ρ and τ are respectively the reflection and transmission coefficient of the plane wave on the tested module.

In this decomposition, the first contribution is the one of interest (also called active noise), while the last two components result from reflections at the duct terminations via scattering across the source itself (passive noise). The same decomposition can be made on the other side of the source for p^+_b. This results in the following set of equations:

$$\begin{aligned} p^+_a &= \rho_a p^-_a + \tau_a p^-_b + p^s_{a,+} \\ p^+_b &= \rho_b p^-_b + \tau_b p^-_a + p^s_{b,+} \end{aligned} \tag{5}$$

Generalizing this formulation to higher order modes, Equation (5) can be written in matrix form:

$$\mathbf{P}^+ = \mathbf{S}\mathbf{P}^- + \mathbf{P}^s \tag{6}$$

where $\mathbf{P}^+$ and $\mathbf{P}^-$ are vectors containing the amplitudes of the left- and right-going acoustic modes at the two microphone stations A and B. The modal scattering matrix $\mathbf{S}$ of the source contains the modal reflection and transmission coefficients of the different modes through the module. This formulation is the basis permitting the extraction of the acoustic field that would be produced by the source ($\mathbf{P}^s$) in an ideal test rig with perfectly anechoic terminations, following the practical procedures described below.

3.3. Experimental methodology

The methodology aims at isolating the two unknowns $\mathbf{S}$ and $\mathbf{P}^s$ of Equation (6). This requires two sets of experiments here called the *passive measurements* and the *active measurements*. The flowchart methodology used during this campaign is given in Figure 5 and relies on the modal decomposition based on Equation (4).

The passive measurements yield the scattering matrix $\mathbf{S}$: loudspeakers are used to produce an acoustic field inside the duct with a level that is sufficiently larger than the noise produced by the source itself for the following approximation to hold:

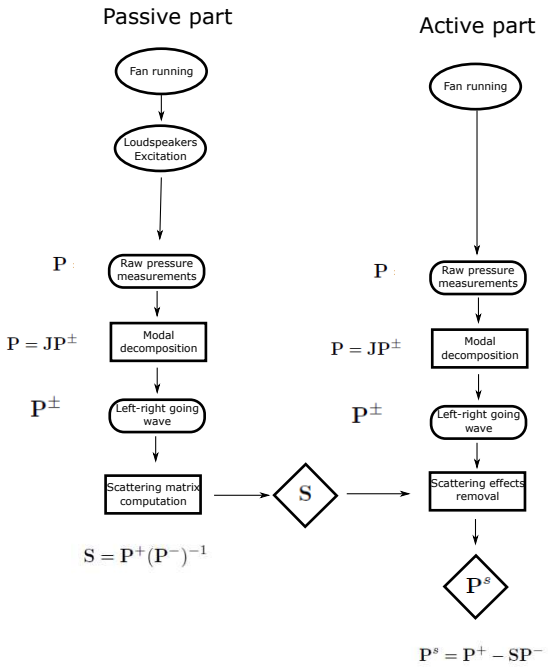

Figure 5: Flowchart of the experimental process.

$$\mathbf{P}^+ = \mathbf{S}\mathbf{P}^- + \mathbf{P}^s \overset{\mathbf{P}^s << \mathbf{P}^-, \mathbf{P}^+}{\Longrightarrow} \mathbf{S} \approx \mathbf{P}^+ \left(\mathbf{P}^-\right)^{-1} \tag{7}$$

In order to enable the inversion of $\mathbf{P}^-$, a minimum of $2N$ independent[1] measurements obtained using different loudspeaker locations and combinations must be obtained. This does not require to know explicitly the exact position of the loudspeakers as long as they yield to independent excitations:

$$\mathbf{P}^- = \begin{pmatrix} p^-_{a_{-N,0}}|_{\mathrm{I}} & \cdots & \cdots & \cdots & \cdots & p^-_{a_{-N,0}}|_{2N} \\ \vdots & \cdots & \cdots & \cdots & \cdots & \vdots \\ p^-_{a_{+N,\mu}}|_{\mathrm{I}} & \cdots & \cdots & \cdots & \cdots & p^-_{a_{+N,\mu}}|_{2N} \\ p^-_{b_{-N,0}}|_{\mathrm{I}} & \cdots & \cdots & \cdots & \cdots & p^-_{b_{-N,0}}|_{2N} \\ \vdots & \cdots & \cdots & \cdots & \cdots & \vdots \\ p^-_{b_{+N,\mu}}|_{\mathrm{I}} & \cdots & \cdots & \cdots & \cdots & p^-_{b_{+N,\mu}}|_{2N} \end{pmatrix}$$

The measurement of the scattering matrix can be quite time-consuming since $2N$ loadcases are required for each tested frequency, and because long acquisition times are necessary to ensure statistical convergence. Two methods have been applied in this work

[1] It is adviced to take more than $2N$ loadcases to have an overdetermined system and improve the accuracy of the computations. In this experiments 24 loadcases were used at each frequency

to accelerate the acquisition process. Firstly, a specific hardware made it possible to generate 4 different loadcases simultaneously by providing loudspeaker signals with 4 different frequencies (not sharing any common harmonic) simultaneously. Secondly, instead of measuring the scattering matrix for every single frequency, the scattering matrix is computed at specific frequencies and later interpolated at the other frequencies of interest. This interpolation method allows very substantial time savings and was shown to be accurate as long as the scattering properties of the source evolve slowly with respect to the frequency. It cannot be used within a frequency interval that includes the cut-on frequency due to the change of the size **S** at that frequency. Therefore, the frequencies in those frequency bands can be poorly resolved. But in any case, the very low axial propagation phase velocity of the acoustic modes around the cut-on frequencies cause a poor conditioning of the matrix **J**, which does actually alter much more significantly the inversion accuracy around those frequencies.

The active measurements are then performed with the loudspeaker's excitation switched off. The modal decomposition on the measurements provides the modal content of the noise produced by the source, reflected at the duct terminations and scattered by the source. But the latter effects can now be removed using the scattering matrix obtained in the passive part:

$$\mathbf{P}^s = \mathbf{P}^+ - \mathbf{S}\mathbf{P}^- \tag{8}$$

This formulation permits the extraction of the acoustic field produced by the sources within the module investigated $\mathbf{P}^s$ without the scattering effects of the duct that would contaminate the acoustic measurements otherwise. However, it does not removes the influence of the TBL pressure fluctuations.

This is why, traditionally, Equation (8) is reformulated using the explicit formulation of the duct terminations reflection coefficients **R** [5] such as:

$$\begin{aligned}\mathbf{P}^s &= [\mathbf{E} - \mathbf{S}\mathbf{R}]\mathbf{P}^+ \\ &= [\mathbf{E} - \mathbf{S}\mathbf{R}](\mathbf{J}\mathbf{T})^{-1}\mathbf{P} \\ &= \mathbf{C}\mathbf{P}\end{aligned}$$

where **E** is the unity matrix and with :

$$\mathbf{T} = \begin{bmatrix} \mathbf{E} & \mathbf{0} \\ \mathbf{R}_a & \mathbf{0} \\ \mathbf{0} & \mathbf{E} \\ \mathbf{0} & \mathbf{R}_b \end{bmatrix}$$

This new formulation has the advantage to reduce the number of variables by two as we only need $\mathbf{P}^+$ form the modal decomposition. The other half microphones reading can be used to compute another equivalent source term $\mathbf{P}_2^s$. Since the TBL pressure fluctuations are not correlated over large distance and assuming that the distance between microphones is sufficient, the TBL pressure fluctuations can be removed by computing the cross-correlations between the two source term:

$$\mathbf{G}^s = \mathbf{P}_1^s(\mathbf{P}_2^s)^* \tag{9}$$

where $(..)^*$ denotes the complex conjugate and transpose. This formulation requires accurate measurements of the duct terminations reflection coefficients. $\mathbf{R}_a$ and $\mathbf{R}_b$ are computed using passive measurements only with loudspeakers situated on the opposite side of the test object, meaning that $\mathbf{R}_a$ is computed using only loudspeakers at station B and viseversa. For this experimental campaign, this poses an issue as the test object is composed of a smaller diameter module and therefore has different cut-on frequencies. Indeed, higher order modes are only passing when they reach the larger cut on frequency of the small diameter module.

This effects has strong consequences on the measurements of the reflection coefficients at the duct terminations for frequencies above $f_{\pm 1,0}$. Indeed, after the first cut-on frequency, additional modes will start propagating in the vicinity of the loudspeakers locations. However, those modes will not be able to be transmitted to the other side of the smaller diameter tested module as it possesses higher cut-on frequencies. This results in poor measurements of the reflection terminations coefficients due to low signal-to noise ratio.

As an illustration, Figure (6) shows non-physical values (above 1) of the reflection coefficient for the first azimuthal mode in the frequency range [1327 Hz - 2010 Hz] which corresponds respectively to the first cut-on frequency of the large and small duct.

To be able to use the traditional method for the active part in Equation (3.3), it would be better to rely on independent measurements of the reflection coefficients obtained with an empty duct. Unfortunately, even with an empty duct relatively high reflection coefficients in the plane wave regim, below $2010Hz$, were observed in Figure (6). It was recently shown [15] that high reflection coefficients also result in high condition number of the matrix **C** and low accuracy for the active part formulation of Equation (3.3). To

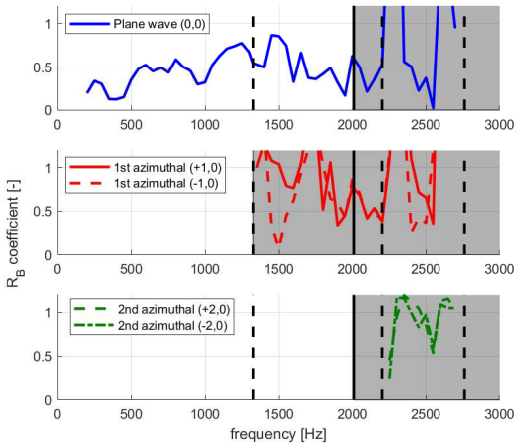

Figure 6: Direct reflection coefficient R_b with the smaller adaptive module. The vertical dashed lines represent the cut-on frequency of the large duct and the vertical lines the one of the small diameter module. The gray areas indicate the zone of low signal-to-noise ratio

avoid all those problems related to the determination of accurate reflection coefficients, it was preferred to use Equation (8) which does not rely on them explicitly. The TBL influence was removed in this experimental campaign by taking long acquisition time and computing averaged spectra on separated time windows [16].

3.4. Acoustic power

According to Myers [14], the acoustic energy is a conserved quantity in an irrotational and isentropic flow. The acoustic power can be integrated across the duct cross-section with normal $\mathbf{n}$:

$$W = \int_S \langle \mathbf{I} \cdot \mathbf{n} \rangle \, dS \tag{10}$$

with the acoustic intensity defined by

$$\mathbf{I} = (\rho_0 \mathbf{v} + \rho \mathbf{v}_0) \left(\frac{p}{\rho_0} + \mathbf{v}_0 \cdot \mathbf{v} \right). \tag{11}$$

Introducing the modal description of the acoustic pressure p and velocity $\mathbf{v}$ in a duct introduced in Equation (1), the axial power across the duct section becomes [11]:

$$P = \pi\beta^4 \sum_{\text{cut-on}} \left[\frac{\sigma^+_{m\mu} |\hat{p}^+_{m\mu}|^2}{(1 - M\sigma^+_{m\mu})^2} + \frac{\sigma^-_{m\mu} |\hat{p}^-_{m\mu}|^2}{(1 - M\sigma^-_{m\mu})^2} \right]$$
$$+ 2\pi\beta^4 \sum_{\text{cut-off}} \frac{\tau_{m\mu}}{(1 + M^2\tau^2_{m\mu})^2} [(1 - M^2\tau^2_{m\mu}) Im(\hat{p}^+_{m\mu} \bar{\hat{p}}^-_{m\mu})$$
$$- 2M\tau_{m\mu} Re(\hat{p}^+_{m\mu} \bar{\hat{p}}^+_{m\mu})] \tag{12}$$

with

$$\beta = \sqrt{1 - M^2} \quad , \quad \sigma^\pm_{m\mu} = \pm \sqrt{1 - \left(\frac{\alpha_{m\mu}\beta}{\omega} \right)^2}$$

and

$$\tau_{m\mu} = i\sigma^+_{m\mu} = -i\sigma^-_{m\mu}.$$

The second term of Equation (12) describes the influence of the cut-off modes on the acoustics power propagating inside the duct, which only contributes through interactions between left- and right-going modes. However, given that cut-off modes decrease exponentially, the product between the two is usually considered negligible. In practical applications, this term is often neglected [17].

When measuring the acoustic power from the multi-ports methodology using Equation (8), it is important to remember that $\mathbf{P}^s$ describes the noise source *as if* it were in an infinite duct. In that context, the terms including $p^+_{m\mu}$ describes the power propagating upstream of the source and $p^-_{m\mu}$ the one downstream.

4. Installation effects

The noise emitted by the fan was first evaluated under uniform inflow profile to serve as a baseline to be compared with the different non-uniform ingested flows generated by the grids. All the fan noise measurements presented in this section have been done at the design point rotational speed Ω.

4.1. Fan with uniform flow condition

The initial raw measurements are obtained before the application of the multi-port technique (Fig. 7, blue curve △). They are contaminated by turbulent pressure fluctuations of the wall boundary layer and acoustic scattering effects (this includes reflections on the duct terminations, standing waves, etc).

Once the modal decomposition is performed, the results can be used to reconstruct an image of the initial measurements (red curve □). Since this image

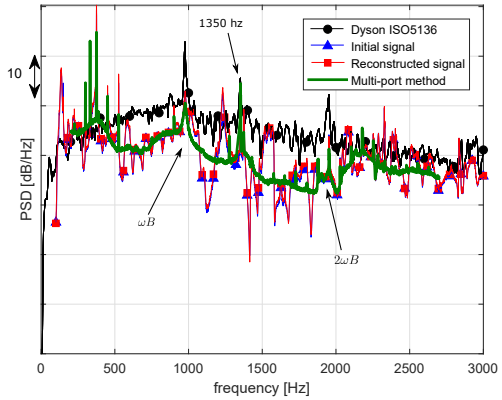

Figure 7: Power spectral density of the fan noise from the multi-ports eduction technique on the microphone 5 and ISO-5136 at similar flow rate and rotational speed. Color: Dyson - black, initial - blue, reconstructed - red and multi-port - green

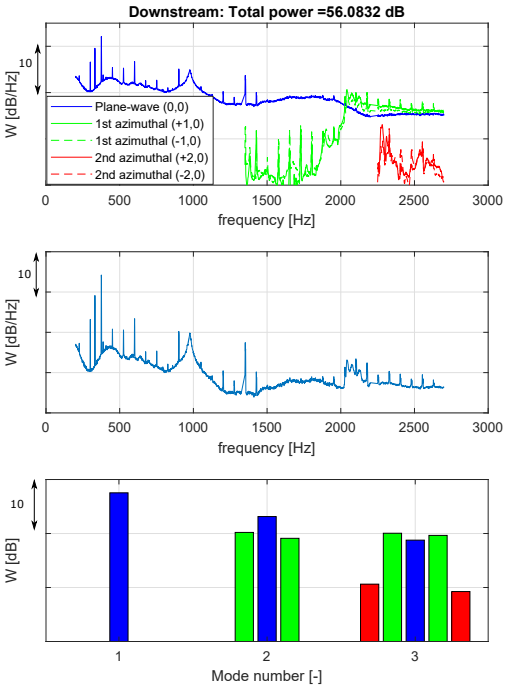

Figure 8: Modal acoustic power downstream of the fan

was obtained by a fitting of the experimental results to a theoretical solution of the acoustic field inside the duct, it does not account for turbulent pressure fluctuations. The small differences between the raw and the reconstructed signals indicates that, at such a low volume flow rate, the turbulent boundary layer pressure fluctuations barely affect the microphone readings.

The green curve corresponds to the results obtained after applying the multi-port eduction on the initial measurements. It appears to have removed most of the large amplitude oscillations that were likely caused by constructive/destructive interferences from acoustic standing waves within the duct. Figure 7 also shows independent results performed on a different setup following the ISO-5136 methodology [18]. Globally, the two spectra obtained are in good agreement. They perfectly match at high frequency, but lower amplitudes are observed in the low to mid-frequency range.

Above the first cut-on frequency of the duct, the spectrum analysed in Figure 7 changes with the microphones position due to the 3D modal structure of the acoustic wave inside the duct. For this reason, it is preferable to analyze the acoustic power in the duct section where the microphones are situated using Equation 12.

In opposition to the traditional induct acoustic measurement methods, the multi-port approach allows to measure the respective contribution of each modes in the overall acoustic power. It can be observed in Figure 8 that the first azimuthal modes $(\pm 1, 0)$ only show significant contribution to the acoustic power after the cut-on frequency of the small diameter module where the fan is installed. The cut-on for the second azimuthal modes being above the frequency range available, it never propagates.

The obtained spectra can be analysed in line with the theoretical framework developed by Ffowcs Williams and Hawkings [19], according to which the noise generated by a rotating machine can be decomposed into three main components: the thickness noise, the turbulence noise and the loading noise. At low Mach number and for thin rotor/stator blades, the unsteady loading noise dominates the sound production. This loading noise is characterized by a broadband and a tonal component. The latter is emitted at the blade passing frequencies $n\omega B$ (with B being the number of rotor blades) and produced by the unsteady forces acting on the blades [12]. The blade passing frequencies (BPF) are well identified in both ISO-5136 and multi-ports measurements.

An additional tonal peak at the frequency $1350Hz$ is also observed in both measurement series. Such harmonic, which cannot be related to a tonal sources attached to the rotor blades, could be due to a coherent flow structure in the blade tip region that interact with the fan blade and rotate at the different angular veloc-

ity than the fan itself [20]. Unfortunately, the resulting peak frequency for this phenomenon also corresponds to the first cut-on frequency $f_{1,0}$ of the duct for which the conditioning of the modal decomposition is poor, hence degrading the measurement accuracy.

4.2. Aerodynamic performance installation effects

To generate installation effects, grids are used upstream of the fan to condition the flow. Those grids (Figure 1) have been selected to induce large radial and azimuthal mean flow distortions (Fractal and Half) and increase turbulence level (Grid). It is expected that those distortions will change the tonal and broadband noise of the fan.

However, non-uniformities in the flow change the velocity triangle seen by the blades of the fan which in turns affect its aerodynamic performances. Figure 9 shows how the performance curves of the fan are affected by the different distorted inflows. The performances of the fan ares evaluated using a Kiel probe at the rear of the duct to avoid the influence of swirl past the fan. The change in operating condition of the fan was done by closing a butterfly valve situated in the exhaust circuit of the wind tunnel. Finally, in order to account for the pressure losses in the duct, additional measurements performed without the fan are used to correct the total pressure measured by the Kiel probe.

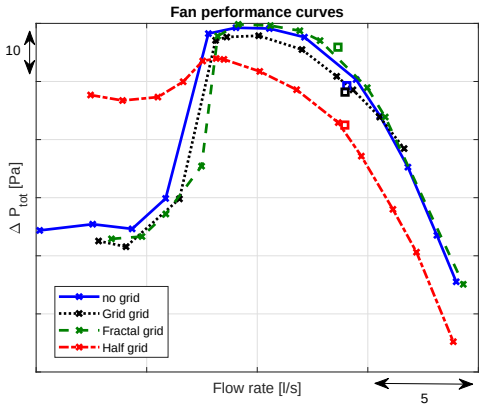

Figure 9: Performance curve of the Dyson fan at constant rotational speed for different inflow conditions. The square dots indicate the operating conditions for the multi-port tests

As it can be seen in Figure 9, the fan no longer works in ideal conditions. Its performances are thus diminished as it is illustrated with the drop in total pressure for the different obstructions. This adds in the complexity of the investigations of acoustic installations effects. Indeed, even though all the tests were performed at similar volume flow rate and rotational speed, the pressure rise of the fan differs depending on the grids installed inside the duct. Since pressure rise across a fan is a critical parameter of the noise it generates, it therefore matters to unveil if the acoustic installation effects observed are strictly due to change in total pressure operating point or more subtle effects.

To determine whether the changes in acoustic power observed are due to a modification of the fan operating point, a similarity law is used [2]:

$$W_2 = W_1 + 10log\left(\frac{Q_2}{Q_1}\right) + 20log\left(\frac{\Delta P_2}{\Delta P_1}\right) \qquad (13)$$

This law, based on dimensional analysis, scales the acoustic power of a fan (W_2) from previous measurements (W_1) performed on the fan under uniform inflow condition at the same rotational speed. In Table 3, the prediction obtained using Equation (12) is compared to the acoustic power measured for the different grids.

Obstruction	No grid	Fractal
Acoustic Power [dB]	56.1 (+0)	59.0 (+2.9)
Similarity [dB]	56.1 (+0)	56.4 (+0.3)
Obstruction	Grid	Half
Acoustic Power [dB]	63.8 (+7.7)	70.1 (+14)
Similarity [dB]	56 (-0.1)	55.7 (-0.4)

Table 3: The acoustic power computed with Equation. (12) downstream of the fan for the different obstructions and their increment compared to the uniform flow case. The similarity is obtained with Equation. (13) and the fan performance conditions described by the square dots in Figure (9)

It can be seen that the increase in noise power observed through Equation (12) is completely different from what is obtained with the similarity law. Equation (13) only predicts small changes in the acoustic power while the measured power levels are strongly increased depending of the obstruction considered. This shows that installation effects cannot be reduced to changes in the aerodynamic performances of the fan only. It also highlights that this similarity law is not well adapted to account for installation effects.

4.3. Acoustics scattering and ingested flow installation effects

Figure (10) shows the scattering coefficients of the small diameter module with the fan installed and the different flow conditioners. The coefficients are no

longer symmetric for A and B ports when the fan is installed inside the duct. Indeed, even though the transmission coefficient τ_a and τ_b are identical, ρ_a and ρ_b exhibit strong differences.

The grids tend to decrease the transmission and increase the reflection compared to the no grid case. This is even more marked at high frequencies. In addition, a systematic and strong reduction of the transmission coefficient can be seen at 2000 Hz for all obstructions, at the first cut-on frequency of the small diameter module.

The acoustic power of the fan is computed under the different inflow conditions in Table (3). As expected, for all the obstructions, the noise is increased compared to the uniform flow configuration. The "Half" distortion led to the strongest increase of noise while the "Fractal" grid had only limited effects.

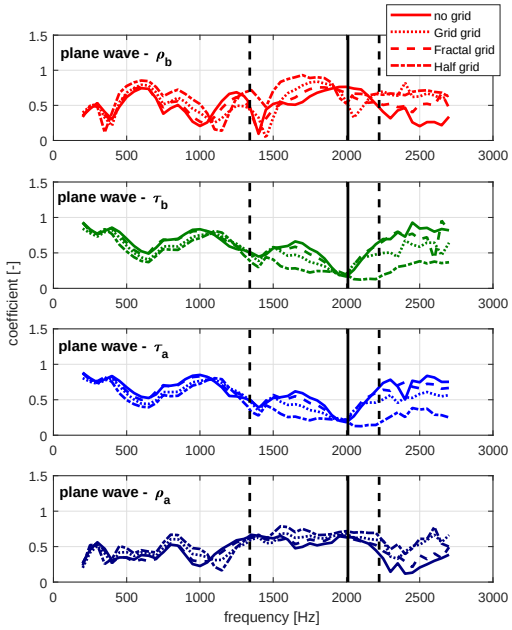

Figure 10: Plane wave scattering coefficients for all the modes in the empty adaptive module with the fan for the different flow conditioners

For further analysis of the influence of inflow conditions on the perceived broadband noise, the acoustic power spectrum was computed in Figure (11) upstream of the fan. The flow distortions set by the "Grid" and "Half" obstructions increased the broadband noise by respectively 5 and 10 dB at high frequencies. This is an indicator of how turbulence in the ingested flow affects the fan noise. Indeed, those are strong and disruptive obstructions that likely increase

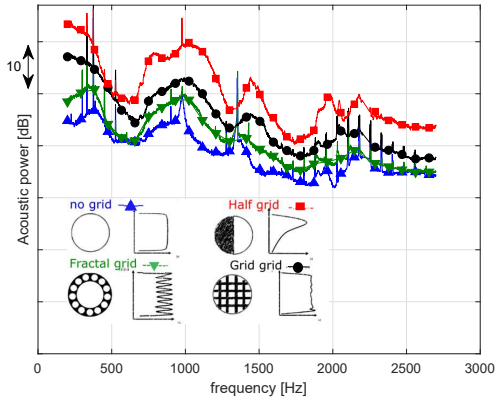

Figure 11: Acoustic power upstream of the fan under different inflow conditions at the same rotational speed.

the turbulence and both were accompanied with an increase in broadband noise.

The last obstruction named "Fractal" was meant to induce a mean inflow distortion with the same azimuthal order as the number of rotor blades, while minimizing the blockage. It was therefore expected to generate a substantial increase in the tonal noise of the fan with limited broadband effect. Surprisingly, only a small increase of acoustic power can be seen around the blade passing frequency. In addition, the amplitude of the noise at high frequency seems to remain unchanged compared to the uniform flow case. This indicates no or little increase in broadband noise. It should be noted that other attempts were made to generate tonal noise using different grids with the same azimuthal order, but none of those obstructions led to significant tonal noise increase.

It was expected, from previous investigations [9; 10], to see an increase in broadband and tonal noise resulting from respectively the turbulence and azimuthal mean flow distortions. Although the increase of broadband noise with added turbulence is well represented, only the "Half" obstruction led to significant increase in the tonal noise.

5. Conclusion

The proposed methodology was shown to permit a detailed analysis of the noise emitted by a ducted axial fan subjected to different inflow conditions. Eliminating spectral features that could be related to the noise being reflected at the duct terminations and further scattered through the fan itself, it was demonstrated to be a key element enabling this investigation.

However, some issues were encountered regarding the application of the multi-port methodology on a fan within a smaller diameter duct: the reduction of the diameter section changes the cut-on frequencies of the module where the fan is installed and prevent accurate measurements of the duct terminations reflection coefficients. As a result, the traditional method to reconstruct the source terms, which relies on an explicit formulation of those reflections, could not be used and an alternative methodology had to be considered.

The extracted active tonal spectrum exhibits peaks that can be associated to the rotor blade passing frequencies and others occurring at a different frequency, which have been hypothesized to be caused by coherent flow structure in the blade tip region. Other than that, the inflow distortions were shown to have strong impact on the acoustic power radiated and aerodynamic performance of the fan. Using similarity laws, it was shown that those aerodynamic performance changes alone were not sufficient to explain the full impact of distorted inflows on the fan acoustic power. In addition, the active broadband noise was shown to be very sensitive to the turbulence shed by the grids, with additional noise of the order of 10 dB at some frequencies. However, the expected increase in tonal noise with azimuthal mean flow distortions were not observed for all obstructions.

The grids have strong effects on the scattering of the module, which complicates the investigation of the installation effects. An additional deconvolution procedure, consisting in dividing the extracted modal content of the (fan+grid) system by the scattering matrix of the grid, may improve the interpretation, and should be considered in future investigations.

Acknowledgments

This research was partly supported by the European Union's Horizon 2020 research and innovation programme under the Marie Sklodowska-Curie project SMARTANSWER (grant agreement No 722401).

References

[1] W. Neise, Generation mechanisms and control method. Fan noise, Proceeding of inter-noise 88, Avignon, France, 1988.

[2] A. Guedel, Generation du bruit et moyens de reduction. Acoustique des ventilateurs, CETITA, France, 1990.

[3] A. Bolton, Installation effect on fan system. National Engineering Laboratory, Germany, 1990.

[4] W. De Roeck, Hybrid methodologies for the computational aeroacoustics analysis of coffined subsonic flow. Katholieke Universiteit te Leuven, Belgium, 2007.

[5] S. Sack, M.Abom, G.Efraimsson, On Acoustic multi-port characterisation including higer order modes, Acta Acustica 102, 2016.

[6] J.Lavrentjev, M.Abom and H.Boden, A measurement method for determining the source data of acoustic two-port source, Journal of sound and vibration 183 (3), 1996

[7] J. Lavrentjev, M. Abom, Characterisation of fluid machines as acoustic multi-port sources. Journal of Sound and Vibration, 197(1),1996.

[8] M. Abom, H. Boden, Modeling of fluid machines as source of sounds in duct and pipe system, Acta Acustica 3, 1995.

[9] M. Shur et al, Effect of inlet distortions on ducted fan noise, 22nd AIAA/CEAS Aeroacoustics Conference, Lyon, France, 2016.

[10] S. Allam, M. Abom, Investigation of aerodynamic installation effects for an axial Fan, 19th AIAA/CEAS Aeroacoustics Conference, Berlin, Germany, 2013.

[11] S.W. Rienstra, An introduction to Acoustics. Eindhoven University of Technology, Netherlands, 2016.

[12] C. Schram, Introduction to acoustics and aerocoustical analogies. von Karman Institute lectures, Rhode-St-Genese, Belgium, 2016.

[13] L. Morfey, Sound transmission and generation in ducts with flow. Journal of Sound and Vibration, 1971.

[14] M. Myers, An exact energy corollary for homotropic flow. Journal of Sound and Vibration, 1986.

[15] E.Garnell, M.Abom and G.Bandwell, Designing, building and validating a test rig to measure two-port data of small fans, Proceedings of FAN2018, Darmstad, 2018

[16] S.Sack and M.Abom, Investigation of orifice aeroacoustics by mean of multi-port methods, Journal of sound and vibration 1-17, 2017

[17] H. Denayer, Acoustic power dissipation and generation by multi-port elements, Katholieke Universiteit te Leuven, Belgium, 2017.

[18] ISO 5136, Determination of sound power radiated into a duct by fans and other air-moving devices, International Standardization Organization, 2003.

[19] J. E. Ffowcs Williams and D. L. Hawkings, Sound generation by turbulence and surfaces in arbitrary motion, Philosophical Transactions of the Royal Society of London, 1969.

[20] F. Kromer, Sound emission of low pressure axial fans under distorted inflow conditions Der Technischen Fakultat der Friedrich-Alexander-Universitat, Nurnberg, 2018

Investigation of Turbulence-Surface Interaction Noise Mechanism and their Reduction using Porous Materials

Riccardo Zamponi

Environmental and Applied Fluid Dynamics Department, von Karman Institute for Fluid Dynamics, Belgium, riccardo.zamponi@vki.ac.be

Supervisor: Christophe Schram

Full Professor, Aeronautics and Aerospace Department & Environmental and Applied Fluid Dynamics Department, von Karman Institute for Fluid Dynamics, Belgium, christophe.schram@vki.ac.be

University Supervisor: Fulvio Scarano

Full Professor, Aerospace Engineering, TU Delft, Netherlands, f.scarano@tudelft.nl

Abstract

The effectiveness of the use of porous materials for reducing airfoil turbulence-impingement noise is investigated experimentally by means of boundary layer characterization and acoustic beamforming measurements. An innovative design for the implementation of melamine foam in a NACA-0024 profile is proposed. Results show that the use of porosity leads to a turbulence-impingement noise decrease in the low frequency range.

Keywords: aeroacoustics, leading-edge noise, porous materials, noise reduction

1. Introduction

The investigation of the noise generation mechanisms involved in the interaction of a wing profile with incoming turbulence represents a core topic for applications of large societal interest, including airframe noise, aeronautical propulsion systems, HVAC systems for automotive and construction. In these instances, the turbulence is typically produced by elements such as protection grids or heat exchangers that are installed upstream of the airfoil and create inflow distortions. From the physical point of view, the sound is radiated as a consequence of the rapid changes of the turbulent vortexes inertia due to the interaction with the surface of the airfoil. Historically, the phenomenon has been studied by several authors. Paterson and Amiet [1], Migliore and Oerlemans [2] and Moreau *et al.* [3] demonstrated that turbulence-impingement noise, referred to also as leading-edge noise, is predominantly a low-frequency source when the turbulent eddies, related to the acoustic generation, result to be large scale structures. Moreover, the Amiet theory [4; 5; 6] showed that the noise radiation pattern depends on the airfoil compactness with reference to the acoustic wavelength. Additional studies concerning the effect of a real airfoil geometry on the interaction with a turbulent flow can be found in the work of Gill *et al.* [7; 8] and Kim *et al.* [9]. The study of the mechanism with whom the turbulence-impingement noise is generated and radiated is instrumental in designing novel sound mitigation approaches. Since acting on the ingested turbulent field is often challenging, one promising strategy to reduce the turbulence-impingement noise is to make the airfoil acoustic response less sensitive to the turbulent flow. Geometrical or structural changes of the airfoil design or the usage of absorbing materials can achieve this objective.

The scope of the present work is to evaluate the effectiveness of a porous airfoil with an impenetrable core line in the reduction of the noise produced by turbulence impinging on its surface. The implementation of porous material as part of the structure of a wing profile has been already addressed in the past by several authors. Among them, Roger *et al.* [10; 11] filled a NACA-0012 airfoil with steel wool to investigate the leading-edge noise reduction in a grid-generated turbulent flow. In their study, the use of porous materials

showed to grant a reduction effect with a maximum of 5 dB, even though no optimization of the material parameters had been attempted. An analogous method has been adopted by Geyer *et al.* [12; 13], who tested different porous materials and different turbulence-generator grids and performed acoustic measurements on leading-edge noise using microphones array techniques. The experiments lead to a noticeable noise reduction for most of the porous profiles when compared with the non-porous cases. Similar designs for a porous airfoil have been considered also by Sarradj and Geyer [14], Geyer *et al.* [15; 16], Tinetti [17] and Herr and Reichenberg [18] in the framework of trailing edge noise mitigation. Most of the conducted studies state that the application of porous materials may have a significant potential for flow noise mitigation but also that it is necessary to improve the understanding of the influence of the porous material parameters. The already mentioned Geyer *et al.* [12; 13] and Sarradj and Geyer [14] focused their analysis on the characterization of this influence by comparing results of aeroacoustic wind tunnel tests on several porous and non-porous airfoils. They found that not only the overall sound pressure level but also the spectral characteristics depend on the properties of the porous material, especially on the static air flow resistivity. A deeper insight about these correlations should lead to a better comprehension of the physical mechanism responsible for noise reduction, since no agreement about the mode of operation of the porous treatments has been found yet, despite the numerous investigations.

This manuscript describes acoustic far-field noise and hot-wire anemometer measurements that were performed in the testing facility of von Karman Institute for Fluid Dynamics (VKI) on a NACA-0024 airfoil in a non-porous and a porous version. Specifically, the porous material considered has been melamine foam. A particular emphasis has been put on the characterization of the parameters of the material. The comparison between the two cases has been carried out considering one angle of attack and one flow velocity. The experimental setup consists of a rod-airfoil configuration, already used by de Santana [19]. In this arrangement, firstly proposed by Jacob *et al.* [20] as benchmark problem for noise computation and modeling, the wing profile undergoes a broadband perturbation dominated by a preferred shedding frequency, similarly to what is observed in most turbo-machinery applications [21]. Indeed, as stated by Roger and Moreau [11], the analysis of the turbulence-impingement noise reduction that can be achieved with the use of porous treatment provides similar results for a rod-airfoil and a tandem airfoil configuration.

Finally, the objective of the present effort is to demonstrate the potential benefits of this technology, rather than carrying out an in-depth investigation of its applicability. For instance, the aerodynamic performance loss that the porous airfoil may experience in comparison with the reference one and that has been observed in similar works [14; 16] has not been evaluated.

2. Design and Characterization of the Porous Airfoil

The porous NACA-0024 airfoil has been designed with a chord of 0.157 m, corresponding to a maximum thickness of approximately 0.038 m, and a span of 0.200 m. The choice of the chord has been made in order to ease the manufacturing and the instrumentation of the model. In order to avoid the cross-flow between the two sides of the profile, the core line has been made impenetrable. The volume of the airfoil has been filled with melamine foam, easy to cut to the desired shape. A porous hard plastic exoskeleton has the function to contain the foam and to ensure the proper shape fidelity and is made of two components, one per each side of the airfoil surface, assembled on the solid center plane and glued in correspondence with the leading edge and the trailing edge. The same manufacturing technique has been adopted to produce the solid airfoil, whose exoskeleton does not present any porosity. All the profiles have been finally coated with the same metallic wire mesh, which protects the materials and guarantees a good surface roughness quality.

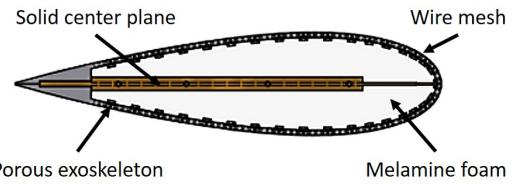

Figure 1: Scheme of the porous NACA-0024 used in the experiments

In Fig. 1 a scheme illustrating the different parts constituting the porous airfoil is depicted. With the aim of investigating the acoustic influence of the exoskeleton and the wire mesh, a third airfoil just made of melamine foam has been fabricated. The porous

Table 1: JCAL model parameters characterizing the melamine foam of the porous airfoil.

σ [Pa· s · m^{-2}]	ϕ [-]	α_∞ [-]	Λ [m]	Λ' [m]	k_0 [m^2]	k_0'[m^2]
13003.9	0.986	1.02	1.344×10^{-4}	1.942×10^{-4}	1.410×10^{-9}	2.382×10^{-9}

material has been cut in the shape of a NACA-0024 and glued on the solid center plane, without any other hard plastic component. Although this design does not represent a technological solution for the implementation of a porous material in the structure of the airfoil, it constitutes a basis of comparison.

As mentioned above, the porous medium parameters play an important role in the investigation of noise reduction mechanisms. According to the Johnson-Champoux-Allard-Lafarge (JCAL) model, the six parameters considered necessary to fully characterize the material are the static air flow resistivity, σ, the porosity, ϕ, the tortuosity, α_∞, the viscous characteristic length, Λ, the thermal characteristic length, Λ' and the thermal permeability, k_0'. Besides these, another parameter that is used to define a porous medium is the viscous permeability, k_0, which is directly linked to σ. Indeed, it is defined as the ratio of the dynamic viscosity of air to the static air-flow resistivity.

The characterization of the above-mentioned quantities has been performed in collaboration with Laboratoire d'Acoustique de l'Université du Maine (LAUM). For their estimation, an inverse method based on the measurement of the melamine foam scattering matrix by means of a 4-microphones impedance tube has been considered [22]. The inversion is done in the Bayesian framework, whereas the model used for describing the porous medium is the JCAL one. The results of the characterization are listed in Table 1. The estimation is considered reliable since a good match has been found with other results from ultrasonic measurements conducted on the same sample and not discussed in this work.

Concerning the parameters of the hard plastic exoskeleton and the metallic wire mesh, the first has been designed to have ϕ of 80%, whereas the second to have ϕ equal to 60.8%. Static air flow resistivity measurements have been performed at Centre de Transfert de Technologie du Mans (CTTM), in Le Mans, with samples of the two materials. As expected, the σ of the two layers was negligible, confirming the fact that the static air flow resistivity of the porous airfoil is governed by the σ of the melamine foam.

3. Experimental Set-up and Data Processing

In this section, the experimental setups and analysis tools used to carry out the aerodynamic and aeroacoustic tests are presented.

3.1. Rod-airfoil Configuration

The experimental facility consists of a jet installed in a semi-anechoic room with dimensions 4 m × 3 m × 4 m and a cut-off frequency of 200 Hz. A wooden circular-to-rectangular contraction, designed by de Santana [19] and characterized by an area ratio of 2.35 to 1, adapts the circular geometry of the duct to the rectangular geometry needed for the rod-airfoil configuration. The dimensions of the nozzle exit are 0.20 m for the span and 0.15 m for the width. The airfoil and the rod are held vertically by two side-plates, designed not to have sharp corners. The experimental setup with the relative distances is depicted in Fig. 2. The cylindrical rod has a diameter of 0.02 m that corresponds to the one of the leading edge circle of the airfoil. The distance between the rod axis and the leading edge is 0.174 m.

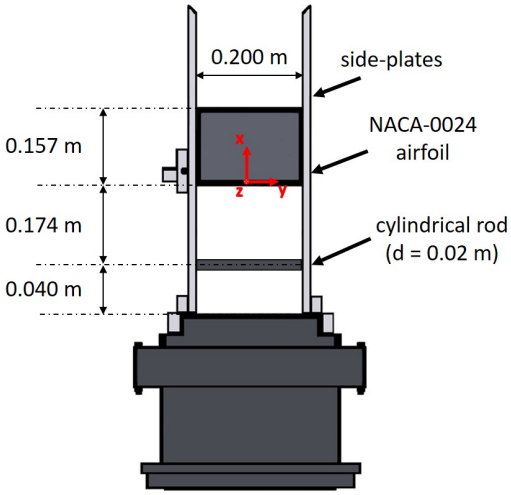

Figure 2: Scheme of the rod-airfoil configuration installed on the cylindrical-to-rectangular contraction

The following coordinate system is used for the description of both acoustic and hot-wire measurements: the x-axis is aligned with the jet axis and therefore

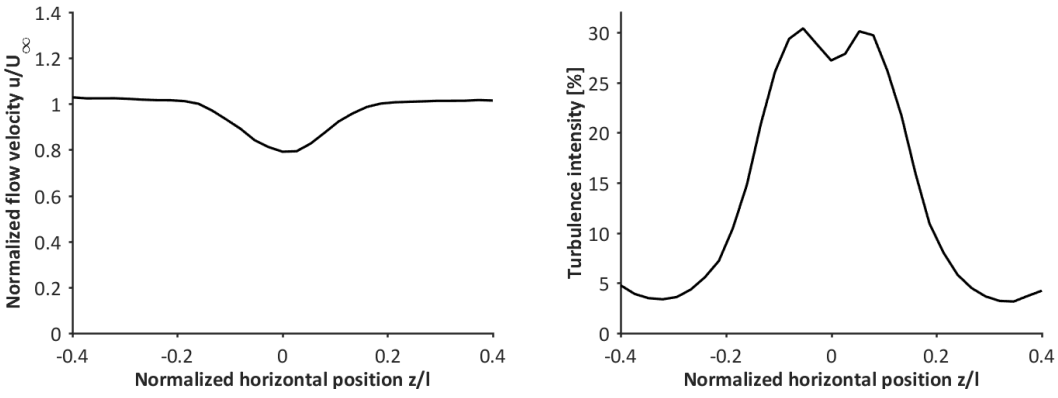

(a) (b)

Figure 3: Mean velocity (a) and turbulence intensity (b) profiles at 20 mm upstream of the airfoil leading edge level. l is the width of the nozzle (0.150 m).

with the flow direction, the y-axis is aligned with the spanwise direction of the airfoil and the z-axis is oriented in order to form a right-handed coordinate system. The origin is set in the midspan of the profile at the level of its leading edge.

All the measurements have been carried out at a 0° angle of attack of the airfoil and at a flow velocity of 30 m/s, corresponding to a chord-based Reynolds number of $3.2 \cdot 10^5$. The angle of attack and the alignment between rod and airfoil have been verified by comparing the static pressure distributions on the two sides of the airfoil.

The facility has been characterized by means of hot-wire anemometry in order to determine the mean velocity, $\bar{u}$, and the turbulence intensity, TI, profiles for different configurations. $\bar{u}$ is normalized by the flow free-stream velocity U_∞, whereas TI is defined as the ratio of the root-mean-square of the turbulent velocity fluctuations to U_∞. All the acquisitions have been performed with a single hot-wire probe connected to an in-house system and corrected in order to take into account the temperature variations during the tests. The sampling frequency has been set to 51.2 kHz, which leads to an anti-aliasing filter set to 25.6 kHz. The acquisition time for the velocity has been set at 5 s with the purpose of ensuring convergence of the results. In free-stream conditions, TI resulted to be about 0.4% in the potential core of the jet at a distance of 1 mm from the nozzle exit, proving that there is almost no inflow turbulence. Figure 3 shows the $\bar{u}$ and TI profiles along the z-axis at 20 mm upstream of the leading edge and 44 mm downstream of the rod axis. In the figure, the z-axis is normalized by the width of the nozzle (l = 0.150 m). The effects of the wake of the cylindrical rod at this level consist of a 20% reduction of $\bar{u}$ and a significant increase in the value of TI, whose peak is about 30%.

3.2. Steady Pressure Measurements

In order to perform static pressure distribution measurements, the NACA-0024 profiles have been equipped with 35 static pressure sensors. In each surface there are 17 transducers at the midspan that correspond to the 1.4%, 3.4%, 5.7%, 8.4%, 12.5%, 16.7%, 21.0%, 26.7%, 32.4%, 38.1%, 49.5%, 55.2%, 60.9%, 66.5%, 72.6% and 77.8% of the chord. An additional measurement position has been considered in correspondence to the leading edge.

The static pressure ports are connected to an in-house acquisition system that leads to the estimation of the pressure coefficient, C_p, along with the chord, defined as

$$C_p = \frac{p - p_\infty}{p_0 - p_\infty}, \tag{1}$$

where p is the static pressure acquired, p_0 is the stagnation pressure in the free-stream, and p_∞ is the static pressure in the free-stream. Finally, the data have been acquired at a sampling frequency of 500 Hz and with an acquisition time of 15 s.

3.3. Hot-Wire Measurements

The airfoil boundary layer has been characterized by means of constant temperature anemometry, with a single wire in-house system. The probe has been

placed in a carriage system which allows a movement within the plane xz, at a y corresponding to the midspan of the airfoil. The wire has been oriented perpendicular to the streamwise velocity component. As in the case of the facility characterization, the sampling frequency has been set to 51.2 kHz, whereas the data have been acquired for 5 s. The first 0.5 s of acquisition have been discarded in the post-processing phase in order to consider the effect of the vibrations of the probe during the traverse system movement.

The static calibration of the hot-wire anemometer has been performed in-situ on a daily basis, using a Prandtl tube to measure the reference velocities. In order to take into account the significant effect of the temperature on the measurements, an appropriate correction has been applied considering the model proposed by Bruun [23]. For the characterization of the boundary layer, nine chordwise coordinates have been chosen along the airfoil. Since the profile is symmetric and mounted with an angle of attack of 0°, only one surface has been investigated. The x-axis positions along the airfoil correspond to the 2%, 5%, 10%, 20%, 30%, 40%, 50%, 62.5% and 75% of the chord. Approximately 30 measurement positions have been considered in the z-direction for each traverse. The distance between the points is variable and the step is 0.5 mm, 1 mm and 4 mm for respectively the first 7.5 mm, the following 10 mm and the last part. In order to avoid the contact between the wire and the metallic cloth coating the airfoil, the minimum distance of the probe from the surface has been evaluated using a dummy sensor with exactly the same geometry as the hot-wire probe. In this way, it has been possible to optically determine the exact position in which the prongs of the sensor touch the surface of the airfoil.

3.4. Acoustic Measurements

Acoustic far-field measurements have been performed to study the eventual noise reduction achievable by the use of a porous treatment. The antenna used for the tests is a 64-microphones seven arms Dougherty array, characterized by an aperture of 1.5 m and placed out of the flow at 1.16 m from the airfoil. The center of the array is approximately aligned with the center of the airfoil leading edge. The microphones installed are capacitor-based Knowles electrets. The data have been acquired with a sampling frequency of 51.2 kHz and a total of 3072000 samples per channel. The cross-spectral matrix (CSM) of the measured signals is computed by using the Welch method [24], with blocks of 8192 samples windowed using a Hann-weighting function characterized by 50% of data overlap, thus providing a frequency resolution of 6.25 Hz. The background noise corresponding to the configuration with the rod and without the airfoil has been recorded to be taken into account during the analysis of the results.

The data have been post-processed with a Generalized Inverse Beamforming (GIBF) technique developed at VKI and validated through the application to an experimental [25; 26] and a numerical [27] benchmark dataset. The isolation of the different noise sources that is possible to achieve with beamforming resulted to be essential for the analysis of turbulence-impingement noise. In this way, the contribution of the noise coming from the open jet, of the rod self-noise and of the noise sources generated at the juncture of the side-plates and the airfoil due to the scattering of the turbulent boundary layer forming along the plates can be discarded. A similar approach has been used also by Geyer *et al.* in the framework of leading-edge noise analysis for a grid-generated turbulent flow impinging on an airfoil [12; 13].

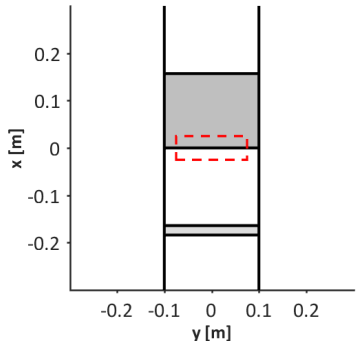

Figure 4: Source distribution map configuration

Two different analyses have been carried out using GIBF, namely, the evaluation of noise source distribution maps referred to several one-third octave band frequencies and the calculation of the one-third octave band spectra. Corrections for accounting the convection of the flow and the refraction of the shear layer have been applied, following the approach proposed by Sijtsma [28]. In addition, proper handling of the background noise plays an important role in the successful visualization of the noise-sources positions and has been performed through an advanced subtraction method based on the eigenvalue decomposition of the measured CSM [29]. It should be mentioned that the source maps generated by GIBF display the source distribution contours and not the peak source intensity [30]. Therefore, the source intensity can be

evaluated only after the integration procedure. This feature is practically useful for the analysis of distributed sources and represents one of the reasons why GIBF has been chosen for the post-processing of the acoustic data. For the source maps visualization, the experimental setup is represented as shown in Fig. 4. The vertical black lines indicate the test section sidewalls, the horizontal ones indicate rod, leading edge and trailing edge of the model. The flow goes from the bottom to the top of the map. Concerning the spectra, they are determined by summing the pressure values of each scanning grid point within a rectangular region surrounding the leading edge center. The red dashed lines in the figure indicate the integration area, whose dimension is 0.15 m × 0.05 m. The width has been chosen in order to include the noise sources eventually distributed along the leading edge and to exclude the ones generated at the juncture with the side-plates. Finally, special care must be taken for the choice of the frequency range to be analyzed. The upper limit has been set to 5 kHz, mostly due to limitations in the calibration procedure of the electret microphones. For the lower one, the constraint is normally represented by the non-compactness condition [31], which states that for a complete separation between the noise generated at the leading edge and the one at the trailing edge the considered wavelength should be smaller than the airfoil chord length. In the present case, this limit approximately corresponds to 2.15 kHz. However, the use of an advanced phased array technique such as GIBF makes it possible to separate noise sources at frequencies even below this value. The lowest one-third octave band center frequency investigated in the present study is therefore 1 kHz. Below this threshold, the resolution of the map was found to be too poor to provide meaningful results due to the beamwidth characteristics of the microphone antenna.

4. Results and Discussion

In this section, the results of the different measurements conducted at 30 m/s for a 0° angle of attack for both solid and porous airfoil are presented and discussed.

4.1. Static Pressure Distribution

The C_p distributions for the solid and the porous airfoil are presented in Fig. 5. These curves have been obtained by averaging the static pressure measured on the two sides of the airfoil for each chord position.

From the comparison of solid and porous airfoil, it is possible to notice that the minimum C_p for the two profiles in correspondence with the 17% of the chord is almost preserved. However, the porous profile reaches the peak in a more gradual way. This discrepancy is probably due to the circulation of flow through the pores of the melamine foam that is originated in the first part of the profile and tends to level out the pressure differences along its surface. Furthermore, in the second half of the airfoil, the two C_p distributions coincide. The reason for this trend is currently under investigation.

Finally, the decrease of C_p experienced by the porous profile may reflects a loss of lift in case of higher angles of attack. Nevertheless, as already mentioned in Section 1, it is out of the scope of this paper to evaluate the aerodynamic performances of the two airfoils.

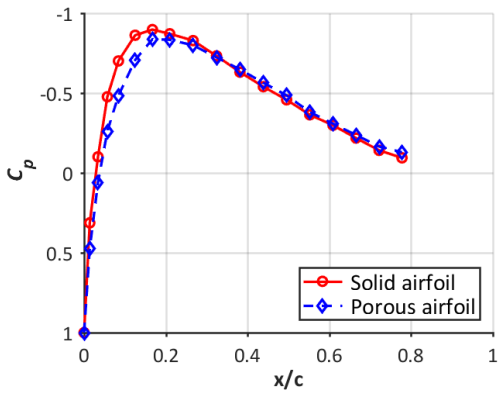

Figure 5: C_p distribution along the chord of the airfoil for the solid and the porous airfoil

4.2. Boundary Layer Results

The ū profile for both airfoil configurations is presented in Fig. 6. The z-axis is normalized by the airfoil maximum thickness, t = 0.038 m. All the plots show the ū profile up to 0.446t, equivalent to about 17 mm, from the surface, whereas the minimum distance between the hot-wire probe and the airfoil is variable and ranges from 0.5 to 0.8 mm.

In general, the comparison shows that the distribution of ū is lower in the boundary layer of the porous case with regard to the solid one. The reason for this mass flow deficiency is probably linked to the presence of the circulation of fluid flow through the pores of the melamine foam due to the possibility for part of the incident velocity to penetrate the medium. This phenomenon can lead to better hydrodynamic absorption of the turbulent vortical structures generated by

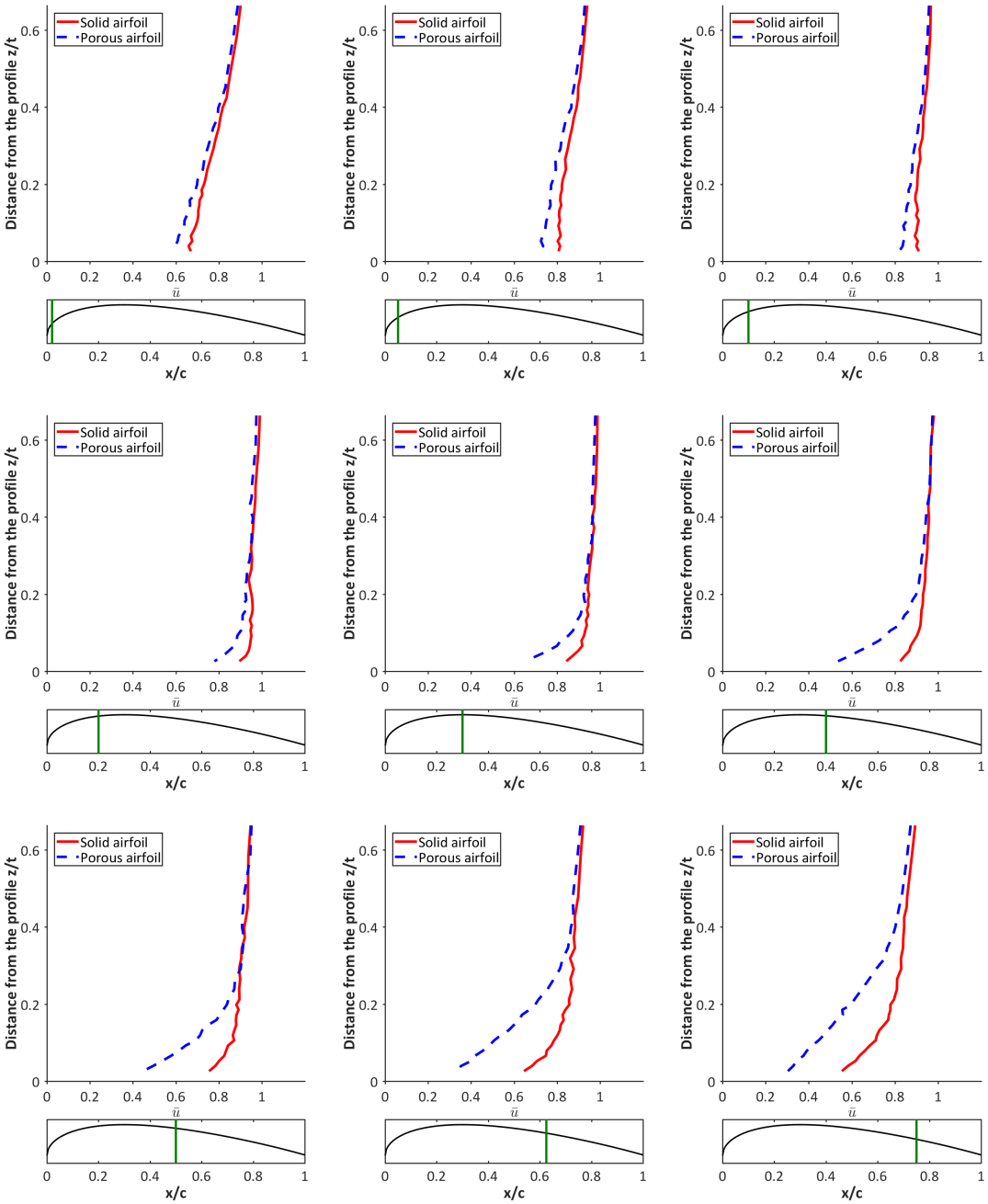

Figure 6: Mean velocity profiles of the solid and porous airfoil for the different chordwise positions depicted in Fig. **??**. t is the airfoil maximum thickness (0.038 m). The free-stream velocity is 30 m/s.

the rod, which is assumed to be one of the possible mechanisms for the airfoil turbulence-impingement reduction. Interestingly, the magnitude of the hydrodynamic absorption within the porous medium increases with the increasing chordwise position. Future PIV measurements can shed light on this trend.

4.3. Aeroacoustic Results

In this section, the qualitative one-third octave band source maps and the quantitative one-third octave

band spectra are presented.

4.3.1. One-third octave band source maps

The noise source maps related to the one-third octave band center frequency of 1.25 kHz, 1.6 kHz, 2.5 kHz, 3.15 kHz, 4 kHz and 5 kHz for both solid and porous airfoil are shown and compared respectively in Fig. 7. The resolution of each map is 20 mm, whereas the dynamic range is set to 20 dB and it is the same for the two cases. In the results shown, the facility background noise has been already subtracted for more clear visualization of the noise sources. This procedure is more effective the more incoherent the background noise is with respect to the investigated sources since the subtraction method is based on the eigenvalue decomposition of the measured CSM[1]. In addition, a Gaussian filter has been exploited with the mere purpose of improving the readability of the maps.

From a general qualitative analysis, in all sound maps, the main noise sources are located at the airfoil leading edge and this is most probably due to the impingement with the turbulent flow generated by the rod. The contribution of the turbulent boundary layer scattering at the trailing edge is not visible. At $f_{1/3}$ = 1.25 kHz, the porous airfoil effectively reduces noise. Indeed, as it is possible to see in the map, the source intensity levels surrounding the leading edge area are lower than the ones of the solid airfoil. However, due to the frequency-dependent beamwidth characteristics of the antenna, the resolution of the localization is limited and it is not possible to observe the expected distributed nature of the source. An analog conclusion can be drawn for $f_{1/3}$ = 1.6 kHz. In this case, a spurious source generated upstream of the airfoil and on the right side-plate is also present. Its origin is still unknown with certainty but could be linked to a residual of the background subtraction procedure. In addition, a downstream shift of the source intensity main peaks for the solid airfoil can be observed if compared with the porous case. This can be related to the low resolution of the map at the investigated frequency. At $f_{1/3}$ = 2.5 kHz, the porous treatment of the airfoil is not effective anymore and an increase instead of a reduction of turbulence-impingement noise is noticed. For the solid case, the main source intensity contours are distributed along the leading edge and in correspondence of the rod. At this range of frequencies, the subtraction method is not able to fully suppress the contribution of the rod self-noise, which is dominant. This may be due also to a partial coherence between turbulence-impingement noise and the trailing edge noise of the rod. In addition, the presence of a noise source can be seen also at the trailing edge of the airfoil. For the porous case, three main peaks are present at the leading edge, one at the midspan and two in the proximity of the juncture with the side-plates. The reason for the detected noise increase could be related to higher surface roughness, given by the melamine foam and by the pores of the hard plastic exoskeleton. The choice of the wire mesh, common to both airfoils, might also influence the noise reduction. A deeper investigation will be required for a better understanding of this phenomena. The same trend can be observed also at $f_{1/3}$ = 3.15 kHz. In this case, the localization accuracy improves with the increasing frequency and it is possible to detect the distributed nature of the leading-edge noise. For the solid airfoil, the main source intensity peaks are still located along the rod, whereas the porous one presents the same two peaks in the vicinity of the side-plates already discussed before. At $f_{1/3}$ = 4 kHz, the increase of noise due to the melamine foam results to be significant. Moreover, the analysis at this frequency shows an interesting aspect concerning the position of the source region. Particularly, in the solid airfoil, the main source intensity peaks are distributed exactly along the leading edge, whereas in the porous one their position is slightly shifted downstream. This may indicate a different noise generation mechanism linked to the circulation of flow through the pores of the porous medium. The investigation of the related phenomenon can bring light to the effective operating principle of porous materials in the framework of turbulence-impingement noise reduction. Finally, the same outcomes can be deduced also for $f_{1/3}$ = 5 kHz, even if the noise increase due to the porous treatment appears lower.

4.3.2. One-third octave band spectra

The integrated one-third octave band spectra processed by GIBF and referred to the center of the array for one-third octave band frequency centers ranging from 1 kHz to 5 kHz are shown in Fig. 8a. The performances of the solid and the porous airfoil are compared with the ones of the profile just made of melamine foam, already mentioned in Section 2 and referred to as "melamine airfoil". For a better representation of the noise reduction given by the porous treatment, in Fig. 8b the difference between the one-third octave sound pressure level, $L_{p(1/3)}$, between the

[1]Each eigenmode of the decomposed CSM is linked to a coherent source distribution [30].

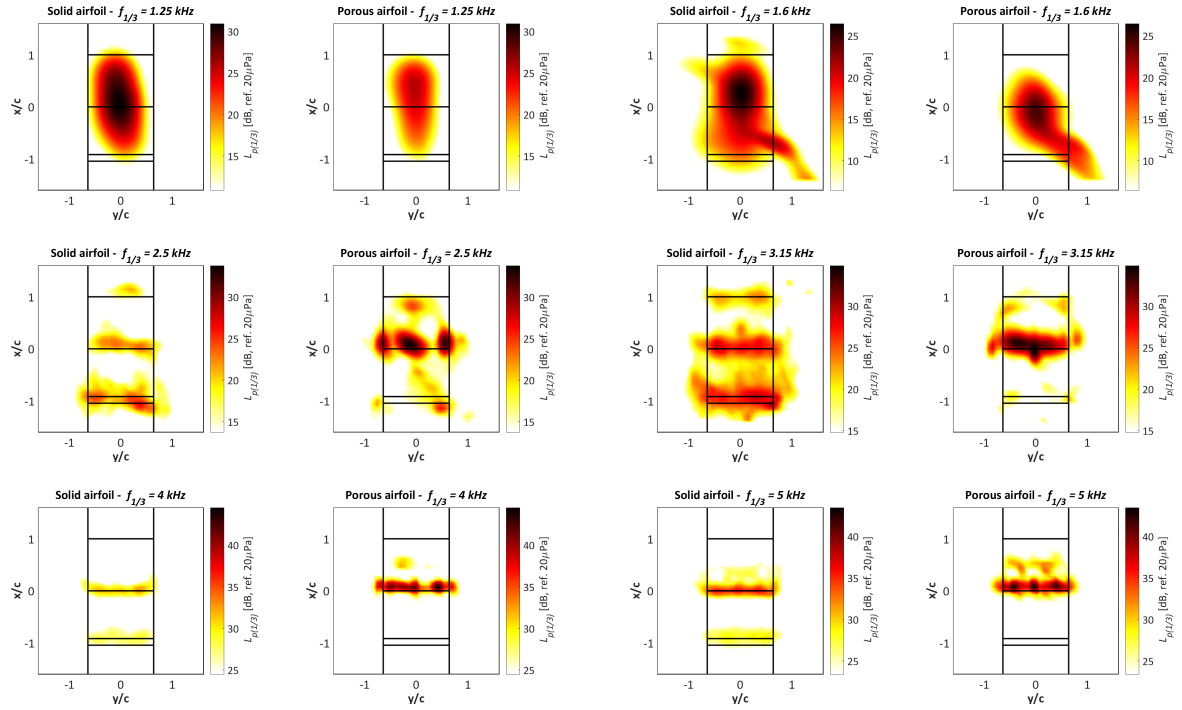

Figure 7: Noise source distribution maps for the solid (on the left) and porous (on the right) airfoil processed with GIBF at different $f_{1/3}$. The maps referred to the same $f_{1/3}$ are plotted with the same dynamic range

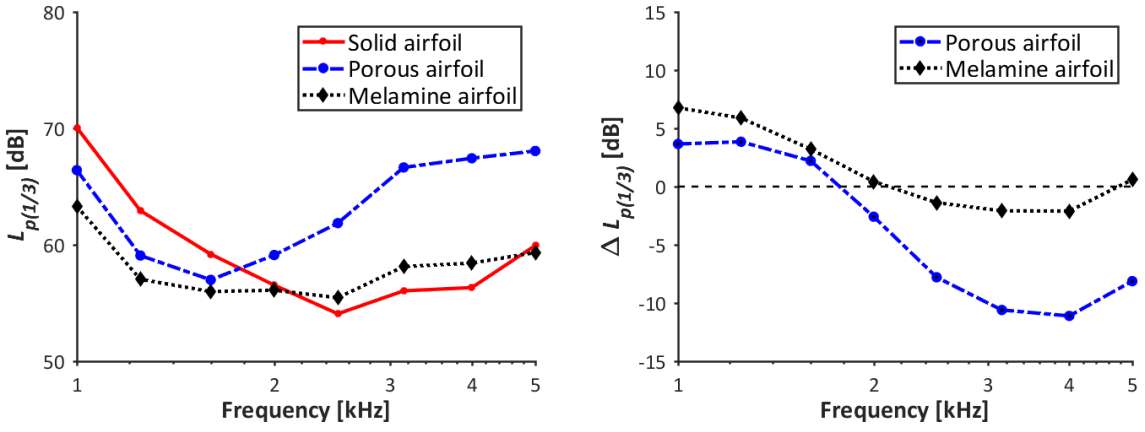

(a) (b)

Figure 8: (a) Integrated one-third octave band spectra processed by GIBF considering a rectangular region surrounding the leading edge and referred to the one-third octave band frequency centers ranging from 1 kHz to 5 kHz. The solid airfoil (in red), the porous airfoil (in blue) and the melamine airfoil (in black) are investigated. (b) Relative noise reduction due to the porous treatment of the airfoil with respect to the solid case. The black dashed line indicates the boundary between reduction and increase of noise.

solid and the porous case and between the solid and the melamine case is plotted.

As can be noticed, the trend of noise reduction follows what has been already qualitatively observed with the GIBF source maps. For frequencies up to almost 2 kHz, the porous treatment is effective and

turbulence-impingement noise results to be mitigated, with a maximum reduction of about 4 dB that may be linked to the hydrodynamic absorption given by the porous medium that has been discussed in the previous section. Above the aforementioned threshold, the surface roughness noise becomes dominant and the noise increases, reaching a maximum value of almost 12 dB at 4 kHz. Concerning the melamine airfoil, it performs better than the porous one, as it could have been expected. Up to 1.6 kHz, the one-third octave sound pressure level of the two profiles follows the same trend, with a maximum scattering of about 2 dB. However, above 1.6 kHz, they start diverging, reaching a maximum $\Delta L_{P(1/3)}$ of 8 dB, and this affects also the cross-over frequency with the solid airfoil, which is at 2.1 kHz. Once overcome this value, also the melamine case results to be noisier than the solid case, mostly due to the increment of surface roughness noise. Anyway, the increase is significantly lower than the one for the porous airfoil, suggesting that the hard plastic exoskeleton has a drastic impact in $L_{P(1/3)}$ at high frequencies. The physical mechanism behind this phenomenon is still under investigation. Concerning the effect of the wire mesh, it contributes to the surface roughness noise, but since the same grid has been applied to both profiles its influence does not affect the reduction. New wire meshes will be tested in future studies.

One possible way to improve the noise mitigation process can be the implementation of a different porous material in the exoskeleton. In the studies conducted by Geyer et al. [12; 13], they stated that the materials able to grant the highest turbulence-impingement noise reduction were those with a low static air flow resistivity, effect which is assumed to be caused by the larger pores that characterize them. In these regards, the use of polyurethane foams represents a promising solution that can be applied in the proposed design.

5. Conclusion

The results of various tests have been presented in this paper to evaluate the effectiveness of the use of melamine foam as part of the structure of a wing profile for the reduction of turbulence-impingement noise on a NACA-0024 in a rod-airfoil configuration.

Specifically, hot-wire anemometry, static pressure distributions and beamforming measurements have been performed. The outcomes of the hot-wire tests show that the boundary layer around of the airfoil is affected by the presence of the porous medium, resulting in a lower mean velocity distribution in the proximity of the porous profile if compared with the solid one. Moreover, the static pressure distribution measured on the airfoil surface is influenced by the circulation of flow through the pores of the porous medium, that tends to level out the pressure differences. Concerning the acoustic measurements, inverse beamforming is able to properly isolate the leading-edge noise due to impingement with the rod-generated turbulence. The source intensity strength is evaluated by integration of the source distribution maps within a rectangular region surrounding the airfoil leading edge. The comparison between the one-third octave integrated spectra shows that for frequencies up to almost 2 kHz the turbulence-impingement noise is effectively reduced, with a promising maximum reduction of about 4 dB. The noise mitigation in the low-frequency regime may be connected to the hydrodynamic absorption of part of the incident velocity through the porous medium, phenomenon confirmed by hot-wire and static pressure distribution measurements. Above 2 kHz, the surface roughness noise of the porous treatment overcomes the surface roughness noise of the solid profile, reaching a maximum value of almost 12 dB. Furthermore, the noise increase at high frequencies is also significantly affected by the way the porous material is implemented in the airfoil, as the use of a third profile just made of melamine foam has shown.

Further studies will be necessary to fully understand the operating principle of porous materials in the noise reduction mechanism. In particular, the relationship between hydrodynamic absorption and noise mitigation needs to be deeply investigated. Finally, new porous materials characterized by different properties will be tested with the proposed design in order to extend the analysis and to optimize the turbulence-impingement noise reduction.

Acknowledgments

This project has received funding from the European Union's Horizon 2020 research and innovation programme under the Marie Skłodowska-Curie grant agreement No. 722401.

References

[1] R. Paterson, R. Amiet, Acoustic radiation and surface pressure characteristics of an airfoil due to incident turbulence, in: 3rd Aeroacoustics Conference, American Institute of Aeronautics and Astronautics, Palo Alto,CA,U.S.A., 1976.

[2] P. Migliore, S. Oerlemans, Wind Tunnel Aeroacoustic Tests of Six Airfoils for Use on Small Wind Turbines*, Journal of Solar Energy Engineering 126 (4) (2004) 974–985.

[3] S. Moreau, M. Roger, Effect of Angle of Attack and Airfoil Shape on Turbulence-Interaction Noise, in: 11th AIAA/CEAS Aeroacoustics Conference, Aeroacoustics Conferences, American Institute of Aeronautics and Astronautics, 2005. doi:10.2514/6.2005-2973.

[4] R. K. Amiet, Acoustic radiation from an airfoil in a turbulent stream, Journal of Sound and Vibration 41 (4) (1975) 407–420.

[5] R. K. Amiet, High frequency thin-airfoil theory for subsonic flow, AIAA Journal 14 (8) (1976) 1076–1082.

[6] R. K. Amiet, Noise due to turbulent flow past a trailing edge, Journal of Sound and Vibration 47 (3) (1976) 387–393.

[7] J. Gill, X. Zhang, P. Joseph, Symmetric airfoil geometry effects on leading edge noise, The Journal of the Acoustical Society of America 134 (4) (2013) 2669–2680.

[8] J. R. Gill, X. Zhang, P. Joseph, Effects of Real Airfoil Geometry on Leading Edge Gust Interaction Noise, in: 19th AIAA/CEAS Aeroacoustics Conference, American Institute of Aeronautics and Astronautics, Berlin, Germany, 2013.

[9] D. Kim, G.-S. Lee, C. Cheong, Inflow broadband noise from an isolated symmetric airfoil interacting with incident turbulence, Journal of Fluids and Structures 55 (2015) 428–450.

[10] M. Roger, C. Schram, L. De Santana, Reduction of Airfoil Turbulence-Impingement Noise by Means of Leading-Edge Serrations and/or Porous Material, in: 19th AIAA/CEAS Aeroacoustics Conference, American Institute of Aeronautics and Astronautics, Berlin, Germany, 2013.

[11] M. Roger, S. Moreau, Airfoil Turbulence-Impingement Noise Reduction by Porosity or Wavy Leading-Edge Cut: Experimental Investigations, in: InterNoise16, INTER-NOISE and NOISE-CON Congress and Conference Proceedings, Hamburg, DE, 2016, pp. 5848–6840, pp. 6366–6375(10).

[12] T. Geyer, E. Sarradj, J. Giesler, M. Hobracht, Experimental assessment of the noise generated at the leading edge of porous airfoils using microphone array techniques, in: 17th AIAA/CEAS Aeroacoustics Conference (32nd AIAA Aeroacoustics Conference), American Institute of Aeronautics and Astronautics, Portland, Oregon, 2011.

[13] T. Geyer, E. Sarradj, J. Giesler, Application of a Beamforming Technique to the Measurement of Airfoil Leading Edge Noise, Advances in Acoustics and Vibration 2012 (2012) 1–16.

[14] E. Sarradj, T. Geyer, Noise Generation by Porous Airfoils, in: 13th AIAA/CEAS Aeroacoustics Conference (28th AIAA Aeroacoustics Conference), American Institute of Aeronautics and Astronautics, Rome, Italy, 2007.

[15] T. Geyer, E. Sarradj, C. Fritzsche, Porous Airfoils: Noise Reduction and Boundary Layer Effects, International Journal of Aeroacoustics 9 (6) (2010) 787–820.

[16] T. Geyer, E. Sarradj, C. Fritzsche, Measurement of the noise generation at the trailing edge of porous airfoils, Experiments in Fluids 48 (2) (2010) 291–308.

[17] A. F. Tinetti, On the Use of Surface Porosity to Reduce Wake-Stator Interaction Noise, Ph.D. thesis, Virginia Tech (Sep. 2001).

[18] M. Herr, J. Reichenberger, In Search of Airworthy Trailing-Edge Noise Reduction Means, in: 17th AIAA/CEAS Aeroacoustics Conference (32nd AIAA Aeroacoustics Conference), American Institute of Aeronautics and Astronautics, Portland, Oregon, 2011.

[19] L. D. de Santana, Semi-analytical methodologies for airfoil noise prediction, Ph.D. thesis, KU Leuven (2015).

[20] M. C. Jacob, J. Boudet, D. Casalino, M. Michard, A rod-airfoil experiment as a benchmark for broadband noise modeling, Theoretical and Computational Fluid Dynamics 19 (3) (2005) 171–196.

[21] V. Lorenzoni, M. Tuinstra, F. Scarano, On the use of time-resolved particle image velocimetry for the investigation of rodairfoil aeroacoustics, Journal of Sound and Vibration 331 (23) (2012) 5012–5027.

[22] M. Niskanen, J.-P. Groby, A. Duclos, O. Dazel, J. C. Le Roux, N. Poulain, T. Huttunen, T. Lhivaara, Deterministic and statistical characterization of rigid frame porous materials from impedance tube measurements, The Journal of the Acoustical Society of America 142 (4) (2017) 2407–2418.

[23] H. H. Bruun, Hot-Wire Anemometry: Principles and Signal Analysis, Measurement Science and Technology 7 (10).

[24] P. Welch, The use of fast Fourier transform for the estimation of power spectra: A method based on time averaging over short, modified periodograms, IEEE Transactions on Audio and Electroacoustics 15 (2) (1967) 70–73.

[25] R. Zamponi, N. V. de Wyer, C. Schram, An Improved Regularization of the Generalized Inverse Beamforming Applied to a Benchmark Database, in: 7th Berlin Beamforming Conference, BeBeC, Berlin, DE, 2018.

[26] R. Zamponi, N. Van de Wyer, C. F. Schram, Benchmark Assessment of an Improved Regularization Technique for Generalized Inverse Beamforming, in: 2018 AIAA/CEAS Aeroacoustics Conference, American Institute of Aeronautics and Astronautics, Atlanta, Georgia, 2018.

[27] R. Merino-Martinez, P. Sijtsma, A. Rubio Carpio, R. Zamponi, S. Luesutthiviboon, A. M. N. Malgoezar, M. Snellen, N. Van de Wyer, C. Schram, D. G. Simons, Integration methods for distributed sound sources, International Journal of AeroacousticsAccepted for publication.

[28] P. Sijtsma, Phased Array Beamforming Applied to Wind Tunnel And Fly-Over Tests, Tech. rep., National Aerospace Laboratory NLR (Oct. 2010).

[29] C. J. Bahr, W. C. Horne, Advanced Background Subtraction Applied to Aeroacoustic Wind Tunnel Testing, in: 21st AIAA/CEAS Aeroacoustics Conference, American Institute of Aeronautics and Astronautics, Dallas, TX, 2015.

[30] T. Suzuki, L1 generalized inverse beam-forming algorithm resolving coherent/incoherent, distributed and multi-pole sources, Journal of Sound and Vibration 330 (24) (2011) 5835–5851.

[31] W. K. Blake, Mechanics of Flow-Induced Sound and Vibration, Volume II: Complex Flow-Structure Interactions, 2nd Edition, Academic Press, 2017.

Low-Order Aeroacoustic Prediction of Low-Speed Axial Fan Noise

Alessandro Zarri

Environmental and Applied Fluid Dynamics Department, von Karman Institute for Fluid Dynamics, Belgium, alessandro.zarrri@vki.ac.be

Supervisors: Christophe Schram and Julien Christophe

Full Professor, Environmental and Applied Fluid Dynamics Department and Aeronautics and Aerospace Department, von Karman Institute for Fluid Dynamics, Belgium, christophe.schram@vki.ac.be

Senior Research Engineer, Environmental and Applied Fluid Dyanmics Department, von Karman Institute for Fluid Dynamics, Belgium, julien.christophe@vki.ac.be

University Supervisor: Michel Roger

Professor, Laboratoire de Mécanique des Fluides et d'Acoustique, Ecole Centrale de Lyon, France, michel.roger@ec-lyon.fr

Abstract

A numerical simulation study is developed to predict the self-noise emitted by an automotive low-speed cooling fan. A low-order CFD unsteady approach is coupled with semi-analytical far-field acoustic propagation to be used in pre-design optimization cycles. The methodology is analyzed and the preliminary far-field noise results exposed.

Keywords: aeroacoustics, noise prediction, low-order methodology, fan self-noise.

1. Introduction

Low-subsonic cooling fans are employed in several fields such as ground transportation [1], air-conditioning of buildings[2], tunnel ventilation [3; 4] or electronic devices [5]. For instance, to cool down the engine of an automotive vehicle, aerodynamic efficiency is a requirement, in order to extract the maximum amount of heat from the radiator with the minimum power effort. Nevertheless, this often comes with an acoustic annoyance decreasing the comfort of the passengers. The fan noise has been already identified as one of the major acoustic source emitted by an automotive vehicle [6]. Concerning future electric ground transports, although the combustion engine is substituted by the electrical motor, the system still needs to be cooled down, especially during the battery recharging phase. Furthermore, international regulations on noise emissions become requirements for the manufacturers. Much progress has been achieved in the design process of a cooling system, moving from one year to only one month for a new cooling fan module, as highlighted by Demory et al. [1].

This work aims at developing a low-order noise prediction method, that can be easily used in an optimization cycle. As shown in Fig.1, the engine cooling module placed in the under-hood of a car is composed of a low-speed axial fan with a shroud, an electric motor, a heat exchanger or radiator placed before the fan suction-side and the stator vanes or struts, acting as fan supports downstream [7]. Several aerodynamic noise sources are present in such a complex system, both tonal and broadband [8; 9]. Due to the struts downstream of the rotor, periodic flow non-uniformities are a possible tonal source, together with possible upstream installation effects. Nevertheless, the heat exchanger may act as flow redirector and homogenizer, although the flow passing through it acquires a certain level of turbulence. The latter, impinging on the blade leading-edges, gives rise to an important broadband noise source mechanism called turbulent-interaction noise or leading-edge noise. The velocity fluctuations of the turbulent flow produce a local random variation of the angle of incidence of the blades and therefore random fluctuations of pressure are created on the leading-edge, generating a broad-

band source [8]. This is supposed to be the dominant one in case of high turbulence intensity going across the fan [10], but results to be negligible in case of a laminar impinging flow [11]. Another important broadband noise generation [12] is due to the boundary-layer vortical structures that interact with the trailing-edge. As demonstrated by Wright et al. [13], this noise source called trailing-edge noise or self-noise, is the minimum source always present on rotating fans and wind turbines [14; 15]. Another noise mechanism known as tip-clearance or tip-leakage noise is due to the tip-gap between the blade tip and the shroud. In particular, for highly loaded fans, the pressure difference between the pressure and the suction sides at the tip of the blade, gives rise to recirculating structures interacting with the blade leading and trailing edges. This noise source, with a signature in the low-frequency region of the noise spectrum [16; 17], has been studied and reduced since the work of Longhouse et al. [18], thanks to the use of L-shaped ring shrouds. Nevertheless, the ring-gap noise remains a significant broadband noise source [19; 20].

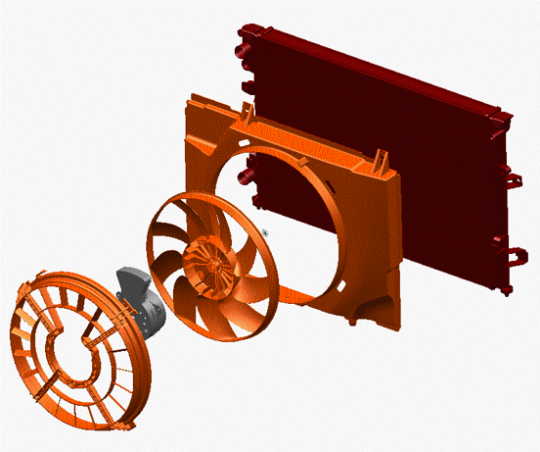

Figure 1: Typical automotive engine cooling module.

To numerically predict these noise mechanisms, direct aeroacoustic simulations exploiting Lattice Boltzmann Method (LBM) have started to be achievable [21; 20], but they are still too computationally expensive to be included in an industrial optimization design [11]. To reduce the computational cost, hybrid methods are considered, based on a decoupling of the fluid dynamic near-field computation and the acoustic far-field propagation [22].

In the present research work, the focus will be put on the trailing-edge far-field noise prediction, for which semi-analytical theories as Amiet's theory have been firstly developed for airfoil turbulence-interaction cases [23]. Then, they have been generalized to take into account a turbulent flow past a trailing edge [24], as well as the presence of finite chords by Roger & Moreau [25]. Moreover, the semi-analytical method has been extended to rotating blades trailing edge noise for helicopters by Schlinker & Amiet [26] and then applied to low-speed cooling fans [27]. In such a theoretical approach, the most important inputs given by the CFD computation are the wall-pressure fluctuations at the trailing-edge, in the form of frequency-dependent Power Spectral Density (PSD). The methodology adopted for this study consists of extracting the trailing-edge boundary layers to model the wall-pressure spectrum. Two families of methods have been exploited in literature to achieve this goal: semi-empirical wall-pressure models, based on experimental databases, and statistical approaches, carried out by integrating the Poisson equation across the boundary layer. A comparison between them is given by Lee & Villaescusa [28] and by Kucukosman et al. [29]. Although the validity of semi-empirical methods is often somewhat limited to the databases used for their derivations, they remain appealing since the velocity profile parallel to the blade surface is the only input they need to calculate the wall-pressure spectrum. In the present study, the Rozenberg model [30] is employed. Unsteady Reynolds Averaged Navier-Stokes Simulations (URANS) are carried out in the near-field fluid dynamic domain. Once the CFD computation is obtained, the fan blade is divided into iso-radius cuts in order to apply the airfoil noise theory. This is performed to take into account span-wise flow variations. At these blade regions, the boundary layer velocity profiles are retrieved.

2. Fan Geometry and CFD Computations

A typical case of L-shaped ring fan, shown in Fig. 2, has been selected for the present study. It has 7 swept blades, with varying chord and stagger angle. The hub diameter is 142 mm, whereas the total diameter consists of 380 mm. The operating condition of this rotor is a rotational speed of 3500 rpm with a volumetric flow rate of 3500 m^3/h. The Reynolds number based on the chord at the tip of the blade is 2.45×10^5, stating that the fan is working in the laminar-turbulent transition region [31]. The Mach number at the tip, related to a rotational speed of 3500 rpm, is 0.19 and thus, a subsonic incompressible regime can be considered. CFD computations are car-

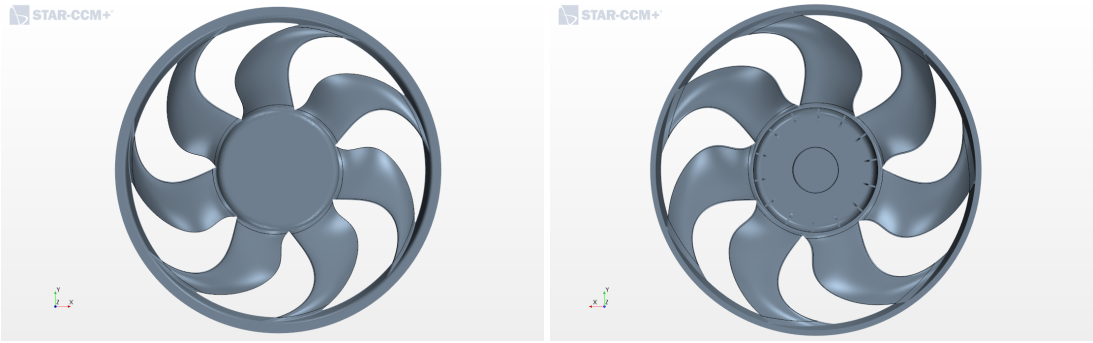

(a) (b)

Figure 2: Equally-spaced fan blades: (a) Fan suction side. (b) Fan pressure side.

ried out with Star CCM+ Version 13.04. Four computational domains are considered: the mass flow inlet, a porous medium to represent the pressure drop caused by the radiator, the moving reference frame (MFR) where the fan is settled and the pressure outlet, including struts, transmission shaft and motor support. Both inlet and outlet regions are chosen sufficiently large to allow free-field atmospheric conditions as boundary conditions. A polyhedral mesh of approximately 40 million cells has been created with refinements in particular around the blade edges, similarly to what has been done by Henner et al. in [32]. URANS are considered in this work as a compromise between computational cost and accuracy to describe unsteady flow features. A steady computation is run to initialize the solution and an unsteady simulation of 200 time steps, representing 2 rotations of the fan at 3500 rpm, is carried out. The aim of this CFD simulation is to collect the velocity profiles around the blade trailing-edge to calculate the wall pressure spectrum. A closer look to the polyhedral mesh and the velocity magnitude is shown in Fig. 3. The relative velocity around iso-radius cuts of the blade at the mid-span and tip regions are shown in Fig. 4. In both regions, the flow appears to be fairly attached along the airfoil suction line, allowing the use of the Rozenberg's model, not suited to calculate the wall-pressure spectrum of separated flows. In Fig. 5, the pressure field is observed to be fairly similarly distributed among the blades, with important loads on the leading-edge region.

3. Wall-Pressure Spectrum Model

As reported by Lee et al. [28], semi-empirical wall-pressure spectrum (WPS) ϕ_{pp} can be generally written:

$$\frac{\phi_{pp}}{\phi^*} = \frac{a(\omega^*)^b}{[i(\omega^*)^c + d]^e + [fR^g\omega^*]^h} \tag{1}$$

where the parameters $a-h$ are set to modify the shape of the spectra in accordance to the chosen model, R is the time-scale ratio, ϕ^* and ω^* are, respectively, the re-scaled wall-pressure spectrum and the circular frequency.

Rozenberg et al. [30] have developed a WPS model taking into account Adverse Pressure Gradient, starting from the Goody model formulation [33] for Zero Pressure Gradient. For both of the models, the time-scale ratio, defined as the ratio of the outer time scale to the inner time scale, reads $R = R_T = (\delta/U_e)/(\nu/u_t^2)$, where ν is the kinematic viscosity, whereas u_t is the friction velocity. The former model employed in this work, is more suited to the physics of a flow developing around the airfoil suction side, due to the presence of adverse WP gradient, as long as it remains attached to the profile. The wall-pressure spectrum is scaled by boundary layer mixed variables: for Rozenberg model, $\phi^* = \tau_{max}^2\delta^*/U_e$, where δ^* is the boundary layer displacement thickness, whereas $\tau_{max} = \max[\mu(dU/dy)]$ is the maximum shear stress along the boundary-layer normal distance. Similarly, the circular frequency is scaled by $\omega^* = \omega\delta^*/U_e$.

In order to characterize the adverse pressure gradient, 3 parameters are considered: Clauser's equilibrium parameter $\beta_c = (\theta/\tau_w)(dp/dx)$, with θ as momentum thickness [34], Zagarola-Smits' parameter [35]: $\Delta_* = \delta/\delta^*$ and Coles' wake parameter Π [36]. The parameters a, d, and e in Eq. (1) are functions of β_c, Δ_* and Π; more information about their explicit expressions can be found in [28].

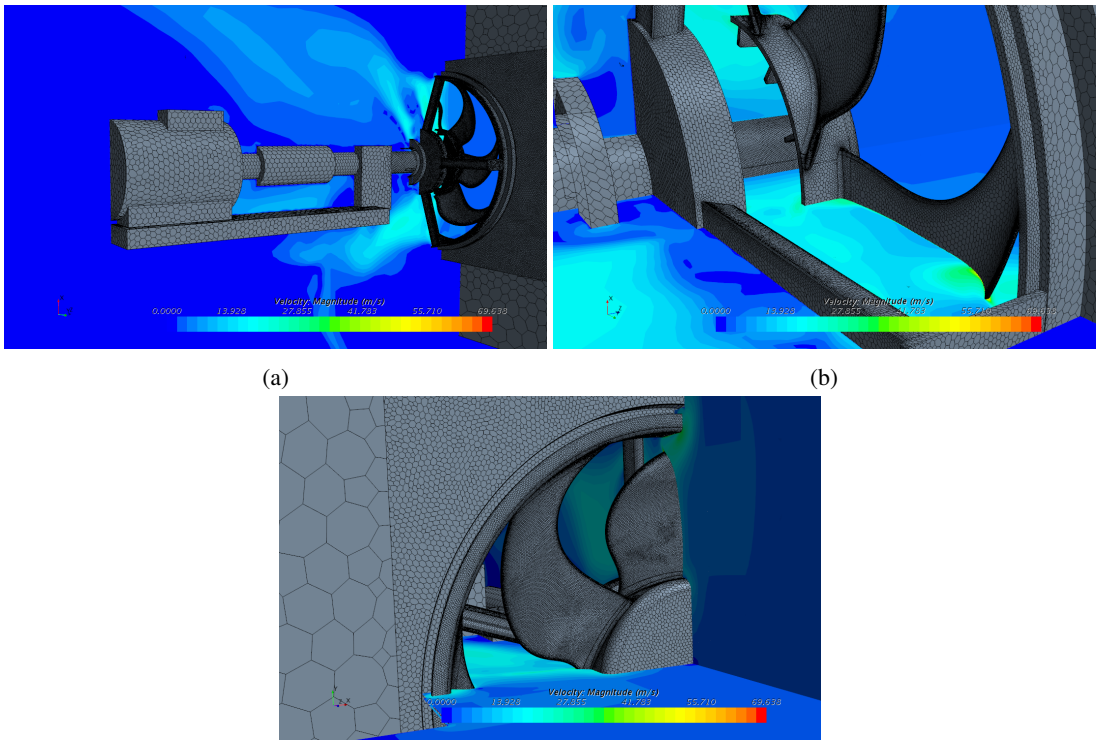

(a) (b)

(c)

Figure 3: Polyhedral mesh visualization with velocity magnitude solution: (a) Back sight with motor support and struts. (b) Back sight close to the pressure side. (c) Front sight of the suction side.

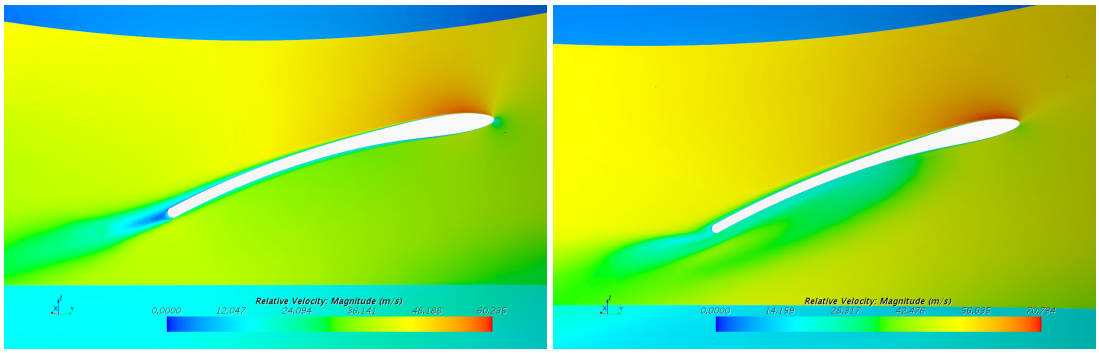

(a) (b)

Figure 4: Relative velocity field around the fan blade: (a) Mid-span iso-radius blade section. (b) Tip-span iso-radius blade section.

4. Acoustic Propagation Approach

The broadband noise emitted by the trailing-edge of stationary isolated aifoils can be predicted by Amiet's theory, firstly published by Amiet [23] for subsonic turbulent streams impinging on the blade leading-edge and then extended for trailing-edge scattering noise in [24]. In 2005, Roger & Moreau [25] generalized Amiet's theory to take into account finite chord lengths, by adding a leading-edge back-scattering contribution. The main assumption to use this theory, derived from flat plates with zero angle of incidence, is that the turbulence is frozen, meaning that it is stationary in a statistical sense, resulting as unaffected

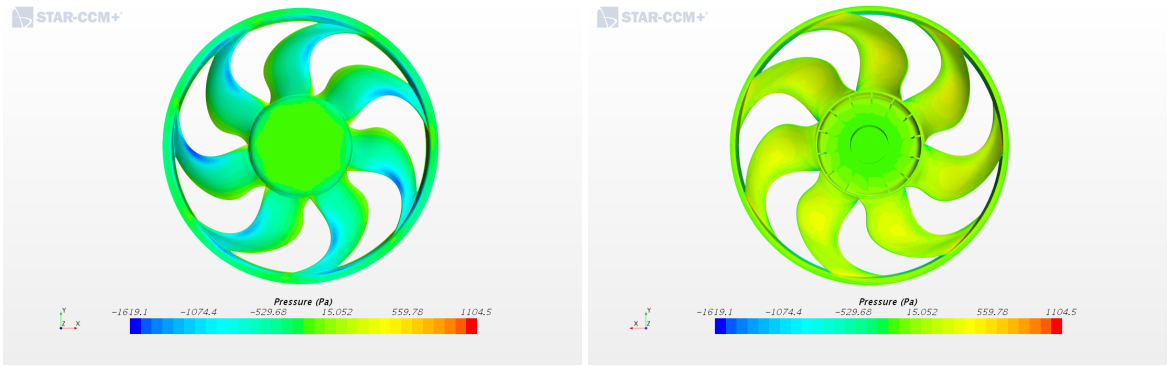

(a) (b)

Figure 5: Pressure field on the fan surface: (a) Suction side. (b) Pressure side.

by the presence of the trailing-edge. The chord-wise unsteady lift distribution, acting as acoustic source, is carried out applying the Schwarzschild's technique [37] and the classical formula for a radiating dipole [38] in a uniform flow is applied to evaluate the far-field sound, via statistical analysis. Large aspect ratio (d/c) is assumed [39], such that for each listener position $\mathbf{x}$ in Fig. 6(a), only one radiating span-wise aerodynamic wave number k_y will be present. The power spectral density of the sound pressure in the

$$S_{pp}(\mathbf{x},\omega) = \left(\frac{\omega c z}{2\pi c_0 S_0^2}\right)^2 \frac{d}{2}\left|\mathcal{L}\left(\frac{\omega}{U_c}\frac{\bar{k}y}{S_0}\right)\right|^2 \Phi_{pp}(\omega) l_y(\omega) \quad (2)$$

where S_0 is the corrected distance for convection effects, ω is the angular frequency, $\mathcal{L} = \mathcal{L}_1 + \mathcal{L}_2$ is the aeroacoustic transfer function; $\mathcal{L}_1$ is the trailing-edge main contributing term, whereas $\mathcal{L}_2$ is the leading-edge back-scattering term. The explicit expressions of these terms can be found in [39]. The span-wise correlation length $l_y(\omega)$ is evaluated employing Corcos' formula [40]:

$$l_y(\omega) = \frac{\omega/(b_c U_c)}{k_y^2 + (\omega/(b_c U_c))^2} \quad (3)$$

with the model constant b_c and the convective velocity of turbulent structures at the trailing-edge U_c. Roger et al. [27] extended the originally developed model for high-speed helicopter blades by Schlinker & Amiet [26], in order to include low Mach number fans operating in a medium at rest. The circular motion is treated to be locally tangent to a translational motion, considering that the flow features on a rotating segment are not essentially different from the ones developing on an isolated airfoil. Thus, as long as the flow remains attached to the blade, a strip method approach is adopted to provide the required information at different radii. Nevertheless, this approximation is acceptable only considering sound frequencies much higher than the rotational frequency [41]. Initially, the single blade segment noise is calculated at the angle $\Psi = \Omega t$, in a reference frame shown in Fig. 6(b), without taking into account the relative motion between the source and the observer. Afterwards, a Doppler-factor correction is applied in a form suited for low-Mach number fans operating in a medium at rest:

$$\frac{\omega_e(\Psi)}{\omega} = 1 + M \sin\Psi \sin\Theta = 1 - M_r \quad (4)$$

with the rotational Mach number $M = \Omega R/c_0$ and the relative Mach number M_r, defined as the Mach number of the source relative to the fluid.

To obtain the overall sound pressure noise, each azimuthal position has to be taken into account, weighted by the Doppler-factor:

$$S_{pp}(\mathbf{x},\omega) = \frac{B}{2\pi}\int_0^{2\pi} \frac{\omega_e(\Psi)}{\omega} S_{pp}^{\Psi}(\mathbf{x},\omega_e) d\Psi \quad (5)$$

in which B is the number of blades and $S_{pp}^{\Psi}(\mathbf{x},\omega_e)$ is the noise spectrum radiated by the single airfoil theory of Eq. (2). In the latter equation, it is worth mentioning that the large aspect-ratio formulation has been preferred to the more general sinus cardinal one, since, as demonstrated by [42], the noise predicted by the sum of the contributions of an airfoil sub-parts can be different if compared to the one emitted by the same non-divided single airfoil.

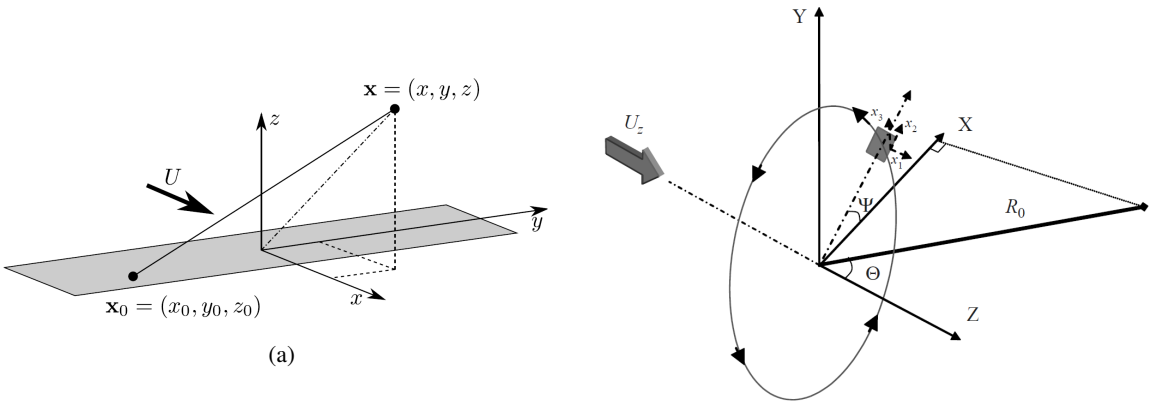

Figure 6: Coordinate reference frame for a single and a rotating segment: (a) Single Amiet's plane. (b) Rotating fan reference frame.

5. Numerical Far-Field Noise Results

The numerical far-field results are shown in this section, considering the fan blade in Fig. 8. In this case, 3 iso-radius cuts have been performed in the hub, middle and tip regions of the span blade. At

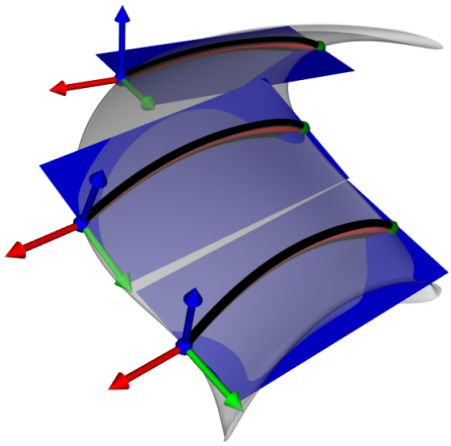

Figure 7: Fan blade divided into three iso-radius cuts with corresponding Amiet's planes.

these locations, the boundary layer velocity profiles have been extracted and the pressure coefficients calculated. They are both shown in Fig. 9. It is worth noticing that the maximum velocity is reached by the strip at the blade-tip, while the most loaded region is the mid-span one. The wall-pressure spectrum predicted using Rozenberg model is shown in Fig. 10 for the three different blade strips. The highest PSD contribution is reached by the blade-tip region in the middle frequency range, with a level of almost 80 dB/Hz. The trailing edge noise fan prediction, obtained by the sum of the far-field acoustic results on the Amiet's planes is plotted in Fig. 11, as well as the directivity plot of the fan noise in function of discrete levels of frequencies. In the latter, it is worth noticing the classical dipolar lobes for $f = 500$ Hz, where the source is compact.

6. Conclusions

In this work, the authors demonstrated the feasibility of a low-order methodology to predict trailing-edge fan noise. A hybrid approach has been employed, consisting of URANS computation to solve the fluid dynamic near-field and Amiet's theory to propagate the acoustic waves to the far-field. As output from the CFD simulation, the velocity profiles around iso-radius cuts of the blade have been extracted and the wall-pressure spectra have been calculated applying the Rozenberg model. They represent indeed the principal input to the Amiet'semi-analytical approach. As future work, a mesh independence study will be performed, whereas more robust models to calculate the wall-pressure spectrum will be considered as alternatives to Rozenberg model. To improve the trailing edge noise prediction, modifications of Amiet's theory may be taken into account, in or-

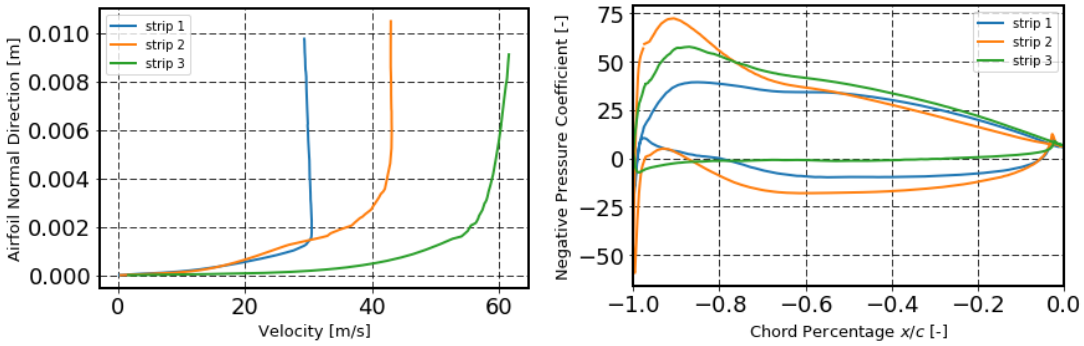

(a) (b)

Figure 8: Velocity profiles and pressure coefficients have been extracted at 3 iso-radius cuts: (a) Boundary-layer velocity profiles. (b) Pressure coefficients.

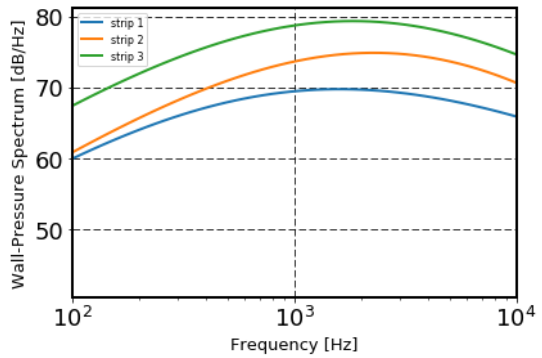

Figure 9: Wall-pressure spectra predicted by Rozenberg model.

der to predict the noise emitted by fan blades with a high swept angle. The Amiet's theory formulation for the leading-edge noise will be implemented as well, to include the influence of the turbulent flow past the radiator as broadband noise source. A validation of the results is planned in order to compare the numerical results with the experimental rotor-alone measurements that will be carried out in the ALCOVES anechoic chamber of the von Karman Institute for Fluid Dynamics.

Acknowledgments

The authors acknowledge the support of the European Commission's Framework Program "Horizon 2020", through the Marie Sklodowska-Curie Innovative Training Networks (ITN) "SmartAnswer - Smart mitigation of flow-induced acoustic radiation and transmission" grant agreement No. 722401 to the present research project. Furthermore, the authors acknowledge Valeo for the received technical support, as well as the École Centrale de Lyon.

References

[1] B. Demory, M. Henner, A. Levasseur, S. Moreau, Optimized efficient quiet automotive fan systems, SIA International Congress on Fluid Dynamics Applications in Ground Transportation.

[2] W. Chen, S. Liu, Y. Gao, H. Zhang, E. Arens, L. Zhao, J. Liu, Experimental and numerical investigations of indoor air movement distribution with an office ceiling fan, Building and Environment 130 (2018) 14–26.

[3] Å. Jan, F. LukÅ, C. JiÅ, Z. JiÅ, Model-based airflow controller design for fire ventilation in road tunnels, Tunnelling and Underground Space Technology 60 (2016) 121–134.

[4] A. Bring, T.-G. Malmstrm, C. A. Boman, Simulation and measurement of road tunnel ventilation, Tunnelling and Underground Space Technology 12 (3) (1997) 417–424.

[5] A. Talbot, Y. Detandt, S. Hatanaka, K. Hirai, G. Minorikawa, Numerical aeroacoustic analysis of small cooling fans for electronic devices (2018) 12.

[6] R. C. Chanaud, D. Muster, Aerodynamic noise from motor vehicles, The Journal of the Acoustical Society of America 58(1) (11) (1975) 31, 38.

[7] S. Moreau, G. Iaccarino, M. Roger, M. Wang, Cfd analysis of flow in an open-jet aeroacoustic experiment.

[8] A. Gudel, Acoustique des ventilateurs, PYC Livres, Villeurbanne, France, 1999.

[9] S. Caro, S. Moreau, Aeroacoustic modelling of low pressure axial flow fans, in: 6th Aeroacoustics Conference and Exhibit, American Institute of Aeronautics and Astronautics, Lahaina,HI,U.S.A., 2000. doi:10.2514/6.2000-2094.

[10] T. Carolus, M. Schneider, H. Reese, Axial flow fan broadband noise and prediction, Journal of Sound and Vibration 300 (1-2) (2007) 50–70.

[11] S. Moreau, M. Roger, Competing broadband noise mechanisms in low-speed axial fans, AIAA Journal 45 (1) (2007) 48–57. doi:10.2514/1.14583.

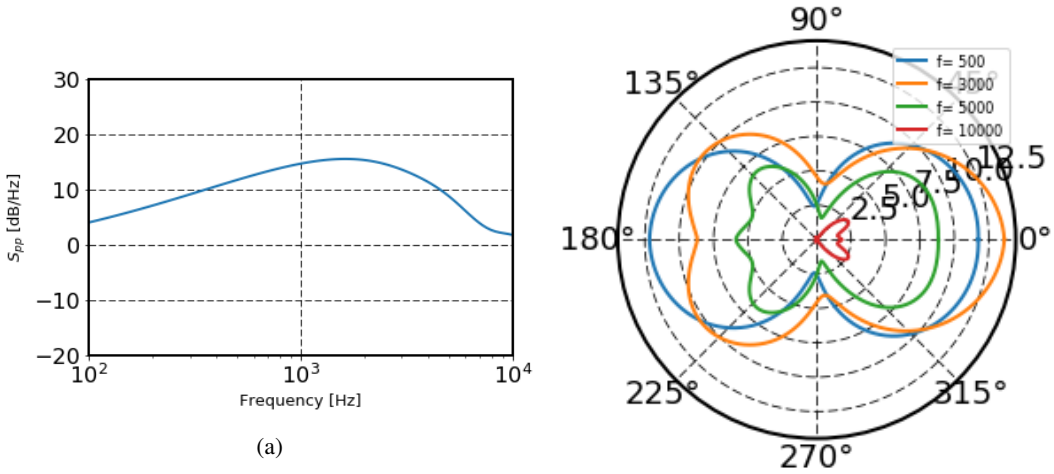

(a) (b)

Figure 10: PSD far-field noise in logarithmic and polar axes: (a) Predicted trailing-edge fan noise sound pressure spectrum. (b) Directivity results in function of frequency.

[12] T. Fukano, Y. Kodama, Y. Senoo, Noise generated by low pressure axial flow fans, i: Modeling of the turbulent noise, Journal of Sound and Vibration 50 (1) (1977) 63–74. doi:10.1016/0022-460X(77)90551-X.

[13] S. Wright, The acoustic spectrum of axial flow machines, Journal of Sound and Vibration 45 (2) (1976) 165–223. doi:10.1016/0022-460X(76)90596-4.

[14] S. Glegg, S. Baxter, A. Glendinning, The prediction of broadband noise from wind turbines, Journal of Sound and Vibration 118 (2) (1987) 217–239. doi:10.1016/0022-460X(87)90522-0.

[15] M. F. Barone, Survey of techniques for reduction of wind turbine blade trailing edge noise., Tech. Rep. SAND2011-5252, 1029824 (Aug. 2011). doi:10.2172/1029824.

[16] S. Moreau, M. Sanjose, Sub-harmonic broadband humps and tip noise in low-speed ring fans, The Journal of the Acoustical Society of America 139 (1) (2016) 118–127. doi:10.1121/1.4939493.

[17] E. Canepa, A. Cattanei, F. Mazzocut Zecchin, G. Milanese, D. Parodi, An experimental investigation on the tip leakage noise in axial-flow fans with rotating shroud, Journal of Sound and Vibration 375 (2016) 115–131. doi:10.1016/j.jsv.2016.04.009.

[18] R. Longhouse, Control of tip-vortex noise of axial flow fans by rotating shrouds, Journal of Sound and Vibration 58 (2) (1978) 201–214. doi:10.1016/S0022-460X(78)80075-3.

[19] M.-J. Park, D.-J. Lee, Sources of broadband noise of an automotive cooling fan, Applied Acoustics 118 (2017) 66–75. doi:10.1016/j.apacoust.2016.10.007.

[20] M. Sanjose, D. Lallier-Daniels, S. Moreau, Aeroacoustic analysis of a low-subsonic axial fan, in: Volume 1: Aircraft Engine; Fans and Blowers; Marine, ASME, Montreal, Quebec, Canada, 2015, p. V001T09A015. doi:10.1115/GT2015-43737.

[21] F. Perot, S. Moreau, M.-S. Kim, M. Henner, D. Neal, Direct aeroacoustics predictions of a low speed axial fan, in: 16th AIAA/CEAS Aeroacoustics Conference, American Institute of Aeronautics and Astronautics, Stockholm, Sweden, 2010. doi:10.2514/6.2010-3887.

[22] S. Redonnet, Aircraft noise prediction via Aeroacoustic Hybrid Methods - Development and Application of Onera Tools over the last Decade: Some Examples, AerospaceLab Journal, Issue 7, June 2014; ISSN: 2107-6596.

[23] R. Amiet, Acoustic radiation from an airfoil in a turbulent stream, Journal of Sound and Vibration 41 (4) (1975) 407–420. doi:10.1016/S0022-460X(75)80105-2.

[24] R. Amiet, Noise due to turbulent flow past a trailing edge, Journal of Sound and Vibration 47 (3) (1976) 387–393. doi:10.1016/0022-460X(76)90948-2.

[25] M. Roger, S. Moreau, Back-scattering correction and further extensions of Amiet's trailing-edge noise model. Part 1: theory, Journal of Sound and Vibration 286 (3) (2005) 477–506. doi:10.1016/j.jsv.2004.10.054.

[26] R. Schlinker, R. Amiet, Helicopter rotor trailing edge noise, in: 7th Aeroacoustics Conference, American Institute of Aeronautics and Astronautics, Palo Alto,CA,U.S.A., 1981.

[27] M. Roger, S. Moreau, A. Guedel, Broadband fan noise prediction using single-airfoil theory, Noise Control Engineering Journal 54 (1) (2006) 5–14. doi:10.3397/1.2888773.

[28] S. Lee, A. Villaescusa, Comparison and Assessment of Recent Empirical Models for Turbulent Boundary Layer Wall Pressure Spectrum, in: 23rd AIAA/CEAS Aeroacoustics Conference, American Institute of Aeronautics and Astronautics, Denver, Colorado, 2017. doi:10.2514/6.2017-3688.

[29] Y. C. Kkosman, J. Christophe, C. Schram, Trailing edge noise prediction based on wall pressure spectrum models for NACA0012 airfoil, Journal of Wind Engineering and Industrial Aerodynamics 175 (2018) 305–316. doi:10.1016/j.jweia.2018.01.030.

[30] Y. Rozenberg, G. Robert, S. Moreau, Wall-Pressure Spectral Model Including the Adverse Pressure Gradient Effects, AIAA Journal 50 (10) (2012) 2168–2179. doi:10.2514/1.J051500.

[31] Y. Lian, W. Shyy, Laminar-trurbulent transition of a low reynolds number rigid or flexible airfoil, AIAA Journal 45 (7).

[32] M. Henner, B. Demory, F. Franquelin, Y. Beddadi, Z. Zhang,

Test rig effect on performance measurement for low loaded large diameter fan for automotive application, in: Volume 1A: Aircraft Engine; Fans and Blowers, ASME, Dsseldorf, Germany, 2014.

[33] M. Goody, Empirical Spectral Model of Surface Pressure Fluctuations, AIAA Journal 42 (9) (2004) 1788–1794. doi:10.2514/1.9433.

[34] Francis H. Clauser, Turbulent Boundary Layers in Adverse Pressure Gradients, Journal of the Aeronautical Sciences 21 (2) (1954) 91–108. doi:10.2514/8.2938.

[35] M. V. Zagarola, A. J. Smits, Mean-flow scaling of turbulent pipe flow, Journal of Fluid Mechanics 373 (1998) 33–79. doi:10.1017/S0022112098002419.

[36] D. Coles, The law of the wake in the turbulent boundary layer, Journal of Fluid Mechanics 1 (02) (1956) 191. doi:10.1017/S0022112056000135.

[37] K. Schwartzschild, Die beugung und polarisation des lichts durch einen spalt, Mathematische Annalen (1902) 177–247.

[38] N. Curle, The Influence of Solid Boundaries upon Aerodynamic Sound, Proceedings of the Royal Society A: Mathematical, Physical and Engineering Sciences 231 (1187) (1955) 505–514. doi:10.1098/rspa.1955.0191.

[39] J. Christophe, Application of Hybrid Methods to High Frequency Aeroacoustics.

[40] G. M. Corcos, The structure of the turbulent pressure field in boundary-layer flows, Journal of Fluid Mechanics 18 (03) (1964) 353. doi:10.1017/S002211206400026X.

[41] Q. Zhou, P. Joseph, A frequency domain numerical method for airfoil broadband self-noise prediction, Journal of Sound and Vibration 299 (3) (2007) 504–519. doi:10.1016/j.jsv.2006.06.061.

[42] J. Christophe, J. Anthoine, P. Rambaud, S. Moreau, Numerical Issues in the Application of an Amiet Model for Spanwise-Varying Incoming Turbulence, in: 14th AIAA/CEAS Aeroacoustics Conference (29th AIAA Aeroacoustics Conference), American Institute of Aeronautics and Astronautics, Vancouver, British Columbia, Canada, 2008. doi:10.2514/6.2008-2865.

LIQUID AND SOLID PROPULSION

Experimental Study of Cavitating Flow and Fluid Hammer in Cryogenic Conditions

Claudia Esposito

Environmental and Applied Fluid Dynamics Department, von Karman Institute for Fluid Dynamics, Belgium, claudia.esposito@vki.ac.be

Supervisor: Jean-Marie Buchlin

Full Professor, Environmental and Applied Fluid Dynamics Department, von Karman Institute for Fluid Dynamics, Belgium, buchlin@vki.ac.be

University Supervisor: Johan Steelant

Associate Professor, Department of Mechanical Engineering, KU Leuven - ESA-ESTEC, Johan.Steelant@esa.int

University Co-Supervisor: Maria Rosaria Vetrano

Associate Professor, Department of Mechanical Engineering, KU Leuven, rosaria.vetrano@kuleuven.be

Abstract

This report presents a research work on cavitating flows in cryogenic conditions. An orifice configuration is chosen at this purpose. Thermodynamic effect will be addressed by using a thermosensitive fluid such as $LN2$. The first task of the project is the comparison of the experimental results from the cryogenic campaign with the ones from the isothermal one. The aim is to determine if and in which conditions a geometric similitude between these two test cases is possible. Then, the relevance of the so-called thermodynamic effect is investigated.

Keywords: cavitation, orifice, thermodynamic effect

1. Introduction

1.1. Motivation

Cryogenic multiphase phenomena are easily induced within the propulsion system of liquid rocket engines. In fact, the activation of spacecraft propulsion systems generally consists of four phases. The first two are the main responsibles of multiphase cryogenic flow. The first phase includes the launch and the separation of the spacecraft from the launcher vehicle. During this phase, the propulsion system is inactive and the propellant tanks are isolated from the combustion chamber by means of a set of valves. The second phase starts with the pressurization of the tanks and the opening of the latch valve, which results in the filling and pressurization of the propellant lines of the spacecraft. Those are initially vacuum pumped or filled with a non-condensable gas at low pressure. This operation is called *priming* and, once done, the propulsion system is fully operational. It is during this phase that a bubble flow is produced by the combination of several phenomena such as boiling (due to the chilldown of the propellant line), cavitation (due to the passage of the fluid through a valve) or to other phenomena such as fluid hammer.

Pipelines and subsystems, which constitute the feeding system, must be properly designed to avoid alterations in the proper operation of the whole system. Thus, a correct characterization of these phenomena is essential. Unfortunately, their prediction and control is still hampered by the unavailability of validated theoretical models for each sub-process. The limiting factor is the difficulty of describing highly non-equilibrium thermodynamic processes in terms of simplified and computationally efficient models, based on equilibrium thermodynamic assumptions.

In this context, the creation of a reliable and consistent experimental database is crucial for assessing the accuracy of model predictions and their range of

validity. Nevertheless, the physical properties of the propellant used, generally cryogenic fluids, and the complexity of the multiphase process strongly limits the possible measurement techniques to use. The most common measurements are about stationary and unstationary temperature and pressure. Both are usually performed with ad-hoc cryogenic sensors, sometimes flush mounted. Even if many non-intrusive techniques, optical based, already exist for two-phase flows, their use is limited to rather standard situation in which the temperature, the velocities and the void fraction level are not extreme.

1.2. Objectives

This work is aimed at characterizing one of the subprocesses happening during the priming operation of a spacecraft propulsion system, namely cavitation. This study will address cavitation both in stationary condition and unstationary one. In particular, the second case refers to the effect of fluid hammer on a cavitating flow. The outcome of this experimental campaign will be the creation of a cryogenic experimental database in terms of pressure, temperature, velocity and flow topology. The purpose is to provide a database that can be used to validate the numerical codes developed to determine damages of valves and pipes due to pressure peaks linked to cavitation and fluid hammer.

Preliminary tests in isothermal environment are carried out as well. Tests with isothermal fluids, such as water, are not considered representative of the cryogenic phenomenon. However, a comparison has already been performed by Pinho [1]. Both water and liquid nitrogen were used as working fluids to test performances of an orifice. Based on his experimental results, he concluded that hydraulic similarity exists between different fluids at single phase condition. Unfortunately, the two-phase cavitating regime has not been investigated experimentally.

Section 2 introduces the thermodynamic effect to underline the peculiarity of cavitation for cryogenic fluids and recalls the theoretical models proposed in literature. The experimental set-up is described in Section 3 while the tested flow regimes are detailed in Section 4. Finally, the hydraulic similitude between the isothermal and the cryogenic test case is discussed Section 5.

2. Cavitation with cryogenic fluids

Cavitation is commonly defined as the breakdown of a liquid medium under very low pressures [2]. Consequently, vapor cavities appear inside the liquid leading to an unstable two-phase flow. The pressure threshold which induces this phase change is assumed to be the saturation pressure, P_{sat}. It is a property of the liquid and a function of the temperature. As an example, Fig. 1 shows the saturation curve for LN2. Above this pressure, nitrogen is in its liquid phase, below it becomes vapor.

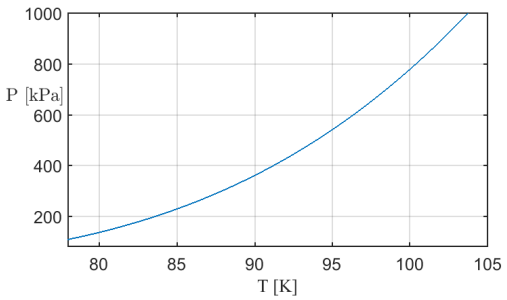

Figure 1: Saturation curve for LN2

2.1. Thermodynamic effect

The thermodynamic effect is a localized cooling process which takes place during the cavitation mechanism [3]. To form and to sustain a vapor bubble, the latent heat is extracted from the surrounding liquid. This effect is usually neglected and cavitation is considered as an isothermal process. However, such an approximation is not always correct. To understand why and when this effect must be taken into account, it is useful to look at the heat balance, Eq. 1, as suggested by [2].

$$\rho_v \cdot V_v \cdot \Delta H = \rho_l \cdot V_l \cdot C_{pl} \cdot \Delta T \tag{1}$$

where C_{pl} is the specific heat of the liquid phase, ΔH is the latent heat of vaporization and the subscripts v and l refer to vapor and liquid phase respectively. A non-dimensional temperature difference, given in Eq. 2, is commonly used [4]. It stands for the temperature drop to apply to a fixed volume of liquid to produce the same volume of water.

$$\Delta T^* = \frac{\rho_v \cdot \Delta H}{\rho_l \cdot C_{pl}} \tag{2}$$

This temperature drop ΔT^* depends only on the physical properties of the liquid. Table 1 shows characteristic properties of water and three cryogenic liquids, namely, nitrogen, hydrogen and oxygen. These values are all referred to a pressure of 5 bar. It appears that the order of magnitude of ΔT^* for water

is much smaller than for the cryogenic liquids. This justifies the distinction into two different kinds of liquids. On the one hand, liquids as water, are isothermal. Cavitation occurs at a constant temperature. On the other hand cryogenic fluids are called thermosensitive. Temperature depression is much more significant and cannot be neglected anymore. This thermal delay also affects the definition of the cavitation parameter. The new expression is written in Eq. 3.

$$\sigma = \frac{P_{up} - P_{sat}(T)}{\Delta P} \tag{3}$$

Table 1: Characteristic values for water compared to cryogenic liquids, [5]

	H_2O	LOx	LN_2	LH_2
T [K]	303.16	108.81	93.99	27.24
C_{pl} [J/g · K]	4.18	1.80	2.20	16.41
ρ_v/ρ_l	$3.05e-5$	0.02	0.03	0.10
ΔH_{vap}	2429.82	191.38	173.32	372.76
ΔT^*	**0.02**	**0.95**	**1.12**	**2.81**

Experimental studies on the thermal effects in cavitating inducers have been performed in [4; 6]. Measurements mainly concern pressure fluctuations. A result was that the temperature depression due to cavitation was increasing with the cavity length.

The importance of the mass-convection across the liquid-vapor interface is discussed in the work by Hosangadi [7]. A cavitating cryogenic flow is simulated over a hydrofoil. As for isothermal cavitation, the vapor bubble has a sharp and distinct interface due to the gap in density across the liquid-vapor interface. It behaves like a limiting streamline and the liquid flows around it. On the contrary, when thermal effects become preponderant, the flow becomes frothy and the vapor volume fraction inside the cavity strongly drops. Since the cavity is more porous, the streamlines flow into it. A small portion of liquid is locally vaporized when it convects into the cavity. The oncoming liquid faces a lower gradient at the interface. The flow slowly deviates and the low pressure region spreads laterally. So the bubble are shorter but they spread laterally allowing a larger entrainment of the liquid.

The rate of this vaporization process is affected by the local geometry and flow conditions. Therefore the shape and the size of the vapor bubble depend on the physical properties of the working fluid as well as on local fluid pressure, temperature and velocity [8].

2.2. Cavitation modeling

Cavitation modeling presents non-negligible difficulties. The flow undergoes to important changes in local density and speed of sound. Moreover the large variance in nuclei number and size and the interaction with turbulence makes cavitation to be a stochastic process. Up to now different models have been proposed in literature [9; 10; 11].

A Hybrid Model will be considered following the approach used by [12; 13]. This model considers the two-phase mixture as a whole. However, Hybrid Models aim to take thermodynamic non-equilibrium into account. Non-equilibrium phenomena within cavitation are vapor bubble nucleation and interphase heat, mass and momentum transfer. Drawback of these models is that they require specific assumptions linked to the particular geometry and conditions. In fact, source terms for the phase change, the evaporation and condensation rates, can be very different according to the specific problem to deal with.

The set of governing equations consists of the conservative form of the Favre-averaged Navier-Stokes equations, a transport equation for the phase change, the enthalpy-based energy equation and the turbulence closure.

$$\frac{\partial \rho_m}{\partial t} + \frac{\partial \left(\rho_m U_j\right)}{\partial x_j} = 0 \tag{4}$$

$$\frac{\partial \left(\rho_m U_j\right)}{\partial t} + \frac{\partial \left(\rho_m U_i U_j\right)}{\partial x_j} = -\frac{\partial p}{\partial x_j} + \frac{\partial}{\partial x_j}\left[(\mu_m + \mu_T)\left(\frac{\partial U_i}{\partial x_j} + \frac{\partial U_j}{\partial x_i} - \frac{2}{3}\frac{\partial U_k}{\partial x_k}\delta_{ij}\right)\right] \tag{5}$$

$$\frac{\partial}{\partial t}\left(\rho_m \left(f_L L\right)\right) + \frac{\partial}{\partial x_j}\left(\rho_m U_j (f_L L)\right) = \frac{\partial}{\partial x_j}\left[\left(\frac{\mu_m}{Pr_L} + \frac{\mu_T}{Pr_T}\right)\frac{\partial h}{\partial x_j}\right] \tag{6}$$

$$\frac{\partial \rho_l \alpha_l}{\partial t} + \frac{\partial \left(\rho_l \alpha_l U_j\right)}{\partial x_j} = \dot{m}^+ + \dot{m}^- \tag{7}$$

In Eqs. 4,5,6,7 the subscripts l and v stand for the liquid and vapor phase respectively. ρ_m is the mixture density, whose expression is written in Eq. 8. α is the volume fraction, U is the velocity and p the pressure. The mixture laminar viscosity is indicated as μ_m and the turbulence one as μ_T. L is the latent heat, h is the enthalpy, Pr_L and Pr_T are the laminar and turbulent Prandtl number respectively.

$$\rho_m = \rho_l \alpha_l + \rho_v \alpha_v \tag{8}$$

Finally $\dot{m}^+$ and $\dot{m}^-$ are the source and the sink term which represent the condensation and evaporation rate, respectively, during the mass transfer process. The equations for the mass transfer are Eqs. 9 and Eqs. 10, where C_{dest} and C_{prod} are two empirical constants. Their values differ significantly from one work to another, [13; 14; 15].

$$\dot{m}^- = \frac{C_{dest}\alpha_l}{t_\infty}\frac{\rho_l}{\rho_v}\frac{MIN(p - p_v(T), 0)}{(0.5\rho_l U_\infty^2)} \tag{9}$$

$$\dot{m}^+ = \frac{C_{prod}(1-\alpha_l)}{t_\infty}\frac{MAX(p - p_v(T), 0)}{(0.5\rho_l U_\infty^2)} \tag{10}$$

Within this model the impact of thermodynamic effect on evaporation and condensation rates is also included [13]. Taylor's series is used at this purpose. The sink and source expressions become functions of the temperature drop. Due to the non-linear relations, the impact of the thermal effects will change according to the working temperature and pressure.

3. Experimental set-up and procedure

Fig. 2 shows a schematic of the CHIlldown Experimental Facility (CHIEF). The cryogenic fluid (LN2) is stored in a ranger with a capacity of 176 litres. This is pressurized through a unit composed of GN2 bottles and pressure regulators in order to supply LN2 at an adjustable and stable pressure (up to 700 kPa). The reservoir is placed outside the laboratory but sufficiently close to the test facility to limit as much as possible long transfer lines. A solenoid valve at the outlet of the reservoir stops the LN2 delivery inside the laboratory in case of emergency. The testing liquid is transferred to the test section by means of a line equipped with a flowmeter and a series of safety valves to protect against over-pressure. Based on the existing data of the facility, the pressure losses through the transfer lines should be around 130 kPa for a flow rate of 0.03 kg/s (tank pressure 700 kPa). These pressure losses are distributed along the line and flow restriction has been limited to reduce as much as possible local evaporation of the liquid phase. A 3-way valve connects the transfer line to both the test section and the bypass line. The latter is used to ensure full-liquid condition at the inlet of the test section. The test section is mounted upwards. It includes the cylindrical orifice and two transparent sections, upstream and downstream the orifice respectively, to allow flow visualizations. Since a precise monitoring of pressure and temperature along the line is of first interest, the test section is instrumented with different pressure and temperature sensors placed at the same locations and whose measurements are taken at once. The characterization of the orifice in terms of pressure drop is obtained from transducers $P2$ and $P3$, Fig. 3, placed, respectively, $4D$ upstream and $8D$ downstream the orifice.

A fast closing valve is placed downstream the orifice to stop abruptly the flow and generate fluid hammer waves in the test line. A vacuum chamber equipped with several electrical and pipe feedthroughs as well as with view ports for flow visualisation surrenders the test section to ensure its thermal insulation from the external environment. The mass flow rate is regulated thanks to two V-control ball valves (30° V-ball) mounted downstream the test section. Both the bypass and exhaust lines are connected to an evaporating tank installed outside the laboratory. It has a capacity of 1.2 m^3 (diameter 1 m and height 2.1 m) and it is not thermally insulated in order to evaporate the liquid phase through a chimney.

In the following we will refer to the cryogenic experimental campaign as Testcase LN2.

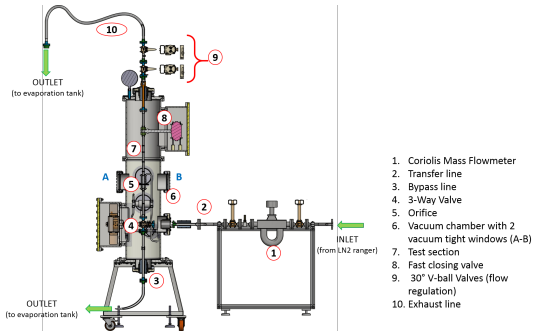

Figure 2: CHIEF facility

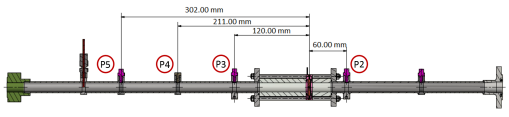

Figure 3: test section with view of pressure sensors positioning

4. Flow regimes for Testcase LN2

Three main flow regimes could be observed during the experimental campaign: single-phase flow, cavitating flow and flashing flow. This classification is

based on the severity of both pressure and temperature drop through the orifice. Flow visualizations have been used as well to discriminate among these regimes.

As it is shown in Fig. 4, both upstream and downstream conditions appear to be above the saturation curve in single-phase regime. In only one case the downstream conditions were found to be at saturation. However, no vapor formation was visualized during the experiments and the flow rate was still linearly dependent on the square root of the pressure drop, so this point was still considered as in fully liquid regime.

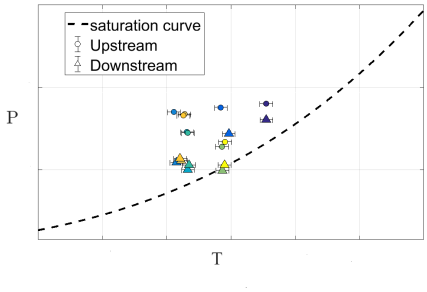

Figure 4: Upstream and downstream P and T in fully liquid conditions

When the pressure drops become larger, from 200 to 500 kPa, and the downstream pressure is at or below the saturation, the cavitation regime starts, Fig. 5. In thiese cases almost no temperature drop occurs during the phase transition. The vapor clouds become visible downstream the orifice but their extension is limited to maximum 3D. Two examples of this regime are depicted in Fig. 6.

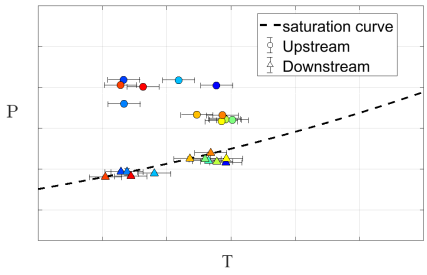

Figure 5: Upstream and downstream P and T in cavitating conditions

Finally, the last regime encountered while testing is the flashing flow. It involves the highest pressure drops up to 650 kPa and it is characterized by the highest vaporization rate. The feature which marks

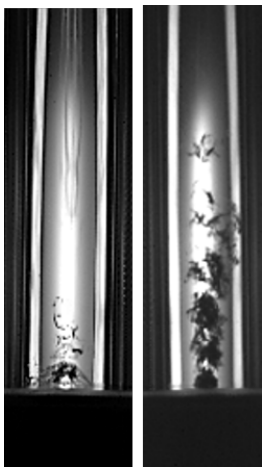

Figure 6: Instantaneous visualizations at: 1) ΔP = 330kPa and $\Delta T \sim 0$ K (left side); 2) ΔP = 456 kPa and $\Delta T \sim 0$ K (right side)

this regime is the high temperature drop which accompanies cavitation and which can arrive up to 7 K. As can be seen from Fig. 7, the downstream points, represented by triangles, are generally below the saturation curve of at least 50 kPa. The result is a very foamy two-phase flow which expands for the whole length of the transparent test section, see for example Fig. 8.

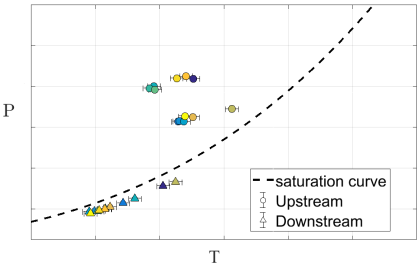

Figure 7: Upstream and downstream P and T in Flashing conditions

5. Hydraulic similitude

As previously stated, the first objective of this work is to study the effect of thermal properties of the liquid on the macroscopic performances of an hydraulic system once cavitation occurs. Therefore, the flow characteristics of Testcase LN2 have been compared to those of a similar orifice tested with an isothermal flow (Testcase H_2O).

For a reliable comparison, the similarity between two orifices must be ensured. It can be stated in terms

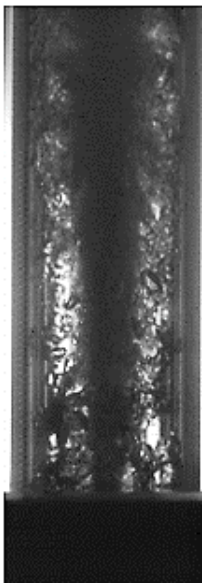

Figure 8: Instantaneous visualization at ΔP = 648 kPa and ΔT = 6K

of the diameter ratio β,Eq. 11, and the thickness ratio T, Eq. 12. Concerning this last parameter, it is used to distinguish between thin and thick orifices. Such a classification becomes necessary because within a thick orifice, $T \geq 0.5$ [16],[17], the flow reattaches to the wall within the orifice. Consequently, the further pressure losses due to this expansion have to be considered.

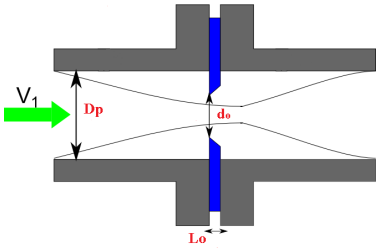

Figure 9: Sketch of an orifice with its main dimensions

$$\beta = \frac{d_o}{D_p} \tag{11}$$

$$T = \frac{L_o}{d_o} \tag{12}$$

From a theoretical point of view, this geometric similarity can be confirmed by looking at the two equations which describe the hydraulic behavior of an orifice in its two main flow stages: the single-phase flow and the choked flow. As for the single-phase regime, different coefficients are proposed in literature to relate the flow to the pressure drop through the orifice, [18]. Within this work, we will refer to the flow coefficient (Kv), which, physically, represents the volumetric flow of water passing through a restriction with a pressure drop of 1 bar. Even if it is very convenient to quantify the flow capacity of an orifice, this parameter is not dimensionless and it also depends on the orifice area. However, it can be easily replaced by a pseudo dimensionless coefficient. In the following it will be referred as SF and its definition is given in Eq. 13.

$$SF = \frac{Kv}{A_o} = \frac{Q}{A_o} \cdot \sqrt{\frac{\rho/\rho}{\Delta P}} \tag{13}$$

The choked flow corresponds to that regime where the cavity size has spread enough to make the flow rate to stabilize around a certain value even for further increases in the pressure drop. To describe such condition, two further parameters have to be introduced apart from the Kv. One is the Liquid critical pressure ration factor F_F, which is defined in Eq. 14,[19]. It takes into account the fact that the liquid vaporizes at a pressure lower than the saturation one because of thermodynamic non-equilibrium effects.

$$F_F = 0.96 - 0.28 \cdot \sqrt{\frac{P_{sat}}{P_{cri}}} \tag{14}$$

In Eq. 14 P_{cri} is the critical pressure of the liquid, which is equal to 22064 kPa for water and to 3395.8 kPa for liquid nitrogen, [5]. The other parameter is the Liquid pressure recovery factor F_L which was introduced by Baumann [20]. It is defined as the ratio between the overall pressure drop through an orifice and the drop between the static pressure at the inlet and the one at the vena contracta (P_{vc}), Eq. 15. For critical flow conditions Eq. 16 is valid.

$$F_L = \sqrt{\frac{P_{up} - P_{dw}}{P_{up} - P_{vc}}} \tag{15}$$

$$Q_{chok} = F_L \cdot Kv \cdot \sqrt{\frac{2 \cdot (P_{up} - P_{vc})}{\rho/\rho_w}} \tag{16}$$

To sum up, the application of the geometric similarity aims at predicting the maximum flow rate at a given inlet condition (P_{up} and T_{up}) for an orifice similar to the one tested, no matter the working fluid. In our case, the intent is to derive teh critical flow conditions

for an orifice in cryogenic environment ($LN2$) by testing a similar orifice in isothermal environment (water).

5.1. Testcase H_2O: flow characteristics

Testcase H_2O was performed in the VKI Becassine facility with a similar cylindrical orifice. The outcome of this campaign in terms of the flow characteristics (pressure drop adn flow rate) is illustrated in Fig. 10.

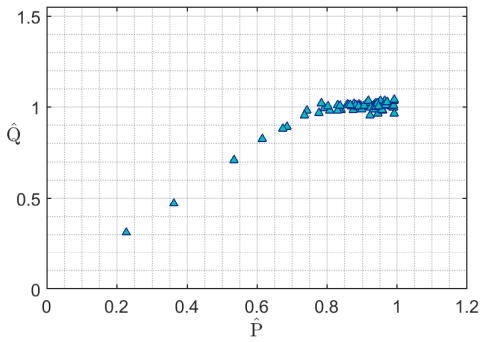

Figure 10: Hydraulic curve for the cylindrical orifice tested in water

The measured flow characteristics are expressed in non-dimensional parameters to compare different working conditions among them. Indeed, during a test campaign, the upstream pressure has been increased to characterize the orifice from the fully liquid condition up to the flashing. Different upstream pressures correspond to different hydraulic curves. Specifically, what is changing is the choked flow rate and the choked pressure drop. So, to obtain a unique curve Q vs. $\sqrt{\Delta P}$, it is suggested to divide Q by Q_{chok},Eq. 16. This ratio will be called $\hat{Q}$. $\hat{P}$ is a dimensionless pressure drop which includes the occurrence of cavitation and its extent. It is defined as in Eq. 17 where the numerator is the actual pressure drop through the orifice. At the denominator there is the cavitation driving term, that is, how much the applied pressure (P_{up}) is close to the saturation pressure (P_{sat}).

$$\hat{P} = \frac{\sqrt{P_{up} - P_{dw}}}{\sqrt{P_{up} - F_f \cdot P_{sat}}} \tag{17}$$

The value of Kv and consequently of SF was extracted from the single-phase data points while the F_L was calculated from the chocked conditions. Table. 2 summarizes these values.

Table 2: Hydraulic parameters for the cylindrical orifice tested in water

Kv [$\frac{m^3/h}{\sqrt{bar}}$]	SF [$\frac{m^3/h}{m^2 \cdot \sqrt{bar}}$]	F_L
1.48 ± 0.02	$4.111 \cdot 10^4 \pm 584$	0.822

5.2. Similitude application: retrieving Testcase LN2 performances from Testcase H_2O characteristics

Firstly, the similitude between Testcase LN2 and Testcase H_2O has been checked in terms of the SF and F_L computed from the respective testing campaign. An F_L of 0.791 was computed from Testcase LN2. As for the SF parameter, the results from both the test cases are depicted in Fig. 11 and they show a good agreement.

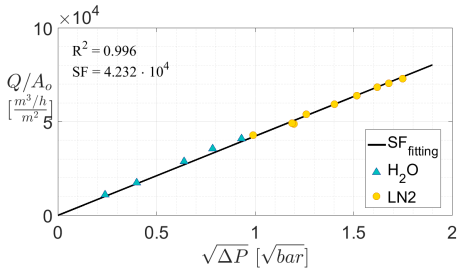

Figure 11: SF from the two experimental campaigns

At this point, the interest is to understand whether isothermal experiments allow to predict the hydraulic performances in the cryogenic case or not. Thus, the F_L and the SF computed in water have been inserted into Eq. 16. Specifically, the Kv to use has been scaled from the SF according to the orifice diameter used in Testcase LN2. Concerning the pressures, P_{up} corresponds to the inlet pressure conditions tested in LN2 and P_{vc} has been assumed to be equal to the saturated pressure at the inlet temperature.

The data points are grouped on the basis of the flow regimes seen in Section 4 and distinguished according to upstream conditions: high inlet pressure (HP) and low inlet pressure (LP).

The calculated maximum flow rate $Q_{chok-calc}$ is compared to the experimental one in Fig. 12. It appears that the critical flow in Testcase LN2 can be predicted within a 2% of error for all the measured points, except for the ones in flashing regime where the thermodynamic effects are preponderant. This means that the pressure at the vena contracta cannot be approxi-

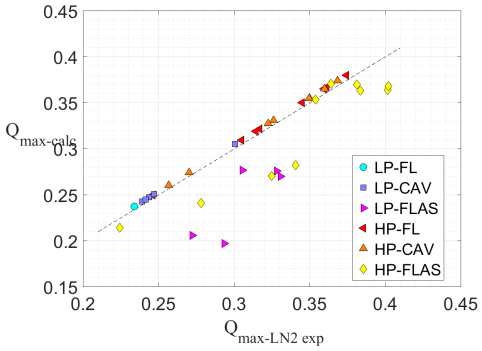

Figure 12: Comparison between the experimental Q_{max} and the calculated one

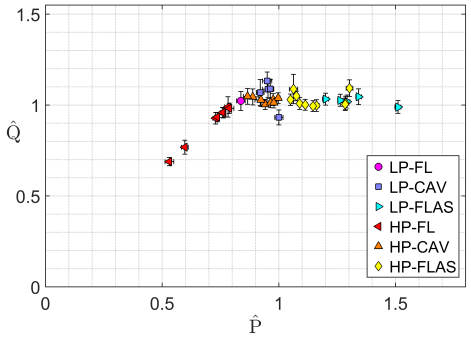

Figure 14: Non-dimensional hydraulic curve for the Testcase LN2

mated by the saturation pressure at the inlet temperature, but it will be much lower. Lower is the pressure value at the vena contracta, higher will be the discrepancy between the calculated maximum flow rate and the experimental one. It is believed that for such cases a better approximation for the vena contracta pressure is the saturation pressure at the downstream temperature. By making such correction, a better correspondence between $Q_{max-calc}$ and $Q_{max-LN2}$, Fig. 13. This correction can be better understood by looking at the hydraulic non-dimensional curve shown in Fig. 14. Here, the flashing points have a $\hat{P} \geq 1$. Practically, it seems that as long as $\hat{P} \leq 1$, that is $P_{dw} \geq P_{sat}(T_{up})$, the maximum flow rate can be predicted from isothermal data. On the other hand, if P_{dw} is lowered more than $P_{sat}(T_{up})$, the similitude as stated in these terms cannot be applied anymore.

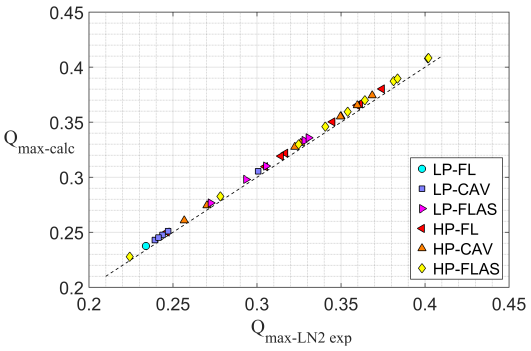

Figure 13: Comparison between the experimental Q_{max} and the calculated one: correction for the flashing regime

6. Conclusion

This work was devoted to investigate a cavitating orifice with LN2. The first aim was to explore the possibility to derive the hydraulic performances of such an orifice by a similar orifice tested with water. Hence, a geometrical similitude was stated and the key parameters to consider were defined. Two testing campaigns with similar orifices were carried out and their results have been compared showing the actual limits in applying such similitude. Finally, this comparison led to have further insights into the physics of the phenomenon, especially in terms of the so-called thermodynamic effect, when it appears and its consequences on the cavitating flow.

Acknowledgments

This research is supported by the ESA's Networking/Partnering Initiative (NPI).

References

[1] J. Pinho, J.-M. Buchlin, S. Chabane, B. Haut, Experimental investigation of cavitation in a safety relief valve using water: extension to cryogenic fluids.

[2] J.-P. Franc, J.-M. Michel, Fundamentals of Cavitation (fluid mechanics and its applications), Kluwer Academic, Dordrecht, The Netherlands, 2004.

[3] M. Billet, D. Weir, Thermodynamic effects on developed cavitation, Journal of Fluids Engineering (1975) 507.

[4] J.-P. Franc, C. Rebattet, A. Coulon, An experimental investigation of thermal effects in a cavitating inducer, Transactions of the ASME-I-Journal of Fluids Engineering 126 (5) (2004) 716–723.

[5] P. Linstrom, W. Mallard, NIST Chemistry WebBook, NIST Standard Reference Database Number 69, National Institute of Standards and Technology, Gaithersburg MD, 20899, retrieved February 11, 2017. doi:10.18434/T4D303.

[6] Y. Yoshida, K. Kikuta, S. Hasegawa, M. Shimagaki, T. Tokumasu, Thermodynamic effect on a cavitating inducer in liquid nitrogen, Journal of Fluids Engineering 129 (3) (2007) 273–278.
[7] A. Hosangadi, V. Ahuja, Numerical study of cavitation in cryogenic fluids, Transactions of the ASME-I-Journal of Fluids Engineering 127 (2) (2005) 267–281.
[8] J. Feng, C. L. Merkle, Numerical modeling of the thermodynamic effects of cavitation, Journal of fluids engineering 119 (1997) 421.
[9] E. Goncalves, R. F. Patella, Numerical simulation of cavitating flows with homogeneous models, Computers & Fluids 38 (9) (2009) 1682–1696.
[10] E. Lauer, X. Hu, S. Hickel, N. A. Adams, Numerical modelling and investigation of symmetric and asymmetric cavitation bubble dynamics, Computers & Fluids 69 (2012) 1–19.
[11] E. Giannadakis, M. Gavaises, H. Roth, C. Arcoumanis, Cavitation modelling in single-hole diesel injector based on eulerian-lagrangian approach, in: Proc. THIESEL International Conference on Thermo-and Fluid Dynamic Processes in Diesel Engines. Valencia, Spain, 2004.
[12] C. C. Tseng, W. Shyy, Turbulence modeling for isothermal and cryogenic cavitation, in: 47th AIAA Aerospace Sciences Meeting including The New Horizons Forum and Aerospace Exposition, 2009, p. 1215.
[13] T. Chen, G. Wang, B. Huang, K. Wang, Numerical study of thermodynamic effects on liquid nitrogen cavitating flows, Cryogenics 70 (2015) 21–27.
[14] R. F. Kunz, D. A. Boger, D. R. Stinebring, T. S. Chyczewski, J. W. Lindau, H. J. Gibeling, S. Venkateswaran, T. Govindan, A preconditioned navier–stokes method for two-phase flows with application to cavitation prediction, Computers & Fluids 29 (8) (2000) 849–875.
[15] A. K. Singhal, M. M. Athavale, H. Li, Y. Jiang, Mathematical basis and validation of the full cavitation model, Transactions-American Society of Mechanical Engineers Journal of Fluids Engineering 124 (3) (2002) 617–624.
[16] G. Kojasoy, F. Landis, P. Kwame-Mensah, C. Chang, Two-phase pressure drop in multiple thick-and thin-orifice plates, Experimental thermal and fluid science 15 (4) (1997) 347–358.
[17] B. Ebrahimi, G. He, Y. Tang, M. Franchek, D. Liu, J. Pickett, F. Springett, D. Franklin, Characterization of high-pressure cavitating flow through a thick orifice plate in a pipe of constant cross section, International Journal of Thermal Sciences 114 (2017) 229–240.
[18] J. P. Tullis, Cavitation guide for control valves, Tech. rep., Nuclear Regulatory Commission, Washington, DC (United States). Div. of Engineering; Tullis Engineering Consultants, Logan, UT (United States) (1993).
[19] G. Stiles, Cavitation and flashing considerations, ISA Handbook of Control Valves, 2nd Edition by Hutchinson, JW (1976) 206–211.
[20] H. D. Baumann, The introduction of a critical flow factor for valve sizing, ISA Transactions 2 (2).

Gas-Liquid Interface Dynamics in Non-Isothermal Sloshing: Experimental Analysis and Simplified Modeling

Domenico Fiorini

Environmental and Applied Fluid Dynamics Department, von Karman Institute for Fluid Dynamics, Belgium, mymail@vki.ac.be

Supervisor: Jean-Marie Buchlin

Full Professor, Environmental and Applied Fluid Dynamics Department, von Karman Institute for Fluid Dynamics, Belgium, buchlin@vki.ac.be

University Supervisor: Johan Steelant

Associate professor, Faculty of Engineering Science, Katholieke Universiteit Leuven, Belgium, Johan.Steelant@esa.int

Abstract

2019 is expected to be a stellar year for space exploration. The EU council has recently approved all the details of the 2021-2027 space program and by the end of the year, the final budget amount will be stated. Three areas are covered by the budget, namely: security, earth observation and satellite navigation. On the latter, advancements can be achieved by improving the guidance navigation systems, which guarantee stable flight conditions. Indeed, the quality of the flight control is dependent on how the the movement of the propellant in the tanks is correctly predicted. The new generation of space propellants is highly sensitive to thermal conditions, moreover the movement of the propellant mass over the walls of the space tanks under different temperatures induces the fuel face extreme thermal phenomena such as boiling and vaporization.

In space, surface tension plays a fundamental role in the fuel motion inside the space tanks, affecting therefore the flight control of the space device. Complex thermal effects influencing the surface tension behavior require still observation and characterization. The impact of these phenomena on the movement of the propellant needs to be predicted through numerical simulations, which still lack experimental data for validation and appropriate models.

The purpose of the project is to scientifically address the open gaps in the literature concerning experiments on phase change dependence on the interface-wall interaction and the characterization of sudden vaporization of space propellants flowing over hot surfaces.

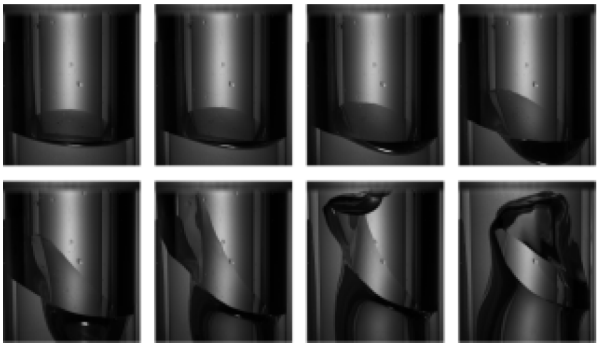

H_2O sloshing image sequence (Simonini 2018. ”Sloshing dynamics investigation by means of non-intrusive measurement techniques.”)

Keywords: dynamic contact angle, non-isothermal phenomena, Leidenfrost effect, microgravity, cryogenic fluids

Multi-Dimensional Design and Optimization of a Hypersonic Propulsion System

Ali Can Ispir

Aeronautics and Aerospace Department, von Karman Institute for Fluid Dynamics, Belgium, ali.can.ispir@vki.ac.be

Supervisors: Bayindir H. Saracoglu and Thierry Magin

Research Manager, Aeronautics and Aerospace Department, von Karman Institute for Fluid Dynamics, Belgium, bayindir.saracoglu@vki.ac.be

Professor, Aeronautics and Aerospace Department, von Karman Institute for Fluid Dynamics, Belgium, magin@vki.ac.be

University Supervisor: Axel Coussement

Professor, Aero-Thermo-Mechanics Department, Universit libre de Bruxelles (ULB), axcousse@ulb.ac.be

Abstract

The goal of this research is to establish an excellent design methodology for transient thermodynamic modeling of combined cycle power plants coupled with an optimization frame work for hypersonic propulsion, in conjunction with detailed design and optimization of the multi-flow path propulsive ducts with heat exchangers through multidimensional unsteady numerical simulation to achieve a propulsion plant operational at any point of the trajectory of the aircraft. This project has received funding from the European Union's Horizon 2020 research and innovation programme under grant agreement No 769246.

Keywords: high speed propulsion, hypersonic aircraft

Numerical Simulations of a Slurry Flow in Horizontal and Vertical Pipes: Effect of Forces Modelling

Maria Teresa Scelzo

Environmental and Applied Fluid Dynamics Department, von Karman Institute for Fluid Dynamics, Belgium, mariateresa.scelzo@vki.ac.be

Supervisors: Jean-Marie Buchlin and Laura Peveroni

Full Professor, Environmental and Applied Fluid Dynamics Department, von Karman Institute for Fluid Dynamics, Belgium, buchlin@vki.ac.be

Research Engineer, Environmental and Applied Fluid Dynamics Department, von Karman Institute for Fluid Dynamics, Belgium, peveroni@vki.ac.be

University Supervisor: Gérard Degrez

Professor, Aéro-Thermo-Mechanics Departement, Université Libre de Bruxelles, Belgium, degrez@ulb.ac.be

Abstract

The use of cryogenic slush -solid liquid mixture at triple point- as future rocket propellant requires new criteria and revised models for a high fidelity design of the engine feedlines. In order to characterize pressure drop and particles distribution of such a fluid in pipes, experiments were performed with an isothermal solid liquid mixture in flow similarity with slush hydrogen. Afterwords, the results were used to validate an Euler-Euler numerical model in OpenFOAM, as shown in this article. CFD simulations were exploited to deepen the understanding of fundamental phenomena discovered in the experiments. It was found that the pressure drop reduction in the vertical pipe configuration is due to a migration of particles from the pipe wall boosted by the off-wall lift force. Also, the strong settling occurring in the horizontal pipe is ruled by the gravity effect and counteracted by the drag force. The present analysis shows as well the influence of the particles diameter on pressure drop and particles distribution. These results lead to the choice of the most effective flow conditions to increase the efficiency of the slush transport in rocket engines.

Keywords: two-phase flow, slurry, Euler-Euler model, OpenFOAM

1. Introduction

The numerical work described in this paper is part of an ongoing project at the von Karman Institute for Fluid Dynamics, intended to characterize and model *slush* flows as a propellant for future launcher engines. Nowadays, cryogenic liquids are widely used as fuel in rocket engines due to the high specific impulse they provide. However, the use of liquid propellants still leads to problems of sloshing, large storage volume requirements and short holding time due to their physical properties and highly thermo-sensitive nature. One promising way to reduce these problems is to use slush instead of pure liquid as fuel [1].

Slush is a solid-liquid mixture at triple point which possesses density and specific enthalpy higher than the liquid state. Recent studies conducted at the SART department of DLR have shown a potential improvement on the gross payload of about 20% if slush replaces the liquid propellant [2]. However, the presence of solid particles in the liquid suspension changes the flow and its thermal properties: the rheological behavior becomes non-Newtonian for high particle concentration and, due to the heat transfer, the solid fraction partially melts changing slush properties in a currently unpredictable process. This implies that the standard correlations for the liquid flow in tubes are no longer valid. Thus, the optimization of the slush transport through circular pipelines requires the

Table 1: Properties of the liquid and solid phase.

	ρ	μ	d
	$[kg/m^3]$	[Pa · s]	[mm]
HFE7200 @ 25C	1430	0.00058	-
Sucrose Crystals	1590	-	0.3 - 1.3

characterization of the slush thermal and fluid dynamics, along with their modeling by means of numerical simulations. The first step of the project was to characterize the pressure drop and the particles distribution in cylindrical pipes of an isothermal solid-liquid mixture [3] in flow similarity with slush hydrogen and methane [4] based on Reynolds number, density ratio and expected pressure drop. Such a mixture, at ambient temperature and atmospheric pressure, is referred to as slurry. The experimental data analysis revealed a number of evidences to drive the design of a slush pipeline and the results were used to validate an Euler-Euler (E-E) numerical model. Numerical simulations are currently being exploited to deepen the understanding of the phenomena observed experimentally, as discussed in the present article.

A summary of the experiments is presented in Section 2. The solver validation for fully liquid and slurry conditions is presented in Section 4. In the same section we present a discussion concerning the modelling of the forces in horizontal and vertical pipe slurry flows.

2. Summary of the experimental results

The slurry chosen for the experiments is a mixture of HFE7200 and sucrose crystals whose properties are reported in Table 1. The facility scales down the main components of a real launcher fuel feeding line [5], with oblique horizontal and vertical test sections as well as two vertical bends. During the experiments the solid volume fraction (α_s) went up to 40% and the mass flow rate (Q) was between 0.2 and 0.7kg/s.

The pressure losses in a concentrated turbulent slurry flow increase because of two components: an inertial contribution, due to increasing mixture density as particles are added, and a viscous term that affects the friction coefficient because of particles-wall interaction. For the mixture considered, the first contribution is almost negligible because the solid liquid density ratio is nearly 1 (see Table 1). Nevertheless, in the horizontal pipe particles undergo strong settling because of the effect of gravity. Therefore, the data show higher pressure drop as α_s increases because the slurry transients from heterogeneous particles distribution to a moving bed of particles in the bottom part of the pipe. Concerning the vertical pipe, past models tend to overestimate the pressure losses. In fact, in this configuration, the particles migrate from wall to the pipe centerline preventing the particles-wall interaction that does not contribute to increase the friction factor.

Therefore, the pressure drop (ΔP) in the vertical pipe (subscript vert), for a given mass flow rate (Q) and solid volume fraction (α_s), is always lower than the horizontal pipe (subscript hor). Figure 1 shows the experimental friction coefficient calculated as in Eq. 1. The subscript l stands for liquid and refers to the experimental pressure coefficient in fully liquid conditions.

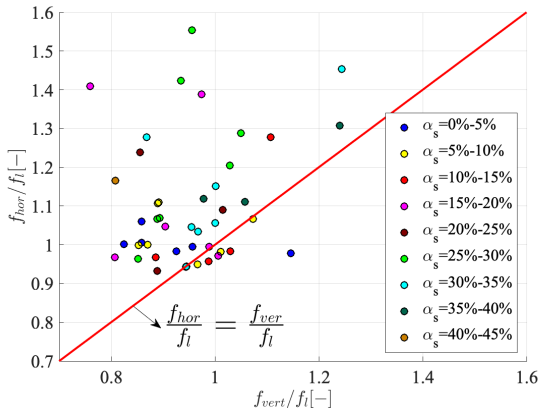

Figure 1: Comparison between the experimental pressure coefficient of slurry in horizontal (f_{hor}) and vertical (f_{vert}) pipe with respect to the correspondent fully liquid conditions (f_l) for different (α_s)

$$f = \frac{2\Delta P_{exp}}{U^2\rho}\frac{D}{L}. \quad (1)$$

In Eq. 1, D is the pipe diameter, L the measurement pipe section length, ρ is the slurry density and U the velocity calculated from the measured mass flow rate as in Eq. 2

$$Q = U\rho D^2/4, \quad (2)$$

where $\rho = \alpha_s\rho_s + (1-\alpha_s)\rho_l$. Based on these results, numerical simulations are exploited to clarify the mechanisms of these phenomena and to identify the mixture features that would possibly lead to a reduction of the pressure.

3. Numerical model

3.1. Governing equations

According to the E-E model, the slurry is constituted by two interpenetrating continua, the liquid phase (denoted by the subscript l) and the solid phase (denoted by the subscript s). Hence, for each domain cell the balance of the two volume fractions (α_l and α_s) is constant and equal to unity. This means that the Navier-Stokes equations are multiplied by the correspondent volume fraction and solved for each phase. The advantage of this approach over the Euler-Lagrange model, where the Newton law is solved for each particle (parcel of particles), is that the computational cost remains low also at high concentrations. The continuity equations of liquid and solid phase are (with k=l,s):

$$\frac{\partial}{\partial \mathrm{t}}\left(\alpha_{\mathrm{k}}\rho_k\right) + \nabla\cdot\left(\alpha_{\mathrm{k}}\rho_k\vec{U_k}\right) = 0 \tag{3}$$

The momentum equation for the liquid phase reads as in Eq. 4:

$$\frac{\partial}{\partial \mathrm{t}}\left(\alpha_k\rho_k\vec{U_k}\right) + \nabla\cdot\left(\alpha_k\rho_k U_k\vec{U}_k\right) = -\alpha_k\Delta P + \\ + \nabla\cdot\left(\overline{\tau_k} + \overline{\tau_{kt}}\right) + \vec{M}_k \tag{4}$$

where $\vec{M}_k$ is the momentum exchange between the tow phases, $\overline{\tau_{kt}}$ are the turbulent stress tensors for liquid and solid phase. The stress tensors $\overline{\tau_k}$ are expressed as in Eq. 5 according to the definition of Newtonian fluid:

$$\overline{\overline{\tau}_k} = \alpha_k\mu_k\left(\nabla\vec{U_k} + \nabla\vec{U_k}^T\right) + \alpha_k\left(\lambda_k - \frac{2}{3}\mu_k\right)\nabla\cdot\vec{U_k}I \tag{5}$$

Eq. 5 for the solid phase supposes the knowledge of the bulk viscosity of the solid particles λ_s and the solid dynamic viscosity μ_s. The bulk viscosity is evaluated with Lun's model as in Eq. 6 [6]:

$$\lambda_s = \frac{4}{3}\alpha_s\rho_S d g_{0,ss}\left(1+e_{ss}\right)\left(\frac{\Theta_s}{\pi}\right)^{1/2} \tag{6}$$

Where d is the particle diameter and $g_{0,ss}$ is the radial distribution, which is the local probability of a particle to collide with another particle, as given by Gidaspow [7]:

$$g_{0,ss} = \left[1 - \left(\frac{\alpha_s}{\alpha_{s,\max}}\right)^{\frac{1}{3}}\right]^{-1} \tag{7}$$

In Eq. 7, α_{max} is the maximum packing volume concentration of particles, measured experimentally and equal to 59% for the present slurry. Θ_s is the granular temperature that describes the kinetic energy of the random motion of solid particles. The transport equation of the granular temperature, reported in Eq. 8, is derived from the Granular Kinetic Theory (GTK) that is a tool developed from the kinetic theory of gases to describe the kinematics (particles collisions) of granular media.

$$\frac{3}{2}\left[\frac{\partial}{\partial t}\left(\alpha_s\rho_s\Theta_s\right) + \nabla\cdot\left(\alpha_s\rho_s\Theta_s\right)\right] = \left(-P_sI + \overline{\tau}_s : \nabla U\right) + \\ + \nabla\cdot\left(\kappa_\Theta\nabla\Theta\right) - \gamma_\Theta + \Phi_\Theta \tag{8}$$

When α_s is high, μ_s accounts also for the friction stresses $P_f sin(\delta)$, where δ is the collisional angle of the particles and P_f is given by Eq. 9:

$$P_f = Fr\frac{\left(\alpha_s - \min\left(\alpha_s\right)\right)^n}{\left(\alpha_{s,max} - \alpha_s\right)^p} \tag{9}$$

Fr, n and p are empirical parameters to be adapted at the specific test case during a parametric study. It is worth mentioning that the models for the closure of the GKT are empirical correlations, thus, they cannot be chosen a priori also because the most of them have been optimized for fluidized beds and not for pipe flows. Examples of the application of this approach can be found in [8] [9] [10].

3.2. Momentum exchange between phases

The coupling between the two phases is achieved by pressure and interphase momentum exchange that takes into account all the forces acting in the mixture:

- Drag force, $F_D = \rho_s\alpha_s C_D(\vec{U_s} - \vec{U_l})|\vec{U_s} - \vec{U_l}|$, where C_D is the drag coefficient (Eq.s 10-11);
- Virtual mass force, $F_{VM} = \rho_l\alpha_s C_{VM}(\vec{U_l}\nabla\vec{U_l} - \vec{U_s}\nabla\vec{U_s})$ where C_{VM} is a constant;
- Lift force, $F_L = \alpha_s\rho_l C_L(\vec{U_l} - \vec{U_s})x\nabla x\vec{U_l}$ where C_L is a constant;
- Body force, $F_g = \alpha_s\rho_s\vec{g}$, where $\vec{g}$ is the gravity acceleration;

$$C_D = \begin{cases} \widetilde{C_d}(1-\alpha_s)^{-1.65} & \text{if } \alpha_S \le 0.2 \\ \frac{200\alpha_s\mu_l}{(1-\alpha_s)d_s\rho_l|u_r|} & \text{if } \alpha_s \ge 0.2 \end{cases} \tag{10}$$

$$\widetilde{C_d} = \begin{cases} \frac{24}{Re_p(1-\alpha_s)}[1 + 0.15((1-\alpha_s)Re_p)^{0.678}] & if Re_p \leqslant 1000 \\ 0.44 & if Re_p \ge 1000 \end{cases} \tag{11}$$

with

$$Re_p = \frac{\rho_s d\,|U_l - U_s|}{\mu_l}. \tag{12}$$

3.3. Geometry

The geometrical domain discretization is performed with the OpenFOAM utility blockMesh, in order to have a structured hexahedral mesh. The pipeline has a diameter of D=22mm. The length of the pipe (Figure 2) is 800mm to allow the full development of the turbulent flow and to have 500mm corresponding to the length of the experimental test section. The wall refinement varies depending on the flow velocity to keep $y^+ < 5$. A mesh independence study has been performed for the number of cells in the three directions, longitudinal, radial and angular direction for each velocity. Details of this study can be found in [11].

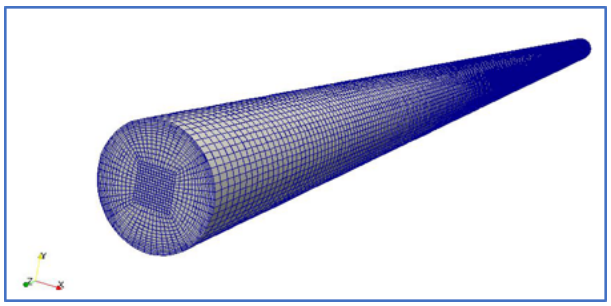

Figure 2: Discretized geometrical domain. The 3D mesh is structured and refined at the pipe wall.

3.4. Boundary conditions

The inlet velocity values of the two phases are uniform and equal to each other, and they range from 0.47 to 0.90 m/s to cover the range of Reynolds number of the experiments. At the pipe outlet the pressure is the atmospheric one and everywhere the temperature is equal to 280K, being an isothermal case. The inlet values for the volume fractions span from 0% to 40 %. At the wall, the Johnson-Jackson boundary condition [12] is used for the velocity of the particles. Considering the balance of the tangential force and energy at the wall, Johnson and Jackson found out two boundary conditions based on two parameters, specularity coefficient (ϵ) and restitution coefficient (ϕ). These parameters represent, respectively, the amount of tangential and normal momentum lost at the wall due to the wall-particle collision. In the expressions of the boundary conditions, these parameters are multiplied by the particle concentration at the wall, so that the flow regime, i.e. the amount of particles at the pipe surface, is accounted for. On the other hand, the particles diameter is not taken into account.

3.5. Numerical settings

A second order upwind discretization scheme is used for the momentum equation while a first order upwind discretization is adopted for volume fraction and turbulent kinetic energy. These schemes ensure, in general, satisfactory accuracy, stability and convergence of the calculation. The convergence criterion is based on the residual value of the calculated variables, i.e., mass, velocity components, turbulent kinetic energies, turbulent energy dissipation rate and volume fraction. Moreover, PIMPLE algorithm is used for the velocity-pressure coupling. A parametric study was performed to ensure the independency of the results from the chosen time step Δt variable with a fixed Courant number (Eq. 13)

$$Cu = \frac{u\Delta t}{\Delta x}, \tag{13}$$

where Δx is the mesh cell size and u the local velocity. For fully liquid simulations, the Courant number is fixed at maximum 0.9; for slurry flow the Courant number decreases down to 0.6 to ensure stability.

3.6. Turbulence modelling

After a comparison between the results with different RANS models, the turbulence model used in the simulations is the $k-\omega$ SST model and the turbulence quantities at the inlet and at the wall are calculated according to [13]. The turbulence intensity is set at 10%.

4. Results and discussion

4.1. Fully liquid conditions

In Figure 3, the pressure drop ΔP resulting from the numerical simulations in fully liquid conditions are compared with the Darcy-Weisbach equation (Eq. 14) for pressure drop in circular pipeline.

$$\Delta P = \frac{1}{2} U^2 \rho f \frac{L}{D} \tag{14}$$

Figure 4 shows the comparison between numerical results and experiments for which the entrance length was not always long enough to ensure fully development of the flow. The comparison allows to identify the segment of the discretized domain corresponding to the measurement section for the comparison in slurry conditions, achieving a partial validation of the solver in not-developed conditions. At higher velocity, the discrepancy between experiments and simulations is higher probably because the level of not development of the flow is more severe.

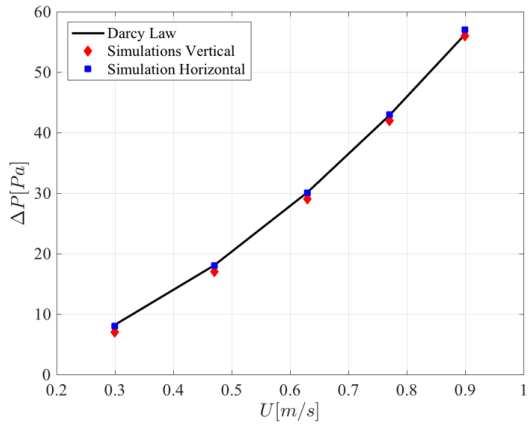

Figure 3: Numerical pressure drop ΔP in function of the flow velocity U in comparison with the Darcy-Weisbach correlation.

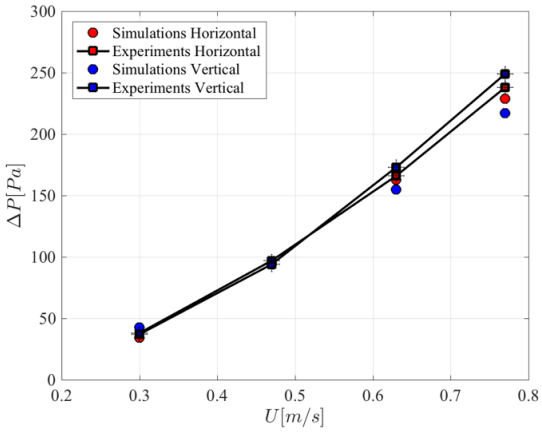

Figure 4: Comparison between the numerical (square markers) and the experimental (circle markers) pressure drop ΔP for horizontal (red markers) and vertical pipe (blue markers), in function of the flow velocity U

4.2. *Slurry conditions*

The solver validation has been achieved by means of a parametric study on the GKT models to perceive the sensitivity of the solver to the different parameters. The final configuration is reported in Table 2.

For the horizontal pipe, the comparison between experimental and numerical results is satisfying, not only for the heterogeneous regime (low concentration in Figure 5) but also for moving bed configuration (high concentration in Figure 6). The same comparison is shown in Figure 7 for the vertical pipe. In this case, in the experiments the effect of increasing flow density on the pressure drop is not visible because it remains within the uncertainty of the measurement.

Table 2: Optimized parameters of the GKT models.

Fr	n	p	α_{max}	e_{ss}	δ
0.05	1	5	0.59	0.1	28.5

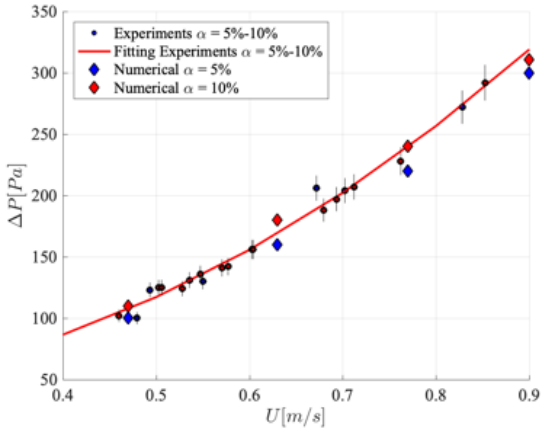

Figure 5: Numerical pressure drop ΔP in function of the the pipe slurry velocity U, for horizontal pipe, for α_s =5% (blue diamonds) and α_s =10% (red diamonds), in comparison with fitting (red line) of the experimental points (small circles)

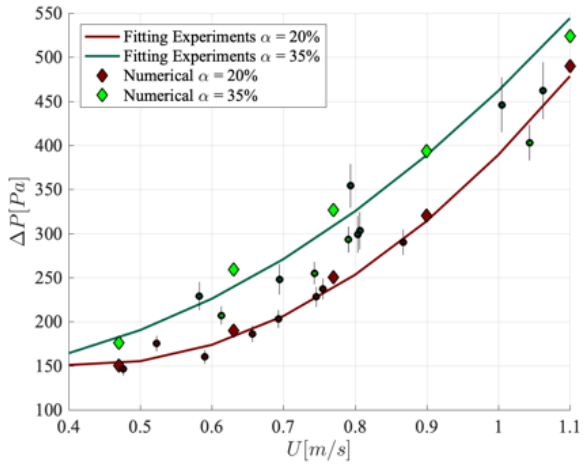

Figure 6: Numerical pressure drop ΔP in function of the the pipe slurry velocity U, for horizontal pipe, for α_s =20% (brown diamonds) and α_s =35% (green diamonds), in comparison with fitting (green and brown lines) of the experimental points (small brown and green circles)

On the other hand, in the simulations, increasing the density of the slurry results in higher pressure drop, that remains anyway lower than the corresponding values of pressure loss in the horizontal pipe.

The particles distribution in the two segments was observed during the experiments by means of High

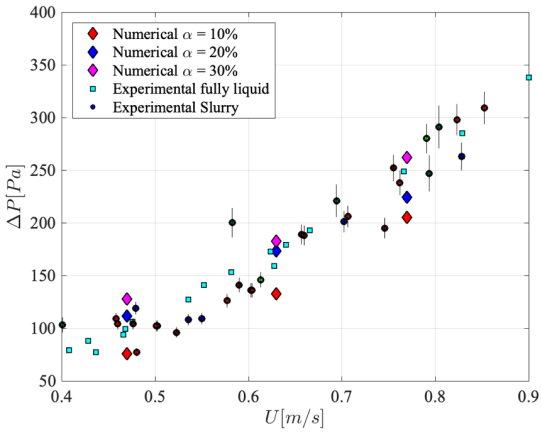

Figure 7: Numerical pressure drop ΔP(diamond markers) in function of the the pipe slurry velocity U in comparison with the experimental slurry points (small circles) and the fully liquid condition (small squares), for vertical pipe

Speed Video (HSV) in background light configuration [4]. Due to the high concentration of particles and their opaque nature, the pictures rapidly reach saturation levels of light. For this reason the quantitative evaluation of the solid volume fraction is somehow difficult. From the qualitative point of view, in the horizontal pipe there is a heterogeneous distribution of particles due to gravity with settling at the bottom part of the pipe, as shown in Figure 8. The simulations show similar qualitative behaviour with strong settling of particles. As for the vertical pipe, a migration of particles toward the pipe centerline is observed (Figure 9). The numerical results confirm that there is a locus of solid volume fraction at the wall. However, the peak of solid volume fraction is located much closer to the wall than to the centerline, resulting in a sort of annular flow. At the moment, this result cannot be confirmed or excluded by the experiments because the optical technique employed for the measurements does not allow the detection of the pipe centerline.

4.3. Forces modelling in the vertical pipe

The migration of particles from the wall towards the pipe centerline in a vertical downward slurry flow has been observed experimentally by Ferre et al. [14] and Shook and Bartosik [15]. The numerical results, shown in Figure 10, confirm that this phenomenon is due to the lift force. In fact, higher lift coefficient C_L leads to fewer particles close to the wall and to lower pressure gradient (Table 3). This is due to the combined action of weaker particles wall interaction and lower relative velocity between the two phases as

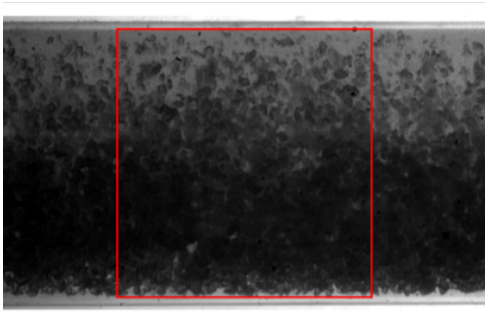

Figure 8: Exemplary HSV frame for the horizontal segment, for slurry at $U = 0.47m/s$ and $\alpha_s = 12\%$ the dark areas are the particles and the clear region is the liquid.The arrows point the liquid film forming at the pipe wall.

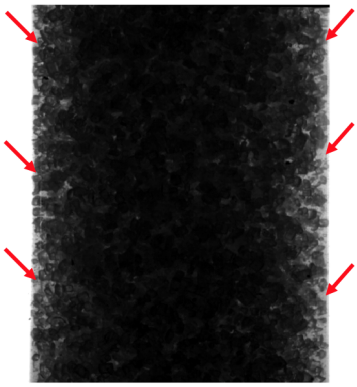

Figure 9: Exemplary HSV frame for the vertical segment, for slurry at $U = 0.47m/s$ and $\alpha_s = 17\%$ the dark areas are the particles and the clear region is the liquid.

C_L rises (Figure 11). The comparison of the pressure drop with the experiments brings to the choice of the $C_L = 0.5$. It is worth noticing that, if the lift is taken into account, the concentration profiles show the maximum peak of concentration far from the pipe center. This was also seen in the experimental results of Summer et al. [16] and reported in [17].

The particles distribution along the pipe diameter depends as well on solid volume fraction and particles size. Concerning the solid volume fraction, as

C_l [-]	0	0.5	1
ΔP_{num} [Pa]	530	267	190
$\frac{\Delta P_{exp}-\Delta P_{num}}{\Delta P_{exp}}$[%]	110	6.8	-24

Table 3: Pressure drop ΔP in vertical pipe and correspondent discrepancy with respect to the experiments for different lift coefficient C_L , U=0.77m/s α_s=17%

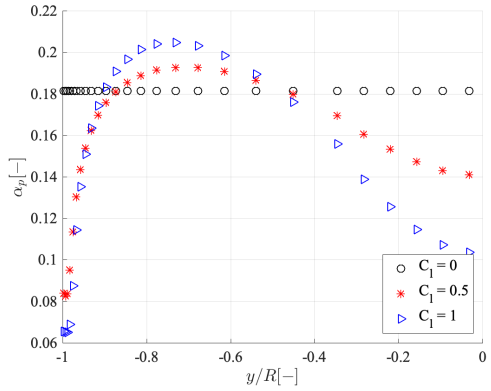

Figure 10: Solid volume α_s fraction along the pipe radius for different lift coefficients C_L

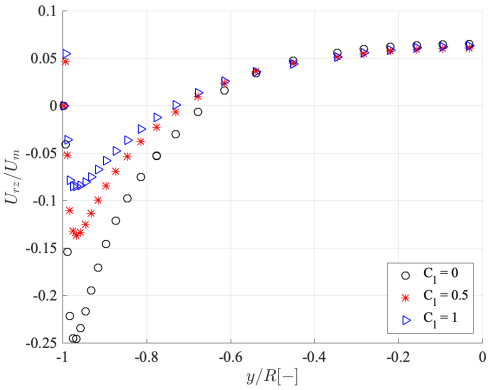

Figure 11: Relative velocity between the phases in the direction of the flow $U_{rz} = U_{s,z} - U_{l,z}$ along the pipe radius, for different lift coefficients C_L

the concentration increases the tendency of the particles to migrate towards the center of the pipe increases (Figure 13). Concerning the particles dimension, the present Euler-Euler model allows the use of only one value for the particles diameter. However, the particles used during the experiments were characterized by a size distribution far from being uniform [4], with an average value of $d_{50} = 0.6mm$. Therefore, a parametric study on the particle diameter (d=0.3mm, 0.6mm, 1.3mm) is performed to assess its effect on the simulations. As the particle size increases the concentration distribution in the near wall region drops and the low concentration region close to the wall enlarges, as shown in Figure 12. The same result was observed experimentally [15] because large particles are unable to travel at the wall, while smaller particles, with a characteristic length smaller than the buffer layer height, are trapped in it and enhance the wall friction coefficient.

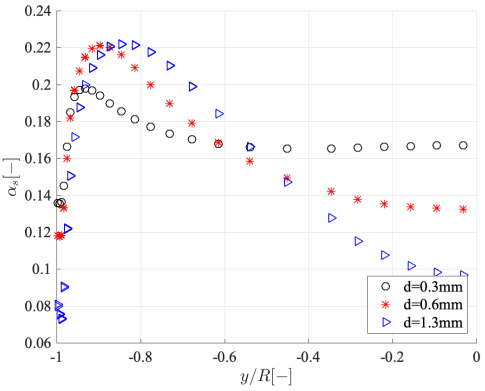

Figure 12: Solid volume fraction α_s along the pipe radius for different particles diameter d.

On the other hand, the comparison of the relative velocity $U_{rz} = U_{s,z} - U_{l,z}$ shown in Figure 14, reveals that where the particles are few they are slower than the liquid, increasing the effect of the off-wall lift force that pushes the particles away from the wall. On the other hand, smaller particles possess smaller response time in the flow, therefore, the relative velocity approaches zero.

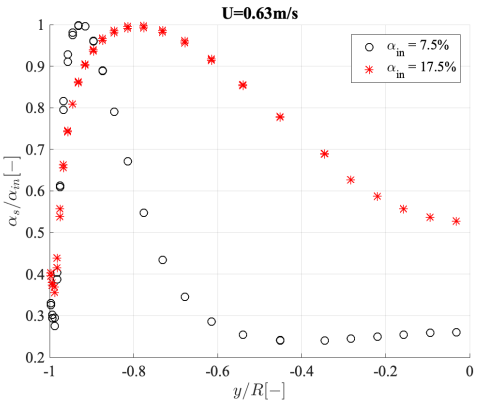

Figure 13: Solid volume distribution α_s for different average inlet concentration α_{in} along the pipe radius.

As a result the pressure drop reaches a minimum for the intermediate particles diameter $d = 0.6mm$, as shown in Table 4.3.

4.4. Forces modelling in the horizontal pipe

According to Wilson [18] and Talmon [19], the off-wall lift force acts also in the horizontal configuration for particles bigger than 0.4mm. This force

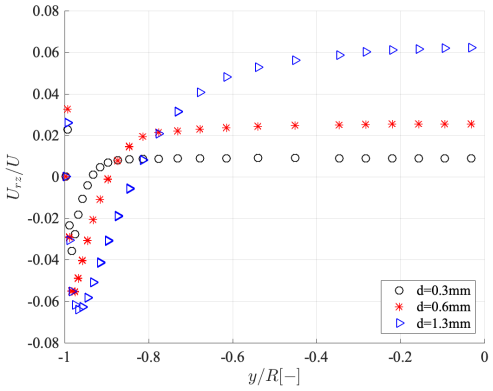

Figure 14: Relative velocity $U_{rz} = U_{s,z} - U_{l,z}$ along the pipe radius for different particles diameter d.

Table 4: Effect of the particles diameter d on the numerical pressure drop ΔP in the vertical pipe, $U = 0.47 m/s$, $\alpha = 17\%$, d=0.3mm (black markers), d=0.6mm (red markers) and d=1.3mm (blue markers)

d	[mm]	0.3	0.6	1.3
ΔP	[Pa]	140	126	130

was not taken into account in any of the CFD studies for slurry flows in horizontal pipe [8] [9] nor in the slush community [10], while the reason of the observed pressure drop reduction at high velocity may be due to this phenomenon. In the present case the lift force does not play any role because particles rapidly settle on the bottom part of the horizontal pipe, under the gravity effect, forming a moving bed. Therefore, the enduring contact between wall and particles enhance the friction coefficient. Instead, the gravity

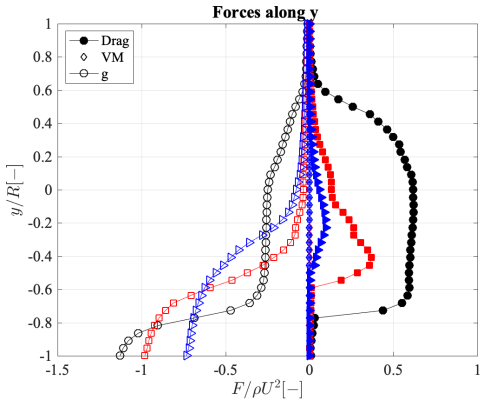

Figure 15: Forces (Drag and Virtual Mass) acting in the direction of gravity (g) acceleration in the horizontal pipe along the pipe radius for particles size, d=0.3mm (black markers), d=0.6mm (red markers) and d=1.3mm (blue markers)

force is counteracted only by the drag force (Figure 15). The drag coefficient C_D is a complex function of the Reynolds number (Re_p) and the solid volume fraction, as well as of the particles diameter. In particular, for a given velocity and particle diameter, the drag coefficient increases with increasing solid volume fraction similarly to what happens for particles in a fluid of high viscosity. Moreover, the drag coefficient increases as the particles are smaller. This results in a higher drag force even if the relative velocity approaches zero when the particles size decreases, as shown in Figure 16.

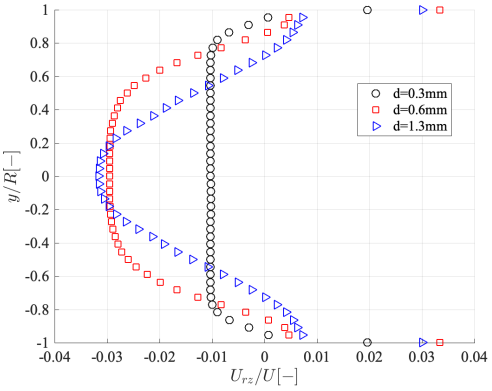

Figure 16: Relative velocity in the direction of the flow (z) along the pipe radius for particles size, d=0.3mm (black markers), d=0.6mm (red markers) and d=1.3mm (blue markers)

5. Conclusions

An Euler-Euler model with Granular Kinetic Theory closure in OpenFOAM has proven capable of simulating isothermal slurry flows in horizontal pipe in challenging conditions such as low velocity, high solid volume fraction and high particle-to-pipe diameter in which the inter-particles collisions and the enduring contact between them and with the wall play a fundamental role. For this slurry, in isothermal similarity with slush hydrogen, the horizontal flow has a strong settling nature that is ruled by gravity and drag force. The off-wall lift force, that would benefit and develop for particles bigger than 0.4 mm, is instead too weak to be effective. Increasing the velocity of the flow would possibly unable the flow to enter the pseudo-homogeneous regime and reduce the pressure drop.

On the other hand, in the vertical pipe, the lift force is responsible for the migration of the particles away from the wall, reducing drastically the pressure drop

in this geometrical configuration. Big particles undergo strong lift effect while smaller particles have lower relative velocity. Therefore, an optimum intermediate particles diameter enables to reach a compromise for lowering pressure drop. From a practical point of view, the particles size in a cryogenic slush flow, is controlled by the slush production method [20] and it is ruled by the *aging* phenomenon. These two aspects will be evaluated as last step of the present research project.

Acknowledgments

This research project is supported by the ESA Networking/Partnering Initiative. The Ph.D. program of M.T. Scelzo is funded by FNRS through the FRIA grant.

References

[1] A. Friedlander, R. Zubrin, T. L. Hardy, Benefits of slush hydrogen for space missions, Cryogenics 52 (7-9) (2012) 428–440.

[2] E. Dumont, S. Stappert, T. Ecker, J. Wilken, S. Karl, S. Krummen, M. Sippel, Evaluation of future ariane reusable vtol booster stages, 9 VKI Ph.D. Symposium, 5-7 March 2018.

[3] M. Scelzo, Experimental characterization of a solid-liquid mixture flowing in circular pipes, 9 VKI Ph.D. Symposium, 5-7 March 2018.

[4] M. T. Scelzo, L. Peveroni, J. Wilken, J.-M. Buchlin, J. Persson, Densified propellants for future launch vehicles: Experimental characterization of an isothermal slurry in circular pipelines in flow similarity with slush hydrogen, Space Propulsion Conference, Seville.

[5] L. Peveroni, M. Vetrano, Propellant densification compatibility predict tn5200: Design and manufacturing of the test bench. (2016).

[6] C. Lun, S. B. Savage, D. Jeffrey, N. Chepurniy, Kinetic theories for granular flow: inelastic particles in couette flow and slightly inelastic particles in a general flowfield, Journal of fluid mechanics 140 (1984) 223–256.

[7] D. Gidaspow, R. Bezburuah, J. Ding, Hydrodynamics of circulating fluidized beds, kinetic theory approach, 7th Engineering Foundation Conference on Fluidization.

[8] D. Kaushal, T. Thinglas, Y. Tomita, S. Kuchii, H. Tsukamoto, Cfd modeling for pipeline flow of fine particles at high concentration, International Journal of Multiphase Flow 43 (2012) 85–100.

[9] G. V. Messa, S. Malavasi, Improvements in the numerical prediction of fully-suspended slurry flow in horizontal pipes, Powder technology 270 (2015) 358–367.

[10] K. Ohira, A. Ota, Y. Mukai, T. Hosono, Numerical study of flow and heat-transfer characteristics of cryogenic slush fluid in a horizontal circular pipe (slush-3d), Cryogenics 52 (7-9) (2012) 428–440.

[11] M. Scelzo, L. Peveroni, J.-M. Buchlin, Propellant densification compatibility - doctoral research thermal effects - tn 4000: Validation of the numerical model in isothermal conditions. (2019).

[12] P. C. Johnson, R. Jackson, Frictional–collisional constitutive relations for granular materials, with application to plane shearing, Journal of fluid Mechanics 176 (1987) 67–93.

[13] H. K. Versteeg, W. Malalasekera, An introduction to computational fluid dynamics: the finite volume method, Pearson education, 2007.

[14] A. L. Ferre, C. A. Shook, Coarse particle wall friction in vertical slurry flows, Particulate science and technology 16 (2) (1998) 125–133.

[15] C. Shook, A. Bartosik, Particle?wall stresses in vertical slurry flows, Powder Technology 81 (2) (1994) 117–124.

[16] R. Sumner, M. McKibben, C. Shook, Concentration and velocity distribution in turbulent vertical slurry flow, J. Solid Liquid Flow 2 (2) (1990) 33–42.

[17] S. Ravikumar, R. Ziazi, F. Chambers, M. McNally, R. Hoffman, Computational prediction of particle-laden slurry flow in a vertical pipe using reynolds stress model, in: ASME 2013 Fluids Engineering Division Summer Meeting, American Society of Mechanical Engineers, 2013, pp. V01CT20A008–V01CT20A008.

[18] K. Wilson, A. Sellgren, Interaction of particles and near-wall lift in slurry pipelines, Journal of Hydraulic Engineering 129 (1) (2003) 73–76.

[19] A. Talmon, Analytical model for pipe wall friction of pseudo-homogenous sand slurries, Particulate Science and Technology 31 (3) (2013) 264–270.

[20] K. Ohira, Study of production technology for slush hydrogen, in: AIP Conference Proceedings, Vol. 710, AIP, 2004, pp. 56–63.

AEROTHERMOCHEMISTRY

Bayesian Parameter Inference for PICA Devolatilization Pyrolysis at High Heating Rates

Joffrey Coheur

Aeronautics and Aerospace Department, von Karman Institute for Fluid Dynamics, Belgium, joffrey.coheur@vki.ac.be

Supervisor: Thierry Magin

Professor, Aeronautics and Aerospace Department, von Karman Institute for Fluid Dynamics, Belgium, magin@vki.ac.be

University Supervisor: Maarten Arnst

Assistant Professor, Aerospatial & Mechanical Engineering, Université de Liège, Belgium, maarten.arnst@uliege.be

University Supervisor: Philippe Chatelain

Professor, Institute of mechanics, materials and civil engineering, Université catholique de Louvain, Belgium, philippe.chatelain@uclouvain.be

Abstract

We present a Bayesian approach for the inference and uncertainty quantification of kinetic parameters for the pyrolysis of Phenolic Impregnated Carbon Ablators (PICA). We first introduce a reparametrization of the pyrolysis equations that facilitates the application of the random walk Metropolis-Hastings and the adaptive Metropolis-Hastings algorithms. We show the effect of this transformation on a problem involving a two-component pyrolysis reaction and synthetic data. We then apply this methodology to the pyrolysis of PICA at high heating rates from the experiments of [1] and we finally quantify the uncertainties on the kinetic parameters and the mass loss of the PICA sample.

Keywords: inverse problem, bayesian, chemical kinetics, pyrolysis, thermal protection materials

1. Introduction

Ablative porous thermal protection materials (TPMs) are used for the heat shield of spacecraft of extra-orbital high-velocity entry missions. They can accommodate the high heating rates and heat loads encountered during hypersonic entry ([2]) through phase change and mass loss ([3]). First, the resin is progressively pyrolyzed, producing pyrolysis gases that percolate through the material and leave a carbonaceous residue on the fibers, the char. Then, this charred material is ablated simultaneously by heterogeneous chemical reactions, sublimation, and mechanical erosion.

Although nowadays baseline predictions are performed using high-fidelity simulation tools, the estimation of their associated uncertainties have received little attention. The first step for the quantification of uncertainty in numerical simulations is the characterization of input uncertainties by means of probability density functions (PDFs) that rely on experimental data; these PDFs can then be propagated through numerical solvers to assess error margins. In this paper, we propose a Bayesian approach to quantify the uncertainties in the parameters of laws governing the pyrolysis process of TPMs.

1.1. Literature review

Studies on ablative materials date back to the 60's with the development of early material response codes ([4; 5]) based on the experiments of [6] and [7]. Since then, these materials have been investigated from both the numerical and experimental perspectives. For predicting the material thermal decomposition, current models are still based on those previous experiments, although nowadays computer solvers allow the use of

more accurate models ([8; 9; 10; 11; 12; 13; 14]). Several experiments have been carried out more recently to get new insight into the pyrolysis of the resin ([15; 16; 17; 18; 19; 1]) and improve models for numerical solvers. In particular, there have been several efforts to infer the kinetic parameters in order to update the models based on these recent experiments. Most of the inference is performed in a deterministic framework, mainly by using optimization solvers to obtain best-fit estimates ([20]). For the application to TPMs, Torres Herrador *et al.* (2018) (see later in this Memorandum) performed deterministic optimization using genetic algorithms on the experiments of [1]. Although those algorithms can be very efficient and the results accurately reproduced the experiments, they do not account for the uncertainty on the parameters stemming from experimental measurement uncertainty, model inadequacy, parameter variability, etc. A correct characterization of those uncertainties is required to obtain a robust estimation of errors in numerical simulations for a better assessment of safety margins.

A few investigations on pyrolysis experiments from a stochastic view have been performed for fire technology ([21]), but to the author's knowledge no study of this kind has been performed in aerospace engineering for the pyrolysis of TPMs. A first study using Bayesian inference was already applied in [22] for parameter inference of the pyrolyis of phenolic materials using thermogravimetric analysis (TGA) data. It was shown however ([23]) that using gas production curves instead of TGA curves provides higher sensitivity for the inference as the production peak can be more clearly identified and more data is available. The objectives of this paper are therefore to perform parameter calibration and uncertainty analysis in a Bayesian framework for the pyrolysis of PICA TPM using gas species production curves.

In Section 2, we present the model for the pyrolysis decomposition. In Section 2 we present the general framework for the Bayesian inference and its implementation. In Section 3, we present a reparametrization of the pyrolysis model that facilitates the convergence of the Markov chains. In Section 4, we apply this methodology to the case of a two-step pyrolysis reaction with parameters taken from the theoretical open-source material TACOT ([24]). With those properties, we simulate synthetic pyrolysis production rate curves in order to apply Bayesian inference and show the feasibility of the method and the effect of the reparametrization. We then apply the proposed methodology to the experimental data of [1] for the pyrolysis of PICA at high heating rates.

2. Multi-component single-step pyrolysis model

We assume that a material sample of initial average virgin matrix density $\varepsilon_{\mathrm{mv}}\rho_{\mathrm{mv}}$ undergoes several independent pyrolysis reactions $p_i \rightarrow \sum_j \zeta_{ij} S_j$ for $i = 1, \ldots, N_{\mathrm{p}}$, where N_{p} denotes the number of components in the pyrolysis decomposition process, and $j = 1, \ldots, N_{\mathrm{g}}$, where N_{g} is the number of gas species. The following general model for the material pyrolysis is used ([13])

$$\partial_t \xi_i = (1-\xi_i)^{m_i} T^{n_i} k_i, \quad \xi_i \in [0,1], \tag{1}$$

$$\pi_j = \sum_i \varepsilon_{\mathrm{mv}}\rho_{\mathrm{mv}} \underbrace{\zeta_{ij} F_i}_{F_{ij}} \partial_t \xi_i, \tag{2}$$

$$\varepsilon\rho = (\varepsilon_{\mathrm{f}}\rho_{\mathrm{f}}) + \varepsilon_{\mathrm{mv}}\rho_{\mathrm{mv}} - \sum_i \varepsilon_{\mathrm{mv}}\rho_{\mathrm{mv}} F_{ij} \xi_i. \tag{3}$$

The ordinary differential equation (1) describes the evolution of the advancement ξ_i of the i-th pyrolysis reaction, where $(1-\xi_i)^{m_i}$ is called the reaction model, m_i is the reaction order and n_i is the temperature exponent which is generally assumed to be equal to zero for pyrolysis processes. The reaction rates for the pyrolysis decomposition in Eq. (1) are modeled using the Arrhenius equation

$$k_i = \mathcal{A}_i \exp\left(-\frac{\mathcal{E}_i}{\mathcal{R}T}\right), \tag{4}$$

which expresses the dependence of the reaction rate k_i on temperature and is widely used in chemical kinetics ([25], [26], [27]). Finally, Eqs. (2) and (3) represent the species production rate π_j and the average density (or mass) loss $\varepsilon\rho$ as a function of time, respectively.

[28] represent the relationship between the observed data d_k^{obs} and the computer model $\eta(\cdot,\cdot)$, here the pyrolysis model, as

$$d_k^{\mathrm{obs}} = \eta(\mathbf{x}_k, \mathbf{p}) + \varepsilon_k, \tag{5}$$

where ε_k is the observation error for the k-th observation among the n_{obs} observations (model error is not considered here). There are two distinct groups of inputs in the computer model η. The first group $\mathbf{p}$ are the calibration parameters, which we wish to learn about. For the pyrolysis decomposition model Eqs. (1)–(3) the uncertain parameter set we assume is $\mathbf{p} = \left\{\mathcal{A}_i, \mathcal{E}_i, m_i, F_{ij}\right\}$ whose size depends on the number of pyrolysis reactions N_{p} as well as on the number of gas species N_{g}. The $\mathbf{x}_k$ are called variable inputs whose value may change during the calibration

process. These are, for example, time or temperature which are supposed to be known.

In a deterministic inverse problem, one estimates a single value $\mathbf{p}_0$ for the parameters with a best fit approach. By contrast, in Bayesian inference, the result of the identification process is the so-called Bayesian posterior probability density

$$\pi(\mathbf{p}|\mathbf{d}^{\text{obs}}) = \frac{\pi(\mathbf{d}^{\text{obs}}|\mathbf{p})\pi_0(\mathbf{p})}{\int_{\Re^m} \pi(\mathbf{d}^{\text{obs}}|\mathbf{p})\pi_0(\mathbf{p})d\mathbf{p}}, \tag{6}$$

in which $\pi_0(\mathbf{p})$ is the prior probability density and $\pi(\mathbf{d}^{\text{obs}}|\mathbf{p})$ is the likelihood function. The **likelihood function** evaluates the plausibility of a value $\mathbf{p}$ of the parameters by calculating the probability of observing the data $\mathbf{d}^{\text{obs}}$ given that value of the parameters. We assume the observation errors to be independent and identically distributed (iid) following a Gaussian density of known variance σ_k (see, for instance, [29] for applications where σ_k is treated as a hyperparameter), thus leading to the following likelihood function

$$\pi(\mathbf{d}^{\text{obs}}|\mathbf{p}) = \frac{1}{(\Pi_k \sigma_k)(2\pi)^{n_{\text{obs}}/2}} \exp\left(-\sum_{k=1}^{n_{\text{obs}}} \frac{\left(d_k^{\text{obs}} - \eta(\mathbf{x}_k, \mathbf{p})\right)^2}{2\sigma_k^2}\right). \tag{7}$$

The **prior density** should compile all the information we know about the parameters before taking into account the data. In the absence of real physical consideration or expert assessment about the distribution of the parameters, we assume a uniform prior distribution whose bounds are large enough so that they do not influence the result of the inference problem. In this work, we assume a uniform prior density that is strictly positive. The **posterior density** is what we know about the parameters after observing the data and is what we want to know. In Bayesian inference, computations with Bayesian posteriors are performed by random explorations of the posterior distribution that provide samples directly drawn from it. These samples can then be used to estimate statistics of the posterior distribution (e.g. mean, variance, etc using Monte Carlo integration), or for propagation through numerical solvers for uncertainty quantification.

2.1. Marko chain Monte Carlo method

Markov Chain Monte Carlo (MCMC) methods are a general class of sampling methods to draw samples from a target distribution, here the posterior distribution $\pi(\mathbf{p}|\mathbf{d}^{\text{obs}})$ ([30]). A fundamental MCMC method is the Metropolis–Hastings algorithm, that was first proposed by [31] and later generalized by [32]. The Metropolis–Hasting algorithm for a multivariate target distribution $\pi(\mathbf{p}|\mathbf{d}^{\text{obs}})$ is summarized in Algorithm 1 ([33]). The Metropolis-Hastings algorithm draws samples from a distribution that is easier to simulate, the proposal distribution J, and the proposed samples $\mathbf{p}^*$ are then accepted or rejected according to the acceptance probability α. The collected samples $\mathbf{p}_l$ in Eq.(9) characterize fully the posterior distribution. Inserting Eq. (6) in the acceptance ratio (8) we obtain

$$r = \frac{\pi(\mathbf{d}^{\text{obs}}|\mathbf{p}^*)\pi_0(\mathbf{p}^*)J(\mathbf{p}^*|\mathbf{p}_{l-1})}{\pi(\mathbf{d}^{\text{obs}}|\mathbf{p}_{l-1})\pi_0(\mathbf{p}_{l-1})J(\mathbf{p}_{l-1}|\mathbf{p}^*)}, \tag{10}$$

for which we need to specify the likelihood function $\pi(\mathbf{d}^{\text{obs}}|\cdot)$, the prior density $\pi_0(\cdot)$ and the proposal distribution J.

Algorithm 1. Metropolis-Hastings algorithm

1: **Initialize** $\mathbf{p}_0$.
2: **Iteration** l:

a) Draw a new value $\mathbf{p}^*$ from proposal density $J(\mathbf{p}^*|\mathbf{p}_{l-1})$.

b) Calculate acceptance probability

$$\alpha(\mathbf{p}^*|\mathbf{p}_{l-1}) = \min\left(1, \frac{\pi(\mathbf{p}^*|\mathbf{d}^{\text{obs}})J(\mathbf{p}^*|\mathbf{p}_{l-1})}{\pi(\mathbf{p}_{l-1}|\mathbf{d}^{\text{obs}})J(\mathbf{p}_{l-1}|\mathbf{p}^*)}\right). \tag{8}$$

c) Sample u from a uniform random variable with values in $[0, 1]$. Set

$$\mathbf{p}_l = \begin{cases} \mathbf{p}^* & \text{if } u \leq \alpha(\mathbf{p}^*|\mathbf{p}_{l-1}), \\ \mathbf{p}_{l-1} & \text{otherwise.} \end{cases} \tag{9}$$

3: **Continue** until convergence.

2.2. Random-walk Metropolis-Hastings algorithms

When the proposal distribution is taken to be symmetric $J(\mathbf{p}_{l-1}|\mathbf{p}^*) = J(\mathbf{p}^*|\mathbf{p}_{l-1})$, and if we assume a uniform prior density, the acceptance ratio simplifies to

$$r = \frac{\pi(\mathbf{d}^{\text{obs}}|\mathbf{p}^*)}{\pi(\mathbf{d}^{\text{obs}}|\mathbf{p}_{l-1})}. \tag{11}$$

In this case, the acceptance ratio is only driven by the ratio of the likelilhood functions. If the new sample $\mathbf{p}^*$ increases the likelihood, the ratio is larger than 1

and $\mathbf{p}^*$ is always accepted. If the likelihood decreases, the proposed value is not necessarily rejected but is accepted with a probability of r. In practice, we only need to sample from J for determining the new value of the estimate $\mathbf{p}^*$. Finally, when the proposal distribution is of the form $J(\mathbf{p}^*|\mathbf{p}_{l-1}) = J(|\mathbf{p}^* - \mathbf{p}_{l-1}|)$ such as a Gaussian distribution, then the algorithm is called random Walk Metropolis-Hastings (RWMH). We choose the proposal distribution to be a multivariate Gaussian distribution centered on $\mathbf{p}_{l-1}$ with covariance matrix Σ

$$J(\mathbf{p}^*|\mathbf{p}_{l-1}) = \frac{1}{\sqrt{(2\pi)^{n_\mathrm{p}} \det\Sigma}} \exp\left(-\frac{1}{2}\left(\mathbf{p}^* - \mathbf{p}_{l-1}\right)^{\mathrm{T}} \Sigma^{-1} \left(\mathbf{p}^* - \mathbf{p}_{l-1}\right)\right). \quad (12)$$

To accelerate the convergence of the Markov chain, a different version of the RWMH, the adaptive Metropolis-Hastings (AMH) ([34]) algorithm updates the covariance matrix based on previous iterations at given interval length i_L. The initial covariance matrix Σ will generally be assumed to be a diagonal matrix where the diagonal elements are tuned by trial-and-error to reach a good acceptance rate.

3. Reparametrization of the pyrolysis model

Convergence of the Markov chain to the posterior distribution can be slow for complex target distributions. It can be the case for strongly correlated parameters for which the covariance matrix is unknown or difficult to estimate and for strongly non-Gaussian posterior PDFs. As the Arrhenius parameter pairs ($\mathcal{A}_i$, $\mathcal{E}_i$) are both strongly correlated and non Gaussian, we propose here to use a reparametrization ([35]) of the Arrhenius equation for pyrolysis modeling based on the work of [36] that we extend to the pyrolysis modeling of TPMs. We show that this reparametrization is suitable for the RWMH and the AMH algorithms since it can achieve fast convergence in a relatively small number of iterations.

We consider the parameter set $\mathbf{p}$ introduced in Section 2 with N_p different reaction rates. We apply the same reparametrization for $\mathcal{A}_i$ and $\mathcal{E}_i$ as in [36] and [37] for deterministic parameter estimation, and we introduce two additional scaling factors for m_i and F_{ij}

$$\tilde{\mathcal{A}}_i = \ln \mathcal{A}_i - \mathcal{E}_i/(\mathcal{R}\overline{T}_i), \quad (13)$$

$$\tilde{\mathcal{E}}_i = \mathcal{E}_i/\overline{\mathcal{E}}_i, \quad (14)$$

$$\tilde{m}_i = m_i/\bar{m}_i, \quad (15)$$

$$\tilde{F}_i = F_{ij}/\overline{F}_{ij}. \quad (16)$$

This parametrization does not affect the reaction rates k_i and the observed data, thus making this expression very convenient for the current modeling. A normalization common in combustion literature was also discussed by [27] for its use in uncertainty quantification, but this normalization does not consider the logarithmic dependence of the pair $\mathcal{A}_i$ and $\mathcal{E}_i$, neither the translation used in Eq. (13).

Considering these new parameters, reaction rates are now expressed as

$$k_i = \exp\left(\tilde{\mathcal{A}}_i + \tilde{\mathcal{E}}_i \tilde{T}_i(t)\right), \quad (17)$$

where $\tilde{T}_i = \overline{\mathcal{E}}_i/\mathcal{R}(1/T + 1/\overline{T}_i)$ is called the local reciprocal temperature ([37]). Both $\tilde{\mathcal{A}}_i$ and $\tilde{\mathcal{E}}_i$ are scaled parameters that now appear in the exponential term, thus making the search more robust and the MCMC proposal covariance matrix easier to tune. We denote the scaling factors by $\overline{\mathbf{p}} = \left\{\overline{\mathcal{A}}_i, \overline{\mathcal{E}}_i, \overline{m}_i, \overline{F}_{ij}\right\}$. An appropriate choice of the scaling factors $\overline{\mathbf{p}}$ is very important and we strive to tune the reparametrization so that it has the effect of rescaling the posterior density to a smaller range of values around 1. We will show in the next section on a two-step pyrolysis process starting from known parameters that this reparametrization improves convergence and facilitates the process of estimating the covariance matrix for the proposal function.

The reparametrization affects the acceptance ratio from Eq. (11). If we denote this transformation by $\tilde{\mathbf{p}} = s(\mathbf{p})$ and the inverse change by s^{-1}, we can show that now

$$r = \frac{\det\left(\dfrac{d(s^{-1}(\tilde{\mathbf{p}}))}{d\tilde{\mathbf{p}}}|_{\tilde{\mathbf{p}}=\tilde{\mathbf{p}}^*}\right)\pi(d|s^{-1}(\tilde{\mathbf{p}}^*))}{\det\left(\dfrac{d(s^{-1}(\tilde{\mathbf{p}}))}{d\tilde{\mathbf{p}}}|_{\tilde{\mathbf{p}}=\tilde{\mathbf{p}}_{i-1}}\right)\pi(d|s^{-1}(\tilde{\mathbf{p}}_{i-1}))}. \quad (18)$$

For linear transformations, we see directly that the acceptance ratio is unaffected by the reparametrization. In the case of non-linear transformations, the determinant of the Jacobian is non constant and must be computed explicitly. In this case, the determinant of the Jacobian of the transformation introduced previously is

$$\det = \prod_i^{N_\mathrm{p}} \exp(\tilde{\mathcal{A}}_i + \tilde{\mathcal{E}}_i \overline{X}_i) = \prod_i^{N_\mathrm{p}} \mathcal{A}_i. \quad (19)$$

4. Reconstructing Arrhenius parameter uncertainties

Synthetic data based on a known set of nominal parameter values are generated and MCMC methods are

	$\mathcal{A}$	$\mathcal{E}$	m	F
Reaction I	541218	74046.7	9.08	0.11
Reaction II	5360000	103680	5.07	0.35

Table 1: Nominal values for the parameters of the two-reaction pyrolysis model.

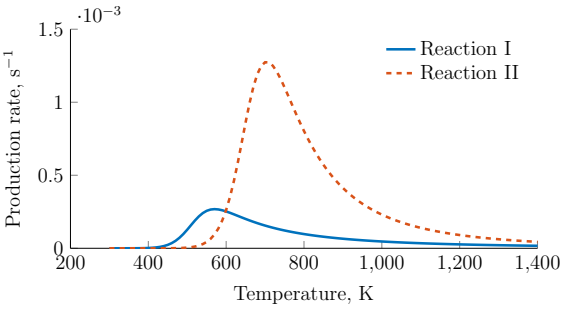

Figure 1: Synthetic production rate curves obtained using values from Table 1.

applied to draw samples from the unknown posterior distribution. The objective of the Bayesian inference here is twofold: firstly, we wish to obtain probability density functions based on simulated data rather than expert judgments, and secondly, we wish to understand the correlation between the parameters and we want to test on this simple case the effect of the reparametrization on the sampling of the posterior distribution.

The following analysis is performed using a Matlab code implementing a 0D pyrolysis model for which the computational cost of a single estimation is cheap. We generate synthetic data as shown in Fig. 1 using the nominal set of parameters summarized in Table 1.

In this case, the pyrolysis model features two equations for the material decomposition ($N_\mathrm{p} = 2$) and we do not make any assumption on the gas composition but we rather consider the pyrolysis gas as a whole ($N_\mathrm{g} = 1$). Synthetic data for the total production rate are assumed to have an additive Gaussian noise with variance σ^2 on the nominal solution, as in Eq. (5). The variance is assumed to be known and constant as a function of temperature. Hence, we choose constant values $\sigma_1 = 0.1490$ s^{-1} and $\sigma_2 = 0.5382$ s^{-1}. We use 1100 data points for each curve between $T_\mathrm{min} = 300$ K and $T_\mathrm{max} = 1400$ K. This number of points is typically higher than what we have in real experiments but it is observed that faster convergence of the MCMC chain is achieved when using a larger amount of data points.

Because we know the production curve of each pyrolysis compound, the two subsets of uncertain parameters are independent and we can perform the Bayesian calibration using the two curves separately. We denote $\mathbf{p}_1$ and $\mathbf{p}_2$ these two subsets such that $\mathbf{p} = \{\mathbf{p}_1, \mathbf{p}_2\}$ with $\mathbf{p}_i = \{\mathcal{A}_i, \mathcal{E}_i, m_i, F_i\}$ and we calibrate those two subsets individually. We apply the reparametrization to the subset of parameters introduced in the previous section with scaling factors obtained from the nominal parameters from Table 1. For the reference temperatures, we use the argument of the maximum production rate of the two curves, which are in this case $\overline{T}_1 = 580$ K and $\overline{T}_2 = 710$ K. The posterior distribution is sampled using the random-walk adaptive Metropolis-Hastings algorithm and in particular, the reparametrization allows the use of the AMH algorithm as the proposal function (unimodal multivariate Gaussian) which is more appropriate to sample the posterior distribution. The number of iterations is 10^5 for each curve and the procedure is run three times to ensure that the algorithm converges towards the target PDF.

The maximum likelihood estimator[1] (MLE) defined as $\mathbf{p}_\mathrm{MLE} = \arg\max_\mathbf{p} \pi(\mathbf{d}^\mathrm{obs}|\mathbf{p})$, reproduces correctly the nominal parameters from Table 1. Results for the bivariate joint PDFs are shown in Fig. 3 and 4 using scatter plots where the density of dots is proportional to the probability density. Blue dots are the parameters obtained from the first reaction and the red dots are for the second reaction. From Fig. 3, the correlation between $(\mathcal{E}_i, \mathcal{A}_i)$ pairs clearly appears: as expected, $\mathcal{A}_i$ varies as the exponential of $\mathcal{E}_i$ and is strongly elongated. For the pairs (F_i, m_i), $(m_i, \{\mathcal{E}_i, \mathcal{A}_i\})$, the scatter plots suggest also a correlation. Nearly horizontal or nearly vertical trends may indicate a low correlation between the remaining parameter pairs $(F_i, \{\mathcal{A}_i, \mathcal{E}_i\})$ but that may also indicate that the scaling of the axis is too large. The correlations are further emphasized from the scatter plots in Fig. 4, where the plots now represent parameter values after the reparametrization. As expected, the same trends as previously are observed. It can be further observed that the pairs $(F_i, \{\mathcal{A}_i, \mathcal{E}_i\})$ show almost no correlation indicated by the nearly circular shape. Still from Fig. 4, we can see that the scatter plots for all parameter pairs almost overlap, showing that the reparametrization is efficient and explains why the sampling works more efficiently. The proposal covariance matrix Σ requires almost no tuning and only a diagonal matrix with a unique value was provided to

[1] When considering a uniform prior in Eq. (6), the MLE is equivalent to the maximum a posteriori (MAP), defined as $\mathbf{p}_\mathrm{MAP} = \arg\max_\mathbf{p} \pi(\mathbf{p}|\mathbf{d}^\mathrm{obs})$, and both are used indifferently.

the algorithm. Adaptation of the covariance proposal was performed by the AMH algorithm thus further enhancing the convergence of the Markov chain. Finally, we can see that the uncertainty on the parameter set $\mathbf{p}_1$ is larger than on the parameter set $\mathbf{p}_2$ indicated by a wider dot density area. We can understand why by computing the coefficient of variations (CVs), defined as the ratio of the standard deviation to the mean, at the peak of the two production rate curves from Fig.1. We have $\mathrm{CV}_1 = 0.1490/0.000268 = 555.97$ and $\mathrm{CV}_2 = 0.5382/0.001273 = 422.78$, showing a higher relative uncertainty on the first pyrolysis curve. Of course, this result depends strongly on the choice for σ_1 and σ_2, which could have been different.

5. Bayesian parameter inference for the pyrolysis of PICA

Here we use the experimental data of [1] for the pyrolysis of PICA and we perform the Bayesian calibration procedure detailed in Sections 3 and 4. There are however two main issues in this case: we do not know what the pyrolysis model we need to use is and we do not have good initial parameter estimates to use in the reparametrization. The following two-step strategy is therefore proposed to overcome those problems. Firstly, we adapt the reparametrization procedure, where the acceptance rate is monitored to a target value. When the acceptance rate becomes very low or too high, we use the current Maximum Likelihood Estimator (MLE) as a new value for rescaling the factors appearing in the reparametrization from Eqs.(13)–(16). Because at every iteration in the MCMC process the likelihood function is computed, it is straightforward to obtain the MLE at the lth iteration. This idea is similar to the AMH algorithm, in which the covariance of the proposal function is directly updated, except that here we directly rescale the posterior distribution so that it fits to the proposal distribution. Secondly, because we do not know what pyrolysis model to use, we build it on-the-fly by first inferring on a one-equation model using a single experimental curve. Once we have converged to the target PDF for the parameters $\mathcal{A}_1$, $\mathcal{E}_1$, m_1 and F_{11}, we increase by one the number of experimental curves in the calibration (we add one species j). If a new reaction peak is observed in the data, we increase the number of equations by one and we need to calibrate the new set of parameters $\mathcal{A}_2, \mathcal{E}_2, m_2$ and F_{21} together with the previous set of parameters (for which we now have an initial guess). If a reaction already exists at the new peak, then we just need to calibrate the new mass fraction F_{12}. This procedure is repeated until the model gives satisfactory results compared to the data. In the end, the following five-equation model was found for the calibration of the experimental production rate curves and comparison of the calibration curves are shown in Fig. 5

$$
\begin{aligned}
&\mathrm{R}_1(s) \xrightarrow{k_1} F_{1,1}\mathrm{H_2O} + F_{1,2}\mathrm{CO_2} + \\
&\quad F_{1,3}(\text{1-propanol}) \\
&\mathrm{R}_2(s) \xrightarrow{k_2} \begin{array}{l} F_{2,1}\mathrm{H_2O} + F_{2,2}\mathrm{CO} + \\ F_{2,3}\mathrm{CO_2} + F_{2,4}\mathrm{Phenol} + \\ F_{2,5}\mathrm{Cresol} + \\ F_{2,6}(\mathrm{Dimethyl\ Phenol}) + \\ F_{2,7}(\mathrm{Trimethyl\ Phenol}) \end{array} \\
&\mathrm{R}_3(s) \xrightarrow{k_3} \begin{array}{l} F_{3,1}\mathrm{CH_4} + F_{3,2}\mathrm{H_2O} + \\ F_{3,3}\mathrm{CO} + F_{3,4}\mathrm{H_2} + \\ F_{3,5}\mathrm{CO_2} + F_{3,6}\mathrm{Xylene} + \\ F_{3,7}\mathrm{Benzene} + F_{3,8}\mathrm{Toluene} \end{array} \\
&\mathrm{R}_4(s) \xrightarrow{k_4} F_{4,1}\mathrm{H_2} \\
&\mathrm{R}_5(s) \xrightarrow{k_5} F_{5,1}\mathrm{H_2} + F_{5,2}\mathrm{CH_4} + \\
&\quad F_{5,3}\mathrm{H_2O} + F_{5,4}\mathrm{CO}
\end{aligned}
$$

This model is not unique and other models could be found. More complex models could better fit the data but are less likely to be general to other pyrolysis experiments and are longer to run, while simpler models could still achieve good fitting with faster run time. Accuracy versus simplicity could be taken into account in the definition of the model structure but it is not performed here and is left for future work.

To obtain the results from Fig. 5, we assume that σ_k in the likelihood function is fixed and known with its value already estimated in [1] although this estimation of σ_k is questionable as it comes from 3 experimental runs. It is also observed experimentally that σ_k varies as a function of the temperature and can be nearly zero where the production rate is zero. This makes the computation of the likelihood close to zero and the calculation of the acceptance ratio undefined. To avoid this problem, we use a constant value for σ_k in the tails of the production rate curves equal to the maximum σ_k over the temperature range. By using the maximum value, we also avoid giving too much importance to the tail of the production rate curves in the calibration process. Using the previous model,

the number of parameters to infer is equal to 40. We run the RWMH algorithm during 10^6 iterations using the final pyrolysis model. The solution of the algorithm provides parameter values sampled from the 40-dimensional posterior PDF, which is quite difficult to characterize. Again, marginal means and standard deviations can be obtained but do not provide information about the correlation of the different parameters. The covariance matrix of size 40×40 can be computed but is not shown here. The rejection rate computed after the 10^6 iterations is equal to 78%.

5.1. Uncertainty propagation

Samples from the posterior PDF can be propagated individually through the model and statistics can be obtained using Monte Carlo integration. This approach is feasible here as the numerical model we use is sufficiently cheap. Samples were already used for the simulation of species production curves during the Bayesian inference process as it was computed for the estimation of the likelihood function (7). Individual species gas production curves are shown in Fig. 5. The shaded area represents all the possible outcomes from the propagated solutions through the model. Results are consistent with the experimental data provided and the uncertainty bounds.

Individual samples are propagated to simulate sample mass loss (simulated TGA curve) and the result is compared with the experimental data in Fig. 2. Results of the propagation show a good agreement with the experimental results. There is a slight underestimation of the mass loss starting at 500 K due to underestimation of the CO production rate curve, which in terms of mass is the most dominant produced species. This could be improved by incorporating CO production into the first reaction R_1. The uncertainty on the mass loss increases with temperature and in particular after the steep mass decrease. The uncertainty of the final mass also implies uncertainty on the final mass of char, which is given by the final mass of the sample assuming all pyrolysis reactions have occurred. It is found here that the average final mass loss is equal 80% of its initial mass with a 95% confidence interval CI = [77%, 82%] and a Gaussian-shaped PDF.

6. Conclusions

A Bayesian approach to the challenge of model calibration for the devolatilization of PICA thermal protection material has been presented.

We showed using a simple two-component pyrolysis reaction that the reparametrization of the pyrolysis

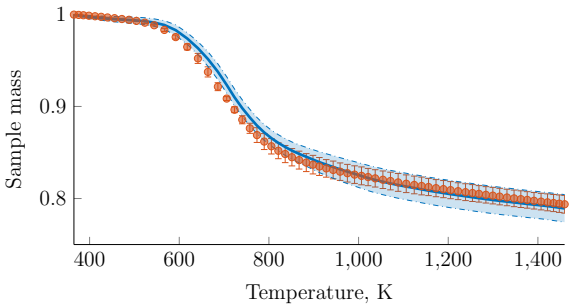

Figure 2: Propagation of the MCMC samples for the prediciton of the normalized mass sample. The symbols with the error bars represent the experimental results from [1]. The continuous line is the result of the propagation for the MLE and the shaded area with dashed lines represent all the possible outcomes of the propagation using every samples from the posterior distribution.

equations rescales and translates the marginal posterior distribution around unit value, rendering it more like a multivariate Gaussian density and therefore allowing the use of a proposal density that is easy to tune. We showed that the proposed Bayesian calibration methodology leads to a posterior distribution whose mode is concentrated around the correct nominal parameter values and we observed the correlation between the parameters. In particular, we observed the non-linear relation and the strong correlations between the Arrhenius parameters $\mathcal{A}$ and $\mathcal{E}$. In future studies, samples from the joint PDF could be directly used for sensitivity analysis and propagation through simulation tools such as the material-response code PATO ([13]) in order to perform uncertainty quantification. Characterizing the full joint posterior distribution is however challenging, in particular for a high-dimensional posterior.

We presented the results of the Bayesian inference on experimental data on the pyrolysis of PICA ([1]) and we showed that this approach was capable of reproducing experimental species production curves and their errors with good accuracy. Samples from the posterior distribution characterizing the uncertainties on model parameters were propagated to obtain the uncertainty on the final mass loss. In the future, we need to consider more experimental data in the inference procedure including, for example, the different heating rates from [1] or the piecewise linear constant heating rate from [18]. It is however likely that a multi-component single step pyrolysis model as studied in this work may lack generality and may not be able to reproduce experiments from different heating rates. This issue will be discussed later in this Techni-

cal Memorandum.

Improvement of the Bayesian calibration methodology presented here is sought as future work. Ideally, it could be interesting to perform a first model inference providing a set of plausible models in a Bayesian inference framework ([38]) and secondly to perform an optimization search for obtaining a best estimate (Torres Herrador *et al.* (2018)). The model could then be fixed and the MCMC procedure could be started from this value. In the case of model inference, we would consider N_p varying and we would apply model inference for quantifying which model is more appropriate, while fostering simple models. MCMC jumps between the model with different number of reactions then need to be incorporated ([38]).

Finally, we used here cheap computational models. For computationally expensive models however, other methods for uncertainty propagation must be sought such as building surrogate models and reduced order models. Then the individual samples from the posterior PDF can be propagated.

Acknowledgments

The first author work is supported by the Fund for Research Training in Industry and Agriculture (FRIA) provided by the Belgian Fund for Scientific Research (F.R.S.-FNRS) and by the Wallonie-Bruxelles International (WBI) fellowship for excellence (WBI.World). The first author would like to thank F. Torres Herrador for the valuable discussions about pyrolysis modeling and results from the deterministic inference. Finally, the first author is indebted to Dr. Nagi Mansour and to the NASA Advanced Supercomputing Division for welcoming and for providing me the opportunity to carry out this work at NASA Ames Research Center.

References

[1] B. K. Bessire, T. K. Minton, Decomposition of phenolic impregnated carbon ablator (PICA) as a function of temperature and heating rate, ACS Appl. Mater. Inter. 9 (2017) 21422–21437.

[2] J. D. Anderson, Hypersonic and High Temperature Gas Dynamics, 2nd Edition, AIAA Education Series, 2006.

[3] G. Duffa, Ablative thermal protection systems modeling, American Institute of Aeronautics and Astronautics, Inc., Reston, Virginia, 2013.

[4] R. M. Kendall, E. P. Barlett, R. A. Rindal, C. B. Moyer, An Analysis of the Coupled Chemically Reacting Boundary Layer and Charring Ablator: Part I., CR-1060, NASA (1968).

[5] Y.-K. Chen, F. S. Milos, Ablation and thermal response program for spacecraft heatshield analysis, Journal of Spacecraft and Rockets 36 (3) (1999) 475–483.

[6] G. F. Sykes, Decomposition Characteristics of a Char-Forming Phenolic Polymer Used for Ablative Composites, Tech. rep., NASA TN D-3810 (1967).

[7] H. E. Goldstein, Pyrolysis Kinetics of Nylon 6-6, Phenolic Resin, and Their Composites, Journal of Macromolecular Science: Pt. A - Chemistry 3 (4) (1969) 649–673.

[8] D. Bianchi, A. Turchi, N. Francesco, O. Marcello, Coupled CFD analysis of thermochemical erosion and unsteady heat conduction in solid rocket nozzles, in: 48th AIAA/ASME/ASEE Joint Propulsion Conference & Exhibit, Atlanta, GA, 2012, pp. 1–15. doi:10.2514/6.2012-4318.

[9] A. Martin, Volume averaged modeling of the oxidation of porous carbon fiber material, in: 44th AIAA Thermophysics Conference, San Diego, CA, 2013, pp. 1–14.

[10] Y.-K. Chen, T. Gökçen, Implicit coupling approach for simulation of charring carbon ablators, Journal of Spacecraft and Rockets 51 (3) (2014) 779–788.

[11] A. Martin, I. Boyd, Strongly coupled computation of material response and nonequilibrium flow for hypersonic ablation, Journal of Spacecraft and Rockets 52 (1) (2015) 89–104.

[12] P. Schrooyen, K. Hillewaert, T. E. Magin, P. Chatelain, Fully Implicit Discontinuous Galerkin Solver to Study Surface and Volume Ablation Competition in Atmospheric Entry Flows, International Journal of Heat and Mass Transfer 103 (2016) 108–124. doi:http://dx.doi.org/10.1016/j.ijheatmasstransfer.2016.07.022.

[13] J. Lachaud, J. Scoggins, T. Magin, M. Meyer, N. Mansour, A generic local thermal equilibrium model for porous reactive materials submitted to high temperatures, International Journal of Heat and Mass Transfer 108 (2017) 1406–1417. doi:10.1016/j.ijheatmasstransfer.2016.11.067.

[14] J. Coheur, A. Turchi, P. Schrooyen, T. Magin, Development of a unified model for flow-material interaction applied to porous charring ablators, in: 47th AIAA Thermophysics Conference, American Institute of Aeronautics and Astronautics, Denver, CO, US, 2017, pp. 1–13. doi:https://doi.org/10.2514/6.2017-3684.

[15] K. A. Trick, T. E. Saliba, Mechanisms of the pyrolysis of phenolic resin in a carbon/phenolic composite, Carbon 33 (11) (1995) 1509–1515.

[16] K. A. Trick, T. E. Saliba, S. S. Sandhu, A kinetic model of the pyrolysis of phenolic resin in a carbon/phenolic composite, Carbon 35 (3) (1997) 393–401.

[17] H.-W. Wong, J. Peck, R. Bonomi, J. Assif, F. Panerai, G. Reinish, J. Lachaud, N. Mansour, Quantitative determination of species production from phenol-formaldehyde resin pyrolysis, Polymer Degradation and Stability 112 (2015) 122–131.

[18] H.-W. Wong, J. Peck, J. Assif, F. Panerai, J. Lachaud, N. Mansour, Detailed analysis of species production from the pyrolysis of the phenolic impregnated carbon ablator, Journal of Analytical and Applied Pyrolysis 122 (2016) 258–267.

[19] B. K. Bessire, S. A. Lahankar, T. K. Minton, Pyrolysis of Phenolic Impregnated Carbon Ablator (PICA), ACS Appl. Mater. Inter. 7 (3) (2015) 1383–1395.

[20] C. Lautenberger, C. Fernander-Pello, Optimization algorithms for material pyrolysis property estimation, Fire Safety Science 10 (2011) 751–764. doi:10.3801/IAFSS.FSS.10-751.

[21] M. Bruns, Inferring and propagatin kinetic parameter uncertainty for condensed phase burning models, Fire Technology 52 (2016) 93–120.

[22] J. Coheur, M. Arnst, P. Chatelain, T. Magin, A first step towards the bayesian inference of uncertain kinetic parameters of pyrolysis decomposition laws, in: 9th VKI PhD Symposium, Rhodes-Saint-Genèse, Belgium, 2018, pp. 1–9.

[23] F. J. Torres Herrador, Thermal characterization of ablative materials, Master's thesis, von Karman Institute for Fluid Dynamics, Rhode-Saint-Genèse, Belgium (2016).
[24] J. Lachaud, A. Martin, T. Van Eekelen, I. Cozmuta, Ablation test-case series #2, in: 5th Ablation Workshop, Lexington, Kentucky, 2012, pp. 10–18.
[25] B. L'vov, Thermal Decomposition of Solids and Melts, english Edition, Springer, 2007.
[26] F. V. Domingo, L. C. Rodrigo, A. R. Greus, Thermal characterisation of polymeric materials, Universitat Politcnica de Valncia, 2008.
[27] J. Urzay, N. Kseib, P. G. Constantine, D. F. Davidson, G. Iaccarino, Uncertainty-quantifying models for chemical-kinetic rates, Center for Turbulence Research Annual Briefs.
[28] M. C. Kennedy, A. O'Hagan, Bayesian calibration of computer models, Journal of the Royal Statistical Society 63 (3) (2001) 425–464.
[29] H. Najm, R. Berry, C. Safta, K. Sargsyan, B. Debusschere, Data-free inference of uncertain parameters in chemical models, International Journal for Uncertainty Quantification 4 (2014) 111–132.
[30] C. P. Robert, G. Casella, Monte Carlo Statistical Methods, Springer N.-Y., 1999. doi:10.1007/978-1-4757-3071-5.
[31] N. Metropolis, A. W. Rosenbluth, M. N. Rosenbluth, A. H. Teller, T. E., Equation of state calculations by fast computing machines, Journal of Chemical Physics 21 (1953) 1087–1092.
[32] W. K. Hastings, Monte Carlo sampling methods using Markov chains and their applications, Biometrika 5 (1) (1970) 97–109.
[33] R. C. Smith, Uncertainty Quantification: Theory, Implementation, and Applications, Society for Industrial and Applied Mathematics, Philadelphia, 2014.
[34] H. Haario, E. Saksman, J. Tamminen, An adaptive Metropolis algorithm, Bernoulli 7 (2) (2001) 223–242.
[35] W. R. Gilks, S. Richardson, D. J. Spiegelhalter, Markov Chain Monte Carlo in Practice, Chapman & Hall/CRC, London, 1996.
[36] O. E. Rodionova, A. L. Pomerantsev, Estimating the parameters of the arrhenius equation, Kinetics and Catalysis 46 (3) (2005) 305–308. doi:10.1007/s10975-005-0077-9.
[37] A. L. Pomerantsev, A. V. Kutsenova, O. Y. Rodionova, Kinetic analysis of non-isothermal solid-state reactions: multistage modeling without assumptions in the reaction mechanism, Physical Chemistry Chemical Physics 19 (5) (2017) 3606–3615. doi:10.1039/c6cp07529k.
[38] N. Galagali, Y. M. Marzouk, Bayesian inference of chemical kinetic models from proposed reactions, Chemical Engineering Science 123 (2015) 170–190. doi:10.1016/j.ces.2014.10.030.

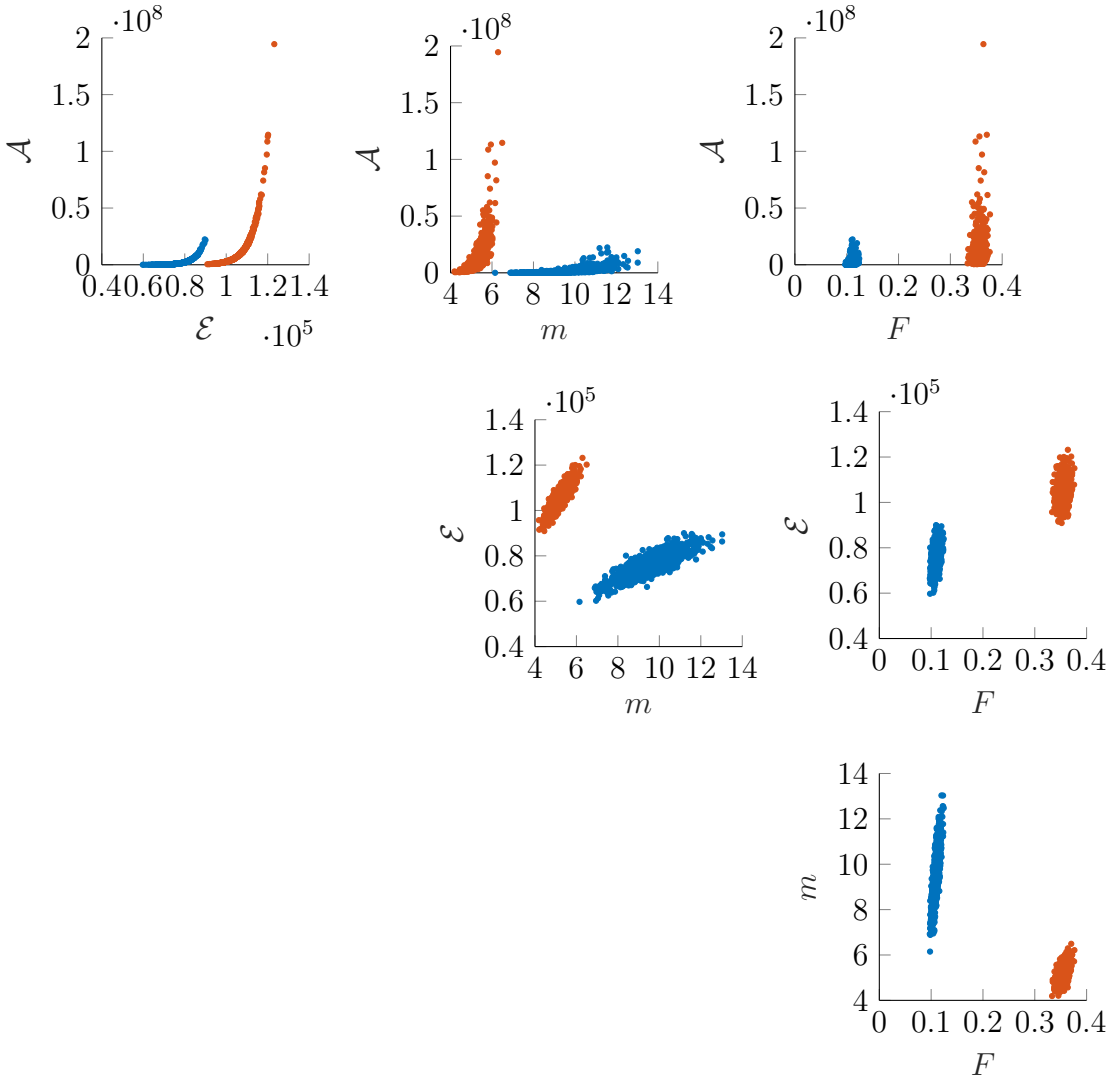

Figure 3: Scatter plots for the unscaled parameter values representing pairwise bivariate posterior distributions. Blue dots are the parameters obtained from the first reaction and the red dots are for the second reaction.

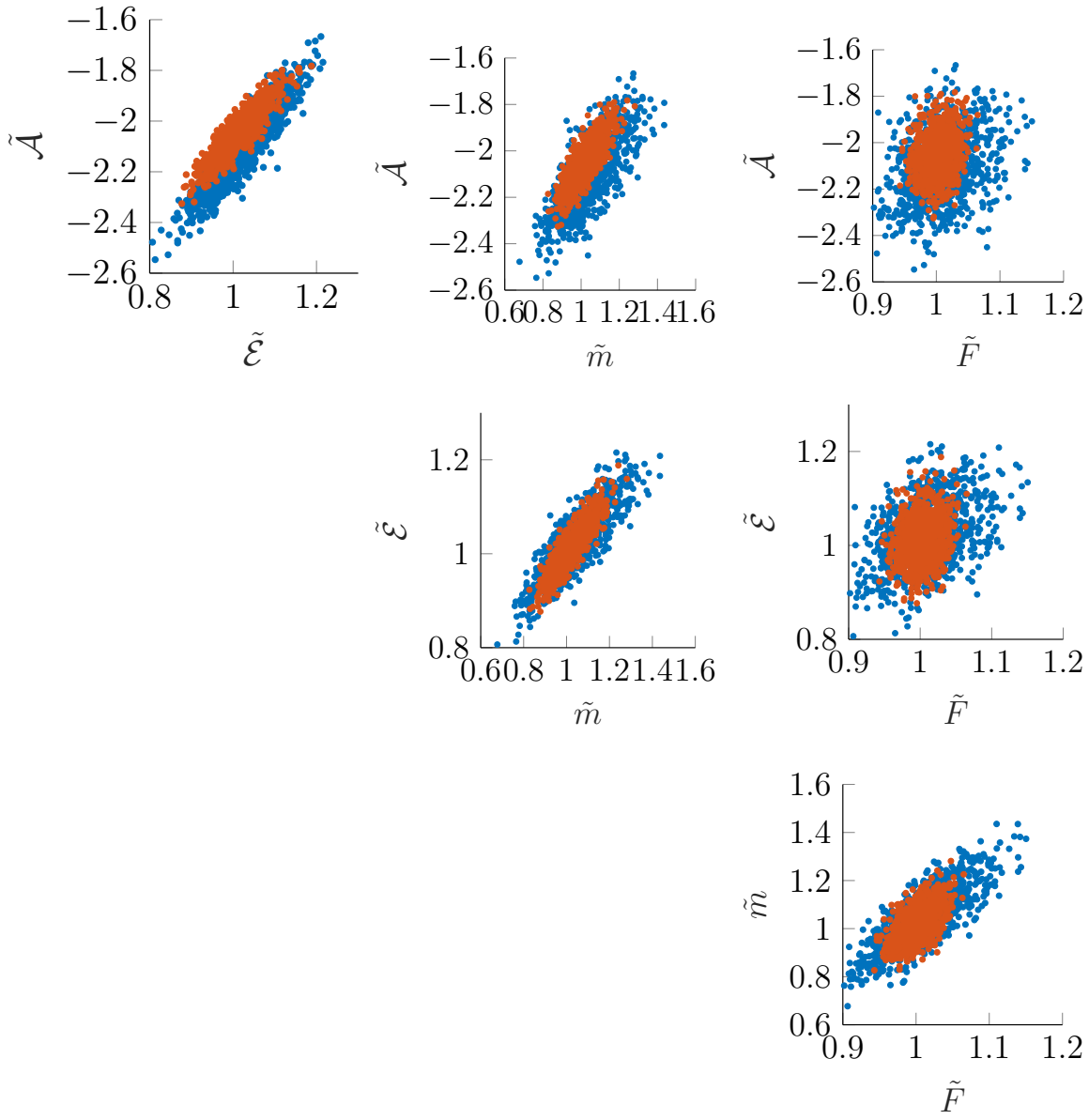

Figure 4: Scatter plots after the reparametrization representing pairwise bivariate posterior distributions. Blue dots are the parameters obtained from the first reaction and the red dots are for the second reaction.

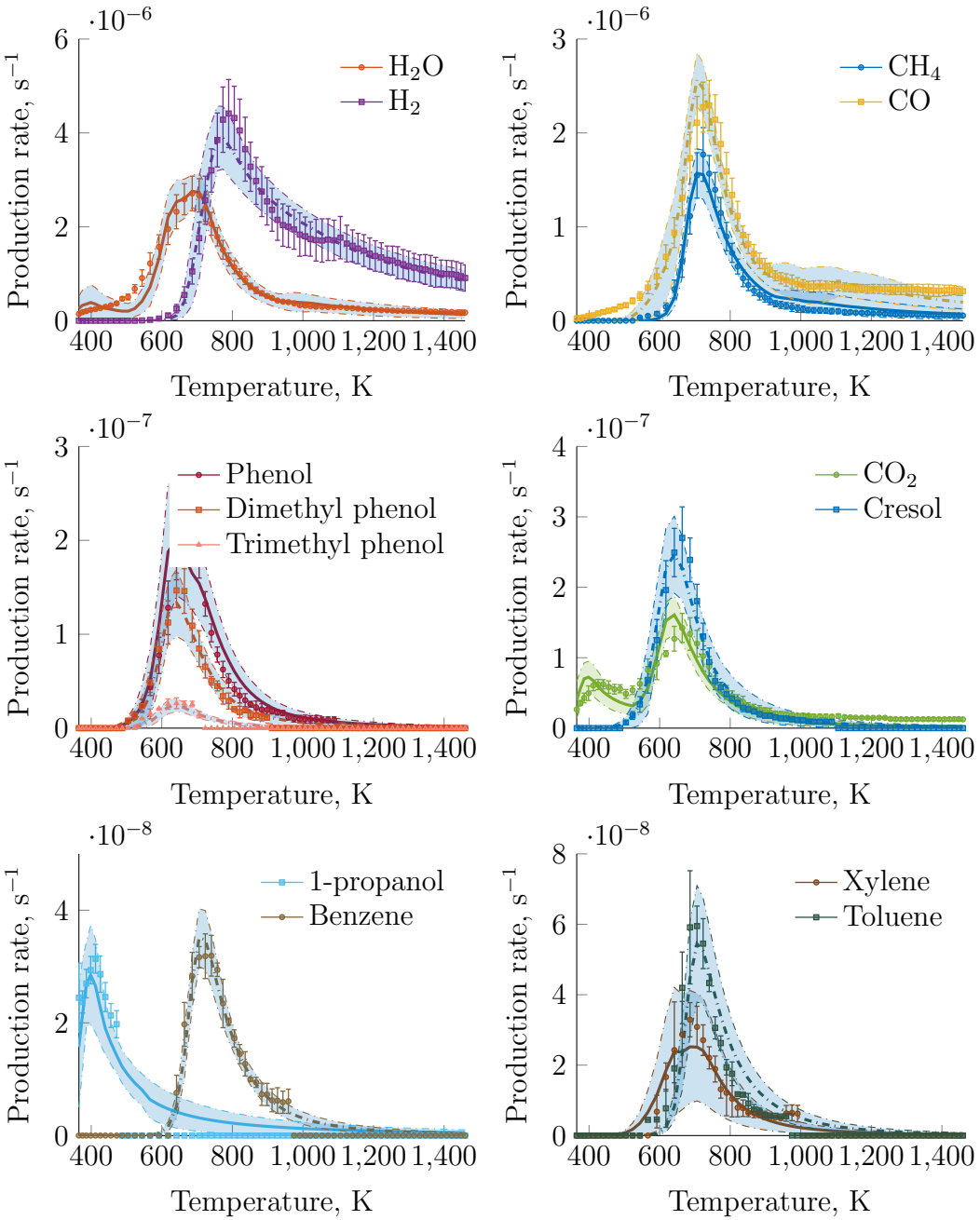

Figure 5: Production rate curves of each species as a function of temperature obtained after the propagation of the MCMC samples. The symbols with the error bars represent the experimental results from [1]. The continuous lines are the results of the propagation for the maximum likelihood estimator and the shaded areas with dashed lines represent all the possible outcomes of the propagation using every samples from the posterior distribution.

Towards a Systematic Framework for the Design of Experiments: Application to Catalytic Phenomena in Plasma Wind Tunnels

Anabel del Val

Aeronautics and Aerospace Department, von Karman Institute for Fluid Dynamics, Belgium, ana.isabel.del.val.benitez@vki.ac.be

Supervisors: Olivier Chazot and Thierry Magin

Head of Department and Professor, Aeronautics and Aerospace Department, von Karman Institute for Fluid Dynamics, Belgium, chazot@vki.ac.be

Professor, Aeronautics and Aerospace Department, von Karman Institute for Fluid Dynamics, Belgium, magin@vki.ac.be

University Supervisor: Pietro Congedo

Research Scientist, DeFI Team (INRIA Saclay Île-de-France, École Polytechnique). Centre de Mathématiques Appliquées (CMAP), École Polytechnique, France, pietro.congedo@inria.fr

Abstract

The underlying interplay between model, experiments and simulations lies at the core of engineering applications. In this work, state-of-the-art uncertainty quantification techniques are applied to the characterization of catalytic thermal protection system using plasma wind tunnel experiments. A Bayesian inference framework, derived in a previous work, is now extended to other testing methodologies and testing conditions. A 3-probes testing methodology is evaluated to extract catalytic values for the reference material commonly used for ground testing. A discussion and evaluation of both methodologies is included, comparing the quality of results that can be achieved and the consequences of the experimental conditions. To assess whether or not the calibration of the reference parameter can be extrapolated to other testing conditions, a hypothesis testing analysis is also included. The computation of the Bayes factor relates the comparison between two different marginal likelihoods or evidences attached to two alternative hypotheses. The results from this analysis determine the suitability of one hypothesis or the other opening up the discussion about model selection and the influence of the experimental conditions for optimal testing. This contribution offers a deeper insight to the experiments performed in this domain and how to improve our model upon experimental evidence.

Keywords: Uncertainty Quantification, Bayesian Inference, Plasma Flow Experiments, Catalysis, Thermal Protection Systems, Hypothesis Testing

1. Introduction

Historically, experiments have been the main source of knowledge since the dawn of scientific pursuit. The invention of computers lead to a raise in computational methods that are widely used in modern engineering to reduce time and costs during the design phase of a complex system, often as an alternative to experiments when our confidence in the models is very high. Another use for computational methods is the capability of solving complex equations which otherwise would remain unsolved or would require a considerable amount of human resources [1]. Since the beginnings of the computational era, experiments and simulations have been used alongside one another to uncover deep physical laws and to understand nature. As our knowledge of the world is never perfect and so far we cannot account for all its different multiscale details, uncertainties must play a role in the understanding process.

When dealing with complex physical phenomena, it is important to resort to all the available tools: experiments, simulations and uncertainty quantification studies are used to assess the reliability of our pre-

dictions as well as the quality of our models. The study of the aerothermal environment surrounding a vehicle during atmospheric entry is extremely complex, as such, experiments and models are put to the test to avoid critical mission failure. In this context, inductively-coupled plasma (ICP) wind tunnels represent the best option to characterize this kind of flows together with the thermal protection material used to protect the spacecraft and equipment during the entry phase. In particular, these facilities allow to accurately analyze complex gas-surface interactions, such as catalysis and ablation. The von Karman Institute (VKI) Plasmatron facility uses a state-of-the-art ICP torch [2] to collect relevant data to study this flow-material interaction phenomenon. Depending on the material to be characterized, different testing techniques can be used to assess different aspects of their performance. In this case, we focus our interest in reusable materials for which the characterization of their surface properties are done in an indirect manner by using several measurement techniques. The fact that the properties we want to measure are derived through a combination of experimental data and numerical rebuilding, means that there is more room for error, literally. Uncertainties affecting each part of the rebuilding must be accounted for, from the measurement errors, to the methodology used to measure, to the model used to perform the rebuilding.

In a previous work, we addressed the development of a Bayesian framework to calibrate the catalytic parameters of some materials. The experimental and computational techniques used to rebuild the catalytic parameters were addressed. One of the shortcomings of the computational model was the fact that it relies on inputs that are unknown though some of them are measured. To overcome this issue, the likelihood function where model and measurements are compared, was optimized with respect to these nuisance input parameters. This procedure let the Bayesian problem depend only on the quantities of interest. The posterior distributions obtained were accurate and meaningful showing well-defined peaks and a reduced support. Robustness was achieved by using a surrogate model for the log-likelihood.

In this work, we extend the Bayesian framework by answering the following questions: Can the estimation of the catalytic parameter be improved through another experimental methodology? When doing so, can the Bayesian framework be extended to include new parameters and give accurate posteriors? Is the calibration useful in other testing conditions? The purpose of this part is to address them all through the use of the Bayesian framework previously developed.

The article is arranged as follows. Section 2 recalls the tools and data conventionally used. Section 3 introduces the 3-probes testing methodology in terms of its experimental set-up and the theoretical foundation behind it. In Section 4, the hypothesis testing strategy is explained and the Bayes factor is derived for the two different hypotheses posed. Section 5 presents the reader the results of the 3-probes testing methodology for different testing conditions in terms of the posterior distributions of the three catalytic parameters. Section 5 also deals with the results from the hypothesis testing, showing the value obtained for the Bayes factor. Finally, Section 6 summarizes the outcomes of the analyses and discusses the possible perspectives for future work.

2. Recall on the Numerical Tools and Experimental Data

The Bayesian inference framework relies on the modeling of the chemically reacting boundary layer of re-entry vehicles and experimental data taken from plasma wind tunnels, i.e. the VKI Plasmatron. In the following subsections, the numerical tool encoding the model adopted in this study and the methodology used for experiments are briefly depicted.

2.1. The Boundary Layer Code

The numerical framework used in this study reproduces the stagnation region of a chemically reacting boundary layer flow. The outer edge conditions and the wall conditions are given. The former one is achieved through and external fluid dynamics computation of the flowfield in the Plasmatron chamber, while the latter one assumes a certain catalytic parameter γ as a boundary condition on the wall. The code relates the functional $q_w = f(H_\delta, P_s, P_{st}, T_w, \gamma_i)$ through inputs-outputs relationship. All the parameters can be measured except the enthalpy H_δ and the catalytic parameter γ_i which can be assumed or derived experimentally in some cases.

The details of the numerical schemes and implementation of the code itself can be found in [3].

2.2. 2-probes Testing Methodology

The experimental side of the inference involves a testing methodology which relies on the characterization of two different materials. A reference material with an assumed γ_{ref} parameter is immersed in the plasma flow first and its heat flux q_{cw} and wall

temperature T_{cw} are measured. These quantities and the fact that the catalytic parameter is assumed, give us the computation of the enthalpy at the edge of the boundary layer H_δ that it is unknown and not directly measurable.

During the same experimental run, the probe with the protection material in question is exposed to the plasma as well, this time knowing the free stream enthalpy levels computed previously. Measurements of the heat flux q_w and the wall temperature through radiative equilibrium $q_w = \sigma\epsilon T_w^4$ are performed and the material catalytic parameter γ_{prob} is finally extracted.

The previous methodology is the one used conventionally for the deterministic extrapolation of catalytic parameters of materials [4]. Through the Bayesian framework, no hypothesis on the γ_{ref} is needed and the uncertainty levels of both parameters can be computed simultaneously.

3. 3-probes Testing Methodology: Mini-Max

The Mini-Max methodology consists of using 3 different materials (quartz, copper and silver) where two of them have a very well-known catalytic behavior, being in the upper and lower catalytic limits, and the other one being ranked in between them for catalytic reactions. In this case, the problem is the same as the previous methodology but with an extra *dimension* in the search space of catalytic parameters (3). This approach is mostly used to characterize the catalytic parameter of copper, often used in ground testing as reference material [5].

3.1. Experimental Approach

The approach presented here relies on two well-known catalytic parameters that live on the extremes of the catalytic parameter spectrum. This fact lowers the epistemic uncertainty that the assumption of catalytic behaviors introduces in the system. As a natural consequence, the determination of copper catalytic parameter is more reliable and one can expect to obtain more peaky distributions for such parameter, showing that this experimental reasoning proves to be a better way of dealing with these materials.

Mathematically, the problem is represented in Fig. 1 following the same nomenclature than previously seen.

The experimental procedure follows the same guidelines than the 2-probes methodology but keeping the wall temperature of the 3 probes under control and at a low level (350K), except for the quartz probe

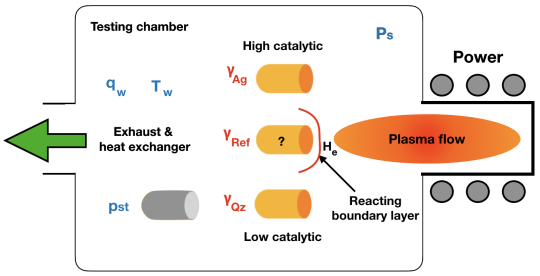

Figure 1: Sketch of the 3-probes testing methodology. Here the catalytic parameter of copper (γ_{Cu}) is determined in a plausible range between two extremes of this behavior, materialized on the silver and quartz probes

for which a slightly higher temperature is achieved (750K) [6]. One can assume that this effect is small and that all probes measure the same wall temperature for the purpose of this study. By doing so, we can be sure that the different heat fluxes measured on the different materials are only due to the differences in their nature and not on the surface temperature they can reach under the plasma flow influence, making this a suitable experimental strategy for determining such characteristic parameter.

Heat fluxes can be measured through water pipes and the heat exchange between the water running on the surface of the probes and the plasma impinging on it. Once the 3 probes have been subjected to the plasma jet and we have measured all three different heat fluxes, we can rebuild the parameters of interest for this experimental run.

3.2. Computational Rebuilding

The boundary layer code uses as inputs the heat flux, wall temperature, static pressure and stagnation pressure measured. It also needs to input the enthalpy at the boundary layer edge and the catalytic parameter. This methodology provides upper and lower bounds to the determination of the copper catalytic parameter, that is why the name “Mini-Max”. It develops as follows:

First, the 3 S-shaped curves for the 3 materials are derived using the boundary layer code as depicted in Fig. 2.

Referring to the low catalytic values for quartz and the high catalytic values for silver, we can close up an interval for the enthalpy H_δ which reflected upon the curve for copper, gives back another interval for the γ_{cu} we are looking for. It is common practice to

take the mean value of this interval as the catalytic parameter we want to characterize.

From this methodology a few remarks are clear: There is a dependence of the free stream enthalpy on the assumptions made for the behavior of quartz and silver and these assumptions are more reliable as these materials have a more predictable behavior under characteristic Plasmatron conditions. It is these peculiarities and the fact that we use two different materials to asses a third one, that the results will be different from the ones obtained for the 2-probes testing methodology.

4. Hypothesis Testing: Derivation of the Bayes Factor

The reference material used for ground testing is proven to be a key factor in the deterministic approach previously mentioned. The current literature state-of-the-art does not largely agree on a specific value for it [7; 8; 9; 10; 11; 12; 13; 14; 15; 16] and the 3-probes testing methodology was derived by the experimentalists to deal with this uncertainty. It is important to assess its validity across different testing conditions where the calibrated value can be re-used for this purpose. To do so, the Bayes factor is computed [17] giving an estimation on the ratio between the evidences for the two alternative hypotheses stated [18].

In this section, we derive the two hypotheses that *compete* in the Bayes factor setting. Hypothesis 1 reads: γ_{ref} does not change significantly across different testing conditions versus hypothesis 2: γ_{ref} has to be assessed for each condition. Two different experiments are accounted for to compute the different evidences [4]. Each experiment is aiming at characterizing a different thermal protection material by using the same copper calorimeter as reference. Schematically, we have the following Fig. 3. In it, the two experiments are depicted as S_1 and S_2 (S_8 in [4]) and they differ in the material they aim to characterize (M_1 and M_2, respectively) while using the same γ_{ref} material. The notation of γ_{prob_1} and γ_{prob_2} denote the catalytic parameters of both materials.

4.1. Formulation of the Evidence for Hypothesis 1

Hypothesis 1 comprises the assumption of having a unique γ_{ref} for both experimental conditions. Let $p(\gamma_{\text{ref}})$, $p(\gamma_{\text{prob}_1})$ and $p(\gamma_{\text{prob}_2})$ be the prior distributions for the three catalytic parameters to be calibrated and S_1, S_2 two independent measurement sets. The evidence of H_1 is therefore given by the averaged value of $L(S_1, S_2|\gamma_{\text{ref}}, \gamma_{\text{prob}_1}, \gamma_{\text{prob}_2})/p(S_1, S_2)$ over the priors $p(\gamma_{\text{ref}})$, $p(\gamma_{\text{prob}_1})$, $p(\gamma_{\text{prob}_2})$,

$$
\begin{aligned}
&P(S_1, S_2|H_1) = \\
&= \int_{\gamma_{ref}} \int_{\gamma_{prob_1}} \int_{\gamma_{prob_2}} \frac{L(S_1, S_2|\gamma_{ref}, \gamma_{prob_1}, \gamma_{prob_2})}{P(S_1, S_2)} \\
&p(\gamma_{ref})\; p(\gamma_{prob_1})\; p(\gamma_{prob_2})\; d\gamma_{ref}\; d\gamma_{prob_1}\; d\gamma_{prob_2}.
\end{aligned}
\tag{1}
$$

4.2. Formulation of the Evidence for Hypothesis 2

For H_2, on the contrary, the evidence considers different values for γ_{ref} in independent experiments as depicted in Fig. 4. A general view on the ground testing hypothesis 2 is represented, where the reference calorimeter catalytic behavior differs from one experiment to the other, reason why different colors are used to depict this phenomenon. The physical probes remain the same from one experiment to the other.

The formulation of the evidence for hypothesis 2 is derived as

$$
\begin{aligned}
&P(S_1, S_2|H_2) = \int_{\gamma_{ref_1}} \int_{\gamma_{prob_1}} \frac{L(S_1|\gamma_{ref_1}, \gamma_{prob_1})}{p(S_1)} \\
&p(\gamma_{ref_1}) p(\gamma_{prob_1})\; d\gamma_{ref_1}\; d\gamma_{prob_1}\; x \\
&x \int_{\gamma_{ref_2}} \int_{\gamma_{prob_2}} \frac{L(S_2|\gamma_{ref_2}, \gamma_{prob_2})}{p(S_2)} \\
&p(\gamma_{ref_2}) p(\gamma_{prob_2})\; d\gamma_{ref_2}\; d\gamma_{prob_2},
\end{aligned}
\tag{2}
$$

where the two experiments are considered independent and four catalytic parameters are used within the model to explain the data.

Finally, we should compare both alternative hypothesis through the Bayes factor as

$$
I_H = \frac{P(S_1, S_2|H_1)}{P(S_1, S_2|H_2)}. \tag{3}
$$

If $I_H < 1$, then H_2 is more likely than H_1 and viceversa. It is important to notice that there will be a range of values, close enough to one, where it is difficult to assess the result of the hypothesis testing. Further discussions can give an estimation on how small compared to one the Bayes factor can be to have a significant impact on our hypothesis choice.

5. Results

In this section we discuss the two main applications for the Bayesian framework. Concerning the

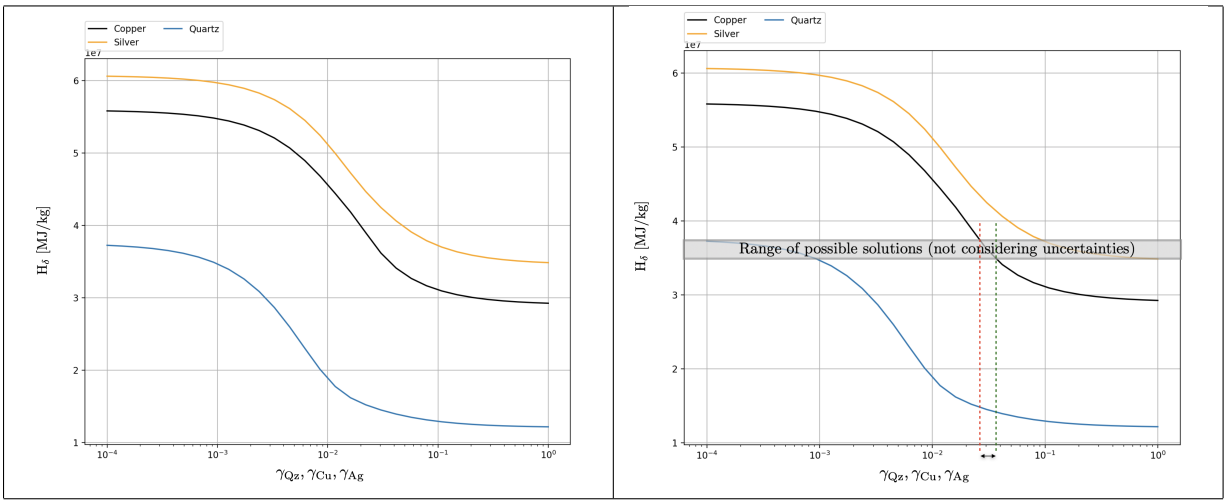

Figure 2: Rebuilding methodology for the Mini-Max. Unlike the 2-probes methodology, the assumptions behind this methodology are better founded, providing a tight interval for the copper parameter

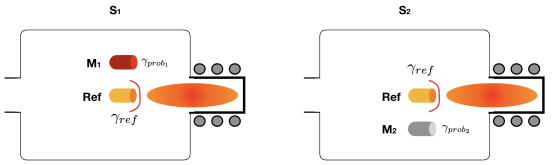

Figure 3: Sketch of testing scenarios for samples 1 and 2 where the reference calorimeter is assumed to behave catalytically the same in both conditions

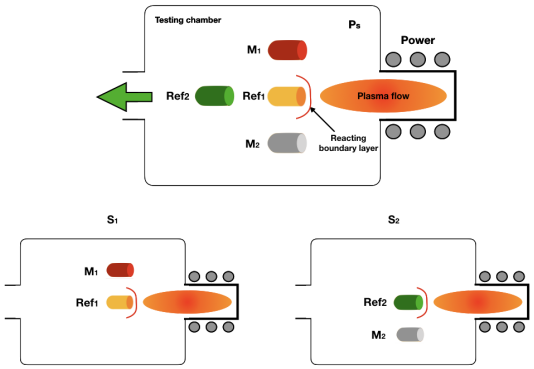

Figure 4: Sketch of testing scenario according to hypothesis H_2 where it is assumed that the same reference probe behaves differently for each condition

3-probes testing methodology, results are explained and compared to the previous case study for the 2-probes testing methodology. Hypothesis testing results are also included here. The two applications prove the Bayesian framework to be an enhancement of the state-of-the-art compared to the deterministic approach giving us the way forward in the field when looking at performing experiments.

5.1. 3-probes Testing Methodology

This methodology comprises the use of an extra calorimeter, therefore, giving an extra catalytic parameter to be calibrated with our framework when compared to the 2-probes testing methodology. Our two-dimensional plane where we performed surrogate evaluations and sampling of the posterior distributions becomes a cube where γ_{Qz}, γ_{Cu} and γ_{Ag} are the *dimensions*. Not only the number of parameters to be calibrated increases but also the number of measurements taken in each experimental run, elevating the dimensions of the simplex used for the optimization of the log-likelihood. All this, complexity of the simplex and the fact that we have to sample a cube instead of a plane, add computational time to our problem.

As a result, different measures are put in place. For starters, a smarter way of sampling our quantities of interest space by using Latin Hypercube Sampling (LHS) techniques [19], together with a sequential approach to the posterior sampling. This approach starts with a LHS sparse grid upon which we build our Gaussian Process (GP) surrogate [20] and run Markov Chain Monte Carlo (MCMC) [21]. An additional sampling process is undertaken but focused only on the part of the cube where MCMC is drawing samples from, refining the accuracy of the GP in that part.

Iteration of this process leads to good results with acceptable computational time.

5.1.1. *Experimental Data and Associated Uncertainties*

Three different experiments are considered for this case and they are part of Viladegut's work [5]. They are chosen to be different in terms of the overlapping of the S-shaped curves to see their effects on the final results. The following table depicts the experimental data used for each run and their uncertainties.

The aforementioned experimental data is an input provided to us from the experimentalists in the field. The treatment of the data and the computation of their uncertainties can be subjected to question and changes in future work. The values of the different measured quantities are the results of averaging the time series obtained for each quantity. The overall uncertainties are the results of two different sources: the accuracy of the measurement chain and the measurement error or the spread of each measurement point in time. For the second term, t-Student distributions are obtained [22] and the corresponding assumed normal distributions are corrected with the t-Student factor as a result. The overall values are obtained as the squared sum of the quadratic errors stemming from the two sources.

5.1.2. *Nominal Results*

The deterministic results obtained for cases 9b, 9c and 3a are depicted in Fig.5 showing their corresponding S-shaped curves where one can extrapolate the γ_{Cu} for each of them. It is important to focus on their relative position and the size of their enthalpy overlap to extract conclusions about their posterior distributions hereafter and where the origin of their differences is.

The main differences among these cases are the relative position of the S-shaped curves and their consequent overlapping in the enthalpy sense, in a range where the three curves can have the same simultaneous H_δ.

5.1.3. *Surrogate Modeling and MCMC*

The log-likelihood is approximated using Gaussian Processes (GP) as surrogate model. Building this surrogate requires the evaluation of the log-likelihood along the different dimensions of the cube. Initially, a LHS strategy is followed for a cube in the logarithmic scale:

It was noticed that for values of γ_{Qz} under a certain threshold, the Boundary Layer Code would not converge. This is due to the very different enthalpy levels require for those cases given that all simulations start from the same initial conditions. According to the S-shaped curves:

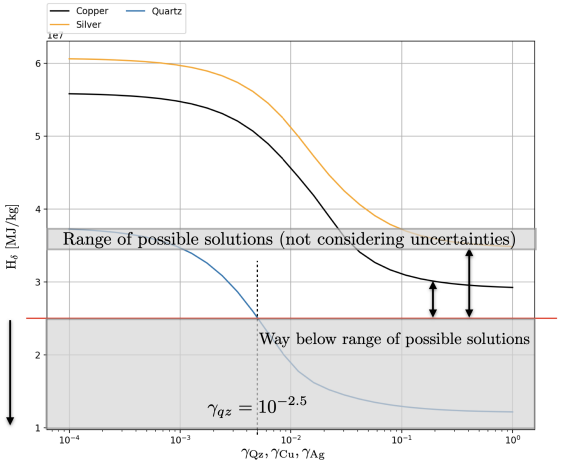

Figure 6: S-shaped curves sketch where the range of possible physical solutions is shown and the shorter prior support for the γ_{Qz} can be justified graphically

In turn, the domain can become smaller and the prior distributions are chosen to be:

The idea resides in the fact that it is not important how good our surrogate is for those far away points, which is a way of reducing your initial domain. Around 200 samples are evaluated in this initial grid. After that, additional samples are taken in the portion of the cube where the MCMC draws samples from the posterior in the low-fidelity initial surrogate. This portion of the cube is depicted hereafter together with its canonical transformation. These additional samples are taken using conventional Monte Carlo techniques.

It can be seen that indeed, the domain of interest for the quartz is the one comprised between $10^{-4}, 10^{-2.5}$, although the whole domain is represented in Fig. 7. Copper and silver are contained in a sub-domain between $10^{-2}, 10^{0}$.

Once this issue is settled, the procedure is run iteratively to obtain a good GP surrogate. The approximation and its standard deviation are depicted in the following figures.

As can be appreciated in Figs.8-9, the standard deviation in all the domain does not exceed 1% of the values of the log-likelihood, which represents a good accuracy for the GP surrogate. At this stage, 300 samples in total were used to build the GP, which represents almost double the amount than with the 2-probes case study, which is a good compromise when having an extra dimension to sample in terms of accuracy.

Table 1: Mini-Max Experimental Data and Uncertainties

Case 9b	q_{cw}^{Qz} [kW/m^2]	q_{cw}^{Cu} [kW/m^2]	q_{cw}^{Ag} [kW/m^2]	T_{cw}^{Qz} [K]	T_{cw}^{Cu} [K]	T_{cw}^{Ag} [K]	P_s [Pa]	P_{st} [Pa]
Mean (μ)	822.7	2000	2379.8	750	350	350	5000	152.7
Std deviation (σ)	37.3	88.8	105.7	37.5	17.5	17.5	30	2.3
Case 9c								
Mean (μ)	897.6	2000	2203.8	750	350	350	10000	60.9
Std deviation (σ)	40.7	88.8	97.9	37.5	17.5	17.5	60	0.9
Case 3a								
Mean (μ)	273.2	700	720.7	750	350	350	1500	396.9
Std deviation (σ)	12.4	31.1	32	37.5	17.5	17.5	7.6	6

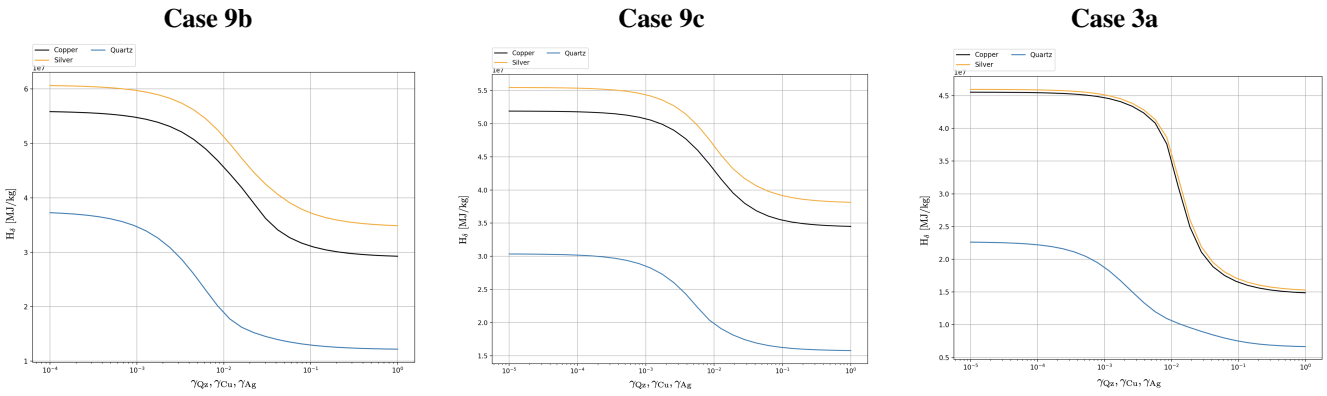

Figure 5: Nominal S-shaped curves for the different experimental cases with different relative overlapping with respect to the boundary layer edge enthalpy

Table 2: Initial sampling domain for the log-likelihood

γ_{Qz}	γ_{Cu}	γ_{Ag}
$[10^{-4}, 10^{0}]$	$[10^{-4}, 10^{0}]$	$[10^{-4}, 10^{0}]$

Table 3: Prior distributions used to sample the log-likelihood

γ_{Qz}	γ_{Cu}, γ_{Ag}
LogU $[10^{-4}, 10^{-2.5}]$	LogU $[10^{-4}, 10^{0}]$

Subsequently, the MCMC algorithm is run for the three quantities of interest and the chains mix well and present no correlation which gives us good estimation of the posterior distribution.

In Fig.10, the chain samples are depicted for the different catalytic parameters. In general, it can be appreciated that quartz and silver samples are confined in a certain area of same size in both parameters. In the lower part for quartz and upper part for silver, as it was expected. On the other hand, copper samples are confined in a much smaller region, making this methodology ideal for the accurate determination of copper catalytic behavior.

5.1.4. Discussion on the Posterior Distributions

The MCMC algorithm provides the samples that conform the joint posterior distribution. Three marginal distributions are derived from the chain samples of each catalytic parameter. In Fig. 11, several things can be noticed. The support of both the γ_{Cu} and γ_{Ag} is significantly reduced to higher catalytic parameter values. The support of the quartz parameter remains the same once the initial domain was reduced to accommodate possible solutions for the optimization of the log-likelihood.

The marginal posteriors of quartz and silver are quite flat which can be expected due to the S-shaped curves behavior in the limits of the catalytic behavior, meaning that the molecular recombination contribution to the heat flux for their cases is negligible. The positions in the gamma "spectrum" are totally coherent, being quartz the least catalytic, silver the most catalytic and copper somewhere in between. It is important to notice that this experimental methodol-

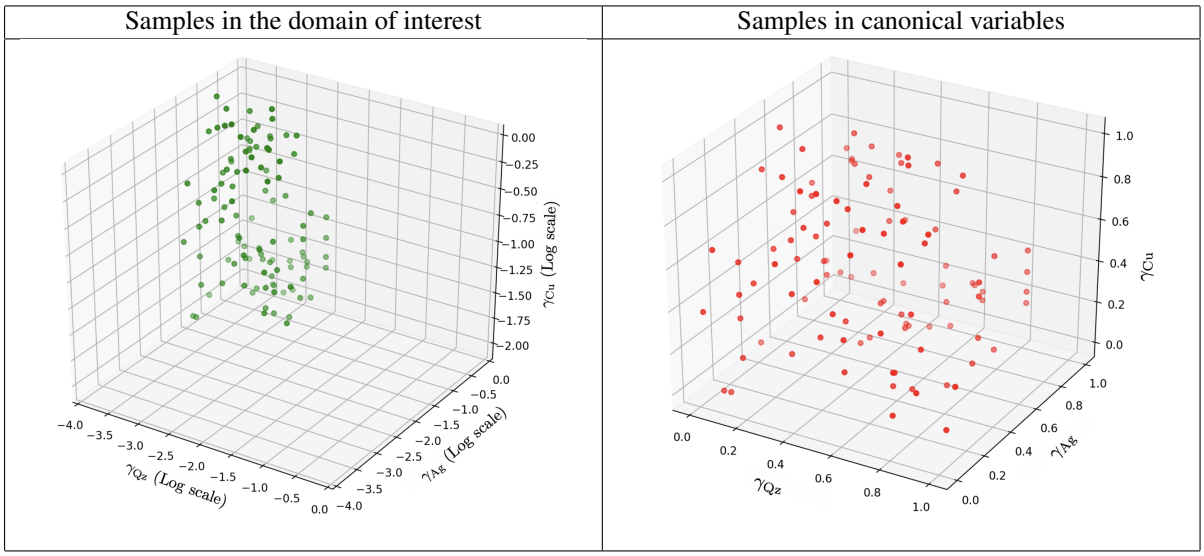

Figure 7: Samples in the area of interest in both logarithmic scale in the variables domain as well as in the canonic space

ogy can achieve a good knowledge of the copper catalytic behavior but cannot expect to know accurately either quartz or silver for which the supports are what give the information needed to characterize the copper probe.

To illustrate the explanation of the shapes of the distributions better, we should take a look at Fig. 12, where we can see the relative position of the MCMC samples with the S-curves. The support of each of them can be appreciated together with the density of points within the support, explaining the observed probability density functions shapes.

5.1.5. Additional cases: 9c and 3a

The procedure showed for case 9b is repeated for other cases with other testing conditions as depicted in Sec. 5.1.1. Here we show the final results as the posterior distributions obtained in both cases. Fig. 13 shows the posteriors for the conditions of case 9c. This particular set of conditions leaves no overlapping in the enthalpy sense, meaning that, using the conventional model, our experimental measurements cannot be explained. One can think that this is due to not accounting for the uncertainties of the measurements in the S-shaped curves. By looking at the results of Fig. 13 we can extrapolate that the points drawn with MCMC are further apart than what would be expected from the uncertainties. The log-likelihood optimization algorithm still finds solutions but they are not physical. The model is showing its shortcomings.

In Fig. 14, results from case 3a are depicted. This case shows the opposite behavior than 9c, the overlapping is even bigger. S-shaped curves of copper and silver are very closed together, therefore, yielding very similar posteriors with the same support. Due to the increased overlapping, the points of the quartz distribution are shifted towards the steep part of the S-shaped curve and this translates into a more peaky behavior in the posterior. From the S-shaped curves sketch of Fig. 14, one can see that the optimization algorithm finds the optimum by "moving" more the points of the quartz probe than the others. This is due to the lower increase of the error when changing the wall temperature of the quartz probe than the heat fluxes of the copper and silver ones.

5.2. Hypothesis Testing

Different testing conditions for the same set up can lead to very different conclusions. In this context, it is important to assess the variability on the reference calorimeter behavior under such different conditions. Common practice in the field dictates that the catalytic parameter for copper is assumed and well-known across all testing conditions. The Bayesian framework targets this assumption and "liberates" the determination of the catalytic parameter of a given thermal protection material from its uncertainties. It is inevitable then to test whether or not the changes in γ_{ref}, referred to copper, with the testing conditions are important.

For this matter, two different experiments performed in different conditions are considered. Experi-

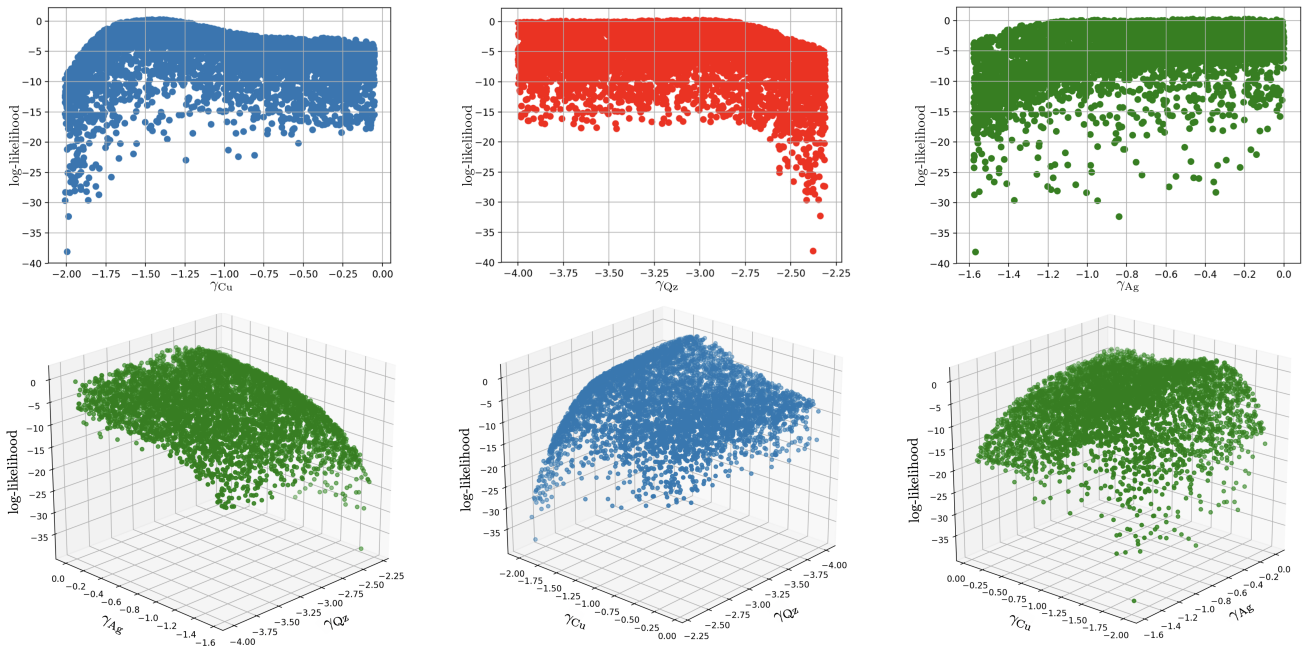

Figure 8: Log-likelihood GP surrogate evaluated on the area of interest depicted in Fig. 7

ment S_1 and experiment S_2, which are depicted in Table 4, are used to compare two alternative hypotheses through the computation of the Bayes factor [23].

5.2.1. *Experimental Data and Associated Uncertainties*

The two experiments used here are part of Panerai's work [4] and they are chosen to be different in terms of the testing conditions. Table 4 depicts the experimental data and related uncertainties.

5.2.2. *Computation of the Bayes Factor*

The Bayes factor is what gives quantitative consistency to alternative hypotheses. As depicted in Sec. 4, the way to do that is by deriving the evidences for each hypothesis. In our case, we want to test whether or not the testing conditions make a difference in the determination of γ_{ref}. We formulate two alternative hypothesis: one in which we assume that γ_{ref} remains unchanged for different testing conditions (H_1) and another one where γ_{ref} is different for each condition (H_2).

Based on this, we compute the evidences from Eqs. 1 and 2. The resulting Bayes factor results in

$$I_H = \frac{P(S_1, S_2|H_1)}{P(S_1, S_2|H_2)} = 0.71. \tag{4}$$

The result depicts disagreement between both hypotheses in the sense that the evidence for H_2 based on the available data is larger. An inference assuming H_1 can lead to wrong conclusions when these experiments are considered. The generalization to all conditions cannot be made based on the mathematical description of the Bayes factor. A deeper look into the physics could provide a more meaningful generalization if needed.

6. Concluding Remarks

A comprehensive experimental study is carried out concerning the catalytic properties of thermal protection materials. The Bayesian framework already developed is extended to accommodate a 3-probes testing methodology used by the experimentalists in the field to improve the characterization of the reference calorimeter catalytic behavior. To deal with the increment in complexity due to the inclusion of an extra catalytic parameter, a sparse sampling strategy is adopted. This strategy gives accurate results while needing less number of samples than the previously used uniform distribution. The posteriors obtained are meaningful, managing to reduce the support, and accurate.

The 3-probes testing methodology proves to be a good experimental approach to the problem of char-

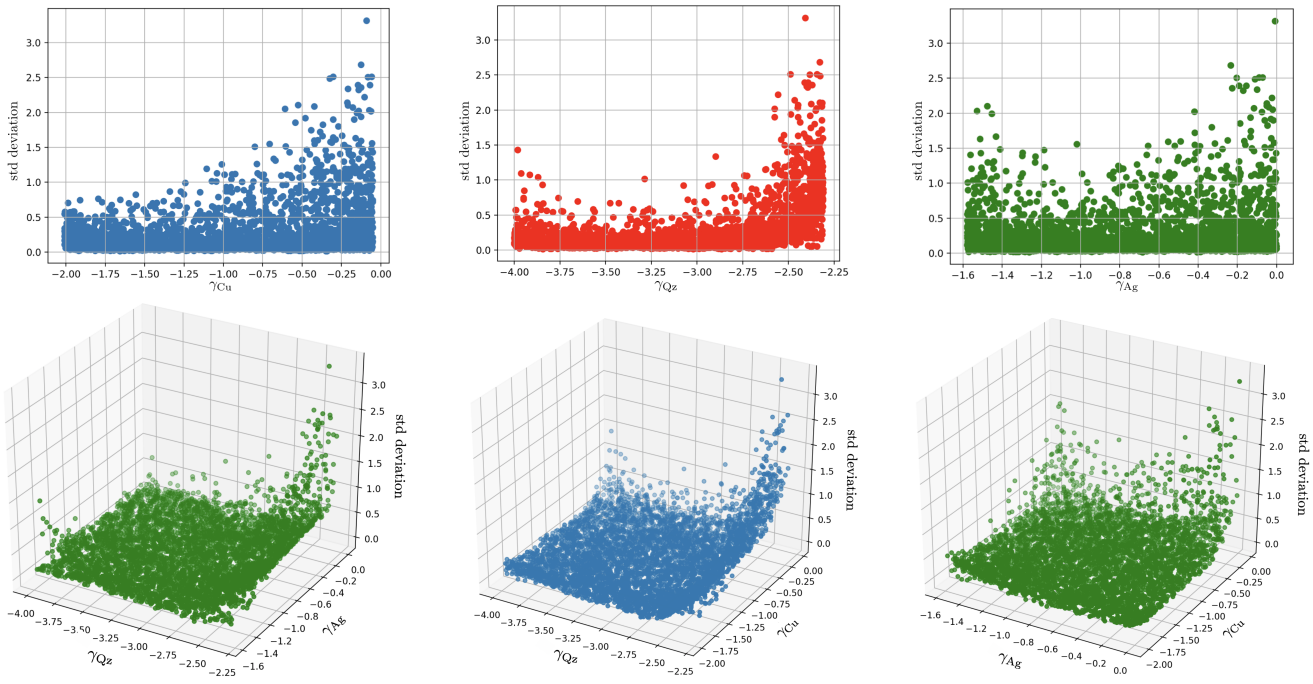

Figure 9: Log-likelihood GP surrogate standard deviation evaluated on the area of interest depicted in Fig. 7

Table 4: 2-probes testing methodology experimental data and uncertainties

Sample S_1	q_{cw} [kW/m^2]	T_{cw} [K]	P_s [Pa]	P_{st} [Pa]	T_w [K]	ϵ
Mean (μ)	195	350	1300	75	1200	0.78
Std deviation (σ)	6.5	11.7	1.3	1.5	4	0.013
Sample S_2						
Mean (μ)	410	350	3000	64	1400	0.88
Std deviation (σ)	13.7	11.7	3	1.3	4.7	0.015

acterizing reusable thermal protection materials. The fact that the reference material must be catalytically in between two materials at the opposite limits of this behavior makes its determination more certain with resulting more peaky distributions for nominal cases. Extended to other testing conditions, the relative "overlapping" of the S-shaped curves in terms of the enthalpy H_δ where all the curves "coexist" becomes either larger or non-existent. For these limit cases, the resulting posteriors for γ_{Cu} become more spread as a consequence of the physics adopted by this particular model. A next natural step concerning this part of the contribution would be to design the experiments that help gain knowledge about this parameter.

Another question that arises is how the parameter calibrated can be used in other testing conditions different from the ones used for calibration. A hypothesis testing study is carried out where two alternative hypotheses are tested against each other. The evidences ratio shows disagreement between the two hypotheses. A further study could clarify the range of validity of the hypothesis where the γ_{ref} is assumed the same across conditions. This could be used to avoid performing the calibration for every test.

The Bayesian inference framework proves to be a reliable way to extract information from your experiments in the form of parameters with uncertainty distributions. The assessment of different experimental methodologies can be done to improve the significance and knowledge that can be extracted from each experiment. Other conditions are considered and the methods shows robustness when dealing with extreme situations. The Bayes factor calculation can be extrapolated to more conditions to have a more complete un-

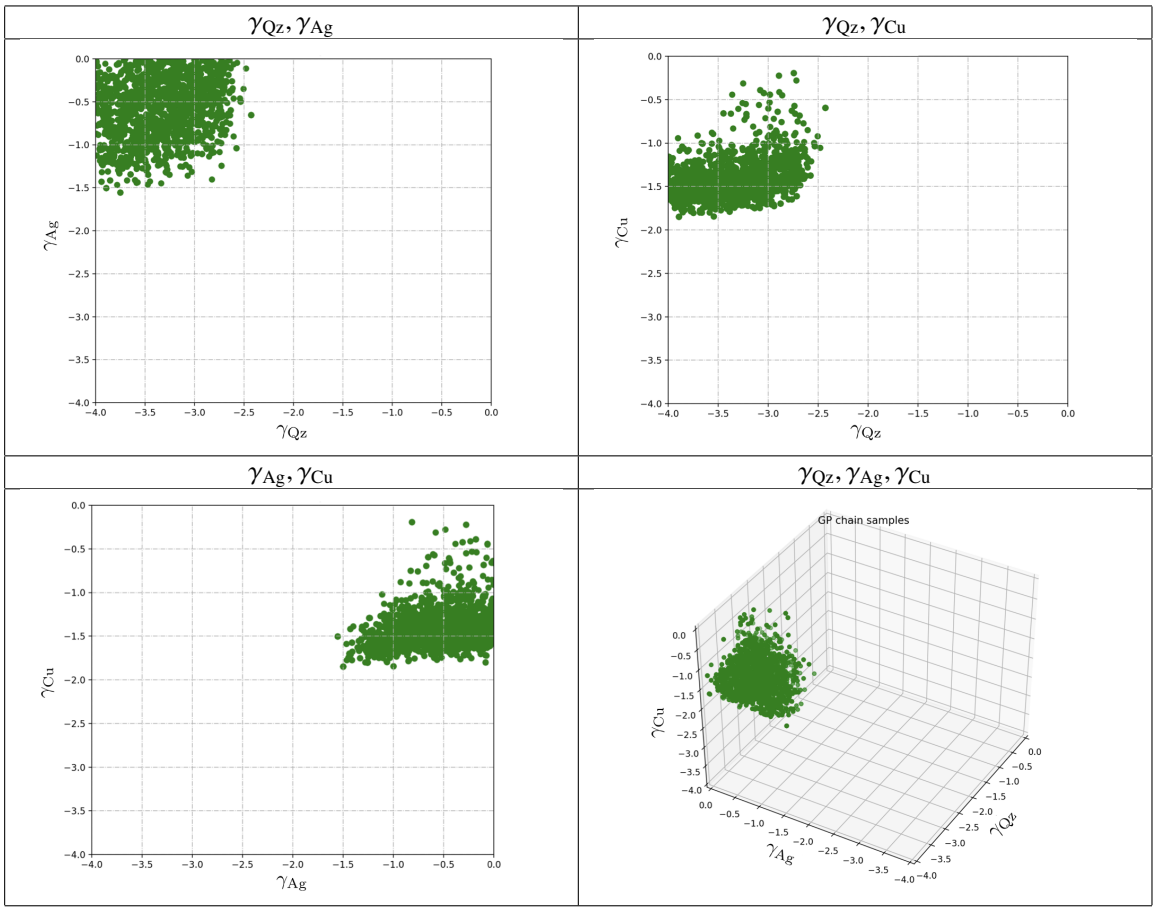

Figure 10: MCMC sample points in the log-scale for the different quantities of interest

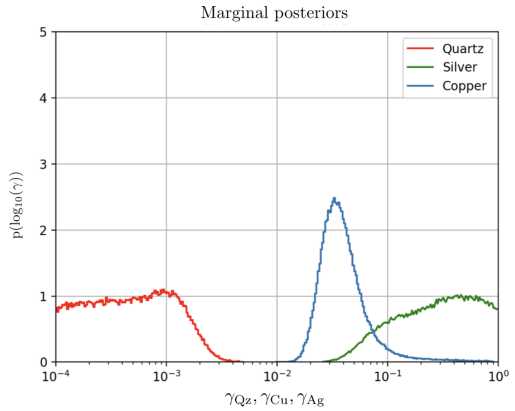

Figure 11: Marginal posterior distributions for the three materials

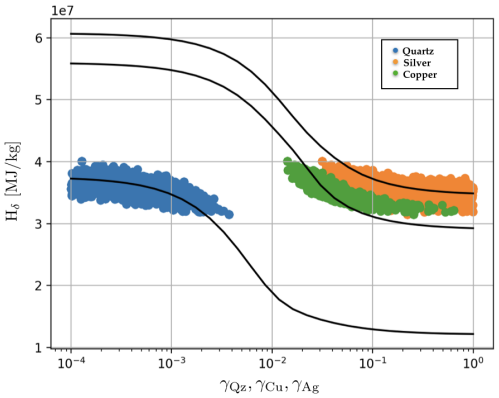

Figure 12: MCMC samples superimposed to the S-shaped curves where the range of their variability together with the part of their morphology where the samples are drawn from can be appreciated

derstanding of the changes in γ_{ref} on the experimental conditions.

Other reusable protection materials (such as ceramics) can be tested to assess their performance and its confidence while replacing the deterministic method

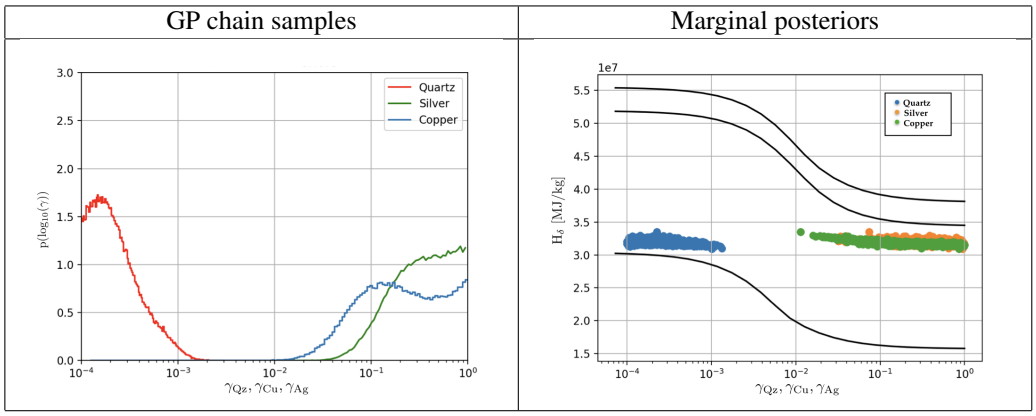

Figure 13: Left: Marginal posterior distributions for case 9c testing conditions. Right: Distributions of the MCMC samples over the S-shaped curves

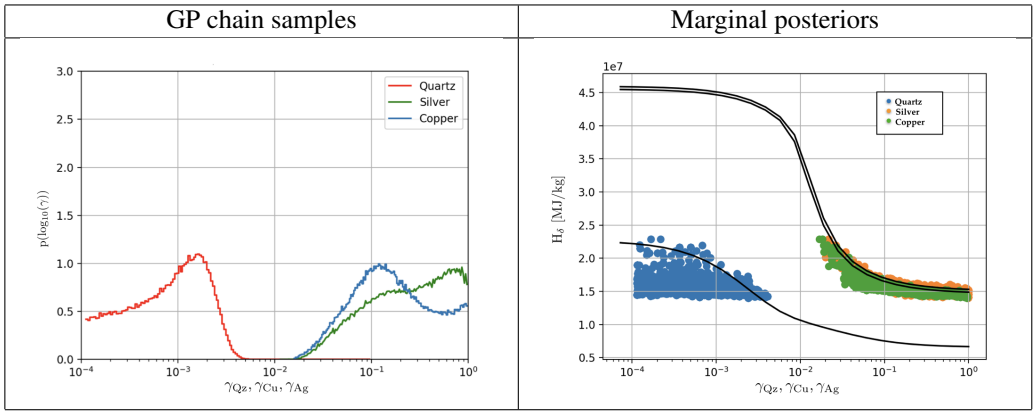

Figure 14: Left: Marginal posterior distributions for case 3a testing conditions. Right: Distributions of the MCMC samples over the S-shaped curves

where assumptions could lead to wrong results and no confidence measure is explicitly stated.

Acknowledgments

This work is fully funded by the European Commission H2020 programme, through the UTOPIAE Marie Curie Innovative Training Network, H2020-MSCA-ITN-2016, Grant Agreement number 722734.

References

[1] B. Golemba, Human computers: The women in aeronautical research, Tech. rep., NASA Langley Archives (1994).

[2] B. Bottin, O. Chazot, M. Carbonaro, V. V. der Haegen, S. Paris, in: Measurement Techniques for High Temperature and Plasma Flows, RTO-EN 8, pp. 6–1, 6–24.

[3] P. F. Barbante, Accurate and efficient modelling of high temperature nonequilibrium air flows, Ph.D. thesis, ULB/VKI (2001).

[4] F. Panerai, Characterization of gas/surface interactions for ceramic matrix composites in high enthalpy, low pressure air flow, Materials Chemistry and Physics 134 (2-3) (2012) 597–607.

[5] A. Viladegut, Assessment of gas-surface interaction modelling for lifting body re-entry flight design, Ph.D. thesis, VKI/UPC (2017).

[6] A. Kolesnikov, A. Gordeev, S. Vasilevskii, Study of catalytic heating effects on metals and quartz for exomars entry conditions, in: 5TH European Conference for Aeronautics and Space Sciences (EUCASS), 2013.

[7] J. C. Greaves, J. W. Linnett, The recombination of oxygen atoms at surfaces, in: Trans. Faraday Soc., Vol. 54, pp. 1323–1330.

[8] J. C. Greaves, J. W. Linnett, Recombination of atoms at surfaces - part 5: Oxygen atoms at oxide surfaces, in: Trans. Faraday Soc., Vol. 55, 1959, pp. 1346–1354.

[9] R. A. Young, Measurements of the diffusion coefficient of atomic nitrogen in molecular nitrogen and the catalytic efficiency of silver and copper oxide surfaces, The Journal of Chemical Physics 34 (1961) 1295.

[10] P. G. Dickens, Recombination of oxygen atoms on oxide surfaces. part 1.-activation energies of recombination, in: Trans. Faraday Soc., Vol. 60, 1964, pp. 1272–1285.

[11] R. A. Hartunian, W. P. Thompson, S. Safron, Measurements of catalytic efficiency of silver for oxygen atoms and the o-o2 diffusion coefficient, The Journal of Chemical Physics 43 (1965) 4003.
[12] A. L. Myerson, Exposure-dependent surface recombination efficiencies of atomic oxygen, The Journal of Chemical Physics 50 (1969) 1228.
[13] G. A. Melin, R. J. Madix, Energy accommodation during oxygen atom recombination on metal surfaces, in: Trans. Faraday Soc., Vol. 67, 1971, pp. 198–211.
[14] P. Cauquot, S. Cavadias, J. Amouroux, Thermal energy accomodation from oxygen atoms recombination on metallic surfaces, Journal of Thermophysics and Heat Transfer 12 (2) (1998) 206–213.
[15] J. M. Meyers, W. P. Owens, D. G. Fletcher, Surface catalyzed reaction efficiencies in nitrogen and oxygen plasmas from laser induced fluorescence measurements, in: 44th AIAA Thermophysics Conference, AIAA, 2013-3139.
[16] D. M. Driver, S. Sepka, Side arm reactor study of copper catalysis, in: 45th AIAA Thermophysics Conference, AIAA, 2015-2666.
[17] R. Morey, J. Romeijn, J. Rouder, The philosophy of bayes factors and the quantification of statistical evidence, Journal of Mathematical Psychology 72 (2016) 6–18.
[18] Data Analysis: A Bayesian tutorial, Oxford Science Publications, 2006.
[19] M. D. McKay, R. J. Beckman, W. J. Conover, A comparison of three methods for selecting values of input variables in the analysis of output from a computer code, Technometrics 21 (2) (1979) 239–245.
[20] C. E. Rasmussen, C. K. I. Williams, Gaussian processes for machine learning, the MIT Press.
[21] Statistical and Computational Inverse Problems, Springer-Verlag, New York, 2005.
[22] Introduction to Mathematical Statistics, New York: Macmillan, 1978.
[23] Theory of Probability, Oxford University Press, New York, 1961.

Ablation Modelling for the Simulation of the Atmospheric Entry of Meteors

Bruno Dias Barros

Aeronautics and Aerospace Department, von Karman Institute for Fluid Dynamics, Belgium, barros@vki.ac.be

Supervisor: Thierry Magin

Professor, Aeronautics and Aerospace Department, von Karman Institute for Fluid Dynamics, Belgium, magin@vki.ac.be

University Supervisor: Philippe Chatelain

Assistant Professor, Thermodynamics and fluid mechanics - TFL, Université catholique de Louvain, Belgium, philippe.chatelain@uclouvain.be

Abstract

The meteor phenomenon occurs constantly into our planet. The discrepancy of meteoroid flux varies from 50 to 100 tonnes according to aeronomy experts. A better understating of the phenomenon allows to track the meteoroid to the parent comet/asteroid and eventually to prevent catastrophic events by knowing the respective trajectory and composition. This type of events are characterized by complex shock layer physics such as radiation, evaporation of the meteoroid surface and the resulting chemistry process with the air constituents. In this work we present the analysis of a meteor entry using Computational Fluid Dynamic tools where a boundary condition for evaporation is implemented. Moreover the radiative source terms are derived by solving a 1D radiative transfer equations using a tangent slab method. Form the preliminary results it is shown that for a small radius the radiative heating is negligible compared to the convective heating.

Keywords: radiation, evaporation, meteor, CFD

1. Introduction

The meteor phenomenon occurs daily around the planet Earth. From 50 to 100 tonnes of these interplanetary objects enters Earth's atmosphere every day with a range of velocities from 11.5 km/s to 72 km/s [1]. Although a large number of the arriving particles are considered dust (micron-size grains) occasionally a large bolide burst into the atmosphere. The latter may represent a threat to the population as experienced during the Chelyabinsk event in 2013 [2]. A better understanding of such phenomenon is important on a variety of fields such as aeronomy, astronomy, geophysics, evolutionary biology and planetology. Tracing a large number of meteoroid orbits in the Solar System allows to clarify the association of meteoroids with asteroids, comets, or the zodiacal cloud. At the range of velocities typical of meteor phenomena, radiation becomes highly significant, the intense light observed during a meteor entry is mainly due to the radiation of the air and metallic species, where the latter are coming from ablation products. The current models to study meteor entries are focus in the ablation of small particles in the upper atmosphere. They usually rely on a zero dimensional approach providing lack of an accurate treatment of the particle interaction with the atmosphere, from the fluid dynamic point of view. Therefore, for meteoroids big enough to survive this first phase of the atmospheric entry, a different approach has to be sought.

In this work we propose to study the meteor ablation with a numerical approach similar to those used in the aerospace community to model the gas-surface interaction over Thermal Protection System (TPS) materials. A 1D Stagnation-Line solver is used to resolve the multicomponent, reacting governing equations including radiative source terms computed by a tangent slab radiative transfer solver using the HSNB formulation (presented in the next section).

2. Model description

2.1. Physico-Chemical Models

The following sections describe briefly the physico-chemical models. These models are used to close the governing equations which in turn are solved by numerical methods. The evaporation model described is used as a boundary conditions between the gas and the surface. Finally the radiation model provides source terms to the governing equations.

2.1.1. Thermodynamics

From quantum mechanics it follows that the energy levels of atoms and molecules are discrete [3]. In the case of atoms this energy is contained into the translational movement of the particle (translational energy) and into the electronic energy modes (associtated to the electron orbit around the nucleus). In the case of molecules, they have two additional energy modes which corresponds to the rotational and vibrational energy levels. Even thoughh the translational energy levels are discrete, the spacing between them are generally very small therefore they are considered continuum [4]. The internal modes of molecules (electronic, rotational and vibrational modes) are dependent of each other. Very often for simplicity, one considers the separation between the internal modes by assuming that the molecule behaves as a rigid-rotator and an harmonic oscillator (RRHO).

The focus of this section concerns only with the derivation of the thermodynamics properties for metallic atoms. For atoms the separation between translational and electronic modes is valid since they are independent. Thermodynamic properties such as specific heat, enthalpy and entropy is computed based on the system partition function (eq. 1). Typically metallic species are characterised by having a low ionization energy and hundreds of energy levels, turning the evaluation of the partition function computational expensive due to its exponential nature.

To circumvent this problem a binning strategy [5] was employed, which consists in grouping the energy levels into bins over an energy grid $[\varepsilon_k, \varepsilon_{k+1}[$, (Fig. 1) follow:

$$I_k = \{i \in I_e \text{ such that } (\varepsilon_k \leq E_i < \varepsilon_{k+1})\}, \quad k \in K_e$$

where K_e is the set of the indices for the bins. An average energy for bin k follows:

$$\overline{E}_k = \frac{\sum_{i \in I_k} g_i E_i}{\overline{g}_K}, \quad k \in K_e$$

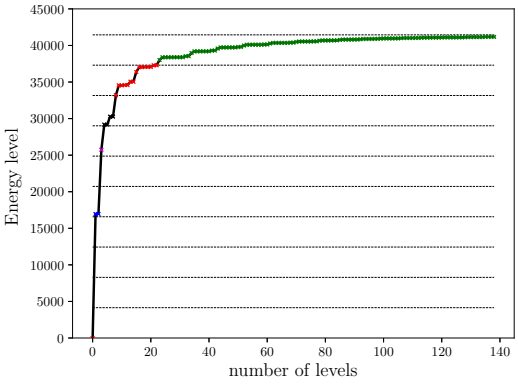

Figure 1: Energy Levels for Na

based on the degeneracy of the bin as $\overline{g}_k = \sum_{i \in I_k} g_i$. Finally the electronic partition function assuming a reduced number of energy levels estimated for each bin is computed by eq. 1.

$$\overline{Q}_i^E(T_{ele}) = \sum_{k \in K_e} \overline{g}_k \exp\left(\frac{-\overline{\theta}_k}{T}\right), \quad i \in N_s \tag{1}$$

where the characteristic temperature $\overline{\theta_k} = \overline{E}_k / k_b$ and k_b is the Boltzmann constant. As mentioned previously once the electronic partition function is known the computation of the thermodynamic properties become trivial. The electronic enthalpy follow:

$$h_i^E(T_{ele}) = R_i T^2 \frac{\partial \ln \overline{Q}_i^E}{\partial T}, \quad i \in N_s \tag{2}$$

where R_i is the specific gas constant for species i. The total enthalpy of the atom as:

$$h = \sum_{i \in N_s} y_i (h_i^T + h_i^E) \tag{3}$$

where the translational contribution is defined as $h_i^T(T) = 5/2 R_i T$.

The electronic levels for atoms are either observed through spectroscopy measurements or computed from quantum mechanics. The Nist database [6] comprises a big amount of data regarding the electronic levels for several atoms. In fig. 1 the total 140 electronic levels for Na are shown. The bars shown in the same figure represent the bins and the symbols concerns the total number electronic levels per bin. Using the reduction technique mentioned above it was possible to pass from 140 to 6 electronic levels. The non-dimensional enthalpy for Na is show in 2 for the

total number of electronic levels extracted from Nist and for the reduced number.

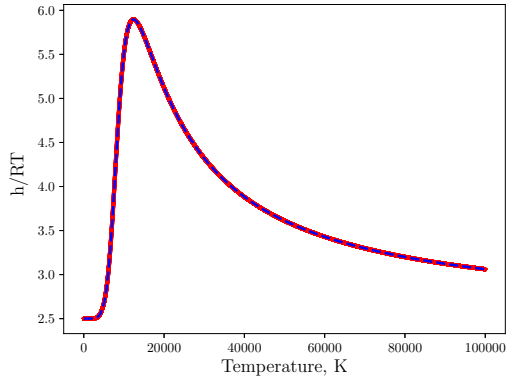

Figure 2: Non-dimensional total enthalpy for Na; line: 140 electronic levels, broken line: 6 electronic levels

From the figure one can conclude that the reduction system works well being able to reproduce the same thermodynamic quantity as the entire number of electronic levels. Finally fig. 3 shows the equilibrium composition based on the Gibbs free energy minimization [7] for a Na elemental system. A comparison was made between the RRHO model and the Nasa polynomials database [8], where the later is more accurate up to 20000 K. Initially only NaO is present in the mixture, around 2500 K the species starts to dissociate forming Na and O. Around 5000 K Na starts to ionize forming Na^+ and finally at 12000 K the mixture becomes fully ionized. The agreement between both models is very good up to 17000 K , limit where the Nasa polynomials become invalid and the composition becomes unrealistic.

2.1.2. *Hybrid Statistical Narrow Band Model*

By solving the radiative transfer equations (RTE) one can determine the spectral radiative intensity, therefore, the radiative source terms, $\mathcal{P}^{rad}$ and $\mathcal{P}^{rad,VE}$ and $\dot{\omega}_i^{rad}$. The production or destruction of species, $\dot{\omega}_i^{rad}$, due to radiative processes such as photoionization and photodissociation and the radiative source terms. Solving the RTE by conventional methods such as Line-by-Line (LBL) becomes computationally very expensive for complex molecular spectra. Recently, [9] presented a hybrid statistical narrow band model (HSNB) showing an accurate description of the radiative flux with low CPU costs for non-ablative materials. Later [10], extended this approach for ablative TPS material.

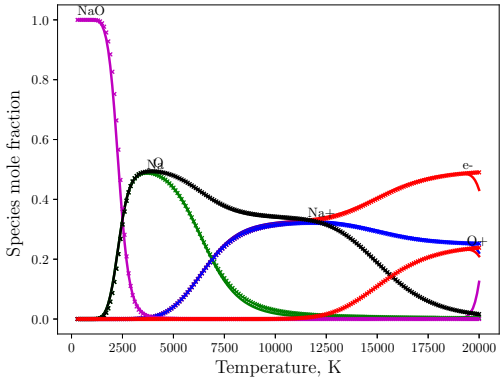

Figure 3: Equilibrium composition for {NaO, Na, O, Na^+, O^+, e^-}; lines: Nasa database, symbols: RRHO

The feature of the HSNB is that if the radiative mechanisms are statistically uncorrelated one can divide the spectra into narrow bands and compute the intensity in terms of averages. The different mechanism can be separated into 3 contributions: optically thick molecular systems, optically thin molecular systems and continua, atomic lines. Due to the weak spectral density of atomic lines, this contribution has to be solved by LBL methods. Details about the HSNB can be found in Refs. [9; 10].

2.1.3. *Gas-Surface Interaction*

The evaporation of a molten layer can be modeled by limiting the control volume to a infinitesimal thin lamina where the surface is located. Typically mass conservation for the generic species i can be written in terms of a surface mass balance (SMB):

$$J_{i,w} + \dot{m}_{evap,i} = (\rho v)_w y_{i,w} \quad \mathrm{i} \in \mathrm{N_s} \tag{4}$$

where $(\rho v)_w$ is the gas blowing, $y_{i,w}$ is the mass fraction of species i in the gaseous mixture at the wall, $\dot{m}_{evap}$ is the evaporation/condensation rate and $J_{i,w}$ is the species mass diffusion.

To solve this balance a suitable model to compute the surface reactions is needed, which in general can be solved by heterogeneous finite-rate chemistry. The evaporation/condensation of the material $\dot{m}_{evap,i}$ is estimated by the Knudsen-Langmuir law:

$$\dot{m}_{evap,i} = \left(\frac{\mathcal{M}_i}{2\pi \mathcal{R} T}\right)^{\frac{1}{2}} (\alpha_{evap} p_{vap,i} - \alpha_{cond} p_i) \quad \mathrm{i} \in \mathrm{N_s} \tag{5}$$

where the equilibrium vapor pressure , $p_{vap,i}$, can be compute through a multiphase equilibrium solver

such as Magma [11]. The Magma solver has been extensively validated for silicate melt compositions. The solver it uses the ideal mixing of complex components (IMCC) model which considers the deviation of ideal mixture into the melt. In other words it uses complex pseudospecies to compute activity coefficients of metal oxides in non-ideal molten compositions. In fig. 4 is shown the equilibrium vapour pressure of each species for a wide range of temperatures.

The term $(\mathcal{M}/2\pi\mathcal{R}T)^{1/2}\, p_i$ represents the flux of incident particles on the surface while the therm $(\mathcal{M}/2\pi\mathcal{R}T)^{1/2}\, p_{vap,i}$ represents the mass flux emerging from the wall. The α_{evap} and α_{cond} are respectively the evaporation and condensation coefficient. In equilibrium both coefficients are the same and the net flux of evaporating and condensating particles is zero [12]. The non-equilibrium evaporation implies a formation a of layer called Knudsen layer where the rarefaction effects become dominant thus the use of continuum methods becomes impossible [13]. [14] defines the α_{evap} coefficient as the ratio of the number of particles evaporated with respect to the equilibrium conditions, while the α_{cond} is the ratio of the number of particles condensating with respect to the impinging particles at the wall (both coefficients are bounded between 0 and 1). He observed these coefficients experimentally for water and concluded that they can vary significantly depending on the conditions. One possible way to estimate these coefficients is trough molecular dynamics (MD) [15] which becomes prohibited expensive for a large system. Hereafter a sensitivity analysis was made to these coefficients which will be shown later on.

By summing Eq. 4 over all species, one obtains:

$$\dot{m}_{evap} = (\rho u)_w$$

Once the gas composition is known and the mass blowing rate, $\dot{m}_{evap}$, is computed, the surface blowing velocity can be easily computed.

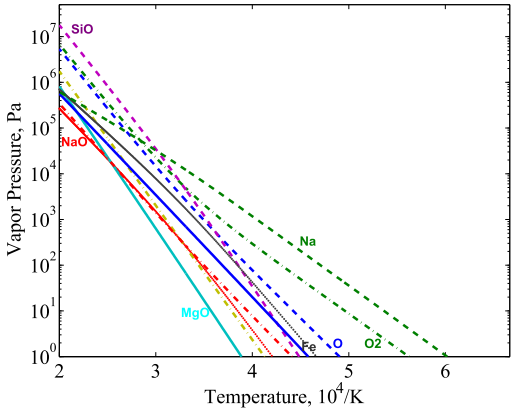

Figure 4: Vapor pressure for a silicate composition

2.2. Numerical tools

The flow governing equations are solved through a CFD code where the SMB boundary condition, explained the in previous section, is implemented. The flow properties are computed with the VKI physico-chemical library (Mutation^{++}). Energy and chemical (photoionization and photodissociation) source terms to account for radiation are included into the Navier-Stokes. These source terms are computed by solving the radiative transfer equations (RTE).

2.2.1. Stagnation-Line Code CFD Solver

The 1D Stagnation-Line solver developed at the VKI by Munafò [16], resolves the Navier-Stokes equations along the stagnation line of spherical or cylindrical bodies, where an illustration is shown by Fig. 5. This model leads to an efficient way to calculate hypersonic flows with low computational costs.

In this code the three-dimensional Navier-Stokes equations are reduced to a one-dimensional approximation for the stagnation streamline by a system called "Dimensionally Reduced Navier Stokes Equations" (DRNSE). The spatial discretization is done by finite volume method and the time integration is computed by a Backward-Euler method. The stagnation-line equations read as:

$$\frac{\partial}{\partial t}\mathbf{U} + \frac{\partial}{\partial r}\mathbf{F}^{\mathbf{inv}} + \frac{\partial}{\partial r}\mathbf{F}^{\mathbf{vis}} + \frac{\mathbf{G}^{\mathbf{inv}} + \mathbf{G}^{\mathbf{vis}}}{r} = \mathbf{S}^{\mathbf{c}} + \mathbf{S}^{\mathbf{r}} \quad (6)$$

Where $\mathbf{U}$ denotes the volume-specific balance quantities, $\mathbf{F}^{\mathbf{inv}}$ are the inviscid fluxes, $\mathbf{F}^{\mathbf{vis}}$ the viscous terms, $\mathbf{S}^{\mathbf{c}}$ and $\mathbf{S}^{\mathbf{r}}$ are respectively the chemical and ra-

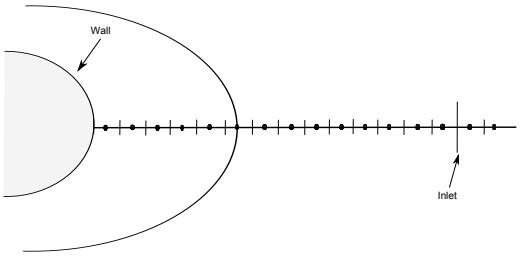

Figure 5: 1D Stagnation-Line illustration

diative source terms:

$$
\begin{aligned}
\mathrm{U} &= \left[\rho_i,\ \rho u,\ \rho v,\ \rho E,\ \rho e^{VE}\right]^T \\
\mathbf{F^{inv}} &= \left[\rho_i u,\ \rho u^2 + p,\ \rho uv,\ \rho uH,\ \rho u e^{VE}\right]^T \\
\mathbf{F^{vis}} &= \left[\mathrm{J}_{ri},\ \bar{\tau}_{rr},\ \bar{\tau}_{r\theta},\ q_r + \bar{\tau}_{rr}u,\ q_r^{VE}\right]^T \\
\mathbf{G^{inv}} &= [2\rho_i(u+v),\ 2\rho u(u+v),\ 3\rho v(u+v) - 2\bar{p}, 2\rho H(u+v), \\
&\rho e^{VE^T} \\
\mathbf{G^{vis}} &= [\mathrm{J}_{ri},\ 2(\bar{\tau}_{rr} - \bar{\tau}_{\theta\theta} + \bar{\tau}_{r\theta}),\ -\bar{\tau}_{\theta\theta} + 3\bar{\tau}_{r\theta},\ 2(q_r + \bar{\tau}_{rr}u + \bar{\tau}_{\theta\theta}u + \bar{\tau}_{r\theta}v), \\
&2q_r^{VE^T} \\
\mathbf{S^c} &= \left[\dot{\omega}_i^{\mathbf{c}},\ 0,\ 0,\ 0,\ \Omega^{VE}\right]^T \\
\mathbf{S^r} &= \left[\dot{\omega}_i^{\mathbf{rad}},\ 0,\ 0,\ \mathcal{P}^{rad},\ \mathcal{P}^{rad,VE}\right]^T
\end{aligned}
\tag{7}
$$

The variables $\mathbf{G^{inv}}$ and $\mathbf{G^{vis}}$ are inviscid and viscous source terms arising from the DRNSE transformation, respectively. The therm ρe^{VE} stands for vibrational-electronic-electron energy. Details regarding the radial heat fluxes, q_r and q_r^{VE} as well the energy transfer source term, Ω^{VE} are given by [10].

2.2.2. MUlticomponent Thermodynamic And Transport properties for IONized plasmas in C++ (Mutation^{++})

The closure of the multi-temperature Navier-Stokes equations is done by computing thermodynamic and transport properties. Mutation^{++} is a library built at the VKI by [17] where thermodynamic properties are computed by the Rigid Rotor Harmonic Oscillator model while transport properties are derived by the Chapman-Enskog expansion from Kinetic Theory [18].

3. Results and Discussion

A two-temperature model was used for these simulations, i.e., T = T_{rot} and T_{vib} =T_{ele} and the wall temperature was imposed at 2600 K. The choice of this temperature was based on experimental and numerical observations of a melting ordinary chondrite [19].

The first analysis concerns a sensibility study of both the evaporation and condensation coefficient (respectively α_{evap} and α_{cond}) in eq. 5. This analysis is made to understand the influence of such coefficients in terms of the overall mass blowing rate. The concept of these coefficients is explained in section 2.1.3 as well the difficulty to access such properties, which motivates the following study. It was considered a 0.1 meter radius object with a 15 km/s velocity at 60 km altitude.

The second part of the discussion concerns the influence of radiation coupled to the flow/ablation and the overall effects for two different sizes (0.1 and 1 meter radii). The radiation source terms (section 2.1.2) are computed and updated to the flow after a determined number of iterations. The conditions were the same as the previous analysis.

3.1. Sensitivity analysis on the evaporation law

The choice of the Knudsen-Langmuir (eq. 5) parameters is shown by table 1. For all the cases the major vapour species are Na followed by NaO being in agreement with meteor observations since these species are considered the most volatiles.

Table 1: Eq. 5 coefficient parameters

Case #	coefficient
Case 1	α_{evap} = 0.1
	α_{cond} = 0.1
Case 2	α_{evap} = 0.1
	α_{cond} =0.0
Case 3	α_{evap} = 1.0
	α_{cond} = 1.0

Figure 6 shows a comparison between case 1 and 2 of Na and Na^+ along the stagnation streamline. It is seen a large difference between both cases regarding

the concentration of Na at the surface. Even if both cases have the same evaporation coefficient the null condensation coefficient, for case 2, does not allow for this species to condensate. The species Na^+ is not a direct product from the evaporation but instead from the ionization of Na. The choice of a different condensation/evaporation coefficient not only influences the ablation rate but also changes the behaviour of the shock layer increasing substantially the electron concentration. The low ionization coefficient for this type of species leads to a fast ionization making the electron concentration a the wall different than zero, which can make an impact to the material (material electric conductivity). Moreover due to the high evaporation rate of Na for the case 2, the composition becomes strongly ionized close to the wall.

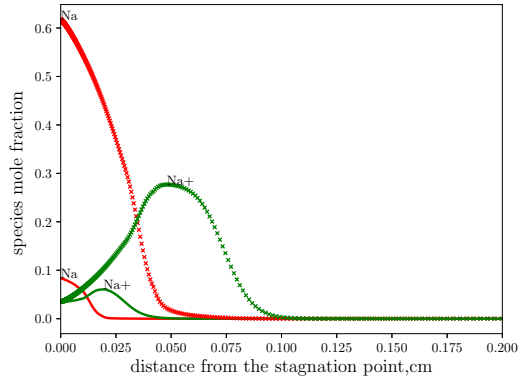

Figure 6: Evaporated species along the stagnation streamline; —— case 1, , $*$ case 2

In figure 7 the temperature profile along the stagnation streamline is shown. The shock translation temperature reaches a maximum of 70000 followed by a decrease to a plateau of 12000 K where both the internal and translational reaches equilibrate. This decrease is due to a transfer of energy between translational to internal mode caused by chemical reactions of dissociation and ionization. For the case 1 the shock is roughly located at 0.7 cm while for the case 2 it is slight shifted upstream. The thermal boundary layer is also affected. These effects are a consequence of a stronger blowing rate from the material shown in table 2.

For case 1 and 3 the evaporation rates are similar (around 10 % of Na at the surface, fig 8). The blowing rates for the evaporated species are slightly higher for the case 3, when compared with case 1, explaining why the concentration of Na is higher leading also to a

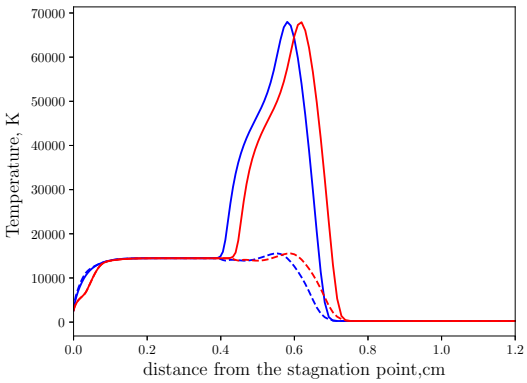

Figure 7: Temperature profile along the stagnation streamline at 60 km; —— translational temperature, −− internal temperature; case 1, case 2

higher ionization. Even though in the case 3 the evaporation coefficient is ten times higher than case 1 also the condensation coefficient follows the same trend. Meaning a balance between evaporation/condensation fluxes is established.

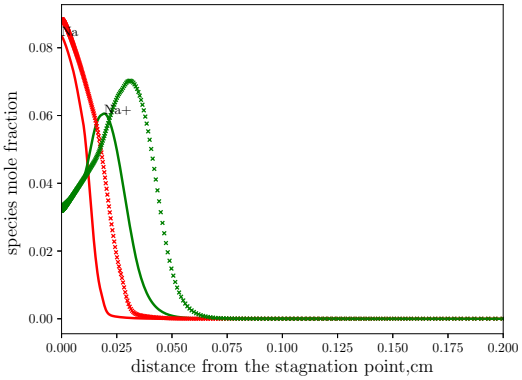

Figure 8: Evaporated species along the stagnation streamline; —— without radiation, , $*$ with radiation

In figure 9 the temperature profile for both case 1 and 3 are shown. The difference at the thermal boundary layer is quite small and the position of the shock for case 3 is slightly shifted upstream due to a higher blowing rate

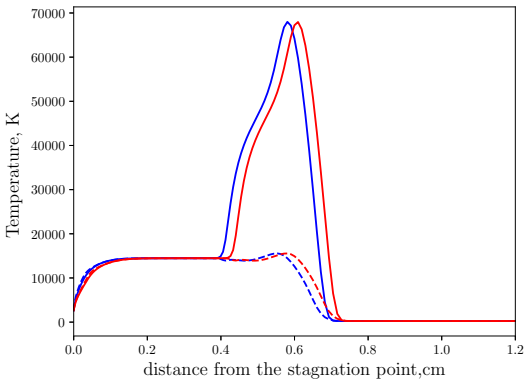

Figure 9: Temperature profile along the stagnation streamline at 60 km; —— translational temperature, −− internal temperature; case 1, case 3

Table 2: Blowing rates for major species

Case #	blowing rates
Case 1	$\dot{m}_{Na} = 0.133 \times 10^{-1}$
	$\dot{m}_{NaO} = 0.296 \times 10^{-2}$
	$\dot{m}_{SiO} = 0.597 \times 10^{-2}$
Case 2	$\dot{m}_{Na} = 0.226$
	$\dot{m}_{NaO} = 0.232 \times 10^{-2}$
	$\dot{m}_{SiO} = 0.597 \times 10^{-2}$
Case 3	$\dot{m}_{Na} = 0.119 \times 10^{-1}$
	$\dot{m}_{NaO} = 0.218 \times 10^{-1}$
	$\dot{m}_{SiO} = 0.297 \times 10^{-2}$

3.2. Radiation coupling with the flow

The final analysis was to include radiative source terms and to compare a 1 dm to a 1 m radius OC at the same conditions as the case 1 mentioned above

In figure 10 the temperature profile is shown. he shock position is roughly located at 0.6 cm showing a smaller shock layer when compared to the non-radiative case (fig 7) for the same conditions. The reduction of the shock layer is explained by a cooling down due to a strong emission (also observed by the equilibrium plateau after the shock). The highly excited particles emit photons in all the directions due to a decrease of the electronic levels. The emitted photons is absorbed by thermal boundary layer (increasing the internal energy of the particles) and also by the free-stream. A departure of non-equilibrium is also observed in the free-stream, where the internal temperature is higher than the translational. Since the atmosphere at 60 km is optically thin, this departure of non-equilibrium is observed up to 12 cm way from the surface. Once the free-stream particles absorbs this energy it result in photochemical processes such as photoionization and photodissociation.

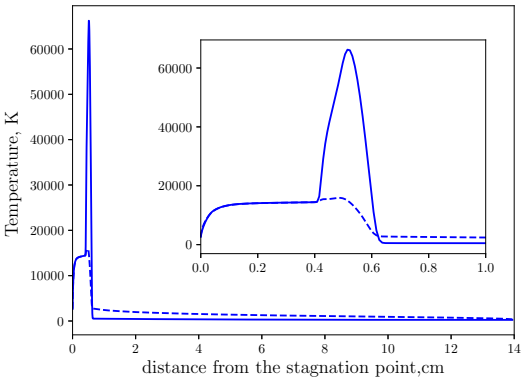

Figure 10: Temperature profile along the stagnation streamline at 60 km for 0.1 meter; —— translational temperature, −− internal temperature

The consequence of the photochemical processes is shown by fig. 11 where free stream is no longer formed by only N_2 and O_2 but also atoms and ions.

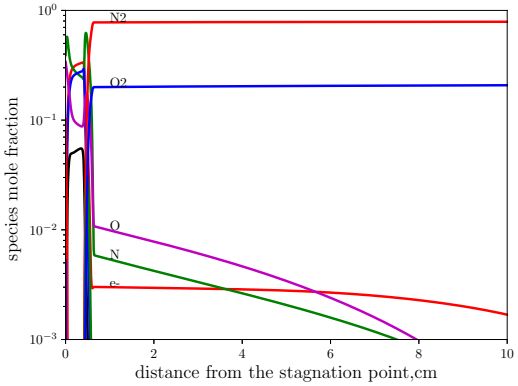

Figure 11: Air composition along the stagnation streamline at 60 km for 0.1 meter (log scale)

The effects of the shock layer coll down is also seen by fig 12. For a non-radiative field a constant plateau until the thermal boundary layer is expect for the species composition, meaning chemical equilibrium, which in this case is not observed.

For a bigger radius the radiation effects become stronger. For the 1 m radius body this departure is

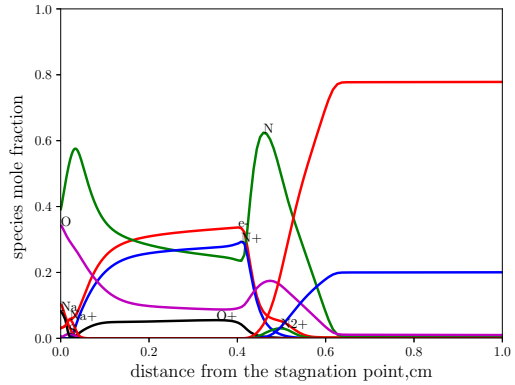

Figure 12: Air composition along the stagnation streamline at 60 km for 0.1 meter

strong enough to have an exchange of energy between the internal and translation mode rising the translation temperature (fig. 13). The non-equilibrium departure becomes more pronounced than for the smaller radius.

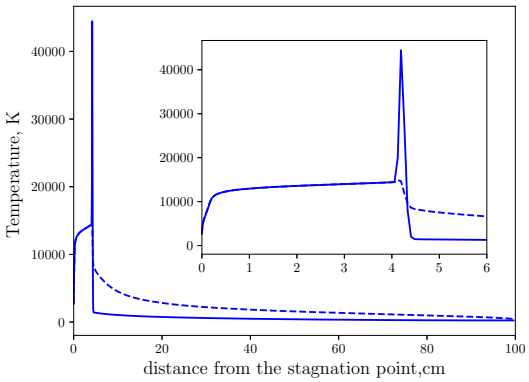

Figure 13: Temperature profile along the stagnation streamline at 60 km for 1 meter; —— translational temperature, −− internal temperature

This rise of the translation temperature leads to a strong dissociation of O_2 (fig 14) since the chemical rate is controlled by a geometrical temperature $T = \sqrt{TT_i}$.

The composition of the shock layer is also shown in fig 15 where the chemical non-equilibrium becomes also stronger.

In terms of evaporation rate not substantially differences were noticed comparing with the non-radiative flow because the surface temperature was imposed to be same for all the cases. In reality the surface tem-

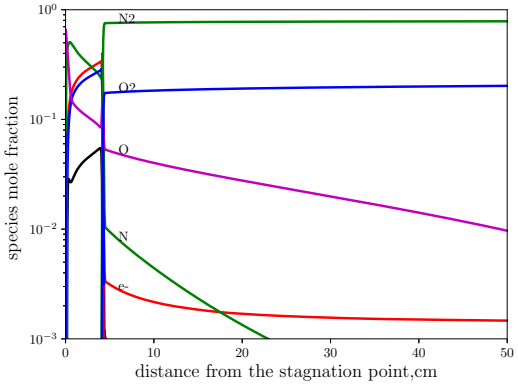

Figure 14: Air composition along the stagnation streamline at 60 km for 1 meter (log scale)

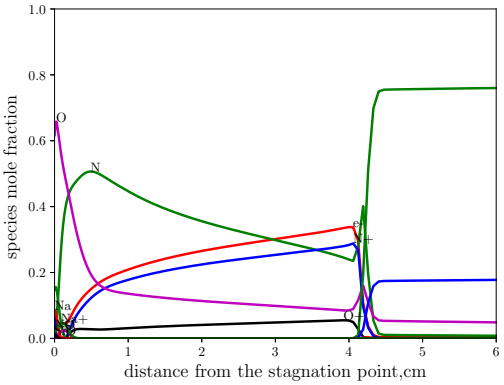

Figure 15: Air composition along the stagnation streamline at 60 km for 1 meter

perature should be estimated by an surface energy balance (SEB), similar to the surface mass balance. For the calculation of the SEB the incoming radiative flux will enter to the balance which might change significantly the surface temperature, deepening how strong the radiative field is.

4. Conclusion

A model to study the meteor ablation at low altitude has been proposed and implemented. The chosen parameters (trajectory, entry velocity and material size) were selected arbitrarily with the purpose of presenting a different approach from the one proposed by the state of the art. The model takes the clue from the strategy used to evaluate the gas-surface interaction on the heat shields of re-entry capsules.

The first step was to gather thermodynamic properties for the metallic species produced by evaporation. Taking the full electronic levels can become computationally expensive when used by CFD solvers. A reduction method was presented which has shown to preserve its accuracy when compared with the full data set.

An evaporation model based on kinetic-theory was also presented. Do to the kinetic nature of the evaporation processes, approximations are made when extended to macroscopic properties. A sensitivity analysis was made to the evaporation and condensation coefficients from the Knudsen-Langmuir law. These coefficients range from 0 to 1 and not big difference was observed when both coefficients are the same for lowest and highest bond. On the other hand if both coefficients are different a significant effects is observed in the flow field.

In this work a flow/radiation/ablation methodology was presented to study the meteor entry. It was observed that a stronger radiative field for bigger bodies which explains the stronger luminosity for bolides. For both radii it was observed a decrease of temperature in the shock layer due to the radiant emission increasing of the heat flux at the surface. The radiative field becomes stronger for the 1 m case due to a larger shock layer. The ablation rate did not change significantly since the wall temperature as chosen to be the same as the first analysis. Interestingly, due to the strong shock emission the flow upstream of the shock undergoes photochemical processes. These processes leads to photoionization and photodissociation reactions increasing the electron density. In our case only photoionization mechanisms are considered. Moreover a departure from thermal equilibrium is also observed in the free-stream. In this case the surface energy balance was not considered. Further analyses will be made to compute the energy balance considering the incoming radiative flux to the surface.

Acknowledgments

This research is sponsored by the Belgian Research Action Through Interdisciplinary Networks “METRO: Meteor trajectories and origins”. Research of B. Dias is sponsored by fellowship from the “Fonds pour la Formation la Recherche dans l’Industrie et dans l’Agriculture.”.

References

[1] Z. Ceplecha, J. Borovicka, W. Elford, D. ReVelle, R. Hawkes, V. Porubcan, M. Simek, Meteor phenomena and bodies, Space Science Reviews 84 (3-4) (1998) 327–471.

[2] O. P. Popova, P. Jenniskens, V. Emelyanenko, A. Kartashova, E. Biryukov, S. Khaibrakhmanov, V. Shuvalov, Y. Rybnov, A. Dudorov, V. I. Grokhovsky, et al., Chelyabinsk airburst, damage assessment, meteorite recovery, and characterization, Science 342 (6162) (2013) 1069–1073.

[3] N. Laurendeau, Statistical thermodynamics: fundamentals and applications, Cambridge University Press, 2005.

[4] A. D. Mario Capitelli, Gianpiero Colonna, Fundamental Aspects of Plasma Chemical Physics: Thermodynamics, 1st Edition, Springer Series on Atomic, Optical, and Plasma Physics 66, Springer-Verlag New York, 2012.

[5] T. E. Magin, M. Panesi, A. Bourdon, R. L. Jaffe, D. W. Schwenke, Coarse-grain model for internal energy excitation and dissociation of molecular nitrogen, Chemical Physics 398 (2012) 90 – 95.

[6] Atomic spectra database, https://www.nist.gov/pml/atomic-spectra-database.

[7] J. Scoggins, T. Magin, The gibbs function continuation method for linearly constrained multiphase equilibria, Combustion and Flame 162 (12) (2015) 4514–4522.

[8] B. J. McBride, S. Gordon, M. A. Reno, Thermodynamic data for fifty reference elements, NASA TP-3287-REV1, Glenn Research Center, Cleveland, Ohio (February 2001).

[9] J. Lamet, P. Rivière, M. Perrin, A. Soufiani, Narrow-band model for nonequilibrium air plasma radiation, Journal of Quantitative Spectroscopy and Radiative Transfer 111 (1) (2010) 87–104.

[10] J. Scoggins, L. Soucasse, P. Riviere, S. Soufiani, T. Magin, Coupled flow, radiation, and ablation simulations of atmospheric entry vehicles using the hybrid statistical narrow band model, in: 45th AIAA Thermophysics Conference, Dallas, Texas, 2015, AIAA 2015–3112.

[11] L. Schaefer, B. Fegley, A thermodynamic model of high temperature lava vaporization on io, Icarus 169 (2004) 216–241.

[12] Y. Zudin, Non-equilibrium evaporation and condensation processes : analytical solutions, Mathematical engineering, Springer, 2017.

[13] T. Ytrehus, S. stmo, Kinetic theory approach to interphase processes, International Journal of Multiphase Flow 22 (1) (1996) 133 – 155.

[14] R. Marek, J. Straub, Analysis of the evaporation coefficient and the condensation coefficient of water, International Journal of Heat and Mass Transfer 44 (1) (2001) 39 – 53.
[15] A. Frezzotti, P. Barbante, Kinetic theory aspects of non-equilibrium liquid-vapor flows, Mechanical Engineering Reviews.
[16] A. Munaf, T. E. Magin, Modeling of stagnation-line nonequilibrium flows by means of quantum based collisional models, Physics of Fluids 26 (9) (2014) 097102. doi:10.1063/1.4894842.
[17] J. Scoggins, Development of Mutation++: MUlticomponent Thermodynamics And Transport properties for IONized gases library in C++, Tech. Rep. VKI PhD Symposium (2013).
[18] T. E. Magin, G. Degrez, Transport algorithms for partially ionized and unmagnetized plasmas, Journal of Computational Physics 198 (2004) 424–449.
[19] B. Dias, F. Bariselli, A. Turchi, A. Frezzotti, P. Chatelain, T. Magin, Development of a melting model for meteors, AIP Conference Proceedings 1786 (1) (2016) 160004.

Comprehensive Characterization of the Aerothermomechanical Response of Space Debris to Atmospheric Entry Plasmas

Andrea Fagnani

Aeronautics and Aerospace Department, von Karman Institute for Fluid Dynamics, Belgium, andrea.fagnani@vki.ac.be

Supervisor: Olivier Chazot

Head of Department and Professor, Aeronautics and Aerospace Department, von Karman Institute for Fluid Dynamics, Belgium, chazot@vki.ac.be

University Supervisor: Annick Hubin

Professor at Department of Materials and Chemistry, Vrjie Universiteit Brussel, Belgium, annick.hubin@vub.be

Abstract

Satellites orbiting Earth offer unrivalled possibilities for research and commercial applications, including space science, Earth observation, telecommunication and meteorology. However, space activities over the last six decades have led to an unanticipated hazard: space debris, that is, the objects in Earth's orbit which are no longer functional. Due to their motion at speeds in the order of 10 km/s, collision of fragments with new and existing missions can lead to a catastrophic break-up, rapidly increasing the amount of debris in a cascade effect. To achieve a sustainable space environment, the Design for Demise (D4D) strategy proposes to conceive any new space object for the end-of-life disposal through a destructive atmospheric re-entry. Aerothermal heating and aerodynamic forces should be exploited to break up and completely destroy any spacecraft component. Experience, however, has demonstrated that several parts, mostly made up of titanium, steel and silicate materials, can survive re-entry almost intact, thus representing risk on ground.

To safely implement the D4D strategy, accurate computational models are required for the prediction of the spacecraft thermal degradation. In turn, these models need empirical data for validation. The main objective of this research is to advance the predictive capabilities of the aerothermal demise of space debris by performing multi-scale experiments and modelling to characterize the thermal decomposition of metallic and silicate components.

The project is articulated on three main axes. First, we will provide a comprehensive theoretical framework for the thermal degradation of metallic and silicate materials in high-enthalpy reacting flows, also addressing the ground-to-flight scaling methodology. Next, the experimental conditions will be carefully studied using computational codes developed at the von Karman Institute for Fluid Dynamics (VKI) and NASA Ames Research Center. However, these tools need to be improved in order to include the physics of the melting ablation problem. Finally, the core of the work will focus on the multi-scale experimental characterization, with plasma wind tunnel tests and micro-scale post-test analysis, leveraging competences and facilities of the VKI and the Electrochemical and Surface Engineering research group (SURF) at the VUB.

Keywords:
Space debris, aerothermochemistry, plasma wind tunnels, oxidation

Development of High-Fidelity Numerical Methods for the Simulation of the Aerothermal Ablation of Space Debris during Atmospheric Entry

David Henneaux

Aeronautics and Aerospace Department, von Karman Institute for Fluid Dynamics, Belgium, david.henneaux@vki.ac.be

Supervisor: Thierry Magin

Professor, Aeronautics and Aerospace Department, von Karman Institute for Fluid Dynamics, Belgium, magin@vki.ac.be

University Supervisor: Philippe Chatelain

Professor, Institute of Mechanics, Materials and Civil Engineering, Université catholique de Louvain, Belgium, philippe.chatelain@uclouvain.be

Abstract

The number of space debris orbiting the Earth is becoming increasingly problematic for the integrity of operational satellites and the future access to space. The many space debris mitigation projects currently under study require an accurate prediction of the degradation of these objects when they re-enter the atmosphere in order to comply with the severe re-entry safety requirements.

Dedicated engineering softwares are used to assess the survivability of these debris. However, the correlation-based models implemented in these softwares lack accuracy and they do not allow to gain insight into the complex flow phenomena taking place near the surface of the body, yet essential for the conception of new satellites designed for demise. That is why CFD methods are needed to study this complex situation. But the methods currently available rely on simplifying assumptions that compromise the reliability of the results.

The objective of this project is to develop new high-fidelity numerical methods able to deal with the presence of the three phases in the same domain and their complex interactions. They will be grouped into the ARGO code under development at CENAERO, VKI, and UCL, using a discontinuous Galerkin discretization of the governing equations. To do so, a highly- accurate multiphase method coupled with evaporation and surface tension models and based on a sharp interface approach will be employed for the treatment of the gas-liquid interface, while a state of the art melting method accounting for the diffuse character of the liquid-solid interface will be considered. Both methods will be built to work with multicomponent compressible equations. The code will then be validated with experimental data from the VKI Plasmatron facility.

At the end, this new numerical tool should make it possible to perform space debris ablation simulations of unprecedented reliability, allowing the validation of the models used in space debris re-entry softwares and contributing to the design of new material components that will ensure the complete destruction of future debris.

Keywords: Compressible multiphase flow, multispecies, discontinuous Galerkin, phase transition, sharp interface

Pyrolysis Modeling for Aerospace Applications

Francisco Torres Herrador

Aeronautics and Aerospace Department, von Karman Institute for Fluid Dynamics, Belgium, fratorhe@vki.ac.be

Supervisor: Olivier Chazot

Head of Departement and Professor, Aeronautics and Aerospace Department, von Karman Institute for Fluid Dynamics, Belgium, chazot@vki.ac.be

Supervisor: Thierry Magin

Professor, Aeronautics and Aerospace Department, von Karman Institute for Fluid Dynamics, Belgium, magin@vki.ac.be

University Supervisor: Julien Blondeau

Professor, Thermo and Fluid dynamics (FLOW), Faculty of Engineering, Vrije Universiteit Brussel, Belgium, jublonde@vub.ac.be

Abstract

When the Phenolic Impregnated Carbon Ablator (PICA) is submitted to high temperatures, it undergoes a series of irreversible chemical reactions in a process known as pyrolysis. This process has been modeled using different approaches depending on the application field. In this document, we review two pyrolysis models: the (aerospace) devolatilization and the (biomass) competitive reaction models exposing advantages and disadvantages for each approach as well as providing results on the pyrolysis modeling of PICA using each method.

Keywords: pyrolysis, kinetic modeling, heat shield

1. Introduction

In an atmospheric entry, the high kinetic energy of the spacecraft is converted into heat. The high temperatures achieved (10 000 K) require an appropriate Thermal Protection System (TPS) to protect the payload. In the recent years, a new generation of ablative TPS has gained attention due to their applicability to different entry scenarios. These materials are composites made up of short carbon fibers bound together with a phenolic resin [1]. A good example of such material is the Phenolic Impregnated Carbon Ablator (PICA) developed by NASA, which has been successfully used in missions such as Mars Science Laboratory (MSL) or Stardust Sample Return Capsule (SRC).

PICA has shown a great ablation performance due to several factors. The high porosity (80 %), which reduces the effective thermal conductivity, combined with high heat capacity of the components reduces the heat flux towards the interior of the TPS. In addition, the phenolic resin will undergo an endothermic thermal degradation process known as pyrolysis. In this process, the polymeric chains break up, leading to a carbonaceous char and the release of gases [2]. These gases are of great importance since they will be blown into the boundary layer generating an additional protection for the TPS [3]. Therefore, an accurate prediction of the pyrolysis gases is required for an appropriate TPS design.

Several researchers have studied the thermal degradation of different phenolic composites. The first experimental studies were carried out in the 1960s by Goldstein [4] and Sykes [5] on similar materials. In late 1990s, Trick and Saliba [6; 7] developed the first kinetic model for the pyrolysis of a carbon/phenolic ablator. In these studies, the mass loss and the species produced were investigated by means of Thermogravimetric Analysis (TGA) and Gas Chromatography (GC). More recently, Lachaud *et al.* [8] developed a new pyrolysis model by compiling information from the aforementioned experiments. How-

ever, these studies were carried out at heating rates ($\beta \approx 10\,\mathrm{K}\cdot\mathrm{min}^{-1}$) that are much lower than actual atmospheric entry applications. Different studies [9; 10] have shown that the extrapolation of kinetic data towards higher heating rates may result in erroneous predictions on the material decomposition due to differences on the chemical reactions occurring.

In fact, several studies [11; 12; 13] suggest that the decomposition behavior of phenolic resin varies considerably at different heating rates. The current models used in the aerospace sector cannot accommodate such behavior. The pyrolysis of biomass ([14; 15]) is somewhat similar to that of phenolic resin, following different kinetic pathways under different heating conditions. This can be explained by the degrees of freedom and the difference of time that the molecule chains have to break up and get released. In addition, the –competitive– models developed for biomass pyrolysis seem appropriate to model the decomposition of phenolic.

In this work, firstly we do a review of the state of the art on modeling of thermal degradation of solid materials showing the different models currently in use. Secondly, we present results obtained applying the aforementioned models on the thermal degradation of PICA.

2. Modeling

Pyrolysis is a complex and poorly understood process which has been historically treated using different modeling approaches. Di Blasi [15] presents an extensive review of the different approaches. Among the different methods, there are two methods that have been widely used: devolatilization and competing reaction mechanisms. In the following, we describe the two methodologies from the physical description to the mathematical modeling.

2.1. Devolatilization reaction mechanism

The devolatilization pyrolysis reaction mechanism (also known as parallel or multi-component mechanisms) considers that a solid phase $\mathcal{S}$ is composed of N_p different sub-phases. Each sub-phase P_i undergoes a determined number of pyrolysis reactions $R_{i,j}$ that release gaseous species A_k in a proportion given by stoichiometric coefficients $\gamma_{i,j,k}$ (Fig. 1). The remaining solid after the completion of pyrolysis is known as char. This model can be generically formulated as:

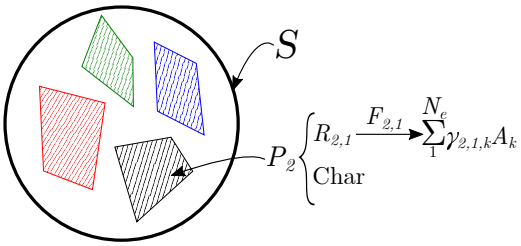

Figure 1: Example of a Solid $\mathcal{S}$ made up of 4 sub-phases (colors). The sub-phase 2 (black) undergoes 1 pyrolysis step which produces a mass loss $F_{2,1}$ and releases elements A_k given by $\gamma_{2,1,k}$.

$$\mathcal{S} \rightarrow \sum_{i}^{N_P} \sum_{j}^{N_{R_i}} R_{i,j} + \mathrm{Char} \tag{1}$$

$$R_{i,j} \rightarrow \sum_{k}^{N_*} \gamma_{i,j,k} A_k, \quad * \begin{cases} e = \text{elements} \\ s = \text{species} \end{cases} \tag{2}$$

Each reaction $R_{i,j}$ is modeled using an Arrhenius-like equation, of the following form:

$$\frac{\mathrm{d}\chi_{i,j}}{\mathrm{d}t} = \mathcal{A}_{i,j}(1-\chi_{i,j})^{n_{i,j}} \exp\left(\frac{-\mathcal{E}_{i,j}}{\mathcal{R}T}\right), \tag{3}$$

where the advancement of reaction ($\chi_{i,j} \in [0,1]$) evolves as function of the kinetic parameters ($\mathcal{A}_{i,j}, \mathcal{E}_{i,j}, n_{i,j}$) and the temperature.

The initial –virgin– density of the solid is expressed as the sum of each sub-phase as:

$$\rho_{\mathrm{s,v}} = \sum_{i}^{N_P} \rho_{i,\mathrm{v}} \tag{4}$$

The density evolution of the solid can be computed as the contribution of each advancement of reaction $\chi_{i,j}$ scaled by the fraction density loss $F_{i,j}$. This constant expresses the fraction of density that is lost when reaction $R_{i,j}$ reaches completion (i.e $\chi_{i,j} = 1$):

$$\rho_\mathrm{s}(t) = (\rho_{\mathrm{s,v}} - \sum_{i}^{N_P} \sum_{j}^{N_{R_i}} \rho_{i,\mathrm{v}} \chi_{i,j} F_{i,j}) \tag{5}$$

Similarly, the gas production rate of A_k (element or species) can be expressed as:

$$\pi_{A_k} = \sum_{i}^{N_P} \sum_{j}^{N_{R_i}} \rho_{i,\mathrm{v}} F_{i,j} \gamma_{i,j,k} \frac{\mathrm{d}\chi_{i,j}}{\mathrm{d}t} \tag{6}$$

Using multicomponent volatilization mechanisms, one may assume that products which have production peaks at the same location, are produced by the same reaction and can thus be grouped.

Furthermore, the production of each species A_k in the reaction i, j can be assumed to be independent, and the use of stoichiometric coefficients can be replaced for k pyrolysis reactions which keep the same kinetic triplet, but they use a weighted F parameter $\tilde{F}$ such that

$$\tilde{F}_{i,j,k} = \gamma_{i,j,k} F_{i,j}. \tag{7}$$

This allows to decouple the problem and removes the need of adding a unit sum optimization constraint to the stoichiometric coefficient ($\sum_{k}^{N_*} \gamma_{i,j,k} = 1$), which could be a difficult constraint for reactions producing more than two gases.

However, it can be seen that the final state and the amount of gases produced are pre-defined due to the use of the mass fraction loss $F_{i,j}$.

2.2. Competitive reaction mechanisms

In the competitive reaction mechanisms, a solid $\mathcal{S}_r$ can get decomposed into gases $\mathcal{G}_i$ and different new solids $\mathcal{S}_i$, which may further react over and over again in a chained process (Eq. 8). This model considers that the thermal decomposition of a solid can be described by the combination of different kinetic pathways. Indeed, the name of the mechanism comes from the fact that one reactant is generating different products at once, so that different kinetic pathways *compete* with each other to consume the reactant and, depending on the heating conditions, one pathway will be favored over others due to the different kinetic constants k_i. These different pathways allow to cover a broad range of heating conditions. A competing mechanism on the solid phase $\mathcal{S}_\mathrm{r}$ can be described as:

$$\mathcal{S}_r \xrightarrow{k_i} \gamma_i \mathcal{S}_i + (1-\gamma_i)\mathcal{G}_i, \quad i \in N_\mathrm{product}. \tag{8}$$

The rate of production/destruction of a solid $\mathcal{S}_i$ is expressed as a balance by the contributions from reactions that generate solid $\mathcal{S}_i$:

$$\frac{\mathrm{d}\rho_s}{\mathrm{d}t} = \underbrace{\sum_{r,s\neq reac} \gamma_s k_r \cdot \rho_{reac}^{n_r}}_{\text{generation term}} \underbrace{- \sum_{r,s=reac} k_r \cdot \rho_s^{n_r}}_{\text{destruction term}} \tag{9}$$

Where the reaction rate k_r is defined by the pre-exponential factor $\mathcal{A}_r$ and the activation energy $\mathcal{E}_r$:

$$k_r = \mathcal{A}_r \exp\left(\frac{-\mathcal{E}_r}{\mathcal{R}T}\right), \quad r \in N_r \tag{10}$$

In Eq. 9, the order of the reaction n_r is commonly set to 1 (in biomass applications) to reduce the number of model parameters to be calibrated.

In this model, the final state is not pre-defined since each pathway can generate different gases and/or char yields. However, their ability to predict gas yields in different heating conditions does not ensure extrapolation. The competing model is developed for a specific range of conditions, and extrapolation should be carefully studied [2].

By considering competitive reactions, we mean that a single density variable can be decomposed by several reaction rates, that are "in competition" with each other, as the reaction rate depends on temperature. We also assume that a given density variable can become activated[1] and further reacts, leading to multi-step reactions with density variables that can be a function of each other. Intermediate variables start at zero density, become positive when they are created by another pyrolysis reaction and can ultimately become again zero if consumed. With this assumption, it is therefore hard to express the problem is terms of a set of advancement coefficients since χ_i has to be monotonic to give meaning to the advancement of a reaction, although some attempts have been made using the cumulative production of a given solid species in the definition of the advancement coefficient [16]. Indeed, if an activated variable is consumed, then the advancement could go backward which would have no physical meaning; also it is not possible to define the completion of a variable that starts at 0 and is 0 at the end of the pyrolysis process because it has been consumed.

2.2.1. A basic example on competitive reactions

Let us consider a solid $\mathcal{S}$ which decomposes into two solid plus two gaseous products as shown in Figure 2.

The system of equations can be expressed as follows:

[1] This is sometimes refer to as a depolimerization step [14].

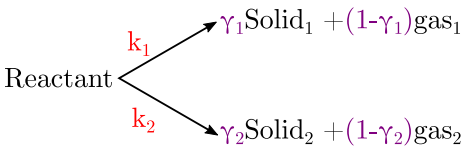

Figure 2: Basic example of competing scheme: one reactant produces two different product plus two gases

Table 1: Kinetic constants

Reaction	1	2
A	$4 \cdot 10^2$	$3 \cdot 10^{11}$
E	$60 \cdot 10^3$	$170 \cdot 10^3$
γ	0.6	0.8

$$
\begin{aligned}
\frac{\mathrm{d}\rho_r}{\mathrm{d}t} &= -(k_1 + k_2)\rho_r \\
\frac{\mathrm{d}\rho_{s1}}{\mathrm{d}t} &= \gamma_1 k_1 \rho_r \\
\frac{\mathrm{d}\rho_{s2}}{\mathrm{d}t} &= \gamma_2 k_2 \rho_r \\
\frac{\mathrm{d}\rho_{g1}}{\mathrm{d}t} &= (1-\gamma_1) k_1 \rho_r \\
\frac{\mathrm{d}\rho_{g2}}{\mathrm{d}t} &= (1-\gamma_2) k_2 \rho_r
\end{aligned}
\tag{11}
$$

Let us also consider that *reaction 1* occurs at low temperatures and is slow, and that *reaction 2* occurs at higher temperatures, but it is faster.

We can also assume that the proportion of gases produced by *reaction 1* is higher than by *reaction 2*. For example: $\gamma_1 = 0.6$ and $\gamma_2 = 0.8$. The parameters chosen for this case are presented in Table 1.

We will simulate this case using four different heating rates $\beta = 0.05, 0.5, 5, 50\,\mathrm{K \cdot s^{-1}}$. Figure 3a presents the density loss for the different heating rates. It seems that *only* one pyrolysis *step* has occurred, however this is not the case. In Figure 3b, the evolution of the two products can be better observed. For slow heating rates ($\beta = 0.05\,\mathrm{K \cdot s^{-1}}$), *reaction 1* will have enough time to convert *Reactant* into Sol_1. As the heating rate is increased, *reaction 1* will not have enough time to consume the reactant before *reaction 2* gets active, and since it is much faster, it will consume reactant, generating Sol_2. It can be seen that the density of the *char* in Figure 3a is not a equal for the different simulated cases, but it is related to γ_1, γ_2 and to the temporal evolution of the process (thus indirectly related to β).

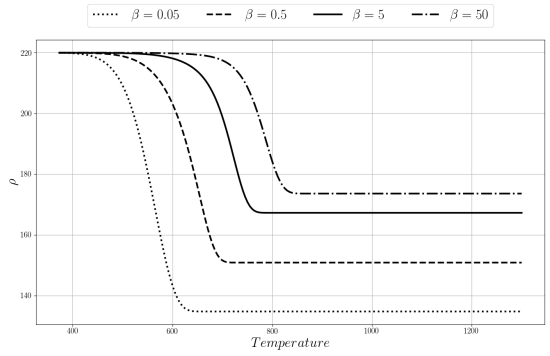

(a) Density loss of the reactant

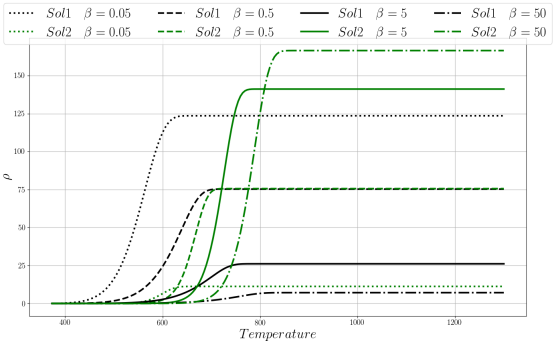

(b) Density evolution of the products

Figure 3: Simulated results for 2 competing reactions with $\gamma_1 < \gamma_2$

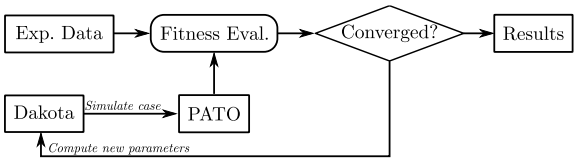

Figure 4: Basic structure of the optimization setup

This is a **key difference** with respect to the parallel multi-component mechanisms currently used to simulate the decomposition of phenolic resin. Using parallel schemes, the final state is pre-defined by the F's associated to each pyrolysis reaction.

3. Calibration methodology

Model parameters presented in Section 2 need to be adjusted in order to reproduce the experiments. The basic structure of the calibration methodology has been essentially the same in the different models presented and it is depicted in Figure 4. We use the optimization tool Dakota ([17]) developed by Sandia National Laboratories to calibrate the model parameters. In each iteration of the optimization, Dakota will set up the appropriate parameters for the pyrolysis mechanism. With those parameters, the numerical solver Porous media Analysis Toolbox based on OpenFOAM (PATO [8]) will carry out a simulation of the pyrolysis process with the given conditions of heating rate, geometry, material properties, etc. In most cases, the sample can be considered isothermal, so the case can be reduced to a 0D geometry, consisting of one cell.

This soft coupling between PATO and Dakota allows great flexibility: access to a large variety of optimization methods (gradient based and evolutionary), and also allows to choose which model (multicomponent, competing, etc) or level of fidelity we want to use to simulate the solid thermal decomposition in PATO.

4. Results

Hereafter we present results for both devolatilization and competitive mechanisms derived from experimental data. For the devolatilization mechanism, the experimental results of Bessire and Minton [18] are used, and for the competitive, data from Stokes [12] at a broad range of heating rates is used.

4.1. A high heating rate elemental model for PICA[2]

Bessire and Minton [18] carried out Mass Spectroscopy (MS) experiments using PICA samples, in which 14 significant pyrolysis products were identified. These products are organic compounds of the form $C_xH_xO_x$, therefore one can then consider the element (C, H and O) contributions of each compound to construct a finite rate elemental model for PICA. If required, the species composition may be obtained assuming chemical equilibrium in the porous media.

The proposed devolatilization scheme consists of 4 parallel reactions [4; 5; 8] in which C, H and O are released following stoichiometric coefficients γ_i.

The optimized parameters are shown in Table 2, we can observe that the 3rd reaction is the most important, consuming 33.6 % of the resin content which mostly produces carbon and oxygen (in terms of mass).

Table 2: Summary of the kinetic parameters identified for the element-based model.

R	F(-)	log($\mathcal{A}$)(-)	$\mathcal{E}$(kJ/mol)	m (-)	γ(-)	
1	0.032	5.67	51.4	7.74	C	0.32
					H	0.06
					O	0.62
2	0.089	7.02	87.4	4.02	C	0.40
					H	0.07
					O	0.53
3	0.336	7.03	103.7	4.33	C	0.42
					H	0.12
					O	0.46
4	0.086	6.9	194.4	9.25	C	0.25
					H	0.21
					O	0.54

Figure 5 shows the comparison between the experimental data and the optimized parameters. It can be observed that the agreement is great for the most produced elements (C and O), while for hydrogen the peak is slightly shifted towards higher temperature because the optimizer tends to favor the most produced elements.

In addition, the density loss evolution can be obtained by integrating the element production rates as shown in Figure 6 also presenting great agreement with the results of Bessire and Minton.

[2]These results are part of a journal publication.

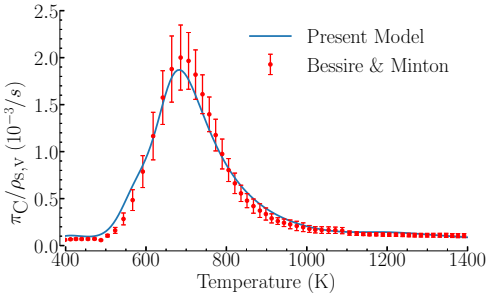

(a) Carbon

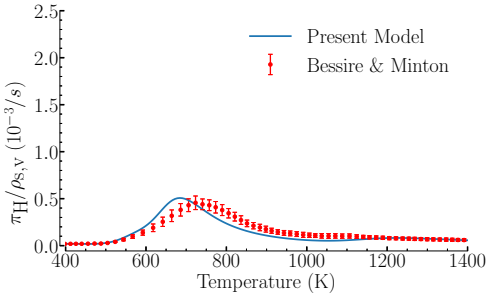

(b) Hydrogen

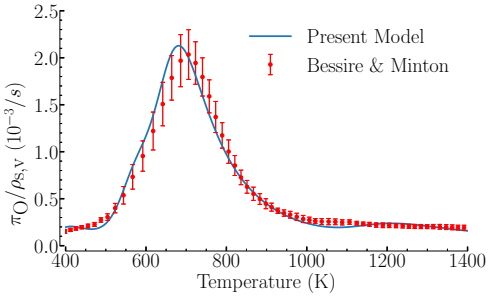

(c) Oxygen

Figure 5: Results from the parameter calibration. Simulations (——) show good agreement with Experiments (•). The error-bars represent 1σ experimental uncertainty.

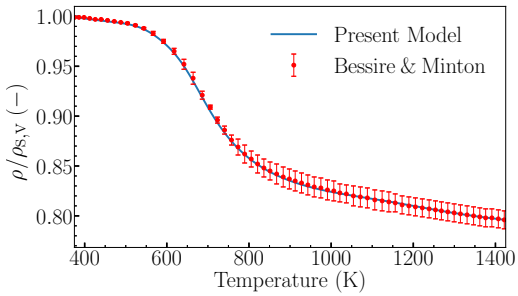

Figure 6: Reconstructed TGA curve from the element production rate.

4.2. *A first competitive mechanism for SC1008 resin*

Back in 1995, Stokes [12] did measurements on SC1008 and found out that at largely varying heating rates ($\beta \in [20, 1000]\text{K} \cdot \text{min}^{-1}$) the main pyrolysis peak was shifting towards low temperatures at high heating rates. These observations remained however forgotten until Bessire and Minton [18] observed a similar behavior during their experiments. This behavior may be explained at the molecular scale by differences in the depolimerization process, however in this section we will focus on developing a global reaction mechanism which is capable of phenomenologically recovering those results.

The proposed scheme is depicted in Figure 7. There are two kinetic paths, for the low and high heating rates. At low heating rates, the slow process k_1 will consume the *Reactant* producing $Activation_{slow}$ which will react at high temperatures producing $Solid_1$ and Gas_1 (Figure 8a). At high heating rates, the fast process k_3 will gain importance consuming the *Reactant* and producing $Activation_{fast}$ which will further react into $Solid_2$ and Gas_2 (Figure 8b). Both $Solid_1$ and $Solid_2$ could be grouped as Char, but here we keep them separated for illustration purposes.

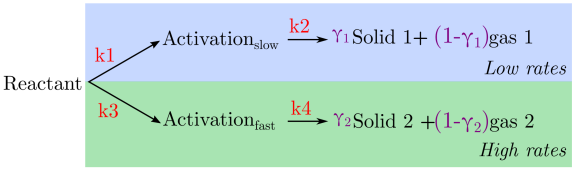

Figure 7: Proposed competitive scheme for the pyrolysis of SC1008 resin

Figure 9 shows the results of the optimization procedure using the kinetic scheme aforementioned. It can be observed that the kinetic scheme is capable of capturing the shift towards lower temperatures when the heating rate is increased.

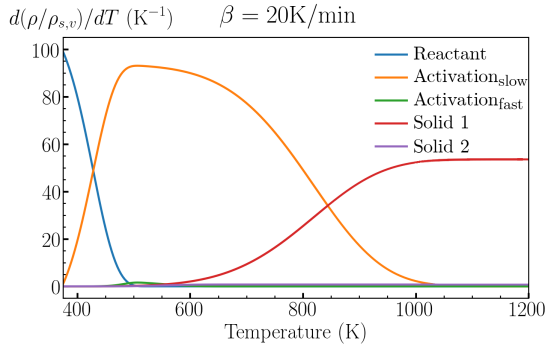

(a) 20 K · min^{-1}

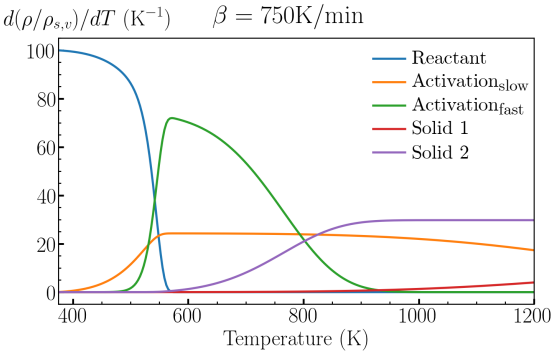

(b) 750 K · min^{-1}

Figure 8: Production/Destruction rates of the different solids.

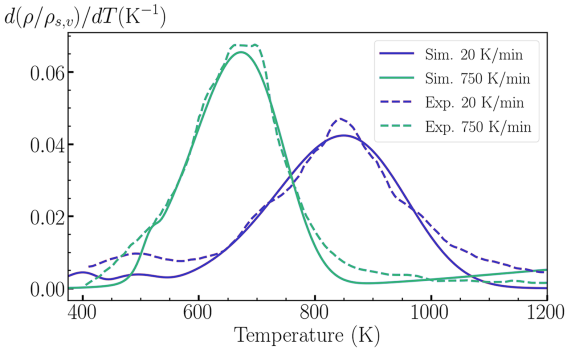

Figure 9: Competitive pyrolysis calibration results for SC1008.

5. Conclusions

In this report, we have revised two different approaches to the pyrolysis process: the devolatilization model currently used in the aerospace sector, and the competitive reaction model commonly used in biomass.

The devolatilization model is rather simple since it assumes that reactions occur in parallel without any kind of interactions. This allows to fully decouple the problem and even have analytical solutions in some cases. This type of model has shown great agreement to match experimental data at a given condition of heating rate and in some cases even to extrapolate it. However, experimental findings show that this model is not capable of reproducing the complexity of the pyrolysis process at largely varying heating rates.

The alternative proposed is to use competitive mechanisms. In this model, a reactant can take different kinetic paths depending on the time evolution of the environment conditions (heating rate). These preliminary results have shown that we are now capable of capturing major pyrolysis features occurring at two largely different heating rates (20 and 750 K · min^{-1}). These results suggest that pyrolysis modeling based on competitive reactions should be further investigated, which we plan to carry out when more experimental data become available.

Acknowledgments

The research of F. Torres Herrador is supported by SB PhD fellowship 1S58718N of the Research Foundation Flanders (FWO).

The authors would like to acknowledge Dr. Brody Bessire for the useful discussions and comments on this work.

References

[1] J. C. Ferguson, F. Panerai, J. Lachaud, A. Martin, S. C. C. Bailey, N. N. Mansour, Modeling the oxidation of low-density carbon fiber material based on micro-tomography, Carbon 96 (2016) 57–65. doi:10/f74dqb.
URL http://www.sciencedirect.com/science/article/pii/S0008622315302153

[2] J. Blondeau, H. Jeanmart, Biomass pyrolysis at high temperatures: Prediction of gaseous species yields from an anisotropic particle, Biomass and Bioenergy 41 (2012) 107–121. doi:10/f3zmcx.
URL http://www.sciencedirect.com/science/article/pii/S0961953412001043

[3] G. Duffa, Ablative Thermal Protection Systems Modeling, American Institute of Aeronautics and Astronautics, 2013.

[4] H. E. Goldstein, Pyrolysis Kinetics of Nylon 66, Phenolic Resin, and Their Composites, Journal of Macromolecular Science: Part A - Chemistry 3 (4) (1969) 649–673. doi:10.1080/10601326908053834.
URL http://dx.doi.org/10.1080/10601326908053834

[5] G. F. Sykes, Decomposition Characteristics of a Char-Forming Phenolic Polymer Used for Ablative Composites., Tech. Rep. TN D-3810 (1967).

[6] K. A. Trick, T. E. Saliba, Mechanisms of the pyrolysis of phenolic resin in a carbon/phenolic composite, Carbon 33 (11) (1995) 1509–1515. doi:10.1016/0008-6223(95)00092-R.
URL http://www.sciencedirect.com/science/article/pii/000862395000092R

[7] K. A. Trick, T. E. Saliba, S. S. Sandhu, A kinetic model of the pyrolysis of phenolic resin in a carbon/phenolic composite, Carbon 35 (3) (1997) 393–401. doi:10.1016/S0008-6223(97)89610-8.
URL http://www.sciencedirect.com/science/article/pii/S0008622397896108

[8] J. Lachaud, J. B. Scoggins, T. E. Magin, M. G. Meyer, N. N. Mansour, A generic local thermal equilibrium model for porous reactive materials submitted to high temperatures, International Journal of Heat and Mass Transfer 108, Part B (2017) 1406–1417. doi:10.1016/j.ijheatmasstransfer.2016.11.067.

[9] R. K. Agarwal, On the use of the arrhenius equation to describe cellulose and wood pyrolysis, Thermochimica Acta 91 (1985) 343–349. doi:10/fr8tn3.
URL http://www.sciencedirect.com/science/article/pii/0040603185852278

[10] P. Åimon, Isoconversional methods, Journal of Thermal Analysis and Calorimetry 76 (1) (2004) 123. doi:10/bmrvgn.
URL https://link.springer.com/article/10.1023/B:JTAN.0000027811.80036.6c

[11] W. M. Jackson, R. T. Conley, High temperature oxidative degradation of phenolformaldehyde polycondensates, Journal of Applied Polymer Science 8 (5) (1964) 2163–2193. doi:10/cbfhmp.
URL https://onlinelibrary.wiley.com/doi/abs/10.1002/app.1964.070080516

[12] E. H. Stokes, Kinetics of pyrolysis mass loss from cured phenolic resin, Journal of Thermophysics and Heat Transfer 9 (2) (1995) 352–358. doi:10.2514/3.667.
URL https://doi.org/10.2514/3.667

[13] B. K. Bessire, S. A. Lahankar, T. K. Minton, Pyrolysis of Phenolic Impregnated Carbon Ablator (PICA), ACS Applied Materials & Interfaces 7 (3) (2015) 1383–1395. doi:10/f62x9w.
URL https://doi.org/10.1021/am507816f

[14] R. S. Miller, J. Bellan, A Generalized Biomass Pyrolysis Model Based on Superimposed Cellulose, Hemicelluloseand Liqnin Kinetics, Combustion Science and Technology 126 (1-6) (1997) 97–137. doi:10.1080/00102209708935670.

[15] C. Di Blasi, Modeling chemical and physical processes of wood and biomass pyrolysis, Progress in Energy and Combustion Science 34 (1) (2008) 47–90. doi:10.1016/j.pecs.2006.12.001.
URL http://www.sciencedirect.com/science/article/pii/S0360128507000214

[16] C. Lautenberger, A. C. Fernandez-Pello, Optimization Algorithms for Material Pyrolysis Property Estimation, Fire Safety Science 10 (2011) 751–764.
URL http://www.iafss.org/publications/fss/10/751

[17] B. M. Adams, L. Bauman, W. J. Bohnhoff, K. R. Dalbey, M. Ebeida, J. P. Eddy, M. S. Eldred, P. Hough, K. Hu, J. Jakeman, J. Stephens, L. P. Swiler, D. Vigil, T. Wildey, DAKOTA : a multilevel parallel object-oriented framework for design optimization, parameter estimation, uncertainty quantification, and sensitivity analysis. Version 6.7, user's reference manual., Tech. Rep. SAND2014-4633, Sandia National Laboratories (Nov. 2017). doi:10.2172/991841.

[18] B. K. Bessire, T. K. Minton, Decomposition of Phenolic Impregnated Carbon Ablator (PICA) as a Function of Temperature and Heating Rate, ACS Applied Materials & Interfaces 9 (25) (2017) 21422–21437. doi:10.1021/acsami.7b03919.
URL http://dx.doi.org/10.1021/acsami.7b03919

Massively Parallel and Robust High-Order Methods for Transitional Hypersonic Flow Modelling on Unstructured Grids

Ray Vandenhoeck

Aeronautics and Aerospace Department, von Karman Institute for Fluid Dynamics, Belgium, vandenhoeck@vki.ac.be

Supervisor: Andrea Lani

Guest Research Expert, Aeronautics and Aerospace Department, von Karman Institute for Fluid Dynamics, Belgium

Research expert-project manager, Centre for Mathematical Plasma Astrophysics, KU Leuven, Belgium, andrea.lani@kuleuven.be

University Supervisor: Johan Steelant

Professor, Mechanical Engineering Department, KU Leuven, Belgium, johan.steelant@kuleuven.be

Abstract

The high-order finite element-type method Flux Reconstruction (FR), or Correction Procedure via Reconstruction (CPR), is a promising scheme with a high computational efficiency and favorable properties for massively parallel computing. However, the main pacing item for this method is its lack of robust shock capturing techniques for high-speed viscous flows. The present work proposes a modified Localized Laplacian Artificial Viscosity (LLAV) scheme combined with a positivity preservation method to handle hypersonic viscous flows. In order to avoid the stringent CFL constraints encountered in explicit time marching schemes, the proposed shock capturing method is adapted to implicit schemes. The FR method combined with the present shock capturing scheme was implemented in an efficient way within the open-source COOLFluiD platform. The proposed method was successfully applied to heat flux prediction of viscous hypersonic test cases.

Keywords: High-Order CFD, Hypersonics, Flux Reconstruction, Artificial Viscosity

1. Introduction

Over the past decade, compact high-order methods have drawn considerable attention due to an increased computational efficiency over their low-order counterparts. High-order methods generally introduce less numerical dissipation and allow for the use of coarser meshes to obtain the same accuracy as compared to low-order methods. The Flux Reconstruction (FR) or Correction Procedure via Reconstruction (CPR) formulation in particular represents one of the most recent and promising family of schemes. The FR approach is readily adaptable to high-performance parallel architectures due to its element-local nature and is capable to deal with complex unstructured geometries. However, adoption of these types of methods for both academic and industrial applications has remained limited up to now due to their reduced robustness and lack of adequate shock capturing techniques.

The present paper presents a novel FR shock capturing scheme for handling viscous hypersonic flows and its implementation within the world-class open-source framework for multi-physics modeling and simulations COOLFluiD[3]. More information on the development of this platform can be found in [1; 2]. The proposed method combines Localized Laplacian Artificial Viscosity with a positivity preservation scheme and is well-suited to both explicit and implicit time marching methods. The scheme was subsequently used to obtain to the authors' knowledge the first high-order FR viscous hypersonic results.

After giving an overview of the Flux Reconstruction method in section 2, the proposed shock capturing scheme is presented in section 3. Subsequently the implementation of the method is discussed in sec-

[3] https://github.com/andrealani/COOLFluiD/wiki

tion 4. Finally, section 5 presents two viscous hypersonic test cases in order to verify the shock capturing scheme.

2. Flux Reconstruction Method

The FR method was originally developed by Huynh in [3]. The formulation of the FR approach proposed by Huynh is applicable to 1D advection problems and can be extended to quadrilateral elements in 2D through tensor products of the one-dimensional base and correction functions. In 2009, the FR scheme was extended to diffusion problems. In this case, the flux also depends on the gradient of the solution, and the reconstruction procedure is applied to both the solution and the flux [4]. In 2011, Huynh proposed a method to extend FR to deal with advection-diffusion problems on triangles [5].

Vincent, Castonguay, and Jameson proposed a class of FR schemes for linear advection problems in 1D, called Vincent-Castonguay-Jameson-Huynh (VCJH) schemes in [6] and extended the schemes to 2D and 3D advection-diffusion problems in [7; 8]. This method is characterized by a single parameter that determines the analytical form of the correction functions. By choosing a particular value for this scalar, the FR method can reduce to several existing methods, including Nodal Discontinuous Galerkin, Spectral Difference, and the g_2 scheme proposed by Huynh in [3].

2.1. FR in One Dimension

This section presents a review of the Flux Reconstruction method in one dimension equivalent to the method presented in [6; 9]. Consider solving the one-dimensional advection-diffusion problem on an arbitrary domain Ω, given by:

$$\frac{\partial u}{\partial t} + \frac{\partial f}{\partial x} = 0 \quad \text{with} \quad x \in \Omega = [x_L, x_R] \quad \text{and} \quad f = f\left(u, \frac{\partial u}{\partial x}\right). \tag{1}$$

In equation 1, x represents the one dimensional coordinate, t is the time variable, $u(x,t)$ is a conservative variable, and f is the flux which is a scalar for the 1D case. The Euler and Navier-Stokes equations can be written as a system of conservation equations, equivalent to expression 1. The FR method is classified as a Finite Element (FE)-type method. Hence, the spatial domain Ω is partitioned into a finite number N of non-overlapping, non-empty, open sub-domains Ω'_n such that:

$$\Omega'_n = \{x \mid x_n < x < x_{n+1}\} \text{ with } x_1 = x_L,\ x_{N+1} = x_R. \tag{2}$$

The closed domain corresponding to the union of the open sub-domain Ω'_n and its boundary $\Gamma_n = \{x_n, x_{n+1}\}$ is called an element and is denoted by $\Omega_n = \Omega'_n \cup \Gamma_n$ such that:

$$\bigcup_{n=1}^{N} \Omega_n = \Omega \quad \text{with} \quad \bigcap_{n=1}^{N} \Omega_n = \emptyset. \tag{3}$$

The exact solution u of the conservation law 1 is approximated by a function u_n^δ within each element Ω_n. This function u_n^δ corresponds to a polynomial of degree P within Ω_n and is identically zero on $\Omega \setminus \Omega_n$. These polynomials are generally discontinuous across elements. u^δ is constructed through summation of the elemental solutions u_n^δ. In the same manner, the exact flux f is approximated by a polynomial of degree $P+1$ within each sub-domain Ω_n, denoted by f_n^δ. The overall approximate flux f^δ in the entire domain Ω is given by the sum of the elemental approximate fluxes such that:

$$u^\delta(x,t) = \sum_{n=1}^{N} u_n^\delta(x,t) \text{ and } f^\delta(x,t) = \sum_{n=1}^{N} f_n^\delta(x,t). \tag{4}$$

Each element Ω_n together with the approximate solution u_n^δ and flux f_n^δ inside it, is transformed to a standard reference element $\Omega_S = \{\xi \mid -1 \le \xi \le 1\}$. In this manner, the computations for all elements are done in the same reference domain Ω_S. Consequently, the same algorithm can easily be applied to all elements. The transformation between Ω_n and Ω_S is carried out by means of a mapping function $\Theta_n(\xi)$.

The solution u_n^δ within each sub-domain Ω_n can be obtained by solving the transformed conservation equation within the reference element Ω_S:

$$\frac{\partial \hat{u}^\delta}{\partial t} + \frac{\partial \hat{f}^\delta}{\partial \xi} = 0 \quad \text{with} \quad \xi \in \Omega_S, \tag{5}$$

with the transformed physical quantities given by:

$$\hat{u}^\delta = \hat{u}^\delta(\xi,t) = J_n u_n^\delta(\Theta_n(\xi),t) \quad \text{and} \quad \hat{f}^\delta = \hat{f}^\delta(\xi,t) = f_n^\delta(\Theta_n(\xi),t). \tag{6}$$

In equation 6, J_n represents the Jacobian of the mapping $\Theta_n(\xi)$.

The FR method for solving equation 5 within the reference element Ω_S consists of seven subsequent steps. In the first step, a specific form for the approximate solution $\hat{u}^\delta$ within Ω_S is defined. To this end, a set of $P+1$ distinct solution points ξ_i are chosen within Ω_S at which the values of $\hat{u}^\delta$ are assumed to be

known. The two end-points of the standard element Ω_S are referred to as the flux points.

The approximate solution $\hat{u}^\delta$ is defined as a degree P polynomial of the following form:

$$\hat{u}^\delta = \sum_{i=1}^{P+1} \hat{u}_i^\delta l_i(\xi), \tag{7}$$

where $\hat{u}_i^\delta$ is the value of $\hat{u}^\delta$ at the i-th solution point, and $l_i(\xi)$ is the 1D Lagrange polynomial associated with the i-th solution point.

The second step consists of determining a common interface solution $\hat{u}^{\delta I}$ at the boundaries of the standard element Ω_S, i.e. $\xi = \pm 1$, where the flux points of two neighboring elements coincide. In order to compute this interface value, the approximate solution $\hat{u}^\delta$ must first be evaluated in the flux points by means of equation 7. The approximate solutions evaluated at the left and right boundaries are denoted as $\hat{u}_L^\delta = \hat{u}^\delta(-1)$ and $\hat{u}_R^\delta = \hat{u}^\delta(1)$. Following the second approach of Bassi and Rebay (BR2), $u^{\delta I}$ is then computed as the average of the two solutions in a flux point [10]. The common interface solutions corresponding to the left and right ends of Ω_n are denoted by $u_L^{\delta I}$ and $u_R^{\delta I}$. Figure 1 illustrates the process of computing the common interface values.

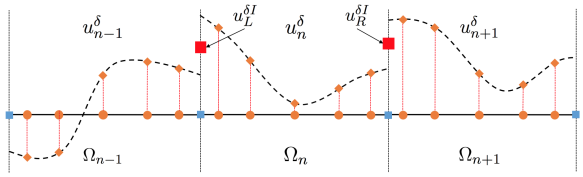

Figure 1: Computation of the common interface solutions $u_R^{\delta I}$ and $u_L^{\delta I}$ at the left and right boundary of Ω_n

The third step of the FR method consists of calculating a corrected solution gradient $\hat{q}^\delta$. The corrected solution gradient $\hat{q}^\delta$ is defined in terms of two correction functions $g_L(\xi)$ and $g_R(\xi)$ of degree $P+1$, which approximate the zero function within the reference element Ω_S, and satisfy the following boundary conditions: [9]

$$g_L(-1) = 1,\ g_R(-1) = 0,\ g_L(1) = 0,\ g_R(1) = 1. \tag{8}$$

Furthermore, the correction function for the right boundary $g_R(\xi)$ is defined as the reflection of the correction function $g_L(\xi)$ with respect to the vertical axis: $g_L(\xi) = g_R(-\xi)$.

The corrected solution gradient $\hat{q}^\delta$ is then computed via the following expression:

$$\hat{q}^\delta = \frac{\partial \hat{u}^\delta}{\partial \xi} + (\hat{u}_L^{\delta I} - \hat{u}_L^\delta)\frac{dg_L}{d\xi} + (\hat{u}_R^{\delta I} - \hat{u}_R^\delta)\frac{dg_R}{d\xi}. \tag{9}$$

The VCJH scheme is used to define the exact polynomial expression of g_L and g_R, as found in [7].

The fourth step consists of calculating the approximate discontinuous flux $\hat{f}^{\delta D}(\xi)$ on the reference element Ω_S. To this end, the flux is computed at each solution point ξ_i. In general, the flux depends on the solution and the solution gradient. Consequently, the discontinuous flux is evaluated using the approximate solution $\hat{u}^\delta$, and the corrected solution gradient $\hat{q}^\delta$. The approximate discontinuous flux $\hat{f}^{\delta D}$ is then constructed as a polynomial of degree P in the same manner as $\hat{u}^\delta$ in equation 7:

$$\hat{f}_i^{\delta D} = f(\hat{u}_i^\delta / J_n, \hat{q}^\delta / J_n) = \sum_{i=1}^{P+1} \hat{f}_i^{\delta D} l_i(\xi). \tag{10}$$

The fifth step of the FR framework involves computing the transformed common interface fluxes $\hat{f}^{\delta I}$ at the flux points of the standard element Ω_S. In order to compute these interface fluxes, it is necessary to first obtain the values of the approximate solution $\hat{u}^\delta$ and the corrected gradient $\hat{q}^\delta$ at the boundaries of the standard element by using equations 7 and 9. The common interface flux at the left and right ends of the standard element Ω_S is denoted as $\hat{f}_L^{\delta I}$ and $\hat{f}_R^{\delta I}$, respectively. The methodology for calculating the interface fluxes depends on the system of equations that needs to be solved. In the case of the Navier-Stokes equations, it is computed as the sum of a convective and a diffusive term. For the convective interface flux, an upwind biased approximate Riemann solver, like the Roe scheme [11], can be used. The diffusive interface flux is often calculated following the BR2 scheme, which uses the average approximate solution $((u^{\delta-} + u^{\delta+})/2)$ and the average corrected gradient $((q^{\delta-} + q^{\delta+})/2)$ as demonstrated by Bassi and Rebay [10] and applied to the FR approach in [9].

The flux must be continuous across element boundaries in order to obtain a conservative scheme. Therefore, the sixth stage of the FR framework consists of adding a correction flux function $\hat{f}^{\delta C}$ to the approximate discontinuous flux $\hat{f}^{\delta D}$ resulting in the continuous flux $\hat{f}^\delta$. The correction flux $\hat{f}^{\delta C}$ is a polynomial of degree $P+1$ defined in such a manner that the continuous flux $\hat{f}^\delta$ equals the common interface flux in the flux points, while approximating the discontinuous flux $\hat{f}^{\delta D}$ within the standard element Ω_S. In order to satisfy the aforementioned requirements, $\hat{f}^{\delta C}$ is constructed by means of the degree $P+1$ correction functions $h_L(\xi)$ and $h_R(\xi)$. These polynomials are

equivalent to the correction functions g_L and g_R used to define the corrected gradient $\hat{q}^\delta$ and have the same properties as expressed in 8.

The correction flux function $\hat{f}^{\delta C}$ takes the form:

$$\hat{f}^{\delta C} = (\hat{f}_L^{\delta I} - \hat{f}_L^{\delta D})h_L(\xi) + (\hat{f}_R^{\delta I} - \hat{f}_R^{\delta D})h_R(\xi), \quad (11)$$

where $\hat{f}_L^{\delta D} = \hat{f}^{\delta D}(-1)$ and $\hat{f}_R^{\delta D} = \hat{f}^{\delta D}(1)$ are the values of the approximate discontinuous flux at the left and right boundaries, evaluated from equation 10. The continuous flux $\hat{f}^\delta$ within the standard element Ω_S is then written as the sum of the approximated discontinuous flux and the correction flux:

$$\hat{f}^\delta = \hat{f}^{\delta D} + (\hat{f}_L^{\delta I} - \hat{f}_L^{\delta D})h_L + (\hat{f}_R^{\delta I} - \hat{f}_R^{\delta D})h_R. \quad (12)$$

A schematic of the flux correction procedure within the reference element Ω_S is given in figure 2.

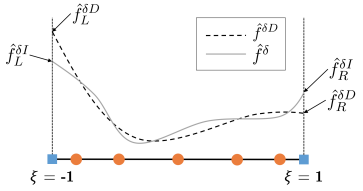

Figure 2: Correction procedure of the discontinuous flux $\hat{f^{\delta D}}$ within Ω_S such that the values of the total flux $\hat{f}^\delta$ at the boundaries are equal to $\hat{f}_L^{\delta I}$ and $\hat{f}_R^{\delta I}$

.

The final step consists of computing the divergence of the total flux $\hat{f}^\delta$ at each solution point ξ_i, which is trivial as the derivatives of both the Lagrange polynomials and correction functions are exactly known.

Finally, a time marching strategy such as a backward Euler method is applied to advance the approximate solution $\hat{u}^\delta$ in time using the following expression:

$$\frac{d\hat{u}_i^\delta}{dt} = -\frac{\partial \hat{f}^\delta}{\partial \xi}(\xi_i). \quad (13)$$

For quadrilateral and hexahedral elements, the extension to 2D and 3D is straightforward: it suffices to define a tensor product basis based on the one-dimensional Lagrange polynomials on the reference element, as shown in [3]. Subsequently the steps of the FR method are analogous to FR in one dimension.

3. Shock Capturing

Robust shock capturing is the main pacing item for high-order FE-type CFD methods. In the vicinity of discontinuities within the flow field, spurious oscillations appear due to the Gibbs phenomenon. This effect is more severe for higher orders and for stronger shocks. The oscillations near the shock generally cause numerical instabilities and negative pressures or densities. Several schemes have been investigated in [12; 13; 14; 15; 16] to avoid spurious oscillations around shock waves. However these schemes have not been successfully applied to viscous hypersonic flows and are generally only applicable to explicit time stepping. The present paper proposes a modified LLAV scheme combined with a positivity preservation method in order to alleviate oscillations caused by the Gibbs phenomenon as well as the harsh transient effects of hypersonics.

3.1. Localized Laplacian Artificial Viscosity

The localized artificial viscosity method adds an artificial diffusive flux that depends on the local properties of the flow field in order to spread out the shock over one or more elements. In this way oscillations due to the Gibbs phenomenon around shocks are attenuated. Within the Localized Laplacian Artificial Viscosity (LLAV) framework, the artificial viscosity is of a Laplacian type, as proposed in [17; 15]. The local artificial viscosity is only activated in areas of the flow field where discontinuities are present. To this end, a smoothness detector is used, of which several are proposed in [15].

LLAV shows better convergence characteristics compared to traditional limiters developed for FR, such as Multi-Dimensional Limiting Process (MLP) [13], especially for steady-state cases. Furthermore, LLAV is readily adaptable to implicit time-marching schemes. However, LLAV cannot guarantee positivity of the solution for hypersonic test cases and requires fine-tuning of the maximum amount of artificial viscosity added. A modified LLAV scheme is proposed to alleviate these difficulties.

Within the LLAV framework, an extra flux is added to the system of equations:

$$\frac{\partial \mathbf{u}}{\partial t} = -\nabla \cdot \mathbf{f}_c + \nabla \cdot \mathbf{f}_d + \nabla \cdot \mathbf{f}_{av}, \quad (14)$$

where $\mathbf{f}_c$ is the convective flux, $\mathbf{f}_d$ the diffusive flux and $\mathbf{f}_{av}$ the flux due to the artificial viscosity. $\mathbf{f}_{av}$ is constructed as follows:

$$\mathbf{f}_{av} = \varepsilon \nabla \mathbf{u}, \quad (15)$$

where ε is the artificial viscosity. Within the FR framework, this means that the space discretization procedure is also applied to a third flux. The gradients $\nabla \mathbf{u}$ are approximated using the corrected solution gradients $\mathbf{q}$ as computed in equation 9. As such, the

FR procedure, as described in section 2.1, is applied to $\mathbf{f}_{av} = \varepsilon \mathbf{q}$.

The value of the artificial viscosity ε is computed in such a way that it is only active in discontinuous regions:

$$\varepsilon = \begin{cases} 0 & \text{if } S < S_0 - \kappa, \\ \frac{\varepsilon_0}{2}\left(1 + \sin\frac{\pi(S - S_0)}{2\kappa}\right) & \text{if } S_0 - \kappa \leq S \leq S_0 + \kappa, \\ \varepsilon_0 & \text{if } S > S_0 + \kappa, \end{cases} \tag{16}$$

where S is the smoothness in the current element, S_0 the reference smoothness, κ a parameter to control the working spectrum of the artificial viscosity and ε_0 the maximum artificial viscosity.

The smoothness for a P-th order FR method can be computed as follows, using the smoothness detector found in [15]:

$$S = \log_{10} \frac{\langle u_m - u_m^{P-1}, u_m - u_m^{P-1} \rangle}{\langle u_m, u_m \rangle}, \tag{17}$$

where u_m is the state variable that is monitored in order to detect discontinuities. For the Navier-Stokes equations, typically the density ρ or pressure p is used. u_m^{P-1} represents the monitored state variable projected on a $(P-1)$-th order polynomial. The operator $\langle \cdot, \cdot \rangle$ is the element-wise scalar product over the solution points. The reference smoothness is generally set equal to $S_0 = -3\log_{10} P$ as suggested in [18]. However, it was found that a value of

$$S_0 = -5\log_{10} P - 0.5 \tag{18}$$

produces more robust resusts. The $P-1$-projected state variable can be computed by projecting the solution polynomial, which is expressed in a Lagrange polynomial basis, on a modal basis using the Vandermonde matrix. Next, the sum over the first $P-1$ polynomials is made to determine u_m^{P-1}.

A novel scheme to compute the maximum artificial viscosity is proposed. In order to match the flux dimensions, ε must be expressed in $\left[\frac{m^2}{s}\right]$, or a length-scale times a velocity-scale. Since a higher artificial viscosity is needed at higher speeds and in bigger elements (in order to spread out the shock over the element), ε_0 is set to be:

$$\varepsilon_0 = f(P) h |\lambda|_{max}, \tag{19}$$

where h is the characteristic length of the current element and $|\lambda|_{max}$ the maximum eigenvalue of the inviscid part of the system of equations. In order to take into account the order P of the FR method, following the approach of [15], $f(P)$ is set to:

$$f(P) = c(2 - \Delta\xi_{max}(P)), \tag{20}$$

where $\Delta\xi_{max}(P)$ is the subcell resolution, i.e. the largest distance between two solution points within the reference domain and c a constant. In order to avoid the need for fine-tuning the constant c, an approximate relation between this parameter and the number of cells over which a shock is spread.

For shocks where viscosity is present, the following Reynolds number is of order of magnitude 1:

$$\frac{\delta_s \Delta u \rho^*}{\mu^*} \approx 1, \tag{21}$$

where δ_s is the shock thickness, Δu the velocity difference over the shock, ρ^* and μ^* respectively the density and dynamic viscosity in the shock at $M = 1$. Consider the following assumptions:

$$\rho^* \sim \rho_\infty \quad \text{and} \quad \mu^* \sim \varepsilon \rho_\infty. \tag{22}$$

Combining these two relations, the following scaling relation is found:

$$\varepsilon \rho_\infty \sim \delta_s \Delta u \rho_\infty. \tag{23}$$

Using the expression for the velocity drop Δu over a shock:

$$\varepsilon \sim \delta_s \frac{2}{\gamma + 1} \frac{M_\infty^2 - 1}{M_\infty^2}, \tag{24}$$

combining with expression 19:

$$c(2 - \Delta\xi_{max}) h |\lambda|_{max} \sim \delta_s \frac{M_\infty^2 - 1}{M_\infty^2}, \tag{25}$$

rearranging and setting $h^* = (2 - \Delta\xi_{max})h$ the characteristic subcell length:

$$c \sim \frac{\delta_s}{h(u_\infty + \frac{u_\infty}{M_\infty})} \frac{M_\infty^2 - 1}{M_\infty^2}, \tag{26}$$

introducing the characteristic shock thickness $\delta_s^* = \frac{\delta_s}{h^*}$, this expression becomes:

$$c \sim \delta_s^* \frac{M_\infty - 1}{M_\infty}. \tag{27}$$

Using expression 27, the LLAV scheme can be characterized by a characteristic shock thickness δ_s^* which is a measure for the number of elements over which the shock is spread out. By calibrating c as:

$$c = \alpha \delta_s^* \frac{M_\infty - 1}{M_\infty} + \beta. \tag{28}$$

If there is no viscosity present, the characteristic shock thickness is zero. As a consequence, β can be set to

zero. For the value of α, a calibrating test case can be used. As described in the section 5, the following is found: $\alpha \simeq 0.027$.

By using this scheme, only the parameters κ and δ_s^* need to be specified for the LLAV method. The spectral sensitivity κ is only related to the smoothness detector and is independent of the specific conditions of the test case. As proposed in [15], a value of κ ranging from 1 to 5 generally produces robust results. However it was found that smaller values of κ, ranging from 0.5 to 1.5 generate more robust results, especially in combination with the expression for S_0 in equation 18. The characteristic shock thickness is a measure for the amount of elements over which the shock is spread, as a consequence, if $\delta_s^* < 1$ there is a risk of spurious oscillations, while if $\delta_s^* > 2$, the shock will be spread over more than two elements, and accuracy may be deteriorated due to superfluous artificial viscosity. The LLAV scheme based on these two parameters requires little fine-tuning and generally produces robust results, independent of the characteristic length h of the elements near the shock, of the Mach number of the far field, etc.

3.2. Positivity Preservation Scheme

When solving the Navier-Stokes equations, a negative density or pressure leads to an unphysical state which causes to solver to crash or become unstable. As such the following conditions must be satisfied during the iterative solution process:

$$\rho > 0 \quad \text{and} \quad p = (\gamma - 1)\left(\rho e_t - \frac{1}{2}\frac{\|\rho \mathbf{v}\|^2}{\rho}\right) > 0. \quad (29)$$

Here the pressure is expressed as a function of the conservative variables $\mathbf{u} = (\rho, \rho\mathbf{v}, \rho e_t)$, where $\mathbf{v}$ is the velocity and e_t the specific total energy.

A shock capturing method based on artificial viscosity cannot guarantee that 29 is satisfied. Especially in hypersonic test cases where very strong shocks and severe transients are present, artificial viscosity is inadequate in preserving positivity. In order to alleviate this, a positivity preservation scheme is proposed for FR. This scheme limits the state at each iteration such that each violation of equation 29 is corrected. The proposed scheme is similar to the one presented in [19] that was developed for the Discontinuous Galerkin method, with the difference that now the limiting procedure must limit the states based on the evaluation of the approximate solution polynomials in the flux points.

The first step is to limit the density. To this end the average state $\bar{\mathbf{u}}$ on the each element is computed. Based on $\bar{\mathbf{u}}$, the average density $\bar{\rho}$ and pressure $p(\bar{\mathbf{u}})$ are known. A small number ϵ is defined to which ρ will be limited:

$$\epsilon = \min(10^{-13}, \bar{\rho}, p(\bar{\mathbf{u}})), \quad (30)$$

where $p(\bar{\mathbf{u}})$ denotes the pressure computed using the element average state. Next, ρ is recomputed in each solution point i, in order to obtain a new positive density $\tilde{\rho}_i$:

$$\tilde{\rho}_i = t_1(\rho_i - \bar{\rho}) + \bar{\rho} \text{ with } t_1 = \min\left(\frac{\bar{\rho} - \epsilon}{\bar{\rho} - \rho_{min}}, 1\right). \quad (31)$$

ρ_{min} is computed in the following way:

$$\rho_{min} = \min_j\left(\rho_j\right), \quad (32)$$

where the subscript j refers to the j-th flux point. In this way, the density in each solution point of an element is limited such that all the densities in the flux points remain larger than or equal to ϵ.

The state $\tilde{\mathbf{u}} = (\tilde{\rho}, \rho\mathbf{v}, \rho e_t)$ obtained after limiting the density, is now used to limit the pressure: if in the j-th flux point $p_j < \epsilon$, a coefficient t_j is computed such that:

$$p(t_j(\tilde{\mathbf{u}}_j - \bar{\mathbf{u}}) + \bar{\mathbf{u}}) = \epsilon. \quad (33)$$

$\tilde{\mathbf{u}}_j$ represents the state after limiting the density in the j-th flux point. This can be computed by evaluating the approximate solution polynomial, as defined in equation 7, in the j-th flux point. The value of t_j can be obtained from equation 33 by solving a second order equation. Note that the expression $0 < t_j < 1$ is used to select the correct solution of the second order equation. Next, the whole state in each solution point i is limited using the minimum value of the t_j coefficients computed in the current element, obtaining $\tilde{\tilde{\mathbf{u}}}_i$:

$$\tilde{\tilde{\mathbf{u}}}_i = t_2(\tilde{\mathbf{u}}_i - \bar{\mathbf{u}}) + \bar{\mathbf{u}} \quad \text{with} \quad t_2 = \min_j(t_j). \quad (34)$$

This scheme guarantees that the density and pressure remain positive in the flux points. For a $P1$ extrapolation, the most negative value will always be attained inside a flux point rather than a solution point, since they are situated on the boundary of the element. For higher order it is theoretically possible that a negative state appears first in a solution point. As such, the same procedure outlined above can be applied to the solution points.

Interaction between LLAV and positivity preservation

Generally for a high maximum artificial viscosity, which is accomplished by specifying a large δ_s^*, positivity is only enforced during the transient of the simulation. However if δ_s^* is chosen lower, typically $\delta_s^* \simeq 1$,

the positivity preservation scheme remains active until convergence, as is shown later in section 5. Since the positivity preservation scheme is applied outside of the residual computation, it causes the residuals to stall at convergence: the positivity preservation scheme exactly matches the contribution of the non-zero residuals to the solution at the next time step. As a consequence the solution remains unchanged, despite non-zero residuals. As proposed in [16], a solution for this is to monitor $\frac{u(t+\Delta t)-u(t)}{\Delta t}$ instead of the residual.

4. Implementation

The FR solver computes the divergence of the reconstructed flux in each element at every time step. For this purpose, the FR algorithm is divided into different parts. The flux is split up in a convective, diffusive, and artificial part:

$$\frac{\partial \mathbf{u}}{\partial t} = -\boldsymbol{\nabla}\cdot\mathbf{f}_c(\mathbf{u}) + \boldsymbol{\nabla}\cdot\mathbf{f}_d(\mathbf{u},\boldsymbol{\nabla}\mathbf{u}) + \boldsymbol{\nabla}\cdot\mathbf{f}_{av}(\boldsymbol{\nabla}\mathbf{u}). \quad (35)$$

The three parts of the flux divergence are computed separately. As such there are three main parts in the developed solver: a convective, diffusive and shock capturing part. These parts interact with the correction functions, the interface flux schemes and the boundary conditions. The algorithm as a whole takes the current states, the geometric data of the elements and the specification of the FR parameters (point distributions, flux scheme, correction function) as inputs. The solver then at each iteration computes the residuals and flux Jacobians. The different implementations of the correction functions and interface flux schemes are separated from the core solver. As a consequence, a new type of correction function, interface flux scheme, boundary condition, etc. can simply be implemented by adding a new class without changing the existing solver.

Within each of the three parts of the flux divergence computation, the solver performs a loop over the elements, the inner faces and the boundary faces. For the convective part, the following computations are performed in each loop:

loop over elements:

$$\boldsymbol{\nabla}_{\boldsymbol{\xi}}\cdot\hat{\mathbf{f}}_C^{\delta D}(\hat{\mathbf{u}}) - \sum_{i=1}^{N_f}\boldsymbol{\nabla}_{\boldsymbol{\xi}}\cdot\mathbf{h}_i(\boldsymbol{\xi})\left(\hat{\mathbf{f}}_C^{\delta D}(\hat{\mathbf{u}}(\boldsymbol{\xi}_i))\cdot\hat{\mathbf{n}}_i\right), \quad (36)$$

loop over inner faces:

$$\sum_{i=1}^{N_f}\boldsymbol{\nabla}_{\boldsymbol{\xi}}\cdot\mathbf{h}_i(\boldsymbol{\xi})\left(\hat{\mathbf{f}}_{C,i}^{\delta I}(\hat{\mathbf{u}}(\boldsymbol{\xi}_i))\cdot\hat{\mathbf{n}}_i\right), \quad (37)$$

loop over boundary faces:

$$\sum_{i=1}^{N_f}\boldsymbol{\nabla}_{\boldsymbol{\xi}}\cdot\mathbf{h}_i(\boldsymbol{\xi})\left(\hat{\mathbf{f}}_{C,i}^{\delta I}(\hat{\mathbf{u}}_{ghost}(\boldsymbol{\xi}_i))\cdot\hat{\mathbf{n}}_i\right), \quad (38)$$

where $\boldsymbol{\nabla}_{\boldsymbol{\xi}}\cdot\mathbf{h}_i(\boldsymbol{\xi})$ denotes the divergence of the correction field. For 1D this reduces to the correction function $h(\xi)$. Furthermore, for quadrilaterals and hexahedra, $\boldsymbol{\nabla}_{\boldsymbol{\xi}}\cdot\mathbf{h}_i(\boldsymbol{\xi})$ can be constructed using a tensor product of the 1D correction functions $h(\xi)$, as discussed in [3]. $\hat{\mathbf{u}}_{ghost}(\boldsymbol{\xi}_i)$ refers to the ghost state applied in the boundary in order to impose the proper boundary condition.

By splitting up the computation in a loop over elements and a loop over faces, no calculation has to be performed twice: all computation related to the interface valuesof the states as well as the fluxes, are computed in the loop of the faces. All computations related to the discontinuous fluxes on the other hand, are computed within the loop over elements, since only element-local quantities must be known.

Both the diffusive and artificial viscosity part perform the same computations, except for the computation of the flux $\mathbf{f}$. However, these two parts require the corrected gradients, which in themselves would require additional loops over the elements and faces. In order to avoid performing another set of loops, the corrected gradients are computed during the convective flux divergence computation. Afterwards the diffusive and artificial viscosity computations are performed.

4.1. Implicit time stepping

For implicit time stepping, the core solver remains unchanged, however, in addition to the residual, the Jacobian matrix of the residuals is needed. Consider as an example the backward Euler implicit time marching scheme that can be written as follows:

$$\mathbf{u}_{ce}(t+\Delta t) = \mathbf{u}_{ce}(t)+\Delta t\,\mathbf{R}(\mathbf{u}_{ce}(t+\Delta t),\mathbf{u}_{ne}(t+\Delta t)), \quad (39)$$

where *ce* refers to the current element and *ne* to a neighboring element. $\mathbf{R}$ is the residual. The appearance of $\mathbf{u}(t+\Delta t)$ in the right-hand side of this equation confirms that this is an implicit method. The value of Δt can be determined by a CFL number specified by the user. At time t, the value of

$\mathbf{R}(\mathbf{u}_{ce}(t+\Delta t), \mathbf{u}_{ne}(t+\Delta t))$ is not readily available since $\mathbf{u}(t+\Delta t)$ is unknown. Because $\mathbf{R}$ is non-linear for the Navier-Stokes equations, expression 39 is a non-linear equation that has to be solved during each iteration. It also needs to be solved for each element in the spatial domain, resulting in a system of non-linear equations:

$$\mathbf{u}(t+\Delta t) = \mathbf{u}(t) + \Delta t\, \mathbf{R}(\mathbf{u}(t+\Delta t)). \tag{40}$$

Here the subscripts *ce* and *ne* are omitted since here $\mathbf{u}$ represents the vector of all state vectors in the spatial domain. The system of equations 40 is linearized as follows:

$$\mathbf{u}(t+\Delta t) = \mathbf{u}(t)+\Delta t \left(\mathbf{R}(\mathbf{u}(t)) + \left.\frac{\partial \mathbf{R}}{\partial \mathbf{u}}\right|_t (\mathbf{u}(t+\Delta t) - \mathbf{u}(t))\right), \tag{41}$$

where $\left.\frac{\partial \mathbf{R}}{\partial \mathbf{u}}\right|_t$ is the Jacobian matrix of the residuals with respect to the state vectors, evaluated at time t. The resulting large linear system is then solved with for example a Generalized Minimal Residual approach (GMRES). [20] The residual Jacobian matrix is determined by numerically approximating the partial derivatives with a simple first order finite difference scheme in the i-th element:

$$\frac{\partial \mathbf{R}}{\partial \mathbf{u}_i} = \frac{\mathbf{R}(\mathbf{u}_i + \varepsilon_u) - \mathbf{R}(\mathbf{u}_i)}{\varepsilon_u}. \tag{42}$$

After solving the time marching equation 41, the positivity preservation scheme is applied to all elements on the newly computed state $\mathbf{u}(t+\Delta t)$.

5. Results

5.1. Viscous Hypersonic Flow over a Cylinder

The proposed shock capturing scheme is tested for a hypersonic cylinder test case, presented in [21]. The considered geometry consists of a cylinder with radius 1m. The free-stream values imposed are the following:

Table 1: Free stream values

M_∞	$\rho_\infty\ [kg/m^3]$	$V_\infty\ [m/s]$	$T_\infty\ [K]$
17.637	0.001	5000	200

The mesh used is presented in figure 3. The mesh consists of curved quadrilateral elements of second order and contains 297 elements: 11 in the circumferential direction and 27 in the direction normal to the cylinder. The inlet boundary is imposed as a Dirichlet boundary condition that set the states to the free stream values. For the outlet, a supersonic outlet boundary condition is used. The cylinder is represented by an iso-thermal no-slip wall at a temperature T_{wall} of 500K.

The FR method is used with a VCJH scheme for the correction functions. The distribution of both the solution and flux points is the Gauss-Legendre distribution. For the convective interface fluxes, the AUSM$^+$ scheme is used, as proposed in [22; 23]. For the diffusive and artificial interface fluxes, the second Bassi-Rebay scheme is used, as proposed in [10; 9]. For the LLAV scheme, κ is set to 0.5. This value is more centered around the values of S found in the shock region, as can be seen in figure 4.

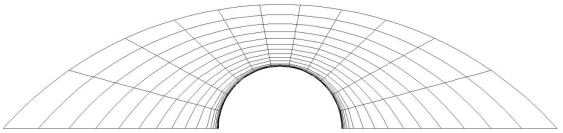

Figure 3: Mesh with 297 curved quadrilateral elements used for the hypersonic cylinder test case

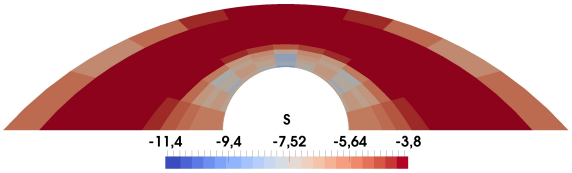

Figure 4: Smoothness field for P3

The pressure coefficient field for a second-order and fourth-order of accuracy FR method are presented in respectively figure 5 and 6. Here the pressure coefficient is computed as follows:

$$Cp = \frac{p - p_\infty}{0.5\rho_\infty V_\infty}. \tag{43}$$

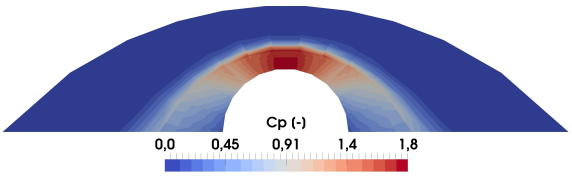

Figure 5: Pressure coefficient field for P1

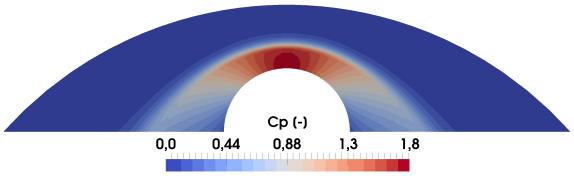

Figure 6: Pressure coefficient field for P3

Figures 7 and 8 show the artificial viscosity for the two cases. It is clear that the LLAV method is only active in the shock area. Figure 9 shows the Stanton number of the second- to seventh-order of accuracy solutions (P1-P6) compared to the one found in [21]. The Stanton number is the adimensionalized heat flux and is computed in the following way:

$$St = \frac{q_{wall}}{c_p \rho_\infty V_\infty (T_{t,\infty} - T_{wall})}, \tag{44}$$

where q_{wall} is the wall heat flux and $T_{t,\infty}$ the total free stream temperature. For P1 to P3 the heat flux is over estimated, while for higher orders it coincides with the reference heat flux.

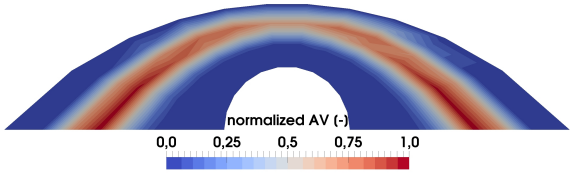

Figure 7: Artificial viscosity field for P1

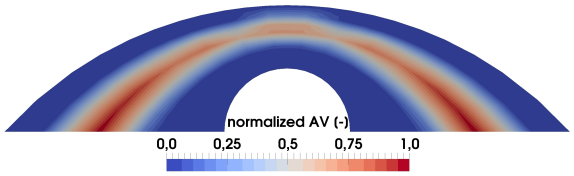

Figure 8: Artificial viscosity field for P3

Figure 10 shows the influence of the LLAV parameter c on the computed shock thickness. This result is used to calibrate the relation between c and δ_s^*. From equation 28:

$$\alpha = \frac{c\, M_\infty}{\delta_s^*(M_\infty - 1)} \tag{45}$$

For $c = 0.2$, the shock is spread over about 8 elements, as shown in figure 10c. Substituting $c = 0.2$ and $\delta_s^* = 8$ in equation 45, gives $\alpha = 0.027$. Figure 10b shows that for $c = 0.1$, the shock is spread over about 4 elements, which gives the same result for α.

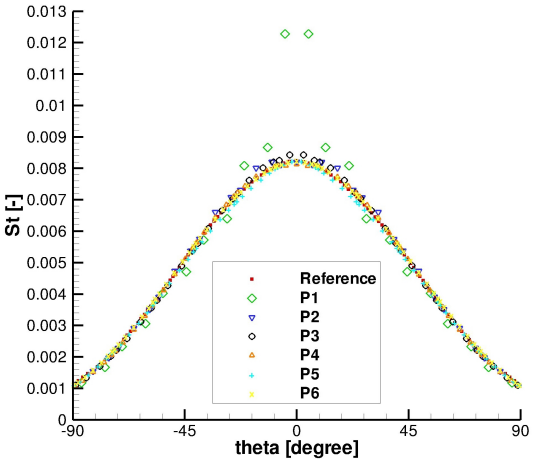

Figure 9: Stanton number for the hypersonic cylinder test case

For $c = 0.05$ the shock is spread over about two elements, as shown in figure 10a, which again confirms $\alpha = 0.027$. However, for this value of c, the positivity preservation scheme remains active until convergence.

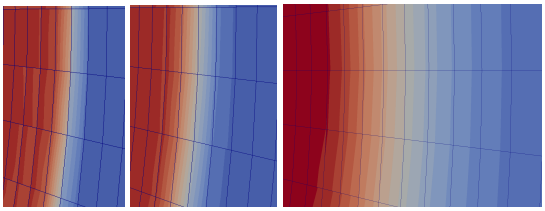

(a) $c = 0.05$ (b) $c = 0.1$ (c) $c = 0.2$

Figure 10: Shock thickness for different values of c, density ρ is shown

Figure 12 presents the Stanton number for different settings of κ, c and S_0 of the LLAV scheme for the P1 case on a finer mesh of 2679 elements shown in figure 11. For the smoothness detector S, in all present cases, the pressure is used. However the final case in figure 12 shows the Stanton number when the density ρ is used to compute S instead of the pressure. It is clear that in this test case the influence of the LLAV settings on the predicted Stanton number is not very significant.

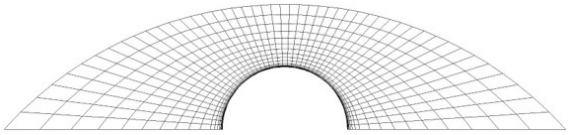

Figure 11: Mesh with 2679 curved quadrilateral elements for the hypersonic cylinder test case

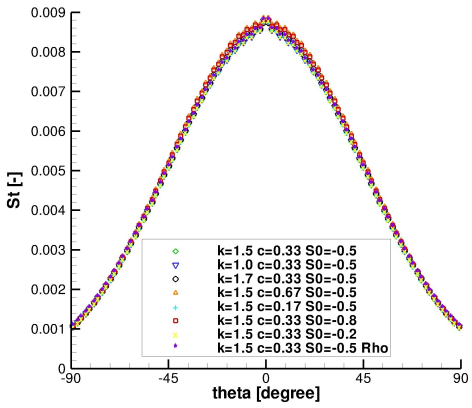

Figure 12: Stanton number for different κ, c and S_0

The present test case is also executed on a coarser mesh, in order to obtain a tenth-order of accuracy solution (P9). The mesh is presented in figure 13 and contains 77 curved quadrilateral elements. The pressure coefficient field for the tenth-order of accuracy solution is presented in figure 14.

Figure 15 shows the Stanton number for 3 cases with approximately the same amount of degrees of freedom: the present P9 case with 77 elements (7700 DoF), the P4 case presented previously with 297 elements (7425 DoF) and a P1 case on a mesh with 1824 elements (7296 DoF). Despite having the same amount of degrees of freedom, it is clear that P4 and P9 significantly outperform P1 and have a much better agreement with the reference Stanton number.

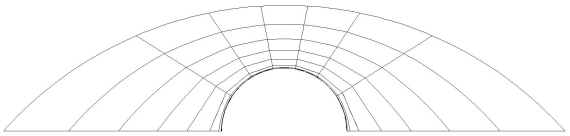

Figure 13: Coarse mesh with 77 curved quadrilateral elements for the hypersonic cylinder test case

5.2. *Viscous Hypersonic Flow over a Cone*

The second test case considered to test the LLAV shock capturing scheme is the flow of nitrogen gas

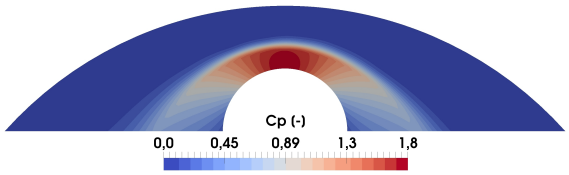

Figure 14: Pressure coefficient field for P9

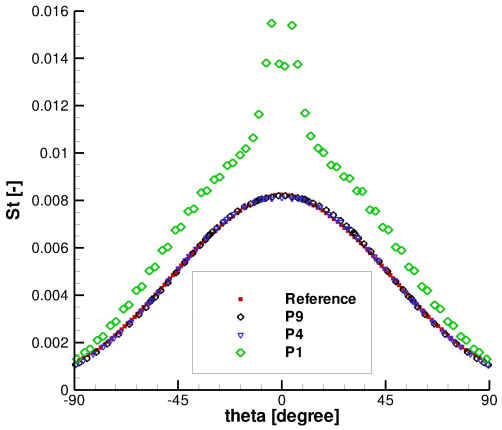

Figure 15: Stanton number for three cases with the same amount of degrees of freedom: P1, P4 and P9

over a rounded cone. The considered geometry consists of a 25° half-angle cone with a rounded nose of radius 1mm. The total length of the cone in the x-direction considered is 9cm. The free stream values imposed are presented in table 2. This corresponds to Run 35 conditions as presented in [24].

Table 2: Free stream values

M_∞	ρ_∞ $[kg/m^3]$	V_∞ $[m/s]$	T_∞ $[K]$
11.3	0.5515	2713	138.9

The mesh used is presented in figure 16. The mesh consists of curved quadrilateral elements of second-order and contains 3000 elements: 100 along the cone and 30 in the direction normal to the cone. The inlet boundary is imposed as a Dirichlet boundary condition that sets the states to the free-stream values. For the outlet, a supersonic outlet boundary condition is used. The cone is represented by an iso-thermal no-slip wall at a temperature T_{wall} of 296K.

The FR method is used with a VCJH scheme for the correction functions. The distribution of both the solution and flux points is the Gauss-Legendre distribution. For the convective interface fluxes, the AUSM$^+$

scheme is used. For the LLAV scheme, κ is set to 2 and the reference smoothness to $S_0 = -3\log_{10} P$. In order to simulate the flow over a cone on a 2D mesh, axisymmetric source terms are added to the Navier-Stokes equations.

The pressure contours are presented in figure 17a. Figure 17b shows the artificial viscosity distribution. It is clear once again that the LLAV method is only active in the shock area.

Figure 18 presents the density residual history and the CFL number for both the P1 and P3 cases. For hypersonic test cases the CFL number is chosen smaller than for the previous subsonic cases in order to preserve stability. However, for both P1 and P3 the CFL number is still much larger than the CFL limit explicit time marching methods would impose: $CFL_{max} = 0.5$ and $CFL_{max} = 0.25$ for respectively P1 and P3. For the P3 case it should be noted that at iteration 660 the AV field was frozen (ε is no longer recomputed at each iteration) in order to speed up convergence.

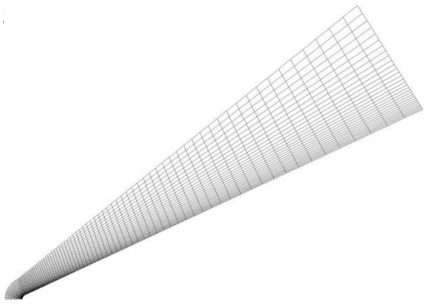

Figure 16: Mesh used for the hypersonic cone

Figure 19 shows the Stanton number of the cone for different heights of the first cell near the wall. This was done for P1 solutions. As the mesh gets finer near the wall, the heat flux coincides with the reference heat flux. The reference was obtained as the grid-converged heat flux solution for the second-order FV solver within COOLFluiD, which has been well validated for hypersonic test cases [25]. As such it is clear that if the mesh is fine enough, the FR solver computes the correct heat flux.

Finally, figure 20 shows three cases with the same amount of degrees of freedom, namely 12000 (for P1 the mesh in figure 16 is used). These cases are a P1 FR solution, a P3 FR solution and a second-order FV solution. Despite having the same amount of degrees of freedom, the P3 FR solution is the most accurate. This illustrates the higher computational efficiency per degree of freedom of high-order methods.

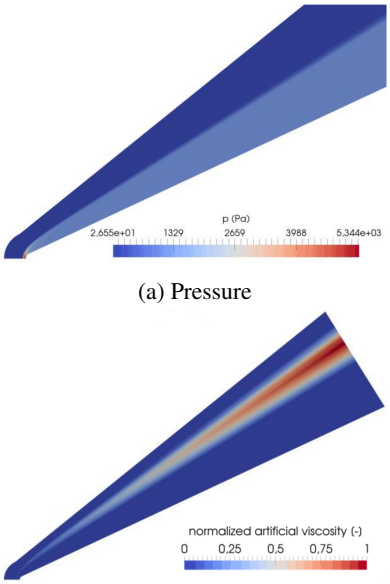

(a) Pressure

(b) Artificial viscosity

Figure 17: Flow field of the hypersonic cone for P3

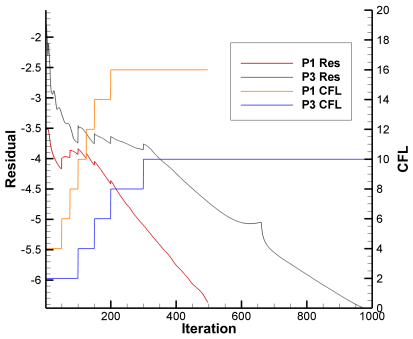

Figure 18: Logarithm of the density residual and CFL as a function of the iteration for P1 and P3

6. Conclusion

A novel shock capturing scheme for the FR method was proposed and successfully applied to a viscous hypersonic test case. Additionally, the test case was solved using implicit time marching, contrary to most current shock capturing schemes for high-order finite element-type methods. To the author's knowledge this is the first time a viscous hypersonic test case was successfully run with the FR method. As future work, the shock capturing scheme will be tested for different hypersonic test cases, in order to verify the calibration of the LLAV scheme. Furthermore, the applicability of the shock capturing scheme to heat flux prediction will be investigated and the results compared to a ref-

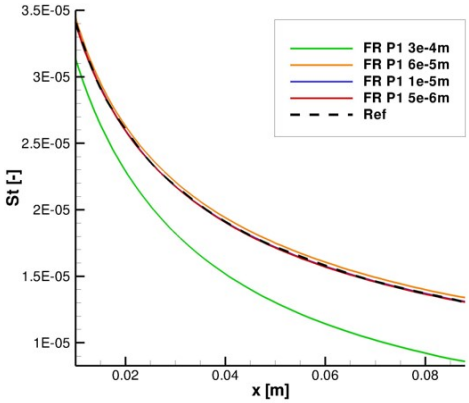

Figure 19: Stanton number for different first cell height (P1)

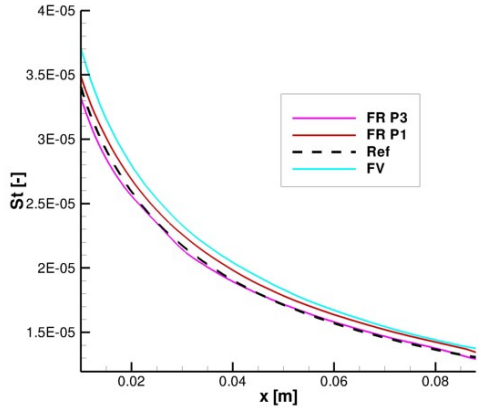

Figure 20: Stanton number for FR P1, P3 and FV with the same number of DoFs

erence numerical solution.

Acknowledgments

The research of Ray Vandenhoeck is supported by SB PhD fellowship 1S19918N of the FWO.

References

[1] A. Lani, An object oriented and high performance platform for aerothermodynamics simulation, Ph.D. thesis, Université Libre de Bruxelles (2008).

[2] T. Quintino, A component environment for high-performance scientific computing: design and implementation, Ph.D. thesis, Ph. D. Thesis, KU Leuven, von Karman Institute for Fluid Dynamics, Leuven (2008).

[3] H. Huynh, A flux reconstruction approach to high-order schemes including discontinuous galerkin methods, AIAA paper 4079 (2007) 2007.

[4] H. T. Huynh, A reconstruction approach to high-order schemes including discontinuous galerkin for diffusion, AIAA paper 403 (2009) 2009.

[5] H. Huynh, High-order methods including discontinuous galerkin by reconstructions on triangular meshes, AIAA Paper 44 (2011) 2011.

[6] P. E. Vincent, P. Castonguay, A. Jameson, A new class of high-order energy stable flux reconstruction schemes, Journal of Scientific Computing 47 (1) (2011) 50–72.

[7] P. Castonguay, P. Vincent, A. Jameson, Application of high-order energy stable flux reconstruction schemes to the euler equations, in: 49th AIAA Aerospace Sciences Meeting, Vol. 686, 2011.

[8] P. Castonguay, P. E. Vincent, A. Jameson, A new class of high-order energy stable flux reconstruction schemes for triangular elements, Journal of Scientific Computing 51 (1) (2011) 224–256.

[9] P. Castonguay, D. M. Williams, P. E. Vincent, M. Lopez, A. Jameson, On the development of a high-order, multi-gpu enabled, compressible viscous flow solver for mixed unstructured grids, AIAA paper 3229 (2011) 2011.

[10] F. Bassi, S. Rebay, A high-order accurate discontinuous finite element method for the numerical solution of the compressible navier–stokes equations, Journal of computational physics 131 (2) (1997) 267–279.

[11] P. L. Roe, Approximate riemann solvers, parameter vectors, and difference schemes, Journal of computational physics 43 (2) (1981) 357–372.

[12] A. Sheshadri, A. Jameson, Shock detection and capturing methods for high order discontinuous-galerkin finite element methods, in: 32nd AIAA Applied Aerodynamics Conference, 2014, p. 2688.

[13] J. Park, T. Chang, C. Kim, Higher-order multi-dimensional limiting strategy for correction procedure via reconstruction, in: 52nd Aerospace Sciences Meeting, 2014, p. 0772.

[14] J. Du, C.-W. Shu, M. Zhang, A simple weighted essentially non-oscillatory limiter for the correction procedure via reconstruction (cpr) framework, Applied Numerical Mathematics 95 (2015) 173–198.

[15] M. Yu, F. X. Giraldo, M. Peng, Z. J. Wang, Localized artificial viscosity stabilization of discontinuous galerkin methods for nonhydrostatic mesoscale atmospheric modeling, Monthly Weather Review 143 (12) (2015) 4823–4845.

[16] Y. Li, Z. J. Wang, A convergent and accuracy preserving limiter for the fr/cpr method, in: 55th AIAA Aerospace Sciences Meeting, 2017, p. 0756.

[17] P.-O. Persson, J. Peraire, Sub-cell shock capturing for discontinuous galerkin methods, in: 44th AIAA Aerospace Sciences Meeting and Exhibit, 2006, p. 112.

[18] J. S. Park, M. Yu, C. Kim, Z. Wang, Comparative study of shock-capturing methods for high-order cpr: Mlp and artificial viscosity, in: Proceedings of the 8th International Conference on CFD, ICCFD8-2014-0067, 2014.

[19] X. Zhang, On positivity-preserving high order discontinuous galerkin schemes for compressible navier–stokes equations, Journal of Computational Physics 328 (2017) 301–343.

[20] Y. Saad, M. H. Schultz, Gmres: A generalized minimal residual algorithm for solving nonsymmetric linear systems, SIAM Journal on scientific and statistical computing 7 (3) (1986) 856–869.

[21] P. Gnoffo, J. White, Computational aerothermodynamic simulation issues on unstructured grids, in: 37th AIAA Thermophysics Conference, 2004, p. 2371.

[22] M.-S. Liou, C. J. Steffen, A new flux splitting scheme, Journal of Computational physics 107 (1) (1993) 23–39.

[23] M.-S. Liou, On a new class of flux splitting, Lecture Notes in Physics 414 (1993) 115.
[24] G. Candler, I. Nompelis, M.-C. Druguet, M. Holden, T. Wadhams, I. Boyd, W.-L. Wang, CFD validation for hypersonic flight-hypersonic double-cone flow simulations, in: 40th AIAA Aerospace Sciences Meeting & Exhibit, 2002, p. 581.
[25] A. Lani, Development of an object oriented framework for PDE solvers on unstructured grids, Master's thesis, Université Libre de Bruxelles, Faculté des Sciences Appliquées (Sep 2003).

Nonlinear Parabolized Stability Analysis of Chemically Reacting Boundary-Layers

Ludovico Zanus

Aeronautics and Aerospace Department, von Karman Institute for Fluid Dynamics, Belgium, ludovico.zanus@vki.ac.be

Supervisor: Fabio Pinna

Senior Research Engineer, Aeronautics and Aerospace Department, von Karman Institute for Fluid Dynamics, Belgium, fabio.pinna@vki.ac.be

Supervisor: Olivier Chazot

Professor and Head of the Aeronautics and Aerospace Department, von Karman Institute for Fluid Dynamics, Belgium, chazot@vki.ac.be

University Supervisor: Gérard Degrez

Professor and Head of the École Polytechnique de Bruxelles, Université Libre de Bruxelles, Belgium, gdegrez@ulb.ac.be

Abstract

Stability of hypersonic boundary-layers is studied by means of Parabolized Stability Equations (PSE). After verification of the algorithm by comparisons against the Texas A&M University EPIC code, the numerical method is used to investigate the influence of high-temperature effects on the nonlinear transition stages. Results reveal that perturbations amplitudes relative evolutions are highly affected by the flow assumption considered.

Keywords: Transition, stability, PSE, nonlinearities, hypersonic, boundary-layer

1. Introduction

Laminar-to-turbulent boundary layer transition is still a poorly understood phenomenon, especially in hypersonic regimes. High temperature gas effects and, in general, physics complexity, increase the number of parameters influencing the flow stability and transition, when compared to lower Mach flows [1]. Studies to describe the overall process and systematically assess the influence of each one of these parameters are therefore complicated. Moreover, the difficulties, and sometimes the unfeasibilities, to conduct ground test and in-flight experiments lead to lack of data for the validation of numerical simulations, which often remain the only analysis tool available. On the other hand, this understanding is of fundamental importance for transition prediction and control in the design phase of hypersonic vehicles. It is well known that higher level of drag and heat flux are expected on surface surrounded by turbulent flows, compared to laminar ones [2]. Hence, accurate estimations of transition locations become important to reduce drag and thus fuel consumption on cruise spaceplanes, or to properly size Thermal Protection Systems (TPS) on re-entry capsules, optimizing the amount of material utilized [3]. In addition, knowledge about the phenomenon can be used not only to delay the transition process, but also to promote turbulent flows, as it is preferred for example at the inlet of scramjet engine, where fuel-oxidizer mixing must be enhanced [4].

High temperatures in hypersonic boundary layers may produce excitation of the molecules different energy modes and eventually activation of chemical reactions. Comparison of the reactions time with the characteristic flow time allows the distinction between frozen, finite-rate (or Chemical Non-Equilibrium, CNE) and infinite-rate (or Local Thermodynamic Equilibrium, LTE) chemical reacting flows [5]. These effects lead to modifications of the fluid thermodynamic and transport properties, with consequences on the boundary layer stability [6]. In the past, most of

the studies on this subject focused on the linear stages of the transition process. Local analysis by means of Linear Stability Theory (LST) were performed both for flows in LTE and CNE conditions (see respectively Malik et al. [7] and Stuckert et al. [8]). The same types of flows were also investigated by Linear Parabolized Stability Equations (LPSE) (see for example Chang et al. [9], Malik [10] and Johnson et al. [11]) and by Direct Numerical Simulations (DNS) (Marxen et al. [12; 13]). No general conclusions about the role of high temperature effects on stability and transition were drawn from these studies.

When perturbations reach finite amplitudes, nonlinearities become important and they may eventually lead to transition by following different mechanisms: oblique breakdown [14] or secondary instability [15], the latter expressed by a fundamental or subharmonic resonance. Previously related studies, as the works of Kuehel et al. [16], Perez et al. [17] and Moyes et al. [18] by means of Nonlinear PSE (NPSE) and Mayer et al. [19] by means of DNS, were dealing mainly with supersonic and hypersonic flows in Calorically Perfect Gas (CPG) conditions, thus neglecting high temperature effects. Very few investigation of the nonlinear transition processes included chemical reactions and proper modeling of the gas thermodynamics and transport properties typical of high Mach regimes; among them the DNS results of Marxen et al. [13] for flows in frozen and CNE conditions are noteworthy. At author knowledge, no NPSE simulations were performed with aerothermodynamic models other than CPG.

This work aims to extend the NPSE analysis of the nonlinear transition mechanisms in presence of high temperatures effects. The PSE code used is part of the VKI Extensible Stability and Transition Analysis (VESTA) toolkit, originally developed by Pinna et al. [20]. The article is divided in the following part. In §2 the general problem is formulated and the equations are reported. In §3 the numerical method and the tools used are explained. Next, the result are described in §4, divided into two parts. The first part deals with the verification of the PSE algorithm, by comparing the linear and nonlinear stability analyses of different instabilities, against the results obtained with the Euonymous Parabolized Instability Code (EPIC) [21], of the Computational Stability and Transition Laboratory of Texas A&M University. In the second part, the PSE algorithm is applied to study the nonlinear perturbations evolution up to the transition onset in adiabatic flat plate LTE flows, and compared against the results obtained assuming CPG conditions. In particular, an oblique-type breakdown at Mach 3 and a secondary instability in a form of fundamental resonance in an hypersonic boundary layer at Mach 10 are investigated. Finally, in §5 a summary and the conclusions are presented.

2. Problem formulation

2.1. Governing equations

The Navier-Stokes equations for a gas mixture in local thermodynamic equilibrium do not formally change compared to the ones describing a calorically perfect gas. The fact that chemical reactions occur, in this case at an infinite rate, leads to variable specific heats, and makes internal energy and transport properties depend on any two thermodynamic variables (here chosen as pressure and temperature) instead of the sole temperature dependence for CPG flows. Being the continuity and momentum equations purely mechanical in nature, they are not influenced by the chemistry, while the energy equation slightly modifies compared to the one in CPG conditions, since the effect of diffusion has to be included and enthalpy can not longer be written as a simple multiplication of temperature and specific heat at constant pressure. The Navier-Stokes equations are given in nondimensional invariant form for a gas in LTE conditions, in absence of body forces. Superscripts q^i denote vectorial contravariant variables, whereas subscripts q_i denote vectorial covariant variables (see Pinna et al. [22]). Also, indexes following a comma denote spatial derivatives (e.g. $u^i_{,j} = \partial u^i / \partial x^j$).

$$\frac{\partial \rho}{\partial t} + (u^j \rho)_{,j} = 0 \,, \tag{1a}$$

$$\rho \frac{\partial u^i}{\partial t} + \rho u^j u^i_{,j} = -g^{ij} p_{,j} + \frac{1}{Re} \mathbb{T}^{ij}_{,j} \,, \tag{1b}$$

$$\begin{aligned} \rho \frac{\partial h}{\partial t} + \rho u^j h_{,j} = Ec \left(\frac{\partial p}{\partial t} + u^j p_{,j} \right) \\ + \frac{1}{RePr} q_f{}^j_{,j} + \frac{Ec}{Re} g_{ik} \mathbb{T}^{kj} u^i_{,j} \,, \end{aligned} \tag{1c}$$

where g^{ij} is the metric tensor, ρ the density, u^i the velocity component in different spatial directions, p the pressure, h the enthalpy and $\mathbb{T}$ the stress tensor defined as:

$$\mathbb{T}^{ij} = \lambda g^{ij} u^k_{,k} + \mu \left(g^{jk} u^i_{,k} + g^{ik} u^j_{,k} \right) , \tag{2}$$

where μ and λ are respectively the first and second viscosity coefficients. Moreover, the heat flux, neglecting

radiation and the Dufour's effect, takes the form

$$q_f{}^j = -\kappa_{fr} g^{ij} T_{,j} + \sum_{s=1}^{n_s} h_s J_s^j = \kappa_{eq} g^{ij} T_{,j} \,, \qquad (3)$$

where T is the temperature, κ_{fr} the "frozen" thermal conductivity, J_s^j the diffusion mass-flux of the sth species and κ_{eq} is an equivalent thermal conductivity, here used to rewrite the equation in terms of a Fourier's law. Nondimensionalization, whose details are described in §2.2.2, leads to the appearance of the Reynolds number Re, Prandtl number Pr and the Eckert number Ec.

The system of equations given by Eq. (1) is completed by the equation of state, which can be written as:

$$Hp = \rho T \zeta \,, \qquad (4)$$

where ζ is the compressibility factor and $H = Ec \cdot c_{pe}/R_e$, with c_{pe} the specific heat at constant pressure and R_e the specific gas constant of the undissociated gas.

The problem is finally closed by proper modeling of the transport and thermodynamic properties. For gases in local thermodynamic equilibrium these are computed from the library MUTATION++ based on kinetic theory (see Magin et al. [23] and Scoggins et al. [24]), whereas for flows in CPG conditions Sutherland's law together with the assumption of constant Prandtl number are utilized. If not otherwise specified, coefficients are fixed to the values proposed by White [25]. For further details the reader should refer to Zanus et al. [26].

2.2. Parabolized Stability Equations

Parabolized Stability Equations are derived by following the classic approach adopted in perturbation theory. Every flow quantity q is decomposed into a mean part $\bar{q}$ (the laminar base flow) plus a perturbation q':

$$q(x^i, t) = \bar{q}(x^i) + q'(x^i, t) \,, \qquad (5)$$

Perturbations of dependent quantities, such for example transport and thermodynamic properties, are obtained by Taylor expanding them around zero, with respect to their dependencies. The perturbation of the $\mu(p, T)$ variable, for example, is decomposed as:

$$\mu' = \frac{\partial \overline{\mu}}{\partial \overline{p}} p' + \frac{\partial \overline{\mu}}{\partial \overline{T}} T' + \dots \,, \qquad (6)$$

The total disturbance q' is assumed periodic in time and in the spanwise direction, and within the NPSE theory it is represented by the double Fourier series:

$$q'(x^1, x^2, x^3, t) = \sum_{n=-N_m}^{N_m} \sum_{m=-M_m}^{M_m} \tilde{q}_{(n,m)}(x^1, x^2) \exp(i\,\Theta) + \; c.c. \qquad (7)$$

where $c.c$ denotes the complex conjugate, and the argument of the exponential term is:

$$\Theta = i \left(\int_{x_0^1}^{x^1} \alpha_{(n,m)}(\xi) d\xi + m \beta_0 x^3 - n\, \omega_0\, t \right). \qquad (8)$$

The couple of indexes (n, m) identifies the mode having as frequency and spanwise wavenumber respectively n and m times the frequency and spanwise wave number of the fundamental or primary mode (i.e. ω_0 and β_0). The streamwise wavenumber is defined by the phase-conditioned constraint:

$$\alpha_{(n,m)} = \frac{n}{n_p} \alpha_{r(n_p,m_p)} + \alpha_{i(n,m)} \,. \qquad (9)$$

where $\alpha_{r(n_p,m_p)}$ is the real part of the primary mode streamwise wavenumber. Contrary to LST, the parallel flow assumption is not enforced within the PSE framework, meaning that the base flow and the perturbation shape functions $\tilde{q}_{(n,m)}$ depend not only on wall-normal direction, but also on the streamwise one. The latter dependence though is considered "weak", in the sense that the flow variation over one disturbance wavelength is negligible [27]. This allows to drop second order derivatives along this direction.

By inserting the Eq. (5) into the Navier-Stokes equations, subtracting the equation satisfied by the base flow, substituting the NPSE ansatz in Eq. (7), and applying the aforementioned hypotheses, the NPSE equations are obtained. Every single mode (n, m) has thus to satisfy the following equation written in matrix form:

$$\underline{\underline{L}}\,\underline{\tilde{q}} + \underline{\underline{M}}\,\underline{\tilde{q}}_{,1} + \alpha_{,1} \underline{\underline{Na}}\,\underline{\tilde{q}} \Big|_{(n,m)} = \underline{F}_{(n,m)} \,, \qquad (10)$$

where $\tilde{q} = [\tilde{u}^1, \tilde{u}^2, \tilde{u}^3, \tilde{T}, \tilde{p}]$ is the vector of the perturbation variables, the $\underline{\underline{L}}$, $\underline{\underline{M}}$ and $\underline{\underline{Na}}$ matrices are functions of the mean flow quantities and the stability parameters, and $\underline{F}_{(n,m)}$ is the forcing vector for mode (n, m).

In order to solve the problem, a closure relation needs to be applied, thus assuring the weak streamwise dependence of every mode shape function. This can be obtained by a normalization through the following integral norm:

$$\int_\Omega \underline{\tilde{q}}^\dagger \underline{\tilde{q}}_{,1} dy \Big|_{(n,m)} = 0 \,, \qquad (11)$$

where Ω indicates the domain in x^2. Different normalization conditions can be employed depending on the selected $\underline{\tilde{q}}$ components. Chang et al. [28] showed that the PSE results are basically independent on the chosen norm. In this work we chose to normalize by considering all five elements of the $\underline{\tilde{q}}$ vector.

2.2.1. Initial and boundary conditions

Eq. (10) and Eq. (11) constitute an initial boundary value problem. Hence, proper initial and boundary conditions are required both for the primary disturbance and the successively generated modes. Homogeneous Dirichlet boundary conditions are applied for the temperature and velocity components both at the wall and at the boundary layer edge. A compatibility condition is instead applied on the pressure disturbance by enforcing the x^2-momentum equation at the boundaries. An exception to this procedure is applied to the MFD: an homogeneous Neumann boundary conditions is imposed at the boundary layer edge to the wall-normal velocity component, to allow for the growing of the boundary layer.

Initial conditions for the primary modes are obtained by LST calculations. Before marching the solution with the PSE, the computed eigenvector is normalized by the maximum of one of the variables forming it, normally the streamwise velocity component, if not otherwise specified. Higher harmonics are initialized in a different way, since in these cases nonlinear effects cannot be neglected even during the first simulation steps. A reasonable initialization is obtained by assuming the locally streamwise derivatives of these modes equal to zero, thus:

$$\underline{\underline{L}}\,\underline{\tilde{q}}\,\Big|_{(n,m)} = \underline{F}_{(n,m)}\,, \tag{12}$$

where the forcing $\underline{F}_{(n,m)}$ is computed by considering only the modes already activated. The MFD is instead set always to zero. In order to solve Eq. (12), a guess for the streamwise wavenumber $\alpha_{(n,m)}$ need to be chosen. In accordance with Salinas [29], the following relations are used:

$$\alpha_{(n,m)} = \begin{cases} 0 & \text{if } n = 0 \wedge m = 0, \\ \alpha_{(n_p,m_p)} & \text{if } n = 0 \wedge m \neq 0, \\ \frac{n}{n_p}\alpha_{(n_p,m_p)} & \text{if } n \neq 0. \end{cases} \tag{13}$$

2.2.2. Nondimensionalization and scaling considerations

Most variables are nondimensionalized with respect to their free stream values, denoted by the subscript e. Exceptions to this are the spatial coordinates, normalized with the Blasius length ℓ:

$$\ell_e = \sqrt{\frac{\mu_e\,\hat{x}^1}{U_e\,\rho_e}}\,, \tag{14}$$

the reference time scale ℓ/U_e and the reference pressure $\rho_e\,U_e^2$.

LST uses the local edge quantities at every $\hat{x}$ location as the reference, meaning that ℓ will slowly grow as the boundary layer develops. PSE however uses constant reference values for all $\hat{x}$ locations. These are obtained at a single $\hat{x}_0$ location, and are identified as: U_{e0}, μ_{e0}, ρ_{e0} and $\delta_{e0} = \ell_e(\hat{x}_0)$. The Reynolds number based on this reference Blasius length δ_{e0} thus identically:

$$Re_0 = \hat{x}_0^1/\delta_{e0} = x_0^1\,. \tag{15}$$

The nondimensional reduced frequency is defined as $F = 2\pi\hat{f}\,\mu_{e0}/(U_{e0}^2\,\rho_{e0}) = \omega/Re_0$, whereas the reduced spanwise wavenumber is $b = \hat{\beta}\,\mu_{e0}/(U_{e0}\,\rho_{e0}) = \beta/Re$.

2.2.3. Measures of amplitudes and growth rates

While in the linear case amplitudes are defined up to a constant, in the nonlinear problem this is no longer true. The choice of initial modes amplitudes actually defines a specific nonlinear problem. NPSE results are usually displayed in terms of the evolution of the modes maximum amplitude value. For a generic quantity q of a mode (n, m), this is computed as:

$$A_{(n,m)_q}(x^1) = r_n\,r_m\,|\tilde{q}_{(n,m)}(x^1)|_{max}\,\mathcal{A}_{(n,0)}\,, \tag{16}$$

where

$$\begin{aligned} \mathcal{A}_{(n,0)} &= \exp\left(-\int_{x_0^1}^{x^1}\alpha_{i(n,0)}(\xi)d\xi\right), \\ r_n &= \begin{cases} 1 & \text{if } n = 0 \\ 2 & \text{if } n \neq 0 \end{cases}. \end{aligned} \tag{17}$$

For comparison with experimental measures, amplitudes in terms of Root-Mean-Square (RMS) values are presented as:

$$\begin{aligned} A''_{(n,m)_q} &= C_n(A_{(n,m)})_q\,, \\ C_n &= \begin{cases} 1 & \text{if } n = 0 \\ 1/\sqrt{2} & \text{if } n \neq 0 \end{cases}. \end{aligned} \tag{18}$$

Finally, the growth rate of a quantity q of a mode (n, m), can be expressed as:

$$\gamma_{(n,m)_q} = -\Im(\alpha_{(n,m)}) + \Re\left(\frac{\tilde{q}_{(n,m),1}}{\tilde{q}_{(n,m)}}\right). \qquad (19)$$

3. Methodology

The present NPSE code was developed within the VESTA toolkit [20]. One of its basic blocks is the Automatic Derivation and Implementation Toolkit (AD&IT) [22], a software algebra module able to derive stability equations in an automatic way, thus minimizing the possibilities of errors due to manual manipulations of lengthy equations. Thanks to its flexibility and general approach the AD&IT can provide results for different stability theories, coordinate systems, flow assumptions and set of variables. Once the equations are derived, the algorithm places each term of them in the correct position within the matrices describing the stability problem, in this case Eq. (10). When nonlinear terms are taken into account, the user can choose up to which nonlinearity order terms should be retained. To this purpose, it is worthy to point out that, for consistency, dependent quantities should be Taylor expanded up to the order of nonlinearity considered as in Eq. (6). In most PSE codes, only linear terms are retained in the expansion of dependent quantities. Since the simulations performed in this work represent the first computations made with this newly implemented NPSE algorithm, it was decided, for verification purposes, to follow the practice in the literature. Two distinct NPSE solvers have been developed to study respectively flows in CPG and LTE conditions. This means that results in CPG are not obtained as limiting solutions of LTE equations.

PSE constitutes an initial boundary value problem, solvable by a marching technique. A first order backward Euler method is used to discretize the streamwise derivatives, while the wall-normal ones are approximated by a Chebyshev spectral collocation method based on Lagrangian polynomia defined on Gauss-Chebishev-Lobatto points. A Malik mapping is adopted to cluster points close to wall, to have a better resolution of the boundary layer. All mean flows considered were calculated from the self-similar boundary layer solution, both for the CPG and LTE assumption. For further details about the numerical method generally used in VESTA and the structure of the PSE algorithm refer respectively to Pinna [20] and Zanus [30].

4. Results

The VESTA PSE solvers were verified in the past against literature results, for simple flow configurations, mainly self-similar flows like flat plates and straight cones at zero angle of attack. Nonlinear calculations in CPG were presented in Zanus et al. [31], whereas linear PSE studies of high Mach flows in LTE conditions were reported in Zanus et al. [26]. In the following, before investigating the influence of high temperature effects on the nonlinear stages of the transition process, the VESTA PSE algorithm is verified against the EPIC code for a variety of instability types, in complex flow configurations and calorically perfect gas conditions.

4.1. Verification of PSE solvers against EPIC code

For verification purposes, different kinds of instabilities were taken into account, allowing to check the correct implementation of several features of the VESTA PSE code. The mean flows and the EPIC stability results were kindly provided by A. J. Moyes.

4.1.1. 1st mode on a supersonic flat plate flow

The first case investigated is a 1st two-dimensional Mack-mode on a flat plate at Mach 1.6, previously studied by Bertolotti[32]. Figure 1 displays the growth rate evolution for a reduced frequency $F = 4 \cdot 10^{-5}$, computed with both a first and second order Euler backward marching scheme. The comparison between VESTA and EPIC results shows a good overall agreement, retrieving the same trend for both the schemes. Minor discrepancies are visible only at the simulation start, and they were found to be caused by different strategies used to compute the perturbations streamwise derivatives.

4.1.2. 2nd mode on a hypersonic flow over a compression cone

The stability of a 2nd Mack-mode is studied for a boundary layer flow over a compression cone. This is an axisymmetric circular cone at 0° angle of attack, with a streamwise flare and a 0.49 meters length. The pre-shock freestream conditions correspond to a Mach 6 flow, with $T_\infty = 52.6\,K$, $P_\infty = 611.1\,Pa$ and a cone surface temperature of $T_w = 300\,K$. Additional details about the mean flow can be found in [33]. The compression cone is ideal to create a constant-height boundary-layer, thus exciting a single frequency disturbance over a long distance. In this case the linear stability of a $\hat{f} = 286\,kHz$ perturbation is analyzed, and the results displayed in terms of N factor, based on the mass-flux variable. Simulations were

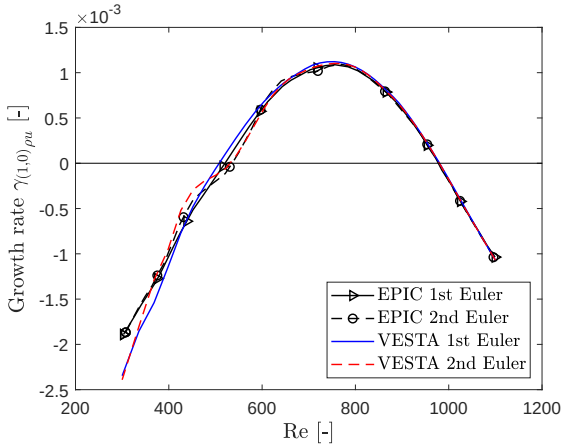

Figure 1: Evolution of the mode (1,0) linear growth rate, based on the mass-flux variable, $F = 4 \cdot 10^{-5}$: comparison between VESTA and EPIC codes, for different marching schemes. Supersonic flat plate flow: $M_e = 1.6$, $T_e = 206\,K$

performed both in Cartesian and orthocurvilinear coordinate systems. Figure 2 shows the comparison between VESTA and EPIC results: the curves superpose and reveal that curvature effects in this case are negligible, with respect to stability analyses.

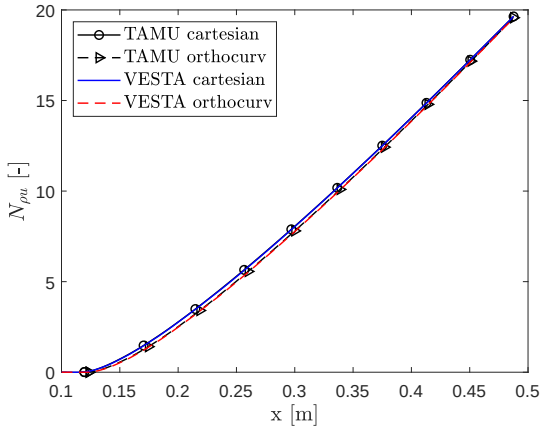

Figure 2: Linear N factor of mode (1,0), based on the mass-flux variable, $\hat{f} = 286\,kHz$: comparison between VESTA and EPIC codes, for different coordinate systems. Compression cone: $M_\infty = 6$, $T_\infty = 52.6\,K$

The evolution of the same disturbance was also investigated in the nonlinear framework. A bi-dimensional resonance was simulated, by considering 5 super-harmonics of the primary wave (mode (1,0)). The comparison between the two algorithm is reported in Fig. 3. Generally, the agreement is very satisfactory, considering the differences between the codes: mainly the modes initialization and the computation of the nonlinear terms.

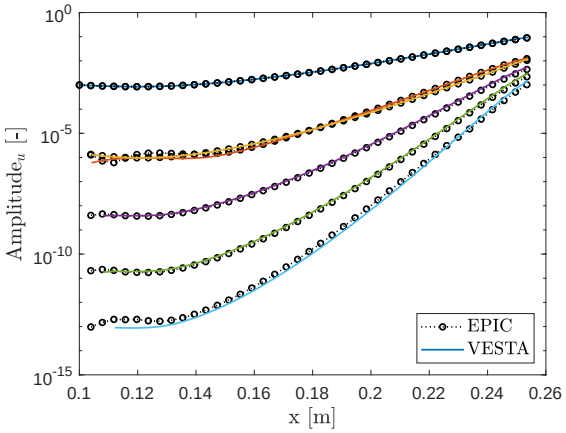

Figure 3: Nonlinear amplitude evolution, based on the maximum of the streamwise velocity component, $\hat{f} = 286\,kHz$, $A_{(1,0)_u} = 10^{-3}$: comparison between VESTA and EPIC codes. Compression cone: $M_\infty = 6$, $T_\infty = 52.6\,K$

4.1.3. Crossflow on a hypersonic flow over a yawed straight cone

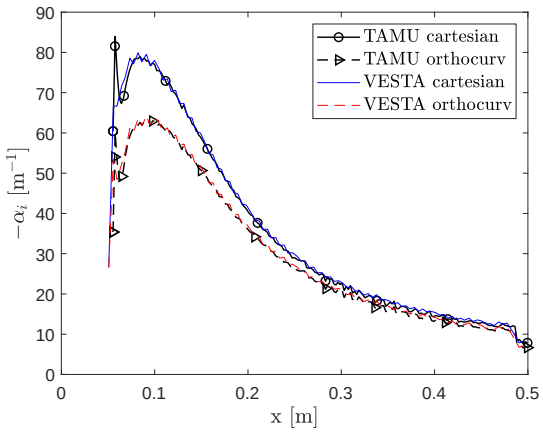

Figure 4: Growth rate component of mode (0,1), based on the streamwise dimensional wavenumber component, $\hat{f} = 0\,kHz$: comparison between VESTA and EPIC codes, for different coordinate systems. Yawed straight cone: $M_\infty = 6$, $T_\infty = 53.42\,K$

The last instability studied is the linear stationary crossflow evolution over a 7°-half-angle yawed

straight cone, previously analyzed by Oliviero et al.[21]. The upstream flow conditions are: $M_\infty = 6$, $T_\infty = 53.42\ K$, $P_\infty = 611.28\ Pa$, and the unit Reynolds number is $Re' = 10.09 \cdot 10^6\ [m^{-1}]$. The perturbation is tracked along the crossflow vortex's path emerging from the generalized ρw inflection point [21]. Figure 4 shows the dimensional growth rate component, solely based on the streamwise wavenumber, computed in both Cartesian and orthocurvilinear coordinate systems. The results were found to be quite sensitive to the streamwise discretization and marching scheme used, particularly around the growth rate peak. However, the displayed curves obtained with a 2nd order backward Euler agree very well in both coordinate systems. To this end, it is evident the relevant stabilizing effect due to surface curvature.

4.2. *Study of high temperature effects during transition nonlinear stages*

4.2.1. *Oblique-mode breakdown at Mach 3*

High temperature effects are investigated on a Mach 3 supersonic flow. The freestream temperature and pressure values are respectively $T_e = 103.6\,K$ and $p_e = 2282.4\,Pa$. At this Mach number the most unstable wave is a three-dimensional first Mack mode. This suggests the oblique-type breakdown mechanism to be the most likely to occur. The full transition process for a flow with the same freestream conditions was studied in details by Mayer et al. [19] by means of DNS, and compared against NPSE in Mayer et al. [34]. In their calculations a Prandtl number of $Pr = 0.71$ was set, while the Sutherland's law fit was based on the coefficients: $\mu_{ref} = 2.1543 \cdot 10^{-5}\,kg\,m^{-1}\,s^{-1}$, $T_{ref} = 103.6\,K$, $S_\mu = 110.4\,K$. A disturbance (1,1) of frequency $\hat{f} = 6.36\,kHz\,(F = 3 \cdot 10^{-5})$ and spanwise wavenumber $\hat{\beta} = 211.52\,m^{-1}\,(\beta = 9.698 \cdot 10^{-5})$ was introduced in the boundary layer and the transition evolution investigated with high spatial resolution. As pointed out in Mayer et al. [34], a direct comparison PSE against DNS was not possible, due to the quite large amplitude of the DNS forcing, causing nonlinear effects in the receptivity process. This was verified by performing a NPSE simulation initialized by inserting the mode (1,1) very close to the first branch point. Its initial very small amplitude was set to match the DNS one further downstream. The disagreements between the higher modes amplitudes computed by DNS and NPSE proved that indeed the receptivity process was not linear. In Fig. 5 the result of this NPSE study in CPG conditions (see Fig. 10a in Mayer et al. [34]) are reproduced and compared. The mode (1,1) is introduced with a RMS amplitude $A''_{(1,1)_u} = 1.53 \cdot 10^{-3}$ at position $x = 0.07\,m$ ($\approx Re = 390$). Since no information was given about the number of terms at which the Fourier series were truncated a convergence study was made. Increasing the number of modes considered clearly improves the agreement with literature. Minor discrepancies persist in the initial evolution of mode (2,2) (△ in Fig. 5), but they vanish further downstream.

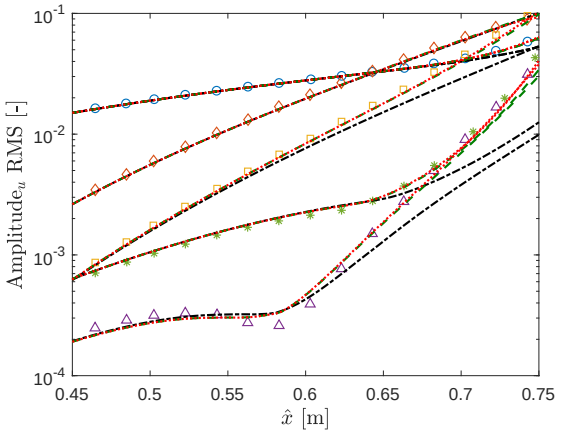

Figure 5: Evolution of the maximum RMS modes amplitude of the streamwise velocity component in CPG conditions: comparison against Mayer [34] (symbols). Supersonic flat plate flow: $M_e = 3$ and $T_e = 106.3\,K$, $p_e = 2282.4\,Pa$. Mode (1,1) (○), $F = 3 \cdot 10^{-5}$, $\beta = 9.698 \cdot 10^{-5}$, $A''_{(1,1)_u} = 1.53 \cdot 10^{-3}$, at $x = 0.07\,m$

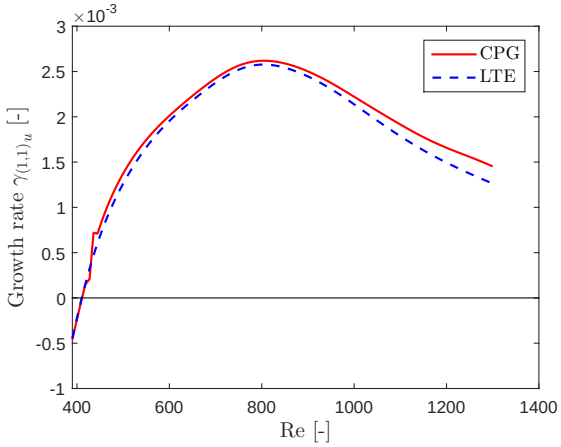

Figure 6: Evolution of the mode (1,1) linear growth rate, $F = 3 \cdot 10^{-5}$, $\beta = 9.698 \cdot 10^{-5}$: comparison between CPG and LTE flow assumptions. Supersonic flat plate flow: $M_e = 3$ and $T_e = 106.3\,K$, $p_e = 2282.4\,Pa$

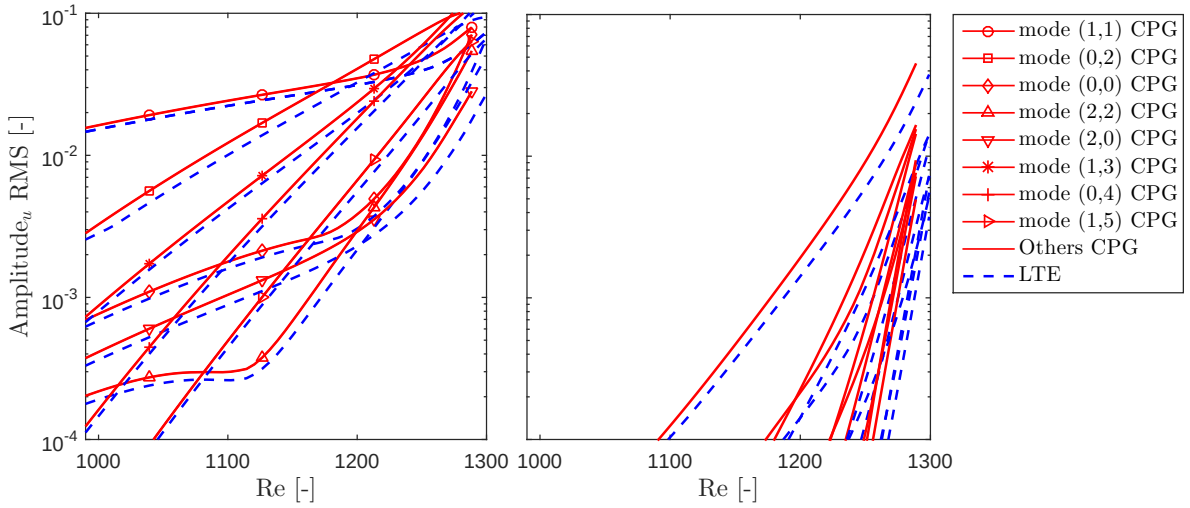

Figure 7: Evolution of the maximum RMS modes amplitude of the streamwise velocity component: comparison between CPG and LTE flow assumptions. Supersonic flat plate flow: $M_e = 3$, $T_e = 106.3\,K$, $p_e = 2282.4\,Pa$. Mode (1,1), $F = 3{\cdot}10^{-5}$, $\beta = 9.698{\cdot}10^{-5}$, $A''_{(1,1)_u} = 1.53{\cdot}10^{-3}$, at $Re = 450$

In order to study the influence of high temperature effects, the gas properties were slightly modified for the CPG calculation: the standard Sutherland's coefficients proposed in White [25] and a $Pr = 0.7$ were employed. The same nondimensional quantities of the Mayer et al. [19] study were considered, but due to the different nondimensionalization the new analyzed oblique wave has a frequency and spanwise wavenumber respectively equal to $\hat{f} = 19,1\,kHz$ and $\hat{\beta} = 634.56\,m^{-1}$.

Figure 6 displays the comparison between the linear grow rates of the primary mode (1,1), computed by PSE in CPG and LTE conditions. In this case, high temperature effects act on the boundary layer similarly to the cooling effect: they tend to stabilize the first Mack mode.

The slightly lower growth rate in LTE of the primary disturbance, results in lower amplitudes evolution when modes nonlinear interactions are analyzed. The NPSE simulation is started close to the first branch point ($Re = 450$), by inserting the same disturbance used to reproduce the data of Mayer et al. [19] in Fig. 5. The Taylor series were truncated at N=5 and M=5. Because the initial amplitude of the primary wave is very low, it takes some space for the generated harmonics to reach comparable values. Figure 7 displays the modes amplitude evolutions in the Re range 1000-1300, where, according to the linear analysis, the growth rate of (1,1) is positive but decreasing. The influence of high temperature effects involves all the harmonics. In particular, the longitudinal vortex (0,2), directly fed by the primary mode, seems to exhibit the larger differences (NB: the plot is in logarithmic scale). The discrepancies between the two solutions are carried on with the simulation, and they increase as the strong nonlinear stages of the transition process are approached. As final consequence, higher modes are activated earlier within the CPG regime, and the simulation stops slightly before compared to the LTE case. Nevertheless, for this specific problem the overall high temperature effects influence can be considered weak.

4.2.2. Fundamental resonance at Mach 10

A secondary instability mechanism in a form of a fundamental resonance is studied in an hypersonic flow at Mach 10, $T_e = 350\,K$, $p_e = 3596\,Pa$. The mean flow correspond to the benchmark test case of Malik et al. [7], analyzed by numerous authors by means of different stability theories. In particular, Marxen et al. [12; 13] analyzed the linear stability features of this flow in frozen, LTE and CNE conditions, and the weakly nonlinear transition aspects in presence of frozen and finite-rate chemistry. In Zanus et al. [26] a linear PSE study with LTE flow assumption was presented. Figure 8 compares the self-similar velocity and temperature profiles for both aerothermodynamic models. Chemical reactions cool

down the boundary layer, decreasing the nondimensional wall temperature almost by half. For boundary

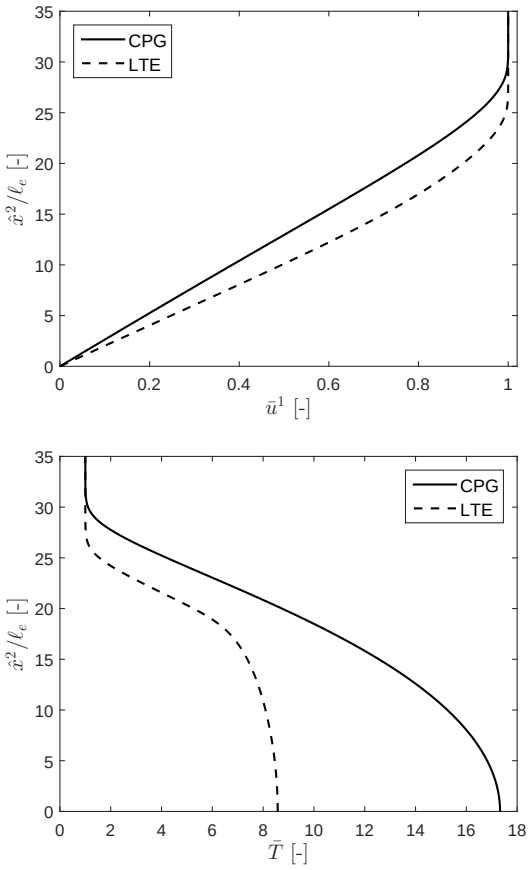

Figure 8: Streamwise velocity and temperature nondimensional mean flow profiles at Mach 10, $T_e = 350\,K$, $p_e = 3596\,Pa$: comparison between CPG and LTE flow assumptions

layers with Mach number greater more or less than 4, the most unstable disturbance is usually a two dimensional acoustic mode, the so called second Mack mode [35]. This is true both for CPG and LTE conditions, thus the expected mechanism triggering transition would be a secondary instability type breakdown. In this test case, a fundamental resonance is initialized by introducing a 2D wave (1,0) of reduced frequency $F = 3.4 \cdot 10^{-5}$ and an oblique mode (1,1) with spanwise wavenumber $b = 1.6 \cdot 10^{-5}$, at the position $Re = 1500$. Figure 9 depicts the comparison of the linear stability characteristic of the primary mode (1,0), computed by PSE. High temperature effects destabilize the second Mack mode, shifting the maximum peak towards lower Re numbers.

Figure 10 shows the nonlinear modes amplitude

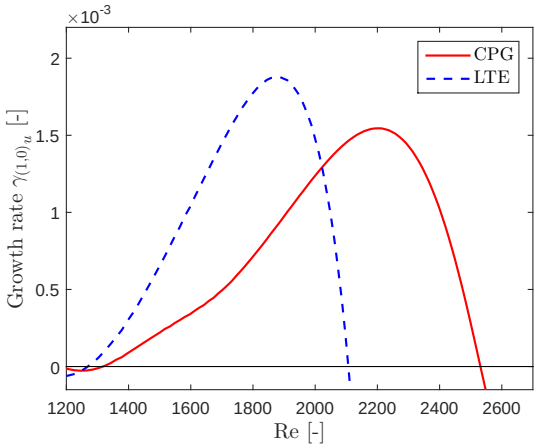

Figure 9: Evolution of the mode (1,0) linear growth rate, $F = 3.4 \cdot 10^{-5}$: comparison between CPG and LTE flow assumptions. Hypersonic flat plate flow: $M_e = 10$, $T_e = 350\,K$, $p_e = 3596\,Pa$

evolution obtained with an initial amplitude $A''_{(1,0)_u} = 5 \cdot 10^{-3}$ for the primary wave, and $A''_{(1,1)_u} = 10^{-3}$ for the secondary one. Nonlinear computations were obtained only for LTE flow assumption, truncating the Fourier series to N=2 and M=4. In CPG conditions the primary 2D mode reaches amplitudes of the order $O(10^{-1})$, due to the wider instability region of the perturbation, causing the simulation to diverge. On the other hand, decreasing the initial amplitude of the primary wave would not promote strong enough nonlinear interactions between the modes. The occurrence of a fundamental-type resonance is highlighted by the appearance of the stationary vortex (0,1), direct consequence of the primary and secondary waves interaction [15]. The amplitude of this mode increases up to the point it overcomes the amplitude of the secondary disturbance. Second harmonics of the primary wave and of the stationary vortex also develop. From the implementation point of view it is worthy to mention that because nonparallel effects become important as the Mach number increases [26], strong transient may occur at the beginning of the simulations, if solutions coming from LST are provided as initial conditions. Both for the Mach 3 and Mach 10 test cases, it was necessary to damp out this transient phase. Its undesired effect can indeed accumulate during the marching path, affecting the perturbations amplitude calculation through the growth rate integral contribution, as in Eq. (16).

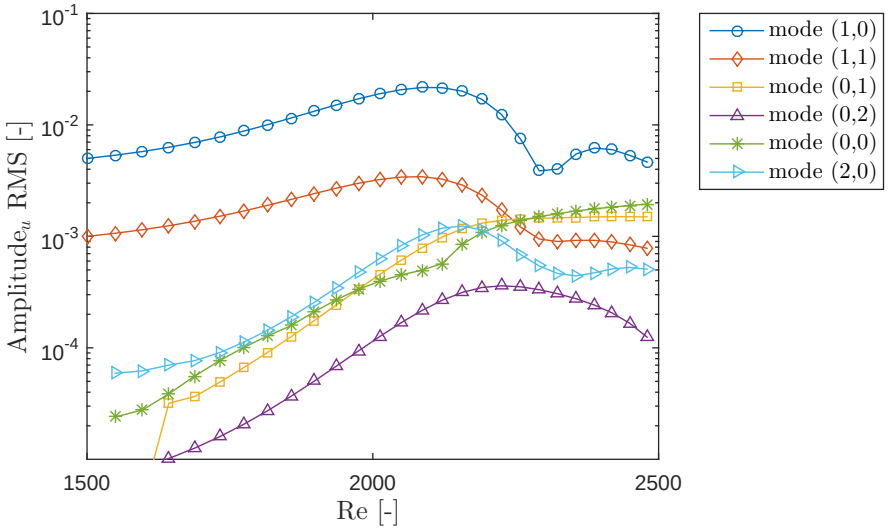

Figure 10: Evolution of the maximum RMS modes amplitude of the streamwise velocity component in LTE flow conditions. Hypersonic flat plate flow: $M_e = 10$, $T_e = 305\,K$, $p_e = 3596\,Pa$. Mode (1,0), $F = 3.4 \cdot 10^{-5}$, $A''_{(1,0)_u} = 5 \cdot 10^{-3}$; mode (1,1), $\beta = 1.6 \cdot 10^{-5}$, $A''_{(1,1)_u} = 10^{-4}$

5. Conclusion

Laminar-to-turbulent transition in hypersonic boundary layers was studied in its linear and weakly nonlinear stages by means of PSE. A newly algorithm, recently developed within the VESTA toolkit, was proved to solve nonlinear PSE in CPG and LTE flow conditions.

The code was first verified against the results provided by the PSE code EPIC of Texas A&M University, for different types of instabilities and flow configurations. Next, the algorithm was used to investigate the influence of high temperature effects on the nonlinear transition stages, for an oblique-type breakdown at Mach 3 and a fundamental resonance transition mechanism at Mach 10. In the mid-supersonic test case, high temperature effects lead to slightly lower modes amplitudes, due to the more stable oblique primary disturbance. Consequently, higher modes appear earlier and the simulation reaches saturation first in CPG conditions. Nevertheless, for this specific problem, the overall influence of the flow assumption can be considered negligible. Including high temperature gas physics in the analysis was proved to be essential in order to reproduce the fundamental resonance phenomenon at Mach 10. Because the primary disturbance is unstable over a wider region in CPG conditions, unsustainable amplitude are reached, preventing the simulation to converge. The LTE NPSE solver, on the other hand, is able to retrieve the main characteristic of the transition mechanism, without any numerical instability.

Results obtained by means of this LTE NPSE solver encourage the utilization of the NPSE technique for stability and transition prediction in hypersonic flows. Investigation of nonlinear stages of the transition process in high Mach flows are nowadays accessible only to DNS simulations. The coupling of the NPSE technique with proper modeling of high temperature gas effects, will bring undeniable advantages in this type of studies, providing results with comparable DNS accuracies, but at a much lower computational cost.

Acknowledgments

This research is made possible thanks to the financial support provided by the Fonds de la Recherche Scientifique through their FRIA fellowship program. The author wants to thank Alexander J. Moyes for providing the base flows and for performing the related PSE analyses with the EPIC code, for the verification cases.

References

[1] R. L. Kimmel, Aspects of hypersonic boundary-layer transition control, in: AIAA (Ed.), 41st Aerospace Sciences Meeting and Exhibit, no. 2003-772, Reno, Nevada, 2003.

[2] H. L. Reed, E. Perez, J. Kuehl, T. Kocian, N. Oliviero, Verification and validation issues in hypersonic stability and transition prediction, Journal of Spacecraft and Rockets 52 (1) (2014) 29–37.
[3] H. L. Reed, R. Kimmel, S. Schneider, D. Arnal, Drag prediction and transition in hypersonic flow, in: AIAA (Ed.), 28th Fluid Dynamics Conference, Snowmass Village, Colorado, 1997.
[4] L. Krishnan, N. D. Sandham, Shock-wave/boundary-layer interactions in a model scramjet intake, AIAA Journal 47 (7) (2009) 1680–1691.
[5] J. D. Anderson, Hypersonic and High Temperature Gas Dynamics, American Institute of Aeronautics and Astronautics, 2006.
[6] K. J. Franko, R. W. MacCormak, Effects of chemistry modeling on hypersonic boundary layer linear stability prediction, in: AIAA (Ed.), 40th Fluid Dynamics Conference and Exhibit, no. 2010-4601, Chicago, Illinois, 2010.
[7] M. R. Malik, E. C. Anderson, Real gas effects on hypersonic boundary-layer stability, Physics of Fluids A 3 (5) (1991) 803–820.
[8] G. Stuckert, H. L. dd, Linear disturbances in hypersonic chemically reacting shock layers, AIAA Journal 32 (7).
[9] C.-L. Chang, H. Vinh, M. R. Malik, Hypersonic boundary-layer stability with chemical reactions using pse, in: AIAA (Ed.), 28th Fluid Dynamic Conference, 1997.
[10] M. R. Malik, Hypersonic flight transition data analysis using parabolized stability equations with chemistry effects, Journal of Spacecraft and Rockets 40 (3).
[11] H. B. Johnson, G. V. Candler, Pse analysis of reacting hypersonic boundary layer transition, in: AIAA (Ed.), 30th Fluid Dynamics Conference, 1999.
[12] O. Marxen, T. Magin, G. Iaccarino, S. G. Shaqfeh, A high-order numerical method to study hypersonic boundary layer instability including high-temperature gas effects, Physics of Fluids 23.
[13] G. Marxen, O. Iaccarino, T. Magin, Direct numerical simulations of hypersonic boundary-layer transition with finite-rate chemistry, Journal of Fluid Mechanics 755 (2014) 35–49.
[14] C. L. Chang, M. R. Malik, Oblique-mode breakdown and secondary instability in supersonic boundary layers, Journal of Fluid Mechanics 273 (1994) 323–360.
[15] T. Herbert, Secondary instability of boundary layers, Annual Review of Fluid Mechanics 20 (1988) 487–526.
[16] J. J. Kuehl, E. Perez, H. L. Reed, Jokher: Npse simulations of hypersonic crossflow instability, in: AIAA (Ed.), 50th Aerospace Science Meeting, 2012.
[17] E. Perez, H. L. Reed, J. J. Kuehl, Instabilities on a hypersonic yawed straight cone, in: AIAA (Ed.), 43rd Fluid Dynamics Conference,, San Diego, California, 2013.
[18] A. J. Moyes, P. Paredes, T. S. Kocian, H. L. Reed, Secondary instability analysis of crossflow on a hypersonic yawed straight circular cone, Journal fo Fluid Mechanics 812 (2017) 370–397.
[19] C. S. J. Mayer, D. A. vonTerzi, H. F. Fasel, Direct numerical simulation of complete transition to turbulence via oblique breakdown at mach3, Journal fo Fluid Mechanics 674 (2011) 5–42.
[20] F. Pinna, Numerical study of stability of flows from low to high mach number, Phd thesis, Von Karman Institute - Università degli Studi di Roma La Sapienza (2012).
[21] N. B. Oliviero, T. S. Kocian, A. J. Moyes, H. L. Reed, Epic: Npse analysis of hypersonic crossflow instability on yawed straight circular cone, in: AIAA (Ed.), 45th AIAA Fluid Dynamics Conference, 2015.
[22] F. Pinna, K. Groot, Automatic derivation of stability equations in arbitrary coordinates and different flow regimes, in: AIAA (Ed.), 44th Fluid Dynamic Conference, 2014.
[23] T. E. Magin, G. Degrez, Transport algorithms for partially ionized and unmagnetized plasmas, Journal of Computational Physics 198 (2004) 424–449.
[24] J. B. Scoggins, T. E. Magin, Development of mutation++: Multicomponent thermodynamic and transport properties for ionized plasmas written in c++, in: AIAA (Ed.), 11th AIAA/ASME Joint Thermophysics and Heat Transfer Conference, no. AIAA 2014-2966, 2014.
[25] F. M. White, Viscous Fluid Flow, McGraw-Hill, 2006.
[26] L. Zanus, F. Miró Miró, F. Pinna, Parabolized stability analysis of chemically reacting boundary layer flows in equilibrium conditions, in: 7th EUCASS Conference, Milan, 2017.
[27] T. Herbert, F. P. Bertolotti, Stability analysis of nonparallel boundary layers, Bulletin of the American Physical Society 32 (1987) 2079.
[28] C.-L. Chang, M. R. Malik, G. Erlebacher, M. Y. Hussaini, Linear and nonlinear pse for compressible boundary layers, Icase report n. 93-70, NASA (1993).
[29] H. Salinas, Stabilité linéaire et faiblement non linéaire d'une couche limite laminaire compressible tridimensionnelle par l'approche pse, Phd thesis, École National Supérieure de l'Aéronautique et de l'Espace (1998).
[30] L. Zanus, Analysis of a compressible boundary layer flow by means of parabolized stability calculations, Research Master report 2016-28, von Karman Institute for Fluid Dynamics (June, 2016).
[31] L. Zanus, F. Miró Miró, F. Pinna, Nonlinear parabolized stability analysis of hypersonic flows in presence of curvature effects, AIAA paper 2018-2087.
[32] F. P. Bertolotti, Linear and nonlinear stability of boundary layers with streamwise varying properties, Phd thesis, The Ohio State University (1991).
[33] A. Moyes, E. Beyak, T. S. Kocian, H. L. Reed, Accurate and Efficient Modeling of Boundary-Layer Instabilities, AIAA Paper 2019-1907 (2019) 1–26.
[34] C. S. J. Mayer, H. F. Fasel, Detailed comparison of dns to pse for oblique breakdown at mach 3, in: AIAA (Ed.), 40th Fluid Dynamic Conference and Exhibit, Chicago, Illinois, 2010.
[35] L. M. Mack, Boundary-layer linear stability theory:, in: AGARD (Ed.), Special Course on Stability and Transition of Laminar Flows, no. R-709, 1984.

AEROTHERMODYNAMICS

Laminar to Turbulent Transition Prediction in Hypersonic Flows with Neural Networks Committee

Florian Danvin

CEA-CESTA, France and

Aeronautics and Aerospace Department, von Karman Institute for Fluid Dynamics, Belgium, danvin@vki.ac.be

Supervisors: Olivier Chazot and Fabio Pinna

Head of Department and Professor, Aeronautics and Aerospace Department, von Karman Institute for Fluid Dynamics, Belgium, chazot@vki.ac.be

Senior Research Engineer, von Karman Institute for Fluid Dynamics, Belgium, pinna@vki.ac.be

University Supervisor: Herman Deconinck

Professor, Aero-Thermo-Mechanics Department, Université Libre de Bruxelles, Belgium

Full Professor, Aeronautics and Aerospace Department, von Karman Institute for Fluid Dynamics, Belgium, deconinck@vki.ac.be

CEA Supervisor: Marina Olazabal-Loume

Senior Research Engineer, CEA-CESTA, France, marina.olazabal@cea.fr

Abstract

Simulating the full reentry trajectory of a general spacecraft is cumbersome, especially when real gas effects and surface ablation typical from hypersonic regimes come into play. In the continuous layer of the atmosphere, a boundary layer develops around the spacecraft's body. The development of instabilities among the initially laminar boundary layer, may cause its transition to a turbulent state, which is for hypersonic regimes synonym of a rise in the wall heat fluxes and skin friction. Accordingly a metamodel of LST (Linear Stability Theory) was developed not only to ease computations, but also to improve the spacecraft performances accounting for boundary layer transition. The metamodel is able to predict accurately and instantaneously the evolution of Mack's second mode, characteristic of hypersonic regime, on sharp and slightly blunted cones at Mach 6 using either a self-similar flow or a Navier-Stokes solution.

Keywords: LST, metamodel, artificial neural network, active learning, hypersonics

Nomenclature

U: streamwise velocity component $[m.s^{-1}]$
V: normal to the flow velocity component $[m.s^{-1}]$
W: spanwise velocity component $[m.s^{-1}]$
P: static pressure $[Pa]$
R: density $[kg.m^{-3}]$
α: Non-dimensional streamwise wavenumber $[-]$
β: Non-dimensional spanwise wavenumber $[-]$
ω: Non-dimensional frequency $[-]$
A: perturbation amplitude $[-]$
N: N factor $[-]$
Tr: ratio of the adiabatic temperature over the wall temperature $[-]$
β_H: Hartree parameter
Re: Reynolds number based on Blasius length scale $[-]$
f: frequency $[Hz]$
ϵ: relative error $[\%]$

Subscripts

e: boundary layer edge value
∞: far field value
0: initial state value
r: real part
i: imaginary part
tr: value at transition point
w: value at the wall

Abreviations
LST: Linear Stability Theory
PSE: Parabolized Stability Theory
$RANS$: Reynolds Averaged Navier-Stokes
CFD: Computational Fluid Dynamics
$SSIFL$: Smart Sampling and Incremental Function Learning
NN: Neural Network
RBF: Radial Basis Functions
PL: Passive Learning
AL: Active Learning
N_{pts}: Number of points

1. Introduction

Since the first hypersonic flight in 1949 by the German $V-2$ rocket, the hypersonic field still carries many unknowns and obstacles to be overcome before considering routinely hypersonic flights. Both scientists and engineers are "facing the heat barrier" [1] problem whenever a spacecraft is submitted to an atmospheric reentry. In the continuous layer of the atmosphere, a boundary layer forms around the spacecraft and it can transition towards a turbulent state, causing both an increase of heat transfer and drag, ultimately leading to surface deterioration.

The prediction of boundary layer transition on a general spacecraft remains nowadays challenging. This is especially due to the lack of comprehension in the intrinsic physics of the phenomenon, and to the variety of factors either triggering or delaying its onset. Though the physics of an hypersonic flow around a sharp cone is known, the apparently simple flow around blunt cones at hypersonic speeds is still under active research [2] [3], especially due to the blunt body paradox evidenced by Reshotko [4]. Several numerical methods are nevertheless able to reproduce boundary layer transition. The best method is undoubtedly direct numerical simulation in terms of completeness but requires serious computational resources. While these requirements are acceptable for one particular case to study, it quickly becomes intractable for studying the full reentry phase of an hypersonic vehicle with real gas effects or surface ablation. To overcome these difficulties RANS coupling with either stability calculations or empirical correlations is usually preferred significantly lowering the resource requirements per case. LST has demonstrated the adequate compromise between performances, computational cost, and physical considerations to predict boundary layer transition in hypersonics on simple geometries [5] [6], and the development of a metamodel based on this theory was firstly undertaken by Pinna et al in [7] and extended by Danvin et al in [8]. The methodology adopted in this article was to couple a RANS simulation to an LST metamodel in order to reduce the computational time to the one of the CFD as the metamodel predictions can be considered instantaneous. The main advantages of using this metamodel lie in its flexibility in terms of geometry and Mach range over empirical correlations. Indeed an expansion in one or the other direction is just a matter of increasing a database with meaningful cases, and to directly reproduce the boundary layer perturbation amplification as the LST would. Nevertheless the construction of a meaningful database can be quite long and tedious if no prior knowledge on the function to approximate were acquired. This article is focused on the improvement of the metamodel presented in [8], but also aims at extending the metamodel applicability on blunt cones.

2. Metamodel establishment

A metamodel or a surrogate model, consists in building an approximator $\tilde{f}$ of a chosen oracle function $\bar{f}$. The approximator elaboration requires, on one hand, a database of points linking some meaningful input parameters X to the corresponding oracle output $Y = \bar{f}(X)$. On the other hand it also requires a multidimensional regression method to construct the approximator $\tilde{f}$ here chosen to be artificial neural networks. The following subsections describe the different steps of the metamodel improvement.

2.1. Generating a validation Benchmark

A sound benchmark composed of several examples is needed, in order to test and validate our metamodel. For this purpose, two kinds of examples can be distinguished. The first kind is a self-similar flow (SS), whereas the other one is a CFD flow coming from a RANS code. The main advantage of using the former compared to the latter is the computational cost. For now, examples used as references are all flows past a 7° half-angle cone at different freestream conditions of the VKI-H3 Mach 6 blow-down tunnel. For self-similar flows, the boundary-layer edge

quantities are computed with the Taylor-Maccoll relations, contrary to the CFD flows for which they are directly taken from the flow field using the 99% of the freestream total enthalpy criterion, as suggested by Demange [9]. From a previous study of Grossir et al [10], three VKI-H3 flow conditions were selected, the $Re_\infty = 15 \cdot 10^6/m$ case, the $Re_\infty = 18.1 \cdot 10^6/m$ and the $Re_\infty = 22.8 \cdot 10^6/m$ for which both a self-similar flow, and a CFD flow were computed. The respective freestream conditions, and boundary layer edge quantities are given in Tab 1 and .7 (given in Annex). The example denominations will be Re15-SS7 and Re15-CFD7 respectively for the self-similar and CFD flow at $Re_\infty = 15 \cdot 10^6/m$, similarly Re18-SS7 / Re18-CFD7 and Re23-SS7 / Re23-CFD7 for the other cases.

Table 1: Freestream conditions for both the self-similar and CFD examples.

$Re_\infty\ [m^{-1}]$	M_∞	$T_\infty\ [K]$	$P_\infty\ [Pa]$	$T_w\ [K]$
$15 \cdot 10^6$	6	61.18	1140.1	293
$18.1 \cdot 10^6$	6	59.6	1317.4	300
$22.8 \cdot 10^6$	6	60.97	1721.1	295

2.2. Previous results

Some preliminary results were presented in [8], on the first two flow conditions mentioned in the previous section. The behaviour of the metamodels on the Re15 cases was depicted by Fig 1. The blue curves represent the LST results, and the dashed lines are metamodel predictions depending on the training database or the training algorithm used. One can firstly note this frequency shift causing a delay in the instability amplification predicted by the different metamodels on either the self-similar flow or the CFD flow. Furthermore the best metamodels prediction were not achieved each time by the same neural network, causing our general method to lack consistency. For all these reasons, some modifications on both the database input parameters and on the regression part were brought and are detailed in the following sections.

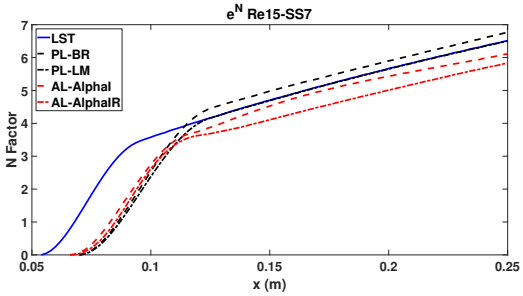

a) Re15-SS7 case

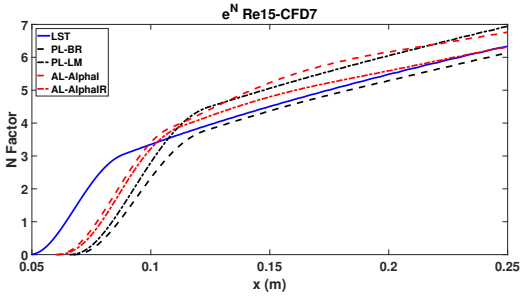

b) Re15-CFD7 case

Figure 1: Envelope curves comparison between the growth rate obtained with LST vs different metamodel predictions.

2.3. Database modifications

The previously built databases were based on the input parameters found by Demange [9] and Pinna et al [7]. The approximator function $\tilde{f}$ was linked to the oracle function $\bar{f}$ (the LST) via the following parameters,

$$\alpha = \tilde{f}(M_e, T_e, T_r, \beta_H, Re, f). \quad (1)$$

As this set of parameters proved to be insufficient to give an accurate enough description of the LST, the boundary layer edge pressure p_e and points of the non dimensional velocity and temperature derivatives with respect to the wall normal coordinate were further included. The inclusion of p_e was observed to cure the frequency shift. The derivatives inclusion was thought to help coping with blunt geometries and also to increase the overall accuracy. The probing locations along the boundary layer for the velocity and temperature derivatives were based on an even partition between the wall and the minimum of the non dimensional total enthalpy derivative with respect to y as can be seen in Fig 2. This criterion was preferred instead of a more classical percentage of the freestream total enthalpy as it places the boundary layer height just after the total enthalpy maximum

and bump. The non-viscous flow variations are consequently excluded, producing minor discrepancies between a self-similar and a CFD profile, as these variations are neglected for a self-similar flow.

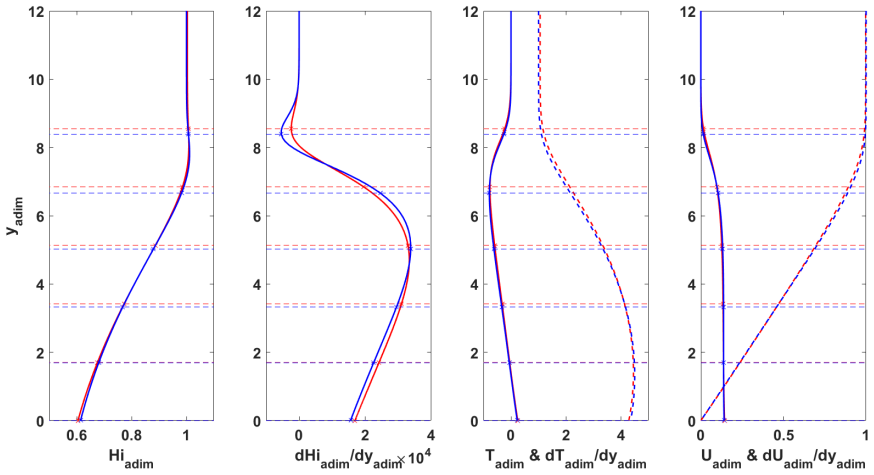

Figure 2: Derivatives extraction comparison between a CFD profile (red) and a self-similar profile (blue), for the Re18-CFD7 flow conditions at x=15cm.

Table 2: Derivatives influence on the metamodel performances

Probing N_{pts}	$1pt$		$2pts$		$2pts0060$		$5pts$	
Case	ϵ_P (%)	ϵ_N (%)	ϵ_P (%)	ϵ_N (%)	ϵ_P (%)	ϵ_N (%)	ϵ_P (%)	ϵ_N (%)
$Re15-SS7$	2.31	1.40	1.37	0.48	3.96	1.76	1.68	1.63
$Re15-CFD7$	6.94	4.31	7.90	8.27	12.26	4.49	6.29	14.10
$Re18-SS7$	2.88	2.60	2.03	2.66	3.96	1.86	3.06	3.22
$Re18-CFD7$	1.81	9.92	4.24	4.41	14.36	6.55	4.92	9.92
$Re23-SS7$	3.57	5.54	1.78	3.22	2.97	2.93	4.50	7.25
$Re23-CFD7$	2.43	1.51	2.30	5.18	14.82	5.10	3.10	6.33
TOTAL:	19.94	25.28	**19.62**	**24.22**	52.33	22.69	23.55	42.45

The number of probing locations and the position of particular interest were chosen after a brief parametric study detailed hereafter in Tab 2. This study was run with neural network committees, whose descriptions are presented in the following section. A comparison was made between adding gradually the points in the database, except for the $2pts0060$ case, where the chosen derivatives are taken at the wall and at 60% of our boundary layer height. This study revealed that considering the first two points was providing us the best results, and the lowest error on the ϵ_P, ϵ_N couple. This configuration is consequently retained, for the following sections.

Table 3 presents the chosen range of variation for the new database input parameter. As its predecessors it was computed with self similar profiles on a 7° half angle cone. Ranges of velocity and temperature derivatives were voluntarily not included for the sake of clarity.

Table 3: Database input range of fluctuations.

Parameter	Unit	Range
Me	$[-]$	$5-6$
Te	$[K]$	$65-95$
Tr	$[-]$	$0.6-0.8$
β_H	[-]	0
Re	$[-]$	$1000-3000$
f	$[kHz]$	$100-800$
Pe	$[Pa]$	$2000-5000$
N_{pts}	$[-]$	$\approx 8,400,000$

2.4. Regression method modifications

2.4.1. Performance evaluation

The estimation of the metamodel performances remains unchanged comparing with [8]. The accuracy is given firstly by the relative growth rate peak error P_{Err}, i.e., the point where $-\alpha_i$ is maximum. Nevertheless, other measures of the prediction accuracy are needed to estimate independently the accuracy on the N-factor curve prediction N_{Err}. For a single frequency f_j with $j \in [1; M]$, the peak error P_{Err} and respectively the N-factor error N_{Err} are given by:

$$P_{Err}(f_j) = \frac{\mid max[-\alpha_{I-NN}(f_j)] - max[-\alpha_{I-LST}(f_j)] \mid}{max[-\alpha_{I-LST}(f_j)]} \tag{2}$$

Considering only positive values of $-\alpha_I$, $N_{Err}(f_j)$ is given by:

$$N_{Err}(f_j) = \frac{\mid \int_x -\alpha_{I-NN}(f_j)dx - \int_x -\alpha_{I-LST}(f_j)dx \mid}{\int_x -\alpha_{I-LST}(f_j)dx} \tag{3}$$

N_{Err} computation can be illustrated with Fig. 3, where the surface A represents one integral term either for the LST or the metamodel prediction used in Eq. 3. Denoting the mean function by $\bar{m}$, then the previous quantities mean value are obtained with:

$$\epsilon_P = \bar{m}(P_{Err}(f_j), j = 1..M) \tag{4}$$

and

$$\epsilon_N = \bar{m}(N_{Err}(f_j), j = 1..M). \tag{5}$$

In order to study the predictions error dispersion, the variance and respectively the median of both the peak error and of the N-factor error are computed with:

$$Var(P_{Err}) = \frac{\sum_{i=1}^{M}(P_{Err}(f_j) - \epsilon_P)^2}{M-1} \tag{6}$$

$$Var(N_{Err}) = \frac{\sum_{i=1}^{M}(N_{Err}(f_j) - \epsilon_N)^2}{M-1} \tag{7}$$

$$Med(P_{Err}) = median(P_{Err}) \tag{8}$$

$$Med(N_{Err}) = median(N_{Err}) \tag{9}$$

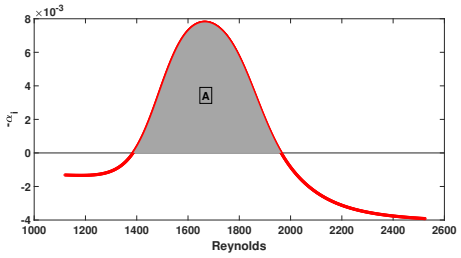

Figure 3: Unstable area illustration, plotting the growth rate vs Reynolds number for a single frequency f_j

2.4.2. Neural Network Committee

As mentioned in the beginning of the section, having an absolute oracle with the class of neural network and training method chosen is not straightforward. Hence the individual metamodels were lacking precision and robustness, an approach by committee, as suggested by [11], was retained. Each metamodel output is weighted with the others in order to match our prediction objectives. Following Eq 10, a_i is the individual neural network prediction, and N the total number of metamodels composing the committee. The weights are denoted w_i are equal to 1 for now but can be changed towards some more sophisticated method either benefiting from the committee disagreement [11] or such as the one presented in [12].

$$a = \Sigma_{i=1}^{N} \frac{w_i * a_i}{N} \tag{10}$$

The committee is composed of a total of six performers among eighty different neural networks, three among the six, further denoted $NN_P{-}i$ gave the best ϵ_P error on the benchmark examples, and the three others, referred as $NN_N - i$ gave the best ϵ_N error on the following examples. Their accuracy on each example are provided in Tab 4 through 6. These networks differs from each other by both their neuron partition and their number of hidden layers. They were individually trained with the Adam optimizer training algorithm from Kingma et al [13] using TensorFlow™ library [14].

Table 4: Metamodel performances on Re15 cases

Cases	$Re15-SS7$		$Re15-CFD7$	
Networks	ϵ_P (%)	ϵ_N (%)	ϵ_P (%)	ϵ_N (%)
NN_P-1	2.04	1.45	1.93	6.10
NN_P-2	1.52	1.82	3.66	3.23
NN_P-3	0.38	0.59	4.79	2.43
NN_N-1	0.38	0.59	4.79	2.43
NN_N-2	1.52	1.82	3.66	3.23
NN_N-3	4.15	0.85	12.25	5.99
NN Com.	0.70	0.55	4.04	3.07

3. Metamodel predictions on 7° half-angle sharp cones

The committee and individual best neural networks performers predictions are presented in Fig 4 for every case considered. At first sight it can be noted that the frequency shift is cured, and that the committee predictions lies perfectly on top of the LST for each cases. A slightly higher disagreement within the committee is also noticeable for CFD cases, as the database was build with self-similar flows, cf Tab 4, 5 and 6. Consequently, provided the domain of application lies within the database range, the committee should be able to predict accurately the stability of the conical flow for 7° half-angle cones. As this is quite restrictive regarding the geometry considered, an extension of the metamodel applicability towards blunt cones and cones with different half-angle is sought. Some preliminary results for slightly blunted cones are presented hereafter.

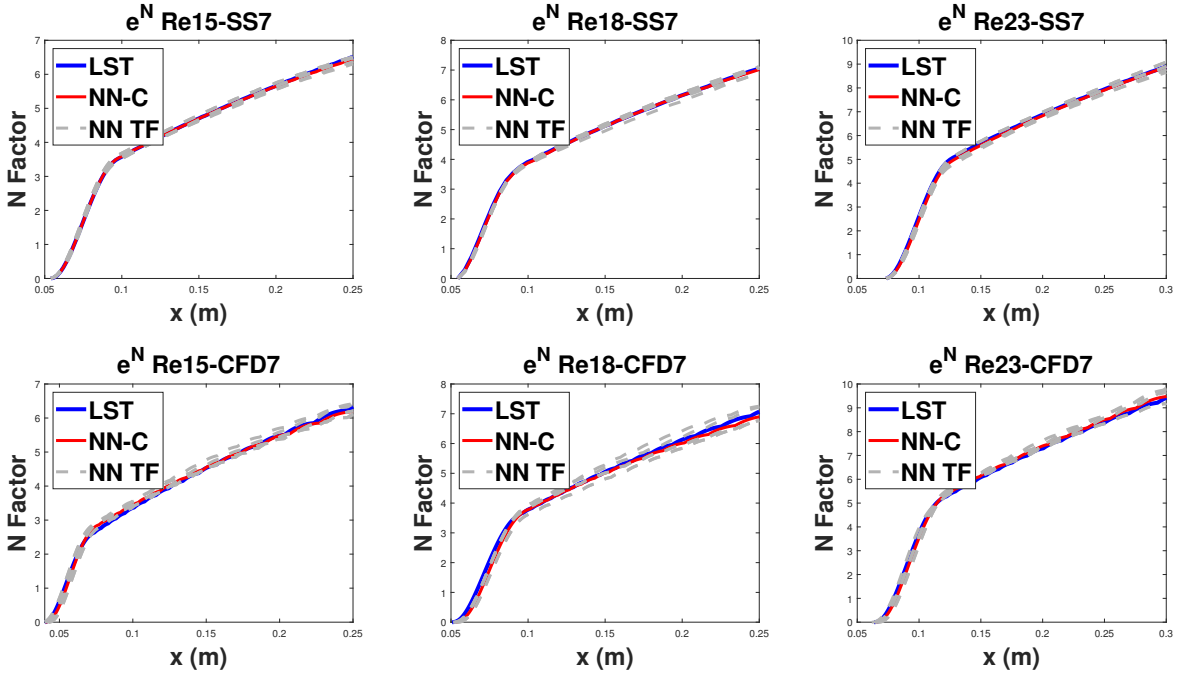

Figure 4: Committee predictions for all the examples considered.

Table 5: Metamodel performances on Re18 cases

Cases	$Re18-SS7$		$Re18-CFD7$	
Networks	ϵ_P (%)	ϵ_N (%)	ϵ_P (%)	ϵ_N (%)
NN_P-1	3.64	5.01	1.69	6.06
NN_P-2	1.67	2.31	2.25	6.38
NN_P-3	2.96	3.84	4.93	6.99
NN_N-1	2.96	3.84	4.93	6.99
NN_N-2	1.67	2.31	2.25	6.38
NN_N-3	4.19	2.45	9.08	5.22
NN Com.	2.26	2.73	2.91	5.31

Table 6: Metamodel performances on Re23 cases

Cases	$Re23-SS7$		$Re23-CFD7$	
Networks	ϵ_P (%)	ϵ_N (%)	ϵ_P (%)	ϵ_N (%)
NN_P-1	2.57	2.27	1.55	5.21
NN_P-2	1.58	4.49	3.04	4.38
NN_P-3	1.93	2.94	2.73	2.53
NN_N-1	1.93	2.94	2.73	2.53
NN_N-2	1.58	4.49	3.04	4.38
NN_N-3	5.95	4.00	8.23	4.14
NN Com.	1.08	0.99	1.34	2.85

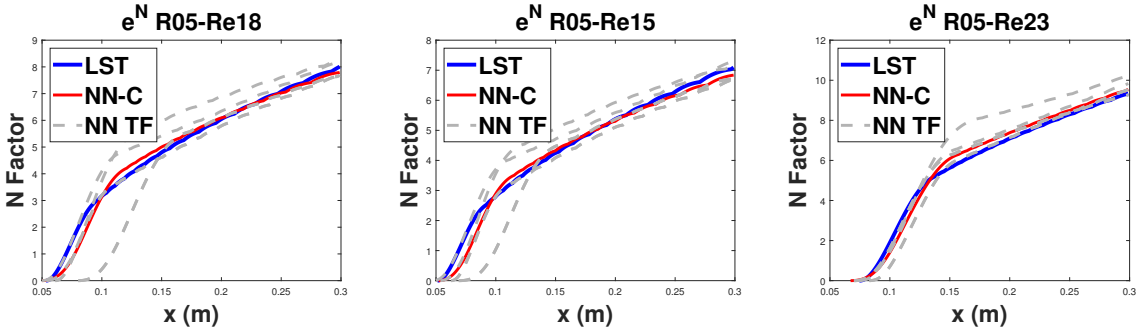

Figure 5: Committee predictions for all the 500μm blunt cones.

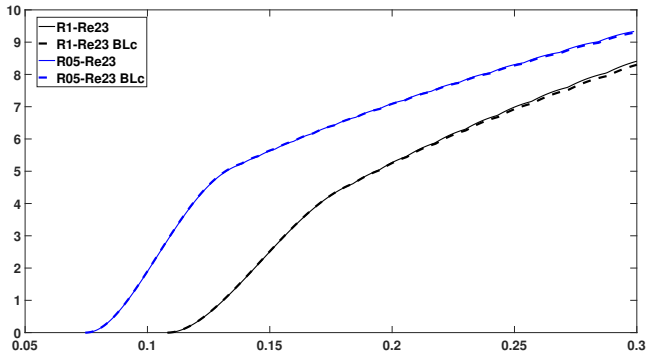

Figure 6: Effect of input pre-processing on stability for blunt Re23 cases

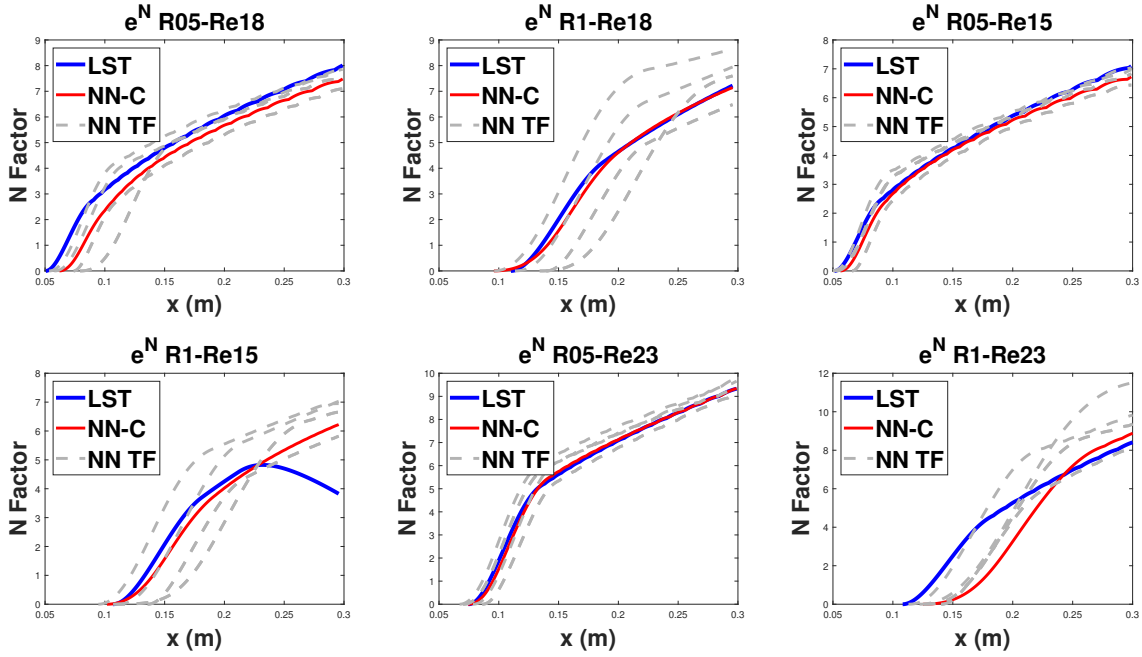

Figure 7: Committee predictions for blunt cones with input treatment.

4. Metamodel predictions on 7° half-angle slightly blunted cones

4.1. Raw input predictions

As most of the geometries flying at hypersonic speeds are blunted in order to decrease the intense heat fluxes the object is submitted to, it was decided to test our metamodels on slightly blunted cones for the same freestream conditions. The nose radii considered are $500\mu m$, $1mm$, and $2mm$. The committee predictions are presented in Fig 5. Results on blunter geometries are not presented in this section due to the significant impact of the entropy swallowing phenomenon on the flow stability that strongly affects the accuracy of the metamodel predictions. The effects of which are not at the present moment accounted for in the database. Although the committee predictions present a higher disagreement, it is able to perfectly

retrieve the perturbations amplification rate for every flow conditions. On all these examples presented in Fig 5, the entropy layer swallowing length is about $7-8cm$, according to Rotta's [15] correlation. This length increase to $17.5-20.5cm$ for $1mm$ blunt cases, and to $44.5-51.5cm$ for the $2mm$ one. The latter case was then dropped as the maximum possible object length fitting the VKI-H3 test section is 30 cm.

4.2. Predictions considering input treatment

As CFD and self-similar profiles differs in the inviscid region of the flowfield, the effect of neglecting the CFD profiles variations in this region was investigated. This can be seen as "straightening" the CFD profiles. Fig 6 represents LST predictions for both $500\mu m$ and $1mm$ blunted cones in Re23 freestream conditions either considering or not this input preprocessing. Curves obtained from the pre-processed input are referred to as "R..-Re.. BL*c*". The flow stability seems not to be affected by this pre-processing, at least for the considered examples and for the range of applicability we are targetting. However this preprocessing considerably helps the committee providing the results displayed in Fig 7. The committee predictions are almost in perfect adequation with the LST in each example. As expected the disagreement in the committee is quite higher than for the sharp cases and increases with the nose bluntness, highlighting a higher uncertainty in the predictions. The frequency shift observed by the committee predictions for the R1-Re23 case are not yet explained. To sum up, the metamodel exhibit fair predictions, when considering slightly blunted geometries for which transition can be observed in the VKI-H3 facility. This is encouraging as only self-similar flows were considered to build the database.

5. Conclusions

After improving the metamodel performances for transition prediction on sharp cones in hypersonics, its ability to cope with slightly blunted geometries was demonstrated for the VKI-H3 freestream conditions, provided a moderate entropy layer swallowing length. Thus motivates the metamodel improvement and extension in order to account for either blunter cases and cones of various half angle before an extension towards higher Mach numbers.

Acknowledgements

The authors would like to acknowledge F. Mirò Mirò as well as S. Demange and L. Zanus for fruitful discussions.

References

[1] T. A. Heppenheimer, Facing the heat barrier: a history of hypersonics, Vol. 4232, Government Printing Office, 2009.

[2] P. Paredes, M. M. Choudhari, F. Li, J. S. Jewell, R. L. Kimmel, E. C. Marineau, G. Grossir, Nosetip bluntness effects on transition at hypersonic speeds: experimental and numerical analysis under nato sto avt-240, in: 2018 AIAA Aerospace Sciences Meeting, 2018, p. 0057.

[3] J. S. Jewell, R. L. Kimmel, Boundary layer stability analysis for stetson's mach 6 blunt cone experiments, in: 54th AIAA Aerospace Sciences Meeting, 2016, p. 0598.

[4] R. E., Transient growth: A factor in bypass transition, Physics of Fluids 13 (5) (2001) 1067–1075.

[5] F. Pinna, Numerical study of stability flows from low to high mach number, Ph.D. thesis, Università Degli Studi Roma La Sapienza Facoltà di Ingegneria (2012).

[6] D. Arnal, Boundary layer transition: predictions based on linear theory, in: Special Course on Progress in Transition Modelling AGARD 793, 1993.

[7] F. Pinna, L. Zanus, M. Olazabal-Loumé, Reduced model for transition prediction in hypersonic flows, 2018 AIAA Aviation and Aeronautics Forum and Exposition, Atlanta, GA.

[8] F. Danvin, M. Olazabal-Loumé, F. Pinna, Laminar to turbulent transition prediction in hypersonic flows with metamodels, 2018 AIAA Aviation and Aeronautics Forum and Exposition, Atlanta, GA.

[9] S. Demange, Fast method for the prediction of the transition in the boundary layer for hypersonic flows (2016).

[10] G. Grossir, D. Masutti, O. Chazot, Flow characterization and boundary layer transition studies in vki hypersonic facilities, in: 53rd AIAA Aerospace Sciences Meeting, 2015, p. 0578.

[11] A. Krogh, J. Vedelsby, Neural network ensembles, cross validation, and active learning, in: Advances in neural information processing systems, 1995, pp. 231–238.

[12] Y. H. Hu, J.-N. Hwang, Committee machines, 2000.

[13] D. P. Kingma, J. Ba, Adam: A method for stochastic optimization, arXiv preprint arXiv:1412.6980.

[14] M. Abadi, P. Barham, J. Chen, Z. Chen, A. Davis, J. Dean, M. Devin, S. Ghemawat, G. Irving, M. Isard, et al., Tensorflow: A system for large-scale machine learning., in: OSDI, Vol. 16, 2016, pp. 265–283.

[15] S. R. Pate, Effects of nose bluntness on the boundary layer characteristics of conical bodies at hypersonic speeds rotta, n. r., Tech. rep., New-York University Report NYUAA-66-66 (1966).

Appendix

Table .7: Examples input range of fluctuations.

Unit Case	Me $[-]$	Te $[K]$	Tr $[-]$	Re $[-]$	f $[kHz]$	Pe $[Pa]$
$Re15 - SS7$	5.36	74.47	0.67	974.4 – 2190.1	100 – 800	2242.2
$Re15 - CFD7$	5.49 – 5.52	70.67 – 71.18	0.67	859.5 – 2332.8	375 – 775	2261.7 – 2295.8
$R05 - Re15$	5.51 – 5.61	68.53 – 70.62	0.69	1040.2 – 2549.2	325 – 650	2259.4 – 2273.6
$R1 - Re15$	5.52 – 5.63	67.96 – 70.45	0.69	1480.5 – 2539.2	375 – 450	2252.9 – 2262.1
$Re15 - SS5$	5.58	69.07	0.67	938.3 – 2298.2	200 – 800	1749.3
$Re15 - SS10$	4.99	83.53	0.67	1028.3 – 2518.9	200 – 1000	3181.9
$Re18 - SS7$	5.36	72.55	0.71	961.6 – 2416	100 – 800	2591
$Re18 - CFD7$	5.47 – 5.49	69.53 – 69.89	0.71	1121 – 2525	375 – 750	2612.9 – 2640.3
$R05 - Re18$	5.52 – 5.61	66.69 – 68.78	0.71	1143.2 – 2799.2	375 – 700	2610.9 – 2625.4
$R1 - Re18$	5.31 – 5.36	66.13 – 68.63	0.71	1627.9 – 2787.7	400 – 475	2601.9 – 2613.2
$Re18 - SS5$	5.59	69.07	0.69	1027.8 – 2517.6	100 – 800	2099.2
$Re18 - SS10$	4.99	83.53	0.69	1126.5 – 2759.3	100 – 800	3818.3
$Re23 - SS7$	5.36	74.21	0.69	934.2 – 2697	100 – 800	3383
$Re23 - CFD7$	5.50 – 5.52	70.23 – 70.66	0.68	1394.4 – 3641.2	375 – 750	3402 – 3434
$R05 - Re23$	5.52 – 5.55	69.62 – 70.32	0.68	1500.6 – 3139.7	425 – 675	3405.2 – 3420.8
$R1 - Re23$	5.52 – 5.65	67.33 – 70.19	0.68	1833.2 – 3619.3	350 – 550	3391.1 – 3407.0
$Re23 - SS5$	5.59	69.07	0.68	1156.7 – 2833.4	200 – 800	2659.0
$Re23 - SS10$	4.99	83.53	0.68	1267.8 – 3105.5	400 – 1000	4836.5

Review of the VKI Longshot Hypersonic Tunnel Operation for Martian Entries

Zdeněk Ilich

Aeronautics and Aerospace Department, von Karman Institute for Fluid Dynamics, Belgium, zdenek.ilich@vki.ac.be

Supervisor: Olivier Chazot

Head of Department and Professor, Aeronautics and Aerospace Department, von Karman Institute for Fluid Dynamics, Belgium, chazot@vki.ac.be

University Supervisor: Herbert Olivier

Professor, Shock Wave Laboratory, RWTH Aachen University, Germany, olivier@swl.rwth-aachen.de

Abstract

The Longshot gun tunnel, operated at the von Karman Institute for Fluid Dynamics, is a short duration hypersonic facility used for aerothermodynamic investigations of entry flows in terms of Mach and Reynolds numbers. The present work aims to extend and better quantify its operational capabilities for Martian entries. Carbon dioxide is therefore considered as the test gas. The operation of the wind tunnel is discussed and numerically simulated. The numerical investigations focus on the compression process generating sufficiently high reservoir conditions and lead to the definition of the reservoir operational map. The rebuilding method needed for determination of the free-stream conditions is reviewed and modified for carbon dioxide. Different technical and physical constraints which must be considered for the successful tunnel operation are pointed out.

Keywords: Hypersonic, Longshot, ground testing, Martian entries

Nomenclature

Symbols

A	area, m^2
a	specific Helmholtz energy, J/kg
c_p	specific heat at constant pressure, J/(kg.K)
c_v	specific heat at constant volume, J/(kg.K)
D	diameter, m
f	Darcy-Weisbach friction factor
g	specific Gibbs energy, J/kg
h	specific enthalpy, J/kg
$\bar{h}$	reduced enthalpy, $\bar{h} = h/(rT_{\text{ref}})$, $T_{\text{ref}} = 273.15\,\text{K}$
K_L	pipe-fitting loss coefficient
L	length, m
M	Mach number
m	mass, kg
Nu	Nusselt number
p	pressure, Pa
$\dot{q}$	heat flux, W/m^2
r	specific gas constant, J/(kg.K)
R_N	nosetip radius, m
Re	Reynolds number
T	temperature, K
u	velocity, m/s
w	speed of sound, m/s
y	distance along meridian profile, m

Greek Symbols

α	reduced Helmholtz energy
δ	reduced density
ρ	density, kg/m^3
μ	dynamic viscosity, Pa.s
τ	inverse reduced temperature
ϕ	quantity defined in eq. 2
ψ	quantity defined in eq. 3

Subscripts

c	relative to the critical point
driven	relative to the driven tube
max	maximum; in front of the check valves
p	relative to the piston
ref	reference value
t	stagnation condition
unit	based on a unit length of 1 m
s	stagnation condition at the edge of the boundary layer
w	at the wall
0	stagnation conditions in the reservoir
1	condition upstream a normal shock
2	condition downstream a normal shock
∞	free-stream value

Superscripts

0	relative to the perfect gas behavior
r	relative to the residual real gas behavior
*	relative to the critical flow conditions

Abbreviations

CEA	Chemical Equilibrium & Applications program
EDL	Entry Descent and Landing mission phase
ESA	European Space Agency
L1d	Lagrangian 1-dimensional code
VKI	von Karman Institute for Fluid Dynamics

1. Introduction

1.1. Background

Martian atmospheric entry is a challenging task which concludes a several-month travel to Mars for missions that involve surface operations. This final phase called EDL (entry descent and landing) begins even before a significant atmosphere is present and aerodynamic controlling of the vehicle is thus not possible yet. The final phase of EDL is typically divided into three parts: hypersonic entry, supersonic decent phase, and final descent. Although flawless completion of all of them is necessary for the successful mission, the present study will focus only on the first phase – hypersonic entry.

Hypersonic entry starts when the entry vehicle first comes into a sensible atmosphere. During this phase, the peak heating followed by the peak deceleration occurs [1]. If not fully understood, these processes may be potential mission killers. Hypersonic flows are characterized not only by high Mach numbers but more importantly also by the presence of specific phenomena such as real-gas effects, high enthalpies, chemistry, or non-equilibrium effects [2]. Since an acquisition of flight data is prohibitively expensive (infrequent operations, sharing of useful payloads), ground testing in hypersonic facilities is an attractive option to gain useful information about these phenomena. However, there is no ground facility capable of duplicating the full flight environment. Therefore, ground testing relies on the partial duplication when only some of the physical phenomena are respected. The whole picture of the hypersonic entry is then collected from different facilities operating in, more or less, narrow envelope.

The Longshot is a short-duration hypersonic facility operated at the von Karman Institute for Fluid Dynamics (VKI), in Belgium. It is based on the gun tunnel principle and used for aerothermodynamic investigation of hypersonic entry flows.

By far the most frequent test gas used in the VKI Longshot facility is nitrogen which serves Earth entry investigations. However, about 140 tests utilizing carbon dioxide have been performed so far aiming to partially duplicate the Martian entries. The tunnel operating conditions for CO_2 were systematically investigated during the ESA supported program [3] in the mid 90's. Since then, many improvements have been made regarding numerical simulations of the facility and the free-stream flow characterization.

1.2. Objectives

The main goal of the present study is to review the operation of the VKI Longshot facility with carbon dioxide and to prepare all tools necessary for the definition of the new operational map for Martian entry investigations.

First, a brief overview of the VKI Longshot facility and its working principle is given (§2). The core of the present work is organized into two main paragraphs: wind tunnel modeling (§3), represented by the numerical investigations of the Longshot compression process (§3.1), and determination of the free-stream flow properties (§4). Finally, §4.3 discusses the typical Mars entry conditions.

2. The VKI Longshot wind tunnel

2.1. General characteristics

The VKI Longshot hypersonic gun tunnel has been described extensively by Grossir in [4]. The Longshot was designed by R.W. Perry and his team at the Republic Aviation Corporation (U.S.). It was moved

to the premises of the von Karman Institute for Fluid Dynamics (Belgium) in 1967. Although the Longshot has been used for different applications, its primary goals have been to simulate environments associated with reentry conditions in terms of Mach/Reynolds numbers and to develop corresponding aerothermodynamic databases.

Pure nitrogen is used as the main test gas, with moderate total enthalpies which are sufficiently low not to induce flow chemistry. As such, the Longshot is regarded as a "cold" hypersonic facility, i.e. where no chemical reactions take place, and as a perfect gas reference wind tunnel for the validation of numerical models.

The first use of carbon dioxide in the Longshot is dated back to 1995, aiming to partially simulate the so-called high-temperature gas effects. Since then, CO_2 has been utilized for many purposes, e.g. investigation of the Martian entries [5], boundary-layer transition studies, and the development of different measurement techniques as the tunable diode laser absorption spectroscopy [6]. Regardless of the test gas, nitrogen is used as the only driver gas pushing the piston.

The sketch of the wind tunnel is given in Fig. 1 with a description of its main parts:

- a 127 mm internal diameter and 6.1 m long driver tube, initially filled with nitrogen at high pressure and ambient temperature.
- a 76.2 mm internal diameter and 27.5 m long driven tube[1], containing the test gas initially at ambient temperature and at moderate pressure, the latter depending on the test conditions to be reached.
- a piston, initially located at the interface between the driver and driven tubes and preventing gas mixing between the two tubes. Its mass can be altered in order to achieve different reservoir stagnation conditions.
- a set of 48 small check valves at the end of the driven tube which is used to trap the gas at the peak stagnation conditions in the reservoir.
- conical/contoured nozzles, discussed hereafter.
- a test section, vacuumed prior to an experiment to $p < 20\,\mathrm{Pa}$, in which an instrumented model and probes are located.
- and two diaphragms: a first one attached to the piston, and a second one isolating the driven tube from the vacuumed nozzle and test section.

[1] The beginning of the driven tube is further reduced in diameter (63.5 mm over a length of 36 mm) by a mechanical device holding a primary diaphragm. This driven tube was heavily nitrided during fabrication to reduce abrasion by the piston [8].

2.2. *Working principle*

Being a gun tunnel, the Longshot relies on a high-velocity piston moving in the driven tube and directly compressing the driven (test) gas[2]. The compression cycle of the Longshot wind tunnel using *nitrogen* has been analyzed (theoretically) in [9; 10] and more recently (numerically) in [11; 7].

The piston is set in motion by the controlled rupture of the primary diaphragm and the large pressure difference existing between the driver and driven tubes[3], Fig. 2a. Its typical acceleration is on the order of $10^5\,\mathrm{m/s^2}$. Shortly after the release of the piston, compression waves focus and generate a shock wave ahead of the piston, Fig. 2b. The piston quickly approaches its final velocity, traveling within the driven tube at about $600\,\mathrm{m/s}$. This compresses nearly adiabatically the test gas located ahead.

Once the primary shock wave reaches the end of the driven tube it is partially reflected back towards the piston and partially transmitted through the system of check valves, Fig. 2c. Upon incidence of the reflected shock wave on the front face of the piston, the latter initiates its deceleration whose maximal value can be as high as $10^6\,\mathrm{m/s^2}$ for nitrogen and even higher for CO_2. Multiple shock wave reflections between the piston and the end of the driven tube follow. The pressure rapidly increases and the piston decelerates, transferring its kinetic energy to the test gas. The secondary diaphragm is automatically ruptured as the pressure increases.

Then, the piston reaches its maximum axial location and peak stagnation conditions are achieved. The nozzle flow is rapidly established. As the piston rebounds in the driven tube, the 48 check valves are closed automatically by the pressure difference acting on them, Fig. 2d. This prevents the reservoir conditions from being influenced by the rebounding motion

[2] Similarly, the free-piston wind tunnels employ moving pistons as well. However, unlike what is achieved in the gun tunnels, their pistons are used to compress the driver gas.

[3] The larger diameter of the driver with respect to the driven tube creates a chambrage effect, well described in [12], which benefits to the work done on the piston by the driver gas, as evaluated for the Longshot in [9; 13].

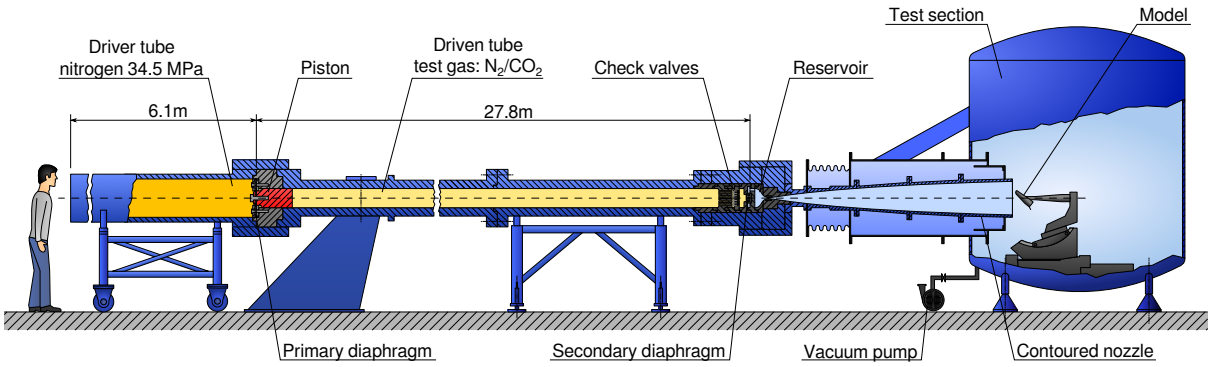

Figure 1: Sketch of the VKI Longshot hypersonic gun tunnel, redrawn from [7].

of the piston. The test time is typically extended by an order of magnitude thanks to the presence of the check valves. The gas trapped in the constant volume reservoir is then expanded through a nozzle thereby generating the desired free-stream flow in the test section.

Two nozzles are currently available. The first one is a 6 ° half-angle conical nozzle whose throat diameter can be varied between 2 and 5.96 mm. The corresponding exit diameter is 360 mm and can be extended up to 600 mm to reach the largest Mach numbers. Alternatively, a 3 m long contoured nozzle for nitrogen, targeted to Mach 14, with an exit diameter of 426 mm and an area ratio of $A/A^* = 4362$, is available.

Stagnation conditions are decaying with time because of the mass flow out of the finite volume reservoir. The temporal decay is sufficiently slow to regard the flow as a succession of quasi-steady events for most flow configurations, as demonstrated in [4]. Similarly, the free-stream Reynolds number exhibits a temporal decay. In most cases, a single experiment in the Longshot wind tunnel, therefore, offers the possibility to scan a range of Reynolds numbers, increasing its productivity.

2.3. *Initial conditions for* CO_2

In the VKI Longshot wind tunnel, reservoir stagnation conditions resulting from the compression process can be adjusted by three independent parameters: the initial pressure in the driver tube, the initial pressure in the driven tube, and the mass of the piston.

The initial driver pressure is kept constant at 34.5 MPa for CO_2. The initial pressure in the driven tube varies typically between 140 and 300 kPa. The mass of the piston falls between 1.3 and 3.8 kg.

Different combinations of these parameters can be used to produce different test conditions. Table 1 lists four representatives of the performed tests in the Longshot tunnel using carbon dioxide. The case 1 will be regarded as a *reference*, because it is the only carbon dioxide test where a new free-stream diagnostic technique was used (the free-stream conditions are discussed in §4)[4].

Table 1: Typical initial conditions used in the past for the operation of the Longshot wind tunnel with CO_2.

	Driver pressure	Driven pressure	Piston mass
case 1	**34.5 MPa**	**144.1 kPa**	**1.592 kg**
case 2	34.5 MPa	275.8 kPa	1.592 kg
case 3	34.5 MPa	227.5 kPa	3.215 kg
case 4	34.5 MPa	227.5 kPa	3.700 kg

3. Wind tunnel modeling

3.1. *Compression process*

The purpose of this section is to compute the new operational map in terms of reservoir pressure and temperature as a function of the initial conditions. To this point, the compression process is numerically investigated using a quasi-1D solver.

3.1.1. *L1d solver*

The L1d is the quasi-one-dimensional Lagrangian solver developed by P. Jacobs from the University of Queensland (Australia) [14] and significantly customized at VKI during past years. The modeling of the Longshot compression process using the L1d solver is extensively detailed in [11; 7]. The behavior of nitrogen is described by the Span & Wagner

[4]The experimental data for this reference test is available only for the contoured nozzle designed for nitrogen.

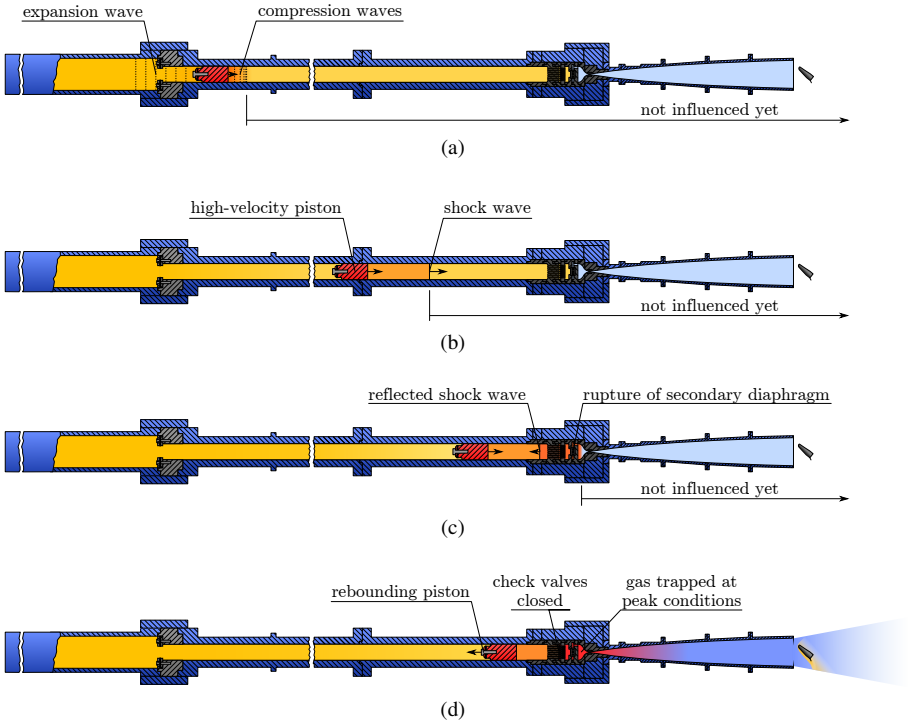

Figure 2: Illustration of the Longshot compression process, redrawn from [7].

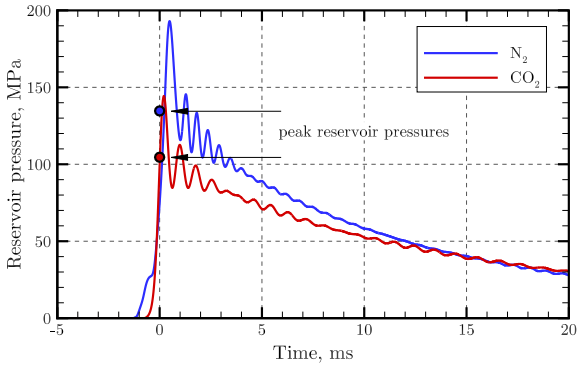

Figure 3: Stagnation pressures measured in the Longshot reservoir for initial conditions corresponding to the reference case 1 (Table 1) using different gases. The contoured nozzle with a throat diameter of 6.45 mm was used for both.

reference equation of state [15] implemented in the code through a look-up table approach. For the present case, modifications of the code have been made allowing it to handle different real gases for the driver and the driven tubes (nitrogen is still used as the driver gas). The equation of state for CO_2 reported in [16], which is valid up to 1100 K, has been implemented. This equation is of a type which usually allows reasonable extrapolation to higher temperatures (often up to the limits of chemical stability), nevertheless without guaranteed accuracy.

Look-up table approach

Span & Wagner's equations are formulated using the reduced Helmholtz energy ($\alpha = a/(rT)$) which is split into a part for the perfect gas behavior (α^0), and a second one for the residual behavior of the real gas (α^r). Therefore, the general functional form of this equation can be written as:

$$\frac{a(\rho,T)}{rT} = \alpha(\delta,\tau) = \alpha^0(\delta,\tau) + \alpha^r(\delta,\tau), \qquad (1)$$

where $\delta = \rho/\rho_c$ is the reduced density and $\tau = T_c/T$ is the inverse reduced temperature. This enables an accurate description of gas states over a wide range of flow conditions. On the other hand, their complex form is not appropriate within CFD methods since their implementation leads to expensive algorithms. Moreover, the direct determination of all gas properties (i.e. without iteration) is possible only if density and temperature are given. For the remaining cases, iterative procedures are required, making the computational cost even larger.

In order to moderate the computational cost, a look-

up table approach can be used. This takes advantage of the structure of the L1d code in which the look-up table approach is already used for gas data issuing from the CEA library [17; 18]. The main idea is to tabulate a set of quantities from which all gas properties of interest can be easily calculated and to store them within a data file which is then read by the L1d code. A similar approach is reported in [19], where the set of tabulated quantities consists of derivatives of Gibbs energy with respect to temperature and pressure. Since the L1d code requires to determine gas thermodynamic properties for given internal energy and density, the set of tabulated quantities is chosen as T, $(g-a)$, $\alpha_{\tau\tau}$, ϕ, and ψ. The last two quantities are defined in eqs. 2 and 3, whereas $\alpha_{\tau\tau} = \alpha^0_{\tau\tau} + \alpha^r_{\tau\tau}$ is the second partial derivative of the reduced Helmholtz energy with respect to τ.

$$\phi = (1 + \delta\alpha^r_\delta - \delta\tau\alpha^r_{\delta\tau})^2 \tag{2}$$

$$\psi = 1 + 2\delta\alpha^r_\delta + \delta^2\alpha^r_{\delta\delta} \tag{3}$$

These quantities are calculated for a prescribed range of temperature and density using the Span & Wagner equation. Then, they are reordered according to the corresponding internal energy and density and stored in a binary data file. During the computation, the L1d solver uses bilinear interpolation techniques to reconstruct their values for any given internal energy and density. The remaining gas properties are then calculated according to eqs. 4 – 7. This approach has been verified against the direct implementation of the complete Span & Wagner's equation of state within the L1d code for nitrogen. Identical results have been obtained for computational times decreased by an order of magnitude when using the look-up table approach.

$$p = (g-a)\rho \tag{4}$$

$$c_v = -r\tau^2\alpha_{\tau\tau} \tag{5}$$

$$c_p = r\left(-\tau^2\alpha_{\tau\tau} + \frac{\phi}{\psi}\right) \tag{6}$$

$$w = \sqrt{rT\left(\psi - \frac{\phi}{\tau^2\alpha_{\tau\tau}}\right)} \tag{7}$$

Although the same approach is followed for carbon dioxide, the implementation of the look-up table is generaly complicated by the location of the critical region of carbon dioxide ($T_c = 304.1282\,\mathrm{K}$, $\rho_c = 467.6\,\mathrm{kg/m^3}$). Besides the fact that wide-range equations of state themselves have a more or less compromised accuracy in the critical region, a single table of discrete points distributed in the T-ρ space cannot capture a nonanalytic behavior of the isochoric heat capacity and the speed of sound in the immediate vicinity of the critical point[5]. Moreover, a systematic error, which is discussed also in [19], exists in areas with a pronounced curvature of thermophysical properties, e.g. in the vicinity of the critical point or along the saturation vapor/liquid lines.

Since CO_2 is used only as the driven gas in the present work (i.e. starting at ambient temperature and moderate pressures) and the simulations of the compression process is relevant only up to the piston rebound (the closure of the check valves is not taken into account), there is no need to accurately determine gas properties in the two-phase region nor the critical region. Therefore, only a single table with no additional treatment of the critical region and saturation lines is used. However, lower temperatures than T_c must be included hence the two-phase region is filled using the leverage rule from the saturation values.

Since a large number of points would increase the computational time, the final number of points in the table must be a compromise between accuracy and computational speed. The final number of points is 2000 and 500 for temperature and density, respectively. The points are distributed according to the cubic root function centered around the critical point.

Transport properties

Boundary layers along the tubes cannot be directly resolved with the present 1-dimensional formulation of the gas-dynamic equations; instead, engineering correlations must be used. Viscous effects (induced by the boundary layer developing along the wall of the ducts) are taken into account through a wall shear stress which is added to the momentum equation and which is based on the Darcy-Weisbach friction factor f, for more details see [11; 14]. Therefore, a simple Sutherland law is used to determine the gas transport properties.

Heat transfer into the gas is modeled using the modified Reynolds analogy for turbulent flow in pipes [14].

Computational domain

Being a quasi-1D solver, the L1d code enables to take into account the varying tube diameter. Al-

[5] The specific isochoric heat capacity has infinite value at the critical point. Accordingly, the speed of sound vanishes at this point.

though the Longshot system of driver/driven tubes can be essentially represented using such a quasi-1D approach, special attention must be paid to the end of the driven tube, where the check valves, the secondary diaphragm, and the nozzle reservoir are located. The detail of this geometrically complex part is depicted in Fig. 4.

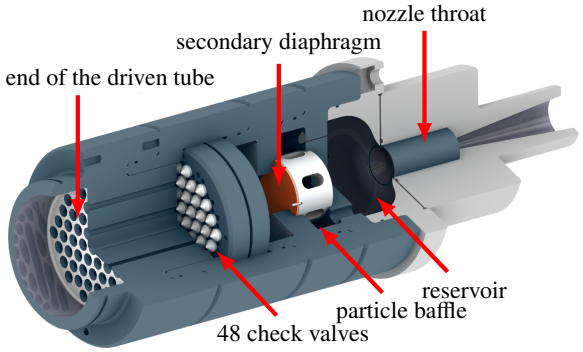

Figure 4: Longshot check valve system at the end of the driven tube.

The selected strategy is to model the end of the driven tube by respecting the equivalent volumes of the different pieces of the check valve assembly. The computational domain is schematically shown in Fig. 5, redrawn from [7]. The secondary diaphragm is also included in the model and its position matches the real case. It is set to rupture for a pressure difference larger than 12MPa. The reservoir is assumed to be closed at the location corresponding to the throat. The useful compressed volume[6] (considered for the present study equal to 413.573 cm^3) is located downstream the check valves. The origin of the coordinate system is chosen as the surface of the primary diaphragm facing the driven tube.

Beside the viscous losses, the pipe-fitting losses defined in eq. 8 are expected where sudden variations of the tube cross-section are present. The present simulations will use a single loss coefficient K_L applied to the entrance of the check valve layout (point 6 in Fig. 5). Due to the lack of theoretical formulations, this loss coefficient is found by comparison with experimental data of the selected reference case. For the detailed implementation of these losses to the momentum equation, see [14].

In order to retrieve the peak reservoir pressure for numerical simulations, a special procedure based on

[6]The useful compressed volume is the volume of gas which will be expanded through the nozzle. It actually depends on the used nozzle and its throat diameter since the contours of the convergent part are different.

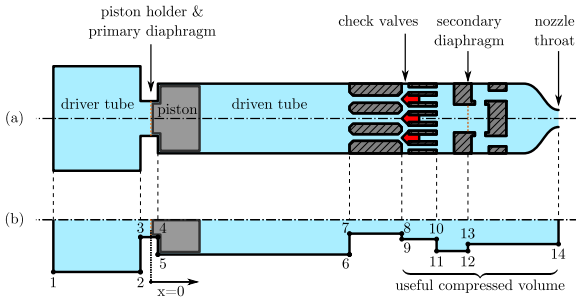

Figure 5: Definition of the computational domain for the L1d solver. (a) Sketch of the Longshot geometry up to the nozzle throat. (b) The geometry representation in quasi-1D approach.

the total energy stored in the final compressed volume is followed as discussed in [7].

$$\Delta p = -K_L \frac{1}{2} \rho u |u| \tag{8}$$

3.1.2. *Numerical investigation of the compression process*

All cases listed in Table 1 have been numerically simulated using CO_2. The reference case 1 has been computed for nitrogen as well. First, nitrogen and carbon dioxide are compared for the reference case and with the available experiments. Then, the results for the other cases are reported.

Currently, the experimental data for validation of the L1d computations come from pressure measurements using fast-response Kistler sensors at several locations along the driven tube. These measurements are reported in details in [20].

Reference case

First, the loss coefficient K_L mimicking the pipe-fitting losses of the check valves must be found. The peak reservoir pressure measured for the reference case 1 is used to set the right value. The value 14.42 ensures the perfect agreement between the experiment and the numerics for the reference case. The same value is used for all computations using CO_2.

The comparison of the pressure profiles for CO_2 is reported in Fig. 6 for which the reference time t = 0 ms is chosen as the instant when the piston is released, indicated by the accelerometer mounted on the driven tube. Characteristic events for the experimental pressure traces are labeled as follows:

- event 1: primary shock wave,
- event 2: first reflection (from the end of driven tube),
- event 3: second reflection (from the front face of the piston),
- event 4: *piston* passage (forward),
- event 5: upstream traveling shock due to piston rebound,
- event 6: second *piston* passage (backward).

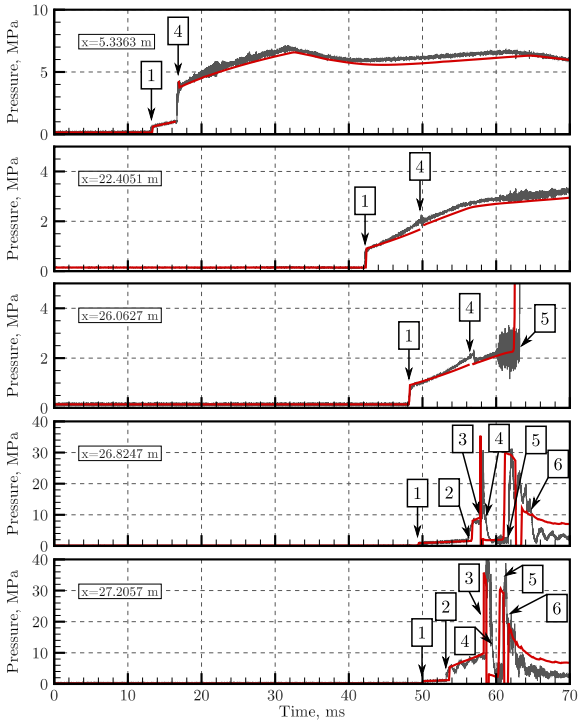

Figure 6: Comparison of the pressure profiles along the driven tube for the reference case 1 using carbon dioxide. Lines (—) represent experimental data, whereas lines (—) denote numerical data.

Overall, a very good agreement is observed. Some discrepancies are presented especially after the piston rebound as the closure of the check valves is not modeled. This can be tolerated since only the peak reservoir conditions are of interest for the present study. A common way to represent the compression process is the utilization of a so-called space-time diagram. These diagrams are presented in Fig. 7 for nitrogen and carbon dioxide where the discrete points represent the characteristic events collected from the experimentally obtained pressure profiles. The primary shock is clearly slower in the case of CO_2 due to the lower speed of sound.

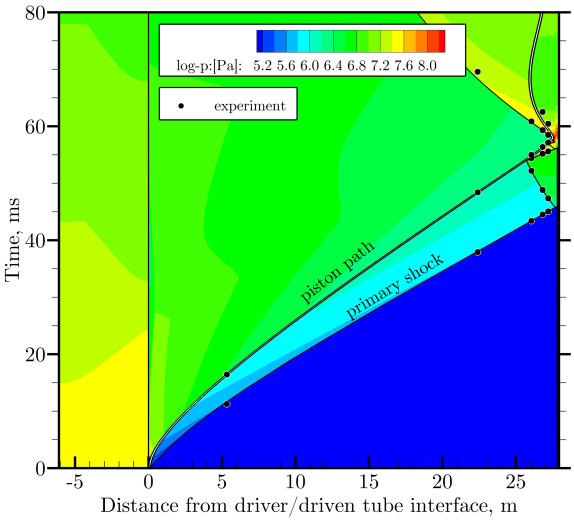

(a) Nitrogen in the driven tube.

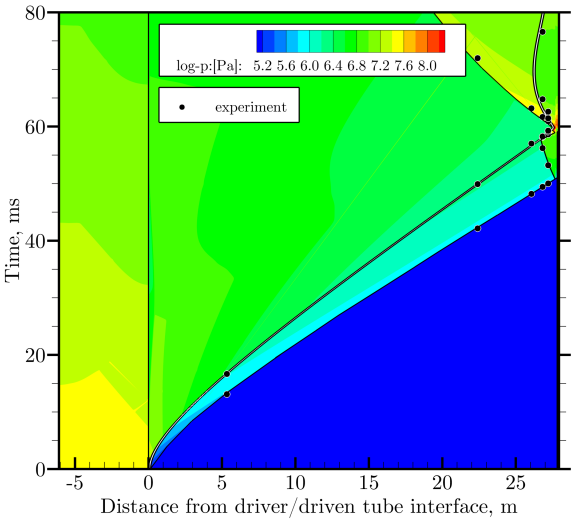

(b) Carbon dioxide in the driven tube.

Figure 7: Space-time diagrams of the compression process with iso-pressure contours (log-scale) resulting from the L1d simulation, case 1 (Table 1). Symbols (•) denote characteristic events measured experimentally along the driven tube.

The piston trajectories for nitrogen and carbon dioxide are very similar as can be seen in Fig. 8a where the trajectory of the piston center is plotted (the piston length is 143 mm for this particular case). The piston stops at 62.3 mm from the end of the driven tube for CO_2 which is about 39 mm closer than for N_2. The deceleration during the piston rebounding is more than two times higher for carbon dioxide (Fig. 8b).

Therefore, the CO_2 test leads to higher forces acting on the piston and a rebound closer to the end of the driven tube.

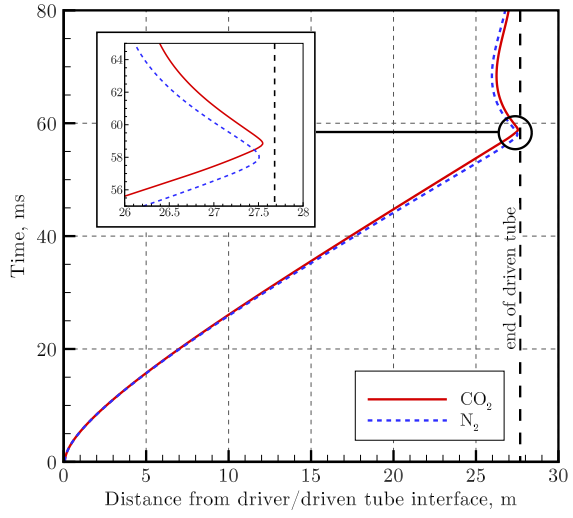

(a) Trajectory of the piston center.

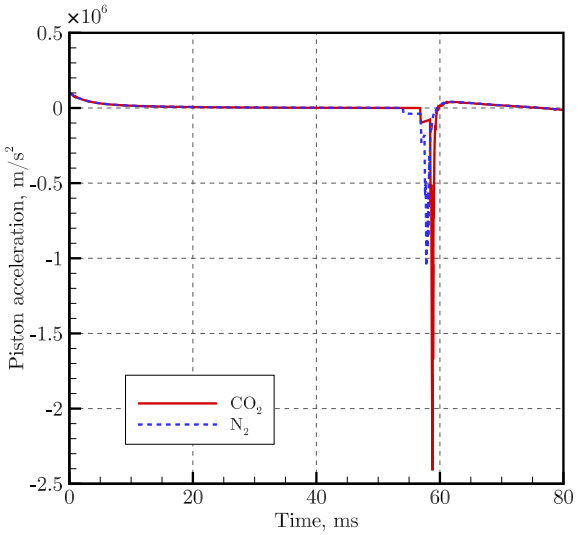

(b) Piston acceleration.

Figure 8: Comparison of the piston path for nitrogen and carbon dioxide for the reference case 1.

Results of the available tests performed

All cases listed in Table 1 have been computed using the same settings as for the reference case. The results are summarized in Table 2. Although only a limited number of tests is available, the overall agreement on the peak reservoir pressure is very good. The biggest difference of -3.74% is observed for case 4. Although the numerical code underestimates the reservoir pressure for all considered cases, the differences are of the same order as the accuracy of the peak reservoir pressure measurement (about 1%). The rebounding position of the piston seems to be at sufficient distance from the tube end.

A reliable measurement technique to accurately determine the peak reservoir temperature is not yet available for the Longshot and thus no direct validation of temperature can be conducted.

It is well-known that the check valves may introduce large pressure losses [8]. It means that only a fraction of the gas compressed in front of the check valves is transferred to the reservoir. Therefore, the determination of the stagnation conditions upstream the check valves is as important as the ones in the reservoir for the safe operation of the Longshot wind tunnel and in order to not exceed the structural limits of the wind tunnel (designed for a peak reservoir pressure of 400 MPa). However, the common practice is to tolerate pressures at the end of the drive tube (before the check valves) as high as 600 MPa. This limit is exceeded by all considered cases except case 1 and 2. Therefore, the maximal pressure that builds up ahead of the check valves is the primary limiter for the tunnel operation using carbon dioxide.

The pressure ratio across the check valves (P_{max}/P_0) ranges from 1.7 to 4.6 for the investigated cases. As pointed out in [7], these pressure differences should be seen as a consequence of the different compression process rather than as pure pressure losses. It is shown in [7] that the pressure drop across the check valves increases significantly as the piston-to-driven-gas mass ratio (m_p/m_{driven}) increases. The quantity m_p/m_{driven} is a very important parameter characterizing the final part of the compression process; a low value means a gradual compression with a peak reservoir pressure close to the one upstream of the check valves, whereas a high value leads to a faster compression which does not provide enough time for the high-pressure gas to fill the reservoir.

The pressure ratio across the check valves determined numerically is plotted with respect to the piston-to-driven-gas mass ratio in Fig. 9. The data for CO_2 include the cases from Table 1 as well as cases computed to determine the operational map presented in §3.1.3. The nitrogen data comes from [7].

Although quite a large scatter of the data is present, the trends are clearly visible. The rise of the pressure ratio across the check valves for increasing (m_p/m_{driven}) is much steeper for carbon dioxide (Fig. 9a). However, it is not generally possible to simply limit the operation of the tunnel to low values of the piston-to-driven-gas mass ratio because of

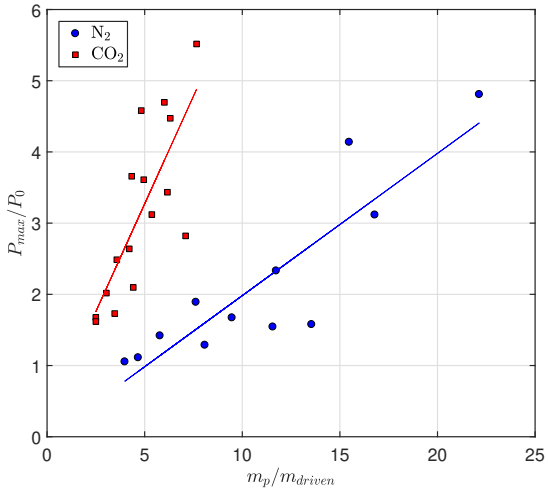

(a) Pressure ratio across the check valves, P_{max}/P_0.

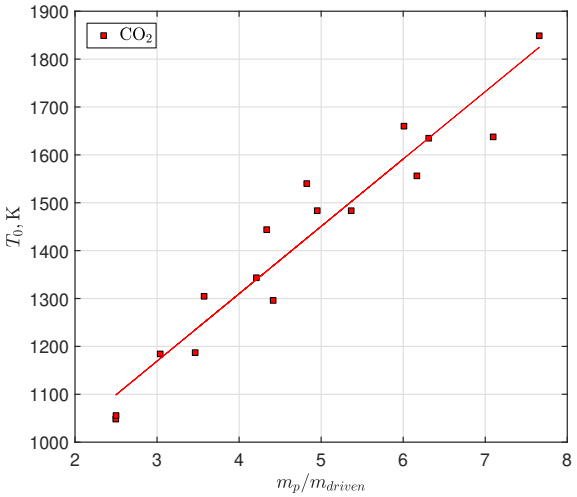

(b) Peak reservoir temperature, T_0.

Figure 9: Effects of the piston-to-driven-gas mass ratio (m_p/m_{driven}) on the pressure ratio across the check valves and on the peak reservoir temperature.

the strong correlation with the reservoir temperature (Fig. 9b), which must be kept sufficiently high to avoid gas condensation in the test section. The solution can be to reduce the reservoir pressure (i.e. using light pistons and low driven pressures). Nevertheless, this approach leads to a reduction of the Reynolds number which may potentially fall short of the entry trajectories of interest.

3.1.3. Operational map of the reservoir conditions

Being validated against the experimental data, the L1d code can be used to compute the operational map in terms of the peak reservoir conditions. An example of such a map for CO_2 covering the piston masses from 1.59 kg to 2.80 kg and the driven pressures from 1.600 bar to 2.758 bar is presented in Fig. 10a.

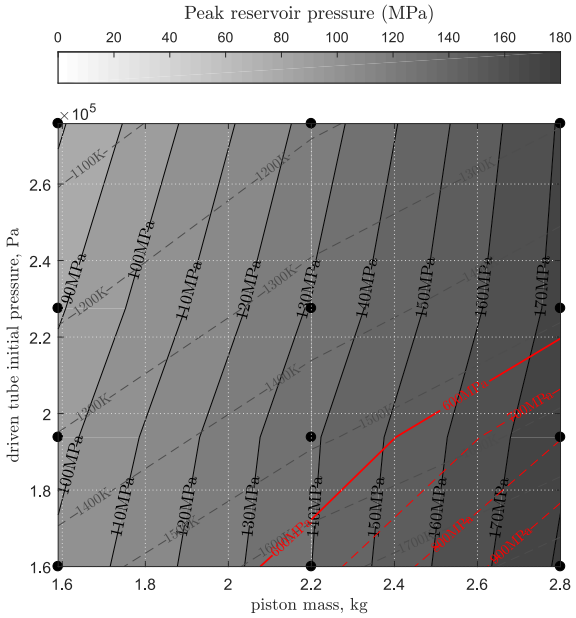

(a) Peak reservoir pressure and temperature, and maximum pressure in front of the check valves.

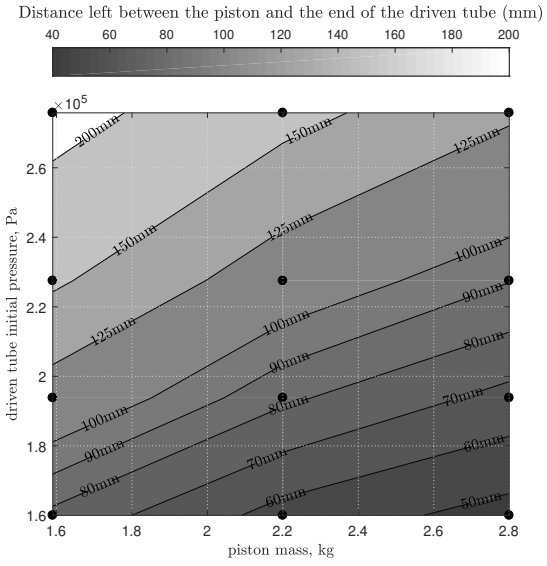

(b) Distance left between the piston and the end of the driven tube.

Figure 10: Operational map of reservoir conditions for carbon dioxide.

The contours correspond to the reservoir pressure (together with the solid isolines) whereas the dashed lines are isolines of the reservoir temperature. Note that the reservoir pressure strongly depends on the piston mass. On the other hand, the reservoir temperature

Table 2: Peak reservoir conditions of the tests performed.

		Numerical results				Experiment	
	gas	P_{max}, MPa	Rebound*, mm	T_0, K	P_0, MPa	P_0, MPa	ΔP_0, %
case 1	N_2	**259.35**	**101.5**	**2326.6**	**135.62**	**134.67**	**0.7**
case 1	CO_2	**478.84**	**62.3**	**1540.1**	**104.53**	**104.58**	**-0.05**
case 2	CO_2	126.62	218.9	1048.2	75.53	76.27	-0.97
case 3	CO_2	708.85	81.5	1556.2	206.43	206.88	-0.22
case 4	CO_2	664.52	72.0	1637.6	235.58	244.72	-3.74

*Minimal distance from the end of the driven tube reached by the piston.

essentially follows the piston-to-driven-gas mass ratio as already discussed.

From a practical point of view, this map eases the tunnel operation as it allows a rapid selection of the initial conditions in order to generate the desired reservoir pressure and temperature. Also, it helps to define the available ranges of the reservoir conditions. However, several constraints related to the compression process must be taken into account. Summarizing [21], the major technical limitations are:

- the minimum piston weight on the order of 1.5 kg, related to the minimum piston length to avoid wobbling motion.
- the maximum allowable pressure in the reservoir and the driven tube, related to the strength limit of the material.
- the maximum reservoir temperature, usually critical for the check valves which have a small thermal inertia.
- the piston collision with the end of the driven tube.

Although the piston generally rebounds close to the end of the driven tube for CO_2, the maximum allowable pressure (reached in front of the check valves) seems to be the main constraints. Figure 10b shows the distance left between the rebounding point and the end of the driven tube. The pressure in front of the check valves is plotted as red lines in Fig. 10a starting from the upper practical limit of 600 MPa.

The flow condensation, which dictates the minimal reservoir temperature, is a very important physical limitation as well.

4. Free-stream flow properties

Characterization of free-stream properties is an essential task for every wind-tunnel test. However, it may be very challenging. This is especially true for hypersonic facilities where relatively short test times may be associated with specific phenomena such as dense-gas effects, high temperatures, chemistry, or non-equilibrium effects. Due to limited measurement techniques which are available, all flow quantities of interest cannot be measured directly. Instead, rebuilding methods are required.

A rebuilding method takes a set of measured quantities, typically at the exit section of a nozzle and in its reservoir, and determines the rest of flow properties, characterizing the free-stream in the test section. The set of measured input quantities is not unique and can be selected to suit a particular facility or test purpose. Thus, two distinct rebuilding methods applied to the same facility may result in different accuracy on the rebuilt conditions and may also involve different assumptions about the nature of the flow.

The first part of this section briefly presents two existing rebuilding methods used in the Longshot along with their assumptions. Then, the specifics of carbon dioxide tests are discussed.

4.1. Existing rebuilding methods

An extensive overview of the methods currently used can be found in [4]. Only the main points important for the present content are pointed out here. The measured inputs needed to rebuild all free-stream properties are illustrated in Fig. 11.

4.1.1. Nozzle method

Although this method is still available, it is not used as a primary tool to characterize the free-stream of the Longshot facility anymore and it is considered only for the old test campaigns where the static pressure measurement is not available. The method relies on measurements of three quantities: the stagnation point heat flux on a hemispherical probe $\dot{q}_w$ and the pitot pressure p_{t2} both measured in the test section, and

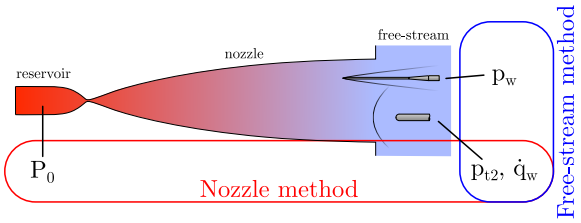

Figure 11: Sketch of the experimental inputs to the rebuilding methods.

the reservoir pressure P_0 monitored by a fast-response Kistler sensor. The main issue which must be overcome is that the reservoir pressure is not the same as the total pressure p_{t1} in the test section due to dense gas effects. Therefore, an iterative procedure is required. The first step is an estimation of the reservoir temperature T_0. Using the measured reservoir pressure P_0 and the real gas equation of state, it is possible to determine entropy and enthalpy of the reservoir gas. The nozzle flow is assumed to be adiabatic and isentropic allowing considering both entropy and enthalpy to be constant all along the nozzle. Corresponding equivalent perfect gas conditions p_{t1} and T_{t1} can be calculated following the work of Culotta and Richards [22]. The Fay-Riddell equation [23] is used to infer the stagnation point heat flux which is then compared to the measured heat flux on the hemispherical probe. The iteration on T_0 is performed until both predicted and measured values of the stagnation point heat flux are equal.

The resulting Mach number usually agrees well with numerical computations of the nozzle flow as well as with the designed Mach number of the nozzle.

4.1.2. *Free-stream method*

Nowadays, this is the main procedure to determine the free-stream properties in the Longshot tunnel. It has been introduced in [4]. It benefits from the fact that all experimental inputs are acquired in the test section. No assumption about the nozzle flow nor the reservoir conditions is needed[7].

The thermal and transport properties are determined using the VKI *Mutation++* thermodynamic library [24; 25] where nitrogen is considered as a mixture of 5 species (N_2, N, N_2^+ , N^+, e^-) following the *thermally* perfect gas law. The method requires measurements of the stagnation point heat flux $\dot{q}_w$, the pitot pressure p_{t_2}, and the free-stream static pressure p_∞. First, two unknown free-stream quantities (the velocity u_∞, and the static temperature T_∞) are prescribed. They, together with the static pressure p_∞, represent a sufficient set to determine the total conditions behind the normal shock (p_{t2}, T_{t2}). Then, the Fay-Riddell equation is applied to find the corresponding stagnation point heat flux. The latter one along with the pitot pressure is compared to the measured values and the free-stream velocity and static temperature are iterated until the match is achieved.

4.2. *Modifications for carbon dioxide*

Although both existing rebuilding methods can be used for carbon dioxide, there are several practical aspects which must be reviewed. First of all, the appropriate equation of state [16] must be used to determine thermal gas properties within the nozzle method[8]. Regarding the free-stream method, gas properties are again determined using the VKI *Mutation++* library where carbon dioxide is considered as a mixture of 6 species (CO_2, CO, C_2, O_2, C, O).

The pressure measured by the static probe p_w is influenced by viscous effects along the probe, and thus the free-stream static pressure p_∞ requires the viscous correction p_w/p_∞ inferred from CFD. Additionally, the Fay-Riddell equation which is needed for both methods has been derived for air (or nitrogen) and hence it is not valid for carbon dioxide.

The viscous correction and a model for the stagnation point heat flux are assessed by numerical means in the following.

4.2.1. *Model for stagnation point heat flux*

Starting from boundary layer equations for global continuity, species continuity, momentum, and energy, Fay and Riddell in [23] have obtained a set of nonlinear ordinary differential equations for the stagnation point. The found self-similar solutions hold for chemically reacting viscous flows of air or nitrogen. This Fay-Riddell equation (depending among others on the heat-transfer parameter $\mathrm{Nu}/\sqrt{\mathrm{Re}}$) relates the wall heat flux at the stagnation point to the free-stream total enthalpy. For the equilibrium boundary layers with Lewis number equal to one, the heat-transfer parameter depends only on the total variation

[7] Currently, it is assumed that the flow is in local thermal equilibrium everywhere.

[8] The available real gas equation of state for CO_2 is valid up to the limits of chemical stability. This may compromise further the accuracy of the nozzle method if the reservoir gas is partially dissociated.

of $\rho\mu$ across the boundary layer. The simple correlation $\mathrm{Nu}/\sqrt{\mathrm{Re}} = 0.67(\rho_s\mu_s/\rho_w\mu_w)^{0.4}$ has been established by fitting numerical data in [23]. The vicinity of the stagnation point of a hemisphere together with the corresponding nomenclature is depicted in Fig. 12.

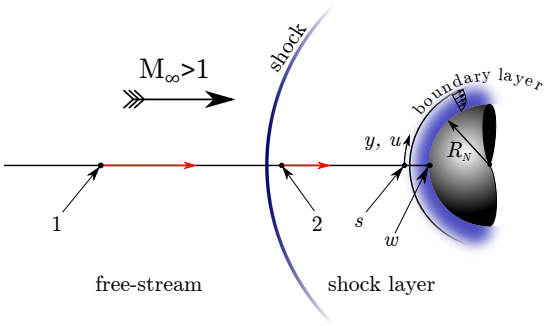

Figure 12: Nomenclature used in the Fay-Riddell equation.

The original formula does not hold for carbon dioxide. Therefore, it is necessary to perform numerical simulations and determine new correlations. For this purpose, the stagnation-line code has been used. It is a quasi-1D code enabling the determination of flow properties along the stagnation streamline of hypersonic (generally non-equilibrium) flows over spheres or cylinders. This solver developed by Munafò [26] can be coupled with the VKI *Mutation++* library. The results obtained using this numerical tool are presented in Fig. 13 (referred to as the "stagline") for the conditions covered the expected range of the enthalpy difference. Also, the numerical data for nitrogen as well as results given by the Fay-Riddell equation from [27] are plotted. Only a simple correlation of the form $\dot{q_w}\sqrt{R_N/p_{t2}} = c_1(h_{t2}-h_w)^{c_0}$ is determined by fitting the present numerical data (black solid line in Fig. 13).

The stagnation-point heat flux was experimentally investigated in the past (e.g. [28; 29]) and some more recent numerical computations over blunt bodies in CO_2 are reported as well [30]. Also, several correlations similar to the Fay-Riddell equation has been established (e.g. [31]). However, they generally focus on much higher velocities (enthalpies) related to planetary atmospheric entries (starting about 1800 m/s). Zoby in [32] introduced an empirical method for computation of the stagnation-point heat flux in arbitrary gas mixtures. For pure gases, he considers a simple equation of the form $\dot{q_w}\sqrt{R_N/p_{t2}} = c_1(h_{t2}-h_w)$. This simple empirical correlation is plotted in Fig. 13 for nitrogen ($c_1 = 3.6391 \times 10^4\,\mathrm{kg/(s\cdot m^{1.5}\cdot Pa^{0.5})}$) and carbon dioxide ($c_1 = 4.3230 \times 10^4\,\mathrm{kg/(s\cdot m^{1.5}\cdot Pa^{0.5})}$).

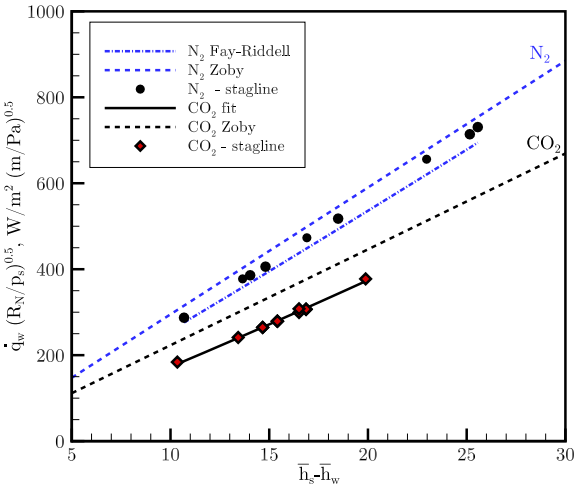

Figure 13: Reduced stagnation point heat flux as a function of reduced enthalpy difference.

4.2.2. *Viscous correction of static probe*

The viscous correction p_w/p_∞ for the Nagamatsu probe (Fig. 14) must be determined in order to relate the measured pressure to the real free-stream static pressure [33]. These corrections are found through numerical simulations using a commercial software and assuming thermally perfect gas.

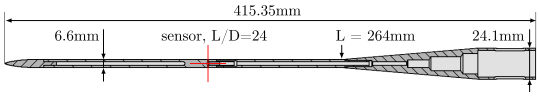

Figure 14: Static pressure probe of Nagamatsu type, redrawn from [33].

The flow around the probe has been computed for several conditions covering ranges: $p_\infty = 300-500\,\mathrm{Pa}$, $T_\infty = 70-170\,\mathrm{K}$, and $u_\infty = 1400-1800\,\mathrm{m/s}$. Since the correction factor p_w/p_∞ varies within 1% around its mean value (equal to 0.97), it can be assumed constant.

An example of the numerically determined pressure ratio p_w/p_∞ along the probe is reported in Fig. 15 for conditions approximately corresponding to a low Reynolds number regime at $t = 5\,\mathrm{ms}$ (i.e. $p_\infty = 482.4\,\mathrm{Pa}$, $T_\infty = 169.4\,\mathrm{K}$, and $u_\infty = 1769.8\,\mathrm{m/s}$).

Figure 16 compares the Schlieren image for the reference case 1 at 5 ms with numerical contours of the density gradient. The agreement on the shock angle is very good.

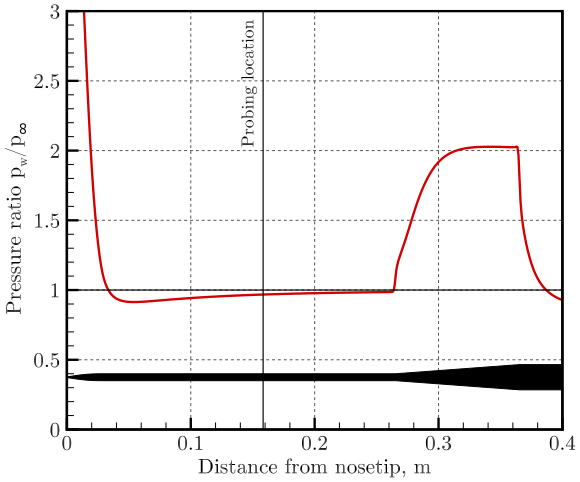

Figure 15: Pressure ratio p_w/p_∞ along the static probe for a low Reynolds number test at $t = 5$ ms.

4.3. Mars entry conditions

The Longshot future operational map for Martian entries should consider only the existing conical nozzle as it has the universal geometry regardless of Mach number or gas used. If the parallel free-stream flow is required by potential experimental work, a new contoured nozzle must be designed[9].

For the conical nozzle, the free-stream Mach number can be altered by exchangeable throats with different diameters. Different free-stream Reynolds numbers can be achieved by altering the stagnation conditions in the nozzle reservoir as discussed in §3.1. However, the varying Reynolds number leads to a different displacement thickness of the boundary layer developing on the nozzle wall thereby changing the effective nozzle area ratio. Therefore, the free-stream Mach number sightly depends on the Reynolds number as well.

Following the work presented in [21], the operational range is theoretically bounded by several limits. The minimum Mach number is determined by the shortest acceptable test time or the smallest tolerable diameter of the core flow, respectively. The maximum Mach number is limited by flow condensation. Since this aspect is more critical for carbon dioxide than for nitrogen, a potential increase of the reservoir temperature is of primary interest. However, a higher reservoir temperature leads to a reduction of the free-stream Reynolds number for given reservoir pressure. This sets the upper limit of the Reynolds number, which is basically dictated by the maximal achievable reservoir density. On the other hand, the lower limit is not of interest as it lies out of the entry trajectories. The lowest Reynolds number is usually limited by the minimal piston weight, currently about 1.5 kg.

Some trajectories of past successful Mars missions are depicted in Fig. 18a redrawn from [34]. In order to convert the trajectories from the altitude-velocity to the Mach-Reynolds variables, the atmospheric conditions must be known. Although the reconstructed atmospheric data are available for some missions (e.g. [1; 35; 36]), both free-stream Mach and Reynolds numbers are estimated using the atmospheric conditions reported in Fig. 17. Figure 18b shows the Mars mission trajectories in terms of the free-stream Mach and Reynolds numbers. The future Longshot operation using CO_2 should target the Mach numbers up to 10 and the Reynolds numbers around 10^6.

5. Conclusions

The Longshot wind tunnel operation for Martian entry flows has been reviewed. The investigation follows the gas flow inside the tunnel from the system of driver/driven tubes to the test section where the free-stream flow properties must be determined using the rebuilding methods.

The compression process generating the reservoir conditions has been investigated by the quasi-1D numerical solver L1d validated by experimental data obtained from the pressure measurements along the driven tube and in the nozzle reservoir. The operational map of the reservoir conditions (P_0 and T_0) as a function of the initial driven pressure and the piston weight has been determined numerically. The structural limits of the facility and the potential risk of the piston collision with the check valves are taken into account. The pressure which is built up in front of the check valves is the main limiting factor for the further increase of the reservoir temperature.

The available rebuilding methods needed for determination of the free-stream flow properties are presented and modified for carbon dioxide. The stagnation point heat flux models has been established replacing the Fay-Riddell equation. The operation of the static pressure probe in carbon dioxide has been assessed by the numerical computations. It has been

[9] As already discussed, the existing contoured nozzle has been designed for nitrogen. Although about 40 tests have been carried out with this nozzle using CO_2 and the reported flow quality seems to be acceptable for some preliminary studies [6], the off-design operation may be questionable.

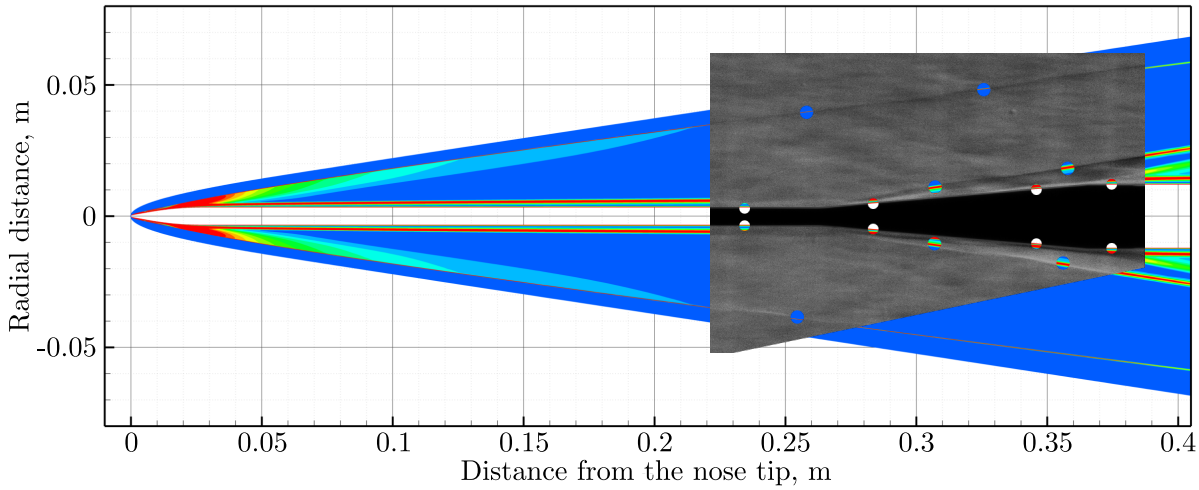

Figure 16: Comparison of density gradients with Schlieren flow visualization.

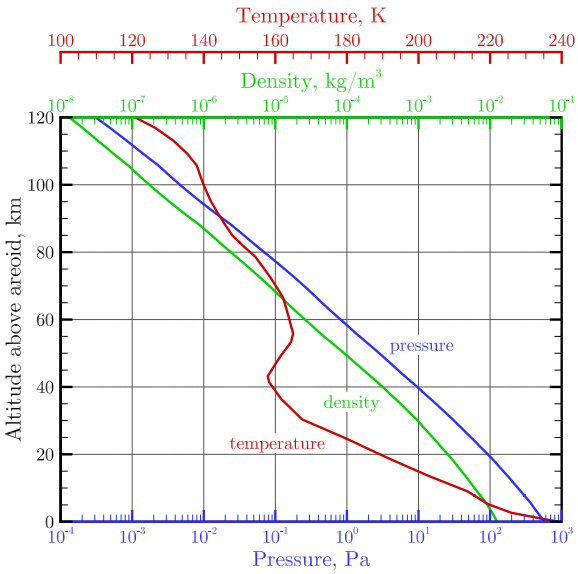

Figure 17: Mars atmospheric pressure, temperature, and density as functions of the altitude relative to the areoid.

found that the viscous correction factor can be regarded as constant within the relevant range of Longshot free-stream flow conditions.

The present work has established a solid background of the auxiliary numerical tools which will allow a future test campaign aiming to precisely define the new operational map in terms of Mach and Reynolds numbers available for experimental investigations of Martian entry flows. The rigorous evaluation of the flow condensation must be carefully performed base on experimental data including the directly measured static pressure which is sensitive to the flow condensation.

Acknowledgments

The author wishes to thank Dr. Grossir and Ing. Paris for their help in designing and conducting the experiments.

References

[1] C. Karlgaard, P. Kutty, J. Shidner, M. Schoenenberger, M. Munk, Mars entry atmospheric data system trajectory reconstruction algorithms and flight results, no. AIAA 2013-0028 in Aerospace Sciences Meetings, American Institute of Aeronautics and Astronautics, 2013. doi:10.2514/6.2013-28. URL `https://doi.org/10.2514/6.2013-28`

[2] J. D. Anderson, Hypersonic and High Temperature Gas Dynamics Second Edition, American Institute of Aeronautics and Astronautics, 2006.

[3] J.-M. Charbonnier, S. Paris, W. Dieudonné, Extension of the operating domain of the vki-longshot tunnel to the use of testing gases with various gamma values, Tech. Rep. VKI RP 1997-40, ONERA, Modane, France (1997).

[4] G. Grossir, Longshot hypersonic wind tunnel flow characterization and boundary layer stability investigations, Ph.D. thesis, von Karman Institute for Fluid Dynamics - Université Libre de Bruxelles (July 2015).

[5] M. Bugel, P. Rynier, A. Smith, Review of European Aerodynamics and Aerothermodynamics Capabilities for Sample Return Missions, in: 6th European Symposium on Aerothermodynamics for Space Vehicles, Vol. 659 of ESA Special Publication, 2009, p. 125.

[6] J. M. Meyers, Tunable diode laser absorption spectroscopy characterization of impulse hypervelocity co_2 flows, Ph.D. thesis, von Karman Institute for Fluid Dynamics - Université Libre de Bruxelles (2009).

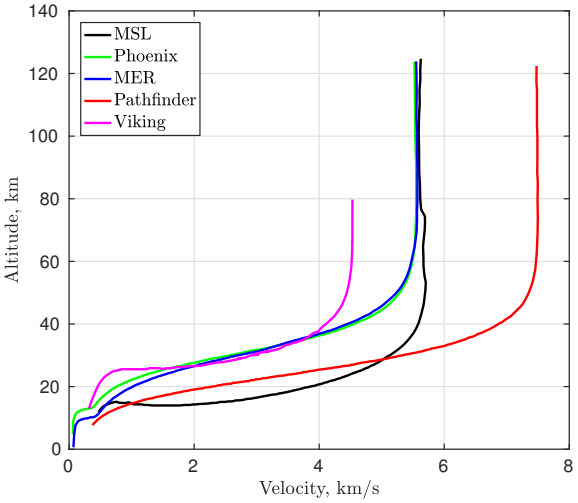

(a) Entry trajectories of Mars missions, redrawn from [34].

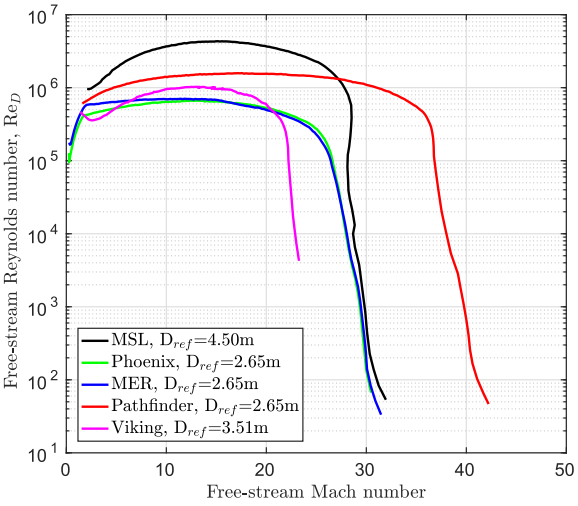

(b) Estimated entry trajectories in terms of Mach and Reynolds numbers.

Figure 18: Mars entry trajectories of some selected missions.

[7] G. Grossir, Z. Ilich, Numerical modeling of the vki longshot compression process, in: Flow Characterization and Modeling of Hypersonic Wind Tunnels, VKI Lecture Series STO-AVT-235, 2018.

[8] R. W. Perry, The Longshot type of high-Reynolds number hypersonic tunnel, in: Third hypervelocity techniques symposium, Advanced experimental techniques for study of hypervelocity flight, 1964.

[9] K. R. Enkenhus, C. Parazzoli, The Longshot free-piston cycle, part I, theory, Technical Note 51, von Karman Institute for Fluid Dynamics (November 1968).

[10] G. Simeonides, Design of a Mach 15 axisymmetric nozzle, Internal Note 82, von Karman Institute for Fluid Dynamics (March 1987).

[11] G. Grossir, Z. Ilich, O. Chazot, Modeling of the VKI Longshot gun tunnel compression process using a quasi-1D approach, in: 33rd AIAA Aerodynamic Measurement Technology and Ground Testing Conference, 2017 AIAA Aviation Forum, no. AIAA 2017-3985, 2017.

[12] A. E. Seigel, The theory of high speed guns, in: AGARDograph 91, NATO, 1965.

[13] B. E. Richards, K. R. Enkenhus, Hypersonic testing in the VKI Longshot free-piston tunnel, AIAA Journal 8 (6) (1970) 1020–1025.

[14] P. A. Jacobs, Quasi-one-dimensional modeling of a free-piston shock tunnel, AIAA Journal 32 (1) (1994) 137–145.

[15] R. Span, E. W. Lemmon, R. T. Jacobsen, W. Wagner, A. Yokozeki, A reference equation of state for the thermodynamic properties of nitrogen for temperatures from 63.151 to 1000K and pressures to 2200MPa, Journal of Physical Chemistry 29 (6) (2000) 1361–1433.

[16] R. Span, W. Wagner, A new equation of state for carbon dioxide covering the fluid region from the triple-point temperature to 1100K at pressures up to 800MPa, Journal of Physical Chemistry 25 (1996) 1509–1597.

[17] S. Gordon, B. J. McBride, Computer program for calculation of complex chemical equilibrium compositions and applications, i. analysis, Reference Publication 1311, NASA (1994).

[18] B. J. McBride, S. Gordon, Computer program for calculation of complex chemical equilibrium compositions and applications, ii. users manual and program description, Reference Publication 1311, NASA (1996).

[19] T. Andresen, Mathematical modeling of CO_2 based heat pumping systems, Ph.D. thesis, Norwegian University of Science and Technology (2009).

[20] Z. Ilich, G. Grossir, S. Paris, O. Chazot, Experimental investigation of the VKI Longshot gun tunnel compression process, in: EUCASS, no. EUCASS 2017-155, 2017. doi:10.13009/EUCASS2017-155.

[21] G. Grossir, Z. Ilich, S. Paris, O. Chazot, Theoretical considerations to extend the operational map of the vki longshot hypersonic wind tunnel, in: AIAA AVIATION Forum, no. AIAA 2016-3818, American Institute of Aeronautics and Astronautics, 2016. doi:10.2514/6.2016-3818.
URL `https://doi.org/10.2514/6.2016-3818`

[22] S. Culotta, B. E. Richards, Methods for determining conditions in real nitrogen expanding flows, Technical Note TN-58, von Karman Institute for Fluid Dynamics (February 1970).

[23] J. A. Fay, F. R. Riddell, Theory of stagnation point heat transfer in dissociated air, Journal of the Aeronautical Sciences 25 (2) (1958) 73–85.

[24] J. B. Scoggins, T. E. Magin, Development of Mutation++: Multicomponent thermodynamic and transport properties for ionized plasmas written in C++, in: AIAA AVIATION Forum, no. AIAA 2014-2966, American Institute of Aeronautics and Astronautics, 2014.

[25] T. E. Magin, A model for inductive plasma wind tunnels, Ph.D. thesis, von Karman Institute for Fluid Dynamics - Université Libre de Bruxelles (June 2004).

[26] A. Munafò, Multi-scale models and computational methods for aerothermodynamics, Ph.D. thesis, von Karman Institute for Fluid Dynamics - École Centrale Paris (2014).

[27] Z. Ilich, G. Grossir, O. Chazot, Evaluation of the stagnation point velocity gradient in low-enthalpy hypersonic flows, in: 33rd AIAA Aerodynamic Measurement Technology and Ground Testing Conference, 2017 AIAA Aviation Forum, no. AIAA 2017-3984, 2017.

[28] L. Yee, H. E. Bailey, H. T. Woodward, Ballistic range measurements of stagnation-point heat transfer in air and in carbon dioxide at velocities up to 18000 feet per second, Technical Note D-777, National Aeronautics ans Space Administration (March 1961).

[29] R. M. Nerem, C. J. Morgan, B. C. Graber, Hypervelocity stagnation point heat transfer in a carbon dioxide atmosphere, AIAA Journal 1 (9) (1963) 9.

[30] M. Sharma, A. B. Swantek, W. Flaherty, J. M. Austin, S. Doraiswamy, G. V. Candler, Experimental and numerical investigation of hypervelocity carbon dioxide flow over blunt bodies, Journal of Thermophysics and Heat Transfer 24 (4) (2010) 673–683. doi:10.2514/1.49386.
URL https://doi.org/10.2514/1.49386

[31] H. Hoshizaki, Heat transfer in planetary atmospheres at supersatellite speeds, ARS Journal 32 (10) (1962) 1544–1552. doi:10.2514/8.6331.
URL https://doi.org/10.2514/8.6331

[32] E. V. Zoby, Empirical stagnation-point heat-transfer relation in several gas mixtures at high enthalpy levels, Technical Note NASA TN D-4799, Langey Research Center (October 1968).

[33] G. Grossir, S. Paris, P. Rambaud, B. Van Hove, Design of static pressure probes for improved free-stream characterization in hypersonic wind tunnels, in: 52nd AIAA Aerospace Sciences Meeting, no. AIAA 2014-1410, 2014.

[34] K. Edquist, A. Dyakonov, M. Wright, C. Tang, Aerothermodynamic design of the mars science laboratory backshell and parachute cone, in: 41st AIAA Thermophysics Conference, no. AIAA 2009-4078 in Fluid Dynamics and Co-located Conferences, American Institute of Aeronautics and Astronautics, 2009. doi:10.2514/6.2009-4078.
URL https://doi.org/10.2514/6.2009-4078

[35] P. Withers, M. D. Smith, Atmospheric entry profiles from the mars exploration rovers spirit and opportunity, Icarus 185 (1) (2006) 133 – 142. doi:https://doi.org/10.1016/j.icarus.2006.06.013.

[36] D. A. Spencer, R. C. Blanchard, R. D. Braun, P. H. Kallemeyn, S. W. Thurman, Mars pathfinder entry, descent, and landing reconstruction, Journal of Spacecraft and Rockets 36 (3) (1999) 357–366. doi:10.2514/2.3478.
URL https://doi.org/10.2514/2.3478

Analysis of the Stability of a Flat Plate High-Speed Boundary Layer with Discrete Roughness

Iván Padilla Montero

Aeronautics and Aerospace Department, von Karman Institute for Fluid Dynamics, Belgium, ivan.padilla@vki.ac.be

Supervisors: Fabio Pinna and Olivier Chazot

Senior Research Engineer, Aeronautics and Aerospace Department, von Karman Institute for Fluid Dynamics, Belgium, fabio.pinna@vki.ac.be

Head of Department and Professor, Aeronautics and Aerospace Department, von Karman Institute for Fluid Dynamics, Belgium, olivier.chazot@vki.ac.be

University Supervisor: Gérard Degrez

Dean of the Faculty and Professor, Aero-Thermo-Mechanics Department, Université libre de Bruxelles, Belgium, gdegrez@ulb.ac.be

Abstract

Two-dimensional linear stability theory is used to analyze the instability of the wake behind a cuboid and a ramp-shaped roughness elements mounted on top of a flat plate in a Mach 6 freestream. Spatial stability results are presented for the streamwise evolution of the leading instabilities along the wake behind the elements, using base flows obtained from steady and laminar Navier-Stokes simulations.

Keywords: boundary layer, stability, transition, hypersonic, roughness

1. Introduction

Boundary-layer transition from a laminar to a turbulent regime is a critical driver in the design of high-speed vehicles. Turbulent hypersonic boundary layers are usually characterized by big heat transfer rates that lead to strong aerothermodynamic loads. For example, for a Reynolds number of 10^7 and a moderate supersonic Mach number, the turbulent heat-transfer coefficient on a flat plate is estimated to be an order of magnitude higher than the corresponding laminar value [1]. Despite being an active research topic for decades, the physical mechanisms governing hypersonic boundary layer transition are not well understood yet, and the existing transition prediction tools for practical applications still rely heavily on empirical correlations and extensive wind tunnel testing [2]. During the design process, this fact implies the need to account for large safety factors (mainly the assumption of fully turbulent flow) that lead to an oversize of the thermal protection systems, with the consequent reduction of payload capacity and an ultimate increase in mission cost. In order to improve the transition prediction capabilities for future high-speed applications, new methodologies involving a higher degree of flow physics for each particular case should be developed. The use of experimental-based correlations should be replaced by methods based on stability theory and transient growth considerations [3]. Nowadays, linear stability theory has become a computationally feasible tool for simple configurations which is able to provide good results in the first stages of the transition process [4].

The natural boundary-layer transition process at hypersonic speeds is known to be strongly influenced by the presence of isolated roughness elements on the surface of a body. Typical examples include damaged heat-shield tiles, rivets or gap fillers, among many others. The perturbations generated by these elements can accelerate the growth of incoming disturbances and introduce additional instability mechanisms in the boundary layer, eventually leading to a premature occurrence of transition. Although a physics-based

prediction of roughness-induced transition is still not available nowadays, several experimental and numerical investigations have recently increased our knowledge, see for example [5; 6; 7; 8; 9; 10]. Three-dimensional elements with heights comparable to the local boundary-layer thickness tend to induce counter-rotating streamwise vortices in the wake flow field. These vortices lift-up low-momentum fluid from the near-wall region and give rise to low-velocity streaks that are surrounded by regions of high shear and can support the growth of different instabilities. Since the flow field in this case presents a strong inhomogeneity in the wall-normal (y) and spanwise (z) directions, classical linear stability theory is no longer a valid technique for this problem. In order to obtain meaningful results, the amplitude functions considered in the stability analysis must depend on both y and z coordinates. This approach, in which the perturbations are inhomogeneous in two spatial directions but homogeneous in the third one and in time, is hereby referred to as two-dimensional linear stability theory, also known as BiGlobal stability theory, as introduced by Theofilis [11].

A significant amount of fundamental studies in roughness-induced transition involving the use of 2D linear instability theory have been carried out over the last years, both for supersonic and hypersonic flows and mostly for elements mounted on top of a flat plate. Groskopf et al. [5] performed temporal analyses of the instability of the wake behind isolated 3D cuboidal roughness elements in a Mach 4.8 boundary layer, and compared the results against direct numerical simulation (DNS), reporting a very good agreement in the disturbance amplitude shapes. Similar analyses were conducted by De Tullio and coauthors [9] at Mach 2.5 and by Paredes [12] and De Tullio & Sandham [13; 10] at Mach 6 for the same geometry, in both cases comparing DNS results against spatial BiGlobal stability theory and three-dimensional parabolized stability equations (PSE-3D). For the two cases investigated, the two-dimensional eigenfunctions obtained from the 2D stability computations and the growth rates extracted from the PSE-3D simulations were both found to be in close agreement with the DNS data. On the experimental side, Kegerise et al. [6] carried out measurements of the disturbance amplitudes behind a diamond element in a flat plate at Mach 3.5, and compared them against the spatial stability analyses of Choudhari and coworkers [14; 8] with satisfactory results, reinforcing the validity of the theory for such configurations. In all the cases analyzed, the dominant wake instability modes were found to be varicose (even) and sinuous (odd) deformations of the low-velocity streak that characterizes the wake flow structure. Nevertheless, whether the leading instability mode has an even or an odd nature appears to be case dependent. Moving to a more practical configuration, Theiss et al. [15; 16] performed 2D and PSE-3D linear stability computations in the wake behind different roughness geometries located on the heat shield of a reentry capsule in a Mach 5.9 freestream. The varicose wake mode was found to be the disturbance undergoing a higher amplification, with the cylindrical roughness element being the most effective shape.

In this work, the instability of the wake behind a cuboidal and a ramp-shaped roughness element is investigated by means of two-dimensional linear stability theory. The elements are mounted on top of a flat plate inside a hypersonic freestream that matches the high Reynolds test conditions of the von Karman Institute H3 wind tunnel. Spatial stability calculations are performed at different streamwise positions and frequencies along the wake behind the roughness elements, employing steady and laminar base flow solutions obtained with the compressible Navier-Stokes equations. Two different inflow conditions are considered in order to investigate the effect of the flat plate leading edge on the instability characteristics of the wake flow field, respectively corresponding to a self-similar boundary layer profile and a flat plate with a circular leading edge. For each case, the dominant instability modes are identified and compared, providing an estimation of the transition onset locations predicted with the e^N method.

2. Governing equations

The governing equations considered in this analysis are the Navier-Stokes equations for a compressible Newtonian fluid. The primitive variables of the flow are denoted by density ρ, pressure p, temperature T and velocity components u_i, with $i = 1, 2, 3$. Considering a Cartesian reference frame, the system of equations can be written in conservation form as

$$\frac{\partial \rho}{\partial t} + \frac{\partial (\rho u_i)}{\partial x_i} = 0, \tag{1}$$

$$\frac{\partial (\rho u_i)}{\partial t} + \frac{\partial (\rho u_i u_j)}{\partial x_j} + \frac{\partial p}{\partial x_i} - \frac{\partial \tau_{ij}}{\partial x_j} = 0, \tag{2}$$

$$\frac{\partial (\rho E)}{\partial t} + \frac{\partial (\rho E u_i + p u_i)}{\partial x_i} + \frac{\partial q_i}{\partial x_i} - \frac{\partial (u_i \tau_{ij})}{\partial x_j} = 0, \tag{3}$$

where t is the time coordinate, x_i is the ith spatial coordinate and $E = e + u_i u_i/2$, with e being the specific internal energy of the fluid. The viscous stress tensor τ_{ij} is defined as

$$\tau_{ij} = \mu\left(\frac{\partial u_i}{\partial x_j} + \frac{\partial u_j}{\partial x_i} - \frac{2}{3}\frac{\partial u_k}{\partial x_k}\delta_{ij}\right), \tag{4}$$

where μ is the dynamic viscosity of the fluid and δ_{ij} is the Kronecker delta. The conductive heat flux vector q_i is modeled using Fourier's law of heat conduction, given by

$$q_i = -k\frac{\partial T}{\partial x_i}, \tag{5}$$

with k denoting the thermal conductivity of the fluid. Under the assumption of a calorically perfect gas, the system is closed by means of the perfect gas equation of state together with two additional thermodynamic relationships, respectively expressed as

$$p = \rho R T, \quad e = c_v T \quad \text{and} \quad c_v = \frac{R}{\gamma - 1}, \tag{6}$$

where R is the specific gas constant, c_v is the specific heat at constant volume and γ is the ratio of specific heats. Air is considered with the values $\gamma = 1.4$ and $R = 287.18$ J/(kg·K). Sutherland's law is used to model the variation of the dynamic viscosity with temperature, such that

$$\mu = \mu_{ref}\left(\frac{T}{T_{ref}}\right)^{3/2}\frac{T_{ref} + S_\mu}{T + S_\mu}, \tag{7}$$

where S_μ is the Sutherland temperature constant and μ_{ref} and T_{ref} are respectively the reference dynamic viscosity and static temperature. The same law is also assumed to take into account the variation of thermal conductivity with temperature, in this case with the parameters S_k and k_{ref}. The corresponding values considered in this work for these quantities are $\mu_{ref} = 1.716\times10^{-5}$ kg/(m·s), $S_\mu = 111$ K, $k_{ref} = 2.41\times10^{-2}$ W/(m·K), $S_k = 194$ K and $T_{ref} = 273.15$ K. The resulting Prandtl number can then be directly obtained from its definition as $Pr = \mu c_p/k$, where c_p denotes the specific heat at a constant pressure. The flow similarity parameters that define the problem are γ and the freestream Reynolds, Mach and Prandtl numbers, respectively denoted by Re_∞, M_∞ and Pr_∞.

2.1. Formulation of the two-dimensional linear stability problem

According to classical linear stability theory, the vector of primitive flow variables $\mathbf{q} = [u, v, w, T, p]^T$ is split into a steady reference state $\bar{\mathbf{q}}$, also known as base flow, and a small unsteady perturbation field $\tilde{\mathbf{q}}$:

$$\mathbf{q} = \bar{\mathbf{q}} + \epsilon\tilde{\mathbf{q}}, \tag{8}$$

with $\epsilon \ll 1$. The base flow is assumed to be locally parallel in the streamwise (x) direction, so that $\bar{\mathbf{q}} = \bar{\mathbf{q}}(y, z)$ at a given x coordinate. As stated before, due to the high shear that characterizes the wake base flow in the wall-normal and spanwise directions, the amplitude of the perturbations is considered to be a function of both y and z. The ansatz of the modal perturbations for this case can be written as

$$\tilde{\mathbf{q}}(x, y, z, t) = \hat{\mathbf{q}}(y, z)\exp[i(\alpha x - \omega t)] + c.c., \tag{9}$$

where $\hat{\mathbf{q}}$ is the two-dimensional amplitude function, α is the wavenumber along the streamwise direction, ω is the angular frequency and $c.c.$ denotes the complex conjugate. In this work, the attention is focused on the spatial growth of the wake instabilities. In the spatial framework, ω is considered to be real and represents the angular frequency of the perturbations. On the contrary, α is complex, with the real part $\alpha_r = \Re\{\alpha\}$ being the streamwise wavenumber of $\tilde{\mathbf{q}}$ and the imaginary part $\alpha_i = \Im\{\alpha\}$ its spatial growth rate. With this definition, a positive value of α_i means a spatial decay of the amplitude function whereas a negative value implies a spatial growth.

The equations governing the linear stability problem are obtained by substituting the splitting given by Eq. (8) together with the ansatz defined by Eq. (9) into the Navier-Stokes system, Eqs. (1) to (3), and then neglecting the resulting non-linear terms, which are of order $O(\epsilon^2)$. In the end, the resulting system of linear partial differential equations can be written in the following compact form

$$\mathbf{A}\hat{\mathbf{q}} = \alpha\mathbf{B}\hat{\mathbf{q}} + \alpha^2\mathbf{C}\hat{\mathbf{q}}, \tag{10}$$

where $\mathbf{A}$, $\mathbf{B}$ and $\mathbf{C}$ are complex and nonsymmetric differential matrix operators. The stability equations are made nondimensional using the boundary layer edge properties, denoted by the subscript e. The following dimensionless quantities are defined

$$\begin{gathered} t^* = \frac{t u_e}{l_e},\ x_i^* = \frac{x_i}{l_e},\ \rho^* = \frac{\rho}{\rho_e},\ u_i^* = \frac{u_i}{u_e}, \\ p^* = \frac{p}{\rho_e u_e^2},\ E^* = \frac{E}{u_e^2},\ T^* = \frac{T}{T_e},\ \mu^* = \frac{\mu}{\mu_e}, \end{gathered} \tag{11}$$

where l_e is the local Blasius length scale at the streamwise location x where the stability analysis is performed, given by $l_e = \sqrt{\mu_e x/\rho_e u_e}$.

After discretization of Eq. (10), an algebraic generalized eigenvalue problem (GEVP) is obtained, which is nonlinear in the eigenvalue α. The problem is linearized by means of the companion matrix method [17], defining the following auxiliary vector: $\hat{\mathbf{q}}^+ = [\hat{u}, \hat{v}, \hat{w}, \hat{T}, \hat{p}, \alpha\hat{u}, \alpha\hat{v}, \alpha\hat{w}, \alpha\hat{T}]^T$, so that the two-dimensional GEVP becomes

$$\mathcal{A}^+\hat{\mathbf{q}}^+ = \alpha\mathcal{B}^+\hat{\mathbf{q}}^+, \tag{12}$$

with

$$\mathcal{A}^+ = \begin{bmatrix} \mathcal{A} & -\mathcal{B}_{\hat{u}:\hat{T}} \\ \mathbf{0} & \mathbf{I} \end{bmatrix} \quad \text{and} \quad \mathcal{B}^+ = \begin{bmatrix} \mathcal{B}_{\hat{p}} & \mathcal{C}_{\hat{u}:\hat{T}} \\ \mathbf{I} & \mathbf{0} \end{bmatrix}, \tag{13}$$

in which $\mathcal{A}$ denotes the discrete matrix operator associated to matrix $\mathbf{A}$. $\mathcal{B}_{\hat{u}:\hat{T}}$ and $\mathcal{C}_{\hat{u}:\hat{T}}$ are non-square matrices that contain the columns from the respective discrete operators $\mathcal{B}$ and $\mathcal{C}$ which correspond to the variables $\hat{u}$, $\hat{v}$, $\hat{w}$ and $\hat{T}$. Similarly, $\mathcal{B}_{\hat{p}}$ is a square matrix that contains only the columns from $\mathcal{B}$ that correspond to the variable $\hat{p}$ and $\mathbf{I}$ is the identity matrix. It is important to note that this procedure significantly increases the size of the system to be solved, from 5 to 9 variables.

3. Numerical methodology

3.1. Computation of the laminar base flow

The roughness elements considered in this study are the two three-dimensional sharp-edged geometries depicted in Fig. 1. The cuboidal geometry allows the design of a high-quality computational grid, making it ideal for fundamental studies and constituting a good case for validation purposes. On the other side, the ramp roughness element is based on a practical design developed by the Hypersonic Airbreathing Propulsion Branch (HAPB) at NASA Langley Research Center, who explored the possibility of using wall-mounted ramp fuel injectors in scramjet combustors [18]. Ramp-shaped injectors shed vortices and produce local flow separation which can enhance mixing and flame holding. This roughness shape has been previously tested at the von Karman Institute during a fundamental experimental campaign in roughness-induced transition by Tirtey [19], and it is considered here with the purpose of obtaining numerical results that can later be compared against the experimental observations and provide additional understanding.

The geometrical configuration of the problem under investigation is represented in Fig. 2. The roughness elements are mounted on top of the flat plate surface

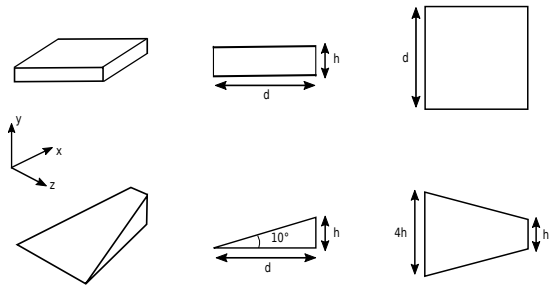

Figure 1: Roughness element geometries (not to scale).

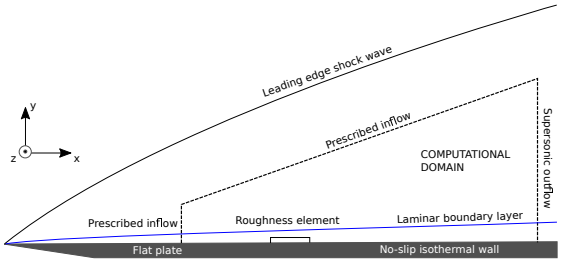

Figure 2: Representation of the geometrical configuration of the problem under study and the computational domain employed for the base flow calculations (not to scale).

at a given distance behind the leading edge and centered along the spanwise direction at $z = 0$ (streamwise symmetry plane). This figure also shows the computational domain used to obtain the base flows for the stability analysis. As it can be observed, the domain is located inside the shock layer established between the surface and the shock wave induced at the flat plate leading edge. This approach has already been employed in similar studies by other authors with successful results [9; 10; 15]. Avoiding the leading edge induced shock wave helps to reduce the computational effort needed to obtain a converged numerical solution while adding flexibility to test different inflow conditions. On the other hand, it requires the imposition of adequate flow profiles at the inflow and top boundaries, which may come from another numerical solution of the Navier-Stokes equations or from a self-similar boundary layer computation. Additionally, the top boundary has a constant slope in order to avoid roughness-induced shock waves to impinge on it, which would complicate the treatment of boundary conditions at this boundary. The spanwise symmetry of the current geometrical configuration is also exploited by reducing the computational domain to solve only half of the flow field.

The dimensions of the computational domain are the same for both roughness geometries and are sum-

Table 1: Dimensions of the computational domain. Units in millimeters. The origin is located at the flat plate leading edge.

x_{in}	x_{out}	y_{in}	y_{out}	z_∞
50	400	7.69	88.49	15

Table 2: Freestream conditions used in the base flow computations.

M_∞	T_∞ [K]	p_∞ [Pa]	Re_∞/l [1/m]
6	60.98	1963.42	2.60×10^7

marized in Table 1, which lists the streamwise coordinate and height of the inlet (x_{in}, y_{in}) and outlet (x_{out}, y_{out}) planes of the domain, as well as the spanwise size (z_∞), which is constant. Regarding the dimensions of the roughness elements, they are fully defined by the roughness height h and the ramp angle, as illustrated in Fig. 1. For comparison purposes, both elements have the same height, which has a value of $h = 0.4$ mm. Finally, the streamwise location of the roughness elements is defined by the streamwise coordinate of the leading edge of the roughness with respect to the flat plate leading edge, hereby denoted by x_r. In the current configuration, both elements are located at $x_r = 60$ mm.

The freestream values considered for the numerical solution are summarized in Table 2. They correspond to the high-Reynolds test conditions of the von Karman Institute H3 hypersonic wind tunnel (see [19]). Because of the low freestream static temperature achieved ($T_0 = 500$ K), no high-temperature effects are expected in the flow field and therefore the assumption of a calorically perfect gas is a good approximation. Due to the short operating time of the wind tunnel, the flat plate wall is considered to be isothermal with a wall temperature of $T_w = 300$ K (room temperature). The numerical solution of the base flow is steady and laminar, and is carried out using the CFD package CFD++® [20] on a block-structured grid consisting of hexahedral cells. The spatial discretization is based on a second-order upwind finite volume scheme which features a limited total variation diminishing (TVD) flux interpolation to minimize numerical oscillations in the vicinity of discontinuities. Concerning time integration, an implicit scheme (backward Euler) with multigrid acceleration and residual smoothing is employed to enhance convergence to the steady state as much as possible.

Regarding the base flow boundary conditions, the primitive flow variables are prescribed at the inlet and the top boundaries of the domain with values that are obtained either from a self-similar boundary layer computation or from another Navier-Stokes solution in a bigger domain without the roughness element. When no roughness is present, the flow field is constant along the spanwise direction and the problem becomes two-dimensional. Therefore, the values to prescribe can be computed through a 2D simulation provided that the 3D domain boundaries are far enough for the influence of the element to be negligible. This is an additional advantage of using a subdomain with prescribed inflow data. At the center ($z = 0$) and the far side ($z = z_\infty$) streamwise planes, symmetry conditions are specified, such that the actual problem would correspond to a spanwise array of discrete roughness elements. At the wall, a no-slip isothermal condition is enforced. Lastly, at the outlet boundary a supersonic outflow condition is specified, in which all the primitive flow variables are extrapolated from the interior of the domain. With respect to the initial conditions, the flow field is initialized with the freestream values reported in Table 2 and the system is integrated in time until a decrease of at least 8 orders of magnitude in the residual norm is achieved.

The computational grids used to obtain the base flow solutions are generated using OpenFOAM's blockMesh [21] utility. For both roughness geometries the grid is clustered towards the element in all directions as well as towards the flat plate wall to maintain a reasonable computational effort. In addition, the transition in cell size between the different blocks is kept as smooth as possible by appropriately adapting the expansion ratios along each edge. The resulting computational grids for the cuboid and ramp roughness elements contain a total number of cells of 65 millions and 76 millions, respectively.

3.2. Solution of the generalized eigenvalue problem

The numerical solution of the stability problem given by Eq. (10) is performed using the von Karman Institute Extensible Stability & Transition Analysis (VESTA) toolkit, originally developed by Pinna [22; 23]. The particular structure of the matrices **A**, **B** and **C** for a given case is automatically derived and implemented in MATLAB® [24] by means of a tool based on the computer algebra system named Maxima [25]. The two-dimensional partial differential eigenvalue problem resulting from the linear stability formulation is assembled and discretized by means of a high-order finite difference scheme with uniform error developed by Hermanns & Hernández [26], also known

as FD-q, as introduced by Paredes et al. [27]. Following the same philosophy as the Chebyshev collocation method [28], the idea behind the FD-q technique is to construct a finite difference scheme in a structured grid with a specific non-uniform point distribution, based on a piecewise Lagrange polynomial interpolation defined on a transformed domain $\xi, \eta \in [-1, 1]$, with ξ and η being respectively the spanwise and wall-normal transformed coordinates. For a given degree q of the interpolating polynomials, an optimal grid point distribution is computed which minimizes the interpolation error. In the limit of $q = N$, with $N + 1$ being the total number of grid points, the Chebyshev-Gauss-Lobatto point distribution is retrieved, making the FD-q discretization identical to the one provided by the Chebyshev collocation method. The advantage of this scheme lies upon the fact that by reducing the order of the discretization to $q << N$, a high degree of sparsity is introduced in the matrices that compose the discrete eigenvalue problem, which can then be exploited to provide a significant reduction of the computational cost at an acceptable decrease in accuracy.

In the majority of practical problems, the transformed grid does not coincide with the physical domain under study, and as a consequence adequate geometrical mappings have to be considered. In the computations presented in this work, the mapping originally introduced by Malik [29] is applied in the wall-normal direction, which allows placing half of the grid points below a given coordinate. In the spanwise direction, a BiQuadratic mapping [30] is employed, which concentrates one-third of the grid points in a desired region. In this way, the grid used for solving the stability problem can be clustered towards the boundary layer and the roughness centerline, which is the region containing the wake induced by the roughness element and is where the strongest base flow gradients are encountered. Even though this process transforms the stability grid into the physical domain, the mapped grid defined by the FD-q point distribution does not coincide with the mesh employed to obtain the base flow solution, which is based on a completely different discretization technique, namely, a finite volume method. As a consequence, before building the eigenvalue problem, the base flow data is interpolated on the FD-q grid by means of a cubic spline interpolation in each spatial direction.

Before solving the stability problem, appropriate boundary conditions have to be imposed on the perturbation quantities to fully define the discrete GEVP. At the wall, the no-slip condition is enforced by setting the velocity perturbations to zero with a homogeneous Dirichlet condition. The same is also applied for the wall temperature disturbance, whereas the pressure fluctuation is determined by means of a compatibility condition satisfying the wall-normal momentum equation at the wall. In the wall-normal far-field boundary, the perturbations are forced to decay by imposing a Dirichlet boundary condition, with the exception of $\hat{p}$, which once again satisfies the compatibility condition. Regarding the spanwise boundaries, periodic boundary conditions are specified for all the perturbation variables, meaning that the value of each disturbance quantity and its first derivative normal to the boundary must be equal at both spanwise boundaries.

The classical algorithm for solving generalized eigenvalue problems is the QZ method [31], which is able to compute the complete eigenvalue spectrum. Nevertheless, its high computational cost makes it feasible for the solution of small problems only. For the cases under consideration, the discrete matrices $\mathcal{A}^+$ and $\mathcal{B}^+$ reach a dimension of order $O(10^5)$, and therefore other options have to be assessed. For large-scale problems, the most common alternative is the implicitly restarted Arnoldi method [32], which is an iterative algorithm that only provides a given number of eigenvalues in the vicinity of a specific region. The solver built in VESTA toolkit makes use of the parallel implementation of the Arnoldi algorithm given by the (P)ARPACK library [33]. The Arnoldi iteration works optimally for extracting eigenvalues near the boundaries of the spectrum. However, in most of the interesting situations, the focus is on the interior values that are closer to the origin. In order to modify the solution region, the so-called shift-invert transformation is applied, which transforms the problem into the following one

$$(\mathcal{A}^+ - \sigma\mathcal{B}^+)^{-1}\mathcal{B}^+\hat{\mathbf{q}}^+ = \nu\hat{\mathbf{q}}^+, \quad \text{with} \quad \nu = \frac{1}{\alpha - \sigma}, \quad (14)$$

where σ is known as the shift-invert parameter, around which the eigenvalues are sought. The large matrix inversion involved in the solution process is based on a LU decomposition that is also performed in parallel by means of the Scalable Linear Algebra PACKage (ScaLAPACK) library [34]. The current solver has been previously tested against experimental data in the case of wake instabilities induced by a micro-ramp mounted on top of a flat plate in incompressible regime by Groot et al. [35], delivering satisfactory results.

4. Results

Four different cases are analyzed in this work by means of linear stability theory, which are summarized in Table 3. The parameter Re_h is known as the roughness Reynolds number, and is defined as $Re_h = u_h h/\nu_h$, where u_h and ν_h are the local streamwise velocity and kinematic viscosity of the fluid evaluated at the streamwise location of the roughness element and at a height of $y = h$ in the corresponding smooth flat plate boundary layer. The important role of this parameter in correlating roughness-induced transition experimental data sets is highlighted in the review work of Reda [2]. For instance, for the case of discrete roughness-induced transition over the Space Shuttle Orbiter centerline, a critical roughness Reynolds number of 344 is found to provide a good data fit. The value of h/δ_{99} describes the ratio between the roughness height and the local boundary layer thickness at the streamwise position of the roughness element, hereby denoted by δ_{99}. The value of δ_{99} is determined by means of the total enthalpy (h_0) criterion $h_0/h_{0,\infty} = 0.995$ [36], using the smooth flat plate boundary layer profiles associated to each particular case. Two different inflow boundary layer profiles are considered for each roughness geometry, namely, a self-similar solution of the compressible boundary layer equations, obtained with VESTA toolkit, and a profile corresponding to the boundary layer developing on a smooth flat plate with a circular leading edge of radius $r_{LE} = 0.1$ mm. The latter is obtained by solving the full Navier-Stokes equations in a 2D mesh with CFD++®. Fig. 3 illustrates the streamwise velocity and temperature profiles of the two different inflow cases. As it can be observed, despite the relatively small bluntness considered (only one tenth of a millimeter), there is a significant difference between the two boundary layer profiles. This is due to the entropy layer introduced by the curved bow shock generated in front of the circular leading edge, which for the hypersonic conditions under study is strong and the entropy gradient persists a long distance downstream. This condition has been chosen to study the effect of leading edge bluntness on the stability of the wake behind the roughness elements.

4.1. Base flow

The main physical features of the obtained base flow solutions are highlighted in Fig. 4, which depicts the Mach number and streamwise velocity contours of the numerical solutions computed for both roughness geometries with a self-similar boundary layer inflow (cases 1 and 3). Focusing on the streamwise flow structure, shown in the xy plane contour plots, it can be observed that the presence of the roughness elements introduces a displacement of the boundary layer upstream of the leading edge, progressively inducing a set of compression waves that eventually merge into an oblique shock wave further downstream. This compression is stronger for the cuboidal element, as it could be expected due to the higher flow displacement introduced by this geometry with respect to the ramp one. As the flow reaches the trailing edge of the elements, it turns and detaches, generating an expansion wave and creating a region of separated flow immediately downstream. Next, as the flow progressively reattaches further downstream, another fan of compression waves is induced which once again merges into an additional oblique shock. This is essentially the same flow behavior encountered in a backward facing step in supersonic flow. It is important to note that in the case of the cuboidal geometry, a region of separated flow is also encountered immediately upstream of the element due to the strong flow blockage

Table 3: Summary of the different cases investigated.

Case	Geometry	Re_h	h/δ_{99}	Inflow data
1	Cuboid	330	0.59	Self-similar
2	Cuboid	233	0.45	$r_{LE} = 0.1$ mm
3	Ramp	330	0.59	Self-similar
4	Ramp	233	0.45	$r_{LE} = 0.1$ mm

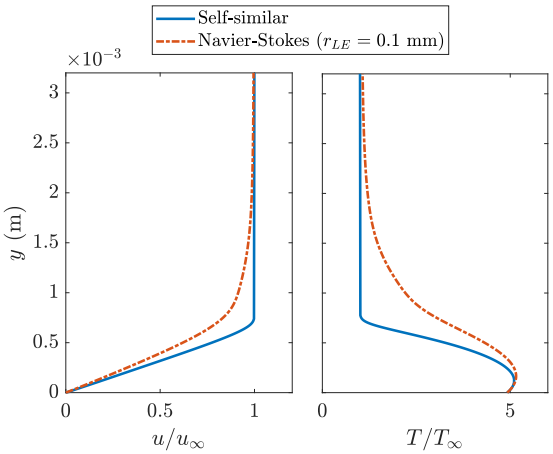

Figure 3: Streamwise velocity and temperature boundary layer profiles imposed at the inlet of the computational domain (x_{in}) for each of the two inflow conditions considered.

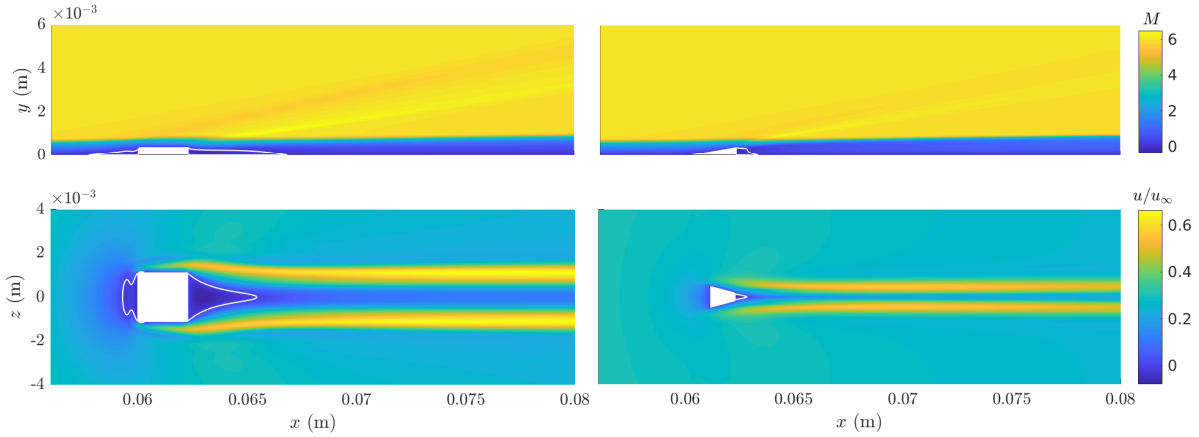

Figure 4: Base flow results obtained for cases 1 (cuboid) and 3 (ramp). (top) Mach number contours on the streamwise plane located at the roughness centerline ($z = 0$ m), illustrating the roughness-induced shock and expansion waves. (bottom) Nondimensional streamwise velocity contours (u/u_∞) on a plane located at $y = 0.5h$, showing the counter-rotating vortex pair induced by each roughness element. The white lines represent isolines of $u = 0$, delimiting regions of separated flow.

imposed by the blunt geometry. Similarly, the extension of the downstream separation bubble is significantly larger for the cuboidal element as compared with the ramp-shaped roughness. The spanwise structure of the flow field is represented in the xz plane contour plots of Fig. 4 and in Fig. 5. Fig. 5 shows contours of the streamwise shear magnitude, defined as

$$u_s = \sqrt{\left(\frac{\partial u}{\partial y}\right)^2 + \left(\frac{\partial u}{\partial z}\right)^2}, \tag{15}$$

on a spanwise (zy) plane located behind the roughness elements at a distance of $x = 0.1$ m with respect to the flat plate leading edge. For both geometries, a pair of strong counter-rotating vortices can be identified, which form at the edges of the roughness elements due to a pressure gradient between their side and top surfaces. These streamwise structures lift-up low-momentum fluid adjacent to the flat plate wall and give rise to a mushroom-shaped low-velocity streak [7; 8], which is surrounded by regions of high streamwise shear and large shear gradients in the wall-normal and spanwise directions. Due to the side angle of the ramp geometry, narrowing the planform shape of the element towards the trailing edge, the counter-rotating vortex pair in this case also presents a small spanwise velocity component in the direction of the roughness centerline. This small lateral momentum brings the vortices closer to each other along the wake, concentrating the vorticity in a smaller region and leading to a narrower but taller streak, as it can be directly observed in the u_s plots for cases 3 and 4 in Fig. 5. On the other hand, this figure also highlights the effect of the leading edge bluntness in the base flow. Focusing on the contour plots for cases 2 and 4, it can be seen that the wake flow structure presents a lower shear magnitude for these configurations and that the distance between contour lines is larger, which indicates that shear gradients are also smaller. Such characteristics point to a less unstable wake in these cases, as it will be shown later.

4.2. *Stability analysis*

Two-dimensional linear spatial stability analyses have been performed in the wake behind the roughness elements for each of the four cases listed in Table 3. Regarding the discretization employed to solve the generalized eigenvalue problem, interpolating polynomials of order $q = 8$ are considered in both spatial directions. For the self-similar inflow cases (cases 1 and 3), a grid resolution of $N_z = 121$ and $N_y = 101$ points is employed, whereas for the blunt leading edge inflow a resolution of $N_z = 101$ and $N_y = 81$ is used. The low-velocity streak induced behind the roughness elements supports the growth of different instability modes. For the roughness geometries under study, the authors have performed, in previous studies, computations of the spatial stability spectrum in a particular streamwise position and frequency in the wake behind the elements. The results can be found in reference [37] for the cuboidal roughness and in reference [38] for the ramp-shaped element. For both cases, the most amplified wake

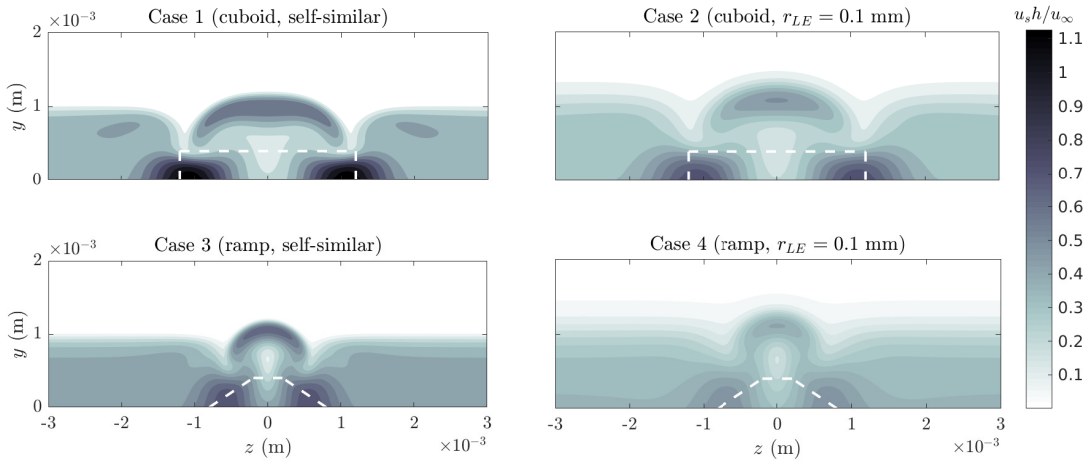

Figure 5: Contours of streamwise shear magnitude on a spanwise plane located behind the roughness elements at a streamwise distance of $x = 0.1$ m from the flat plate leading edge. The white solid lines represent a projection of the roughness element for each case.

modes were found to be varicose and sinuous instabilities developing in different regions around and inside the streak induced by the roughness elements. Several additional unstable modes were also found in the spatial spectra, corresponding to the first and second (Mack) instability modes, which are inherent to compressible boundary layer flows, along with the respective oblique families of modes that can be resolved by the two-dimensional eigenvalue problem discretization considered in the spanwise direction.

In this work, several streamwise locations and frequencies have been analyzed in order to find the most relevant instability mode for each case. Due to its high computational cost, the two-dimensional eigenvalue problem given by Eq. (14) is solved only at selected streamwise locations and frequencies and for a limited number of eigenvalues. This is done in order to find bounds for the stability characteristics of the wake base flow for each particular case. After identifying the most relevant instabilities and frequencies, an iterative algorithm is employed which computes the evolution of a single mode for a given range of positions. The results of the stability calculations performed in this study are summarized in Figs. 6, 7 and 8. Fig. 6 presents the streamwise evolution of the growth rate of the most unstable mode obtained for each case at the range of most amplified frequencies. Fig. 7 displays the magnitude of the two-dimensional streamwise velocity amplitude functions respectively associated to the most amplified instability for each case on the spanwise plane located at $x = 0.1$ m with respect to the flat plate leading edge. The streamwise evolution of the growth rate for each mode is started at the end of the separation bubble generated at the trailing edge of the roughness elements, denoted by $x_{b,TE}$ in Fig. 6, and is carried out all along the wake until the end of the computational domain, located at $x_{out} = 0.4$ m. As it can be observed in the contour plots of Fig. 7, the most unstable mode for all four cases is an instability developing in the low-velocity streak that characterizes the wake flow structure. The most amplified instability for case 1 has a varicose nature, as can be determined from its spanwise symmetric amplitude function, whereas for cases 2, 3 and 4 it manifests as a sinuous perturbation, featuring an antisymmetric eigenfunction in the spanwise direction with zero amplitude in the symmetry plane at $z = 0$. The varicose mode is mainly developing in the regions surrounding the streak while the sinuous mode shows higher amplitude values inside the streak. As shown in the shear magnitude plots in Fig. 5, the streak for the ramp cases is narrower and taller than for the cuboid ones, and as a result the instabilities for cases 3 and 4 develop in a smaller and higher area than in cases 1 and 2. Focusing on the growth rate evolution for each case, it can be seen that the instability modes feature maximum amplification rates just after the trailing edge separation bubble and then progressively decay downstream. This is coherent with the fact that the streamwise counter-rotating vortices induced by the roughness elements lose strength as they evolve downstream due to viscous dissipation. It is interesting to note the big differences in the growth rates achieved by the instability modes when a self-similar

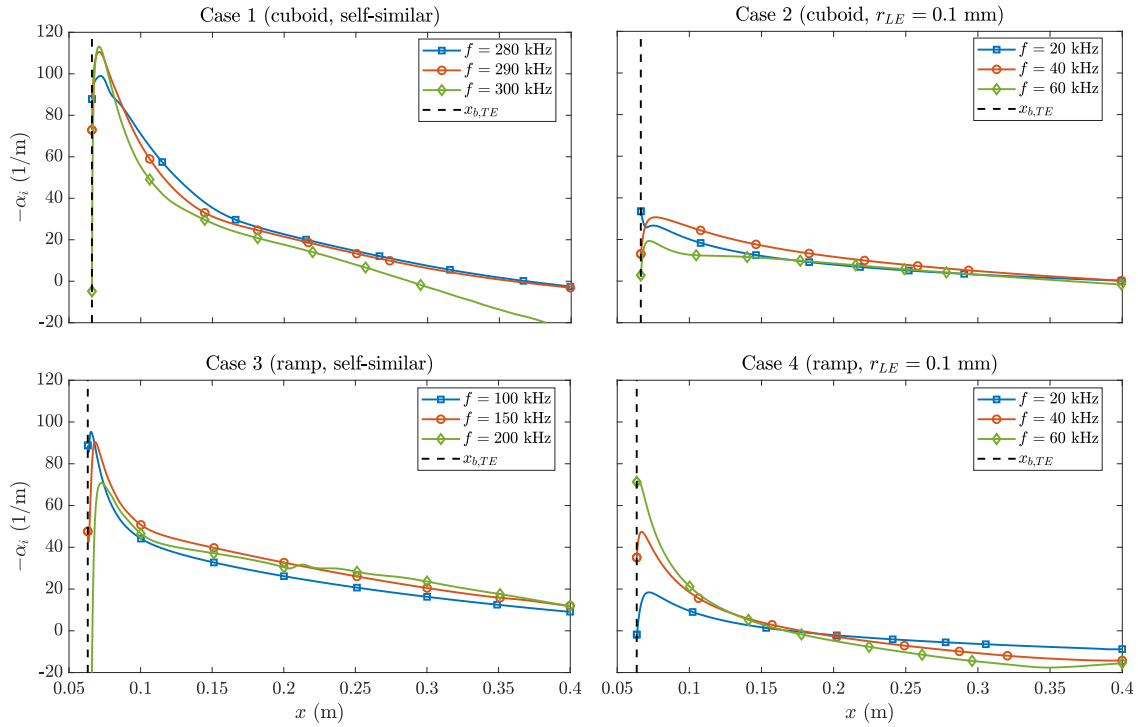

Figure 6: Streamwise evolution of the growth rate of the most unstable mode for each case at the respective range of most amplified frequencies. The dashed line located at $x_{b,TE}$ denotes the location of the end of the separation bubble generated at the trailing of the roughness elements.

inflow is considered (cases 1 and 3) as opposed to the case of the blunt leading edge inflow (cases 2 and 4). The entropy layer induced by the leading edge bow shock is introducing a strong stabilizing effect in the wake instabilities. Moreover, the range of unstable frequencies becomes smaller in the blunt leading edge cases. The stabilizing effect of entropy layers has been previously recognized in literature for the case of smooth blunt flat plates, wedges and cones, see for instance [39]. However, to the best of the authors' knowledge, no theoretical or numerical studies exist in the current literature that investigate this phenomenon in the case of isolated roughness-induced transition. Regarding the effect of the roughness shape, it can be seen that the growth rates reached by the instabilities in the self-similar inflow cuboid wake are significantly higher than the respective ones for the ramp geometry within the first centimeters behind the roughness element (approximately between $x_{b,TE}$ and $x = 0.1$ m). Further downstream, the ramp case (case 3) growth rates remain higher than in case 1. When a blunt leading edge is present, these trends are found to be inverted.

In order to obtain quantitative information about the transition onset location for each case, the integrated logarithmic amplification factors are computed, given by

$$N = \int_{x_0}^{x} -\alpha_i dx, \tag{16}$$

where x_0 is the streamwise location at which the perturbation becomes unstable. An important note must be made here regarding the definition of x_0 in this study. As it can be observed in the growth rate evolution plots (Fig. 6), in many cases the wake instability modes are already unstable at the first streamwise location in which they can be evaluated, namely, the end of the downstream separation bubble. In this situation, the N-factor is assumed to be equal to zero at this location and the integration is carried out from this point onwards. This is the same approach followed by similar studies in literature, see for instance [8; 15; 12]. Fig. 8 shows the N-factor curve obtained for each of the instabilities described before. The dotted line corresponds to the N-factor envelope of the most unstable mode developing in a smooth flat plate when a self-similar boundary layer is considered, which for the freestream conditions used in this work is the Mack mode. In agreement with the previous discussion, the

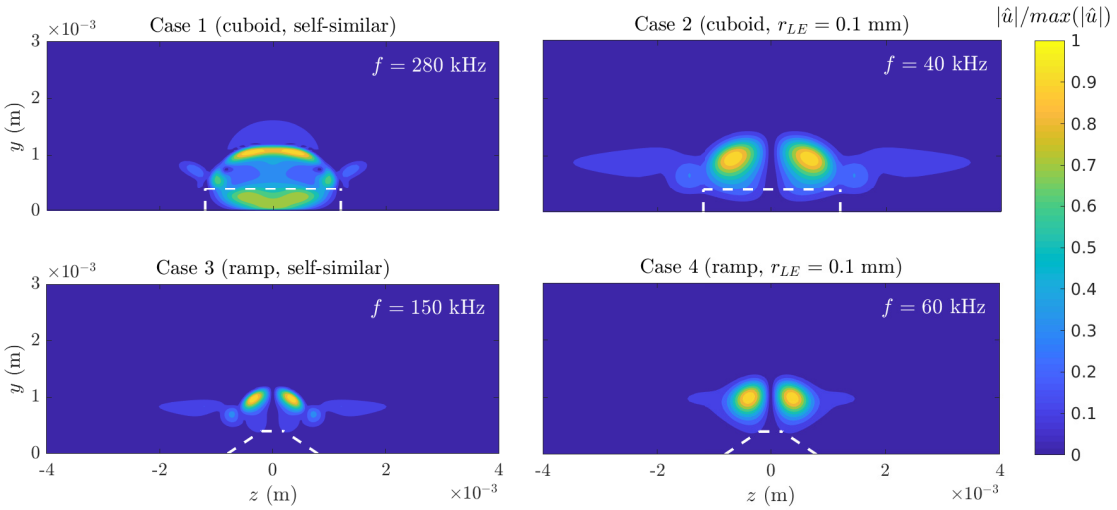

Figure 7: Contours of the normalized magnitude of the streamwise velocity eigenfunction of the most amplified instability mode for each case, on a plane located at a distance of $x = 0.1$ m from the flat plate leading edge.

highest N-factor values are reached by the sinuous instability mode developing in the wake behind the ramp roughness element when a self-similar inflow is considered (case 3). Nevertheless, larger N values are attained by the varicose instability in case 1 for the first half of the computational domain. To assess the impact of the roughness elements in the transition location, quiet and noisy reference values for N are considered. For quiet conditions, representative of a flight environment, a value of $N = 9$ is usually accepted, whereas for noisy conditions, more representative of a standard wind tunnel environment, values of N between 5 and 6 are usually employed. Here, a value of $N = 5.9$ is chosen for the noisy condition. Table 4 summarizes the transition onset locations estimated with the aforementioned criteria for cases 1 and 3 and for the self-similar boundary layer profile. As it can be observed, the presence of the roughness elements is significantly moving the transition location upstream, as compared to the natural transition process in the smooth flat plate as given by the Mack mode envelope. The varicose instability excited by the cuboid geometry (case 1) does not reach a value of $N = 9$ in the current analysis, although it is very close to it. However, it is the first mode to reach the noisy environment threshold at $x = 0.162$ m, 2 centimeters before the ramp wake instability in case 3. Comparing the transition locations against the smooth flat plate values, in-flight transition would be triggered about 27 centimeters earlier in the presence of the ramp roughness element, and about 12 and 10 centimeters before in a noisy environment with the cuboid and ramp geometries, respectively. Finally, cases 2 and 4 barely reach N values of 4 and 2, respectively, so transition is not expected to take place at these conditions. This shows the big influence that the flat plate leading edge can have in the transition onset location also in the presence of isolated roughness.

Table 4: Predicted transition onset locations. Units in meters.

Case	Quiet ($N = 9$)	Noisy ($N = 5.9$)
1 (varicose)	-	0.162
3 (sinuous)	0.294	0.182
Mack mode	0.562	0.278

5. Conclusions

The stability characteristics of the wake behind a cuboid and a ramp-shaped roughness element mounted on top of a flat plate inside a Mach 6 freestream have been investigated using two-dimensional linear stability theory. The base flows needed for the stability analysis were obtained by means of calorically perfect gas, laminar and steady Navier-Stokes simulations employing a second-order finite volume scheme. The roughness elements induce a strong pair of counter-rotating vortices that give rise to a mushroom-shaped streak through the

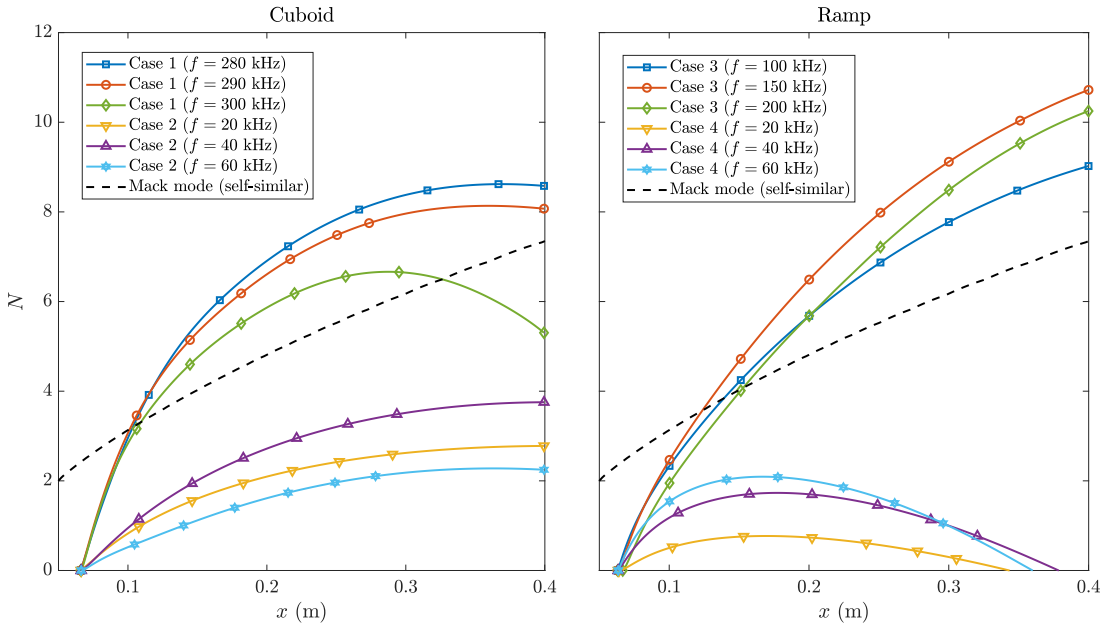

Figure 8: Integrated logarithmic amplification factors (N-factor) of the most unstable modes obtained for each case at the most amplified frequencies. The envelope of the Mack instability mode obtained with the self-similar boundary layer solution (smooth flat plate) is also shown for comparison.

lift-up of low-momentum fluid from the surface of the flat plate. This structure is surrounded by regions of high streamwise shear and large shear gradients in the wall-normal and spanwise directions. The ramp geometry also induces a small spanwise velocity component into the counter-rotating vortices that concentrates the vorticity in a smaller region and increases the lift-up of the streak, leading to a narrower and taller streak than in the cuboid case.

Spatial stability analyses were performed at different streamwise locations and frequencies along the wake behind the elements for four different cases, combining the two roughness shapes and two different inflow boundary layer profiles. The most unstable modes obtained for each case are varicose and sinuous instabilities that develop around and inside the low-velocity streak induced behind the elements. A varicose mode dominates the wake instability in case 1 while a sinuous mode dominates for cases 2, 3 and 4. The instabilities feature the highest amplification rates immediately after the downstream separation bubble generated at the trailing edge of the roughness elements and then decay progressively downstream along the wake. When a blunt flat plate leading edge is considered, lower growth rates are obtained, meaning that the entropy layer introduced by the leading edge bow shock has a strong stabilizing effect in the wake instabilities. In terms of N-factors, case 1 leads to the earliest transition onset in a noisy environment whereas case 3 is the only case that reaches the quiet transition threshold within the studied streamwise range. On the other hand, cases 2 and 4 are considerably less unstable and transition is not triggered at the conditions considered. Overall, the presence of the discrete roughness elements significantly accelerates the transition process as compared to the smooth flat plate boundary layer, indicated by the N-factor envelope of the second instability mode.

Acknowledgments

This work is part of a project that has received funding from the European Union's Horizon 2020 research and innovation programme under the Marie Skłodowska-Curie grant agreement No 675008.

References

[1] E. R. van Driest, The problem of aerodynamic heating, Aeronautical Engineering Review (1956) 26–41.

[2] D. C. Reda, Review and synthesis of roughness-dominated transition correlations for reentry applications, J. Spacecraft Rockets 39 (2) (2002) 161–167.

[3] E. Reshotko, Transition issues for atmospheric entry, J. Spacecraft Rockets 45 (2) (2008) 161–164.

[4] V. Theofilis, Global linear instability, Annu. Rev. Fluid Mech. 43 (2011) 319–352.

[5] G. Groskopf, M. J. Kloker, O. Marxen, Bi-global secondary stability theory for high-speed boundary-layer flows, in: Proceedings of the Summer Research Program 2008, Center for Turbulence Research, Stanford, CA, USA, 2008.

[6] M. Kegerise, R. King, L. Owens, M. Choudhari, A. Norris, F. Li, C.-L. Chang, An experimental and numerical study of roughness-induced instabilities in a Mach 3.5 boundary layer, RTO-AVT-200/RSM-030 29, NATO (2012).

[7] A. I. Ruban, M. A. Kravtsova, Generation of steady longitudinal vortices in hypersonic boundary layer, J. Fluid Mech. 729 (2013) 702–731.

[8] M. Choudhari, C. L. Chang, A. Norris, J. Edwards, Wake instabilities behind discrete roughness elements in high speed boundary layers, in: 51st AIAA Aerospace Sciences Meeting Including the New Horizons Forum and Aerospace Exposition, Grapevine, Dallas/Ft. Worth Region, USA, 7-10 January 2013, AIAA 2013-0081.

[9] N. De Tullio, P. Paredes, N. D. Sandham, V. Theofilis, Laminar-turbulent transition induced by a discrete roughness element in a supersonic boundary layer, J. Fluid Mech. 735 (2013) 613–646.

[10] N. De Tullio, N. D. Sandham, Influence of boundary-layer disturbances on the instability of a roughness wake in a high-speed boundary layer, J. Fluid Mech. 763 (2015) 136–165.

[11] V. Theofilis, Advances in global linear instability analysis of nonparallel and three-dimensional flows, Prog. Aerosp. Sci. 39 (2003) 249–315.

[12] P. Paredes, Advances in global instability computations: from incompressible to hypersonic flow, Ph.D. thesis, Universidad Politécnica de Madrid (2014).

[13] N. De Tullio, N. D. Sandham, Direct numerical simulations of roughness receptivity and transitional shock-wave/boundary-layer interactions, RTO-MP-AVT-200 22, NATO (2012).

[14] M. Choudhari, F. Li, M. Wu, C.-L. Chang, J. Edwards, M. Kegerise, R. King, Laminar-turbulent transition behind discrete roughness elements in a high-speed boundary layer, in: 48th AIAA Aerospace Sciences Meeting Including the New Horizons Forum and Aerospace Exposition, Orlando, FL, USA, 4-7 January 2010, AIAA 2010-1575.

[15] A. Theiss, S. Hein, Investigation on the wake flow instability behind isolated roughness elements on the forebody of a blunt generic re-entry capsule, EUCASS Book Series - Advances in AeroSpace Sciences 9 (2017) 451–480.

[16] A. Theiss, S. Hein, S. R. C. Ali, R. Radespiel, Wake flow instability studies behind discrete roughness elements on a generic re-entry capsule, in: 46th AIAA Fluid Dynamics Conference, Washington, DC, USA, 13-17 June 2016, AIAA 2016-4382.

[17] T. Bridges, P. Morris, Differential eigenvalue problems in which the parameter appears nonlinearly, J. Comput. Phys. 55 (1984) 437–460.

[18] S. D. Stouffer, N. R. Baker, D. P. Capriotti, G. B. Northam, Effects of compression and expansion ramp fuel injector configurations on scramjet combustion and heat transfer, in: 31st AIAA Aerospace Sciences Meeting and Exhibit, Reno, NV, USA, 11-14 January 1993, AIAA 1993-609.

[19] S. C. Tirtey, Characterization of a transitional hypersonic boundary layer in wind tunnel and flight conditions, Ph.D. thesis, Université Libre de Bruxelles and von Karman Institute for Fluid Dynamics (2009).

[20] Metacomp Technologies, CFD++ User Manual (2013).

[21] CFD Direct, OpenFOAM v6 User Guide: 5.3 Mesh generation with blockMesh (2018).

[22] F. Pinna, Numerical study of stability of flows from low to high mach number, Ph.D. thesis, Universitá "La Sapienza" di Roma and von Karman Institute for Fluid Dynamics (2012).

[23] F. Pinna, VESTA toolkit: a software to compute transition and stability of boundary layers, in: 43rd Fluid Dynamics Conference, San Diego, CA, USA, 24-27 June 2013, AIAA 2013-2616.

[24] MATLAB, Release 2018b, The MathWorks Inc., Natick, Massachussets, 2018.

[25] Maxima Manual Version 5.42.0 (2018).

[26] M. Hermanns, J. A. Hernández, Stable high-order finite-difference methods based on non-uniform grid point distributions, Int. J. Numer. Meth. Fluids 56 (2008) 233–255.

[27] P. Paredes, M. Hermanns, S. Le Clainche, V. Theofilis, Order 10^4 speedup in global linear instability analysis using matrix formation, Comput. Methods Appl. Mech. Engrg. 253 (2013) 287–304.

[28] L. N. Trefethen, Spectral Methods in MATLAB, SIAM, Philadelphia, 2000.

[29] M. R. Malik, Numerical methods for hypersonic boundary layer stability, J. Comput. Phys. 86 (2) (1990) 376–413.

[30] A. Esposito, Development and analysis of mapping and domain decomposition techniques for compressible shear flow stability calculations, Tech. Rep. VKI SR 2016-16, von Karman Institute for Fluid Dynamics (2016).

[31] C. B. Moler, G. W. Stewart, An algorithm for generalized matrix eigenvalue problems, SIAM J. Numer. Anal. 10 (2) (1973) 241–256.

[32] R. B. Lehoucq, D. C. Sorensen, Deflation techniques for an implicitly restarted Arnoldi iteration, SIAM J. Matrix Anal. A. 17 (4) (1996) 789–821.

[33] K. J. Maschhoff, D. C. Sorensen, P_ARPACK: An efficient portable large scale eigenvalue package for distributed memory parallel architectures, Lect. Notes Comput. Sc. 1184 (1996) 478–486.

[34] L. S. Blackford, J. Choi, A. Cleary, E. D'Azevedo, J. Demmel, I. Dhillon, J. Dongarra, S. Hammarling, G. Henry, A. Petitet, K. Stanley, D. Walker, R. C. Whaley, ScaLAPACK Users' Guide, Society for Industrial and Applied Mathematics, 1997.

[35] K. J. Groot, Q. Ye, B. W. van Oudheusden, Y. Zhang, F. Pinna, BiGlobal stability analysis of a micro-ramp wake using PIV base flows, in: 46th AIAA Fluid Dynamics Conference, Washington, DC, USA, 13-17 June 2016, AIAA 2016-4383.

[36] D. S. Liechty, S. A. Berry, B. R. Hollis, T. J. Horvath, Comparison of methods for determining boundary layer edge conditions for transition correlations, in: 33rd AIAA Fluid Dynamics Conference and Exhibit, Orlando, FL, USA, 23-26 June 2003, AIAA 2003-3590.

[37] I. Padilla Montero, F. Pinna, BiGlobal stability analysis of the wake behind an isolated roughness element in hypersonic flow, Proceedings of the Institution of Mechanical Engineers, Part G: Journal of Aerospace Engineering.

[38] I. Padilla Montero, F. Pinna, Stability analysis of the boundary layer developing on a flat plate with discrete roughness elements in hypersonic flow, in: 2018 AIAA Aerospace Sciences Meeting, AIAA SciTech Forum, Kissimmee, FL, USA, 8-12 January 2018, AIAA 2018-1079.

[39] P. Balakumar, Stability of supersonic boundary layers over blunt wedges, in: 36th AIAA Fluid Dynamics Conference and Exhibit, San Francisco, CA, USA, 5-8 June 2006, AIAA 2006-3053.

RAREFIED AND PLASMA FLOWS

Elastic and Ionisation Cross Sections for DSMC simulations of Metallic Vapours in Meteor Hyperthermal Environments

Federico Bariselli

Aeronautics and Aerospace Department, von Karman Institute for Fluid Dynamics, Belgium, federico.bariselli@vki.ac.be

Supervisor: Thierry Magin

Professor, Aeronautics and Aerospace Department, von Karman Institute for Fluid Dynamics, Belgium, thierry.magin@vki.ac.be

University Supervisor: Aldo Frezzotti

Professor, Aerospace Science and Technology Department, Politecnico di Milano, Italy, aldo.frezzotti@polimi.it

University Supervisor: Annick Hubin

Professor, Electrochemical and Surface Engineering Department, Vrije Universiteit Brussel, Belgium, annick.hubin@vub.ac.be

Abstract

The transport properties of the ablated vapour are computed following the Chapman-Enskog theory and the DSMC phenomenological parameters are retrieved by fitting the collision integrals over a wide range of temperatures. Semi-empirical inelastic cross sections for direct and electron impact ionisation of metals are computed analytically and casted into DSMC steric factors.

Keywords: transport properties, hyperthermal chemistry, Direct Simulation Monte Carlo, meteor

1. Introduction

About 50 tonnes of small meteoroids enter the terrestrial atmosphere every day [1]. These bodies, from one meter diameter to micron-size grains, originate either from sublimating comets or from colliding asteroids. In their rush to the ground, they intersect the atmosphere at hypersonic velocities up to 72 km/s. As a meteoroid interacts with the atmosphere, its surface temperature can reach several thousands of kelvins causing its ablation, i.e. melting, and evaporation, the latter responsible of the metallic layer in the mesosphere and lower thermosphere for which it plays an essential role as source term of the chemical mechanism [2].

Due to their small size and tremendous speeds, meteoroids often burn up at high altitudes, above 80 km, where the atmosphere is rarefied. Here, the gas cannot be treated in the continuum assumption and the Navier-Stokes equations usually employed in Gasdynamics fail [3]. Moreover, the high energies involved activate coupled physico-chemical phenomena in both the gas and solid phases (strong departure from thermo-chemical equilibrium, radiative heating, ionisation and complex gas-surface interactions), making the prediction of these flows a challenging task.

Ground radar and radio stations are able to detect free electrons concentrations in the meteoroid wake, which are directly influenced by the ablation mechanism (Ceplecha [4] et al. estimated that 90% of the meteor light originates from inelastic collisions of vaporised metallic atoms). In fact, the classic formula for the formation of the ionised trail reads as follows

$$q = -\frac{\beta}{\mu V_\infty}\frac{dm}{dt}, \tag{1}$$

where the number of electrons produced per meter, q, by an ablation meteoroid of mass m, moving at speed V_∞, is function of the ionisation coefficient $\beta(V_\infty)$ [5]. Equation 1 is phenomenological in nature, hence, poorly accounts for the correct evaporation rate of the material, detailed chemistry and diffusion in the vapour phase, and rarefied gas effects.

Classical meteor ablation models were derived under the assumption of free-molecular flow and evaporation into vacuum. The simplest among these models assumes that the mass loss rate is proportional to the kinetic energy imparted on the meteoroid, with the ablation beginning when the surface of the meteoroid reaches the boiling point [6]. Campbell-Brown et al. [7] inferred that this model is not valid for meteoroids of lower densities for which the ablation may start before the boiling temperature is reached. They proposed an ablation model applying the Hertz-Knudsen formula

$$\frac{dm}{dt} = n_{\mathrm{w}}^{\mathrm{eq}} \sqrt{\frac{\mu k_{\mathrm{B}} T_{\mathrm{w}}}{2\pi}}, \tag{2}$$

in which μ is the average meteoric atom, k_{B}, the Boltzmann constant, and T_{w} the surface temperature, coupled with the Clausius-Clapeyron relation to compute the equilibrium number density, $n_{\mathrm{w}}^{\mathrm{eq}}$, of the melt-vapour phase transition.

As reported by Silber [8] in her comprehensive review on meteor shock waves, computational studies in this field are relatively sparse with the consequence of a lack of understanding of the relevant rarefied hypersonic flow. Boyd [9] was the first to address the problem of the ablation of meteors in the rarefied regime by giving a detailed description of the phenomenon from the flowfield perspective. He treated the meteor material as a single species, i.e. magnesium, using a phenomenological ablation model accounting for evaporation of the metal and assuming a vaporisation temperature of 2500 K. No chemical reactions were considered in the gas phase. Bird's Direct Simulation Monte Carlo (DSMC) method [10] was also used by Vinkovic [11] to predict the emission of light by very high altitude meteors detected from the ground, not explainable by means of classical ablation theory. The study focused on the sputtering from the meteoroid surface. Strong assumptions were made, such as no distinction between atomic and molecular species in the gas phase. Other physical processes like vaporisation, ionisation, dissociation, and excitation were not included. A simplified particle-based approach was developed by Stokan et al. [12] to model the space resolved trail luminosity of faint meteors in direct connection to the local number of collisions.

In the attempt to reduce the uncertainties related to the resulting ionisation efficiency for the interpretation of radar/radio detection measurements, in this work, we compute elastic and inelastic cross sections suitable for DSMC simulations and we review them in the light of the experimental and theoretical data available in literature. The meteoric material is assumed to be composed by a mixture of metal oxides which are typically present in ordinary chondritic meteorites [13].

The paper is structured as follows. In the next section, the transport properties of the ablated vapour are computed in the framework of the Chapman-Enskog theory and the DSMC phenomenological parameters are retrieved by fitting the collision integrals over a wide range of temperatures. Finally, in Section 3, inelastic cross sections for direct and electron impact ionisation of metals are computed analytically and recasted into the form of DSMC steric factors.

2. Transport properties of the ablated vapour

Experimental data on transport properties of alkali metal vapours are scarce due to the high temperatures required, low vapour pressures, and corrosive nature [14]. Kinetic theory provides the mathematical framework which allows to link interatomic forces to transport coefficients. As a result of the Chapman-Enskog expansion [15], the binary viscosity coming from the interaction between species i and j reads:

$$\eta_{ij} = \frac{5}{8} \frac{k_{\mathrm{B}} T}{\Omega_{ij}^{(2,2)}} \tag{3}$$

$\Omega_{ij}^{(2,2)}$ represents the so-called *collision integral*, which is obtained by integrating a first time the collision cross section over all the possible impact parameters, b, characterising the binary collision and, a second time, over the near-equilibrium distribution of relative velocities, g:

$$\begin{aligned} \Omega_{ij}^{(2,2)} = & \sqrt{\frac{2\pi k_{\mathrm{B}} T}{\mu_{ij}^{\mathrm{R}}}} \\ & \times \int_0^{+\infty} \int_0^{+\infty} e^{-\gamma_{ij}^2} \gamma_{ij}^5 (1 - \cos^2\chi) b db \, d\gamma \end{aligned} \tag{4}$$

in which $\gamma_{ij}^2 = \frac{\mu_{ij}^{\mathrm{R}} g_{ij}^2}{2 k_{\mathrm{B}} T}$ is a reduced relative velocity and $\mu_{ij}^{\mathrm{R}} = \frac{\mu_i \mu_j}{\mu_i + \mu_j}$ the reduced mass. The scattering angle, $\chi = \chi(b, g, \psi)$, resulting from the dynamic of the binary collision, directly depends on the relevant interatomic potential, ψ. Each type of collision (e.g. neutral-neutral, ion-neutral, etc.) would require a different type of potential. However, this procedure quickly becomes cumbersome. In this work, we employ the Lennard-Jones potential:

$$\psi(r_{ij}) = 4\epsilon_{ij} \left[\left(\frac{\bar{\sigma}_{ij}}{r_{ij}} \right)^{12} - \left(\frac{\bar{\sigma}_{ij}}{r_{ij}} \right)^{6} \right] \tag{5}$$

which consists of two parts: a steep repulsive term and smoother attractive term. ϵ_{ij} is the depth of the potential well, $\bar{\sigma}_{ij}$ is the finite distance at which the inter-particle potential is zero and r_{ij} is the distance between the particles.

In order to obtain theoretical viscosity curves for single species vapours, we compute $\Omega_{ii}^{(2,2)}$. For this procedure the Lennard-Jones (6-12) parameters of Table 1 have been employed.

Combination rules for polyatomic species whose potential parameters are not available in literature are used as proposed in their work by André et al. [16]:

$$\begin{aligned} \bar{\sigma}_{\mathrm{SiO_2\text{-}SiO_2}} &= (\bar{\sigma}^3_{\mathrm{Si\text{-}Si}} + \bar{\sigma}^3_{\mathrm{O\text{-}O}} + \bar{\sigma}^3_{\mathrm{O\text{-}O}})^{1/3} \\ \epsilon_{\mathrm{SiO_2\text{-}SiO_2}} &= (\epsilon_{\mathrm{Si\text{-}Si}}\ \epsilon_{\mathrm{O\text{-}O}}\ \epsilon_{\mathrm{O\text{-}O}})^{1/3} \end{aligned} \tag{6}$$

In Figure 1, a comparison between our prediction and a few sets of available experimental results [19; 20; 21; 22] is provided. Differences between theory and experiments may come from the presence of molecules or ions in the vapours. Important uncertainty on the potential parameters are likely to be present and one could also argue that the Lennard-Jones potential (6-12) does not apply to alkali metals such as potassium. Ghatee et al. [14] stated that it fails in the prediction of transport properties of K, Rb, and Cs metals vapour especially in the low temperature range. Nonetheless, in our study, the comparison turns out to be fair, with Na's viscosity which lays between the two sets of data and the K's extremely close. The comparison for K's conductivity, computed as:

$$\lambda_{ii} = \frac{15}{4}\frac{k_\mathrm{B}}{\mu_i}\eta_{ii} \tag{7}$$

is even excellent.

2.1. DSMC elastic cross sections

In DSMC, the transport properties are the natural result of the simulated binary collisions. DSMC relies on a phenomenological potential to make molecules interact. Although apparently simplistic, these models are able to reproduce to some extent the most salient physics of the collision process, with the advantage of being computationally cheap. In the Variable Soft Sphere (VSS) model, molecules are approximated as rigid spheres of diameter d, which depends on the relative velocity of the impact. The total cross section is written as:

$$\sigma_T\Big|_{\mathrm{VSS}} = \pi d_{\mathrm{ref}}^2 \left(\frac{g_{\mathrm{ref}}}{g}\right)^{2\omega-1} \tag{8}$$

The quantities d_{ref} and g_{ref} are reference values evaluated at a reference temperature T_{ref}, whereas ω is the temperature exponent which allows the variation of the particle diameter with temperature. In this way, molecules with higher impact energies spend less time interacting on the potential energy surface. In the VSS model, the scattering law reads:

$$\chi\Big|_{\mathrm{VSS}} = 2\cos^{-1}\left\{\left(\frac{b}{d}\right)^{1/\alpha}\right\} \tag{9}$$

which allows to model anisotropic scattering events through the exponent α (where $\alpha = 1$ corresponds to an isotropic scattering law). It is well known that such a model fails in the attempt of capturing diffusion processes in mixtures of gases and that the anisotropy of neutral-charged collisions in weakly ionised gases is not accurately described [23]. In DSMC, the collision parameters are obtained by averaging the properties of the collision partners: $d_{\mathrm{ref}_{ij}} = (d_{\mathrm{ref}_i} + d_{\mathrm{ref}_j})/2$, $\omega_{ij} = (\omega_i+\omega_j)/2$, $\alpha_{ij} = (\alpha_i+\alpha_j)/2$. The collision integrals of Equation 4, $\Omega_{ii}^{(2,2)}$ can be expressed as function of the VSS model parameters:

$$\begin{aligned} \Omega_{ii}^{(2,2)}\Big|_{\mathrm{VSS}} = \frac{4\alpha_i}{(\alpha_i+1)(\alpha_i+2)}\frac{\pi d_{\mathrm{ref}_i}^2}{2}\sqrt{\frac{k_\mathrm{B}T}{2\pi\mu_{ii}^\mathrm{R}}} \\ \times\left(\frac{T_{\mathrm{ref}_i}}{T}\right)^{\omega_i-1/2}\frac{\Gamma(9/2-\omega_i)}{\Gamma(5/2-\omega_i)} \end{aligned} \tag{10}$$

Starting from Equation 10, an independent least squares fitting is performed to obtain the VSS parameters for each collision pair (see Figure 2) $T_{\mathrm{ref}} = 1000$ K has been chosen as reference temperature. The fitting has been done in such a way that the error is minimised in the range of temperatures between 800 K and 4000 K. This is indeed the range of temperature of the metallic species, which are emitted from the surface with temperatures in the vaporisation range. Table 2 reports the VSS parameters obtained through this procedure.

3. Ionisation chemistry resulting from hyperthermal collisions

In meteors, free electrons are mostly produced by collisions of metal atoms with atmospheric molecules [24]. Meteor spectra give an indication in this sense, as they are dominated by atomic lines of meteoric origin, mostly neutral atoms, but also singly ionised ions [25]. The physico-chemical processes leading to the

Table 1: Lennard-Jones interatomic potential parameters employed to compute collision integrals for neutral-neutral collisions of metallic species.

Interaction	$\bar{\sigma}$ [A]	ϵ/k_B [K]	Reference
Si-Si	2.910	3036.0	[17]
Mg-Mg	2.926	1614.0	[17]
Al-Al	2.655	2750.0	[17]
Fe-Fe	2.468	7556.0	[18]
Ca-Ca	4.517	50.000	[18]
Na-Na	3.567	1375.0	[17]
K-K	4.250	850.00	[18]
SiO-SiO	3.516	461.00	Combination rules
SiO_2-SiO_2	3.964	245.94	Combination rules
MgO-MgO	3.527	336.12	Combination rules
Al_2-Al_2	3.345	2750.0	Combination rules
AlO-AlO	3.345	542.00	Combination rules
Al_2O_2-Al_2O_2	4.219	438.75	Combination rules
FeO-FeO	3.235	727.27	Combination rules
CaO-CaO	4.806	59.161	Combination rules
Na_2-Na_2	4.494	1375.0	Combination rules
NaO-NaO	4.004	310.24	Combination rules
Na_2O-Na_2O	4.786	509.61	Combination rules
K_2-K_2	5.354	850.00	Combination rules
KO-KO	4.572	243.93	Combination rules
K_2O-K_2	5.565	369.81	Combination rules

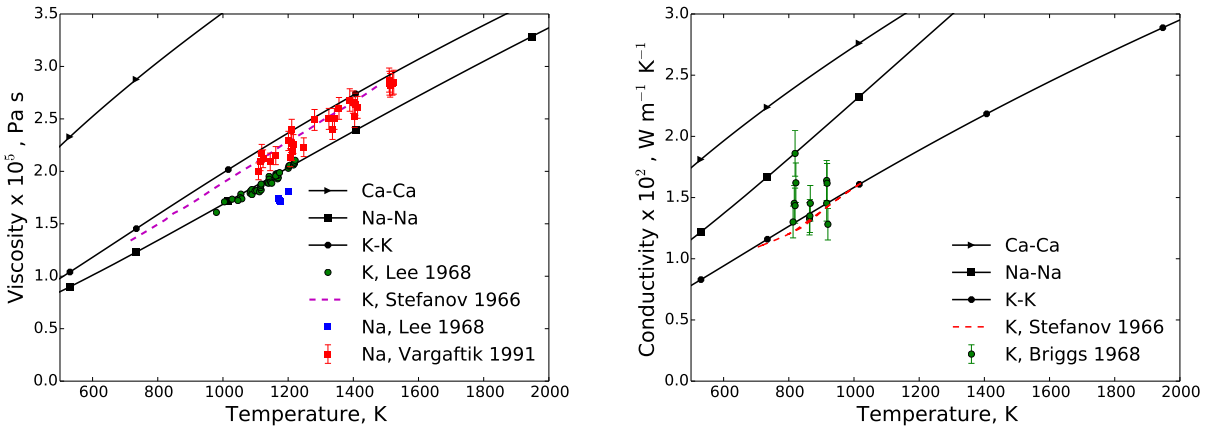

(a) (b)

Figure 1: Shear viscosity (a) and thermal conductivity (b) for some alkali atoms and comparison with available experimental data. Ca, which is not an alkali metal, is kept as a reference.

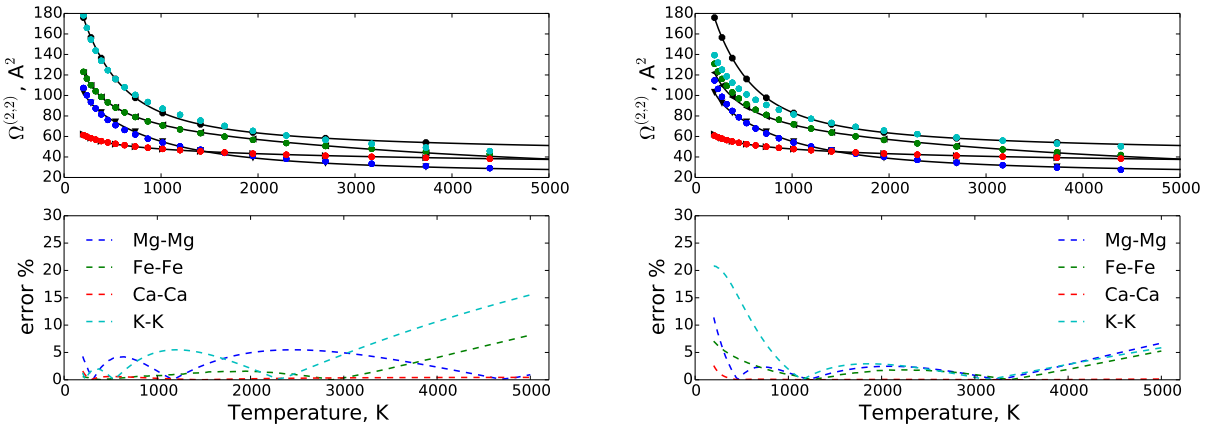

(a) (b)

Figure 2: Fitting procedure of the VSS collision integrals with their exact formulation for some metallic atoms. Two possible choices are proposed, (a) to minimise the error between 200 and 5000 K or to (b) minimise the error between 800 and 4000 K.

Table 2: Variable Soft Sphere (VSS) parameters obtained by fitting the collision integral $\Omega_{ii}^{(2,2)}$ for T_{ref} = 1000 K. This procedure is equivalent to tuning VSS parameters to experimental viscosity data. The average fitting error is reported for the range between 800 K and 4000 K.

Interaction	d_{ref} [A]	ω [-]	α [-]	Error % [-]
Si-Si	5.991	0.985	1.293	0.99
Mg-Mg	5.091	0.962	1.370	1.53
Al-Al	5.362	0.991	1.377	0.77
Fe-Fe	5.605	0.869	1.225	1.09
Ca-Ca	4.117	0.648	1.170	0.04
Na-Na	5.865	0.934	1.250	1.86
K-K	5.862	0.830	1.177	2.04
SiO-SiO	4.071	0.721	1.223	1.23
SiO_2-SiO_2	4.140	0.667	1.181	0.48
MgO-MgO	3.847	0.687	1.213	0.80
Al_2-Al_2	6.771	0.991	1.228	0.77
AlO-AlO	4.021	0.744	1.246	1.48
Al_2O_2-Al_2O_2	4.843	0.715	1.168	1.16
FeO-FeO	4.226	0.797	1.276	1.89
CaO-CaO	4.431	0.648	1.183	0.03
Na_2-Na_2	7.377	0.934	1.356	1.86
NaO-NaO	4.318	0.681	1.180	0.71
Na_2O-Na_2O	5.679	0.735	1.176	1.38
K_2-K_2	7.355	0.830	1.450	2.04
KO-KO	4.771	0.667	1.178	0.47
K_2O-K_2	6.180	0.696	1.171	0.92

excitation and ionisation of metallic atoms are lumped classically into the ionisation coefficient β, that we have introduced in Equation 1 and that is defined as the ratio between the number of electrons produced and the number of vaporised atoms. As shown by Jones [5], this coefficient can be decomposed into two contributions. The first represents the proportion of particles β_0 ionising at the first collision:

$$\beta_0 = \frac{c(V_\infty - V_0)^2 \, V_\infty^{0.8}}{1 + c(V_\infty - V_0)^2 \, V_\infty^{0.8}} \tag{11}$$

where the parameter c is a constant calibrated by experimental data and V_0 the ionisation threshold velocity. The second contribution to the ionisation coefficient is proportional to $(1 - \beta_0)$ and mimics the dynamics of the gas phase, hence the probability with which a collision subsequent to the first one can lead to the formation of an electron.

The most extensive review on the gas-phase chemical dynamics involving metallic species was provided by Dressler [24]. Although a considerable body of literature exists for thermalised metal chemistry, reliable cross sections for hyperthermal collisions (1 to 1000 eV, corresponding to relative velocities of 3-100 km/s) seem to exist only for Na and K, and a substantial experimental effort would be required [2]. While ion beams generator are standard technology and the knowledge about metal-ion inelastic collisions is relatively established, the same cannot be said of metal-neutral interactions, given the associated experimental difficulties.

A source (or a sink) for metal atoms or ions is represented by reactive processes involving molecular or atomic oxygen, and trace species in the atmosphere such as ozone, which, at collision energies below 20 eV, may lead to metal compounds. A study on the formation of molecules in thermochemical equilibrium was conducted by Berezhnoy et al. [25], starting from the experimental evidences of observed spectra. In particular, the process

$$\mathrm{M} + \mathrm{O_2} \rightarrow \mathrm{MO^+} + \mathrm{O} \tag{12}$$

forms ionic oxides which are immediately depleted by the fast dissociative recombination reaction

$$\mathrm{MO^+} + \mathrm{e^-} \rightarrow \mathrm{M} + \mathrm{O} \tag{13}$$

the latter partially responsible of the dissipation of free electrons at altitudes below 80 km [26].

At 100 eV, chemical reactions which lead to the break and formation of new chemical bonds are no longer important processes. Instead, inelastic collisions consisting with transitions to electronically excited atoms are more probable. However, theoretical and experimental studies are sparse and this information is not available even for simple systems. Friichtenicht et al. [27] measured the degree of ionisation of fast particles injected into a thick gas target. They found out an approximate $\sim V_\infty^4$ dependence of the ionisation cross sections, higher than the semi-empirical relation $\sim V_\infty^{3.42}$ from Bronshten [6], but in agreement with the observational investigations by Verniani et al. [28]. Data on fast alkali neutral metal beams with N_2 and O_2 gases were provided by the experiments of Bydin et al. [29] and Cuderman et al. [30]. Although leading to different results, these works showed a similar trend as the O_2 cross sections resulted more than an order of magnitude higher than those for N_2. Very few studies [31; 32] report measurements of fast Ca, Mg, Si, and Fe collisions in N_2 and O_2 gases, producing cross sections generally lower than those observed for the alkali metals, whose ionisation potentials are inferior. However, the accuracy of these data is questionable.

From the analytical point of view, a reliable theory to predict direct impact ionisation is still under developed. Kunc [33] summarised the available approaches. Since ionisation starts with no electrons present, the electron production in the rarefied part of a meteor trajectory must begin with heavy-heavy collisions of the following type:

$$\mathrm{M} + \mathrm{N_2} \rightarrow \mathrm{M^+} + \mathrm{N_2} + \mathrm{e^-} \tag{14}$$

When a sufficient number of electrons has been produced ionisation by electron-heavy impact can take over as the dominant process:

$$\mathrm{M} + \mathrm{e^-} \rightarrow \mathrm{M^+} + 2\mathrm{e^-} \tag{15}$$

Moreover, a substantial contribution to the production of free electrons can be given by photoionisation processes of the following type:

$$\mathrm{M} + h\nu \rightarrow \mathrm{M^+} + \mathrm{e^-} \tag{16}$$

and in minor part by secondary impact ionisation reactions, involving doubly ionised species. However, these two mechanisms will not be considered in this study.

In this work, we employ Drawin semi-empirical cross sections [34] to obtain an estimate of direct and electron impact ionisation processes. For the former,

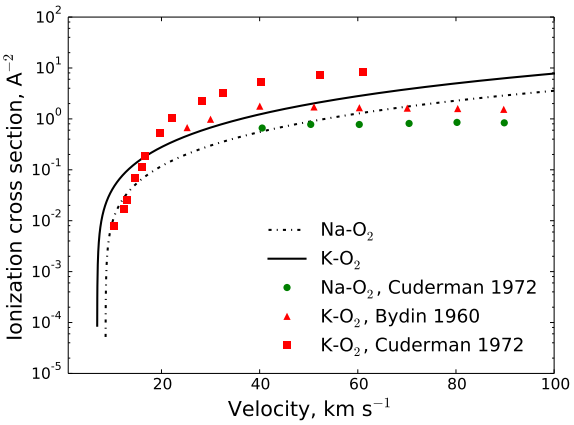

Figure 3: Drawin cross sections computed for direct impact ionisation are compared with available experimental data [29; 30].

the cross section reads

$$\sigma_{\mathrm{I}} = 4\pi a_0^2 \left(\frac{E_{\mathrm{H}}}{E_0}\right)^2 \frac{m_{\mathrm{A}}}{m_{\mathrm{H}}} \xi_0^2 \frac{2m_{\mathrm{e}}}{m_{\mathrm{e}} + m_{\mathrm{A}}} \times (W_0 - 1)\left(1 + \frac{2m_{\mathrm{e}}}{m_{\mathrm{e}} + m_{\mathrm{A}}}(W_0 - 1)\right)^{-2} \quad (17)$$

where $W_0 = E_{\mathrm{c}}/E_0$, being E_{c} the energy of the collision, E_0 the ionisation energy, m_{A} and m_{e} the mass of the incident atom and of an electron. E_{H}, m_{H}, and a_0 are respectively the ionisation energy, the mass, and the first Bohr radius of atomic hydrogen. Finally, ξ_0 represents the number of equivalent electrons in the outer (ground state) shell of the target atom.

In Figure 3 and 4, we provide a comparison of the cross sections obtained in this work with the experimental results of Bydin et al. [29] and Cuderman et al. [30] for direct impact ionisation and the data recommended by Lennon [35] for electron impact ionisation. Results are in reasonable agreement with those reported in literature. In particular, electron impact cross sections by Drawin seem to perform well close to the ionisation threshold for all the species. For Si, Na, and K, however, the analytic cross sections seem to under-predict the recommended values at higher impact energies.

Moreover, electron-heavy ionisation cross sections are characterised by a peak not far from the ionisation threshold and after they decrease (Figure 4). Similarly, this maximum is present in heavy-heavy cross sections, but it occurs at energy values which are higher than those of interest in this work.

3.0.1. DSMC inelastic cross sections

Chemical reactions from the NASA Air-11 mixture [36] are accounted through Bird's Total Collision Energy (TCE) method [10]. This method consists of assuming an analytic form for the collision-dependent reaction cross section:

$$\sigma_{\mathrm{I}}\Big|_{\mathrm{TCE}} = \begin{cases} 0 & \text{if } E_{\mathrm{c}} < E_0 \\ C_1(E_{\mathrm{c}} - E_0^{C_2}(1 - E_0/E_{\mathrm{c}})^{C_3} & \text{if } E_{\mathrm{c}} \geq E_0 \end{cases} \quad (18)$$

When averaging this cross section over a Maxwellian velocity distribution, it is possible to equate it to the known rate coefficient in Arrhenius form. Direct and electron impact ionisation processes of metals have been added to the Park's mechanism which already includes associative and electron impact ionisation of air species. The semi-empirical cross sections of Equation 17 have been fitted into the phenomenological cross section of Equation 18. In DSMC, the algorithm computes the probability with which a collision can result in a reaction according to a steric factor obtained as the ratio $\sigma_{\mathrm{I}}/\sigma_{\mathrm{T}}$ which, on turn, can be expressed as β_0. A comparison between values of β_0 computed by Equation 11 as given by [5] and the DSMC steric factors obtained in this work is given in Figure 5.

4. Conclusions

DSMC is a well established method for the study of transitional flows, where analytical solutions cannot be found and the hydrodynamic regime does not hold. Hence, it is the ideal technique for the study of meteor flows, not least for the simplicity with which it is possible to include physical models.

The transport properties of the ablated vapour have been computed following the Chapman-Enskog theory and the DSMC phenomenological parameters have been retrieved by fitting the collision integrals over a wide range of temperatures. Moreover, we have compared predicted values of viscosity and thermal conductivity with experimental data available in the literature for some neutral alkali species. In a second step, semi-empirical inelastic cross sections for direct and electron impact ionisation of metals have been computed analytically and casted into DSMC steric factors. These new DSMC inelastic cross sections have been compared with classical ionisation efficiencies employed by the meteor community.

We hope that this set of data, comprising of elastic and inelastic cross sections, will be useful for scien-

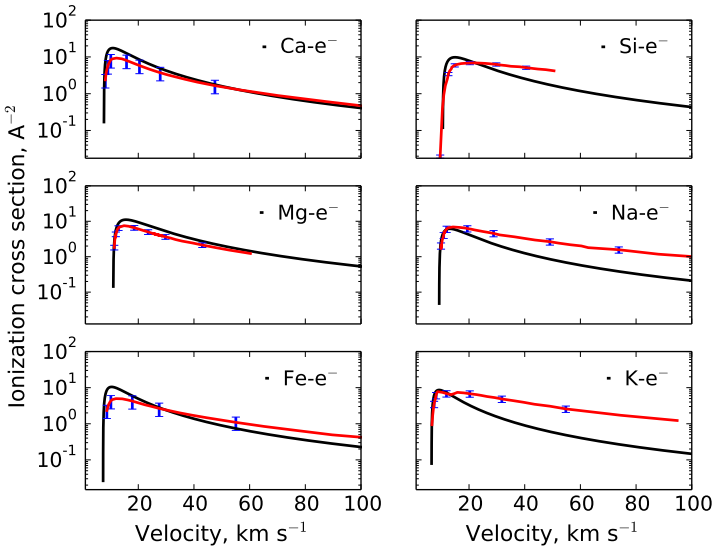

Figure 4: Drawin cross sections computed for electron impact ionisation — are compared with recommended data provided by Lennon [35] —.

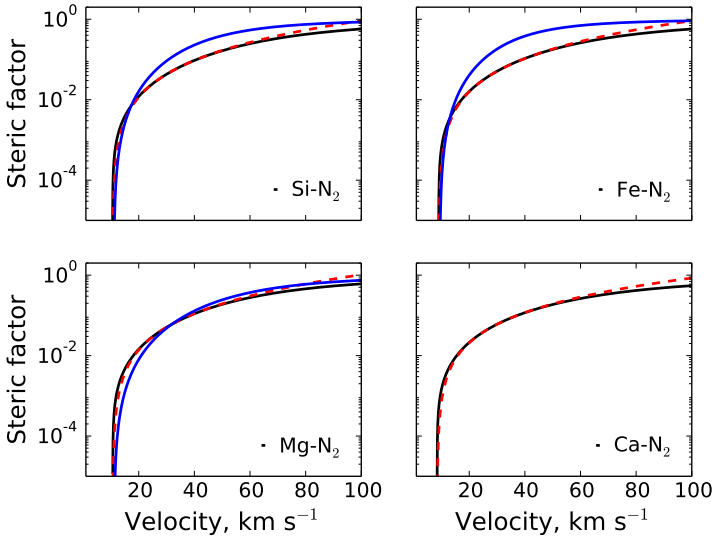

Figure 5: The steric factors computed in this work — and their fitting into a DSMC form — are compared with β_0 coefficients provided by Jones [5] —.

tists as a reference database in future simulations and studies.

Acknowledgments

The research presented here was funded by a PhD grant of the Research Foundation Flanders (FWO).

References

[1] T. Vondrak, J. M. C. Plane, S. Broadley, D. Janches, A Chemical Model of Meteoric Ablation, Atmospheric Chemistry and Physics 8 (23) (2008) 7015–7031.

[2] J. M. C. Plane, W. Feng, E. C. M. Dawkins, The Mesosphere and Metals: Chemistry and Changes, Chemical Reviews 115 (10) (2015) 4497–4541.

[3] E. Josyula, J. Burt, Review of Rarefied Gas Effects in Hypersonic Applications, Tech. rep., RTO-EN-AVT-194 (2011).

[4] Z. Ceplecha, J. Borovicka, W. G. Elford, D. O. ReVelle, R. Hawkes, V. Porubcan, M. Simek, Meteor Phenomena and Bodies, Space Science Reviews 84 (3) (1998) 327–471.

[5] W. Jones, Theoretical and observational determinations of the ionization coefficient of meterors, Monthly Notices of the Royal Astronomical Society.

[6] V. A. Bronshten, Physics of Meteoric Phenomena, D. Reidel Publishing Co., 1983.

[7] M. D. Campbell-Brown, D. Koschny, Model of the Ablation of Faint Meteors, Astronomy and Astrophysics 418 (2) (2004) 751–758.

[8] E. A. Silber, M. Boslough, W. K. Hocking, M. Gritsevich, R. W. Whitaker, Physics of meteor generated shock waves in the earths atmosphere a review, Advances in Space Research 62 (3) (2018) 489 – 532.

[9] I. D. Boyd, Computation of Atmospheric Entry Flow About a Leonid Meteoroid, Earth, Moon and Planets 82 (2000) 93–108.

[10] G. A. Bird, Molecular Gas Dynamics and the Direct Simulation of Gas Flows, Oxford University Press, 1994.

[11] D. Vinković, Thermalization of Sputtered Particles as the Source of Diffuse Radiation from High Altitude Meteors, Advances in Space Research 39 (4) (2007) 574–582.

[12] E. Stokan, M. D. Campbell-Brown, A Particle-Based Model for Ablation and Wake Formation in Faint Meteors, Monthly Notices of the Royal Astronomical Society 447 (2) (2015) 1580–1597.

[13] B. Fegley, A. G. W. Cameron, A Vaporization Model for Iron/Silicate Fractionation in the Mercury Protoplanet, Earth and Planetary Science Letters 82 (1987) 207–222.

[14] M. H. Ghatee, F. Niroomand-Hosseini, Hard-Wall Potential Function for Transport Properties of Alkali Metal Vapors, The Journal of Chemical Physics 126 (1) (2007) 014302.

[15] R. B. Bird, W. E. Stewart, E. N. Lightfoot, Transport Phenomena, John Wiley and Sons, 1960.

[16] P. André, J. Aubreton, S. Clain, M. Dudeck, E. Duffour, M. F. Elchinger, B. Izrar, D. Rochette, R. Touzani, D. Vacher, Transport Coefficients in Thermal Plasma. Applications to Mars and Titan atmospheres, Eur. Phys. J. D 57 (2) (2010) 227–234.

[17] R. Svehla, Estimated Viscosities and Thermal Conductivities of Gases at High Temperatures, Tech. rep., NASA-TR-R-132 (1962).

[18] B. C. McGee, M. L. Hobbs, M. R. Baer, Exponential 6 Parameterization for the JCZ3-EOS, Tech. rep., SAND98-1191 (1998).

[19] D. Lee, C. F. Bonilla, The Viscosity of the Alkali Metal Vapors, Nuclear Engineering and Design 7 (5) (1968) 455 – 469.

[20] N. B. Vargaftik, Y. K. Vinogradov, V. I. Dolgov, V. G. Dzis, I. F. Stepanenko, Y. K. Yakimovich, V. S. Yargin, Viscosity and Thermal Conductivity of Alkali Metal Vapors at Temperatures up to 2000 K, International Journal of Thermophysics 12 (1) (1991) 85–103.

[21] D. E. Briggs, Thermal Conductivity of Potassium Vapor, Ph.D. thesis (1968).

[22] D. I. Stefano, D. Timorot, Y. Y. Totski, Viscosity and Thermal Conductivity of the Vapors of Sodium and Potassium, High Temperature Thermophys. 4 (1966) 131.

[23] K. Swaminathan-Gopalan, K. A. Stephani, Calibration of DSMC Parameters for Transport Processes in Ionized Air Mixtures, in: 45th AIAA Thermophysics Conference, Dallas, TX, 2015.

[24] R. A. Dressler, Chemical Dynamics in Extreme Environments, World Scientific, Advanced Series in Physical Chemistry - Vol. 11, 2001.

[25] A. A. Berezhnoy, J. Borovička, Formation of molecules in bright meteors, Icarus 210 (1) (2010) 150 – 157.

[26] W. Baggaley, The De-Ionization of Dense Meteor Trains, Planetary and Space Science 26 (10) (1978) 979–981.

[27] J. F. Friichtenicht, J. C. Slattery, D. O. Hansen, Ionization from fe atoms incident on various gas targets, Phys. Rev. 163 (1967) 75–80.

[28] F. Verniani, G. S. Hawkins, On the ionizing efficiency of meteors, Astrophysical Journal 140 (1964) 1590.

[29] Y. F. Bydin, A. M. Bukhteev, Ionization of fast na, k, rb, and cs atoms in collisions with h_2, d_2, n_2, and o_2 molecules, Sov. Phys. Tech. Phys. 5 (1960) 512–519.

[30] J. F. Cuderman, Ionization of k atoms in collision with h_2, n_2, o_2, and co, Phys. Rev. A 5 (1972) 1687–1694.

[31] A. M. Bukhteev, Y. F. Bydin, Loss of electrons by fast ca, mg, si and fe atoms in encounters with n2 and o2, Bull. Acad. Sci. USSR, Phys. Ser. 27 (1963) 985.

[32] C. A. Boitnott, H. F. Savage, Light emission measurements of calcium and magnesium at simulated meteor conditions. ii. spectral luminous efficiencies, Astrophysical Journal 167 (1971) 349.

[33] J. A. Kunc, W. H. Soon, Analytical Ionization Cross Sections for Atomic Collisions, The Journal of Chemical Physics 95 (8) (1991) 5738–5751.

[34] H. Drawin, F. Emard, Atom-atom excitation and ionization in shock waves of the noble gases, Physics Letters A 43 (4) (1973) 333 – 335.

[35] M. A. Lennon, K. L. Bell, H. B. Gilbody, J. G. Hughes, A. E. Kingston, M. J. Murray, F. J. Smith, Recommended data on the electron impact ionization of atoms and ions: Fluorine to nickel, Journal of Physical and Chemical Reference Data 17 (3) (1988) 1285–1363.

[36] C. Park, R. L. Jaffe, H. Partridge, Chemical-Kinetic Parameters of Hyperbolic Earth Entry, Journal of Thermophysics and Heat Transfer 15 (1) (2001) 76–90.

Development of High-Order Adaptive algorithms for simulating Magnetic Reconnection processes with Uncertainty Quantification

Firas Ben Ameur

Aeronautics and Aerospace Department, von Karman Institute for Fluid Dynamics, Belgium, firas.benameur@vki.ac.be

Supervisor: Andrea Lani

Research expert-project manager, Centre for Mathematical Plasma Astrophysics, KU Leuven, Belgium, andrea.lani@kuleuven.be

University Supervisor: Stefaan Poedts

Professor, Centre for mathematical Plasma Astrophysics, KU Leuven, Belgium, Stefaan.Poedts@kuleuven.be

Abstract

Space weather (SW) refers to potentially harsh conditions in our space environment mainly originating from the Sun and expanding into the heliosphere through the solar wind (SW). The interaction of the perturbed SW with the magnetosphere of the Earth (and other planets) activates multi-scale phenomena, in particular Magnetic Reconnection (MR) (i.e. the ubiquitous process converting magnetic energy into heating and particle acceleration) [1], occurring both in the Sunward side (across the shock wave) and in the magnetotail. This process plays a crucial role in particular during geomagnetic storms which, besides causing spectacular phenomena such as aurora borealis, can endanger ground-based and space-borne and affect Earth climate and ultimately human health [2]. Todays forecasting systems, however, are either based on (semi-)empirical models that are subject to serious shortcomings or have to rely on inherently incomplete solar observational data, lacking vital information for an educated assessment. The challenge, is to reliably model and simulate the SW interaction with the magnetosphere and to predict those potentially dramatic effects and to ideally take preventive measures.

Keywords: Flux Reconstruction, Adaptive mesh refinement , uncertainty quantification, multi-fluid plasmas, Magnetic reconnection.

1. Introduction

Nevertheless, uncertainties can always affect the input conditions for magnetospheric simulations either provided by models such as EUHFORIA or, as real data, by satellites like Advanced Composition Explorer (ACE) or the Deep Space Climate Observatory (DSCOVR). Parameters that are typically used to simulate magnetospheric MR scenarios numerically, such as ion-to-electron mass ratio or the light speed to Alfven speed ratio, are also affected by uncertainties [3]. A rigorous estimation of the effects of those uncertainties is mandatory to define confidence intervals when analyzing numerical results and this can be accomplished by Uncertainty Quantification (UQ) methods. UQ is rapidly expanding into all branches of computational physics/ engineering but it is far from established for astrophysical applications, due to the high computational costs associated to realistic simulations. As far as MR is concerned, with state-of-the-art second order Finite Volume (FV) plasma solvers very fine grids are typically required in order to get accurate deterministic plasma flow results (i.e. without uncertainty propagation), since a large disparity of scales (ranging from mega-meters to the ion and electron scales) needs to be handled within the same computational domain. This makes MR analysis extremely expensive even for 2D cases within a UQ framework, where it is necessary to evaluate output quantities at several configurations of the uncertain variables, each corresponding to a different run on a potentially different mesh. To make MR simulations with UQ affordable, automatic Adaptive Mesh Refinement (AMR) [4] is mandatory for better resolv-

ing key flow features within the current sheet, near local shocks or plasmoids and mitigating grid-related numerical errors that could be misinterpreted as due to input uncertainties [5]. Moreover, modern High-Order (HO) CFD methods can provide more accuracy per degree of freedom, potentially making more affordable a UQ analysis where runs on finer meshes would be substituted by runs on relatively coarser meshes but with higher order of accuracy [6; 7], therefore reducing mesh generation time. In addition, state-of-the-art validated global magnetospheric models employ the magnetohydrodynamic (MHD) approximation that can only poorly describe the reconnection process, as it is not valid on the length scales at which the reconnection occurs. First principles fully kinetic codes could reliably model reconnection, but global kinetic simulations are not affordable on current or even near-future computers. The multi-fluid models (MF) offers a clever and fast(er) solution to this problem [1]. This research project focuses on investigating and better characterizing the MR process which is key to geomagnetic storms and their possible consequences on Earth systems that will be accomplished by a unique combination of novel MF models and recent developments in numerical techniques.

Acknowledgments

The research of Firas Ben Ameur is supported by SB PhD fellowship 1SC3519N of the FWO

References

[1] A. Alvarez Laguna, A Multi-fluid modeling of magnetic reconnection in astrophysical and laboratory plasmas, Ph.D. thesis, KU Leuven (2017).

[2] J. Pomoell and S. Poedts, EUHFORIA: EUropean Heliospheric FORecasting Information Asset, J. Space Weather Space Clim. 8 (2018).

[3] E. Sousa, G. Lin and U. Shumlak, Uncertainty Quantification of the GEM challenge Magnetic Reconnection problem using the Multilevel Monte Carlo method, International Journal for Uncertainty Quantification 5 (4): 327339 (2015).

[4] Firas Ben Ameur and Andrea Lani, Physics-Based Mesh Fitting Algorithms for Hypersonic Flows Simulations, in: Proceedings, no. AIAA 2019-1997, AIAA Scitech 2019 Forum, San Diego, CA, 2019.

[5] A. Cortesi, Simulations numériques prédictives pour la reconstruction des conditions en amont dans les écoulements de rentré atmosphrique, Ph.D. thesis, U-Bordeaux (2018).

[6] H.T. Huynh, Z.J. Wang and P.E. Vincent, High-order methods for computational fluid dynamics, Computers Fluids 98, 209220, (2014).

[7] Firas Ben Ameur, Andrea Lani and Ray Vandenhoeck, Thermo-Chemical Nonequilibrium High-Speed Flows, in: Proceedings, no. AIAA 2019-1391, AIAA Scitech 2019 Forum, San Diego, CA, 2019.

Modeling of Rarefied and Ionized Flows for Electric Space Propulsion

Stefano Boccelli

Aeronautics and Aerospace Department, von Karman Institute for Fluid Dynamics, Belgium, mymail@vki.ac.be

Supervisor: Thierry Magin

Professor, Aeronautics and Aerospace Department, von Karman Institute for Fluid Dynamics, Belgium, magin@vki.ac.be

University Supervisor: Aldo Frezzotti

Professor, Department of Aerospace Science and Technology, Politecnico di Milano, Italy, aldo.frezzotti@polimi.it

Abstract

The genesis of the ions VDF is analyzed for collisionless Hall thruster discharges and an analytical form is derived, based on fluxes balance in phase space and compared to numerical results. Moments of the distribution function are explicitly obtained. Anisotropic fluid equations are established and closed with Euler fluxes and a phenomenological approximation, assuming a triangular shape for the VDF.

Keywords: Hall thrusters, Vlasov equation, ion kinetic modeling, moment closures.

1. Introduction

From the analysis of nondimensional numbers in average-sized Hall thrusters, it can be observed that the predominant collisional process is the electron-neutral (either non-reactive or ionizing) collision. On the other hand, ions are almost collisionless and once they are produced, they travel through the channel under the influence of the electric field alone. As a result, the axial ion distribution function in Hall thruster discharges is known to be highly non-Maxwellian [1; 2] and is governed by the electric field and the details of the ionization profile. This leads to an inherent limitation for classical fluid models, which are either based on a cold ions approximation [3], or on Euler-like equations [4]. The Chapman-Enskog method is not theoretically appropriate as well, due to the extreme amount of non-equilibrium and the lack of equilibrating processes. The consequences of inappropriate close-to-equilibrium modeling for the ions are appear particularly in the prediction of second order moments of the distribution function (i.e. temperature and pressure), and become even more evident for higher order moments. Besides the thermal analysis of the flow, also the thrust is strongly influenced by the modeling choice, being defined as a second order moment of the velocity distribution function (see Eq. 4).

This work focuses on the axial behavior of ions alone. A a fully collisionless case is assumed, where the effect of nonequilibrium is maximised. Ions are also assumed non-magnetized, which is a typically good approximation in Hall thrusters. These assumptions will be justified in Section 2 from the point of view of nondimensional parameters. The electric field and ionization profiles are assumed as given, as they depend on the neutrals density and electron temperature, which we do not analyze here.

This work starts from an evaluation of the flow regime, through analysis of nondimensional parameters arising from the ions Boltzmann equation (Section 2). The genesis of the distribution function is then analyzed in Section 3, following characteristics in phase space. This gives an intuitive understanding of the general features and also allows to obtain an effective analytical solution. Analytical moments are obtained from the analytical VDF as integrals of the ionization profile and electric field. The analytical solution is then compared in Section 4 to a steady state DVM numerical solution of the ions Vlasov equation. In Section 5, anisotropic fluid equations are expressed and their solution is compared with analytical moments. The final part of this document is aimed at obtaining a phenomenological closure for the heat

flux, derived assuming a simple triangular shape for the distribution function. This closure will provide an easily implementable option for closing the ion fluid equations, allowing for an improved description of the second order moment, for the considered testcase. Not only this allows for a more accurate estimation of thruster performance: it could also lead to more accurate models for the study of thruster instability formation (see for example Lafleur et al. [5]).

2. Order of magnitude analysis

We start by analyzing the order of magnitude of forcing terms and collisional effects on ions. First, the Boltzmann equation is expressed for ions in presence of electrical and magnetic fields as:

$$\frac{\partial f}{\partial t} + \boldsymbol{v} \cdot \frac{\partial f}{\partial \boldsymbol{x}} + \frac{q}{m} \left(\boldsymbol{E} + \boldsymbol{v} \times \boldsymbol{B} \right) \cdot \frac{\partial f}{\partial \boldsymbol{v}} = \mathcal{J} + \mathcal{R} \quad (1)$$

where f is the ions distribution function, $\boldsymbol{v}$ and $\boldsymbol{x}$ the velocity and position axes in phase space, q and m the ion charge and mass respectively, $\boldsymbol{E}$ the electric field and $\boldsymbol{B}$ the magnetic field, which are closed by supplementing this equation by Maxwell equations (or as is more common, the Poisson equation for electric field and constant externally applied magnetic field). Terms $\mathcal{J}$ and $\mathcal{R}$ represent respectively the non-reactive collision and the reactive collision operators. We lump the effect of both elastic and inelastic (but non-reactive) collisions in the term $\mathcal{J}$, since neither of them will show to be of large importance. In order to find the relative importance of the terms, we nondimensionalize the Boltzmann equation, such that nondimensional groups emerge [6]. Characteristic quantities are chosen as: L_0 is the thruster channel size, V the characteristic ion velocity, E_0 and B_0 the characteristic values for the electric and magnetic fields, and ν_{ik}^{nr} and ν^{r} respectively the nonreactive and reactive collision frequencies. Note that term ν_{ik}^{nr} depends on the considered collision partners, i and k, which can be ions (i), electrons (e) or neutrals (n), while the reactive collision frequency is supposed to originate only from electron-neutral collisions. The nondimensional equation reads, for nondimensionalized quantities $\tilde{\bullet}$:

$$\left(\frac{L_0}{V t_0}\right) \frac{\partial \tilde{f}}{\partial \tilde{t}} + \tilde{\boldsymbol{v}} \cdot \frac{\partial \tilde{f}}{\partial \tilde{\boldsymbol{x}}} + \left(\frac{qE_0}{mV^2/L_0}\right) \tilde{\boldsymbol{E}} \cdot \frac{\partial \tilde{f}}{\partial \tilde{\boldsymbol{v}}} + \left(\frac{qB_0V}{mV^2/L_0}\right) \left(\tilde{\boldsymbol{v}} \times \tilde{\boldsymbol{B}}\right) \cdot \frac{\partial \tilde{f}}{\partial \tilde{\boldsymbol{v}}} = \sum_{k \in \mathcal{S}} \left(\frac{\nu_{ik}^{nr}}{V/L_0}\right) \tilde{\mathcal{J}}_{ik} + \left(\frac{\nu^r}{V/L_0}\right) \tilde{\mathcal{R}} \quad (2)$$

Terms appearing in the parentheses are respectively the Strouhal number St, and the inverse of the electric and magnetic Froude numbers Fr_e and Fr_m at the LHS. At the RHS, the inverse Knudsen numbers for non-reactive and reactive collisions appear, $\mathrm{Kn}_{ik}^{\mathrm{nr}}$ and Kn^{r}. To evaluate these terms we consider the literature testcase [7], taking characteristic quantities: $L_0 = 0.02$ m, a characteristic velocity $V = 10\,000$ m/s as estimate of the kinetic energy gained by ions, and $t_0 = 1\,\mu$s for a characteristic period of a thruster instability. Characteristic values for the electric and magnetic field are taken as $E_0 = 100\,\mathrm{kV/m}$ and $B_0 = 400\,\mathrm{G}$. The collision frequencies, computed for every colliding partner species k are obtained as $\nu_k = \sigma_{ik} n_k v$, where v is a characteristic velocity for the collision, that we take as the larger one among collision partners. The cross sections σ_{ik} are taken as: $\sigma_{in} \approx 10^{-18}\,\mathrm{m}^2$ from hard-sphere approximation; $\sigma_{ii} \approx 10^{-20}\,\mathrm{m}^2$ and $\sigma_{ie} \approx 10^{-20}\,\mathrm{m}^2$ from the Coulomb interaction potential [8], considering the temperature of electrons of roughly 5 eV. The cross-section for the parent-child resonant charge-exchange process between Xe and Xe^+ species has a cross-section comparable to the hard-sphere model [9]. Reacting (ionizing) collisions are assumed to originate only from electron-neutral collisions, with $\sigma_{en}^{\mathrm{r}} \approx 5 \times 10^{-20}\,\mathrm{m}^2$.

From the shown parameters, we obtain estimates for the nondimensional groups in Eq. (2), which are reported in Table 1. Apart from the Strouhal number, where the characteristic time depends on the unsteady behavior of the solution (see [10] for a review of thruster instabilities), the regime in which ions are to be simulated appears clear: ions are strongly accelerated by the electric field and hardly feel the magnetic field. Ion collisions are almost negligible for all processes, as shown by the high value of the Knudsen numbers. The only collisional process to be considered is the electron-neutral collision, which generates ions in the first place: while this term is rather small if compared to the LHS, it becomes leading in terms of mass balance, since the initial composition of ions is zero.

In the remaining of this work we will neglect the non-reactive collisions term $\mathcal{J}$ in the Boltzmann

St	$1/\mathrm{Fr}_e$	$1/\mathrm{Fr}_m$	$\mathrm{Kn}^{\mathrm{nr}}_{ie}$	$\mathrm{Kn}^{\mathrm{nr}}_{ii}$	$\mathrm{Kn}^{\mathrm{nr}}_{in}$	Kn^{r}
2	15	0.06	20	10^4	90	0.05

Table 1: Estimation of nondimensional groups for the ions Boltzmann equation.

equation, retaining only the reactive collision term $\mathcal{R}$. This leads to the Vlasov equation with chemical source term:

$$\frac{\partial f}{\partial t} + \boldsymbol{v} \cdot \frac{\partial f}{\partial \boldsymbol{x}} + \frac{q}{m} (\boldsymbol{E} + \boldsymbol{v} \times \boldsymbol{B}) \cdot \frac{\partial f}{\partial \boldsymbol{v}} = \mathcal{R} \qquad (3)$$

3. Genesis of ions VDF

We assume that the only ionizing events are electron-neutral collisions, during which the atom velocity can be approximated to be unchanged. Ions are thus created at the local distribution of neutrals, which we assume as a monoenergetic beam at velocity v_n.Additionally, v_n will be assumed constant along the channel, with value $v_n = 300$ m/s. The effect of this assumption, as well as a more reasonable model for ions injection (such as a drifted Maxwellian centered on the neutrals velocity v_n, in place of the current monoenergetic model) may be argued to quickly become small, if compared to the electrostatic acceleration along the channel.

Ions generation and motion is conveniently analyzed in phase space. Ions originate at position v_n along the velocity axis. Along the thruster channel, the generation of ions typically starts before the electric field reaches its maximum (which in turns roughly corresponds to the maximum of the magnetic field). This situation is depicted in Fig. 1, using electric field and ionization profiles adapted from Boeuf and Garrigues [7]. We start by assuming the simple case of a positive electric field all throughout the domain.

Referring to the case depicted in Fig. 1, the first ions are created around position $x = 0.015$ m. We mark this as the beginning of *Region (a)*. In this first part, the electric field is often very low. As a result, the ions concentration builds up in the phase space: ions slowly drift towards the exit mainly due to their (low) initial velocity $\approx v_n$. The phase-space trajectory is indeed almost vertical and no visible acceleration occurs.

The second phase begins where the electric field starts growing, while still being small with respect to its maximum. Ions produced in this region follow a steeper phase-space trajectory. This trajectory almost

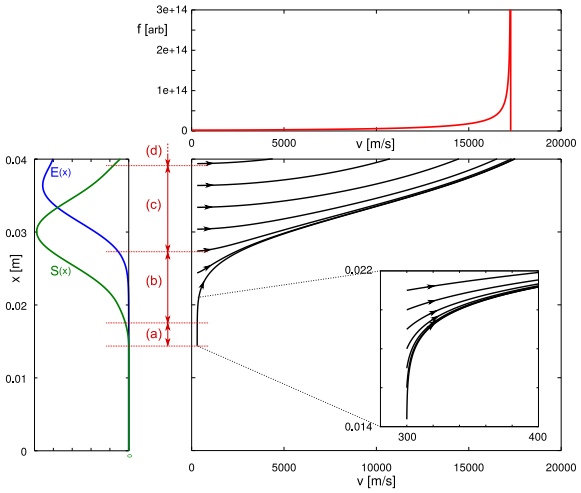

Figure 1: Phase-space trajectory of produced ions (right), and identification of sub-regions, together with chemical and electric field source terms (left), and resulting distribution function (top).

coalesces with that of low speed ions generated in *Region (a)*, that once reached that position start their acceleration. We call this *Region (b)*.

Most of the acceleration happens in *Region (c)*, where both the chemical and electric terms are significant, if not peaking. Until the end of this region, we observe a constant source of ions, whose velocity at the exit will be naturally lower than that of ions originating in *Region (a)*. As will be apparent from the DVM simulations, this creates a sort of low-velocity plateau in the distribution function, or a very heavy tail according to the exact shapes of the E and S profiles.

Finally, *Region (d)* suffers a decrease in the ionization rate, which marks an end to the distribution function. The electric field is typically still present, shifting (and inevitably deforming) the distribution function towards higher velocities.

Note that ions produced in *Regions (a)* and *(b)* will eventually reach the maximum velocity at the end of the thruster, while ions produced in the following, will leave the thruster with a lower velocity, as the potential difference at their disposal is lower. These fast-moving ions can indeed be shown to be the ones producing the higher thrust T, since:

$$T(x) = \int m v_x^2 \, f(\boldsymbol{v}) \, \mathrm{d}\boldsymbol{v} \qquad (4)$$

3.1. Analytic IVDF

The ions velocity distribution function (IVDF) can be easily obtained following the characteristic lines of

the Vlasov equation, which correspond to the particles trajectory in phase space. It is thus clear that the high velocity peak in the ions VDF (shown at top of Fig. 1 at the thruster exit) is composed by all the particles that accumulate in Regions (a) and (b), while the slowly decreasing plateau generate in regions (c) and (d).

First, we start from the steady state Vlasov equation with chemical production term, neglecting the magnetic field, with electric field $\boldsymbol{E}(x)$ and phase-space ion production term $S(x, v)$:

$$\boldsymbol{v} \cdot \frac{\partial f}{\partial \boldsymbol{x}} + \frac{q\boldsymbol{E}}{m} \cdot \frac{\partial f}{\partial \boldsymbol{v}} = S(x, v) \tag{5}$$

Assuming ions are produced from neutrals as a monoenergetic beam at v_n, we have $S(x, v) = S(x)\delta(v - v_n)$. In the collisionless limit, the ion distribution function $f(\boldsymbol{v})$ separates in: $f(\boldsymbol{v}) = f_x(v_x)f_y(v_y)f_z(v_z)$. Putting ourselves in 1D along the chamber axis, the equation reduces to an equation for the x-component only. In the following, we denote for simplicity: $v_x \equiv v$ and $f_x(v_x) \equiv f(v)$.

An analytic expression for the ion VDF can be obtained for a given profile of electric field and chemical production term $S(x)$. A balance of fluxes is easily established in the 1D1V phase space (see for example Harrison and Thompson [11]). In the collisionless case, ions generated between the positions x_0 and $x_0 + \mathrm{d}x$ fall freely along the potential $\phi(x)$, such that their velocity at position x will be:

$$v(x_0, x) = \left[\frac{2e}{m}\left(\phi(x_0) - \phi(x)\right) + v_n^2\right]^{\frac{1}{2}} \tag{6}$$

with the injection velocity v_n equal to the neutrals velocity. Given a position x along the thruster channel, Eq. (6) maps every point along the velocity axis to a space point x_0 where the particle was generated. At position x these ions have a velocity between $v(x_0, x)$ and $v(x_0, x) + \mathrm{d}v$, and the following conservation holds:

$$v f(v)\,\mathrm{d}v = -S(x_0)\,\mathrm{d}x_0 \tag{7}$$

where the minus sign accounts for the inverse relation between a growing x_0 and its corresponding final velocity, and $S(x)$ is the rate of production of ions per unit volume. As the velocity v of a free-falling ion is known in function of x_0, one computes:

$$\frac{\mathrm{d}v}{\mathrm{d}x_0} = \frac{\mathrm{d}}{\mathrm{d}x_0}\left[\frac{2e}{m}\left(\phi(x_0) - \phi(x)\right) + v_n^2\right]^{\frac{1}{2}} = -\frac{e}{m}\frac{E(x_0)}{v(x)} \tag{8}$$

And inserting it into the Eq. (7), one gets the simple analytic expression for the distribution function:

$$f(v(x_0)) = -\frac{S(x_0)}{v}\frac{\mathrm{d}x_0}{\mathrm{d}v} = \frac{m}{e}\frac{S(x_0)}{E(x_0)} \tag{9}$$

In the steady case, it is thus possible to know exactly the IVDF if $S(x)$ and $E(x)$ are known, for example at a given step of a numerical simulation. This VDF will be shown in Section 4, and compared to numerical results.

3.2. Moments of the analytical VDF

Moments can also be computed from the balance in Eq. (7), and are given here as integral expressions, which can be readily evaluated numerically from the values of $S(x)$ and $\phi(x)$. The first four moments of the Vlasov equation, number density n, average velocity u, pressure P_x and heat flux q_x are defined as [12]:

$$n(x) = \int_{-\infty}^{+\infty} f(v)\,\mathrm{d}v \tag{10a}$$

$$n(x)\,u(x) = \int_{-\infty}^{+\infty} v f(v)\,\mathrm{d}v \tag{10b}$$

$$P_x(x) = \int_{-\infty}^{+\infty} m(v - u)^2 f(v)\,\mathrm{d}v \tag{10c}$$

$$Q_x(x) = \int_{-\infty}^{+\infty} \tfrac{m}{2}(v - u)^3 f(v)\,\mathrm{d}v \tag{10d}$$

From the flux balance in Eq. (7), the moments are readily obtained as integrals along the x axis. The number density reads:

$$n(x) = \int_{x_0}^{x} S(x_0)/v(x_0, x)\,\mathrm{d}x_0 \tag{11}$$

where function $v(x_0, x)$ is defined in Eq. (6). The average longitudinal velocity $u(x)$ is obtained from:

$$u(x) = \frac{1}{n}\int_{x_0}^{x} S(x_0)\,\mathrm{d}x_0 \tag{12}$$

The pressure $P_x(x)$, first component of the pressure tensor, can be computed once the average velocity u is known:

$$P_x(x) = \int_{x_0}^{x} m\,\frac{S(x_0)}{v(x_0, x)}\left[v(x_0, x) - u(x)\right]^2\,\mathrm{d}x_0 \tag{13}$$

and finally the heat flux term $Q_x(x)$, first component of the heat flux tensor Q_{ijk} reads:

$$Q_x(x) = \int_{x_0}^{x} \frac{m}{2}\,\frac{S(x_0)}{v(x_0, x)}\left[v(x_0, x) - u(x)\right]^3\,\mathrm{d}x_0 \tag{14}$$

In case the electric field changes sign along the domain, the integrals are to be performed in each region separately, changing the lower integration extreme and the direction of integration accordingly. Analytical moments will be plotted in Section 5.2, for the testcase of Boeuf [7].

4. Comparison with numerical simulations

This section aims at comparing the analytical result with simple solutions of the ions Vlasov equation obtained with a finite volume discretization of phase space.

4.1. Steady case, DVM method

A numerical solution of the Vlasov equation has been obtained following the second order finite-volume formulation of Mieussens [13]. The scheme allows for both steady and unsteady simulations and will be compared here to the steady analytic VDF of Eq. (9).

To discretize the Vlasov equation using the finite-volume formalism, we start by reshaping it to let $x-$ and $v-$fluxes emerge:

$$\frac{\partial f}{\partial t} + \frac{\partial F_x}{\partial x} + \frac{\partial F_v}{\partial v} = S \tag{15}$$

where $F_x = vf$ and $F_v = F/mf$; The equation is integrated over a phase-space cell and this leads to the discretized equation for the cell (i, j), where indices refer to the space and velocity axes respectively:

$$\frac{\partial f_{ij}}{\partial t} + \frac{1}{L_x}\left[F_{x,i+1/2} - F_{x,i-1/2}\right] + \frac{1}{L_v}\left[F_{v,j+1/2} - F_{v,j-1/2}\right] = \frac{1}{L_v} S_{ij} \tag{16}$$

where $L_x = x_{i+1/2} - x_{i-1/2}$ is the spatial dimension of the $i-$th cell, and L_v is the analogous on the velocity axis. Note that the discretized source term is nonzero only in the cell that encloses the neutrals velocity v_n:

$$S_{ij} \equiv \begin{cases} \frac{1}{L_x}\int_{L_x} S_0(x)\,\mathrm{d}x & \text{if} \quad v_n \in \{v_{j-1/2}, v_{j+1/2}\} \\ 0 & \text{otherwise} \end{cases} \tag{17}$$

Fluxes are discretized using an upwind scheme:

$$F_{x,i+1/2} = \frac{1}{2}\left[v_j f_{i,j} + v_j f_{i+1,j} - |v_j|\left(f_{i+1,j} - f_{i,j} - \Phi_{x,i+1/2}\right)\right] \tag{18}$$

$$F_{v,j+1/2} = \frac{1}{2}\left[\frac{qE_i}{m} f_{i,j} + \frac{qE_i}{m} f_{i,j+1} - \left|\frac{qE_i}{m}\right|\left(f_{i,j+1} - f_{i,j} - \Phi_{v,j+1/2}\right)\right] \tag{19}$$

with minmod limiter function Φ. A `C++` OpenSource implementation of the scheme is freely available [14]. Parallelization is performed with OpenMP and performance is discussed in Appendix A.

Numerical results from this formulation are shown in Fig. 2 for a grid of 1600×1600 phase-space cells, and can be seen to match closely the analytical form of the ions VDF in most of the domain. Numerical diffusion is evident around the peak of the VDF, especially at lower x positions, where accumulation of ions is favored by the very low electric field. This is expecially evident if one compares the peak heigth at various channel locations, which should be conserved in the collisionless case ($Df/Dt = 0$), but decreases due to numerical diffusion. However, although not explicitly shown here, moments are less sensitive than the VDF on the computational grid size: good estimations of moments do not necessarily require an exact reproduction of the VDF sharp peak.

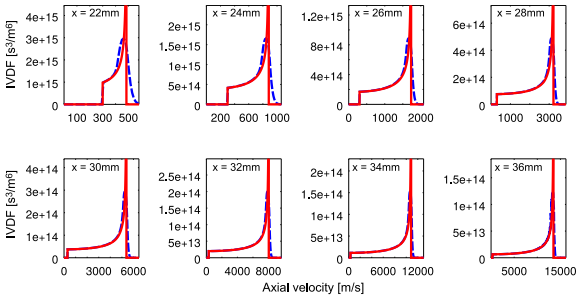

Figure 2: Ions velocity distribution function at various thruster locations, starting from shortly after the position where ionization starts. — analytical solution; - - - DVM method.

Neglecting the injection velocity in the previous model would have a strong impact in the result only in the low electric field region. As ions accelerate, that contribution of energy becomes quickly negligible, as can be see in Fig. 3.

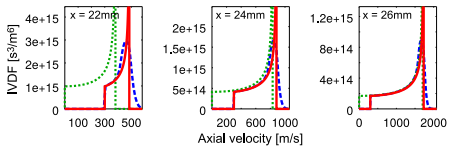

Figure 3: Ions velocity distribution function with and without considering injection velocity v_n. — analytical solution with $v_n = 300\,\mathrm{m/s}$; · · · analytical solution with $v_n = 0$; - - - DVM method.

The biggest advantage of the DVM method over the previously found numerical simulation lies in the possibility to obtain unsteady results. Indeed, such solver could be easily coupled to neutrals and electrons solvers, or fed with ionization profiles and electric fields which vary in time. This would allow to easily simulate low and high frequency thruster instabilities and can be a valuable support in the formula-

tion of unsteady analytical results.

5. Anisotropic fluid formulation

A fluid formulation for the ions equation benefits from a much lower computational cost than DVM or particle solutions of the Vlasov equation. Also, if compared to the analytical result developed above, they have the additional benefit of being applicable to unsteady problems.

Fluid equations for ions in the longitudinal direction x are obtained as moments of the Vlasov equation Eq. (3), [12; 15]. We avoid the commonly employed cold fluid approximation [3], as it may include significant errors in the momentum. The amount of error can be estimated by comparing the contributions of ρu^2 and P from the analytical moment equations (errors go up to 15-20% for the testcase of Section 5.2). Instead we solve an equation for (twice of) the ions energy.

The formulation is anisotropic, as only the longitudinal direction is described: the other two directions evolve separately and can thus develop different values for the pressure and temperature. The mass equation reads:

$$\frac{\partial \rho}{\partial t} + \frac{\partial}{\partial x}\left(\rho u_x\right) = \omega \tag{20}$$

where $\rho = mn$ and $\omega = mS$ is the chemical production term. The momentum equation reads:

$$\frac{\partial}{\partial t}\left(\rho u_x\right) + \frac{\partial}{\partial x}\left(\rho u_x^2 + P_x\right) = nqE + R_x^r \tag{21}$$

Finally, in place of the energy equation, we write a balance for the quantity $\rho u_x^2 + P_x$, which from the kinetic definition in Eq. (10c) can be easily seen to be twice the total energy, since $P_x \equiv 2\rho e_x$. The equation reads:

$$\frac{\partial}{\partial t}\left(\rho u_x^2 + P_x\right) + \frac{\partial}{\partial x}\left[\rho u_x^3 + 3u_x P_x + 2Q_x\right] = 2\,nqEu_x + 2\,C_x^r \tag{22}$$

where the factor 2 multiplying the heat flux and the RHS terms also comes from the fact that we are solving an equation for *twice* the total energy. It is important to stress that these equations include only the longitudinal motion of particles. The relation between temperature and pressure can be easily written by defining the longitudinal energy per unit mass $e_x = k_B T_x/2m$ and from definition in Eq. (10c) we retrieve: $P_x = nk_B T_x$.

Terms R_x^r and C_x^r represent sources for the momentum and energy equations due to the production of ions at a given initial momentum and energy respectively. For ions produced at a given neutrals velocity v_n, these terms read:

$$R_x^r = \omega v_n \quad \text{and} \quad C_x^r = \omega m_n \frac{v_n^2}{2} \tag{23}$$

where the production rate ω is supposed given for the purpose of the present work, being a function of the local neutrals density and electrons population, which we do not treat here.

The equations formulated require a closure, obtained by expressing the heat flux term Q_x in function of the available moments ρ, u_x and P_x. The simplest closure consists in choosing, arbitrarily enough, that $Q_x = 0$. This results in the Euler equations, which are theoretically valid in the infinitely collisional regime, and certainly not for collisionless ions. However one should consider that: (i) the great simplicity makes this closure appealing and (ii) in the particular case of Hall thruster ions, the importance of the heat flux is significant but not extreme, and is thus frequently neglected. On the other hand, the Fourier closure, commonly employed in fluid dynamics, lacks from physical grounds in a fully collisionless context, where the flux of energy is purely generated by the combination of electric field and ionization profile. A simple attempt to overcome these limitations is provided in Section 5.1.

5.1. Triangular phenomenological heat flux closure

In this subsection we aim at deriving a phenomenological closure for the heat flux, inspired from the observed features of the ions VDF. Roughly speaking, the ions VDF consists in a peak accelerated by the electric field, followed by one long tail. As an attempt to mimic this behavior, we consider the oversimplified case of a triangular distribution function, such that:

$$f_T(v) = \begin{cases} \alpha v & \text{for} \quad v \in \{0, v_{\max}\} \\ 0 & \text{otherwise} \end{cases} \tag{24}$$

The two free parameters of this distribution, α and $v_{\max}$ can be written in function of two moments of the distribution. Indeed, for a two-parameters distribution function, moments can be found in function of other two, and the relation is algebric and explicit in the considered triangular case. It is thus possible to relate the heat flux of this distribution, Q_x^T, to two of the lower order moments.

We start considering that, from geometrical considerations, the average velocity u of a triangular distribution defines the maximum velocity as: $v_{\max} = \sqrt{2}u$. Then, the number density definition reads:

$$n = \int_0^{v_{\max}} f_T \, \mathrm{d}v = \int_0^{\sqrt{2}u} \alpha v \, \mathrm{d}v = \alpha u^2 \qquad (25)$$

Therefore, $\alpha = n/u^2$. This defines the two parameters in function of the distribution moments. The heat flux Q_x^T for a triangular distribution can thus be computed as:

$$\begin{aligned} Q_x^T(\rho, u) &= \int_0^{\sqrt{2}u} \frac{m}{2} (v-u)^3 \, \alpha v \, \mathrm{d}v \\ &= \frac{14}{5} \left(\sqrt{2} - 4 \right) \rho u^3 \approx -0.0201 \rho u^3 \end{aligned} \qquad (26)$$

which provides a simple closure for the heat flux in function of the density and velocity. Other moments could be chosen for expressing the heat flux as well, such as the density and pressure. To do this, we first write P_x as function of ρ and u:

$$P_x = \int_0^{\sqrt{2}u} m (v-u)^2 \, \alpha v \, \mathrm{d}v = \left[2 - \frac{4}{3}\sqrt{2} \right] \rho u^2 \qquad (27)$$

and we then subsitute the velocity u appearing in this equation, in the heat flux equation (26), obtaining:

$$Q_x^T(\rho, P_x) = -0.51959 \, \rho \left(\frac{P}{\rho} \right)^{\frac{3}{2}} \qquad (28)$$

Note that despite being analogous for a triangular distribution, when these fluxes are plugged into the ions PDEs, their effect may be different, as no more trivial algebraic relation holds among ρ, u and P in the general case.

5.2. *Comparison of results*

In this subsection, we compare the analytical moments with the solution of the three anisotropic moment PDEs, employing the Euler closure and the two variants of the triangular phenomenologic closure. The electric field and ionization profiles are adapted from [7]. The PDE solution is obtained with the finite-volume scheme, employing Roe numerical fluxes with linear reconstruction on primitive variables ρ, u, P_x following van Leer's MUSCL scheme [16]. The number of cells is 1000 and the (steady) solution is obtained with a linearized point-implicit formulation [17].

As can be seen from Fig. 4 the density and velocity fields for all the closures match closely the analytical results. On the other hand, the pressure field obtained from the Euler closure is significantly different (with a peak error of about the 25%), but can be strongly improved by employing the two phenomenological closures. Some mismatching can be appreciated close to the exit, and can be attributed to the high degree of approximation of the phenomenological heat flux. The behavior can be improved for example by combining the two closures obtained, with a geometrical average:

$$Q_x^T = \mathrm{sign}\left(Q_x^T(\rho, P_x) \right) \sqrt{\left| Q_x^T(\rho, u) \, Q_x^T(\rho, P_x) \right|} \qquad (29)$$

We wish to stress that a good reproduction of the pressure (and thus temperature) field is not only important for the prediction of thruster performance (mainly the thrust), but also for the analysis of plasma instabilities, such as the $E \times B$ electron drift instability [5].

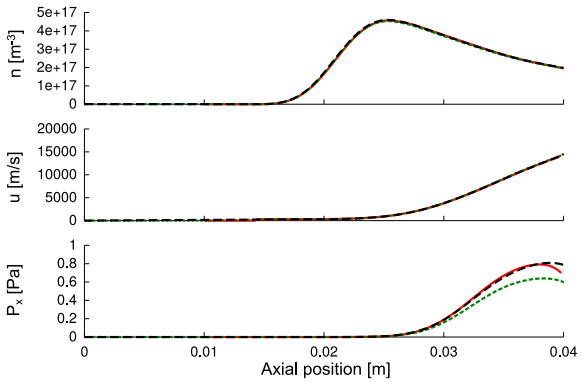

Figure 4: Solution of the first three moment equations compared to analytical moments. — analytical solution; · · · Euler closure; - - - Triangular heat flux $Q_x^T(\rho, u)$.

6. Conclusions

The case of collisionless ions in Hall thrusters has been discussed from the point of view of gas-kinetic theory. The genesis of the axial ions distribution function was described analyzing the ionization profile and axial electric field. A simple analytic VDF was obtained by establishing a balance of fluxes in phase-space, leading to the formulation of the analytic moments as integrals of the ionization profile and electric field. A finite-volume scheme for the solution of the time-dependent Vlasov equation is formulated, and the solution is compared to the analytical results. This verifies the numerical implementation and

Anisotropic fluid equations are formulated for the ions. Their numerical solution is compared to the analytic moments, using the Euler closure for the heat flux. A simple phenomenological closure has been derived for the heat flux, by assuming a triangular shape for the distribution function, and parameters that allow to match the local density and velocity (or pressure). Such closure is very simple in nature, yet allows to increase considerably the accuracy of the computation.

Appendix A - DVM parallelization

The DVM method of Section 4.1 was parallelized using OpenMP. A simple scaling analysis was performed for meshes up to 1000×1000 elements on the x-v plane, for a 12 OpenMP threads parallelization on a 16 cores machine. The speed-up shows to be almost ideal and is reported in Fig. 5).

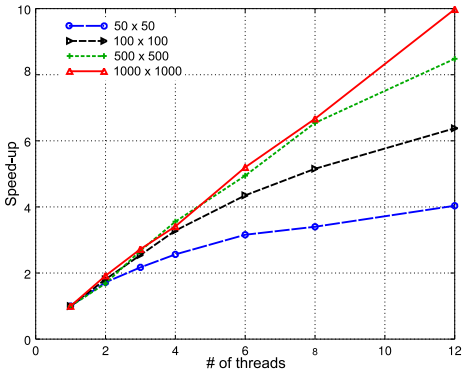

Figure 5: Speedup for different meshes. 12 threads parallelization, 16 cores machine.

References

[1] A. Shashkov, A. Lovtsov, D. Tomilin, A one-dimensional with three-dimensional velocity space hybrid-PIC model of the discharge plasma in a Hall thruster, Physics of Plasmas 24 (4) (2017) 043501. doi:10.1063/1.4979190.

[2] P. Q. Elias, J. Jarrige, E. Cucchetti, F. Cannat, D. Packan, 3d ion velocity distribution function measurement in an electric thruster using laser induced fluorescence tomography, Review of Scientific Instruments 88 (9) (2017) 093511. doi:10.1063/1.5001304.

[3] E. Ahedo, One-dimensional model of the plasma flow in a Hall thruster: Physics of Plasmas: Vol 8, No 6.

[4] S. Barral, N. Gascon, K. Makowski, Z. Peradzyski, M. Dudeck, Numerical study of the current-voltage characteristic of Hall thrusters, in: 27th International Electric Propulsion Conference, IEPC, 2001, pp. 01–27.

[5] T. Lafleur, R. Martorelli, P. Chabert, A. Bourdon, Anomalous electron transport in Hall-effect thrusters: Comparison between quasi-linear kinetic theory and particle-in-cell simulations, Physics of Plasmas 25 (6). doi:10.1063/1.5017626.

[6] M. N. Kogan, L. Trilling, Rarefied Gas Dynamics: Transl. from Russian, Plenum Press, 1969.

[7] J. P. Boeuf, L. Garrigues, Low frequency oscillations in a stationary plasma thruster, Journal of Applied Physics 84 (7) (1998) 3541–3554. doi:10.1063/1.368529.

[8] R. J. Goldston, P. H. Rutherford, Introduction to plasma physics, CRC Press, 1995.

[9] B. M. Smirnov, Tables for Cross Sections of the Resonant Charge Exchange Process, Physica Scripta 61 (5) (2000) 595. doi:10.1238/Physica.Regular.061a00595.

[10] J.-P. Boeuf, Tutorial: Physics and modeling of Hall thrusters, Journal of Applied Physics 121 (1) (2017) 011101. doi:10.1063/1.4972269.

[11] E. R. Harrison, W. B. Thompson, The Low Pressure Plane Symmetric Discharge, Proceedings of the Physical Society 74 (2) (1959) 145–152. doi:10.1088/0370-1328/74/2/301.

[12] J. H. Ferziger, H. G. Kaper, Mathematical theory of transport processes in gases, North-Holland, 1972.

[13] L. Mieussens, Discrete velocity model and implicit scheme for the BGK equation of rarefied gas dynamics.

[14] S. Boccelli, Open Source Finite Volume solver for gaskinetic theory., original-date: 2018-12-18T13:42:10Z (Jan. 2019). URL `https://github.com/sbocce/fvkin`

[15] M. S. Benilov, A kinetic derivation of multifluid equations for multispecies nonequilibrium mixtures of reacting gases, Physics of Plasmas 4 (3) (1997) 521–528. doi:10.1063/1.872151.

[16] B. van Leer, Towards the ultimate conservative difference scheme. V. A second-order sequel to Godunov's method, Journal of Computational Physics 32 (1) (1979) 101–136. doi:10.1016/0021-9991(79)90145-1.

[17] J. Blazek, Computational fluid dynamics: principles and applications, Butterworth-Heinemann, 2015.

Absolute Instability in Plasma Jet

Simon Demange

Aeronautics and Aerospace Department, von Karman Institute for Fluid Dynamics, Belgium, simon.demange@vki.ac.be

Supervisor: Olivier Chazot

Head of department and Professor, Aeronautics and Aerospace Department, von Karman Institute for Fluid Dynamics, Belgium, chazot@vki.ac.be

University Supervisor: Gérard Degrez

Dean, Aéro-Thermo-Mécanique, Université Libre de Bruxelles, Belgium, gdegrez@ulb.ac.be

Abstract

The full impulse response of the high enthalpy axisymmetric jet of the VKI Plasmatron is investigated using the Linear Stability Theory for a set of static pressure and electrical power of the facility. A competition mechanism between shear layer and jet column instability modes is revealed by varying the group velocity of the resulting wave packet. Finally, results are compared against experimental observations.

Keywords: Jet instabilities, Self-Similar jet, Absolute Instabilities, Linear Stability Theory

1. Introduction

Understanding and predicting physical phenomena occurring during the atmospheric re-entry of manned capsules is still one of the most challenging issue of present day space exploration. Due to high orbital and entry velocities, the air in front of the objects approaching the Earth is compressed, forming a bow shock through which pressure and temperature increase drastically until the air dissociates and reaches a state in which the gases are ionized called plasma. To study such high enthalpy flows, the von Karman Institute operates since 1997 the most powerful Inductively Coupled Plasma wind tunnel in the world: the Plasmatron [1]. However, the phenomena studied in this facility, such as the ablation of Thermal Protection System materials and flow laminar to turbulent transition, are strongly coupled with the quality of the plasma jet blown into the test chamber. Moreover, the reproduction of conditions similar to atmospheric entry in the facility is eventually hampered by hydrodynamic instabilities of the jet, as observed by Cipullo et al. in [2] using high speed cameras.

The development and evolution of perturbations inside a jet were first presented by Michalke [3]. In particular, he described "[...] in a certain frequency range additional modes exist which may be called "irregular" [...]" [3], when a sufficient heating of the jet centerline was applied. Such a mode displayed a non-zero growth rate at nil frequencies, implying waves traveling upstream. In a later study by Huerre and Monkewitz [4] for planar shear layer, these modes were correlated with the concept of absolute instabilities, developed by Briggs and Bers [5; 6] for plasma physics. Since then, literature has shown the relevance of using the spatio-temporal formulation of the Linear Stability Theory (LST), assuming waves growing both in time and space, in order to distinguish between the *convective* and *absolute* instabilities. The absolute/convective nature of instabilities has been extensively studied for hot round jets, notably to improve aircraft propulsion performances. Monkewitz and Sohn in [7] showed that absolute instability arises in jet profiles with a density (or temperature) ratio under $S_e = \rho_c/\rho_\infty = 0.72$ at the nozzle exit. Furthermore, it was shown that this ratio could be decreased by increasing the Mach number or the azimuthal mode number or by decreasing the velocity ratio. These results were later confirmed and extended by Lesshafft and Huerre [8], taking into account the full impulse response of the flow to highlight the competition be-

tween the convective and absolute instabilities at different group velocities. This study also showed that increasing viscosity would have a stabilizing effect for both types of instabilities. Interesting additional results were brought by the study of Balestra [9] in 2015 for coaxial heated jets, showing that with more complex profiles, new instability modes could appear and lower temperature ratios could trigger the absolute instabilities leading the stability behavior.
Confinement effect on the convective/absolute transition of jet instability modes has been studied by Juniper in [10], who provided a complete methodology to identify valid saddle points. Centerline heating effects have also been studied for convective instabilities, introduced for supersonic jets by Luo and Sandham in [11], and more recently for viscous, compressible, subsonic jets by Gloor et al. [12].
However, to the author knowledge, all previous study of absolute instabilities with LST were considering perfect gases and profiles shapes far from the one met in the Plasmatron jet. The aim of this study is to compute the spatio-temporal impulse response of the Plasmatron jet for several stream-wise positions and input parameters of the facility and uncover the nature of the instabilities observed. The convective/absolute nature of the instabilities is first investigated, and compared to the experimental observations available in [2].

2. Problem and model description

2.1. Base flow

To generate the plasma jet of VKI Plasmatron, air (in the present case) is blown through an annular inlet into a torch section, where it is heated up by induction reaching ionization [1], and finally enters the test chamber forming a hot jet as seen in Fig. 1. The basic state used for the stability studies relies on CFD simulations of Plasmatron's torch and chamber sections performed in CoolFluid-ICP, taking into account the coupling between fluid dynamics and electromagnetism and high enthalpy effects. The flow in the simulations is assumed axisymmetric and in Local Thermodynamic and Chemical Equilibrium, which is close to experimental conditions for static pressures in the chamber between 100 mbar and 200 mbar [2]. The simulations use the Mutation++ [13] library to obtain the flow composition and properties in LTE. The computational domain is compared to a sketch of the facility in Fig. 1.

Each case is obtained for a combination of the following driving parameters:

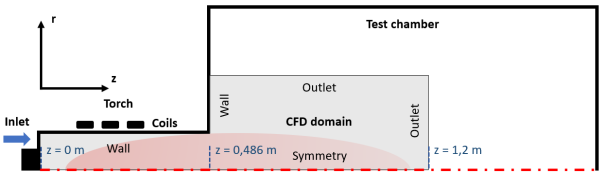

Figure 1: Sketch of the Plasmatron facility and CFD domain.

- $\dot{m}$: The inlet mass flow, kept constant to 16 g/s in this study;
- P_s: The static pressure, imposed at the outlet boundaries of the CFD domain, and kept in the range where the flow is in LTE;
- P_{el}: The power received by the plasma in CoolFluid-ICP. In practice it differs significantly from the facility's power, and estimating the efficiency of Plasmatron remains an open topic [14].

Experimental measurements of the temperature have been carried out by Cipullo at three stream-wise positions: $x_1 = 0.681$ m , $x_2 = 0.806$ m and $x_3 = 0.931$ m [2]. Therefore, the range of positions studied here is comprised between 0.5 and 1.2 m to include these positions. A brief summary of experimental results is reported Table 2. Figure 2 shows the influence of static pressure and electrical power on velocity and temperature profiles. Increasing the power increases both the values of velocity and temperature in the jet, thus the viscosity. On the other hand, increasing the static pressure in the chamber decreases the velocity in the jet and has little influence on the temperature value.

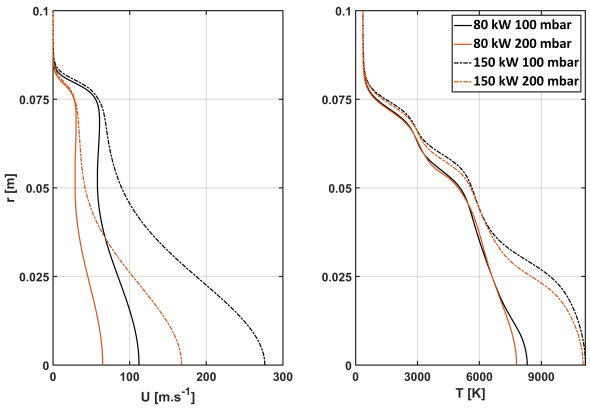

Figure 2: Velocity (left) and temperature (right) profiles evolution with pressure and power.

As linearized stability equations involve up to 2nd order derivatives of the flow quantities with respect to the radial dimension, the MATLAB^{TM} *fit* routine is used to interpolate the velocity and temperature profiles at discrete stream-wise positions using analytical expressions given in the appendix. The derivatives of the flow quantities are then computed analytically. The remaining flow quantities are computed using look up tables generated by DEKAF [15] assuming LTE and a constant static pressure P_s throughout the jet. The reference flow quantities are taken at the centerline of the jet, and the reference length for all positions is the radius of the torch $L_{ref} = r_{torch} = 0.08$ m
One can note that using local fittings does not retrieve a strictly smooth base flow along the stream-wise direction, therefore, a similar behavior is expected for stability features to the shape of the jet.

2.2. Linear Stability Theory

The stability features of the plasma jet are investigated locally using the Linear Stability Theory (LST). The flow is assumed quasi-parallel, as Plasmatron jet remains slender for the whole length of the chamber. The equations are expressed in the cylindrical coordinates (z, r, θ), respectively the stream-wise, radial and azimuthal directions. The physical quantities considered in the equations are (W, U, V, P, T), respectively the components of the velocity along (z, r, θ), the pressure and the temperature. The linearized stability equations are obtained by replacing the flow quantities by the sum of the basic state introduced previously and a small perturbation: $f = \bar{f} + f'$ with $f' << \bar{f}$.
As the early stage of transition are studied here, no interactions between the instabilities are considered, and they take the shape of normal instability modes:

$$f'(z, r, \theta, t) = \tilde{f}(r) e^{(i(\alpha z + q\theta - \omega t))} + c.c. \,, \qquad (1)$$

Where α and q are respectively the stream-wise and azimuthal dimensionless wave-numbers, ω is the dimensionless frequency and $\tilde{f}(r)$ is the shape of the instability considered. The dimensional frequency is retrieved from the real part of ω as $F = \omega_r W_{ctr}/(2\pi L_{ref})$. In the case where $q = 0$, the instabilities are axisymmetric. By imposing either the wave-numbers or the frequency, the linearized stability equations and the appropriate set of boundary conditions reduce to an eigenvalue problem, also called *dispersion relation*, which encapsulate all the information of the normal instability modes for the basic state considered: $\mathfrak{D}(\omega, q, \alpha) = 0$. In this case, $\tilde{f}(r)$ is the eigenfunction associated with α, q and ω.
The spatio-temporal formulation of the LST is used with both α and ω complex numbers, as this study considers waves growing both in time and space. The ensemble of solutions to the *dispersion relation* is called spectrum of instabilities, and the mode with largest tempral growth-rate ω_i leads the stability behavior of the flow.
A first set of linearized compressible Navier-Stokes equations in cylindrical coordinates has been developed by Garcia Rubio in [16], and later completed by Chiatto in [17] to include high enthalpy effects. The latter is used in this study. In both cases, the electro-magnetic terms have been neglected in the stability equations as their effects are mostly confined to the torch section of the Plasmatron.
As seen in Fig. 1, the CFD domain does not reach the physical outer wall of the test chamber, therefore the jet is considered as unconfined. An open outer boundary condition is imposed for which all perturbation vanish. At the jet centerline, three distinct sets of compatibility and Dirichlet conditions are imposed depending on the desired value of the azimuthal integral wave-number q [16].

The absolute/convective nature of the instabilities is determined by analyzing the time asymptotic response of the flow to an impulse. Following Huerre in [18], absolute instabilities reveal the activation of an intrinsic mechanism in the flow, through which instabilities grow without limit in time around their source. Which imposes to consider a nil group velocity $vg = {}^{x}/_{t}$ of the instability. According to the *Briggs-Bers criterion*, the time asymptotic response is given by the sign of ω_i when $i(\frac{x}{t} - \frac{\partial\omega}{\partial\alpha}) = 0$, hence for $vg = 0$, where $\frac{\partial\omega}{\partial\alpha} = 0$, which is the definition of a saddle point outlined by the contours of constant ω in the complex α plane.
However, a saddle point must be formed by the pinching of an α^+ and an α^- branch to be considered valid, in other words, the "hill" sides of the saddle point must extend respectively to the positive and negative values of α_i. The absolute instability found is then characterized by an *absolute frequency* ω_S and an *absolute wave-number* α_S.
To summarise, if the growth rate at a valid saddle is positive for $vg = 0$, the flow is *absolutely* unstable. If the growth rate at the saddle is negative for $vg = 0$, but there exists a vg for which the growth rate is positive, the flow is *convectively* unstable. Otherwise the flow is stable and all perturbations are damped.

2.3. Numerical methods

The implementation of the linearized equations was performed by Garcia Rubio and Chiatto using the Derivation toolkit from the VKI Extensive Stability and Transition Analysis toolkit [19]. The stability computations are also performed using VESTA, calling the *eig* routine from MATLAB^{TM} to solve the *dispersion relation* over the numerical domain discretized using Chebyshev collocation points. The standard discretization is transformed using the TAN mapping technique developed by Bayliss and Turkel in [20], as it proved to be well suited for problems with thick shear layers. The number of collocation points is fixed to $N = 201$, as it proved sufficient to reach an accuracy of two digits on the value of ω. In this study, it can be correlated with an error of the order of 2 Hz when considering reference velocities of order 10^2 m/s. The numerical tools used to find saddle points in the α complex plane and track their evolution along the stream-wise direction have first been developed by Kumar [21] for planar shear layers, and were adapted to cylindrical coordinates for the purpose of this study. The contour of growth rate are obtained by using a *local* stability solver of VESTA and the position of the saddle point is determined by using a Newton-Raphson method to converge toward the point where $\frac{\partial \omega}{\partial \alpha} = 0$, similarly to Rees [22].

3. Results

3.1. Local spatio-temporal analysis

A first analysis of the spatio-temporal instabilities developing in the plasma jet is carried out for a static pressure of P_s = 150 mbar and an electric power of P_{el} =100kW.

The integral azimuthal wave-number q chosen for the stability computations is selected based on experimental observations. The study of Cipullo et al. [2] provides the normal variance distribution of the radiations recorded by high speed camera over the test chamber as seen Fig 3. Assuming that the perturbations recorded are due to hydrodynamic instabilities, these results can be correlated with the temperature eigenfunctions retrieved by the LST. As noticed by Chiatto in [17], for the case studied, the perturbations seems to be non zero at the centerline of the jet, which is only compatible to the centerline boundary conditions obtained for $q = 0$.

A first spectrum of the instabilities obtained by imposing a real value of the stream-wise wave-number

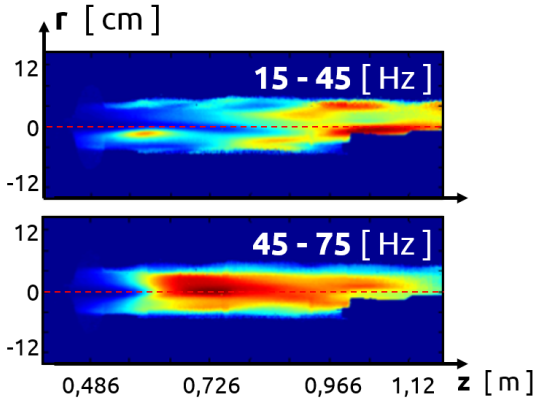

Figure 3: Partial power distributions for P_{el} = 200 kW and P_{tc} = 20 kPa from [2].

$\alpha = 1$ is displayed in Fig. 4, allowing the identification of a single unstable temporal mode. This mode is found at $\omega = 0.1205 + 0.1857i$ for the current value of α and $N = 201$ discretization points. This mode is then tracked across the complex wave-number plane using a local solver to draw the contours of growth rate.

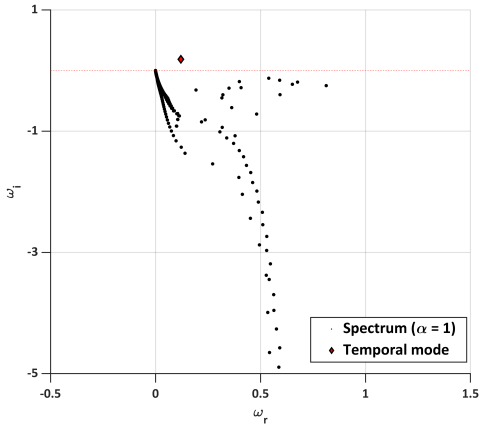

Figure 4: Spectrum obtained for $q = 0$ and $\alpha = 1$, with its least stable mode

Figure 5 shows the contour of the growth rate ω_i obtained over the complex wave-number plane. Several saddle points are found noted from $S0$ to $S2$.

An additional saddle point is also found in the upper α plane, also not displayed here because pinched between two α^+ branches, and therefore not valid. On the other hand, saddles $S0$, $S1$, and $S2$ are all valid from the *Briggs-Bers criterion* point of view. Only the saddle $S0$ located at α_{S0} = 0.4682 - 0.7297i displays a

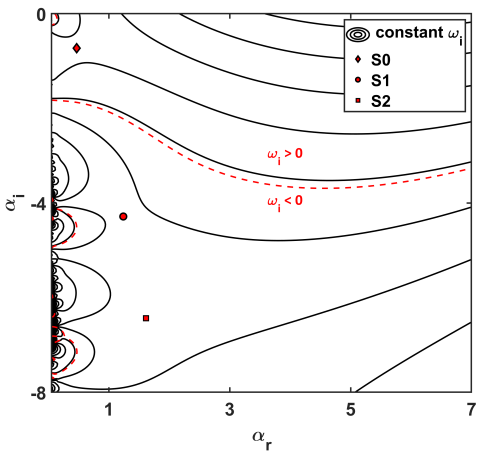

Figure 5: Contour of constant growth-rate ω_i obtained over the complex α plane for z =1.1 m

positive growth rate for the condition studied. Its associated real frequency is $\omega_{r,S} = 0.190295$, corresponding to $f_{S0} = 25.15$ Hz , and its *absolute growth-rate* is $\omega_{i,S} = 0.134455 > 0$. Given the sign of $\omega_{i,S}$, an absolute instability is found to develop at this stream-wise position.

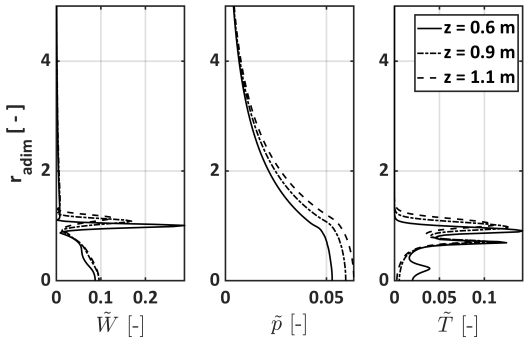

Figure 6: Perturbation functions for $S0$ at the set of stream-wise positions.

The perturbation functions at the saddle are given in Fig. 6. The pressure function is typical of a *mixed* mode described for single and co-flow jets, respectively by Lesshafft and Huerre in [8] and Balestra et al. in [9]. For these modes, the pressure perturbation is amplified both at the centerline and in the shear layer region of the jet. This can be explained as the α^+ and α^- branches pinching at the saddle display pressure perturbations respectively with the shape of shear layer and jet column modes. One can note that the temperature perturbations at the saddle are in agreement with experimental observations given in Fig. 3. Remaining saddle points $S1$ to $S2$ are formed between the pinching of the merged α^+ and α^- branches forming the saddle $S0$ and a set of others α^- branches. Similarly to the study of Lesshafft and Huerre in [8], only the saddle point displaying the highest *absolute growth-rate* $\omega_{i,S}$ is taken into account as it leads the stability behavior of the flow.

3.2. *Influence of the stream-wise position*

Once the spatio-temporal analysis is done for one stream-wise position, the saddles are tracked along the test chamber. This process is repeated iteratively for each stream-wise position with sufficiently small steps along z to allow the local solver to converge from a previous position. The accuracy of the tracking has been checked a posteriori by local spatio-temporal analyses around the supposed location of the saddle in the α plane, and the saddles were retrieved up to machine precision for ω_S and with an error of order 10^{-8} for α_S. The evolution of the main flow parameters with respect to the position in the test chamber is given 1.

z (m)	M_{ctr}	Re	$S = {}^{T_\infty}/_{T_{ctr}}$
0.5	0.036	117.5	0.035
0.7	0.030	131.7	0.047
0.9	0.028	149.4	0.052
1.1	0.027	162.8	0.055

Table 1: Main parameters at discrete stream-wise positions.

One can note that the values of temperature ratio found in Plasmatron are one order of magnitude lower than for most flow studied in the literature ([8; 9; 12]), and that the flow is highly viscous. As the stream-wise position is increased, temperature, viscosity and velocity decrease. However, the Reynolds number based on the torch radius increases.

For this analysis, 25 stream-wise positions between 0.5 m and 1.2 m have been scanned, and only the valid saddles $S0$ to $S2$ are considered. The evolution of the growth-rates and frequency for each position are plotted in Fig. 7. As the saddle $S0$ remains the dominating saddle for the whole length of the test chamber, it is the only one considered for the time being. Its *absolute growth-rate* increases from $\omega_{i,z=0,5\text{ m}} = 0.064$ to $\omega_{i,z=1,1\text{ m}} = 0.126$ in the stream-wise direction. A first significant result is that the jet is found to be *absolutely unstable* for the whole test chamber length at

the set of parameters studied. The evolution of the shape of the saddle point is plotted in Fig. 6, and the mixed nature of the mode remains the same for all the chamber. One can note the presence of an additional peak in the temperature perturbation for positions near the torch exit, assumed to be correlated with the hump in the temperature profile due to ionization.
The *absolute* growth rate is found to increase with the stream-wise position, thus with the increase of the Reynolds number, therefore on can assume that the mode is damped by the jet viscosity at the exit of the torch. Such result is in agreement with the observations of Gloor for co-flow jets done in [12]. Although such observation had not been done for the range of parameters and shapes of profiles studied here.
One can also note that the range of frequencies retrieved differs significantly from the experimental observations reported in Table 2. Hinting that the mode at zero group velocity might not be the one observed in the facility. A discontinuity is observed in the stream-wise evolution of the frequency, which is correlated to the local nature of the analytical fitting done to obtain the basic state. As the discontinuity is not observed in the growth rate curve, it is deduced that ω_r is more sensitive to the basic state than ω_i.

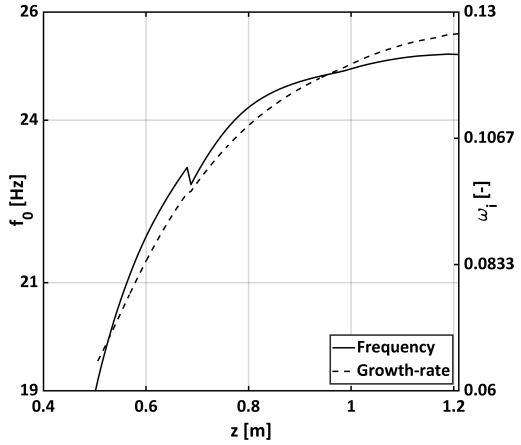

Figure 7: Evolution of saddle growth-rates and frequency along the stream-wise direction for P_s = 150 mbar and P_{el} = 100 kW

One can also observe that the frequency recorded experimentally near the exit of the torch are close to the frequency of the power rectifier of 100 Hz , which is precisely where the growth rate of the instability is the smallest according to LST. Therefore, it seems that the instabilities are firstly dominated by the power rectifier near the torch exit, and further downstream, the hydrodynamic instabilities at lower frequencies take over the stability behavior of the flow.

3.3. *Influence of the electric power and static pressure*

The influence of the driving parameters of the facility on the absolute instability is evaluated for a set of test cases by varying the electric power between 80 and 150 kW, and the pressure between 100 and 200 mbar. For this comparison, the stream-wise position is kept constant to z = 1.1 m , as the qualitative behavior with respect to the position proved to be the same in all tests studied.
The topology of the constant ω_i contours in the complex α plane is found to remain qualitatively similar to the one displayed in Fig. 5 for all the conditions studied. A saddle similar to $S0$ found in section 3.1 is observed for each condition, and remains the leading saddle point. For all parameters studied, the nature and shape of the mode at the saddle points are similar, with quantitative differences in shape being caused by the sharpening of the jet due to an increased power, hinting that the same physical phenomena are leading the stability behavior in all cases.
The evolution of the absolute frequency for the saddle point $S0$ with respect to the driving parameters is given in Figure 8.

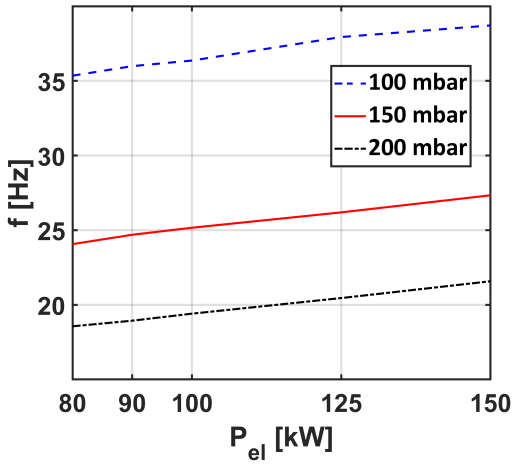

Figure 8: Evolution of f_0 at z = 1. m with respect to power and pressure.

A first conclusion on the hydrodynamic instabilities retrieved by LST, is that the static pressure has more influence on the frequency than the electrical power of the facility. Which is in agreement with the experimental observations of Cipullo [2]. The frequency of the instability is also found to increase with

the electrical power, which is also in agreement with the experimental observations. Although not plotted in figure 8, the *absolute* growth rate of the instabilities is found to be mostly influenced by the power, $\omega_{i,S0}$ decreases when the power is increased, which is when the Reynolds increases. However, the range of frequency obtained by LST is contained between 19 and 37 Hz while the lowest experimental frequency is 50 Hz.

4. Full impulse response

In the previous section, the group velocity vg has been kept to zero in order to asses the nature of the instabilities developing in Plasmatron. However, the maximum amplification of the instabilities is not necessarily obtained for $vg = 0$. The full impulse response is obtained by varying vg, following the work of Huerre and Lessafft [8]. Changes of the group velocity are imposed by shifting the reference frame of the study, modifying the stream-wise velocity basic state as $W_{adim}(vg) = W_{adim}(vg = 0) - vg$. The frequency and wave-number of the instabilities for a given vg are then moved back in the static reference frame as follow: $\omega_{static} = \omega(vg) + \alpha(vg) * vg$ and $\alpha_{static} = \alpha(vg)$.

Figure 9 displays the growth rate of the saddle points tracked for different values of the group velocity. When increasing the group velocity, the saddle $S0$ moves toward nil real wave-numbers and enters the series of sinks and wells located on the α_i axis (see Fig 5) and is no longer a valid saddle point for the *Briggs and Besrs* criteria, saddle $S1$ behaves in a similar way. However, the saddle $S2$ moves toward the upper half of the wave-number plane, and remains a valid saddle point. For $vg = 0.053$, the growth rate of $S2$ is larger than the one of $S0$, and $S2$ becomes the leading saddle point.

Such competition mechanism has already been observed for Perfect Gases jets by Huerre and Lesshafft in [8]. Similarly, the mode prevailing at low vg is the jet column type, as seen from the shape of the pressure perturbation in Fig 10. At higher vg, the shear layer mode associated with $S2$ takes over the stability behavior. According to Huerre and Lesshafft, these modes are typical of the well known Kelvin-Helmholtz instabilities. Therefore, the physical mechanism behind high enthalpy jets seems close to the one of colder perfect gases ones.

Similar analyses have been performed for the whole range of static pressure and electrical power, and the

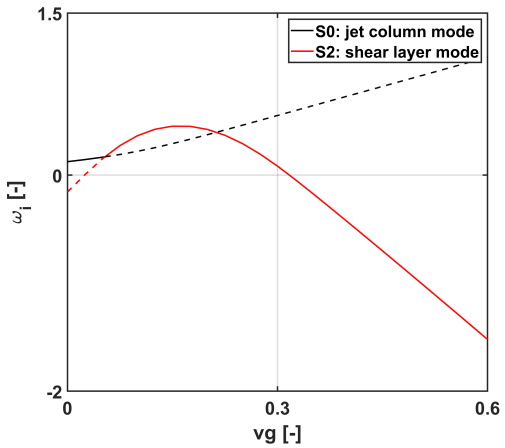

Figure 9: Evolution of the absolute growth rate $w_{i,0}(vg)$ as a function of the group velocity.

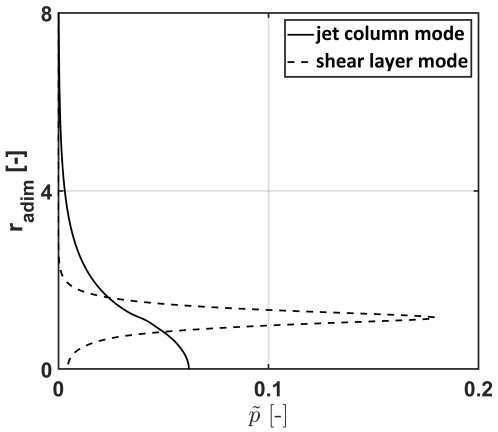

Figure 10: Comparison of pressure perturbation shapes between competing saddles for $vg = 0.1$.

results are qualitatively similar to the one presented above. In all cases, the jet column modes are taken over by the shear layer modes passed a certain value of the group velocity. The frequency of the instabilities displaying the largest amplification ω_i is plotted as a function of the driving parameters of the facility in Fig 11. Results are also compared against experimental observations, assuming that $P_{el}(Exp) = 2 * P_{el}(CFD)$, which is commonly assumed for Plasmatron.

One can note that the behavior with respect to power is inverted when comparing against the instabilities found at $vg = 0$. Hinting that the frequency of jet column modes and shear layer mode respectively increase and decrease with the velocity and tempera-

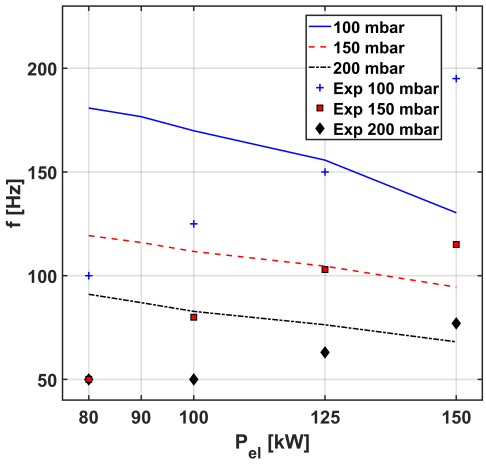

Figure 11: Evolution of the absolute frequency $f_0(vg)$ at maximum amplification with respect to power and static pressure, compared to experimental observations.

ture rise brought by the power increase. A second observation is that the frequencies retrieved by the LST are now in the same range of values as the one observed experimentally. The behavior with respect to static pressure is well in agreement with the experimental observations. However, the behavior with respect to electrical power is inverted. Unfortunately, the uncertainties in the comparison between CFD results against experiments prevents from concluding on the nature of this disagreement.

5. Conclusion

The hydrodynamic instabilities of Plasmatron test chamber have been analyzed using the Linear Stability Theory on analytical fittings of CFD results. The analysis shows that the plasma jet flow is absolutely unstable for all stream-wise positions, static pressure and electrical power, which is coherent with literature results based on the extreme temperature ratio in the jet. The absolute instability at a nil group velocity displays a pressure perturbation function typical of mixed jet column/shear layer modes, also observed by Balestra in co-flow jets. The evolution of the frequency and growth rate for this mode has been studied with respect to the facility's input parameters, and a competition mechanism between the hydrodynamic instabilities and the forcing of the coil has been proposed. However, the frequency of the absolute instability didn't match the experimental observations. Therefore, the full impulse response of the flow has been studied by varying the group velocity. By doing so, a competition mechanism between the jet column and the shear layer modes has been identified, similar to the one observed by Huerre and Lesshafft in [8]. A parametric study showed that the same mechanism is occurring for all conditions studied. Considering the instability at their maximum amplification allowed to match the magnitude of the oscillations frequencies found experimentally. The behavior of the instabilities with respect to the static pressure is well in agreement with the experimental observations. However, uncertainties on the basic state prevent from concluding regarding the trend with respect to the electrical power.

Appendix

Analytical fitting for basic state

The analytical fitting of the CFD velocity and temperature profiles are done for a set of discrete stream-wise positions using the following expressions:

$$W_{adim}(r) = a_w * GN(r,0,b_w) + c_w(1 - tanh(d_w(r - e_w))) + f_w(1 - tanh(g_w(r - h_w))) * GN(r, i_w, j_w) * r^2, \quad (2)$$

$$T_{fit}(r) = a_T * GN(r,0,b_T) + c_T(1 - tanh(d_T(r - e_T))) + f_T(1 - tanh(g_T(r - h_T))) + i_T(1 - tanh(j_T(r - k_T))), \quad (3)$$

Where $r = \frac{r_{dim}}{L_{ref}}$, and GN is the Gaussian function:

$$GN(r,a,b) = \frac{1}{(b\sqrt{2\pi})} exp(\frac{(-(r-a)^2}{2b^2}), \quad (4)$$

The temperature profiles are then shifted to take into account the finite temperature in the outer flow of the test chamber set to $T_\infty = 350$ K as:

$$T_{adim}(r) = (T_{fit}(T_c - T_\infty) + T_\infty)/T_c, \quad (5)$$

Where T_c is the local value of the centerline temperature obtained from the CFD. The value of the coefficients are determined using MATLAB^{TM} *fit* routine. The accuracy obtained with the local fitting is of order 0.1 m/s for the velocity and 10 K with respect to the CFD.

Experimental observations

The results given by Cipullo [2] on the hydrodynamic instability frequencies are summarized in Table 2:

Test label	P_{el} (kW)	P_s (mbar)	$T(x_1)$ (K)	$T(x_2)$ (K)	$T(x_3)$ (K)	f (Hz)
5b	160	200	6500	6390	6290	50
4b	160	150	6490	6359	6108	50
3b	160	100	6541	6388	5958	100
5c	200	200	6830	6628	6523	50
4c	200	150	6858	6576	6458	80
3c	200	100	6853	6594	6465	125
5d	250	200	7131	6940	6708	63
4d	250	150	6939	6792	6623	103
3d	250	100	-	-	-	150
5e	300	200	7374	7198	7118	77
4e	300	150	7388	6908	6858	115
3e	300	100	-	-	-	195

Table 2: Temperature at the centerline and frequency of oscillations from Cipullo [2].

References

[1] B. Bottin, M. Carbonaro, V. Van Der Haegen, A. Novelli, D. Vennemann, The VKI 1.2 MW Plasmatron facility for the thermal testing of TPS materials, 3 rd European Workshop on Thermal Protection Systems, ESTEC,.

[2] A. Cipullo, B. Helber, F. Panerai, F. Zeni, O. Chazot, Investigation of freestream plasma flow produced by inductively coupled plasma wind tunnel, Journal of Thermophysics and Heat Transfer 28 (3) (2014) 381–393.

[3] A. Michalke, Survey on jet instability theory, Progress in Aerospace Sciences 21 (1984) 159–199.

[4] P. Huerre, P. A. Monkewitz, Absolute and convective instabilities in free shear layers, Journal of Fluid Mechanics 159 (1985) 151–168.

[5] R. J. Briggs, Electron-stream interaction with plasmas, M.I.T. Press, Cambridge, 1964, oCLC: 537479.

[6] A. Bers, Space-time evolution of plasma instabilities-absolute and convective, in: Basic plasma physics, 1984, p. 451.

[7] P. Monkewitz, K. Sohn, Absolute instability in hot jets and their control, in: 10th Aeroacoustics Conference, Seattle, WA, U.S.A., 1986.

[8] L. Lesshafft, P. Huerre, Linear impulse response in hot round jets, Physics of Fluids 19 (2) (2007) 024102.

[9] G. Balestra, M. Gloor, L. Kleiser, Absolute and convective instabilities of heated coaxial jet flow, Physics of Fluids 27 (5) (2015) 054101.

[10] M. P. Juniper, The effect of confinement on the stability of non-swirling round jet/wake flows, Journal of Fluid Mechanics 605 (2008) 227–252.

[11] K. H. Luo, N. D. Sandham, Instability of vortical and acoustic modes in supersonic round jets, Physics of Fluids 9 (4) (1997) 1003–1013.

[12] M. Gloor, D. Obrist, L. Kleiser, Linear stability and acoustic characteristics of compressible, viscous, subsonic coaxial jet flow, Physics of Fluids 25 (8) (2013) 084102.

[13] J. B. Scoggins, T. E. Magin, Development of mutation++: Multicomponent thermodynamics and transport properties for ionized gases library in c++, 11th AIAA/ASME Joint Thermophysics and Heat Transfer Conference, AIAA AVIATION Forum, (AIAA 2014-2966).

[14] A. Dorsa, Energy balance for plasmatron facility (2015).

[15] K. J. Groot, F. Miro Miro, E. S. Beyak, A. Moyes, F. Pinna, H. L. Reed, Dekaf: Spectral multi-regime basic-state solver for boundary-layer stability, 2018 Fluid Dynamics, Conference, AIAA AVIATION Forum, (AIAA 2018-3380).

[16] F. Garcia Rubio, Numerical study of plasma jet unsteadiness for re-entry simulation in ground based facilities (2013).

[17] M. Chiatto, Numerical study of plasma jets by means of linear stability theory (2014).

[18] P. Huerre, Open shear flow instabilities, Cambridge University Press, 2000.

[19] F. Pinna, Numerical Study of Stability Fo Flows from Low to High Mach Number, Von Karman Institute for fluid dynamics, 2012.

[20] A. Bayliss, E. Turkel, Mappings and accuracy for Chebyshev pseudo-spectral approximations, Journal of Computational Physics 101 (2) (1992) 349–359.

[21] N. Kumar, Spatio temporal stability of shear layers (2017).

[22] S. J. Rees, Hydrodynamic instability of confined jets & wakes & implications for gas turbine fuel injectors (2008).

Acknowledgments

This work was supported by the Fonds de la Recherche Scientifique - FNRS under the FRIA Grant.

Modeling Strategy for Blackout Analysis of Re-Entry Phases in Space Exploration Missions

Vincent Fitzgerald Giangaspero

Aeronautics and Aerospace Department, von Karman Institute for Fluid Dynamics, Belgium, vincent.giangaspero@vki.ac.be

Supervisor: Andrea Lani

Research expert-project manager, Centre for Mathematical Plasma Astrophysics, KU Leuven, Belgium, andrea.lani@kuleuven.be

University Supervisor: Stefaan Poedts

Professor, Centre for mathematical Plasma Astrophysics, KU Leuven, Belgium, Stefaan.Poedts@kuleuven.be

Abstract

During the re-entry phase of a spacecraft into a planetary atmosphere, the high temperatures generated around the vehicle result in the formation of a plasma flow. Plasma interacts with electromagnetic waves disrupting all communication, navigation and telemetry signals, leading to the well-known radio blackout problem [1]. For re-entry vehicles, radio blackout typically lasts several minutes, depending on the angle of re-entry and the particular flight trajectory of the spacecraft. Communication or radio blackout is an important issue for hypersonic vehicles and it is extremely important to develop strategies for propagating telemetry during hypersonic flight [2]. With future space missions aimed towards Mars, including NASAs Mars 2020 and ESAs Exo-Mars 2020, there is a strong motivation to improve the understanding of the physics regarding the communication blackout.

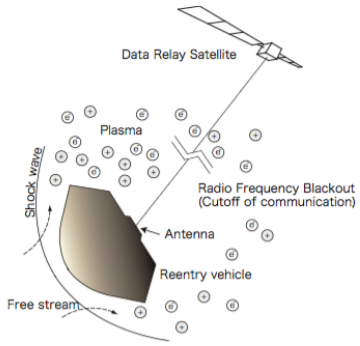

Figure 1: Schematic of communications blackout during atmospheric re-entry

The goal of this research is to develop and validate more effective numerical tools to properly predict radio blackout, both for Earth and Mars re-entry missions, by the development of a multi physics fully-integrated code. This will be accomplished by combining a more accurate computation of the electron density field with improved methods for characterizing the propagation of radio waves through the plasma layer. The specific activities include flow computation of re-entry trajectories, including state-of-the-art modeling of thermo-chemical nonequilibrium effects (as provided by the COOLFluiD [3] aerothermodynamic flow solver in combination with the Mutation++ physico-chemical library). This work will continue a preliminary effort which has lead to develop some promising engineering tools for predicting blackout on 2D axialsymmetric configurations and has been successfully validated on the ExoMars Schiapparelli mission [4]. The existing tools will be significantly extended, generalized and optimized to deal with realistic 3D scenarios.Furthermore, one of the most promising mitigation methods for blackout, which is based on electromagnetic manipulation of plasma [5], will be tested for Mars atmosphere, a novelty for this field. With a limited amount of blackout work performed, this research will create a greater understanding and will contribute filling the unsolved gap in blackout modelling and mitigation methods.

Keywords: CFD, Aerothermodynamics, re-entry flows, plasma flows, blackout, electromagnetics, raytracing

Acknowledgments

The research of Vincent Giangaspero is supported by SB PhD fellowship 1SA8219N of the FWO

References

[1] R. A. Hartunian et al, Causes and Mitigation of Radio Frequency (RF) Blackout During Reentry of Reusable Launch Vehicle, Aerospace Report ATR-2007(5309)-1 (2007).

[2] R.Savino et al, Plasma-Radiofrequency Interactions Around Atmospheric Re-Entry Vehicles: Modelling and Arc-Jet Simulation, The Open Aerospace Engineering Journal (3) (2010) 76–85.

[3] A.Lani, An object oriented and high performance plaoorm for aerothermodynamics simulation., Ph.D. thesis, Universite Libre de Bruxelles (2008).

[4] S.Ramjatan et al, Blackout Analysis of Reentry Vehicles for Maran Missions, IPPW-15, Boulder, Colorado.

[5] Minkwan Kim, Electromagnetic manipulation of plasma layer for re-entry blackout mitigation., Ph.D. thesis, University of Michigan (2009).

Transport Properties in Multicomponent Two-Temperature Magnetized Plasmas: Application to the Sun Atmosphere

Quentin Wargnier

Centre de Mathématiques Appliquées, Ecole Polytechnique, CNRS, Palaiseau, France

Supervisor: Thierry Magin

Professor, Aeronautics and Aerospace Department, von Karman Institute for Fluid Dynamics, Rhode-Saint-Genèse, Belgium

University Supervisor: Alessandro Alvarez Laguna

Laboratoire de Physique des Plasmas, Ecole polytechnique, CNRS, Palaiseau, France

University Supervisor: James Scoggins

Centre de Mathématiques Appliquées, Ecole Polytechnique, CNRS, Palaiseau, France

Research Supervisor: Nagy Mansour

NASA Ames Research Center, Moffett Field, California, USA

University Supervisor: Marc Massot

Centre de Mathématiques Appliquées, Ecole Polytechnique, CNRS, Palaiseau, France

Abstract

A fluid model is developed for multicomponent two-temperature magnetized plasmas in chemical non-equilibrium from the partially- to fully-ionized collisional regimes Graille *et al*. [M3AS 19(04):527-599, 2009] . We focus on the corresponding transport phenomena aiming at representing the atmosphere of the Sun. The governing equations and consistent transport properties are obtained using a multiscale Chapman-Enskog perturbative solution to the Boltzmann equation based on a dimensional analysis. The mass disparity between free electrons and heavy particles is accounted for, as well as the influence of the electromagnetic field. For more general partially ionized conditions, representative of the Sun lower atmosphere, we compute the muticomponent transport properties for a Helium-Hydrogen mixture in local thermodynamic equilibrium. The model is assessed for the 3D radiative magnetohydrodynamic simulation of a pore, at the Sun photosphere.

Keywords: Sun atmosphere, multicomponent transport properties, Helium-Hydrogen mixture, magnetized plasma, partially ionized plasma

1. Introduction

The lower atmosphere of the Sun is a complex and dynamic layer where the plasma is found in a wide range of different regimes – from weakly-ionized and non-magnetized at the bottom of the photosphere to fully ionized and magnetized at the top of the transition region. In the Sun chromosphere, the pressure varies from a thousand pascals just above the photosphere to a few pascals in the high chromosphere ([1]). Similarly, the magnitude of the magnetic field is large in active regions, around thousands of gauss in sunspots, whereas it is just a few gauss in quiet-Sun regions ([2]). It is still nowadays a great challenge to develop a unified model that can be used for both partially- and fully-ionized regimes under the large disparity of plasma parameters in the lower atmosphere.

Two types of fluid models to study the Sun lower at-

mosphere are found in the literature. First, the single-fluid MHD description considers the plasma as a conducting fluid in the presence of a magnetic field. It has the main drawback of assuming thermal equilibrium conditions, where all the species are considered to be at the same temperature. This model is assumed to be valid at the photosphere, in a highly collisional framework, allowing us to study the formation of magnetic field concentrations at the solar surface in sunspots, magnetic pores, and the large-scale flow patterns associated with them ([3]). It is also used for simulating the lower part of the atmosphere of the Sun, *e.g.*, incorporating subgrid-scale turbulence models for the transport of heat and electrical resistivity ([4]). The full MHD equations are solved in [5] accounting for non-grey radiative transfer and thermal conduction outside local thermodynamic equilibrium, in order to study the effects of the partial ionization of the Sun chromosphere.

Multi-fluid MHD models have been used more recently to represent the non-equilibrium conditions of the chromosphere, based on continuity, momentum, and energy conservation equations for each species considered in the mixture ([6; 7; 8; 9; 10; 11]). These models lead to very stiff systems that are difficult to solve numerically as they exhibit characteristic times that range from the convective and diffusive times of each fluid down to the collisional and chemical kinetics time scales ([9]). [6] performed a multi-fluid simulation of magnetic reconnection for a weakly ionized reacting plasma, with a particular focus on the solar chromosphere, by considering collisional transport, chemical reactions between species, as well as radiative losses. [12] has derived rigorous expressions for the transport properties of fully-ionized plasmas starting from the Boltzmann equation. [7] proposed a model for the description of a multi-component partially ionized solar plasma. Deriving rigorous transport properties for such multi-fluid model is complex, and so far, the theory has not yet been developed to the same level of accuracy as Braginskii's.

In this paper, we propose a novel approach for studying the lower Sun atmosphere that is neither a single-fluid nor a multi-fluid MHD model, but a multi-component drift-diffusion model derived by [13] from kinetic theory. This approach is able to capture most of the multi-fluid phenomena. This system of equations is less stiff as it solves for only one momentum equation, like in the single-fluid MHD approach. The transport properties are retrieved through a generalized Chapman-Enskog solution to the Boltzmann equation using a multiscale perturbation method. These developments lead to a model with an extended range of validity from partially- to fully-ionized plasmas, with or without the presence of a magnetic field. We couple this model to the Maxwell equations for the electromagnetic field and derive the corresponding generalized Ohm's law for multicomponent plasmas. Our model includes anisotropy in the transport properties of electrons, that is created by the magnetic field. These properties are computed by solving for the integro-differential. For more general partially ionized conditions representative of the Sun lower atmosphere, we compute the muticomponent transport properties for a Helium-Hydrogen mixture in local thermodynamic equilibrium. Finally, the model is assessed for the 3D radiative magnetohydrodynamic simulation of a pore, in the highly turbulent upper layer of the solar convective zone.

The structure of the paper is as follows. In section 2, the non-dimensonal analysis used for the generalized Chapman-Enskog expansion is presented, together with the multi-component drift-diffusion model for two-temperature magnetized plasmas, the transport fluxes, and the generalized Ohm law. In section 3, we describe the mixture considered, the conditions representative of the Sun lower atmosphere and the method used for computing the transport properties. In section 4, we discuss all the transport properties for a partially ionized case. Additionally, we compute the transport properties and the components of the generalized Ohm's law for 3D radiative MHD simulations of a pore in the low Sun atmosphere.

2. Drift-diffusion model for multicomponent plasmas

In this section, we present the multi-component drift-diffusion model for two-temperature magnetized plasmas. It was derived from kinetic theory by [13] as a generalized Chapman-Enskog solution to the Boltzmann equation, using a multi-scale perturbation method based on a dimensional analysis. Additionally, we compare this model to the multi-fluid description widely used for the Sun lower atmosphere.

2.1. Multi-scale analysis of the Boltzmann equation

We consider a multicomponent plasma composed of electrons, denoted here by the index e, and heavy-particles (atoms and molecules, neutral or ionized), denoted the subscript h. The species are assumed to be point particles, neglecting their internal energy. We combine the equations derived in ([13; 14]) for the

fully magnetized case and the Maxwellian regime for reactive collisions.

In order to apply the Chapman-Enskog method, [13] perform a multi-scale analysis on the non-dimensional Boltzmann equations for electrons and heavy species. The order of magnitude of the different terms in the Boltzmann equation is studied through carefully chosen reference quantities. In the asymptotic fluid limit, the Knudsen number is assumed to be as the same order of magnitude as the square root of the mass ratio between electrons and heavy particles, defined as $\varepsilon = \sqrt{m_\mathrm{e}/m_\mathfrak{h}}$, where m_e and $m_\mathfrak{h}$ are the mass of electrons and reference heavy particles respectively. This small parameter drives thermal nonequilibrium between the electron and heavy-particle baths. In the strongly magnetized regime, the Hall parameter is assumed to scale as $\varepsilon^0 = 1$. The species distribution functions are expanded in the multiscale perturbation parameter ε following Enskog's approach. As opposed to Braginskii, no assumption is made a priori on the zero-order distribution function. The asymptotic analysis of the Boltzmann equation is performed at successive orders of ε. The main results occurring at different time-scales are summarized in [13].

In time scales of order t_e^*, the electron population thermalize at the temperature T_e. The electron distribution function is a Maxwell-Boltzmann distribution obtained by solving the electron Boltzmann equation at the order ε^{-2}. At order ε^{-1} that corresponds to the time scale $t_\mathfrak{h}^*$, heavy particles thermalize at temperature $T_\mathfrak{h}$. At the zeroth order ε^0 that corresponds to the convective time scales, Euler equations for heavy particles and zero-order drift-diffusion equations for electrons are obtained. Finally, at order ε, corresponding to the diffusive time scale, we obtain Navier-Stokes equations for heavy particles and first-order drift-diffusion equations for electrons. It is important to mention that in Braginskii's approach, the macroscopic equations are retrieved by taking moments of the Boltzmann equation by considering only the zero-order Maxwell-Boltzmann distributions. Only a correct scaling deduced from dimensional analysis can yield a sound multicomponent treatment.

2.2. *Multi-component equations*

We denote by symbol H the set of indices for the heavy particles of the mixture considered. First, the mass conservation equations for electron and heavy particles are, as follows,

$$\partial_t \rho_\mathrm{e} + \boldsymbol{\partial_x}\cdot\Big[\rho_\mathrm{e}(\boldsymbol{v}_\mathfrak{h} + \boldsymbol{V}_\mathrm{e})\Big] = \omega_\mathrm{e}, \tag{1}$$

$$\partial_t \rho_i + \boldsymbol{\partial_x}\cdot\Big[\rho_i(\boldsymbol{v}_\mathfrak{h} + \boldsymbol{V}_i)\Big] = \omega_i, \quad i \in \mathrm{H}. \tag{2}$$

Here, ρ_e is the mass density of electrons, ρ_i is the mass density of heavy particle $i \in \mathrm{H}$, $\boldsymbol{v}_\mathfrak{h}$ is the heavy-particle hydrodynamic velocity that has been chosen as the velocity reference frame, $\boldsymbol{V}_\mathrm{e}$ is the electron diffusion velocity, $\boldsymbol{V}_i$, $i \in \mathrm{H}$ is the diffusion velocity of heavy particle i in the reference frame, such that $\sum_{i\in\mathrm{H}} \rho_i \boldsymbol{V}_i = 0$. Quantities ω_e and ω_i, with $i \in \mathrm{H}$, are respectively the chemical production rates of electrons and heavy particles.

Second, a momentum equation for all the particles within the plasma is found to be

$$\partial_t(\rho_\mathfrak{h}\boldsymbol{v}_\mathfrak{h}) + \boldsymbol{\partial_x}\cdot\left[\rho_\mathfrak{h}\boldsymbol{v}_\mathfrak{h}\otimes\boldsymbol{v}_\mathfrak{h} + p\mathbb{I}\right] = -\boldsymbol{\partial_x}\cdot\boldsymbol{\Pi}_\mathfrak{h} + \mathfrak{nq}\boldsymbol{E} + \mathbf{I}\wedge\boldsymbol{B}, \tag{3}$$

where, $p = p_\mathrm{e} + p_\mathfrak{h}$ is the total pressure, which is the sum of the partial pressure of electron p_e and heavy particle $p_\mathfrak{h}$, $\boldsymbol{\Pi}_\mathfrak{h}$ is the viscous stress tensor. The quantity $\rho_\mathfrak{h}$ is the total mass density of heavy particles, $\mathfrak{n} = \mathfrak{n}_\mathrm{e} + \mathfrak{n}_\mathfrak{h}$ is the number density ($\mathfrak{n}_\mathrm{e}$ the number density of electron and $\mathfrak{n}_\mathfrak{h}$ the total number density of heavy particles per unit of volume), $\mathfrak{nq}$ is the total charge of the system defined by $\mathfrak{nq} = \mathfrak{n}_\mathrm{e}\mathfrak{q}_\mathrm{e} + \sum_{i\in\mathrm{H}} \mathfrak{n}_i\mathfrak{q}_i$, where $\mathfrak{q}_i$ is the charge of species i, $\boldsymbol{E}$ is the electric field, and $\mathbf{I}$ is the total current density defined as

$$\mathbf{I} = \mathfrak{nq}\boldsymbol{v}_\mathfrak{h} + \boldsymbol{J}_\mathrm{e} + \boldsymbol{J}_\mathfrak{h} = \mathfrak{nq}\boldsymbol{v}_\mathfrak{h} + \mathfrak{n}_\mathrm{e}\mathfrak{q}_\mathrm{e}\boldsymbol{V}_\mathrm{e} + \sum_{i\in\mathrm{H}} \mathfrak{n}_i\mathfrak{q}_i\boldsymbol{V}_i, \tag{4}$$

where $\boldsymbol{J}_\mathfrak{h}$ is the heavy-particle conduction current density, $\boldsymbol{J}_\mathrm{e}$ is the electron conduction current density, and $\boldsymbol{B}$ is the magnetic field. Note that electrons only participate in the momentum balance through the total pressure gradient and Lorentz force due to the large mass disparity between electrons and heavy particles.

Conservation of energy for free electrons and heavy particles read

$$\partial_t(\rho_\mathrm{e}e_\mathrm{e}) + \boldsymbol{\partial_x}\cdot\left[\rho_\mathrm{e}e_\mathrm{e}\boldsymbol{v}_\mathfrak{h}\right] + p_\mathrm{e}\boldsymbol{\partial_x}\cdot\boldsymbol{v}_\mathfrak{h} + \boldsymbol{\partial_x}\cdot\boldsymbol{q}_\mathrm{e} = \boldsymbol{J}_\mathrm{e}\cdot\boldsymbol{E}' - \Delta E_\mathfrak{h}^0 - \Delta E_\mathfrak{h}^1 + \Omega_\mathrm{e}, \tag{5}$$

$$\partial_t(\rho_\mathfrak{h}e_\mathfrak{h}) + \boldsymbol{\partial_x}\cdot\left[\rho_\mathfrak{h}e_\mathfrak{h}\boldsymbol{v}_\mathfrak{h}\right] + (p_\mathfrak{h}\mathbb{I} + \boldsymbol{\Pi}_\mathfrak{h}):\boldsymbol{\partial_x}\boldsymbol{v}_\mathfrak{h} + \boldsymbol{\partial_x}\cdot\boldsymbol{q}_\mathfrak{h} = \boldsymbol{J}_\mathfrak{h}\cdot\boldsymbol{E}' + \Delta E_\mathfrak{h}^0 + \Delta E_\mathfrak{h}^1 + \Omega_\mathfrak{h}, \tag{6}$$

where $\rho_\mathrm{e}e_\mathrm{e}$ and $\rho_\mathfrak{h}e_\mathfrak{h}$ are the internal energies of electron and heavy particles respectively, and $\boldsymbol{q}_\mathrm{e}$ and $\boldsymbol{q}_\mathfrak{h}$ are the electron and heavy-particle heat flux, respectively. Quantity $\boldsymbol{E}' = \boldsymbol{E} + \boldsymbol{v}_\mathfrak{h}\wedge\boldsymbol{B}$ is the electric field in the heavy-particle reference frame, $\Delta E_\mathfrak{h}^0$ and $\Delta E_\mathfrak{h}^1$ are the relaxation terms at order ε^0 and ε, respectively. Quantities $\boldsymbol{J}_\mathfrak{h}\cdot\boldsymbol{E}'$ and $\boldsymbol{J}_\mathrm{e}\cdot\boldsymbol{E}'$ are respectively the power

that is developed by the heavy particle and electron current density, and $\Omega_{\mathfrak{e}}$ and $\Omega_{\mathfrak{h}}$ are respectively the energy production rate for electron and heavy particles.

Summing Eq. (5) and Eq. (6), with an equation for kinetic energy, the total energy equation is obtained, as

$$\partial_t \mathcal{E} + \boldsymbol{\partial_x} \cdot \left[(\mathcal{E} + p)\, \boldsymbol{v}_{\mathfrak{h}} \right] + \boldsymbol{\partial_x} \cdot (\boldsymbol{\Pi}_{\mathfrak{h}} \cdot \boldsymbol{v}_{\mathfrak{h}}) + \boldsymbol{\partial_x} \cdot \left(\boldsymbol{q}_{\mathfrak{e}} + \boldsymbol{q}_{\mathfrak{h}} \right) = \mathbf{I} \cdot \boldsymbol{E}, \tag{7}$$

where the total energy is $\mathcal{E} = \rho_{\mathfrak{e}} e_{\mathfrak{e}} + \rho_{\mathfrak{h}} e_{\mathfrak{h}} + 1/2 \rho_{\mathfrak{h}} \boldsymbol{v}_{\mathfrak{h}}^2$, and $\mathbf{I} \cdot \boldsymbol{E}$ the power developed by the electromagnetic field.

The system of equations (1-7) is coupled to the set of Maxwell's equations (8) :

$$\begin{aligned} &\boldsymbol{\partial_x} \cdot \boldsymbol{E} = \frac{\mathfrak{nq}}{\varepsilon_0}, \\ &\boldsymbol{\partial_x} \cdot \boldsymbol{B} = 0, \\ &\partial_t \boldsymbol{B} = -\boldsymbol{\partial_x} \wedge \boldsymbol{E}, \\ &\boldsymbol{\partial_x} \wedge \boldsymbol{B} = \mu_0 \mathbf{I} + \mu_0 \varepsilon_0 \partial_t \boldsymbol{E} \end{aligned} \tag{8}$$

where ε_0 is the vacuum permittivity and μ_0 the vacuum permeability.

The electron transport fluxes such as the electron diffusion velocity $\boldsymbol{V}_{\mathfrak{e}}$, the electron heat flux $\boldsymbol{q}_{\mathfrak{e}}$, the electron current density $\boldsymbol{J}_{\mathfrak{e}}$ are composed of two terms: 1- a term at the convective time scale, at order ε^0, corresponding to the Euler equations for heavy species, and 2- a term which is a first order correction, at order ε, at the dissipative time scale corresponding to the Navier-Stokes equations for heavy species. Similarly, the heavy transport fluxes such as the heavy-particle diffusion velocity $\boldsymbol{V}_i, i \in \mathrm{H}$, the heavy-particle heat flux $\boldsymbol{q}_{\mathfrak{h}}$, the viscous stress tensor $\boldsymbol{\Pi}_{\mathfrak{h}}$, the heavy particle current density $\boldsymbol{J}_{\mathfrak{h}}$ are defined at the dissipative time scale, at the order ε of the generalized Chapman-Enskog expansion.

The governing equations (1-8) differ from the multi-fluid models used for partially ionized plasmas. Whereas multi-fluid models consider one hydrodynamic velocity for each species, here we consider one hydrodynamic velocity for the heavy species while each species diffuse in this reference frame. In addition, the structure of the governing equations is symmetrizable hyperbolic ([13]), which can be regarded as an important property for the numerical discretization of the system. Nevertheless, it is necessary to close the model by computing the transport properties. This computation is presented in section 4 for a Helium-Hydrogen mixture. Additionally, by using the definition of the total current density $\mathbf{I}$ and the Maxwell equations Eq. (8), a generalized Ohm's law for this particular model is derived in Section 2.5.

2.3. Transport fluxes for heavy particles

With the same formalism that is used in [13], we introduce some extra notations in order to express the anisotropic transport properties in the presence of a magnetic field. First, a unit vector for the magnetic field $\mathcal{B} = \boldsymbol{B}/|\boldsymbol{B}|$ is defined as well as the three direction matrices

$$\boldsymbol{M}^{\parallel} = \mathcal{B} \otimes \mathcal{B}, \quad \boldsymbol{M}^{\perp} = \mathbb{I} - \mathcal{B} \otimes \mathcal{B}, \boldsymbol{M}^{\odot} = \begin{pmatrix} 0 & -\mathcal{B}_3 & \mathcal{B}_2 \\ \mathcal{B}_3 & 0 & -\mathcal{B}_1 \\ -\mathcal{B}_2 & \mathcal{B}_1 & 0 \end{pmatrix},$$

such that we have for any vector $\boldsymbol{x}$ in three dimensions

$$\boldsymbol{x}^{\parallel} = \boldsymbol{M}^{\parallel} \boldsymbol{x} = \boldsymbol{x} \cdot \mathcal{B}\, \mathcal{B},$$

$$\boldsymbol{x}^{\perp} = \boldsymbol{M}^{\perp} \boldsymbol{x} = \boldsymbol{x} - \boldsymbol{x} \cdot \mathcal{B}\, \mathcal{B},$$

$$\boldsymbol{x}^{\odot} = \boldsymbol{M}^{\odot} \boldsymbol{x} = \mathcal{B} \wedge \boldsymbol{x}.$$

In the $(\boldsymbol{x}, \mathcal{B})$ plane, the vector $\boldsymbol{x}^{\parallel}$ is the component of $\boldsymbol{x}$ that is parallel to the magnetic field and $\boldsymbol{x}^{\perp}$ is the perpendicular component. Therefore, we have $\boldsymbol{x} = \boldsymbol{x}^{\parallel} + \boldsymbol{x}^{\perp}$. The vector $\boldsymbol{x}^{\odot}$ lies in the direction transverse to the $(\boldsymbol{x}, \mathcal{B})$ plane. The three vectors $\boldsymbol{x}^{\parallel}$, $\boldsymbol{x}^{\perp}$, and $\boldsymbol{x}^{\odot}$ are then mutually orthogonal. The anisotropic transport coefficients are expressed by means of the matrix notation

$$\bar{\bar{\mu}} = \mu^{\parallel} \boldsymbol{M}^{\parallel} + \mu^{\perp} \boldsymbol{M}^{\perp} + \mu^{\odot} \boldsymbol{M}^{\odot}. \tag{9}$$

In the weakly or unmagnetized plasma regime the parallel and perpendicular component of the transport coefficients are identical, leading to $\mu^{\parallel} = \mu^{\perp}$. In such framework, the transverse component of the transport coefficient (or in other words, perpendicular to the $(\boldsymbol{x}, \mathcal{B})$ plane), is vanishing, leading to $\mu^{\odot} = 0$.
We recall the heavy particle transport fluxes presented in section (2.2) as:

$$\boldsymbol{\Pi}_{\mathfrak{h}}, \quad \boldsymbol{V}_i, i \in \mathrm{H}, \quad \text{and} \quad \boldsymbol{q}_{\mathfrak{h}}.$$

The viscous stress tensor $\boldsymbol{\Pi}_{\mathfrak{h}}$ is defined as

$$\boldsymbol{\Pi}_{\mathfrak{h}} = -\eta_{\mathfrak{h}} \left(\left[\boldsymbol{\partial_x} \boldsymbol{v}_{\mathfrak{h}} + (\boldsymbol{\partial_x} \boldsymbol{v}_{\mathfrak{h}})^{\top} \right] - \frac{2}{3} (\boldsymbol{\partial_x} \cdot \boldsymbol{v}_{\mathfrak{h}})\, \mathbb{I} \right), \tag{10}$$

where $\eta_{\mathfrak{h}}$ is the viscosity of heavy particles. Then, the heavy particle diffusion velocity $\boldsymbol{V}_i$ is given as

$$\boldsymbol{V}_i = -\sum_{j \in \mathrm{H}} D_{ij} \left(\boldsymbol{d}_j + \chi_{\mathfrak{h}j} \boldsymbol{\partial_x} \ln T_{\mathfrak{h}} \right), \quad i \in \mathrm{H}, \tag{11}$$

where D_{ij} is the multicomponent diffusion coefficient of heavy particles, $\boldsymbol{d}_j$ is the diffusion driving force of

the particle j that is interacting with the heavy particle i, and $\chi_{\mathfrak{h}j}$ is the heavy thermal diffusion ratio of particle j. The diffusion driving force $\boldsymbol{d}_j$ is defined as

$$\boldsymbol{d}_j = \frac{1}{p_{\mathfrak{h}}}\left(\boldsymbol{\partial}_{\boldsymbol{x}} p_j - \mathfrak{n}_j \mathfrak{q}_j \boldsymbol{E}' - \mathfrak{n}_j \boldsymbol{F}_{j\mathfrak{e}}\right), \quad j \in \mathrm{H}, \tag{12}$$

which is composed of three forces: 1- the force due to the gradient of the partial pressure $\boldsymbol{\partial}_{\boldsymbol{x}} p_j$, 2- the Lorentz force, and 3- $\boldsymbol{F}_{j\mathfrak{e}}$ that is an average electron force acting on the heavy particle j. Quantity $\boldsymbol{F}_{j\mathfrak{e}}$ belongs to the category of diffusion driving forces and allows for a coupling between the heavy particles and electrons ([13]). This average force is defined as

$$\boldsymbol{F}_{j\mathfrak{e}} = -\frac{p_{\mathfrak{e}}}{\mathfrak{n}_j}\bar{\bar{\alpha}}_{\mathfrak{e}j}\boldsymbol{d}_{\mathfrak{e}} - \frac{p_{\mathfrak{e}}}{\mathfrak{n}_j}\bar{\bar{\chi}}_{\mathfrak{e}j}\boldsymbol{\partial}_{\boldsymbol{x}}\ln T_{\mathfrak{e}}, \quad j \in \mathrm{H}. \tag{13}$$

where $\bar{\bar{\alpha}}_{\mathfrak{e}j}$ and $\bar{\bar{\chi}}_{\mathfrak{e}j}$ are anisotropic transport coefficients. Finally, the heavy-particle heat flux reads

$$\boldsymbol{q}_{\mathfrak{h}} = -\lambda_{\mathfrak{h}}\boldsymbol{\partial}_{\boldsymbol{x}} T_{\mathfrak{h}} + p_{\mathfrak{h}} \sum_{j\in\mathrm{H}} \chi_{\mathfrak{h}j}\boldsymbol{V}_j + \sum_{j\in\mathrm{H}} \rho_j h_j \boldsymbol{V}_j, \tag{14}$$

where $\lambda_{\mathfrak{h}}$ is the heavy thermal conductivity and $\rho_j h_j$ is the enthalpy of heavy particle j. The second term of Eq. (14) corresponds to thermal diffusion.

In the previous transport fluxes, some of the usual terms can be identified. The viscous stress tensor for heavy particles Eq. (10) is proportional to the strain tensor. Similarly, the first term of $\boldsymbol{V}_i$ in Eq. (11) is a generalized Fick's law where the flux is proportional to the diffusion driving force $\boldsymbol{d}_j$. Also, the first term of the heavy particle heat flux $\boldsymbol{q}_{\mathfrak{h}}$ in Eq. (14) is the usual Fourier's law. In addition, $\boldsymbol{V}_i$ includes a term that is proportional to $\boldsymbol{\partial}_{\boldsymbol{x}}\ln T_{\mathfrak{h}}$, known as the Soret effect, highly described in [15].

In summary, the transport coefficients for heavy particles to be computed in the following sections are

$$\eta_{\mathfrak{h}}, \quad D_{ij}, \quad \chi_{\mathfrak{h}j}, \quad \lambda_{\mathfrak{h}}, \quad i, j \in \mathrm{H}.$$

In addition, the anisotropic transport coefficients associated to the coupling terms between electron and heavy particles are

$$\bar{\bar{\alpha}}_{\mathfrak{e}j}, \quad \bar{\bar{\chi}}_{\mathfrak{e}j}, \quad j \in \mathrm{H}.$$

2.4. Transport fluxes for electrons

The electron transport fluxes are

$$\boldsymbol{V}_{\mathfrak{e}} \quad \text{and} \quad \boldsymbol{q}_{\mathfrak{e}}.$$

The electron diffusion velocity is defined as

$$\boldsymbol{V}_{\mathfrak{e}} = -\bar{\bar{D}}_{\mathfrak{e}}\left(\boldsymbol{d}_{\mathfrak{e}} + \bar{\bar{\chi}}_{\mathfrak{e}}\boldsymbol{\partial}_{\boldsymbol{x}}\ln T_{\mathfrak{e}}\right) + \sum_{i\in\mathrm{H}} \bar{\bar{\alpha}}_{\mathfrak{e}i}\boldsymbol{V}_i, \tag{15}$$

where $\bar{\bar{D}}_{\mathfrak{e}}$ is the tensor of the diffusion coefficient of electrons, $\boldsymbol{d}_{\mathfrak{e}}$ is the electron diffusion driving force and $\bar{\bar{\chi}}_{\mathfrak{e}}$ is the electron thermal diffusion ratio. The electron diffusion velocity $\boldsymbol{V}_{\mathfrak{e}}$ is split into two terms : 1- the terms proportional to $\boldsymbol{d}_{\mathfrak{e}}$ and to $\boldsymbol{\partial}_{\boldsymbol{x}}\ln T_{\mathfrak{e}}$ are at order ε^0, at the heavy particle convective timescale and 2- the terms proportional to $\boldsymbol{V}_i$ are at order ε at the heavy particle dissipative timescale. The electron diffusion driving force is defined as

$$\boldsymbol{d}_{\mathfrak{e}} = \frac{1}{p_{\mathfrak{e}}}\left(\boldsymbol{\partial}_{\boldsymbol{x}} p_{\mathfrak{e}} - \mathfrak{n}_{\mathfrak{e}}\mathfrak{q}_{\mathfrak{e}}\boldsymbol{E}'\right), \tag{16}$$

which is composed of two forces: 1- the force due to the gradient of the partial pressure of electron $\boldsymbol{\partial}_{\boldsymbol{x}} p_{\mathfrak{e}}$ and 2- the Lorentz force. The electron heat flux reads :

$$\begin{aligned}\boldsymbol{q}_{\mathfrak{e}} = &-\bar{\bar{\lambda}}_{\mathfrak{e}}\boldsymbol{\partial}_{\boldsymbol{x}} T_{\mathfrak{e}} + \left(p_{\mathfrak{e}}\bar{\bar{\chi}}_{\mathfrak{e}} + \rho_{\mathfrak{e}} h_{\mathfrak{e}}\right)\boldsymbol{V}_{\mathfrak{e}} \\ &+ p_{\mathfrak{e}} \sum_{j\in\mathrm{H}} \bar{\bar{\chi}}_{\mathfrak{e}j}\boldsymbol{V}_j + \rho_{\mathfrak{e}} h_{\mathfrak{e}} \sum_{j\in\mathrm{H}} \bar{\bar{\alpha}}_{\mathfrak{e}j}\boldsymbol{V}_j\end{aligned} \tag{17}$$

where $\bar{\bar{\lambda}}_{\mathfrak{e}}$ is the electron thermal conductivity tensor and $\rho_{\mathfrak{e}} h_{\mathfrak{e}}$ is the enthalpy of electrons. Quantity $\boldsymbol{q}_{\mathfrak{e}}$ is split into two terms : 1- the terms proportional to $\boldsymbol{\partial}_{\boldsymbol{x}} T_{\mathfrak{e}}$ and $\boldsymbol{V}_{\mathfrak{e}}$ are at the heavy-particle convective timescale, and 2- the terms proportional to $\boldsymbol{V}_i$ that are at the heavy-particle dissipative timescale.

As in the heavy species transport properties, some usual terms can be identified,i.e, Fick's and Fourier's laws. Additionally, terms that couple to the heavy particles diffusion are present at the first order of the generalized Chapman-Enskog expansion. In summary, the anisotropic transport coefficients associated to the transport fluxes for electrons are

$$\bar{\bar{D}}_{\mathfrak{e}}, \quad \bar{\bar{\chi}}_{\mathfrak{e}}, \quad \bar{\bar{\lambda}}_{\mathfrak{e}}.$$

In this section, a list of the transport fluxes and the corresponding transport coefficients has been presented. The method used for computing the latter will be presented in the next section 3.

2.5. Generalized Ohm's law

In the following, we derive a general expression for Ohm's law in the previous set of governing Eqs. (1)-(8). In order to do that, we rewrite the expression of the electric current by grouping the terms in each of

the driving forces. By doing this, we obtain a general algebraic expression for the electric field $\boldsymbol{E}$ as a function of the transport coefficients and the corresponding driving forces. Note that, in this derivation, the displacement current has been neglected.

With the electron diffusion velocity from Eq. (16) and the heavy-particle diffusion velocity from Eq. (11) we find the total current $\mathbf{I}$ as follows

$$\mathbf{I} = \mathfrak{n}\mathfrak{q}\boldsymbol{v}_\mathfrak{h} + \frac{(\mathfrak{n}_\mathfrak{e}\mathfrak{q}_\mathfrak{e})^2}{p_\mathfrak{e}}\bar{\bar{M}}_{\boldsymbol{E}'}\boldsymbol{E}' - \mathfrak{n}_\mathfrak{e}\mathfrak{q}_\mathfrak{e}\Bigg[\bar{\bar{M}}_{p_\mathfrak{e}}\frac{\boldsymbol{\partial_x} p_\mathfrak{e}}{p_\mathfrak{e}} + \sum_{j\in\mathrm{H}}\bar{\bar{M}}_{p_j}\frac{\boldsymbol{\partial_x} p_j}{p_\mathfrak{h}} + \bar{\bar{M}}_{T_\mathfrak{e}}\boldsymbol{\partial_x}\ln T_\mathfrak{e} + \bar{\bar{M}}_{T_\mathfrak{h}}\boldsymbol{\partial_x}\ln T_\mathfrak{h}\Bigg] \quad (18)$$

where the multicomponent electromagnetic matrices $\bar{\bar{M}}$ are defined as:

$$\bar{\bar{M}}_{\boldsymbol{E}'} = \frac{p_\mathfrak{e}}{p_\mathfrak{h}}\left[\sum_{i\in\mathrm{H}}\bar{\bar{\xi}}_{\mathfrak{e}i}\left(\sum_{j\in\mathrm{H}}D_{ij}\bar{\bar{\xi}}_{\mathfrak{e}j}\right) + \bar{\bar{D}}_\mathfrak{e}\right], \quad (19)$$

$$\bar{\bar{M}}_{p_\mathfrak{e}} = \frac{p_\mathfrak{e}}{p_\mathfrak{h}}\left[\sum_{i\in\mathrm{H}}\bar{\bar{\xi}}_{\mathfrak{e}i}\left(\sum_{j\in\mathrm{H}}D_{ij}\bar{\bar{\alpha}}_{\mathfrak{e}j}\right) + \bar{\bar{D}}_\mathfrak{e}\right], \quad (20)$$

$$\bar{\bar{M}}_{p_j} = \sum_{i\in\mathrm{H}}\bar{\bar{\xi}}_{\mathfrak{e}i}D_{ij}, \quad j\in\mathrm{H}, \quad (21)$$

$$\bar{\bar{M}}_{T_\mathfrak{e}} = \frac{p_\mathfrak{e}}{p_\mathfrak{h}}\left[\sum_{i\in\mathrm{H}}\bar{\bar{\xi}}_{\mathfrak{e}i}\left(\sum_{j\in\mathrm{H}}D_{ij}\bar{\bar{\chi}}_{\mathfrak{e}j}\right) + \bar{\bar{D}}_\mathfrak{e}\bar{\bar{\chi}}_\mathfrak{e}\right], \quad (22)$$

$$\bar{\bar{M}}_{T_\mathfrak{h}} = \left[\sum_{i\in\mathrm{H}}\bar{\bar{\xi}}_{\mathfrak{e}i}\left(\sum_{j\in\mathrm{H}}D_{ij}\chi_{\mathfrak{h}j}\right)\right], \quad (23)$$

and the tensor $\bar{\bar{\xi}}_{\mathfrak{e}i}$ is defined as

$$\bar{\bar{\xi}}_{\mathfrak{e}i} = \frac{\mathfrak{n}_i\mathfrak{q}_i}{\mathfrak{n}_\mathfrak{e}\mathfrak{q}_\mathfrak{e}}\mathbb{I} + \bar{\bar{\alpha}}_{\mathfrak{e}i}, \quad i\in\mathrm{H}. \quad (24)$$

After some algebra, using Eq. (18), the general expression of the electric field is obtained as

$$\boldsymbol{E}' = \bar{\bar{M}}^{-1}_{\boldsymbol{E}'}\Bigg[\frac{p_\mathfrak{e}}{(\mathfrak{n}_\mathfrak{e}\mathfrak{q}_\mathfrak{e})^2}(\boldsymbol{J}_\mathfrak{e} + \boldsymbol{J}_\mathfrak{h}) + \frac{p_\mathfrak{e}}{\mathfrak{n}_\mathfrak{e}\mathfrak{q}_\mathfrak{e}}\Big(\bar{\bar{M}}_{p_\mathfrak{e}}\frac{\boldsymbol{\partial_x} p_\mathfrak{e}}{p_\mathfrak{e}} + \sum_{j\in\mathrm{H}}\bar{\bar{M}}_{p_j}\frac{\boldsymbol{\partial_x} p_j}{p_\mathfrak{h}} + \bar{\bar{M}}_{T_\mathfrak{e}}\boldsymbol{\partial_x}\ln T_\mathfrak{e} + \bar{\bar{M}}_{T_\mathfrak{h}}\boldsymbol{\partial_x}\ln T_\mathfrak{h}\Big)\Bigg]. \quad (25)$$

The expression of the multicomponent electromagnetic matrices $\bar{\bar{M}}_{\boldsymbol{E}'}, \bar{\bar{M}}_{p_\mathfrak{e}}, \bar{\bar{M}}_{T_\mathfrak{e}}, \bar{\bar{M}}_{T_\mathfrak{h}}, \bar{\bar{M}}_{p_j}$ can be subdivided into two terms: 1) a term which depends on the coupled heavy-particle/electron transport properties, such as $\bar{\bar{\alpha}}_{\mathfrak{e}j}, \bar{\bar{\chi}}_{\mathfrak{e}j}, D_{ij}, \chi_{\mathfrak{h}j}$, which scales at the dissipative timescale for the heavy particles at order ε, and 2) a term which depends only on the electron transport properties $\bar{\bar{D}}_\mathfrak{e}, \bar{\bar{\chi}}_\mathfrak{e}$, which scales as the convective timescale for the heavy particles at order ε^0.

3. Methodology

For the purpose of this work, a Helium-Hydrogen mixture, composed of 92% Hydrogen and 8% of Helium in mole fractions, which is typical in the Sun atmosphere ([16]), is considered. The set of species considered in this mixture is denoted as

$$S_1 = \{\mathrm{He},\ \mathrm{He}^+,\ \mathrm{H},\ \mathrm{H}_2,\ \mathrm{He}^{++},\ \mathrm{H}^+,\ e-\}. \quad (26)$$

The heavy species such as carbon, oxygen or metals are not taken into account. We assume that they do not impact the transport properties as they are trace elements, i.e., the mole fractions are very small.

We study the transport coefficients for the previous mixture within a range of temperature, pressure, and magnetic field that is largely representative of the sun lower atmosphere ([1; 17]): the temperature varies from 1000 K to 30000 K, the pressure from 1 Pa to 10^4 Pa, and the magnetic field from a few Gauss to thousands of Gauss ([2]). In the following, the plasma beta parameter is defined as $\beta_p = 2\mu_0 p/|\boldsymbol{B}|^2$, where p is the total pressure of the plasma in Pascal and $|\boldsymbol{B}|$ is the magnetic field in Tesla.

Consequently, for a range of temperature between 1000 K and 30000 K, two cases have been considered. The **case A**, where the total pressure is $p = 10^4$ Pa, and $\beta_p = 10$. The **case B**, where the total pressure is $p = 1$ Pa, and $\beta_p = 0.1$. Finally, the case A is chosen as a thermally pressure dominated case whereas, the case B is a magnetically pressure plasma case. In this framework, in the case A, the transport coefficients are shown to be isotropic and in the case B the latter are shown to be anisotropic. Such chosen condition may include conditions that we can find in a cool sunspot (where the average temperature is generally around 4000K and the magnitude of magnetic field is about 1000G [18; 19]), in the quiet sun photosphere, in the lower and upper part of the chromosphere, where the temperature is varying from 5000K to 10000K, and the pressure from 10^4 Pa to 0.1 Pa [1; 20; 16] (in orders of magnitude).

Based on the chosen conditions, we compute the thermochemical equilibrium composition. The mole fraction and the ionization degree of the Helium-Hydrogen mixture S_1 for the **case A** and **case B** are shown in Fig. 1, Fig. 2 and Fig. 3. These results are obtained with a method that is based on the minimization of the Gibbs free energy with suitable mass balance constraints, used by [21] in thermal equilibrium. The compositions that are shown in Figs. 1 and 2 will be used to study the transport properties in the following sections.

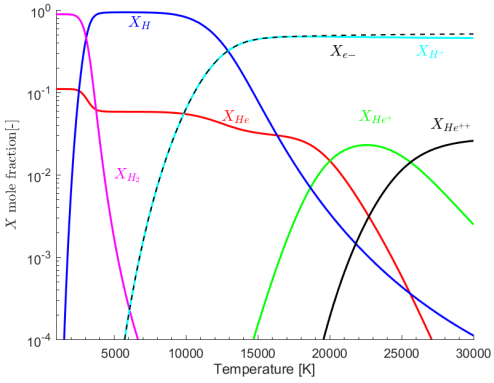

Figure 1: Mole fraction of the Helium-Hydrogen mixture S_1, for $P = 10^4$ Pa (**case A**), as a function of temperature

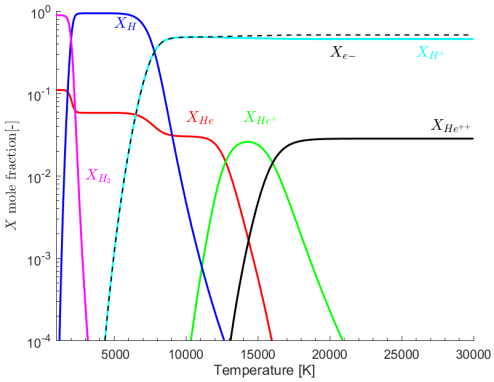

Figure 2: Mole fraction of the Helium-Hydrogen mixture S_1, for $P = 1$ Pa (**case A**), as a function of temperature

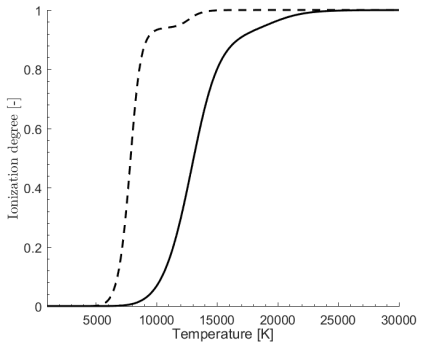

Figure 3: Ionization degree the Helium-Hydrogen mixture of S_1, for **case A** (full line) and **case B** (dashed line) as function of the temperature.

Similarly as in ([22; 23]), the calculation of the transport coefficients is based on the solution of integro-differential equations. In order to solve these equations, a spectral Galerkin method is applied. This method expands the coefficients in a series of orthogonal Laguerre-Sonine polynomials that are truncated at a given order of approximation. The calculation is thus reduced to a linear algebraic system of equations. As a result, the transport coefficients can be obtained by the resolution of linear systems with matrices that are known functions of the macroscopic parameters, i.e., the field variables and the collision integrals between particles. The solution of these systems allows for the transport coefficients to be written as linear combinations of the collision integrals, which take into account the interaction potential for a collision between two particles. These linear combinations are derived by extending the definition and the calculation of bracket integrals introduced by [24] or in ([25; 26; 27]) to the thermal nonequilibrium case, studied in depth by [28]. According to [23], [28] and [29], the transport coefficients involving collisions between heavy particles and electrons converge for expansions in second order non vanishing Laguerre-Sonine polynomials and higher. In this work, we use the third order Laguerre Sonine polynomials approximation in order to compute the transport properties. This method has been widely used in the literature (e.g., [30; 25; 15; 26; 27; 31]). The explicit relations for $\bar{\bar{\alpha}}_{\mathfrak{e}j}, \bar{\bar{\chi}}_{\mathfrak{e}j}$, and $\bar{\bar{D}}_{\mathfrak{e}}, \bar{\bar{\chi}}_{\mathfrak{e}}, \bar{\bar{\lambda}}_{\mathfrak{e}}$ in terms of the solutions to the transport systems can be found in [22].

4. Transport properties for a partially ionized Helium-Hydrogen plasma

4.1. Transport fluxes in thermo-chemical equilibrium

In order to simplify the analysis of the presented transport systems, we consider thermochemical equilibrium $T_{\mathfrak{e}} = T_{\mathfrak{h}} = T$, isobaric mixtures at rest. The total heat flux is entirely a function of the temperature gradient and magnetic field and may be written as

$$\boldsymbol{q}_{\mathfrak{h}} + \boldsymbol{q}_{\mathfrak{e}} = -\left(\lambda_{\mathfrak{h}} + \bar{\bar{\lambda}}_{\mathfrak{e}} + \bar{\bar{\lambda}}_S + \bar{\bar{\lambda}}_R\right)\boldsymbol{\partial}_{\boldsymbol{x}} T, \qquad (27)$$

where the Soret and reactive thermal conductivities may be written as

$$\bar{\bar{\lambda}}_S = -p_{\mathfrak{e}}\bar{\bar{\chi}}_{\mathfrak{e}}\theta_{\mathfrak{e}} - \sum_{j\in \mathrm{H}}\left[p_{\mathfrak{h}}\chi_{\mathfrak{h}j} + p_{\mathfrak{e}}\bar{\bar{\chi}}_{\mathfrak{e}}\right]\theta_i, \qquad (28)$$

$$\bar{\bar{\lambda}}_R = -\rho_{\mathfrak{e}}h_{\mathfrak{e}}\theta_{\mathfrak{e}} - \sum_{j\in \mathrm{H}}\left[\rho_j h_j + \rho_{\mathfrak{e}}h_{\mathfrak{e}}\bar{\bar{\alpha}}_{\mathfrak{e}j}\right]\theta_j, \qquad (29)$$

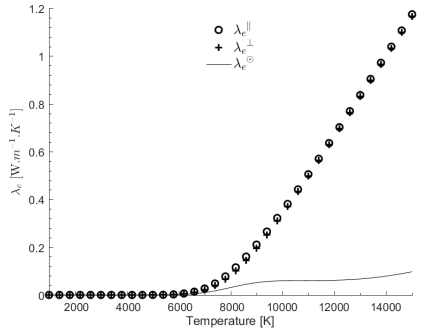

Figure 4: Components of the electron thermal conductivity tensor $\bar{\bar{\lambda}}_{\mathfrak{e}}$ for the isotropic **case A**, at the third-order Laguerre Sonine polynomials, for the Helium-Hydrogen mixture S_1 as a function of temperature

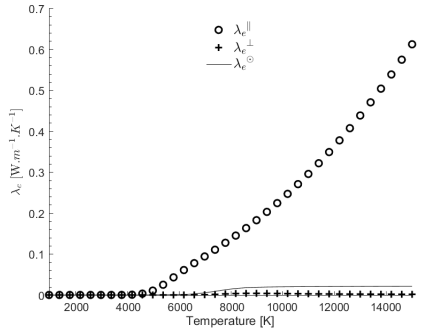

Figure 5: Components of the electron thermal conductivity tensor $\bar{\bar{\lambda}}_{\mathfrak{e}}$ for the anisotropic **case B**, at the third-order Laguerre Sonine polynomials, for the Helium-Hydrogen mixture S_1 as a function of the temperature

where $\theta_{\mathfrak{e}}$ and $\theta_i, i \in \mathrm{H}$ are defined as

$$\theta_{\mathfrak{e}} = -\bar{\bar{D}}_{\mathfrak{e}} \left[\frac{1}{x_{\mathfrak{e}}} \frac{\partial x_{\mathfrak{e}}}{\partial T} + \frac{\bar{\bar{\chi}}_{\mathfrak{e}}}{T} \right], \tag{30}$$

$$\theta_i = \sum_{j \in \mathrm{H}} D_{ij} \left[\frac{1}{1 - x_{\mathfrak{e}}} \left(\frac{\partial x_i}{\partial T} + \frac{\partial x_{\mathfrak{e}}}{\partial T} \bar{\bar{\alpha}}_{\mathfrak{e}j} \right) + \frac{\chi_{\mathfrak{h}j}}{T} + \frac{p_{\mathfrak{e}}}{p_{\mathfrak{h}}} \frac{\bar{\bar{\chi}}_{\mathfrak{e}j}}{T} \right], i \in \mathrm{H}. \tag{31}$$

Here, $\theta_{\mathfrak{e}}$ and θ_i correspond to diffusion velocities for a temperature gradient of 1, i.e, $\boldsymbol{V}_{\mathfrak{e}} = \theta_{\mathfrak{e}} \boldsymbol{\partial_x} T$ and $\boldsymbol{V}_i = \theta_i \boldsymbol{\partial_x} T$. We compute all the transport properties for the Helium-Hydrogen mixture S_1 for **case A**, i.e., weakly magnetized, and **case B** (magnetized case).

Fig. 4 and Fig. 5 present the parallel, perpendicular and transverse components of the electron thermal conductivity tensor $\bar{\bar{\lambda}}_{\mathfrak{e}}$ as a function of the temperature, for both cases. According to Fig. 4 (**case A**), the perpendicular component is equal to the parallel component for the entire range of temperatures, i.e, the electron thermal conductivity is isotropic. Indeed, the pressure forces are dominating the magnetic pressure forces, so the plasma is unmagnetized. On the other hand, in Fig. 5 (**case B**), for temperatures higher than $T = 5000$ K, the electron thermal conductivity $\bar{\bar{\lambda}}_{\mathfrak{e}}$ is anisotropic since the magnitude of magnetic field is higher. This results in a transverse component that is higher than the perpendicular component of $\bar{\bar{\lambda}}_{\mathfrak{e}}$. Similar results have been obtained for the other anisotropic electron transport properties such as $\bar{\bar{D}}_{\mathfrak{e}}$ and $\bar{\bar{\chi}}_{\mathfrak{e}}$.

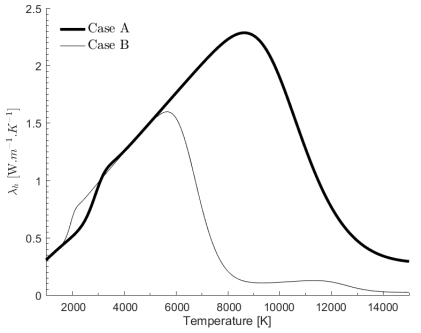

Figure 6: Heavy thermal conductivity $\lambda_{\mathfrak{h}}$, at the second-order of Laguerre Sonine approximation, for **case A** and **case B**, for the Helium-Hydrogen mixture S_1 as a function of temperature

Fig. 6 shows the heavy-particle thermal conductivity $\lambda_{\mathfrak{h}}$, as a function of the temperature, for the **case A** and **case B**. In Fig. 6, strong differences between the two cases for a temperature higher than 6000 K can be seen. In the **case A**, $\lambda_{\mathfrak{h}}$ increases from 1000 K to 9000 K, which is expected since $\lambda_{\mathfrak{h}}$ is an increasing function of the temperature. However, in the **case A** after 9000 K, $\lambda_{\mathfrak{h}}$ decreases. This decrease is due to the ionization of hydrogen. Indeed, the heavy particle thermal conductivity is related to a combination of the cross sections variations of all the heavy species in the mixture, which are proportional to the mole fractions of each heavy particles. This result is coherent with Fig. 1, which shows that the mole fraction of H is decreasing after 9000 K. Similar behavior as the **case A** have been observed for the **case B**, except that the ionization of H starts at 6000 K for this pressure. In Fig. 6, the second modulation observed around 12000 K is due to the ionization of Helium as shown in Fig. 2.

Fig. 7 shows the components of the total heat flux (Eq. 27) as a function of the temperature, for the isotropic **case A**. It is clear that the reactive thermal conductivity $\lambda_R^{\parallel}$ is higher than the other components for certain ranges of temperature between 2200 K and 4300 K, where hydrogen dissociation occurs, and for

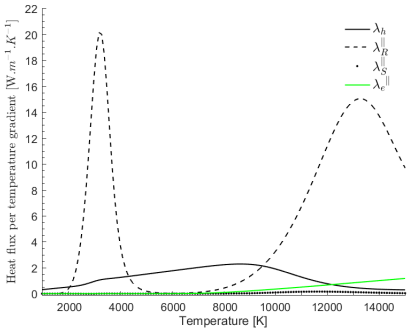

Figure 7: Component of the total heat flux (27) as a function of the temperature for the isotropic **case A** for the Helium-Hydrogen mixture S_1

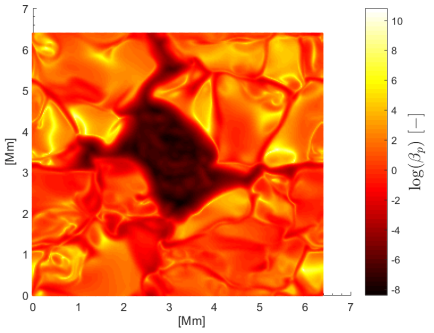

Figure 8: Plasma beta coefficient β_p distribution from the radiative 3D MHD simulations of a pore by [32]

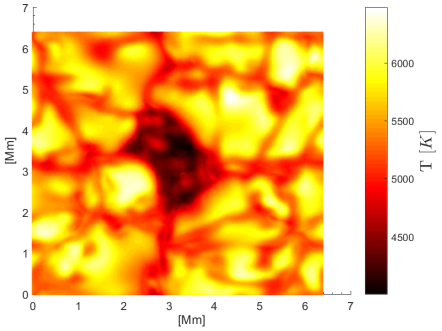

Figure 9: Temperature (K) distribution from the radiative 3D MHD simulations of a pore by [32]

temperature higher than 10000 K, where hydrogen ionization takes place. The heavy thermal conductivity λ_h is the second term which dominates the total heat flux, and is higher than $\lambda_R^{\parallel}$ for a range of temperature between 4200 K and 10000 K. The results obtained here and for all the other transport coefficients, are consistent with those of [22].

4.2. *Transport properties in a pore at the Sun photosphere*

As done in the previous section, the transport coefficients of the previous Helium-Hydrogen mixture are computed for the conditions found in the upper layer of the solar convective zone from the radiative 3D MHD simulations of a pore by [32]. The simulation results are obtained for the computational domain of $6.4\times6.4\times5.5$ Mm^3 with the grid sizes: $50\times50\times43$ km^3, $25\times25\times21.7$ km^3 and $12.5\times12.5\times11$ km^3 ($128^2\times127$, $256^2\times253$ and $512^2\times505$ mesh points). The domain includes a top, 5 Mm-deep, layer of the convective zone and the low Sun chromosphere. In this section, the results and quantities are obtained from simulations of [32] via a single-fluid model. This is a postprocessed calculation for quantities that belong to the multicomponent model presented. Since the electron/heavy-particle collision frequency is high in the conditions chosen, a thermal equilibrium case $T_e = T_h$ has been considered for the computation of the transport coefficients. For the sake of clarity, only results from a slice at a constant geometrical height $z = -0.5Mm$, below the photosphere has been presented in this section.

Figs. 8, 9, and 10 show snapshots of the distribution of the plasma beta parameter β_p, temperature T, and total mass density, respectively. As it can be seen, the temperature is varying from 4000 K to 6500 K, the plasma beta parameter is varying on a large range of magnitude, from weakly- to strongly-magnetized. In the snapshot of the simulation, a characteristic granulation pattern with the relatively hot ($T > 5500$ K) and less dense upflowing weakly-magnetized plasma in the middle of the granular cells can be observed. In addition, the lower temperature ($T < 4500$ K) and higher density downflowing strongly-magnetized plasma at the intergranulation boundaries can be perceived (red lines of granulation). A strongly-magnetized cold plasma can be seen in the middle of the snapshot.

Figs. 11, 12 and 13 present the distribution of the heavy-particle heat flux $\lambda_h|\boldsymbol{\partial_x} T|$ and the ratios $\lambda_e^{\parallel}/\lambda_e^{\perp}$, $\lambda_R^{\parallel}/\lambda_h$, and $\lambda_e^{\parallel}/\lambda_h$, respectively. Fig. 12 shows that the electron thermal conductivity tensor $\bar{\bar{\lambda}}_e$ is almost isotropic everywhere, except in the middle of the snapshot where $\lambda_e^{\parallel}/\lambda_e^{\perp} = 1.08$. Fig. 13 shows that the electron thermal conductivity is small compared to the heavy thermal conductivity. These results are related to the results from Fig. 1 and Fig. 2 that show that

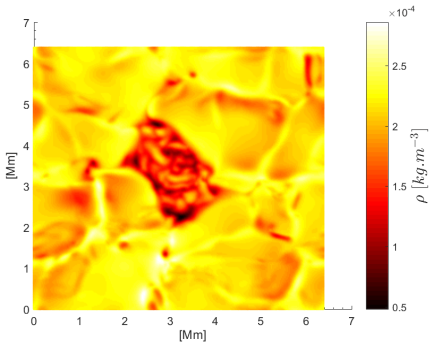

Figure 10: Total mass density ($kg.m^{-3}$) distribution from the radiative 3D MHD simulations of a pore by [32]

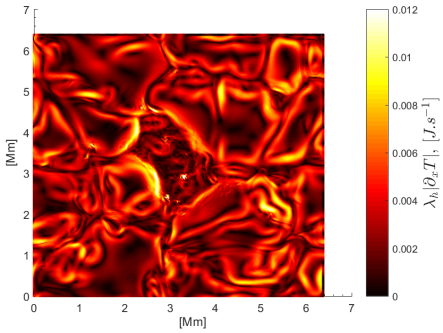

Figure 11: Distribution of the heavy particle heat flux $\lambda_\mathfrak{h}|\partial_{\boldsymbol{x}} T|$, for the Helium-Hydrogen mixture S_1 based on the results of [32]

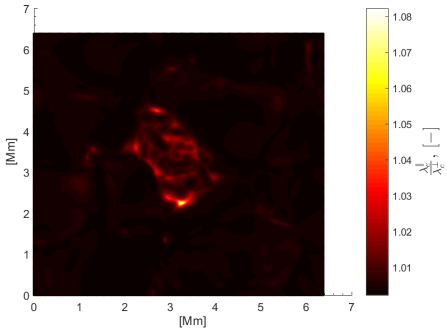

Figure 12: Ratio $\lambda_\mathfrak{e}^{\parallel}/\lambda_\mathfrak{e}^{\perp}$ distribution, for the Helium-Hydrogen mixture S_1 based on the results of [32]

the mole fraction of electrons is very small compared to the mole fraction of heavy particles in that range of temperature between 4000 K to 6500 K.

4.3. Components of the generalized Ohm's law in a pore at the Sun photosphere

As in section 4.2, we compute the components of the generalized Ohm's law from Eq. (25) using a

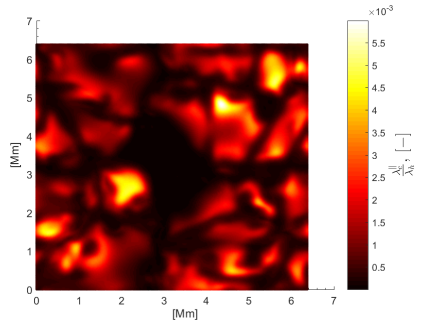

Figure 13: Ratio $\lambda_\mathfrak{e}^{\parallel}/\lambda_\mathfrak{h}$ distribution, for the Helium-Hydrogen mixture S_2 based on the results of [32]

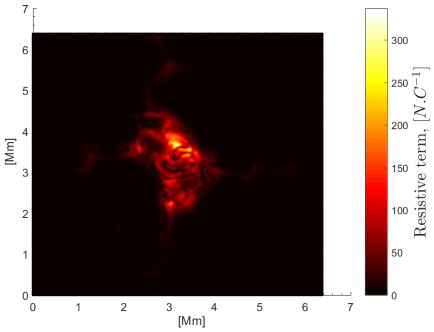

Figure 14: Distribution of the resistive term (first term of (Eq. 25)),for the Helium-Hydrogen mixture S_1, based on the results of [32]

Helium-Hydrogen mixture, from the simulation by [32]. According to the result found in Fig. 12, we assume an isotropic distribution of the transport properties. Fig. 14, 15, 16, 17, and 18 show the distribution of the resistive term, the electron battery term, the heavy-particle battery term and the Soret terms for electron and heavy particles respectively.

Under this condition, the dynamics of the electric field are dominated by the resistive term at the middle of the pore. The battery term for heavy particles appears to be higher at the middle of the pore and at some intergranulation boundaries. Finally, the Soret and battery terms for electrons have higher magnitude at the intergranulation boundaries. The latter is negligible compared to the other terms of the generalized Ohm's law. Indeed, this is due to the mole fraction of electrons which is very small compared to heavy particles under these conditions. These results are coherent with the mole fraction distribution presented in Fig. 1, Fig. 2 and Fig. 3.

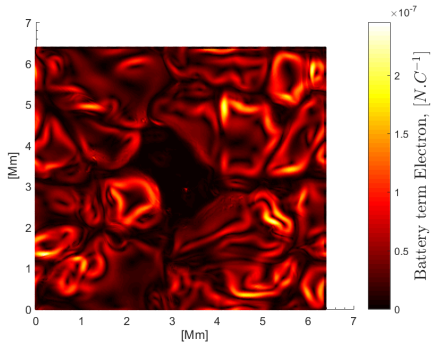

Figure 15: Distribution of the electron battery term (second term of (Eq. 25)), for the Helium-Hydrogen mixture S_1, based on the results of [32]

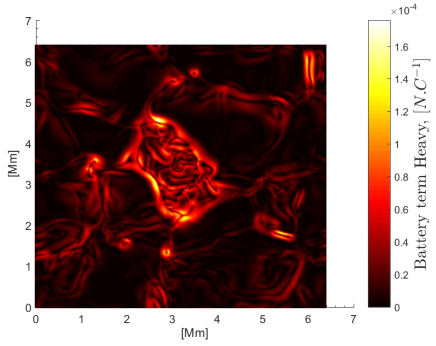

Figure 16: Distribution of the heavy battery term (third term of (Eq. 25)), for the Helium-Hydrogen mixture S_1, based on the results of [32]

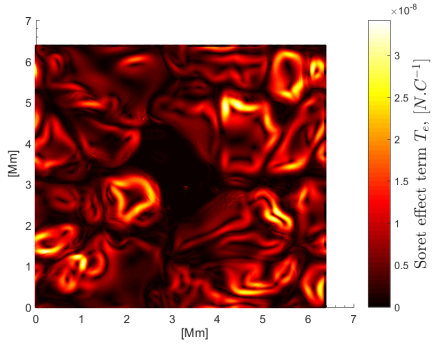

Figure 17: Distribution of the Soret/Dufour term (fourth term of (Eq. 25)), for the Helium-Hydrogen mixture S_1, based on the results of [32]

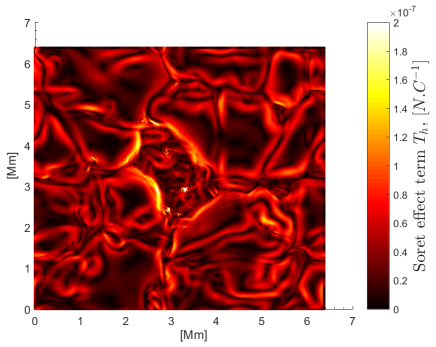

Figure 18: Distribution of the Soret/Dufour term (last term of (Eq. 25)), for the Helium-Hydrogen mixture S_1, based on the results of [32]

5. Conclusion

The present model, derived from the kinetic theory of [13], is neither a single-fluid MHD nor a multi-fluid model. It is an intermediary model between the two, i.e., a drift-diffusion multi-component model. Although the multi-fluid model and the multicomponent model are catching the same physics, their main difference is the scaling that has been used in the generalized Chapman-Enskog expansion. Their scaling leads to a thermal non-equilibrium multicomponent model with one momentum equation, where the electrons and each heavy particle diffuse in the hydrodynamic heavy-particle reference frame. These developments lead to an extended range of validity for partially and fully ionized plasma, non-,weakly- and strongly-magnetized plasmas and for a general multicomponent mixtures, which can be applied to Sun atmosphere conditions. From the numerical point of view, the multicomponent model is prone to less stiffness compared to the conventional multi-fluid models, where source terms and coupling terms are considered in the momentum equations and energy equations of each particle. On the other hand, the single-fluid MHD model is shown to be a thermal equilibrium model with no relaxation term and decoupling between the particles. However, in this framework, this model shows less numerical stiffness in absence of source/relaxation terms. Fluid-models are valid only in cases where the plasma is in collisional regimes leading to small values of the Knudsen number. Thus, only perturbations of Maxwellian distribution functions are considered here.

General conditions largely representative of the Sun lower atmosphere have been chosen in order to compute all the transport properties for a Helium-

Hydrogen mixture S_1. A spectral Galerkin method based on a third-order Laguerre-Sonine polynomials approximation has been used. For convenience, we have implemented the transport model described in the paper in Mutation++, an open-source library[1]. In order to validate our model, a comparison with the model of [12] has been performed in the case of a fully ionized plasma S_2. Both models are derived from the kinetic theory based on a Chapman-Enskog method. Differences are observed in 1-the structure of the governing equations and 2- the nature of the collision operators. While the heavy transport properties are anisotropic in [12], in our model, they remain isotropic. Nevertheless, under the chosen range of conditions, both behave as isotropic. In [12], the corresponding series of Laguerre-Sonine polynomials are truncated at the second order, whereas a third-order accuracy is reached in our model. Good agreement has been obtained for the considered fully ionized S_2 mixture, in the chosen conditions.

Finally, using Mutation++ library, the method allows us to compute all the transport properties for a partially ionized plasma for a given mixture. The obtained results strongly depend on the mole fraction between the species of the mixture. We have been able to identify the behavior of the transport coefficients related to the chemistry of the species in the partially ionized mixture S_1. Considering the complexity of the multicomponent model and the new terms that appear, postprocessing calculations were performed based on the results of a pore simulation for a partially ionized plasma of a mixture of a Helium Hydrogen mixture S_1 in thermochemical equilibrium in the highly turbulent upper layer of the solar convective zone by [32]. These results allow us to both understand the effect and magnitude of these terms under the conditions we chose, especially the terms of the generalized Ohm's law. Generally, the plasma being weakly ionized under these conditions, all the transport fluxes related to the electrons are negligible compared to those from heavy particles. Especially, we show a new formulation of the resistivity which depends on the multicomponent transport coefficients taking into account all possible interactions in the mixture. It appears to be much more general than standard resistivity such as ambipolar resistivity or Spitzer resistivity. Under conditions where the plasma is dominated by electromagnetic forces, which is the case in the center of the pore in section 5, we find qualitatively that this term is dominating the dynamics of the weakly ionized Helium-Hydrogen plasma. On the other hand, at the interboundary granulations (or more generally in the case of quiet sun photosphere conditions), when the plasma is weakly ionized and thermal pressure dominated, the new terms such as the Soret / Dufour effects (related to the temperature gradients) are dominating the plasma dynamics. These new terms, which do not appear in the standard models of single-fluid or multi-fluid type, can play a relevant role in the dynamics of the plasma.

[1]The presented transport systems have been implemented into MUTATION++ Library. The GitHub link repository is https://github.com/mutationpp/Mutationpp

Acknowledgments

The research of Q. Wargnier is funded by an Idex Paris-Saclay interdisciplinary IDI PhD grant, and relies on the the support of NASA Ames Research Center (ARC), Advanced Supercomputing Division, von Karman Institute for Fluid Dynamics, CMAP - Initiative HPC@Maths from Ecole Polytechnique and of Ecole doctorale de Mathématiques Hadamard. T. Magin is supported by a Jean d'Alembert chair of University Paris-Saclay. Part of this work was conducted during the 2018 NASA Summer Program at ARC. We would like to thank I.N. Kitiashvili for providing us with the data in order to evaluate the transport properties in subsection 5.2.

References

[1] J. E. Vernazza, E. H. Avrett, R. Loeser, Structure of the solar chromosphere. III - Models of the EUV brightness components of the quiet-sun, The astrophysical journal 45 (1981) 635–725. doi:10.1086/190731.

[2] T. Wiegelmann, J. K. Thalmann, S. K. Solanki, The magnetic field in the solar atmosphere, AAPR 22 (2014) 78. arXiv:1410.4214, doi:10.1007/s00159-014-0078-7.

[3] T. Hartlep, F. H. Busse, N. E. Hurlburt, A. G. Kosovichev, Magnetohydrodynamic simulations of flows around rotating and non-rotating axisymmetric magnetic flux concentrations, Monthly Notices of the Royal Astronomical Society 419 (3) (2012) 2325–2328.

[4] I. N. Kitiashvili, S. Couvidat, A. Lagg, Using Realistic MHD Simulations for Modeling and Interpretation of Quiet-Sun Observations with the Solar Dynamics Observatory Helioseismic and Magnetic Imager, The astrophysical journal 808 (2015) 59.

[5] J. Martinez Sykora, B. De Pontieu, V. H. Hansteen, M. Carlsson, Impact of the Ion-Neutral Interaction Effects in the Solar Chromosphere, AGU Fall Meeting Abstracts (2015) SH31B–2411.

[6] J. E. Leake, V. S. Lukin, M. G. Linton, Magnetic reconnection in a weakly ionized plasma, Physics of Plasmas 20 (6) (2013) 061202. arXiv:1302.3287, doi:10.1063/1.4811140.

[7] E. Khomenko, M. Collados, A. Daz, N. Vitas, Fluid description of multi-component solar partially ionized plasma, Physics of Plasmas 21 (9) (2014) 092901. arXiv:https://doi.org/10.1063/1.4894106, doi:10.1063/1.4894106.
[8] E. Khomenko, On the effects of ion-neutral interactions in solar plasmas, Plasma Physics and Controlled Fusion 59 (1) (2017) 014038.
[9] A. Alvarez Laguna, A. Lani, H. Deconinck, N. N. Mansour, S. Poedts, A fully-implicit finite-volume method for multi-fluid reactive and collisional magnetized plasmas on unstructured meshes, Journal of Computational Physics 318 (2016) 252–276. doi:10.1016/j.jcp.2016.04.058.
[10] A. Alvarez Laguna, N. Ozak, A. Lani, N. Mansour, H. Deconinck, S. Poedts, A versatile numerical method for the multi-fluid plasma model in partially- and fully-ionized plasmas, Journal of Physics: Conference Series 1031 (2018) 012015.
[11] L. Ni, V. S. Lukin, N. A. Murphy, J. Lin, Magnetic reconnection in the low solar chromosphere with a more realistic radiative cooling model, Physics of Plasmas 25 (4) (2018) 042903. arXiv:1804.05631, doi:10.1063/1.5018351.
[12] S. I. Braginskii, Transport Processes in a Plasma, Reviews of Plasma Physics 1 (1965) 205.
[13] B. Graille, T. E. Magin, M. Massot, Kinetic theory of plasmas: translational energy, Mathematical Models and Methods in Applied Sciences 19 (04) (2009) 527–599.
[14] T. E. Magin, B. Graille, M. Massot, Thermo-chemical dynamics and chemical quasi-equilibrium of plasmas in thermal non-equilibrium, Center for Turbulence Research Annual Research Briefs (2009) 71–82.
[15] T. Magin, G. Degrez, Transport properties of partially ionized and unmagnetized plasmas, Phys. Rev. E 70 (2004) 046412. doi:10.1103/PhysRevE.70.046412.
[16] M. Asplund, N. Grevesse, A. J. Sauval, P. Scott, The Chemical Composition of the Sun, ARAA 47 (2009) 481–522. arXiv:0909.0948, doi:10.1146/annurev.astro.46.060407.145222.
[17] M. Carlsson, R. F. Stein, Does a nonmagnetic solar chromosphere exist?, The astrophysical journal 440 (1995) L29–L32. arXiv:astro-ph/9411036, doi:10.1086/187753.
[18] C. Frhlich, J. Lean, Solar radiative output and its variability: Evidence and mechanisms, Astronomy and Astrophysics Review 12 (2004) 273–320. doi:10.1007/s00159-004-0024-1.
[19] S. Solanki, Sunspots: An overview, Astronomy and Astrophysics Review 11 (2003) 153–286. doi:10.1007/s00159-003-0018-4.
[20] H. N. Russell, On the Composition of the Sun's Atmosphere, The Astrophysical Journal 70 (1929) 11. doi:10.1086/143197.
[21] J. B. Scoggins, T. E. Magin, Gibbs function continuation for linearly constrained multiphase equilibria, Combustion and Flame 162 (12) (2015) 4514 – 4522.
[22] J. B. Scoggins, C. P. Knisely, T. E. Magin, Crossed contributions to electron and heavy-particle transport fluxes for magnetized plasmas in the continuum regime, AIP Conference Proceedings 1786 (1) (2016) 130002. doi:10.1063/1.4967628.
[23] T. E. Magin, G. Degrez, Transport algorithms for partially ionized and unmagnetized plasmas, J. Comput. Phys. 198 (2) (2004) 424–449. doi:10.1016/j.jcp.2004.01.012.
[24] J. H. Ferziger, H. G. Kaper, Mathematical theory of transport processes in gases, American Journal of Physics 41 (4) (1973) 601–603. doi:10.1119/1.1987312.
[25] L. C. Woods, An Introduction to the Kinetic Theory of Gases and magnetoplasmas., Vol. 286, Cambridge University Press, 1995.
[26] V. Zhdanov, Transport Processes in Multicomponent Plasma, Vol. 44, Taylor & Francis Group, 2002.
[27] R. Balescu, Transport Processes in Plasmas, Vol. 1: Classical Transport; Vol. 2: Neoclassical Transport, North-Holland Press, 1988.
[28] A. Kolesnikov, General formulation of multicomponent plasmas transport with ambipolar approach for weakly ionized gases, 41st Aerospace Sciences Meeting and Exhibit.
[29] G. A. Tirsky, Up-to-date gasdynamic models of hypersonic aerodynamics and heat transfer with real gas properties, Annual Review of Fluid Mechanics 25 (1) (1993) 151–181. doi:10.1146/annurev.fl.25.010193.001055.
[30] D. Bruno, M. Capitelli, C. Catalfamo, D. Giordano, Transport properties of high-temperature air in a magnetic field, Physics of Plasmas 18 (1) (2011) 012308. arXiv:https://doi.org/10.1063/1.3533430, doi:10.1063/1.3533430.
[31] M. Capitelli, D. Bruno, A. Laricchiuta, In Fundamental Aspects of Plasma Chemical Physics I, Springer, 2013.
[32] I. N. Kitiashvili, A. G. Kosovichev, A. A. Wray, N. N. Mansour, Mechanism of spontaneous formation of stable magnetic structures on the sun, The Astrophysical Journal 719 (1) (2010) 307.

TURBINE & COMPRESSOR

AERODYNAMICS AND HEAT TRANSFER

Impact of Shrouded Stator Cavity Flow on Axial Compressor Performances

Cedric Babin

Turbomachinery and Propulsion Department, von Karman Institute for Fluid Dynamics, Belgium, cedric.babin@vki.ac.be

Supervisor: Fabrizio Fontaneto

Assistant Professor, Turbomachinery and Propulsion Department , von Karman Institute for Fluid Dynamics, Belgium, fontaneto@vki.ac.be

University Supervisor: Xavier Ottavy

Head of Turbomachinery Department - LMFA , Ecole Centrale Lyon, France

Abstract

The inclusion of technological effects (such as blade fillets, main channel steps, leakage flows...) in the early stage of turbomachinery components design, allows engine manufacturers to obtain a more robust prediction of the performance of the final machine. Technological effects that are responsible for the sealing management between stationary and rotating part generate losses (pressure rise penalty, entropy generation...) therefore playing a fundamental role in the definition of the machine efficiency. In axial compressors with shrouded stator blades, due to the static pressure increase in the main channel, a recirculation flow is generated under the hub platform. The so called cavity flow is then dependent upon the sealing technology used (e.g: labyrinth seals) as well as the design of the stator hub cavities. In this particular case, experience demonstrated that the stability limit of the machine can also be directly affected by the cavity layout.

The goal of the thesis is to investigate the physics of cavity flow and its impact on compressor performance and stability. Supported by the complementary use of experimental end numerical investigations as well as physics based modeling, the loss generative mechanisms associated to the presence of the cavities are investigated. This will make possible to give a precise description of the off design conditions generated at the blade row inlet in different operating conditions. In the mean time it allows to identify and separate the losses generated by the cavities from the losses generated by the blade profile working at off design conditions.

Keywords: axial compressor, cavity flows, leakage flow, shrouded stator blade

An Uncertainty Estimation Method for Turbulence Statistics

Elissavet Boufidi

Turbomachinery and Propulsion Department, von Karman Institute for Fluid Dynamics, Belgium, boufidi@vki.ac.be

Supervisor: Fabrizio Fontaneto

Assistant Professor, Turbomachinery and Propulsion Department, von Karman Institute for Fluid Dynamics, Belgium, fontaneto@vki.ac.be

University Supervisor: Tony Arts

Head of Department and Professor, Turbomachinery and Propulsion Department, von Karman Institute for Fluid Dynamics, Belgium
iMMC, Université catholique de Louvain, Belgium, arts@vki.ac.be

Abstract

A complete uncertainty estimation method for turbulence statistics is presented, which considers both the measurement and the statistical uncertainty contributions. Its step-by-step application to hot wire anemometry measurements performed at the inlet of a short-duration wind tunnel is presented as well.

Keywords: uncertainty, turbulence statistics, statistical convergence

1. Introduction

Reliable experimentally obtained turbulence information is required for both the validation of numerical simulations and the provision of turbulent boundary conditions. Moreover, the development of high fidelity CFD and the ability to simulate the turbulent flow field with Large Eddy Simulations (LES) and Direct Numerical Simulations (DNS) create the need for higher-order turbulence statistics available for validation [1]. For a meaningful validation process, this data should be accompanied by uncertainty bounds.

As suggested by Favier [2], two macro uncertainty sources can be identified for experimental data: the measurement related uncertainty and the uncertainty associated with the statistical data reduction. The first item refers to all bias and random errors that result from the application of a particular instrument and measurement methodology (e.g. sensor, calibration, installation, flow conditions, data reduction, etc.). The second uncertainty contribution refers to the significance of the finite sample size when computing averaged quantities. In the case of turbulence measurements, it is equivalent to the observation time (i.e. the sampling duration) with respect to the period of the phenomenon. Different terms are used in the literature to characterize this uncertainty source: statistical uncertainty [3; 4], sampling uncertainty [5] and random uncertainty [6]. For the remainder of this paper this item will be referred to as statistical uncertainty, while the first item as measurement uncertainty.

The measurement uncertainty budget is in general well documented and is normally evaluated by two widely accepted standards, the ASME Measurement Uncertainty [7] and the ISO Guide to the Expression of Uncertainty in Measurements (GUM) [8]. The two methods differ in terms of classification of uncertainty sources but are consistent in terms of results and computation methodology: the final uncertainty is derived from the propagation of all the uncertainty terms through a first order approximation of a Taylors series expansion. Such a procedure implicitly assumes the linearization of the measurement model and that the input and output quantities would follow a normal or a scaled and shifted t-distribution. According to the GUM [8], when the model features significant non-linearity, the inclusion of higher order terms in the Taylor series expansion is required. This procedure can be algebraically complex and the assumption of the symmetry of the distributions should still be met. When this assumption is not valid, a Monte Carlo method (MC) is suggested to correctly propagate the probability distributions of the variables. The

GUM supplement [9] provides guidelines for the application of MC in measurement uncertainty computations.

The aforementioned works refer to single-sample experiments where only the statistical uncertainty of the population mean is included, evaluated through the variance of a large number of independent samples N. The uncertainty estimation of other statistics due to the sampling of a turbulent process is, on the contrary, much less investigated. The statistical uncertainty is typically computed based on theoretical relationships assuming normal distributions and independent samples. Error estimates for central moments up to the fourth order and Reynolds stresses can be found in Benedict & Gould [3]. The samples are considered independent when the sampling rate is less than $1/(2T_{int})$, with T_{int} being the integral time scale of the turbulent field [10; 11]. When higher sampling rates are used, the uncertainty should be estimated based on the number of independent samples N_{eff} [12]. As the uncertainty of the time-averaged quantities has been observed to decrease with rate $1/\sqrt{N_{eff}}$ [12], the minimization of the uncertainty requires the elongation of the averaging time T (i.e. the signal duration), which can often be bounded by limitations imposed by the experimental setup (e.g. in short-duration wind tunnel tests). Antonia et al. [13] observed that the required averaging time varies dependening on the statistical quantity to be computed (e.g. mean, rms, skewness) and potentially with other parameters of the flow like the Reynolds number and the distance from the wall for boundary layer measurements.

In these conditions, we propose the use of a non-parametric resampling algorithm like the moving block bootstrap method (MBB) to process short time-series. This method maintains the correlation of the time series and it is thus suitable for turbulent flows sampled at a high rate. The MBB technique also allows for the computation of the uncertainty of all statistics without requiring the derivation of complex formulas (see e.g. the expressions for the variance of *r-th* order moments in [3]). Finally, the MBB does not require any assumption about the underlying probability distribution of the population. This is also an essential requirement for the treatment of velocity distributions in turbulent flows that are often non-normal.

The present work aims at developing an uncertainty estimation methodology for turbulence statistics which considers both the measurement and the statistical uncertainty. The former is assessed through the implementation of a MC method in order to take into account the non-linearity resulting from the data reduction process, while the latter is quantified by means of the MBB algorithm. The uncertainty computation method is applied to Hot Wire Anemometry (HWA) measurements performed at the inlet section of a transonic turbine stage tested in a blowdown facility. The limited measurement time (of the order of 100-300 ms) in this type of test rigs increases the statistical uncertainty of turbulence parameters as statistical convergence is not ensured. Therefore, it is necessary that the statistical uncertainty source is included in the total uncertainty budget. With the present methodology, reliable confidence intervals can be computed for all the turbulence parameters of interest.

2. Uncertainty estimation methods

2.1. The Monte Carlo method (MC)

The MC uncertainty computation aims at computing the probability distribution of a certain output quantity by propagating the probability distributions of the inputs through a measurement model. In the present case, it is used to estimate the uncertainty of the velocity time series, taking into account all the uncertainty sources occurring during the measurements and the hot-wire (HW) calibration. As will be explained in the following section, the MBB method is expected to account for the random uncertainty of velocity samples of the same test. Therefore, such uncertainty sources (e.g. random noise of the HW output voltage) should not be included in the MC to avoid considering them twice.

The ASME standard [7] is used for the categorization of uncertainty sources. Uncertainty sources that cause a constant bias to the measured quantity are defined as systematic, while those that cause a variability to the measured quantity are defined as random. The procedure to define the input quantities, following Coleman & Steele [14], is illustrated in Figure 1 for two variables, X_1 and X_2, affected by the uncertainty sources s_1, b_1, b_2 and b_2, b_3 respectively, where s represents a random uncertainty source and b a systematic uncertainty source. At each *i-th* iteration, the input PDFs are randomly sampled so that the input variables to the measurement model Y are computed as: $X_{1i} = \bar{X_1} + s_{1i} + b_{1i} + b_{2i}$ and $X_{2i} = \bar{X_2} + b_{2i} + b_{3i}$, being $\bar{X_1}$ and $\bar{X_2}$ the expected values. Error sources common to multiple variables (such as b_2 in this example) are automatically taken into account, leading therefore to a straight-forward implementation of correlated uncertainty terms. The values X_{1i} and X_{2i} constitute the

inputs to the measurement model $Y = f(X_1, X_2)$ for this iteration. By collecting M realizations (i.e. the number of MC iterations) of the output variable Y, the probability distribution is then constructed by sorting the output values in non-decreasing order, allowing therefore to compute its expected value and any other statistical moments at the desired confidence level p. The algorithm is schematically presented in Figure 2. It should be noted that when the output distribution is asymmetric, different coverage intervals can be defined, including the probabilistically symmetric and the shortest coverage interval [9]. In this study, the shortest coverage interval is used.

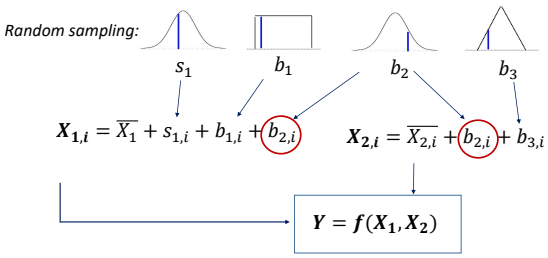

Figure 1: Definition of input variables for the Monte Carlo method.

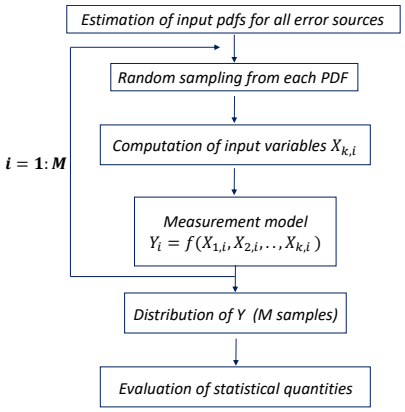

Figure 2: MC algorithm.

The number of iterations M normally results from a trade-off between the statistical significance of the output PDF and the required computational time. According to [9], an a priori estimation of the number of realizations can be obtained by Eq. (1), where p represents the desired confidence interval such that, for $p = 95\%$, M should be equal or higher than 2×10^5. In the present study, the convergence is evaluated a posteriori.

$$M = 10^4 \frac{1}{1-p} \tag{1}$$

The quality of the results of a MC uncertainty computation directly depends on the representativeness of the PDFs of the uncertainty sources. When the latter are not known a priori, a common practice is to assume a normal distribution for random uncertainty sources while the systematic uncertainty items are defined on the basis of the available data and the engineering judgement.

2.2. *The Moving Block Bootstrap method (MBB)*

The bootstrap method is a resampling algorithm that allows computing the statistical inference of a group of samples when its size is statistically too small (i.e. non-representative) or when the probability distribution is unknown. The method, developed originally by Efron [15] in an econometric framework, consists in the generation of B sample series that are constructed by randomly resampling the original data series x. The statistic of interest θ_i is then computed for each sample series, leading therefore to the generation of a population θ_B for which a mean value μ_B and a variance σ_B can then be computed.

Although the bootstrap technique provides a good estimation of the sampling distribution [16], its direct application to turbulence measurements would be inconsistent since, by randomly resampling the original data series, the intrinsic correlation of turbulent phenomena is automatically degraded. In order to overcome this issue, the moving block bootstrap (MBB) methodology by Kunsch [17] is adopted. The procedure firstly splits the original data series x, consisting of N samples, into $N - c + 1$ overlapping blocks. N/c blocks will then be extracted and randomly concatenated, generating therefore a bootstrapped data series $x^*_{b,i}$ of roughly the same size of the original one. The process is then repeated B times in order to create a population of the statistic parameter of interest. A principle sketch of the moving block bootstrap method is shown in Figure 3.

As suggested by Politis et al. [18], the optimal block length c can be determined by retrieving first an estimate of the integral time scale through the computation of the autocorrelation function of the original dataset. Nevertheless, when dealing with limited observation times, the autocorrelation function could present high amplitude oscillations leading to an incorrect evaluation [19]. In the latter case, Theunissen [20] proposed to perform a conservative selection of

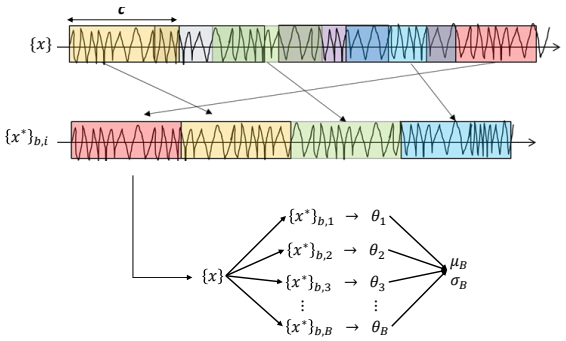

Figure 3: Moving block bootstrap principle.

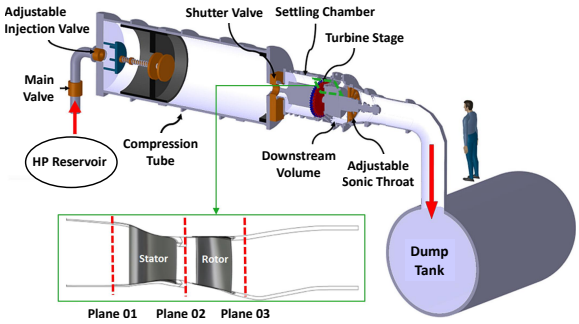

Figure 4: Layout of the facility.

the block length by increasing it by at least a factor of 2. In the frame of the present project, the optimal block length was selected through a sensitivity analysis. The optimum block length coincides with the minimum number of samples per block that provides convergence on the mean value of the bootstrapped integral length scale. Coherently, the number of bootstrap repetitions B was defined by monitoring the convergence on the mean and on the confidence interval limits of all the turbulence statistics of interest.

Garcia et al. [4] validated the MBB method both analytically and experimentally using 80 repeatable tests. The authors reported a good agreement on the computed uncertainty of the turbulence parameters. They concluded that the MBB method is capable of quantifying the statistical errors that produce scatter in repeated measurements. Based on this study, we consider the statistical uncertainty computed by the MBB method to take into account also random errors that produce scatter from sample-to-sample, e.g. noise in the HW voltage. This type of uncertainties is not included in the measurement uncertainty budget.

3. Experimental methods and setup

3.1. The CT3 Compression Tube facility

The turbine tests were conducted in the rotating turbine rig of the von Karman Institute (VKI). This short duration facility operates on the principle of a compression tube and allows testing a high pressure turbine stage at a larger scale while preserving the actual engine Mach and Reynolds numbers and gas-to-wall temperature ratio [21]. The layout of the facility is presented in Figure 4.

The duration of the test is around 0.3 s. In the present experimental campaign, one operating point has been investigated, whose operating conditions are given in Table 1.

Quantity	Value	Units
Turbine inlet Mach number	0.10	–
Inlet total pressure P_{01}	1040	*mbar*
Inlet total temperature T_{01}	463	*K*
Wall-to-gas temperature ratio	0.68	-
Non-dimensional rotation speed	281.3	–
Total-to-static turbine pressure ratio	2.21	–
Reynolds number at plane 2	6.93×10^5	–

Table 1: Experimental test conditions at mid-span.

3.2. The Measurement Plane

The test section in this experimental campaign hosts a single high-pressure stage consisting of a stator with 38 blades and a rotor with 48 blades. The measurements are performed at the inlet of the stage, half a stator axial chord upstream of the stator leading edge. The span at this position is 74.71 mm. The instrumentation used at the measurement plane and their setup are presented in Figure 5. A rake of four Kiel type pressure probes is used to measure the total pressure $P_{0,1}$ along the span and a rake of four thermocouples is used to measure the total temperature $T_{0,1}$. Two reference probes consisting of a thermocouple and a Kiel probe are used to measure $T_{0,1}$ and $P_{0,1}$ at mid-span. All probes are placed at different circumferential positions. The static pressure is measured at the tip and hub endwalls with five static pressure taps distributed over one vane pitch.

Figure 5a shows the employed HW probe as mounted in the test section. It features two HW heads, placed at half span distance from each other. The double-head configuration allows to sweep the channel span (by traversing radially the probe) with a reduced number of tests. The probe is also equipped with a thermocouple in order to measure the total temperature between the HWs. Due to the high inlet total temperature ($\sim$ 440 K), the operating temperature of the HWs had to be increased to reduce the sensitivity to the flow temperature. For this reason, a Platinum and Nickel alloy (90%Pt/10%Ni) was selected as wire

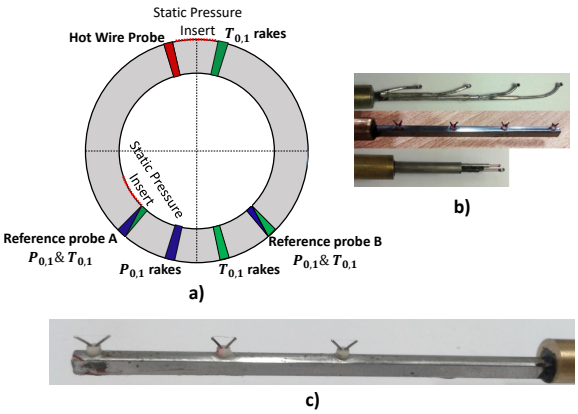

Figure 5: a) Instrumentation and setup at measurement plane, b) total pressure and thermocouple rakes, reference probes, c) HW probe.

material. This allowed using an operating temperature T_w of $\sim$ 540 K and $\sim$ 570 K, for heads 1 and 2 respectively. The Pt-Ni alloy was chosen as it offers high resistance to oxidation compared to conventional Platinum-plated tungsten wires, whose operating temperature limit is $\sim$ 550 K. The wires are of 9 μm diameter and 2 mm long. The actual sensing length of the HW is 1 mm, considering that copper plated stubs, used to eliminate the interference with the prongs, cover the wire along 0.5 mm at each extremity.

3.3. Hot-Wire Calibration Method

In the frame of the present investigation, a non-dimensional HW calibration based on Nusselt (Nu) and Reynolds (Re) numbers is employed, in order to eliminate the effect of the local flow conditions on the HW output [22**?**]. The methodology uses an effective wire temperature and empirical correlations to establish a unique $Nu-Re$ calibration curve.The procedure is only briefly described hereafter as the detailed analysis and evaluation of the performance of the calibration method is provided in [23].

For the present test conditions (Mach $<$ 0.3), the Nusselt number that expresses the convective heat transfer from the wire to the flow can be considered a unique function of the Reynolds number of the flow:

$$Nu = f(Re) \tag{2}$$

The heat transfer balance over the wire is given by

$$I^2 R_{wire} = \pi l_w k (T_w - r T_0) Nu \tag{3}$$

where R_w is the wire resistance, I the supplied current, l_w the active wire length, T_w the wire temperature and T_0 the total temperature of the flow. The recovery factor r can be assumed to be equal to 1 provided the low Mach number of the present application. By expressing the power supplied in terms of bridge voltage E_b, the Nusselt number can be rearranged as

$$Nu = \frac{E_b^2 R_w}{\pi l_w k (T_w - \eta T_0)(R_s + R_{top} + R_w)^2} \tag{4}$$

where R_{top} and R_s are constant resistances which depend on the circuit.

The wire Reynolds number is defined as

$$Re = \frac{\rho U d_w}{\mu} \tag{5}$$

The viscosity μ and the thermal conductivity k of the fluid are evaluated at the total temperature of the flow. T_w is defined as the temperature which collapses a set of $Nu - Re$ data obtained at different flow temperatures on a single curve. The R^2 coefficient of a 4th order polynomial fit is used as the selection criterion. This is the most suitable definition of the wire temperature to represent the true convective heat transfer process from the wire to the flow. In Figure 6, a set of data obtained at different flow total temperatures is presented. When plotted in terms of voltage and velocity, a different curve is created for each temperature level. All the datasets collapse into a single curve when plotted in function of Nu and Re using the effective wire temperature, according to Eq. (2). A single $Nu - Re$ calibration polynomial is obtained that can be employed to retrieve the flow velocity from non-isothermal flows using HWA.

This calibration methodology, based on the fact that Nusselt is a unique function of Reynolds within the flow conditions of the experiment, eliminates the need for an in-situ calibration. Therefore, a simple heater-equipped open jet facility can be employed for the calibration of the HWs. The calibration is performed at a different temperature and velocity compared to the measurement conditions, but at the same Reynolds number as the turbine experiment. The resulting calibration curve for HW head 2 is presented in Figure 6, with the effective operating wire temperature computed at 572 K.

Processing Methodology

The first step in the measurement methodology is to detect the interval for which the flow is stabilized and extract the corresponding signals. In Figure 7,

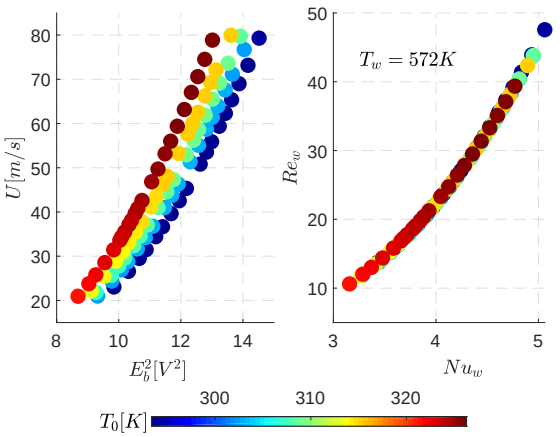

Figure 6: Effect of temperature on the absolute HW calibration (left), non-dimensional HW calibration (right).

the extracted signal parts are indicated for the inlet total temperature $T_{0,1}$, the inlet total pressure $P_{0,1}$, the static pressure at the tip $P_{s,tip}$ and for the HW signal. For this time interval, which lasts approximately 100-150 ms, the $P_{0,1}$ and $P_{s,tip}$ signals are stabilized. The $T_{0,1}$ signal presents some low-frequency fluctuations. The flow temperature variations with time are reflected in the HW raw voltage signal, because of the HW dependency on temperature.

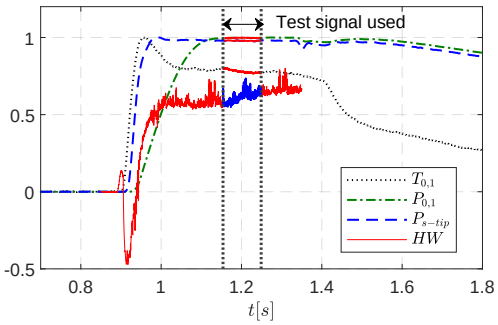

Figure 7: Normalized test signals.

Based on the calibration methodology, the total temperature and the total and static pressure values should be known at the HW location in order to retrieve the instantaneous velocity from the HW. Therefore, the data obtained for all the tests for this operating point are used to build radial profiles of P_0, P_s and T_0. The measurements of T_0 and P_0 are normalized by the reference value at mid-span for each test. Considering the uncertainty in the positioning of the probe, the values are averaged over 2% of the span and fitted with a Fourier fit. The measurements of P_s at the endwalls are normalized by the P_0 value at mid-span for each test and the mean values are fitted with a linear curve to estimate the static pressure values along the span. The non-dimensional profiles and the mid-span values of T_0 and P_0 are used to determine the local values at each HW measurement position. A mean value of the pressure measurements is considered for each test. This operation is valid since the flow pressure values remain very stable (±0.1% of the mean) throughout the entire duration of the turbine run. The fluctuations in total temperature registered during the test duration are taken into account using the time-resolved signal from the thermocouple of the HW probe.

The HW instantaneous voltage is transformed into Nusselt number applying Eq. (4) and the instantaneous T_0 signal. The instantaneous wire Reynolds number is then retrieved from the Nu-Re calibration law. The instantaneous velocity is computed by Eq. (5), where the density and the dynamic viscosity of the fluid are estimated using the local temperature and pressure values. The velocity time series is further processed to compute turbulence statistics.

3.4. Turbulence statistics

The statistical moments of turbulence are computed over the signal time duration ΔT. Since only the longitudinal velocity $U(t)$ is measured, all the following equations refer to this component. The first central moment is the mean velocity, which is computed as

$$\overline{U} = \frac{1}{\Delta T} \int_{t_0}^{t_0+\Delta T} U(t)\,\mathrm{d}t \tag{6}$$

The second central moment is the variance. In turbulence research the root mean square of the velocity fluctuations is most often used, which is the square root of the variance:

$$\overline{u'} = \left[\frac{1}{\Delta T} \int_{t_0}^{t_0+\Delta T} (U(t) - \overline{U})^2\,\mathrm{d}t \right]^{1/2} \tag{7}$$

The square root of the variance defines the turbulence intensity of the flow according to

$$Tu = \frac{\overline{u'}}{\overline{U}} \tag{8}$$

The third central moment, the skewness, is

$$S_u = \frac{1}{\overline{u'}^3} \frac{1}{\Delta T} \int_{t_0}^{t_0+\Delta T} (U(t) - \overline{U})^3\,\mathrm{d}t \tag{9}$$

The skewness is a measure of the lack of symmetry of the distribution and is zero for a symmetric distribution.

To obtain information about the structure of the turbulent flow field, the time autocorrelation coefficient $\rho(\tau)$ is used, which represents the degree of correlation between the flucutating velocity components u at two instants separated by a time interval τ:

$$\rho(\tau) = \frac{\overline{u(t)u(t+\tau)}}{\overline{u^2(t)}} \tag{10}$$

The integral time scale gives an estimate of the time interval for which the velocity signal is correlated. This parameter is calculated as

$$T_{int} = \int_0^\infty \rho(\tau)\,\mathrm{d}\tau \tag{11}$$

Using the Taylors frozen vortex hypothesis [24], the integral length scale L_{int} can be computed multiplying the integral time scale by a convective velocity, usually considered equal to the local mean velocity. Since experimentally obtained autocorrelation coefficients often feature wide oscillations around zero, the integration for the complete signal duration can produce erroneous results. Therefore, different options have been proposed for the upper integration limit of Eq. (11): the time lag for which the amplitude of the function decreases to e−1; or the time lag corresponding to the first root (see for example [20]). The presence of oscillations leads to an unreliable computation of the integral time scale, especially for short time intervals. An alternative method has been proposed by Roach [25] where the integral scale is computed from the power spectrum:

$$L_{int} = \left[\frac{E(f)\overline{U}}{4\overline{u'^2}}\right]_{f\to 0} \tag{12}$$

The micro length scale η, also known as Kolmogorov length scale, is considered representative of eddies that dissipate turbulent energy. It can also be computed following Roach [25] as

$$\eta = \left[\frac{\overline{U}^2\overline{u'^2}}{2\pi^2\int_0^\infty f^2 E(f)\,\mathrm{d}f}\right] \tag{13}$$

4. Uncertainty Analysis

In this section the uncertainty analysis methodology and the uncertainty sources are presented in detail.

4.1. Measurement Uncertainty Sources

The measurement uncertainty consists of two major sources: (a) the uncertainty of the HW calibration polynomial and (b) the uncertainty of the local flow properties at the HW measurement position.

4.1.1. HW calibration uncertainty.

The uncertainty stemming from the HW calibration can be categorized into two parts: the uncertainty of the calibration points and the uncertainty due to the fitting of the calibration curve. The HW voltage, the total temperature, the total and static pressure measurements are used to compute the calibration points (Nu, Re). The points are then fitted with a 4th order polynomial. For each Monte Carlo iteration i, the distributions of the input variables E_b, T_0, P_0 and P_{amb} are randomly sampled, the i-th set of calibration points $(Nu, Re)_i$ is computed and finally this set is fitted with a 4th order polynomial p_i. At the end of M iterations, a distribution of M values is obtained for each coefficient of the polynomial p. If the model used for the fitting correctly represents the physical phenomenon, any fitting errors should be attributed to random errors in the measurements that cause scatter in the calibration points. Therefore, if the random uncertainty in the input variables (in this case E_b, T_0, P_0 and P_{amb}) is correctly estimated, then the curve fitting error should be automatically accounted for by the uncertainty of the polynomial.

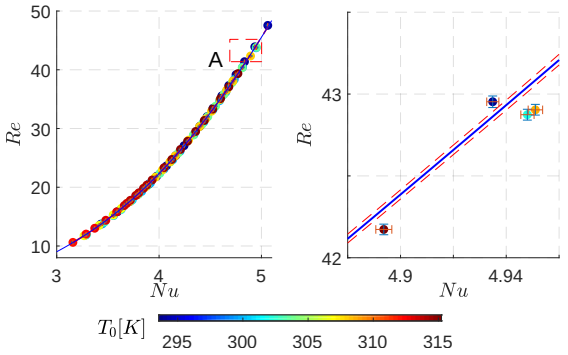

Figure 8: HW calibration curve with uncertainty bars (left), insight view into the calibration curve (right).

Initially, the random uncertainties for the input variables are estimated based on the variance of their output at flow-off conditions (instrument noise). The systematic uncertainties are evaluated based on the instrument documentation and calibration. The total pressure and temperature are measured inside the calibration nozzle by means of a K-type thermocouple

Property	Type	Distribution	Value
HW voltage	random	normal	$s = 0.001$ V
Ambient pressure	systematic	uniform	$a = b = 5$ Pa
PT100	systematic	uniform	$a = b = 0.1$ K
Thermocouple	random	normal	$s = 0.0015$ K
Thermocouple	systematic	uniform	$a = b = 1.1$ K
Druck DPI 610	systematic	uniform	$a = b = 17.5$ Pa
Validyne	random	normal	$s = 0.0012$ V
Validyne	systematic	uniform	$a = b = 32.5$ Pa

Table 2: Elemental uncertainties of instruments used in the HW calibration chain

and a Validyne differential pressure transducer respectively. The static pressure at the measurement point is the ambient pressure, measured by a Druck DPI 150 pressure indicator. The thermocouple and the pressure transducer have been calibrated against a PT100 thermometer and a Druck DPI 610 pressure indicator respectively. The elemental uncertainties originating from the instruments are summarized in Table 2. The uncertainty values s represent the uncertainty at the standard deviation level for normal distributions, while for uniform distributions the values a and b represent the lower and upper limits.

The relative curve fitting error is shown in Figure 9. It can be seen that for some calibration points the deviation from the curve is higher than their measurement uncertainty. Thus, the fitting error is not taken into account automatically by the MC. Hölle et al. [26] encountered the same problem when evaluating the measurement uncertainties of pneumatic multi-hole pressure probes. The authors concluded that the method cannot be used when the fitting error is not negligible compared to the calibration uncertainty. To overcome this limitation, a different approach is applied in the present case. Since the curve fitting error is the result of random errors producing scatter in the calibration points, this error is used as a measure of the random uncertainty and no random uncertainty is assigned to the input values to avoid accounting for it twice. It has to be noted that this approach assumes that the scatter in the calibration points is exclusively due to random errors in the Reynolds values. The distribution of the fitting error (which is computed as $Re_{cal} - Re_{fit}$) has a mean value of zero. Thus, it does not affect the average value of the calibration output, but only its variability. Therefore, a normal distribution is assigned to the fitting error with the computed mean and standard deviation values .The fitting error is therefore treated as an additional error source added to the uncertainty of the measured Reynolds number. The measured Reynolds number for one iteration i is then defined by the following equation:

$$Re_i = p_i(Nu_i) + s_i \tag{14}$$

where Nu_i contains the uncertainty of the measured Nusselt number, p_i the uncertainty of the calibration polynomial parameters and s_i the uncertainty due to the fitting error. The uncertainty s_i is a systematic term for the measured Reynolds number, as the calibration curve is fixed. The parameter s has a mean value of zero and a standard deviation of 0.0273 and 0.1176 for HW1 and HW2 respectively.

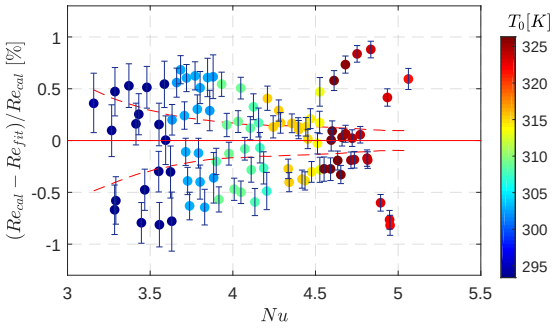

Figure 9: Relative calibration curve fitting error.

4.1.2. Uncertainty of local flow properties.

The flow properties at the HW measurement position are used to retrieve the velocity from the HW calibration. These flow properties are the total temperature T_0, the total pressure P_0 and the static pressure P_s. As previously explained, the profiles of P_0 and T_0 along the span are defined by measurements with different instruments. The values are normalized by the value at mid-span for each test. The non-dimensional profiles and measurement at mid-span at each specific test are used to obtain the local flow data at each HW measurement position. The uncertainty therefore stems from the uncertainty in the determination of the profile and the bias error due to the measurement at mid-span during each test.

The uncertainty of the profiles is computed considering the test-to-test variability of the measurements. Since the measurements are performed with different instruments, the bias errors are not considered separately: they are taken into account in the variability. The non-dimensional measurements are averaged over 2% of the span considering the uncertainty in the positioning of the probes ($\sim \pm 0.5$ mm). The mean value and the standard deviation are computed at each spanwise cluster. The standard deviation for

total pressure and temperature profiles is presented in Figure 10. Since there is no distinct trend in the distribution of the standard deviation along the span, the mean value of the standard deviation std_{mean} is considered representative of the uncertainty in the measurement of T_0 and P_0 due to the test-to-test repeatability and the bias of the different instruments. Since there are not enough measurement points to evaluate the distribution per cluster, the normality assumption is taken. Therefore, the input value of T_0 for one span position k at one MC iteration i is defined as follows:

$$T_{0_{k,i}} = \overline{T_{0_k}} + s_{T_{0_i}} \tag{15}$$

where $\overline{T_{0_k}}$ is the mean value at a certain span location and $s_{T_{0_i}}$ is drawn from a normal distribution with zero mean value and standard deviation equal to std. For each MC iteration i, the values for all H span positions $[T_{0_{k,i}}]_{k=1:H}$ are fitted with a Fourier model to get the spanwise profile $T_{0_{fit,i}}$. The same procedure applies to the measurements of total pressure. An analogue procedure is followed for P_s: the values at hub and tip are computed and the profile fit is obtained by linear interpolation between these two values. The uncertainty of the profiles at the 95% confidence level is shown in Figure 11.

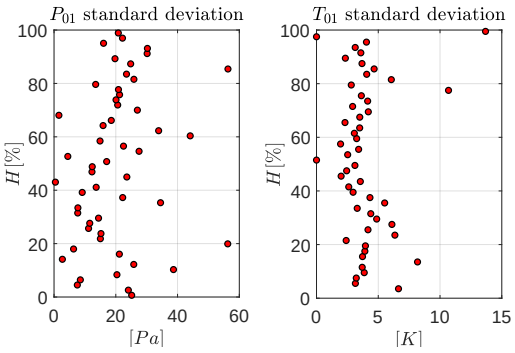

Figure 10: Test-to-test variability of $P_{0,1}$ and $T_{0,1}$ along the span.

The bias error of the T_0 measurement b_{T_0} is assumed to follow a normal distribution with zero mean and standard deviation equal to 0.25 K. The uncertainty of the P_0 measurement, being a differential measurement, originates from two error sources: the error in the measurement of the differential pressure b_{P_0} and the error in the measurement of the ambient pressure $b_{P_{amb}}$. b_{P_0} is estimated to follow a normal distribution with zero mean and standard deviation equal to 0.25 mbar. $b_{P_{amb}}$ follows a uniform distribution with limits at ±0.05 mbar (instruments resolution). The methodology to compute the flow properties at the HW span position for one MC iteration is schematically presented in Figure 12. $T_{0_{ms}}$ and $P_{0_{ms}}$ are the values of the mid-span measurement for the specific test.

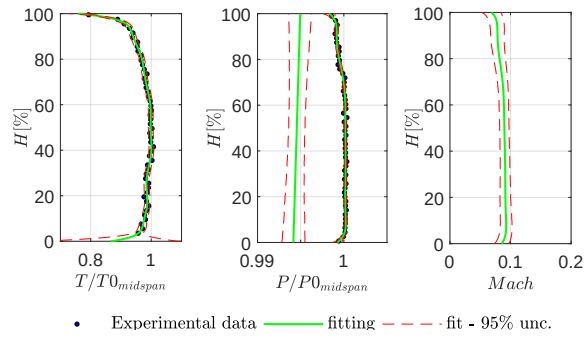

Figure 11: Uncertainty of spanwise profiles at 95% confidence level.

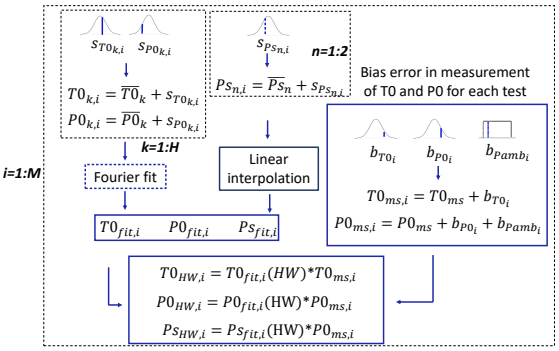

Figure 12: Methodology for the computation of the flow properties T_0, P_0 and P_s at the spanwise position of the HW probe.

4.2. *Uncertainty of the time series*

The uncertainty inputs are inserted in the measurement model to retrieve the velocity time series for each test. For each MC iteration i, each instantaneous velocity sample j is computed as follows

$$U_{i,j} = [p_i(Nu_{ij}) + s_i]\frac{\mu_{ij}}{\rho_{ij} d_w} \tag{16}$$

where

$$Nu_{i,j} = \frac{E_{b_j}^2 R_w}{\pi l k_{ij}(T_w - \eta T_{0_{ij}})(R_s + R_{top} + R_{wire})^2} \tag{17}$$

All the turbulence statistics of interest are also computed at each iteration i. After M iterations, the output

of the MC loop is the distribution GY (composed by M points) for each turbulence parameter Y and a distribution for each sample of the velocity time series. The measurement uncertainty is defined for each parameter by computing the confidence intervals at the 95% level. The methodology is presented in Figure 13. The velocity time series with 95% confidence intervals is presented in Figure 14 and the histograms for two measurement samples A and B are presented in Figure 15. The distributions are slightly skewed and the median value of the velocity is a rather more suitable parameter than the mean value. The same degree of skewness is observed for both points. This is because the systematic uncertainty sources considered mainly affect the ensemble of the time series by introducing a bias. The only factor causing variability is the calibration polynomial uncertainty p_i.

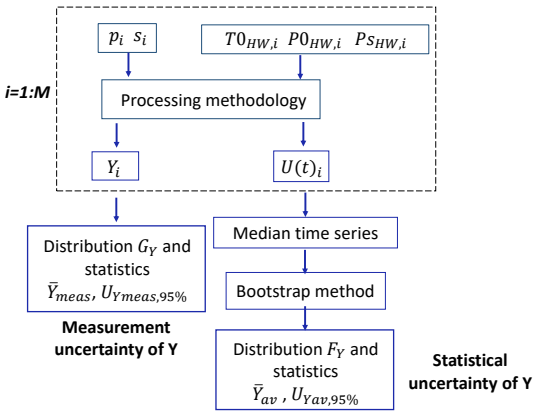

Figure 13: Overall methodology.

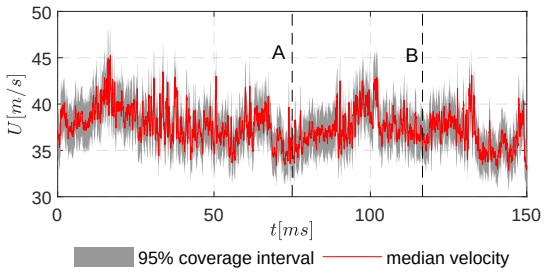

Figure 14: Velocity time series with 95% confidence interval.

4.3. Statistical uncertainty

The statistical uncertainty of the turbulence statistics is computed by applying the MBB to the median

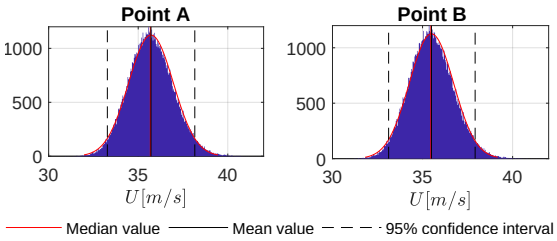

Figure 15: Histograms of points A and B.

velocity time series (Figure 14). The output is a distribution F_Y for each turbulence parameter and the computed confidence intervals express the statistical uncertainty at the 95% confidence level. The statistical uncertainty is independent of the measurement uncertainty, as the latter only considers systematic uncertainty sources. Applying the bootstrap to the mean velocity time series or to any times series $U_i(t)$ (corresponding to the i MC iteration) yields the same statistical uncertainty, only with a small variation on the mean value.

The histogram of the velocity time series for one test is presented in Figure 16. The distribution deviates from normality, featuring positive skewness. This reinforces the necessity to use a non-parametric method which does not require a priori assumptions on the probability function of the velocity distribution.

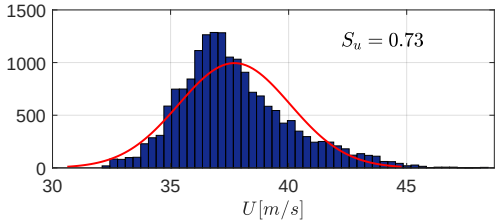

Figure 16: Histogram of the median velocity time series for one test.

The application of the MBB requires the selection of two parameters: the number of the bootstrap series B and the optimal block length c_{opt} for which the intrinsic correlation of the signal is maintained. c_{opt} was selected by a sensitivity analysis as the block length for which the mean integral length scale, computed by Eq. 12, converges to its final value. This indicates the convergence of the power spectrum. Convergence was reached when the block length was approximately one tenth of the whole signal, i.e. c_{opt} = 1800 samples.

B is selected by monitoring the convergence of all

the turbulence statistics of interest. Indicatively, the convergence for the turbulence intensity and the integral length scale are reported in Figure 17 and Figure 18 respectively. It can be seen that the computation of the standard deviation requires a smaller number of iterations compared to the computation of the confidence interval limits. Therefore, the computation of a confidence interval is computationally more expensive compared to the computation of the variance. Moreover, the number of bootstrap series B required for convergence is higher for the integral length scale (78000 series) than for the convergence on the turbulence intensity (35000 series). Considering the convergence histories of all the statistics, $B = 10^5$ was selected.

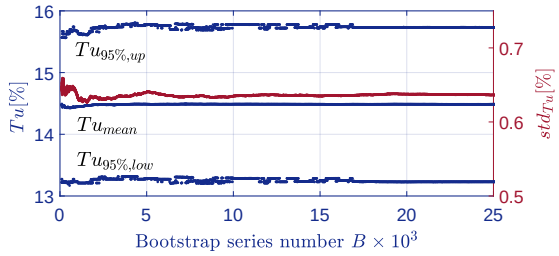

Figure 17: Mean, standard deviation and confidence interval limits of the turbulence intensity, convergence with bootstrap series number B.

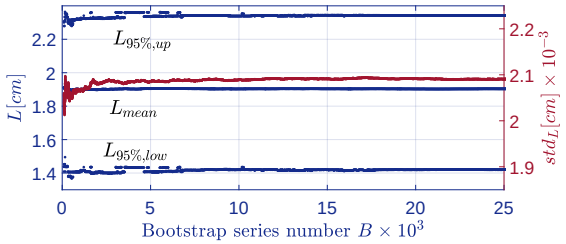

Figure 18: Mean, standard deviation and confidence interval limits of the intergral length scale, convergence with bootstrap series number B.

5. Results and discussion

The spanwise distributions of the uncertainty budget for the turbulence statistics presented at the turbine inlet plane are presented in Figure 19. The uncertainty contributions are expressed as percentage of the total uncertainty.

The measurement uncertainty is the prevalent uncertainty source on the computation of the mean velocity. This contribution is significant due to the propagation of the uncertainty of all the flow properties on the HW signal. For the other statistics, the statistical uncertainty prevails. It can be seen that the measurement uncertainty is important for the length scales as the mean velocity value is required in their computation (Eq. (12) and (13)). The measurement uncertainty of the corresponding time scales is significantly smaller, as they depend mainly on the shape of the power spectrum. Similarly, the measurement uncertainty is almost negligible for the skewness as only the fluctuating velocity component is needed for its computation (Eq. 9).

As the measurement uncertainty does not have a significant effect on the computation of the velocity fluctuations, the measurement uncertainty of the turbulence statistics can be reduced by reducing the uncertainty of the mean velocity. One possibility could be the use of a second measurement of the time-averaged flow velocity by an other instrument feauturing lower uncertainty over the range of test flow conditions (e.g. pneumatic pressure probes). The statistical uncertainty can be reduced by increasing the duration of the velocity signal, which is limited by the test duration in short duration facilities.

6. Conclusions

In this work, a method for the quantification of the uncertainty of turbulence statistics is presented. The method considers both the measurement uncertainty stemming from the experimental process and the statistical uncertainty originating from the statistical treatment of the velocity time series. It is applied to HWA measurements performed at the inlet of a transonic turbine stage, in a short duration wind tunnel. The application is presented in detail, in order to serve as an example for the uncertainty computation in this type of facilities or, more in general, for any time-constrained fluid dynamics experiment.

This work presents a practical application of an uncertainty quantification method for turbulence statistics that can be applied to any type of experiment and measurement technique. In this context, an exhaustive list of uncertainty sources affecting HWA in particular, (eg. turbulence anisotropy, velocity gradients etc.) has not been included in this work. The important statistical uncertainty contributions observed in this analysis confirm the need to consider this type

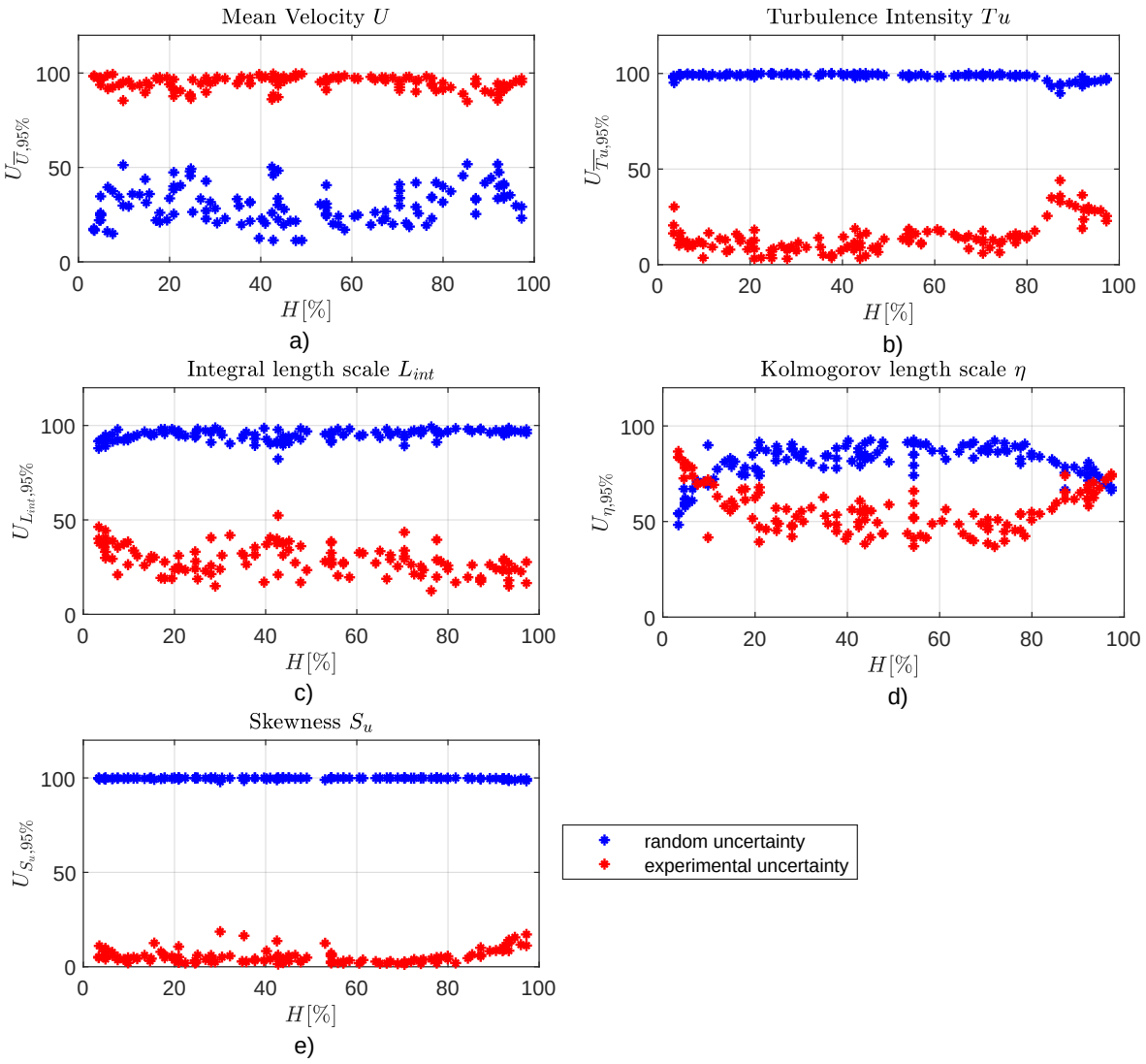

Figure 19: Spanwise distribution of uncertainty budget, expressed as percentage of the total uncertainty for a) Mean velocity, b) Turbulence intensity, c) Integral length scale, d) Kolmogorov length scale, e) Skewness.

of uncertainty in turbulence experiments, in particular for short-duration tests. The proposed method has the advantage of being non-parametric, thus requiring no a priori assumptions on the probability distribution of the turbulent velocity. The computation of the measurement uncertainty requires a reliable estimation of the elemental uncertainties and their probability distributions, but thanks to the MC propagation, it avoids the computation of complex sensitivity derivatives that are required for the common uncertainty propagation based on the Taylor series method. Therefore, besides providing a complete estimation of the uncertainty, the method is also easy to implement and can prove to be a useful tool in turbulence research.

Acknowledgments

The support of the Fonds de la Recherche Scientifique-FNRS, through the award of a FRIA doctoral grant, is greatly acknowledged.

References

[1] P. Sagaut, S. Deck, Large eddy simulation for aerodynamics: status and perspectives, Philosophical Transactions of the Royal Society A: Mathematical, Physical and Engineering Sciences 367 (1899) (2009) 2849–2860. doi:10.1098/rsta.2008.0269.

[2] D. Favier, The role of wind tunnel experiments in cfd validation, Encyclopedia of Aerospace Engineering 1.

[3] L. H. Benedict, R. D. Gould, Towards better uncertainty estimates for turbulence statistics, Experiments in Fluids 22 (2) (1996) 129–136. doi:10.1007/s003480050030.

[4] C. M. Garcia, P. R. Jackson, M. H. Garcia, Confidence intervals in the determination of turbulence parameters, Experiments in Fluids 40 (4) (2005) 514–522. doi:10.1007/s00348-005-0091-8.

[5] T. A. Oliver, N. Malaya, R. Ulerich, R. D. Moser, Estimating uncertainties in statistics computed from direct numerical simulation, Physics of Fluids 26 (3) (2014) 035101. doi:10.1063/1.4866813.

[6] S. T. Salesky, M. Chamecki, N. L. Dias, Estimating the random error in eddy-covariance based fluxes and other turbulence statistics: The filtering method, Boundary-Layer Meteorology 144 (1) (2012) 113–135. doi:10.1007/s10546-012-9710-0.

[7] R. B. Abernethy, R. P. Benedict, R. B. Dowdell, ASME measurement uncertainty, Journal of Fluids Engineering 107 (2) (1985) 161. doi:10.1115/1.3242450.

[8] Joint Commitee for Guides in Metrology, Evaluation of Measurement Data-Guide to the Expression of Uncertainty in Measurement , JCGM 100:2008, 2008.

[9] Joint Commitee for Guides in Metrology (JCGM), Evaluation of Measurement Data- Supplement 1 to the "Guide to the Expression of Uncertainty in Measurement" - Propagation of Distributions using a Monte Carlo Method , JCGM 101:2008, 2008.

[10] W. K. George, P. D. Beuther, J. L. Lumley, Processing of random signals, in: Proceedings of the Dynamic Flow Conference 1978 on Dynamic Measurements in Unsteady Flows, Springer Netherlands, 1978, pp. 757–800.

[11] D. H. Lenschow, J. Mann, L. Kristensen, How long is long enough when measuring fluxes and other turbulence statistics?, Journal of Atmospheric and Oceanic Technology 11 (1994) 661–673.

[12] A. Sciacchitano, B. Wieneke, PIV uncertainty propagation, Measurement Science and Technology 27 (8) (2016) 084006. doi:10.1088/0957-0233/27/8/084006.

[13] R. A. Antonia, B. R. Satyaprakash, A. K. M. F. Hussain, Statistics of fine-scale velocity in turbulent plane and circular jets, Journal of Fluid Mechanics 119 (1) (1982) 55. doi:10.1017/s0022112082001268.

[14] H. W. Coleman, W. G. Steele, Experimentation, Validation and Uncertainty Analysis for Engineers, John Wiley & Sons Inc., 2009.

[15] B. Efron, Bootstrap methods: Another look at the jackknife, in: Springer Series in Statistics, Springer New York, 1992, pp. 569–593. doi:10.1007/978-1-4612-4380-$9_4$1.

[16] B. Efron, R. Tibshirani, An Introduction to the Bootstrap, Taylor & Francis Ltd, 1994.
URL https://www.ebook.de/de/product/3596896/bradley_efron_robert_tibshirani_an_introduction_to_the_bootstrap.html

[17] H. R. Kunsch, The jackknife and the bootstrap for general stationary observations, The Annals of Statistics 17 (3) (1989) 1217–1241. doi:10.1214/aos/1176347265.

[18] D. N. Politis, H. White, Automatic block-length selection for the dependent bootstrap, Econometric Reviews 23 (1) (2004) 53–70. doi:10.1081/etc-120028836.

[19] P. L. O'Neill, D. Nicolaides, D. Honnery, J. Soria, Autocorrelation functions and the determination of integral length with reference to experimental and numerical data., in: 15th Australasian Fluid Mechanics Conference, 2004.

[20] R. Theunissen, A. D. Sante, M. L. Riethmuller, R. A. V. den Braembussche, Confidence estimation using dependent circular block bootstrapping: application to the statistical analysis of PIV measurements, Experiments in Fluids 44 (4) (2007) 591–596. doi:10.1007/s00348-007-0418-8.

[21] V. Andreoli, S. Lavagnoli, G. Paniagua, V. F. Villace, Robust model of a transient wind tunnel for off-design aerothermal testing of turbomachinery, Measurement 82 (2016) 323–333. doi:10.1016/j.measurement.2015.12.032.

[22] H. H. Bruun, Hot-Wire Anemometry: Principles and Signal Analysis, Oxford University Press, 1995.

[23] B.Cukurel, S. Acarer, T. Arts, A Novel Perpesctive to High-Speed Cross-Hot-Wire Calibration Methodology, Experiments in Fluids 53 (4) (2012) 1073–1085.

[24] G. I. Taylor, The spectrum of turbulence, Proceedings of the Royal Society of London. Series A - Mathematical and Physical Sciences 164 (919) (1938) 476–490. doi:10.1098/rspa.1938.0032.

[25] P. Roach, The generation of nearly isotropic turbulence by means of grids, International Journal of Heat and Fluid Flow 8 (2) (1987) 82–92. doi:10.1016/0142-727x(87)90001-4.

[26] M. Hölle, C. Bartsch, P. Jeschke, Evaluation of measurement uncertainties for pneumatic multihole probes using a monte carlo method, Journal of Engineering for Gas Turbines and Power 139 (7) (2017) 072605. doi:10.1115/1.4035626.

Turbine Endwall Contouring and Blade Tip Optimization with Experimental Validation at Engine-Like Conditions

Matteo Burigana

Turbomachinery and Propulsion Department, von Karman Institute for Fluid Dynamics, Belgium, matteo.burigana@vki.ac.be

Supervisor: Sergio Lavagnoli

Assistant Professor, Turbomachinery and Propulsion Department, von Karman Institute for Fluid Dynamics, Belgium, lavagnoli@vki.ac.be

University Supervisor: Tom Verstraete

Visiting Professor, Department of Flow, heat and combustion mechanics, Ghent University, Belgium, tjvrstra.verstraete@ugent.be

Abstract

Nonaxisymmetric endwall profiling and superior blade tip geometries posses the potential to simultaneously mitigate aerodynamic losses and thermal loads in axial turbine. Classical design strategies are usually constrained to a specific type of geometry. The current research presents a multi-objective optimization methodology to explore a broad range of geometry configurations and an experimental validation. A differential evolution optimizer generates and evaluates the individuals. The stage geometry, generated automatically, takes into account real geometrical effects such as rim seal channels and blade fillets. The multi-objective optimization is set to target higher aerodynamic efficiency and simultaneous minimization of heat load or hot gas ingested in the rim seal. RANS simulations, used during the optimization, are verified with time resolved CFD for the best individuals and validated with an experimental campaign. The VKI CT3 test rig is used to evaluate simultaneously the different geometries with a rainbow rotor approach considering purge flow injection.
The aim of the research is to show the potential of such methodology to reach new unexplored stage geometries with enhanced aerothermal performance.

Keywords: turbines, optimization, endwall contouring, blade tip design, experimental validation

On the Influence of High Turbulence on the Convective Heat Flux on the High-Pressure Turbine Vane LS89

Tânia Sofia Cação Ferreira

Turbomachinery and Propulsion Department, von Karman Institute for Fluid Dynamics, Belgium, tania.sofia.cacao.ferreira@vki.ac.be

Supervisor and University Supervisor: Tony Arts

Professor and Head, Turbomachinery and Propulsion Department, von Karman Institute for Fluid Dynamics, Belgium, arts@vki.ac.be
Professor, Institute of Mechanics, Materials and Civil Engineering, Université Catholique de Louvain, Belgium, tony.arts@uclouvain.be

University Supervisor: Vincent Legat

Professor and Head, Applied Mechanics and Mathematics, Université Catholique de Louvain, Belgium, vincent.legat@uclouvain.be

Abstract

Heat transfer measurements on a high-pressure turbine inlet guide vane (VKI LS89 airfoil) are presented in this paper. This contribution focuses on the effect of high freestream turbulence generated by a new turbulence grid allowing a range of turbulence intensities in excess of 10% with representative length scales of the order of 1-2 cm. The experiments are conducted in the Isentropic Compression Tube (CT-2) facility at the von Karman Institute. The exit isentropic Mach (0.70−0.97) and Reynolds numbers ($0.53-1.15\cdot10^6$) and the turbulence intensity (10−26%) are varied independently. The gas-to-wall temperature ratio is fixed (∼1.4). The heat transfer distributions along the vane suction side indicate a strong link between boundary layer transition and the streamwise pressure gradients even at high levels of freestream turbulence intensity. Differences are put in evidence in the dynamics of the transition development. Heat transfer predictions from boundary layer code TEXSTAN are additionally compared to the experiments.

Keywords: thermal effects, boundary layer transition, heat transfer measurements, high-pressure turbines

1. Introduction

The design and optimization of gas turbine components is heavily dependent on numerical tools that rely on available experimental databases for validation of their accuracy. Achieving more realistic engine flow conditions is therefore crucial for more and more representative experimental data.

A considerable source of uncertainty and losses in fluid dynamics is due to transition [1], the inception of a turbulent boundary layer, with rising wall shear stress and wall heat flux rates. The high complexity of laminar to turbulent boundary layer transition on a turbine airfoil surface is difficult to characterize, due to the flow topology (wall bounded, unsteady, 3D) and non-linear interactions between flow variables [2].

A deeper understanding of this fundamental issue is therefore needed to improve performance predictability and efficiency of gas turbines, leading to safer and greener aviation.

In the framework of high-pressure turbines, the main transition mode occurring on the suction side of the blade is bypass transition. This type of transition occurs due to the perturbed freestream environment generated by a combustor chamber where elevated turbulence intensities and length scales are expected. In fact, Laser-Doppler anemometry measurements by Goldstein et al. [3] at the exit of a can-type combustor resulted in turbulence levels in the order of 15-20%. Additionally, Van Fossen and Bunker [4; 5] also surveyed the outlet flow of a similar combustor measuring very high levels of turbulence intensity (up to 30%) and integral length scales (≈ 3 cm). These elevated levels of combustor generated freestream turbulence are extremely challenging for research turbine inlet guide vane testing facilities.

Several researchers have therefore studied the impact of high freestream large scale turbulence on the wall heat transfer distribution and boundary layer evolution on high-pressure nozzle vanes. In general, turbulence increase leads to higher stagnation heat transfer rates and earlier boundary layer transition.

Wang et al. [6] used three turbulence generators to achieve distinct turbulence levels (3, 8 and 18%) and length scales (0.9, 2.6 and 8 cm). The major effect was to move transition upstream and little or no influence was observed on the laminar boundary layer.

Nix et al. [7] developed a turbulence generator reaching 10-12% turbulence intensity with large scale of 2 cm where heat transfer results indicate an increase of 8% for the suction side with respect to the low turbulence case [8]..

Further heat transfer measurements by Carullo et al. [9] report an effect of length scale on the stagnation heat transfer: at similar turbulence levels, a higher heating is observed when the integral length scale is smaller (reduced from 24 mm to 15 mm).

A thorough aero-thermal database was developed at the von Karman Institute (VKI) on a high-pressure inlet guide vane [10] which is still today extensively used for numerical studies [11–17]. Tested turbulence intensities ranged from 1 to 6%. A need for more elevated turbulence levels in the turbine testing facility at the VKI led to the design of a novel turbulence grid in order to achieve freestream turbulence intensities higher than 10% [18].

The aim of the present investigation is hence to study the influence of elevated levels of freestream turbulence on the convective heat transfer and on the behavior of boundary later laminar-to-turbulent transition on the suction side of the VKI LS89 vane.

2. Experimental campaign

2.1. Facility

Tests are performed in the CT-2 facility (Fig. 1) in the "Jacques Chauvin" laboratory of the VKI. The facility is based on an isentropic compression which allows simulating the working conditions of a real engine in terms of temperature ratio and exit isentropic Mach and Reynolds numbers for a short duration of about 0.5 second. More details on the concept and operation principle of this type of test rig can be found in [19; 20]. The gas temperature, the exit isentropic Mach and Reynolds numbers can be set independently by adjusting the overall pressure level and the pressure ratio across the test section. In the present study, the exit Mach number is set by adjusting the opening area of a sonic throat placed at the exit of the test section. This device allows maintaining the operating conditions constant during the complete test duration despite the finite volume of the discharge reservoir. Additionally, a turbulence grid can be placed in one of the five slots available at the inlet of the test section. Therefore, distinct turbulence quantities can be generated for discrete streamwise positions of the grid.

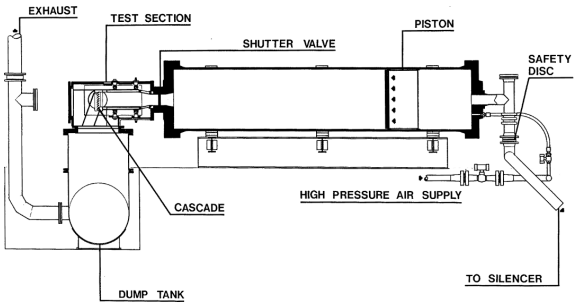

Figure 1: Illustration of CT-2 facility [10].

2.2. Turbulence generator

Downstream of the compression tube, the shutter valve directs the flow into a straight channel towards the cascade. The natural turbulence intensity of the facility inside this channel stands at 0.8%, according to the constant temperature hot-wire measurements of Fontaneto [21]. Increasing the turbulence intensity inside the test section is possible by positioning a turbulence grid in one of the five available slots upstream of the blade leading edge plane. These discrete streamwise positions will define the upstream turbulence intensity. Moving the grid closer to the cascade inlet plane provides higher turbulence intensities and smaller integral length scales.

A novel turbulence grid was manufactured to produce higher turbulence levels than the ones used by Arts et al. [10]; which stood at a maximum of about 5.3% [21]. The new turbulence grid generates turbulence intensity levels higher than 10%; its design and flow field study can be found in [18]. This grid has five bars with a 15 cm square cross section spaced by 45 mm. The grid can be arranged in two different modes, either with the bar faces orthogonal and parallel to the flow direction (squared configuration; Fig. 2, left) or with an angle of 45° to the flow direction (diamond configuration; Fig. 2, right). In the present case, the tests were performed only with the diamond grid configuration due to its higher turbulence generation. Turbulence quantities were characterized by means of

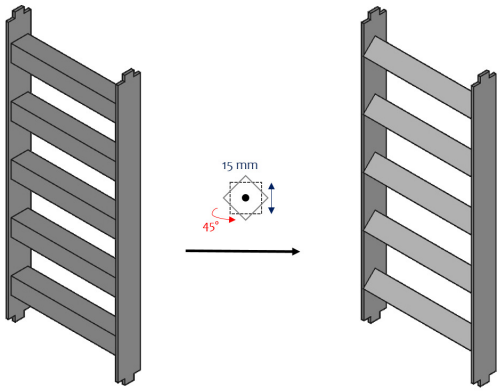

Figure 2: Square (left) and diamond (right) 15mm-bar turbulence grid [18].

a hot-wire probe operated in a constant temperature mode using a Dantec® Streamline hardware and configured through the Dantec® StreamWare software. A Nu_w vs. Re_w calibration procedure as depicted by Cukurel et al. [22] is selected due to the varying total temperature between tests. The hot-wire consists in a platinum-coated tungsten wire of 9 μm diameter and 1 mm active sensor length with an estimated frequency response of 20 kHz. The hot-wire signal for each test is acquired for the duration of one second at 100 kHz and low pass filtered at 30 kHz in order to avoid aliasing effects. The uncertainty on the time-resolved velocity measurements in the facility is of 9.85% for a 95% confidence interval based on the work of Moffat [23]. The average turbulence results provide turbulence intensities between 11 and 26%. Turbulence integral timescales are computed through the autocorrelation method and the length scale is retrieved using the Taylor hypothesis. The integral timescale is integrated by means of a 4th order Gaussian fitted autocorrelation curve until the first zero crossing. Integral length scales are estimated within 1 to 2 cm through the energy spectra [24].

2.3. Instrumentation

The test section (Fig. 3) contains a five-blade linear cascade of a well-known geometry (LS89) which has been used for several test campaigns in the past [10; 21]. The flow is directed to the cascade through a 230x100 mm^2 channel coinciding with the leading edge of the upper and bottom blades. The central blade is used for the heat transfer measurements.

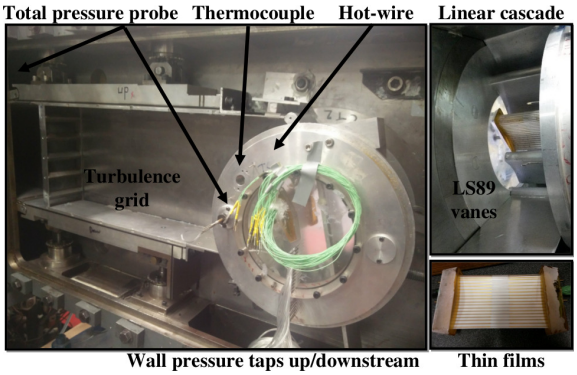

Figure 3: Photograph of the test section, cascade and central blade.

2.3.1. Pressure sensors

Total pressure in the compression tube is measured by a Validyne® variable reluctance differential transducer while National Instruments® semiconductor differential transducers are used for total and static pressure in the test section and static pressure in the dump tank. Pitot probes are installed upstream the cascade and inside the tube while wall tapings are drilled up- and downstream of the cascade for inlet and exit static pressure measurements. The exit static pressure distribution is measured by a Scanivalve® miniature pressure scanner and covers two pitches. The taps are located at 43% axial chord downstream of the trailing edge plane.

2.3.2. Thermocouple

The upstream total gas temperature is measured by a 25 μm type K thermocouple placed half an axial chord upstream of the cascade.

2.3.3. Thin films

Constant current thin film thermometry is used for wall temperature and heat transfer measurements [25; 26]. Forty-five platinum thin films (~0.5 μm of thickness) are painted around the central blade of the cascade. This airfoil is made of Macor® glass ceramic, a good thermal and electric insulator. Further information about the manufacturing characteristics of the thin films are described by Ligrani et al [27]. The temperature measurements are based on the following linear relation between resistance and temperature:

$$R = R_0[1 + \alpha_R(T - T_0)] \quad (1)$$

where R_0 is the thin film resistance at a temperature T_0 and α_R is the temperature coefficient of resistance.

The resistance values are obtained from the measured voltage signals by applying the Ohm's law.

2.3.4. Analog circuits

Heat flux in a semi-infinite substrate can be simulated using electric analog circuits where the Fourier law and the unsteady heat conduction equation are respectively analogous to the Ohm's law and to the transmission line circuit equation. This will result in a heat flux given by the following equation [28]:

$$\dot{q}_w = \frac{V_{out}}{V_0} \frac{\sqrt{\rho c k}}{\alpha_R} \frac{A}{\beta}^* \tag{2}$$

where V_{out} is the thin film Wheatstone bridge voltage, V_0 is the thin film voltage, $\sqrt{\rho c k}$ is the substrate thermal product, α_R is the thin film temperature coefficient of resistance and A/β^* is the analog circuit calibration coefficient. A more detailed analysis of the above-mentioned procedure is reported in [29; 30].

2.3.5. Data acquisition

The signal from the analog circuits is amplified and low-pass filtered at 12 kHz. All the voltage signals (except from the Scanivalve® scanner which possesses a specific hardware and software) are recorded by an acquisition system at a sampling frequency of 50 kHz for a total duration of 1 second.

All pressure, temperature and heat flux measurements are acquired using the TEAM256 software controlling a 64 channel Bakker® data acquisition system except for the outlet pitch-wise static pressure and the hot-wire measurements. The former signals are recorded for a duration of 1.25 sec at a frequency of 50 kHz. Additionally, the analog circuits signals are amplified (x100) and low-pass filtered at 12 kHz before recording. Twenty-two outlet static pressure signals covering two pitches are acquired by means of a Scanivalve® pressure scanner. One-thousand samples are collected at a frequency of 312.5 Hz. The hot-wire is operated using Dantec® Streamline hardware and configured through the Dantec® StreamWare software. The signal for each test is acquired for the duration of one second at 100 kHz and low pass filtered at 30 kHz in order to avoid aliasing effects.

2.4. Uncertainty analysis

The uncertainty analysis was performed based on the work of Moffat [23] within a confidence interval of 95%, Table 1. The uncertainties are estimated from both the calibration curves and from the measurements using the error propagation method. The uncertainties on the outlet isentropic Mach and Reynolds numbers are, respectively, 2.3% and 4.1% while for the temperature ratio it is of the order of 0.8%. The convective heat transfer results have an associated uncertainty of 9.5%. The isentropic inlet velocity from which the turbulence intensities are computed has an uncertainty of 9.9%.

Uncertainty	T_∞/T_w	$M_{is,out}$	$Re_{is,out}$	V_{in}	h
[%]	0.8	2.3	4.1	9.9	9.5

Table 1: Uncertainties within a 95% confidence interval.

3. Influence of freestream turbulence

Assessment of the effect of turbulence intensity is possible by changing the position of the turbulence grid in the test section's inlet channel of the facility. The effects of turbulence intensity are analyzed through the heat transfer coefficient distribution along the suction side of the vane. The link with the boundary layer status is complemented with a numerical prediction of the Mach number distribution.

The thermal boundary layer evolution on the vane suction side can be illustrated by its heat transfer coefficient distribution, defined in the present work as:

$$h = \frac{\dot{q}_w}{T_\infty - T_{w,initial}} \tag{3}$$

Boundary layer heat transfer measurements expect a stagnation region characterized by high heat flux due to elevated heating impinging on a still developing thin laminar boundary layer. Because of its nature, it acts as an insulating layer and the heat transfer decreases continuously downstream of this region. A further variation in heat transfer would be due a change in acceleration, separation bubbles, shocks or transition (which can be also triggered by the former factors).

3.1. Comparison with Arts et al. [10]

The first step of this work has been to compare the heat transfer behavior from the database of [10] with the results from the new grid. In the former work, a turbulence grid of 3 mm cylindrical bars has been used and the maximum turbulence intensity level achieved in the facility was of 5.3%, according to measurements by Fontaneto [21].

Given the significant literature dedicated to predicting the heat transfer distribution of MUR235 (e.g. [12–17]), this test has been selected to be compared with the new result: TUR062. The heat transfer distributions are shown together with a Mach number prediction for $M_{is,out}$ = 0.93 in Fig. 4. Flow conditions for both tests can be found in Table 2.

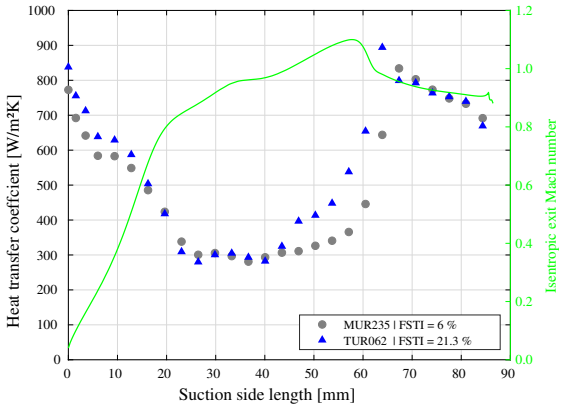

Figure 4: Heat transfer coefficient of MUR235 [10] and TUR062 with a Mach number distribution prediction for $M_{is,out}$ = 0.93 along the suction side.

Test	Tu_∞ [%]	$M_{is,out}$	$Re_{is,out}$	T_∞/T_w
MUR235	6	0.93	$1.15{\cdot}10^6$	1.37
TUR062	22.8	0.93	$1.16{\cdot}10^6$	1.35

Table 2: Flow conditions of MUR235 [10] and TUR062.

Regarding the stagnation region, the effect of the turbulence intensity is to increase the heat transfer by 9%, which then converges to similar heat transfer levels to MUR235 in the laminar region.

The onset of transition is at s = 40 mm, after the velocity plateau. LES results by [14] put into evidence the presence of acoustic waves at this exact position. For test case MUR235 these disturbances are damped and transition develops more energetically due to the adverse pressure gradient starting from s = 60 mm where a shock is expected to occur [14; 31]. However, for the higher turbulence case, we can observe the clear evolution of transition starting from s = 40 mm, even if it is slowed due to the favorable pressure gradient. From the time-resolved heat flux signal, high amplitude fluctuations indicate that the boundary layer was already destabilized since the change in acceleration at about s = 20 mm.

Case	$M_{is,out}$	$Re_{is,out}$	T_∞/T_w	Tu_∞	Λ_x
	[-]	[-]	[-]	[%]	[mm]
A	0.70	$1.15{\cdot}10^6$	1.36	13-26	13-23
B	0.97	$0.53{\cdot}10^6$	1.35	13-22	14-17
C	0.92	$1.15{\cdot}10^6$	1.36	11-21	15-21

Table 3: Flow conditions of test cases.

3.2. Heat transfer coefficient distribution

Heat transfer distributions along the suction side of the vane are displayed to characterize the influence of freestream turbulence. Three distinct levels of turbulence intensity are put side-by-side and compared. Three test cases are selected from the experimental campaign results and their flow conditions are summarized in Table 3.

3.2.1. Case A - subsonic and high Reynolds

The first case study is a fully subsonic experiment ($M_{is,out}$ = 0.70, $Re_{is,out}$ = 1.15x10^6)); the time-averaged suction side heat transfer coefficient distribution is shown in Fig. 5. Each turbulence intensity increment of about 6% allows the advancement of the transition region by one measuring position, corresponding to approximately 3 mm (3.5% of the suction side length).

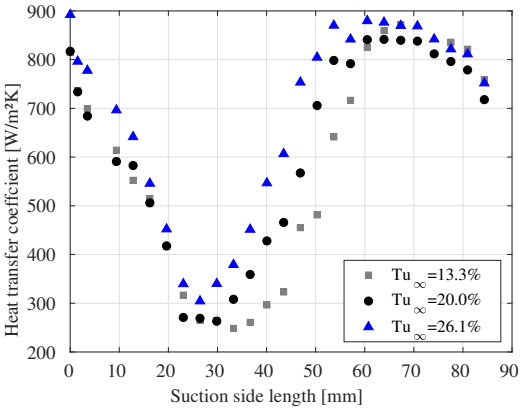

Figure 5: Suction side mean heat transfer coefficient distribution (*Case A*: $M_{is,out}$ = 0.70, $Re_{is,out}$ = 1.15x10^6, T_∞/T_w = 1.36).

An increase of the stagnation heat transfer coefficient is also present but it is not as clear for the two lower turbulence intensities. However, looking at the minimum and maximum heat transfer values presented in Fig. 6, a difference of about 100 W/m^{2}K (~12.5%) is observed on the maximum heat transfer values between tests. These values correspond to

the maximum heat transfer fluctuations due to the increase of turbulence intensity. Regarding the minimum or base heat transfer coefficient, it remains the same except for the lower turbulence intensity case after s = 50 mm. A justification for this can lie on their individual boundary layer evolution: around this position, the highest turbulence intensity cases are almost turbulent whereas the lowest appears to be still half-way through transition, Fig. 5).

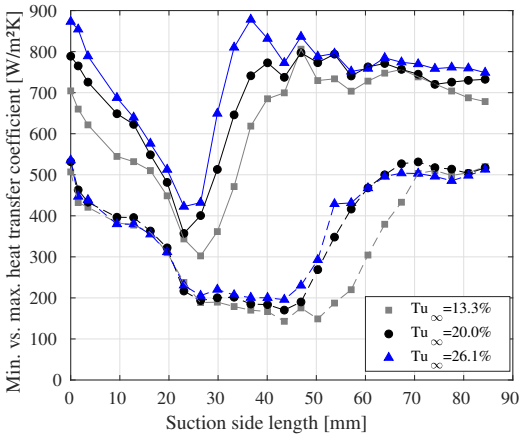

Figure 6: Suction side maximum (solid trace) and minimum (dashed trace) heat transfer coefficient distribution (*Case A*: $M_{is,out}$ = 0.70, $Re_{is,out}$ = 1.15x10^6, T_∞/T_w = 1.36).

If one compares the averaged values of heat transfer to their maximum and minimum, it appears not to add up to the same result. However, it should be pointed out that this is solely due to the post-processing: a typical time-series of a single-position wall heat flux as a function of the time-series of the wall temperature provides the wall heat flux temperature series present in Fig 7.

A linear regression on a selected interval allows to retrieve the original heat flux value given by the isentropic compression for isothermal wall conditions [32]. Therefore, this means that a heat transfer value cannot be compared in absolute value to its fluctuations, which was not the purpose of the previous statements.

3.2.2. Case B - transonic and low Reynolds

Heat transfer measurements for a transonic Mach number distribution at a lower outlet Reynolds number ($M_{is,out}$ = 0.97, $Re_{is,out}$ = 0.53x10^6) result in the rather fixed profiles presented in Fig. 8.

The velocity distribution, expected to be similar to MUR47 in Arts et al. [10] and to the one shown in

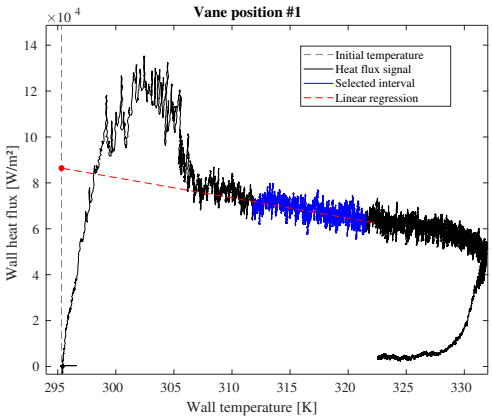

Figure 7: Wall heat flux temperature-series at s = 0 mm: post-processing the averaged value (*Case A*: $M_{is,out}$ = 0.70, $Re_{is,out}$ = 1.15x10^6, T_∞/T_w = 1.36).

this paper (Fig. 4), should have the same variations in acceleration around s = 20 mm and s = 40 mm followed by a steep deceleration at s = 60 mm. From this position, a shock is expected based on previous flow visualizations by Arts et al. [10] at $M_{is,out}$ = 1.03 and $Re_{is,out}$ = 10^6.

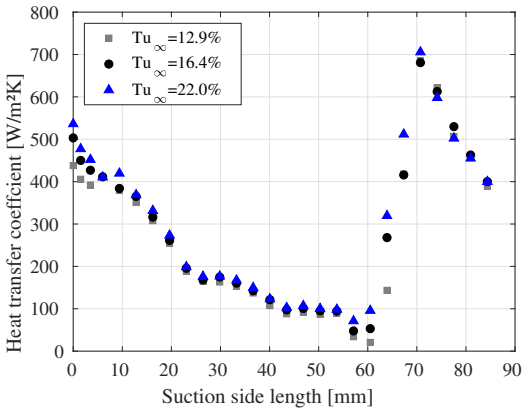

Figure 8: Suction side mean heat transfer coefficient distribution (*Case B*: $M_{is,out}$ = 0.97, $Re_{is,out}$ = 0.53x10^6, T_∞/T_w = 1.35).

Indeed, the above-mentioned velocity variations are clearly reflected in the evolution of the heat transfer slopes. These indicate a laminar boundary layer up to s = 55 mm. An ensuing low heating region between s = 55−60 mm implies the presence of a laminar separation bubble. Its formation is likely due to being in a region with a strong deceleration/shock. Transition is therefore rapidly driven by the shock, within a small spatial domain between s = 60−70 mm where no other

effect of turbulence intensity is perceivable.

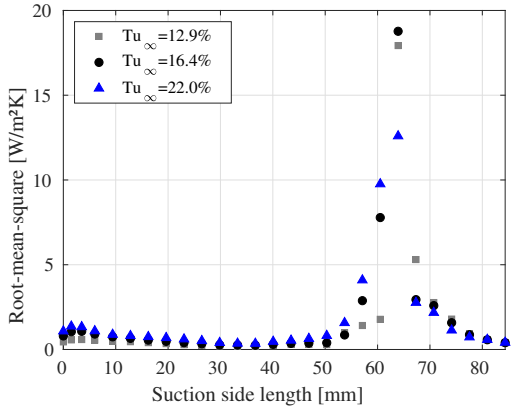

Figure 9: Suction side root-mean-square distribution (*Case B*: $M_{is,out}$ = 0.97, $Re_{is,out}$ = 0.53x10^6, T_∞/T_w = 1.35).

Regarding the differences in heating, they are present on the stagnation region, with an increase in mean heat transfer of about 16%, and on the separation bubble, where the turbulence appears to reduce the size of the bubble.

The latter can be further illustrated through the root-mean-square distribution of the heat transfer coefficient on Fig. 9. While the highest freestream turbulence cases present a continuous evolution into the RMS peak (s = 64 mm, most likely the shock position or reattachment point?), the Tu_∞=12.9% case shows very small heat flux fluctuations up to this point.

Indeed, the reduction of the bubble size has been reported by Castro and Haque [33] due to the higher entrainment rates resulting from increased freestream turbulence. Additionally, research by Isomoto and Honami [34] on the reattachment over a backward-facing step, indicates that the increase of the turbulence level near the wall at the separation point leads to a shorter reattachment length.

3.2.3. Case C - transonic and high Reynolds

For a higher Reynolds number and a slight lower Mach number distribution, still transonic ($M_{is,out}$ = 0.92, $Re_{is,out}$ = 1.02x10^6) the boundary layer status is more varied, Fig. 10.

A Mach number prediction is additionally presented: the velocity distribution displays variations in acceleration around s = 20 and 40 mm and a diffusion region where a shock is expected around s = 60 mm. These are reflected as heat transfer variations and, due to the increase in Reynolds number, a separation bubble is no longer present. After the shock the boundary layer is rapidly evolving to the fully turbulent status however, its behaviour before the shock is distinct. The increase of heat transfer for the highest turbulence case takes place earlier. Boundary layer starts to transition after the velocity plateau at s = 40 mm. A subsequent favorable pressure gradient however, is delaying a strong development of the boundary layer transition. As it had been pointed out by [35], acceleration acts to inhibit the turbulent spots heat transfer, slowing its spanwise growth during the transition process in the thermal boundary layer. Another interesting observation is the difference in the turbulent heat transfer, higher for the lower turbulence intensity cases. Since the lower turbulence case is triggered almost instantaneously by the shock (s = 60 mm), it has a shorter streamwise transition development. This results in a smaller boundary layer thickness compared to the other cases where the boundary layer transition starts around s = 40 mm. A thinner turbulent boundary layer would thus lead to a higher heat transfer from the flow to the wall.

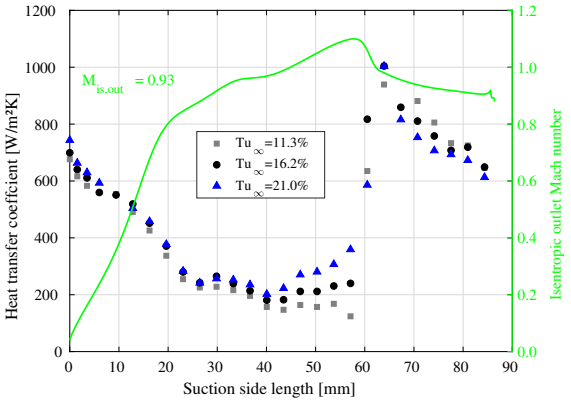

Figure 10: Suction side mean heat transfer coefficient distribution (*Case C*: $M_{is,out}$ = 0.92, $Re_{is,out}$ = 1.02x10^6, T_∞/T_w = 1.36) and Mach number prediction ($M_{is,out}$ = 0.93).

3.3. Stagnation region heat transfer

The present heat transfer measurements are compared to a correlation from Van Fossen et al. [36] for the stagnation region of elliptical leading edges. Turbulence intensity, integral length scale, inlet Reynolds number based on the leading edge diameter and the leading edge diameter itself are considered in the correlation defined as:

$$\frac{Fr_t}{Fr_l} = 0.00851\sqrt{Tu_\infty Re_{d,in}^{0.8}\frac{\Lambda_x}{d}^{-0.574}} + 1 \qquad (4)$$

The turbulent Frossling number Fr_t of the present experimental data is obtained through:

$$Fr_t = Nu \frac{d/c}{\sqrt{Re_{d,in}}} \tag{5}$$

After the heat transfer results were converted in Nusselt number:

$$Nu = \frac{h \cdot c}{k} \tag{6}$$

where k is the air thermal conductivity.

The laminar Frossling number Fr_l depends on the velocity gradient and is given as a function of the body shape. Since the leading edge of the VKI LS89 vane can be approximated to a 1.5:1 aspect ratio ellipse, the correspondent numerical solution for the laminar Frossling number is Fr_l = 0.870 [36].

A comparison between the correlation and the present experimental results is presented in Fig. 11. Even if the correlation itself displayed only 4% of data scatter, stagnation heat transfer data from other authors was fitted into this correlation to within ± 10% [36]. Therefore, the current results are within the model's expected uncertainty except for the lowest turbulence and Reynolds number case (Case B, Tu_∞ = 13%). This might lie on the uncertainty of the heat transfer measurements since a difference in turbulence intensity or scale would still place the point below the uncertainty band.

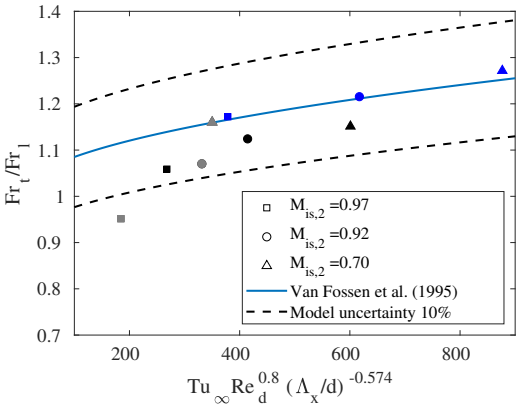

Figure 11: Van Fossen et al. [36] correlation vs. present experimental data: low Tu_∞ (grey), middle Tu_∞ (black), high Tu_∞ (blue).

The correlation considers also the integral length scale since it also affects the stagnation heat transfer. It has been shown that for the same turbulence intensity, smaller length scales will lead to higher levels of heat transfer [36].

Hence, considering that in the present case the lowest turbulence intensity is obtained by placing the grid the furthest away from the cascade inlet section, it results in larger integral length scales since the grow with the streamwise distance [37]. Therefore, maximum stagnation heat transfer levels are still expected for the highest turbulence intensity cases since the produced length scales are the smallest.

In sum, the present freestream turbulence is found to have a moderate effect in increasing the stagnation heat transfer. This is also seen in Wang et al. [6] for turbulence intensity levels between 3 and 18%, where the major effect is to trigger earlier the onset of boundary layer transition, as seen in the present work in the absence of strong pressure gradients (Case A).

3.4. Boundary layer code: TEXSTAN

Heat transfer predictions from the academic boundary layer code TEXSTAN [38] are compared to the experimental values in this section.

TEXSTAN has been selected since it has been validated against several tests cases, including the present one [10]. This software was developed to solve the convective transport of heat, momentum and mass transfer of distinct flow geometries by using a finite difference technique to resolve the 2D parabolic boundary layer equations. Initial conditions are computed at s = 0.5 mm through Falkner-Skan equations for the 2D stagnation point solutions. As boundary conditions, the velocity and wall static temperature distribution on the suction side of the vane are introduced in the code. The inlet total pressure and total temperature, along with the velocity distribution, allow the computation of the static pressure and temperature distribution. The inlet flow velocity and turbulence intensity give the initial value of the turbulence kinetic energy.

TEXSTAN turbulence modelling uses the mean field closure through a choice of the Prandtl mixing length model or one/two equation models. Here, Abu-Ghannam and Shaw's (AG-S) mixing length and Launder-Sharma's (L-S) two equation $\kappa - \epsilon$ model are used with a constant turbulent Prandtl number set to 0.9 for the transition/turbulence modeling.

3.4.1. Case A - subsonic and high Reynolds

The heat transfer prediction of Case A using the AG-S's mixing length model is shown in Fig. 12. Since this model does not account for the stagnation region freestream turbulence effects, it results in an underprediction of this region and the laminar's heat

transfer. The model is also predicting an earlier and shorter boundary layer transition. Freestream turbulence above 20% does not lead however to further hasten the onset of transition. This increase does not affect the correlations due to the correlation formulation: the transition onset momentum thickness Reynolds number is asymptotically approaching the minimum of 163 established in AG-S's correlation. Nevertheless,heating on the turbulent boundary layer is within the experiments uncertainty, yielding a good matching from s = 50−60 mm to the trailing edge.

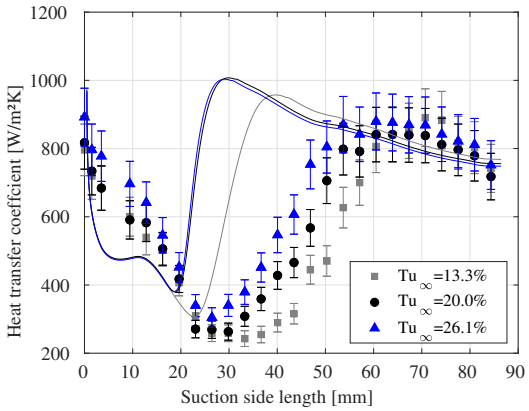

Figure 12: Suction side mean heat transfer coefficient distribution and TEXSTAN prediction through AG-S mixing length model (*Case A*: $M_{is,out}$ = 0.70, $Re_{is,out}$ = 1.15x10^6, T_∞/T_w = 1.36).

As for the predictions using the two-equation model presented in Fig. 13, a much higher leading edge heating is computed. However, for the lowest turbulence case, Tu_∞ = 13.3%, the prediction then converges to heat transfer rates quite close to the measurements from s = 3 mm to s = 9.5 mm. From this point the code predicts an earlier transition onset than that seen in the experiments and on the mixing length model. Nevertheless, it still yields close values for the turbulent boundary layer.

3.4.2. Case B - transonic and low Reynolds

Figure 14 shows the heat transfer predictions using the AG-S mixing length model for case B. The stagnation region does not fall short from the measurements and the laminar part comes close to the experiments. Transition prediction is however, anticipated. Again, we observe a smaller difference in the onset for the highest turbulence cases due to the correlation formulation. The turbulent region is only matching towards the trailing edge: transition in the experiments

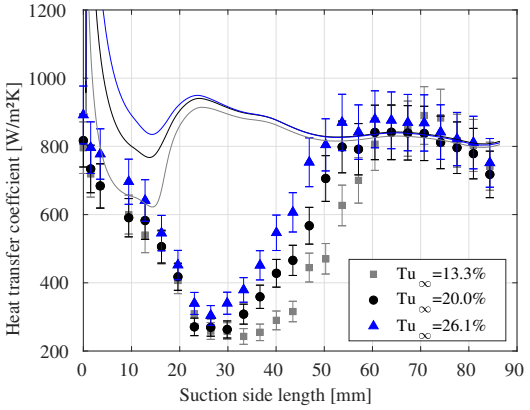

Figure 13: Suction side mean heat transfer coefficient distribution and TEXSTAN prediction through LS two-equation model (*Case A*: $M_{is,out}$ = 0.70, $Re_{is,out}$ = 1.15x10^6, T_∞/T_w = 1.36).

is leading to much higher heating, most likely due to the shock.

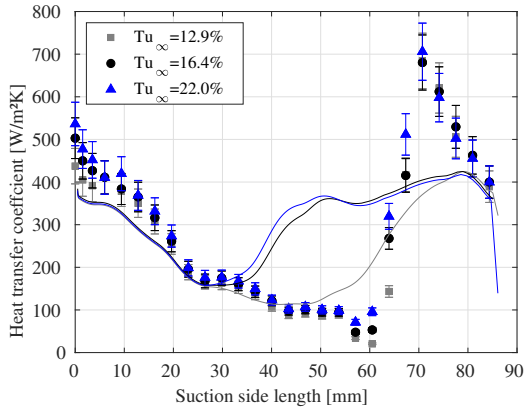

Figure 14: Suction side mean heat transfer coefficient distribution and TEXSTAN prediction through AG-S mixing length model (*Case B*: $M_{is,out}$ = 0.97, $Re_{is,out}$ = 0.53x10^6, T_∞/T_w = 1.35).

Figure 15 displays the two-equation modeling prediction. A very high heating is still present for the early stagnation region, however, from s = 10 mm the prediction converges to the experimental values for all the turbulence cases. Then, transition is once again to rapidly triggered from s = 20 mm whereas the experiments measure a laminar boundary layer up to s = 50 mm. Turbulent boundary layer values are within the uncertainty of the experiments from s = 80 mm.

3.4.3. Case C - transonic and high Reynolds

Case C, presented in Fig. 16 and 17, has a similar prediction behavior to case A except for the turbu-

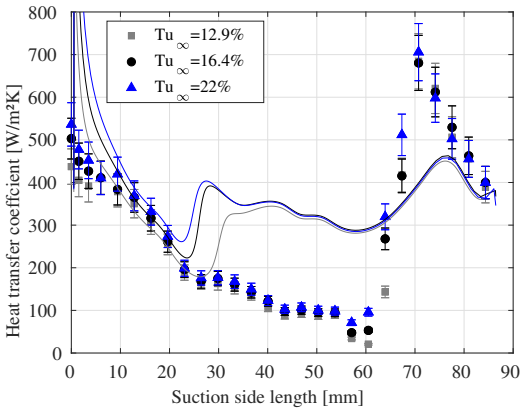

Figure 15: Suction side mean heat transfer coefficient distribution and TEXSTAN prediction through LS two-equation model (*Case B*: $M_{is,out}$ = 0.97, $Re_{is,out}$ = 0.53x10^6, T_∞/T_w = 1.35).

lent region, where it is closer to case B. The mixing length model predicts lower heat transfer rates at the stagnation region but from s = 20 mm it converges to the laminar values as the previous cases. However, an earlier transition is predicted and the end of transition takes place before even the transition onset measurements.

The very high heating seen in the experiments is not shown in the prediction for the turbulent boundary layer. Nevertheless, the code reaches the turbulent levels towards the trailing edge of the vane.

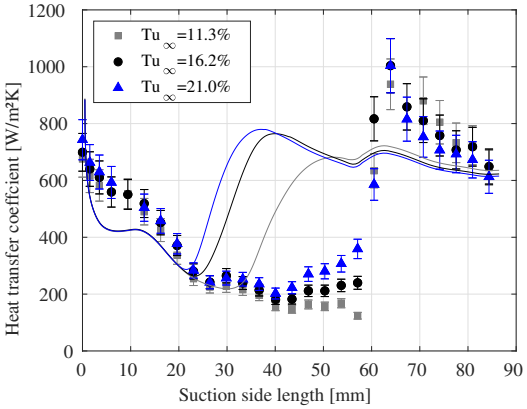

Figure 16: Suction side mean heat transfer coefficient distribution and TEXSTAN prediction through AG-S mixing length model (*Case C*: $M_{is,out}$ = 0.92, $Re_{is,out}$ = 1.02x10^6, T_∞/T_w = 1.36).

The two-equation model prediction renders very good results for the stagnation region of the lowest turbulence intensity case, as in case A. Transition onset prediction again occurs before the mixing length model.

Since the code predicts a similar transition onset between turbulence intensities, the turbulent heat is also alike, opposite to the experiments.

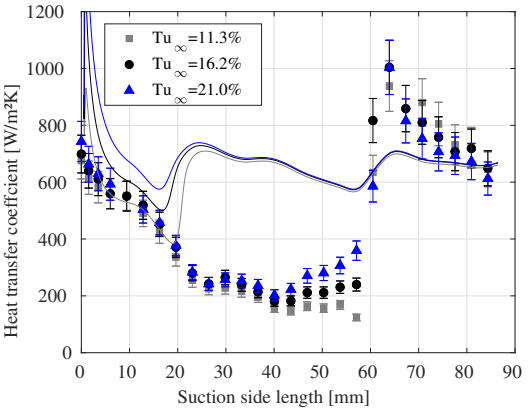

Figure 17: Suction side mean heat transfer coefficient distribution and TEXSTAN prediction through LS two-equation model (*Case C*: $M_{is,out}$ = 0.92, $Re_{is,out}$ = 1.02x10^6, T_∞/T_w = 1.36).

4. Conclusion

Heat transfer measurements were made on the high-pressure VKI LS89 vane under elevated levels of freestream turbulence. A novel grid has been manufactured, generating turbulence intensities within 11-26% and integral length scales between 1-2 cm. In the present paper, three test cases have been studied, for a subsonic and two transonic Mach number distributions. Experimental results find that a considerable increase of freestream turbulence intensity resulted only in a moderate increase of the stagnation heat transfer coefficient. Changes in the boundary layer stability are found to be very dependent on the driving pressure gradients. Nevertheless, the turbulence increase led to earlier transition regions for a mild pressure gradient distribution. For transonic exit conditions, it resulted in a more upstream (acceleration dependent) transition onset and in the reduction of a separation bubble size.

A comparison with the boundary layer code TEXSTAN yielded reasonable results for the laminar and turbulent regions of the boundary layer. An issue remains the accurate prediction of transition at very high turbulence intensities where the pressure gradients stabilizing effect is not completely accounted for as well as for the stagnation region. Using a two-equation model improved the stagnation region pre-

diction for the lowest turbulence intensity ($\approx$ 13%) and Reynolds number ($\approx 5.3\text{x}10^6$) cases.

Acknowledgments

The authors thankfully acknowledge the Mach number predictions from Mr. Riccardo Rubini, the availability of the code from Prof. Mike Crawford and the financial support from Safran Tech.

Nomenclature

Roman symbols

A/β^*	analogue circuits coefficient	$s^{-0.5}$
c	specific heat	J/KgK
c	chord	m
d	diameter (vane leading edge)	m
Fr	Frossling number	$-$
h	heat transfer coefficient	W/m^2K
k	thermal conductivity	W/kgK
M	Mach number	$-$
P	pressure	Pa
Pr	Prandtl number	$-$
$\dot{q}$	heat flux	W/m^2
R	resistance	Ω
$\sqrt{\rho ck}$	substrate thermal product	$J/m^2s^{1/2}K$
Re	Reynolds number	$-$
s	suction side length	mm
T	temperature	K
Tu	turbulence intensity	$\%$
u	axial velocity component	m/s
V	flow velocity	m/s
x	streamwise distance	m

Greek symbols

α_R	temperature coefficient of resistance	K^{-1}
ϵ	turbulence dissipation	m^2/s^3
κ	turbulence kinetic energy	m^2/s^2
Λ	integral length scale	m
μ	dynamic viscosity	kg/ms
ν	kinematic viscosity	m^2/s
ρ	density	kg/m^3

Subscripts

0	stagnation or reference quantity
in	referred to the cascade inlet plane
initial	referred to the initial conditions
is	isentropic quantity
l	laminar
out	referred to the cascade outlet plane
t	turbulent
x	streamwise component
w	referred to the wall
∞	referred to the freestream

Acronyms

AG-S	Abu-Ghannam and Shaw correlation
BLC	boundary layer code
CT-2	Isentropic Compression Tube
HP	high-pressure (turbine)
LS	Launder-Sharma (two-equation turbulence model)
RMS	Root-Mean-Square
VKI	von Karman Institute for Fluid Dynamics

References

[1] J. D. Denton, The 1993 IGTI scholar lecture: Loss mechanisms in turbomachines, Journal of Turbomachinery 115 (4) (1993) 621–656.

[2] R. E. Mayle, The role of laminar-turbulent transition in gas turbine engines, Journal of Turbomachinery 113 (4) (1991) 509–536.

[3] R. Goldstein, K. Lau, C. Leung, Velocity and turbulence measurements in combustion systems, Experiments in Fluids 1 (2) (1983) 93–99.

[4] G. J. Van Fossen, R. S. Bunker, Augmentation of stagnation region heat transfer due to turbulence from a dln can combustor, Journal of Turbomachinery 123 (1) (2000) 140–146.

[5] V. Fossen, G. James, R. S. Bunker, Augmentation of stagnation region heat transfer due to turbulence from an advanced dual-annular combustor, in: ASME Turbo Expo 2002: Power for Land, Sea, and Air, no. 36088 in American Society of Mechanical Engineers, Amsterdam, The Netherlands, 2002, pp. 199–206.

[6] H. P. Wang, R. J. Goldstein, S. J. Olson, Effect of high freestream turbulence with large length scale on blade heat/mass transfer, Journal of Turbomachinery 121 (2) (1999) 217–224.

[7] A. C. Nix, A. C. Smith, T. E. Diller, W. F. Ng, K. A. Thole, High intensity, large length-scale freestream turbulence generation in a transonic turbine cascade, in: ASME Turbo Expo 2002: Power for Land, Sea, and Air, no. 36088, 2002, pp. 961–968.

[8] A. Nix, T. Diller, W. Ng, Experimental measurements and modeling of the effects of large-scale freestream turbulence on heat transfer, Journal of turbomachinery 129 (3) (2007) 542–550.

[9] J. S. Carullo, S. Nasir, R. D. Cress, W. F. Ng, K. A. Thole, L. J. Zhang, H. K. Moon, The effects of freestream turbulence, turbulence length scale, and exit reynolds number on turbine blade heat transfer in a transonic cascade, Journal of Turbomachinery 133 (1) (2011) 011030–011030–11.

[10] T. Arts, Lambert de Rouvroit, Aero-thermal investigation of a highly loaded transonic linear turbine guide vane cascade. A test case for inviscid and viscous flow computations, Journal of Turbomachinery 114 (1) (1992) 147–154.

[11] J. Steelant, E. Dick, Modeling of laminar-turbulent transition for high freestream turbulence., JOURNAL OF FLUIDS

ENGINEERING-TRANSACTIONS OF THE ASME 123 (1) (2001) 22–30.
[12] R. Fransen, E. Collado, F. Duchaine, N. Gourdain, L. Gicquel, L. Vial, G. Bonneau, Comparison of rans and les in high pressure turbines, in: 3me Colloque INCA, ONERA, Toulouse, France, Nov, 2011, pp. 17–18.
[13] N. Gourdain, L. Y. Gicquel, E. Collado, Comparison of rans and les for prediction of wall heat transfer in a highly loaded turbine guide vane, Journal of propulsion and power 28 (2) (2012) 423–433.
[14] E. C. Morata, N. Gourdain, F. Duchaine, L. Gicquel, Effects of free-stream turbulence on high pressure turbine blade heat transfer predicted by structured and unstructured les, International Journal of Heat and Mass Transfer 55 (21-22) (2012) 5754–5768.
[15] E. Rinaldi, R. S. Raspopov, P. Colonna, R. Pecnik, Modeling curvature effects on turbulence transition for turbomachinery flows, in: ASME Turbo Expo 2014: Turbine Technical Conference and Exposition, American Society of Mechanical Engineers, 2014, pp. V02BT39A039–V02BT39A039.
[16] L. Segui, L. Gicquel, F. Duchaine, J. de Laborderie, Les of the ls89 cascade: influence of inflow turbulence on the flow predictions, in: Proceedings of 12th European Conference on Turbomachinery Fluid dynamics and Thermodynamics ETC12. Stockholm, Sweden, 2017, pp. 3–7.
[17] V. Brunet, E. Croner, A. Minot, J. De Laborderie, E. Lippinois, S. Richard, J.-F. Boussuge, J. Dombard, F. Duchaine, L. Gicquel, et al., Comparison of various cfd codes for les simulations of turbomachinery: From inviscid vortex convection to multi-stage compressor, in: ASME Turbo Expo 2018: Turbomachinery Technical Conference and Exposition, American Society of Mechanical Engineers, 2018, pp. V02CT42A013–V02CT42A013.
[18] T. S. Cação Ferreira, T. Arts, Investigation of temperature influence in the production of higher turbulence, in: Proceedings of the Ninth International Symposium On Turbulence, Heat and Mass Transfer, Rio de Janeiro, Brazil, 2018, pp. 171–174.
[19] D. L. Schultz, T. V. Jones, M. L. G. Oldfield, L. C. Daniels, A new transient cascade facility for the measurement of heat transfer rates, High Temperature Problems in Gas Turbine Engines AGARD CP 229 (1978) 1–27.
[20] T. Jones, D. Schultz, A. Hendley, On the flow in an isentropic light piston tunnel, Citeseer, 1973.
[21] F. Fontaneto, Aero-thermal performance of a film-cooled high pressure turbine blade/vane: a test case for numerical codes validation, Ph.D. thesis, von Karman Institute for Fluid Dynamics/Universitá degli Studi di Bergamo, Rhode-Saint-Genèse, Belgium (2014).
[22] B. Cukurel, S. Acarer, T. Arts, A novel perspective to high-speed cross-hot-wire calibration methodology., Experiments in fluids 53 (4) (2012) 1073–1085.
[23] R. J. Moffat, Describing the uncertainties in experimental results, Experimental Thermal and Fluid Science 1 (1) (1988) 3–17.
[24] L. A. El-Gabry, D. R. Thurman, P. E. Poinsatte, Procedure for determining turbulence length scales using hotwire anemometry.
[25] B. E. Richards, Heat transfer measurements related to hot turbine components in the von karman institute hot cascade tunnel, Testing and Measurement Techniques in Heat Transfer and Combustion AGARD CP 281.
[26] H. Consigny, B. E. Richards, Short duration measurements of heat-transfer rate to a gas turbine rotor blade, Journal of Engineering for Power 104 (3) (1982) 542–550.
[27] P. M. Ligrani, C. Camci, M. S. Grady, Thin film heat transfer gage construction and measurement details, Internal Note 72, von Karman Institute for Fluid Dynamics, Rhode-Saint-Genèse, Belgium (1982).
[28] C. Camci, Experimental and theoretical study of film cooling on a gas turbine blade, Phd thesis, Katholieke Universiteit Leuven, Rhode-Saint-Genèse, Belgium (1985).
[29] D. L. Schultz, T. Jones, Heat-transfer measurements in short-duration hypersonic facilities., Advisory Group for Aerospace Research and Development AGARDograph 165.
[30] M. Oldfield, T. Jones, D. Schultz, On-line computer for transient turbine cascade instrumentation, IEEE Transactions on Aerospace and Electronic Systems 5 (5) (1978) 738–749.
[31] T. S. Cação Ferreira, T. Arts, Influence of gas-to-wall temperature on bypass transition, in: ASME Turbomachinery Technical Conference & Exposition, ASME International Gas Turbine Institute, Charlotte, North Carolina, 2017.
[32] T. Arts, C. Camci, Short duration heat transfer measurements, in: von Karman Institute for Fluid Dynamics (Ed.), Measurements Techniques in Turbomachines, Vol. 03, Rhode-Saint-Genèse, Belgium, 1985.
[33] I. Castro, A. Haque, The structure of a shear layer bounding a separation region. part 2. effects of free-stream turbulence, Journal of Fluid Mechanics 192 (1988) 577–595.
[34] K. Isomoto, S. Honami, The effect of inlet turbulence intensity on the reattachment process over a backward-facing step, Journal of fluids engineering 111 (1) (1989) 87–92.
[35] T. P. Chong, S. Zhong, On the momentum and thermal structures of turbulent spots in a favorable pressure gradient, Journal of Turbomachinery 128 (4) (2006) 689–698.
[36] G. J. Van Fossen, R. J. Simoneau, C. Y. Ching, Influence of turbulence parameters, reynolds number, and body shape on stagnation-region heat transfer, Journal of heat transfer 117 (3) (1995) 597–603.
[37] P. Roach, The generation of nearly isotropic turbulence by means of grids, International Journal of Heat and Fluid Flow 8 (2) (1987) 82–92.
[38] M. E. Crawford. TEXSTAN [online] (1996).

Near-Tip Heat Transfer Mechanisms in an Unshrouded Turbine Equipped with Advanced Blade Tip Geometries

Bogdan Cezar Cernat

Turbomachinery and Propulsion Department, von Karman Institute for Fluid Dynamics, Belgium, cernat@vki.ac.be

Supervisor: Sergio Lavagnoli

Assistant Professor, Turbomachinery and Propulsion Department, von Karman Institute for Fluid Dynamics, Belgium, lavagnoli@vki.ac.be

University Promoter: Tony Arts

Professor, Université catholique de Louvain / von Karman Institute for Fluid Dynamics, Belgium, arts@vki.ac.be

Abstract

The casing of shroudless high-pressure turbines is subjected to large unsteady heat fluxes, generated by a combination of high flow recovery temperature and increased heat transfer coefficient. Alternative blade tip sealing solutions can be designed in order to limit the harmful thermal loads on the stationary shroud and rotating airfoils while maximizing the aerodynamic performance of the stage. However, most of the studies available in open literature focus on classical flat tip solutions, while very scarce information is available on the performance of advanced, engine-representative tip designs. The present work provides a detailed characterization of the time-resolved casing heat transfer field over a baseline squealer tip and two high-performance geometries: a fully contoured tip profile and a multi-cavity squealer-like design. A combined experimental and numerical approach is adopted in order to quantify the impact of the aerodynamic and thermal fields on the shroud heat flux distribution. The test article consists of a one stage HP turbine, operated at engine scaled representative conditions in the rotating turbine test rig of the von Karman Institute. A rainbow rotor approach allows the simultaneous testing of multiple rotor blade tips, each one hosted in a dedicated sector. The time-resolved casing heat flux is investigated by means of a high-density instrumented insert hosting 35 double-layer thin film gauges, flush mounted onto the rotor shroud. The investigation region extends between -5% and +105% of the rotor axial chord and covers a full vane pitch to match the stage spatial periodicity. Steady-RANS are performed in Numeca FINE/Open to analyze the casing heat transfer mechanisms over the three tip geometries, separating the aerodynamic and thermal contributions to the global thermal load. Hence, two sets of isothermal calculations are considered, with the wall temperature set to 300 and 310 K respectively, allowing the evaluation of the casing adiabatic wall temperature and heat transfer coefficient for the three tips.

Keywords: HP Turbine, Tip Flows, Aerothermal, Measurements, Pressure, Heat Transfer, Rainbow Rotor

1. Introduction

The stationary shroud of modern high pressure turbines (HPT) is home to severe time-varying heat transfer phenomena, driven by the close proximity of the moving rotor blades. The high temperature tip leakage flow generated in the narrow clearance between the stationary shroud and the rotor tips is responsible for large, high-frequency variations of the over-tip aerodynamic and thermal field [1; 2]. Ever-increasing turbine inlet temperatures are adopted in order to fulfill the demand for improved cycle efficiency. Thus, the design of effective endwall cooling schemes [3] is essential to preserve the component integrity and prevent critical thermally-induced failures [4]. With more than one third of the stage losses due to the tip leakage flow, engine manufacturers demand for novel, high-performance rotor tip designs to improve the aerothermal performance of the HPT. Experience-driven guidelines, based upon expensive engine data

and mainly pertinent to conventional tip sealing solutions, hold no longer as a thrustworthy and effective design strategy. Hence, a detailed assessment of the over-tip aerodynamic and thermal field is needed to support the design of reliable, high-performance machines with improved service life [5].
A significant body of published work performed in low-speed cascades [6] reports the dependency of the tip leakage flow topology on the tip configuration [7; 8]. Low Mach testing performed by Cho et al. [9] showed the strong dependency of the casing heat flux rate on the tip clearance dimension, varied between 0.66% and 2.85% of the rotor chord. Numerical computations employed in support to linear cascade testing [10] allowed to identify significant variations in the heat transfer pattern over a selection of alternative tip geometries.
While these studies provide a qualitative assessment of the driving factors impacting the casing thermal load, an accurate characterization of the over-tip aerothermal field can only be achieved in engine-relevant testing environments[11; 12]. Recent research works demonstrated the importance of correct non-dimensional flow parameters for the establishment of engine-representative rotor tip flows [13]. Dunn et al. [14] and Guenette et al. [15] were among the first to employ full stage rotating rigs to assess the blade-passing event impact on the unsteady heat transfer rates across the rotor airfoils and casing. Significant peaks in heat flux were observed in proximity of the blade pressure side, and a chordwise variation of time-mean heat transfer was highlighted. Experimental studies performed by Thorpe et al. [16] showed an average decrease of flow recovery temperature along the rotor axial chord, as a result of the work extraction across the blade row. Time-resolved measurements, however, demonstrated the presence of over-tip work exchange mechanisms [17; 18], locally increasing the absolute stagnation temperature of the flow above turbine entry levels [19].
In the pursuit of improved component performance and durability, alternative rotor tip geometries [20] have been conceived in recent years to gain control on the over-tip leakage flow. While squealer-like profiles employ rimmed patterns to minimize the fluid bypass in the tip gap [21], carved tips are purposely shaped to control the acceleration of the gap flow up to chocking conditions and minimize the tip heat transfer [22]. Significant potential was shown by non-conventional designs in terms of tip sealing effectiveness and thermal field management [23; 24]. However, very limited information is present in literature about their performance at engine-relevant conditions.
In the present study, the over-tip aerothermal field of three different blade tips is analyzed through a combined experimental and numerical approach. Two optimized rotor tips, a high-performance rimmed profile and a carved tip, are analyzed against a baseline squealer profile. The alternative tip geometries derive from a previous optimization effort [25] targeting improved aerodynamic and thermal performance. The experimental campaign is carried out at engine-scaled flow conditions in the short-duration turbine test rig of the von Karman Institute [26]. The one-stage HPT test section is heavily instrumented for aerothermal tip flow testing, operated in rainbow rotor setup to allow the simultaneous investigation of multiple blade tips [27]. The casing heat transfer field is interrogated for each single profile and the resulting dataset is employed to validate Steady-state RANS computations. Two sets of CFD results are available, characterized by a constant temperature of the wetted surfaces of 300 and 310 K respectively. This approach allows to separate the aerodynamic and thermal contributions to the wall heat flux for the individual tip designs. A quantitative evaluation of the thermal performance of each tip design is provided, supported by a detailed characterization of the inherent time-mean and time-resolved over-tip flow physics.

2. Methodology

2.1. Turbine Test Rig.

The experimental study was carried out in the short duration rotating turbine test rig of the von Karman Institute [28]. The test article, representative of the first stage of a two-stage aeroengine HPT, presents 34 vanes and 48 rotor airfoils. A rainbow rotor configuration is adopted to allow the simultaneous testing of multiple blade tip geometries mounted in seven different sectors along the rotor disk [27].
Engine-relevant thermodynamic flow conditions are maintained through the flow-on time of the facility (250 ms = 23 rotor revolutions), with an average pressure ratio of 2.2 and a thermodynamic speed of 281 $rpmK^{0.5}$. The quasi-isentropic compression experienced by the gas prior to each test ensures the establishment of a representative gas-to-wall temperature ratio of 1.5. High subsonic flow conditions are reached at the stage outlet, with a relative Mach number of 0.78 and a Reynolds number based on the rotor axial chord of 2.76 x 10^5.

2.2. Tip Geometries.

This paper targets the thermal performance analysis of two optimized tip profiles, a squealer-like (AC06D) and a contoured tip (AC07T), against a baseline squealer profile (IN01D).
Blade IN01D correponds to a conventional squealer tip geometry, presenting a continuous perimetral rim. Blade AC06D is the result of a topology optimization approach targeting the design of arbitrary multicavity squealer-like profiles. It features a perimetral rim with two substantial apertures at the blade leading and trailing edge and a closed "island" rim in the central cavity. For both tips, the cavity depth and minimum rim thickness correspond to 4.5% and 2% of the rotor blade span respectively. Blade AC07T presents a continuous surface shaping, aimed at the limitation of the leakage mass flow and blade tip heat transfer through the control of the gap flow acceleration [29], with a maximum tip gap variation of 3% of the rotor blade span. The carved tip operates with a nominal gap of 0.85% h_r, while the two squealer-like tips are tested at a nominal clearance of 1.38% h_r. A more detailed description of the tested profiles is provided by the authors in [27].

2.3. Casing Heat Transfer Measurements.

The unsteady heat flux at the rotor shroud is interrogated by a set of 35 double-layer thin film gauges, installed on a metallic insert which is flush mounted at the turbine casing. The symmetric nature of the instrumented insert allows to apply a 180 degrees rotation to the sensors array to obtain 6 azimuthal x 11 axial = 66 measurement points. The investigation area covers one full vane pitch and extends between -5% and +105% $c_{r,ax}$, allowing to resolve the full spatial periodicity of the HP stage. The high-frequency temperature sensors are constituted of a 200 nm-thick Nickel element with a resistance of ~50 ohm deposited on a thermally insulating layer of Upilex® Polyimide. The sensors are fed with a 15 mA excitation current to convert the resistance into a voltage signal. Conditioning units are employed to boost the sensor voltage by a variable DC gain (1 to 100) and an analog filter stage provides a frequency-dependent gain, varying from a factor of 2.3 at 100 Hz up to 75 at 150 kHz.
The sensor array was calibrated in a controlled-temperature environment to assess the temperature-resistance correlation between 295 and 365 K. A dynamic calibration was performed to characterize the thermal product ($\sqrt{\rho ck}$) and thermal thickness (l/k) of the poyamide sheet and of the metallic substrate [30]. Before digitization, the temperature signals are separated in two components to enable the resolution of the fluctuations at the time scale of the turbine operation (0.5 s) and at the blade passing frequency (~200 µs). A 500 Hz low pass filter is applied to the time-average signal, which is then sampled at 10 kHz for 10 seconds with 16-bit resolution. The high-frequency signal, conversely, is conditioned by an analog band-pass filter ranging between 60 Hz and 200 kHz. The AC component is amplified by a factor of 10 before being sampled on a 16-bit data acquisition board at 1 MHz for 3 seconds (i.e. 210 measurement points per rotor blade passage). The static gain and the dynamic response of the measurement chain are calibrated in the range between 0 Hz and 1 MHz to produce the necessary de-boosting functions [27].

2.4. Time Resolved Data Processing.

The time-resolved heat flux histories are computed from the unsteady temperature signals by numerically solving the 1D unsteady heat conduction in the solid insert [27]. After computing the heat transfer for the entire temperature history (i.e. 23 rotor revolutions), the passage-average flow field is retrieved for the individual tip profiles at each revolution. Only the central passages are considered in the averaging procedure of each sector to ensure an optimal level of flow periodicity. Optical enconders are employed to monitor the rotor angular position with an accuracy of ±0.25% of the rotor pitch at 5900 rpm, allowing to phase-lock the signal over a complete rotor revolution. For each rotor phase position, a time history of temperature and heat flux can therefore be retrieved [31].

2.5. Numerical Setup.

Steady state RANS computations are performed in Numeca FINE/Open 6.1 in support to the experimental study. The numerical study is performed by imposing isothermal wall conditions to allow the assessment of the casing heat transfer field. Two sets of computations are performed, with a wetted surface temperature of 300 and 310 K respectively, enabling the computation of the adiabatic wall temperature (T_{aw}) and heat transfer coefficient (h_{aw}) at the rotor shroud. A single blade passage is modelled for each tip profile, assuming periodic boundary conditions with the adjoining passages. Due to the complexity of the investigated geometries, a fully hexahedral unstructured grid is selected to mesh the numerical domain. The number of cells varies between 21 and $23.8 * 10^6$, leading to a tip region discretizations of 50 radial x

100 axial x 100 azimuthal cells and a maximum y^+ value of 0.7 [32]. The working fluid is modelled as perfect gas, employing the Spalart-Allmaras turbulence model. The experimental boundary conditions are matched at the measurement planes.

Theoretical background

2.6. Heat transfer mechanism

The thermal field of turbine rotor shrouds is characterized by periodic changes in local heat transfer rates and significant axial and circumferential flow recovery temperature variations. Due to its dependency on the thermal boundary conditions, the classical definition of convective heat transfer coefficient, $h = q/(T_{01} - T_w)$, falls short of describing time- and space-dependent convective phenomena. An alternative approach, extensively described in Anderson and Moffat [33], consists in basing the heat flux computation on the difference between the temperature of the solid surface (T_w) and the time-resolved adiabatic wall temperature (T_{aw}). The global heat transfer is therefore quantified in terms of two main driving factors: the time-dependent state of the local boundary layer, represented by h_{aw}, and the thermal contribution, represented by the unsteady variations of T_{aw} .

$$q = h_{aw} * (T_{aw} - T_w) \tag{1}$$

In the present paper, the evaluation of the local T_{aw} and h_{aw} is performed by computing the fluid-to-solid heat transfer in the rotating frame at two diffrerent values of T_w (300 and 310K). By expressing the heat flux as a function of T_w, the local value of T_{aw} is evaluated by linear interpolation as the zero-heat-flux surface temperature. Hence, h_{aw} is then calculated as the slope of the fitting line.

As suggested by [34], the local time-accurate heat flux can be addressed as the summation of a steady and an unsteady component.

$$\bar{q} + q' = (\bar{h}_{aw} + h'_{aw}) * (\bar{T}_{aw} + T'_{aw} - T_w) \tag{2}$$

By rearranging the constitutive terms of Eq.2, it is possible to highlight how the steady thermal load will not depend solely on the mean values of T_{aw} and h_{aw}, but also on the contribution of their unsteady component. The zero-mean oscillations of the two quantities, addressed here as T'_{aw} and h'_{aw}, will in fact produce a non-null average heat flux when out of phase.

$$\bar{q} = \bar{h} * (\bar{T}_{aw} - T_w) + \overline{h'_{aw} * T'_{aw}} \tag{3}$$

Results and discussion

2.7. Over-tip heat flux.

Figure 1 shows the time-resolved shroud heat transfer for the three tips in the rotor-relative frame, with the horizontal axis indicating the pitchwise location along the rotor passage. The experimental data (a) have been averaged in the relative frame, excluding the time-dependent effect of the upstream vane. The measurements are analyzed in comparison to the numerical predictions (b) obtained by imposing isothermal wall conditions ($T_w = 300K$). The heat flux distributions, normalized by the average level of the reference blade (IN01D), demonstrate a remarkable agreement between measurements and numerical predictions.

A gradual decrease of heat transfer levels characterizes the passage region of the three profiles, proceeding from the blade pressure side (PS) to the suction side (SS) of the adjacent airfoil (A). Constant heat flux is observed over the cavity of blade IN01D and central island of blade AC06D (B), while the shaped surface of AC07T generates a gradual decrease of shroud heat transfer from the leading edge up to the SS at 60% $c_{r,ax}$ (C). High heat flux values characterize the stagnation point at the leading edge of the three tips (D), where the flow is locally redirected towards the external shorud. The heat flux peak, however, is not fully captured by the experimental results, possibly due to the coarser axial discretization of the measurement array. The presence of the PS rim drives the flow to impinge on the outlying casing, generating a high heat stripe (E) which extends over the full rim length for blade IN01D and from 25% to 75% of $c_{r,ax}$ for blade AC06D. Similarly, a region of high heat transfer is detected at the PS of AC07T between 25 and 90% $c_{r,ax}$, due to the tight clearance and to the surface contouring emulating a squealer-like geometry. At 50% $c_{r,ax}$ a region of high heat flux is initiated at the SS rim of the two squealer profiles (T), extending up to 70% $c_{r,ax}$ for blade IN01D and up to 60% for blade AC06D.

The over-tip heat flux is maximized between 70% and 90%$c_{r,ax}$ for blade IN01D and between 55% and 90%$c_{r,ax}$ for blade AC06D (G). The rear rim aperture of the latter facilitates the fluid by-pass from the PS to the SS of the blade and the larger clearance is shown to significantly decrease the casing heat load (H). A stripe of high heat transfer is observed over blade AC07T, starting from the PS at 40%$c_{r,ax}$ and reaching its maximum at the blade SS in the last 40% of the axial chord (L). A low-heat spot appears to interrupt this region at 60%$c_{r,ax}$ (F), further developing

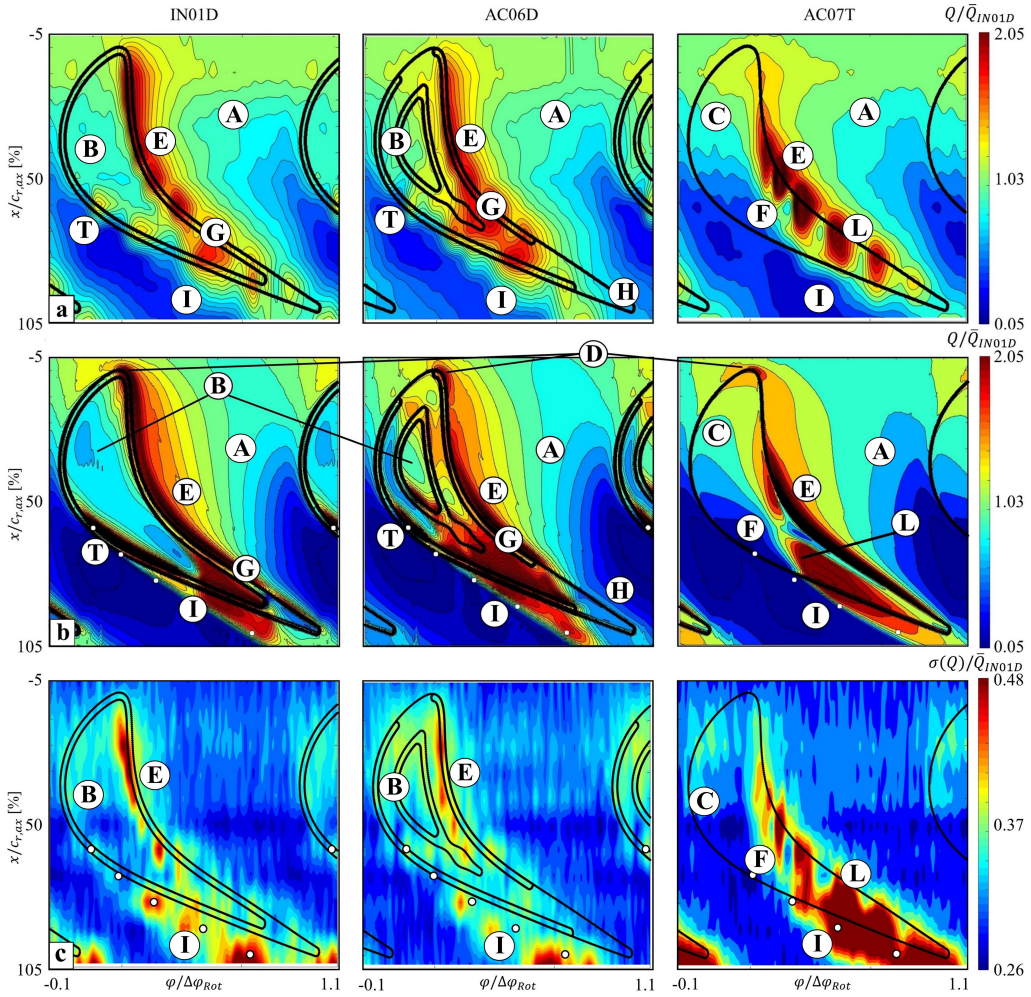

Figure 1: Experimental (a) and numerical (b) normalized casing heat flux and measured random unsteadiness (c) in the rotor frame

in a narrow structure which runs alongside the blade PS up to the trailing edge (F). The tip leakage vortex core (I), displayed by white dots, is computed by applying the vortex tracking method proposed by Kolar [35] and demarks the boundary between high and low heat transfer regions.

Figure 1c shows the non-deterministic component of the measured unsteady heat flux, composed by stochastic fluctuations which are not periodic with the blade passing event. For the squealer profiles, the most significant peaks of random unsteadiness are observed between 10 and 40%$c_{r,ax}$ at the pressure side rim (E), where the ingested flow experiences a local separation, and over the high-turbulence region surrounding the TLV core. As expected, low fluctuation levels are detected over the squealer cavities (B). For the carved profile, conversely, a large random unsteadiness contribution is observed over the aft part of the blade (L), where the highest heat flux levels are generated by the TLV overlaying the tip surface. Contrarily to the heat transfer contours, large stochastic fluctuations are observed on both sides of the TLV cores (I), indicating a significant contribution of the vortex oscillations over the surrounding thermal field.

2.8. Over-tip aerodynamic field.

The over-tip aerodynamic field of the three profiles is displayed in Figure 2 by means of relative velocity streamlines.

The flow entering the tip gap from the blades PS (blue streamlines) shows a strong dependency on the blade tip design. In the case of tips IN01D and AC06D, the

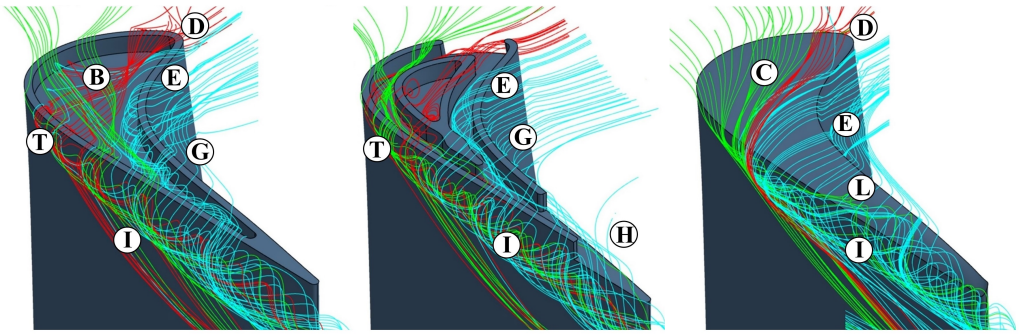

Figure 2: Relative velocity streamlines for blades (left to right) IN01D, AC06D and AC07T

incoming fluid is first diverted radially upwards and accelerated above the perimetral rim (E). The consequent impingement on the external casing originates the high heat transfer stripe observed alongside the pressure side of these profiles in Figure 1. In the cavity of IN01D this stream rolls up in a vortex which follows closely the PS rim, while in blade AC06D the vortical structure is bounded by the rimmed PS channel up to 70% of the axial chord. In blade AC07T the flow ingested in the front PS is shown to closely follow the tip surface, crossing the blade from the PS to the SS.

The red streamlines denote the flow entering the gap from the leading edge region. The front rim aperture of AC06D is shown to facilitate the flow ingress in the overtip gap. This stream is then partly driven over the central island and partly conveyed in the SS rim-bounded channel, where it mixes with the flow entering the gap from the blade suction side (green streamlines). The leading edge of tips IN01D and AC07T is shown to radially divert the incoming flow towards the external casing (D). The ingested flow reattaches then on the cavity floor of blade IN01D while it is gradually redirected in the axial direction by the contoured surface of AC07T.

In both squealer profiles, the over-tip stream is subject to an early suction side ejection in comparison to blade AC07T. The SS rims are shown to promote the outward motion of the gap flow and to increase its tangential velocity component (T), originating the high heat transfer stripes observed in Figure 1.

Starting from 60% $c_{r,ax}$ for blade AC06D and 70% for IN01D, the flow tends to directly bypass the cavity, being discharged at the tip suction side (G). The bypass stream is turned in the tangential direction and lifted towards the external casing, producing a region of high heat flux which entirely covers the tip in the tangential direction (Figure 1). Similarly, the flow entering the tight gap at the carved tip PS is observed to undergo a substantial tangential acceleration starting from 40% $c_{r,ax}$.

The closed end of the squealer bath of tip IN01D is shown to produce a local outward ejection of the cavity stream, which is subsequently entrained by the tip leakage vortex (TLV) at the blade suction side (I). The rear aperture (H) of blade AC06D facilitates the PS-SS fluid bypass and its subsequent entrainment in the TLV. Due to the absence of a rimmed structure in blade AC07T, the flow entering the gap follows closely the carved surface and is constantly accelerated up to 60% of $c_{r,ax}$. At this axial location flow separation occurs over the tip surface and the TLV is observed to partially overhang the tip (L).

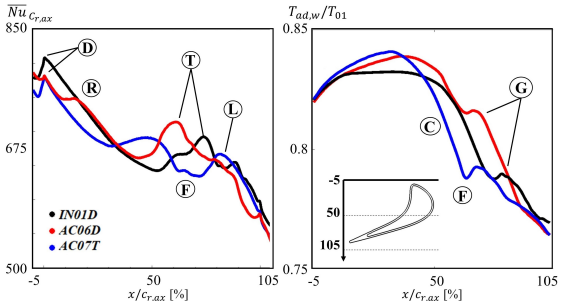

Figure 3: Axial distributions of pitchwise average $Nu_{c_{r,ax}}$ (left) and T_{aw}/T_{01} (right) for the three tips

2.9. Time average heat transfer

The time average components of casing $Nu_{c_{r,ax}}$ and T_{aw}/T_{01} for the three profiles are represented in Fig. 3. The horizontal axis indicates the axial location normalized by $c_{r,ax}$. Blades IN01D and AC07T show significant Nusselt peaks at the leading edge location, where the flow is locally diverted towards the casing (D). A $Nu_{c_{r,ax}}$ value of 810 is reached at this loca-

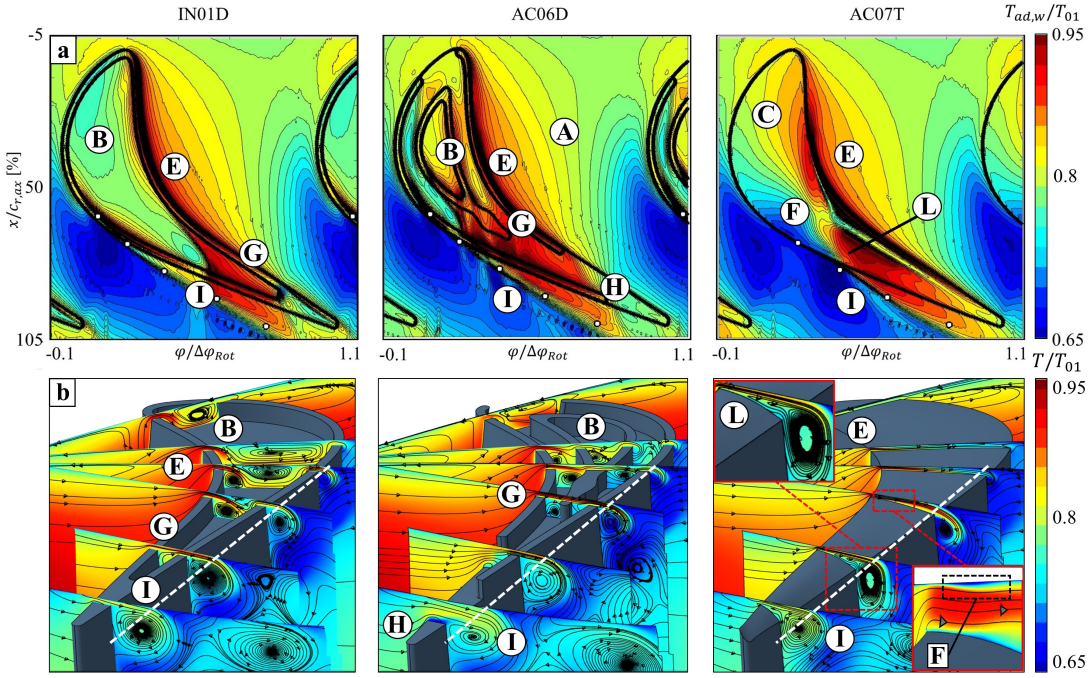

Figure 4: Phase resolved contours of casing T_{aw}/T_{01} (a) and orthogonal cuts with T_0/T_{01} contours and relative velocity streamlines (b)

tion by the baseline squealer, while the carved profile reaches a maximum $Nu_{c_{r,ax}}$ of 750. The front rim aperture of AC06D, providing a larger clearance to the flow entering the gap, appears to mitigate this peak. A local Nusselt plateau is observed in this blade at $15\%c_{r,ax}$, where the over-tip flow is conveyed over the front rim of the central island (R). A decreasing trend is then observed up to 50% $c_{r,ax}$ for the squealer tips and up to 30% $c_{r,ax}$ for the carved profile. The latter shows the highest level of mid-chord Nusselt number, before experiencing a local minimum at $60\%c_{r,ax}$ (F), where the low heat flux region was detected in the time resolved contours (Fig. 1). Another local maximum is detected for AC07T at $80\%c_{r,ax}$, where the tip leakage vortex has been shown to drive the over-tip heat transfer field (L).
A localized increase of $Nu_{c_{r,ax}}$ is shown at $50\text{-}60\%c_{r,ax}$ for blade AC06D and at 50-70% for blade IN01D, reaching values of 710 and 690 respectively. The peaks positions correspond to the axial stations where a high heat transfer stripe was detected along the SS rim of these blades (T). From this location on, a general decreasing trend is shown for the three tips.
The normalized adiabatic wall temperature shows an increasing trend in the front part of the three profiles, reaching a maximum of 0.84 at 40% and 50% $c_{r,ax}$ for blades AC07T and AC06D respectively. After an initial increase up to a value of 0.83 in the first 10% $c_{r,ax}$, the baseline squealer shows a T_{aw} plateau up to mid-chord, in agreement with the constant heat transfer levels registered over the cavity bath (B).
In the second half of the axial chord, the three tips show a quasi monotonous decrease of T_{aw}, interrupted by local peaks at $60\%c_{r,ax}$ for blades AC06D and AC07T and $70\%c_{r,ax}$ for IN01D. This local increase founds its motivation in the initiation of the direct by pass mechanism (G) on the squealer profiles and in the high heat flux region linked to the tip leakage vortex (L) in the carved tip.

2.10. Adiabatic Wall Temperature.

Figure 4 shows the phase-resolved casing adiabatic wall temperature (a) and the evolution of the flow over six planes orthogonal to the blade camber line (b), with normalized total temperature contours completed by relative velocity surface streamlines.

The passage flow shows a similar behavior for the three tips, with the recovery temperature exhibiting a rather uniform increasing trend in the tangential direction from the blade SS to the PS of the neighboring airfoil (A). High temperature stripes are shown at the pressure side of the three profiles (E), where the

flow experiences an abrupt acceleration and tangential redirection before entering the gap. A recirculation region is then observed to arise in the squealer bath of blade IN01D, causing a drop in the recovery temperature of the flow over the entire tangential extent of the cavity (B) up to 70%$c_{r,ax}$.
The fluid ingested in the tip gap of blade AC06D is partly entrained in a vortical structure which develops in the PS channel between the central island and the perimetral rim, with values of T_{aw}/T_{01} ranging between 0.8 and 0.85. A nearly constant distribution of low T_{aw} is observed over the front part of the central island, gradually increasing towards the cavity end (B).
Blade AC07T is characterized by a gradual decrease of adiabatic wall temperature (C) up to 50% of the axial chord, as the over-tip flow is redirected axially by the shaped surface of the tip. A stripe of high T_{aw} is initiated at 20% $c_{r,ax}$ at the blade PS and abruptly interrupted at 60% $c_{r,ax}$ by a local minimum (F). The presence of low temperature fluid in the near casing region at this location is shown in detail in Figure 4b. A better insight on the origin of this cold stream is given in Figure 5, showing the heat transfer distribution at the casing of blade AC07T and relative velocity streamlines in close proximity to the wall. Two distinct fluid streams are observed to enter the gap from the blade SS at 20% and 40% $c_{r,ax}$, traveling towards the blade PS and presenting lower temperature and velocity compared to the main gap flow. After being redirected by the over-tip pressure gradient, the two structures are discharged at the blade SS (70% $c_{r,ax}$) and trailing edge respectively.
Blades IN01D and AC06D show a significant increase of over-tip T_{aw} at 70% and 55% of the axial chord respectively (G), where the fluid ingested in the tip gap

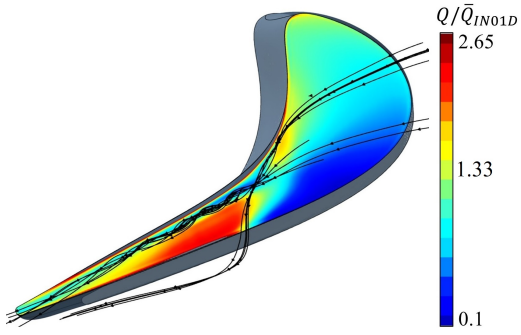

Figure 5: Normalized casing heat flux contours over tip AC07T with near-casing relative velocity streamlines

tends to directly bypass the rimmed pattern instead of being entrained by the cavity vortical structures. The earlier initiation of the process in blade AC06D is motivated by the presence of the central rim. An abrupt increase of heat transfer is observed at 70% $c_{r,ax}$ for blade AC07T, where the relative velocity of the leakage flow presents a high tangential component, the absolute velocity is maximal and the incipient TLV partially overhangs the tip SS.
In the aft region of the three blades the tip leakage flow shows increased values of stagnation temperature, justifying the high heat transfer values already observed in Fig. 1. The vortex cores, indicated by white dots in Fig. 4a and by dashed lines in Fig. 4b, demarcate the boundary between high and low T_{aw} regions (I). Downstream of the vortex center, the high temperature flow is driven inwards by the TLV vortical motion and colder fluid from the main passage flow is conveyed in the near casing region.

2.11. Over-tip work processes.

Rotor blade tips traveling in close proximity to the stationary shroud are responsible for unsteady work processes which can locally increase the flow stagnation temperature well above the stage inlet values. The physical reason for this temperature increment is the increase in angular momentum experienced by the leakage fluid under the action of the pressure gradient between tip PS and SS [36]. As from Eq.4, the increase in flow total temperature can therefore be evaluated as a function of the work produced by the rotor on the over-tip fluid.

$$T_0 - T_{0,2} = \frac{1}{c_p} \cdot U \cdot (V_t - V_{t,02}) \qquad (4)$$

Figure 6a presents the variation of absolute tangential velocity with respect to the rotor inlet at the mid-gap plane of the three tips. While the passage flow is gradually conveyed in the direction imposed by the blade profiles (A), the over-tip aerodynamic field is strongly modulated by the tip design. The pressure side rims of blade AC06 and IN01D are shown to impose an abrupt tangential deviation to the flow entering the tip gap (E), justifying the local increase of T_{aw} highlighted in Figure 4. Conversely, a constant V_t distribution is detected over the central squealer cavities (B), in line with the low thermal contribution observed in these regions. Increased V_t levels are observed at 70% $c_{r,ax}$ of blade IN01D and 55% $c_{r,ax}$ of blade AC06D, where the direct flow bypass mechanism is initiated (G).
In the front part of AC07T, the carved tip surface is

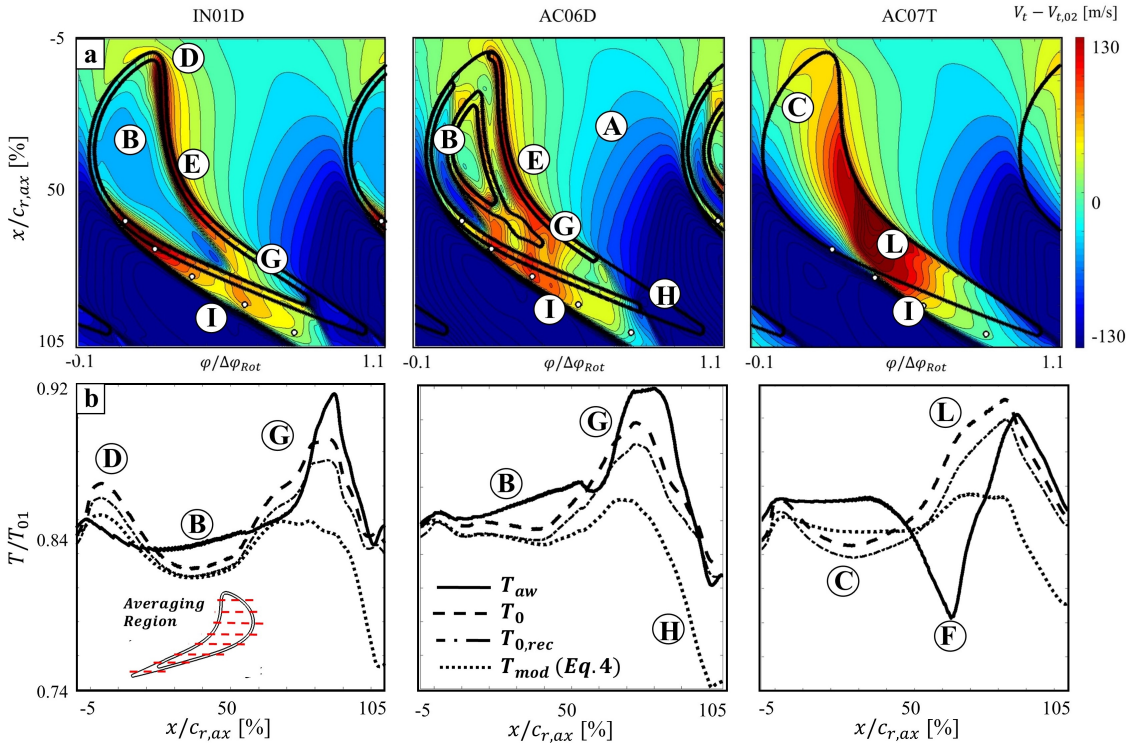

Figure 6: Phase resolved midgap $V_t - V_{t,02}$ (a) and distributions of over-tip pitchwise average T/T_{01} (b)

shown to gradually convey the over-tip fluid in the main flow direction (C). The angular momentum of the flow is decreased from the PS to the SS of the tip, in agreement with the gradual T_{aw} decrease observed in this region. The region of maximum over-tip flow turning is located between 50% and 70% $c_{r,ax}$ (L), matching the region of highest stagnation temperature observed in Figure 4. A higher degree of uniformity is shown, however, by the mid-gap aerodynamic pattern with respect to the casing thermal field. This discrepancy is to be ascribed to the near-casing cold flow structure observed in Fig. 5 (point F in Fig. 4), which does not appear to affect the mid-gap field.

As a common feature for the three profiles, the TLV, developing from 60%$c_{r,ax}$ for AC06D and IN01D and from 70%$c_{r,ax}$ for AC07T, shows high values of V_t upstream of the vortex core (white dots in Fig. 6). As observed in Figure 4, downstream of the TLV core the leakage fluid is conveyed radially inwards while the passage flow, of negative V_t in this case, is entrained in the near-casing region (I).

The phase-resolved flow turning at the mid-gap plane can be employed to compute the pitchwise mean adiabatic wall temperature variation in the over-tip and over-passage regions of the shroud (Eq. 4). Figure 6b shows the evolution of normalized $\bar{T}_{aw}$ over the three tip geometries (solid line) together with the midgap total temperature (dashed line). The recovery temperature (dash-dotted line) is computed from the midgap Mach distribution, considering a recovery factor of $k = Pr^{1/3}$ to account for the thermal behavior of a fully turbulent boundary layer. Additionally, the total

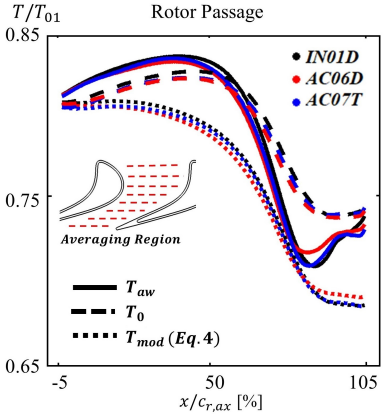

Figure 7: Distributions of pitchwise average casing T_{aw}/T_{01} and extracted and modeled midgap T_t/T_{01}

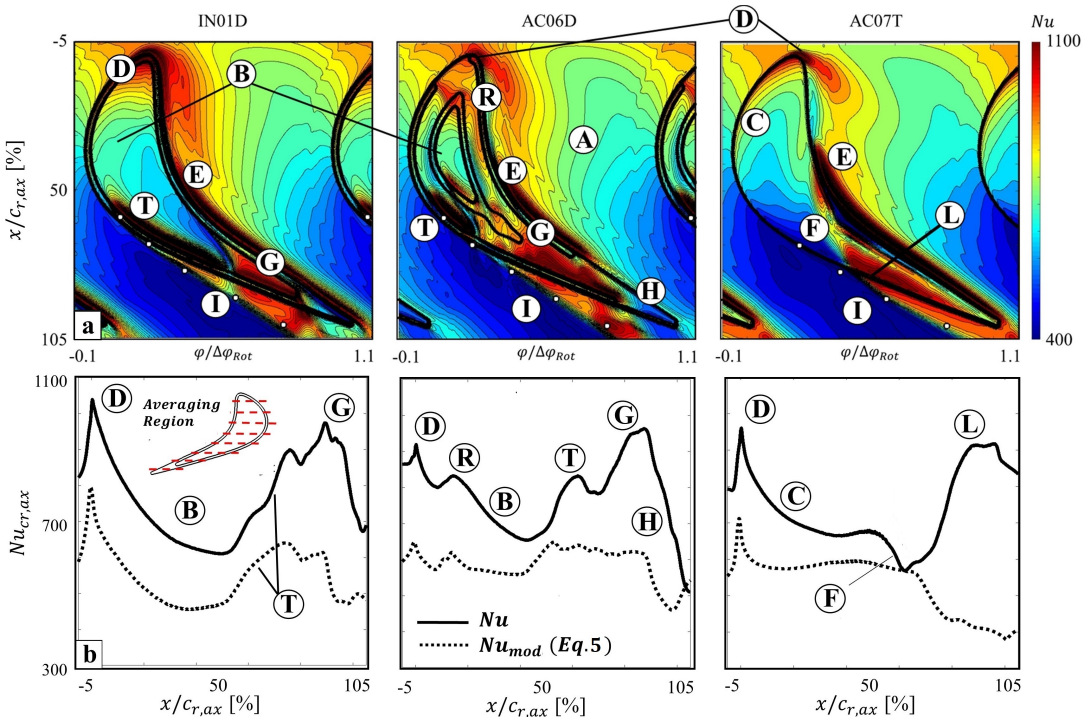

Figure 8: Phase-resolved contours and (a) and over-tip pitchwise average distributions of $Nu_{cr,ax}$ (b)

temperature modeled by Eq.4 is displayed by a dotted line. The horizontal axis represents the axial coordinate normalized by the rotor axial chord, proceeding from the leading edge to the trailing edge of the blade. The midgap recovery temperature is observed to closely follow the trend of $\bar{T}_0$ over the three tips, presenting a negative offset of about 2% of the inlet total temperature. A localized increase of $\bar{T}_0$ is observed at the blades leading edge (D), as the angular momentum of the flow entering the tip gap is incremented under the action of the tip loading. The local maximum, particularly evident in blade IN01D, appears well matched by the model. Between 10 and 30% $c_{r,ax}$, the mid-gap flow temperature of IN01D is shown to decrease significantly due to the presence of the squealer bath (B). Conversely, the rimmed pattern of AC06D is shown to promote higher flow deviation values in this region, contributing to keep a constant level of $\bar{T}_0$ up to 50% $c_{r,ax}$. Between 20 and 50% $c_{r,ax}$, the adiabatic wall temperature reaches higher values than $\bar{T}_0$ for the three blades, indicating a greater flow turning in the near-casing region with respect to the midgap plane. A local minimum is observed, finally, at 25% $c_{r,ax}$ for blade AC07T, consistently with the over-tip negative flow deviation (C) highlighted in Fig. 6a. The casing adiabatic wall temperature, on the other hand, shows a slight increase between 10 and 50% $c_{r,ax}$ for the two squealer tips and a plateau for the carved profile. The model based on Eq. 4 is shown to match closely the variations of $\bar{T}_0$ in the first 50% of the axial chord, confirming the substantial role of the work exchange process in the modulation of the over-tip thermal field.

A steep increase of $\bar{T}_{aw}$ and $\bar{T}_{mid}$ is shown in the second part of the axial chord for both squealer designs, motivated by the initiation of the direct bypass mechanism (G). In agreement with the aerodynamic analysis, a local peak of normalized $\bar{T}_{aw}$ is detected at 85% $c_{r,ax}$ for blade IN01D while a more extended maximum is detected between 70 and 80% $c_{r,ax}$ for blade AC06D. In the case of IN01D, $\bar{T}_{aw}$ reaches values close to 0.91 T_{01} while the midgap total temperature presents a maximum of 0.88 T_{01} at the same axial position. Slightly higher maxima are reached over blade AC06D (+1% T_{01}), while an equivalent offset is observed between $\bar{T}_{aw}$ and $\bar{T}_0$. In the case of blade AC07T, a monotonous increase of $\bar{T}_{mid}$ is observed from 50%$c_{r,ax}$, leading to a global peak at 85% $c_{r,ax}$ of 0.9 T_{01}. Contrarily, the $\bar{T}_{aw}$ is shown to decrease up to a global minimum of 0.78 T_{01} at 60% $c_{r,ax}$, where the near casing cold stream (F) crosses the high heat transfer region initiated at the blade pressure side (L).

The maxima observed in the aft part of the three profiles are only partially replicated by the $\bar{T}_{mod}$, indicating the limited capability of the work exchange model in representing the thermal impact of the tip leakage phenomenon. A generally decreasing trend is shown for the three blades in the last 15%$c_{r,ax}$, with $\bar{T}_{aw}$ reaching the lowest (0.81 T_{01}) and highest (0.86 T_{01}) trailing edge values in blades AC06D and AC07T respectively. This difference is motivated by the larger clearance over the rear rim aperture of blade AC06D (H) in contrast to the tighter clearance at the cut back of blade AC07T.
The pitch-average distributions of normalized $\bar{T}_{aw}$, $\bar{T}_0$ and modeled stagnation temperature over the rotor channel are presented in Figure 7. An increase of about 3% is shown by the three tips in the first 50% $c_{r,ax}$ in terms of both adiabatic wall temperature and midgap temperature. This trend does not appear to be well matched by the model, with a plateau of $\bar{T}_{mod}$ in the first 40% of the axial chord which leads to an underestimation of the temperature at mid-chord of about 5% of the stage inlet vlaue. From 50% to 75% $c_{r,ax}$, a general decreasing trend is shown by the three quantities, indicating a work extraction process operated by the rotor over the passage flow. At 60% $c_{r,ax}$ the adiabatic wall temperature falls below $\bar{T}_0$ to finally reach a global minimum of 0.71 at 75%$c_{r,ax}$. In the last 25% $c_{r,ax}$ the extracted and modeled midgap temperatures show a rather stable trend, while $\bar{T}_{aw}/T_{01}$ increases of about 3% reaching a final value of 0.74 at the trailing edge of the three tips.

2.12. Casing convection mechanisms.

The phase-resolved distributions of casing Nusselt number are presented in form of contour plots in Fig. 8a.
The Nusselt levels over the blade passage are observed to decrease moving along the main flow path, as the absolute velocity of the flow gradually decreases (A). Significant peaks of $Nu_{c_{r,ax}}$ are observed at the leading edge of the three tips (D), where the fluid has been shown to impinge locally on the external shroud. As a difference from the T_{aw} distributions, the local maxima tend to propagate towards the passage at the tip PS. As the flow enters the cavity of tip IN01D and is conveyed towards the squealer floor, the convection levels gradually decrease and lead to a rather uniform distribution of low Nusselt in the central part of the cavity (B). A similar trend is observed over the central cavity of blade AC06D, after an initial Nusselt peak at the island leading edge (R). The increasing clearance over AC07T, conversely, is seen to promote a gradual reduction of the convection levels up to the tip SS at 65% $c_{r,ax}$.
High Nusselt stripes are initiated at 40% $c_{r,ax}$ at the PS of the three tips (E), as an effect of the flow swallowed in the gap above the squealer rims and through the tight running clearance at the carved tip PS. The high convection region is seen to extend up to the trailing edge for blades IN01D and AC07T, while being interrupted abruptly at 70% $c_{r,ax}$ by the aft rim aperture of blade AC06D (H). Similarly, high $Nu_{c_{r,ax}}$ values are registered at the SS rim of the squealer tips, starting from 50% $c_{r,ax}$ and persisting up to the location where the direct bypass mechanism (G) is initiated (60%$c_{r,ax}$ for AC06D, 70% $c_{r,ax}$ for IN01D).
In line with the thermal distributions of Fig. 4, a high convection region (L) develops from the PS of AC07T (40% $c_{r,ax}$) up to the aft part of the blade SS, following the flow path of the tip leakage stream. This region is locally interrupted at 60%$c_{r,ax}$ by the low-velocity flow structure (F) highlighted in Fig. 5. This near casing stream is then seen to generate a low $Nu_{c_{r,ax}}$ stripe traveling in close proximity to the PS up to the blade trailing edge. The TLV core (white dots), marks the boundary between the upstream high Nusselt region, where the flow is driven towards the casing by the vortical motion, and the low-convection region over the rotor passage (I).

2.13. Convection process model.

Fig. 8b shows the pitchwise-average distributions of Nusselt number in the over-tip area of the three profiles. A simplified model is introduced to represent the casing convection mechanism. To this aim two contributions are considered: the forced convection in a turbulent flow, evaluated by means of the Dittus-Boelter correlation, and the local impingement heat transfer contribution based on the radial Reynolds distribution [37].

$$Nu = 0.023 {Re^{0.8}}_{zt,c_{r,ax}} Pr^{0.4} + 0.57 {Re^{0.5}}_{r,c_{r,ax}} Pr^{0.37} \quad (5)$$

The solid lines in Fig. 8b indicate the average adiabatic $Nu_{c_{r,ax}}$ based on the CFD thermal field, while the dashed lines indicate the Nusselt number modeled through Eq. 5. An evident offset is present between the two distributions, with the model underestimating the convection levels by 25% over the first 50% of the axial chord for the three profiles. The discrepancies are more pronounced in the aft part of the blade, especially in tip AC07T, where the tip leakage phenomenon dominates the over-tip aerodynamic field.
A first peak of $\overline{Nu}$ is observed at the leading edge of

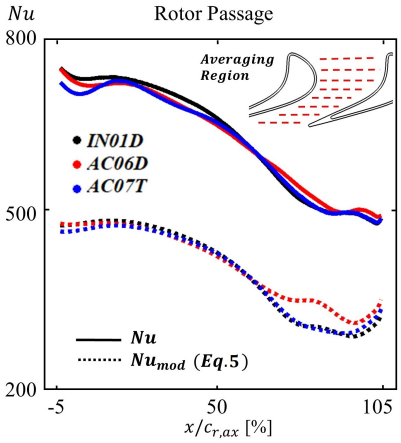

Figure 9: Axial distributions of pitchwise average casing $Nu_{cr,ax}$ (computed and modeled values)

the three profiles (D), significantly reduced in AC06D by the presence of the front rim aperture. A local maximum is present at 15%$c_{r,ax}$ of this profile, where the central island rim diverts the flow towards the external shroud (R). Both squealer cavities are seen to produce a low convection area (B), culminating in the global minimum around 50% $c_{r,ax}$. Similarly, the shaped surface of blade AC07T is seen to produce a monotonous $\overline{Nu}$ decrease (C) up to 50%$c_{r,ax}$.
Starting from 50% $c_{r,ax}$, both squealer tips show a steep $\overline{Nu}$ increment due to the high convection stripe arising at the suction side rim (T). This trend is interrupted by a local minimum at 80%$c_{r,ax}$ for IN01D and 65%$c_{r,ax}$ for blade AC06D, before the direct bypass mechanism (G) contributes to further increase $\overline{Nu}$ up to a value of 1000 for both blades.

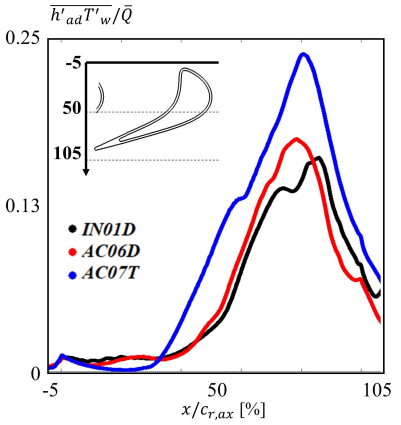

Figure 10: Axial distributions of unsteady h_{aw} and T_{aw} contribution to time mean casing heat flux

In blade AC07T, the global minimum is located at 60%$c_{r,ax}$, where the low-velocity near-casing flow structure was shown to significantly affect the convection mechanism (F). A steep increase of $\overline{Nu}$ is then registered up to 90%$c_{r,ax}$, corresponding to the high heat transfer area generated by the tip leakage over the aft part of the carved surface (L).
Figure 9 presents the pitchwise average distributions of Nusselt number over the passage region of the three blades, with the solid lines indicating the numerical solution and the dashed lines indicating the modeled one. The latter is observed to underestimate by 30% the computed average values over the full length of the axial chord. After a local maximum at 10% $c_{r,ax}$, $\overline{Nu}$ is observed to decrease monotonically up to the 85% of the rotor axial chord, as the absolute Reynolds decreases along the rotor passage. While the three tips show a very similar behavior in the computed distributions, a more evident discrepancy is observed at 85% $c_{r,ax}$ in the modeled $\overline{Nu}$ of blade AC06D. A local maximum of modeled Nu appears at this axial station, corresponding to the position of the rear rim aperture, which is not detected in the computed $\overline{Nu}$. The global Nusselt decrease across the rotor axial chord is equal to 30% of the entry value for both the modeled and computed distributions.

2.14. Unsteady heat transfer contribution.

As observed in Eq.3, both T'_{aw} and h'_{aw} contribute actively to the time-average thermal load of the rotor shroud. Figure 10 presents the relative impact of $\overline{h'_{aw} * T'_{aw}}$ on the time average casing heat transfer for the three tip geometries. The horizontal axis indicates the axial location normalized by the rotor axial chord. As a common feature to the three tips, an initial peak of approximately 1% of the total load is observed at the blade leading edge. This local maximum is followed by a plateau for the two squealer geometries and by a slight decrease in the case of blade AC07T.
A steep increment of the unsteady contribution is then observed in the three profiles, starting at 35% for the carved tip and at 45% for blades IN01D and AC06D. The highest maximum is observed at 80% $c_{r,ax}$ for blade AC07T, reaching almost 25% of the total average thermal load. Lower peaks are registered for blades AC06D and IN01D, at 75 and 85% $c_{r,ax}$ respectively, amounting to 17% and 15% of $\bar{Q}$. This significant rise of $\overline{h'_{aw} * T'_{aw}}$ in the second half of $c_{r,ax}$ is motivated by the presence of strong Nusselt and T_{aw} fluctuations linked to the tip leakage stream. With the former quantity depending on the boundary layer status and the latter depending on the enthalpic content of

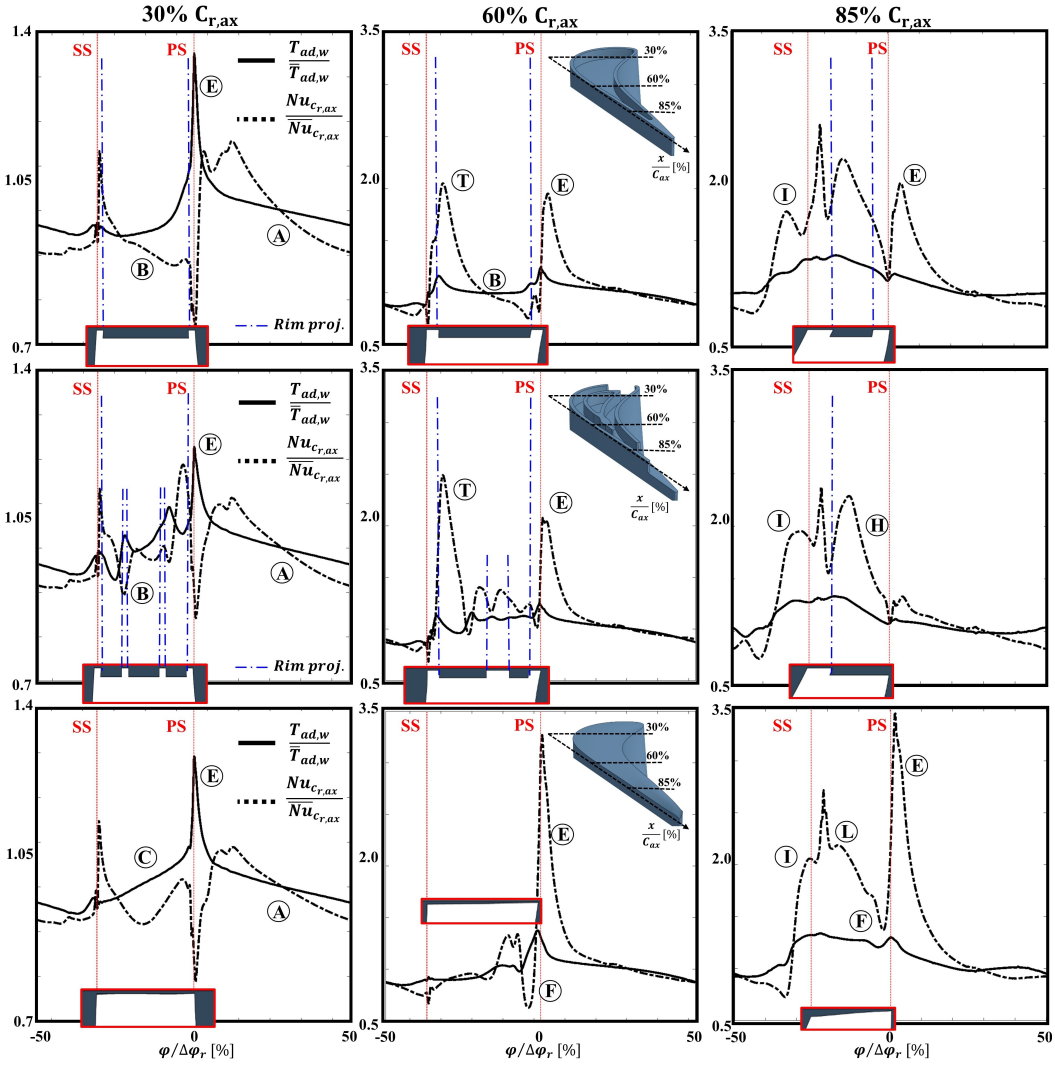

Figure 11: Phase-resolved distributions of normalized $Nu_{cr,ax}$ and T_{aw} at (left to right) 30%, 60% and 85%$c_{r,ax}$ for (top to bottom) blades IN01D, AC06D and AC07T

the flow, the aforesaid fluctuations result out of phase and produce a significant mean thermal load.

Figure 11 presents the phase-resolved histories of T_{aw} (solid line) and $Nu_{c_{r,ax}}$ (dotted line) at a selection of axial stations (30%, 60% and 85%$c_{r,ax}$ from left to right) for the three tips (IN01D, AC06D and AC07T from top to bottom). The distributions have been normalized by their pitchwise average value along the rotor axial chord. The horizontal axis represents the rotor phase normalized by the rotor pitch referred to the position of the blade PS. The airfoils travel from right to left in the plots, red dotted lines indicate the location of the tip SS and PS while the rims projections are displayed by blue dash-dotted lines.

At 30% $c_{r,ax}$ both $Nu_{c_{r,ax}}$ and T_{aw} are observed to grow over the rotor passage from the SS towards the PS (A). The global maximum of adiabatic wall temperature is located at the blade pressure side (E), with values exceeding the average level by 30% in the case of IN01D and AC07T and by 10% in the case of AC06D. As already observed, the local increase of T_{aw} is due to the increment of angular momentum of the fluid ingested in the tip gap at this location. The Nusselt number, contrarily, exhibits a plateau between 5% and 15% $\Delta\varphi_r$, before dropping by 20 to 30% over the blade PS, due to the establishment of the vena contracta in the flow entering the tip gap. After a sudden rise immediately after the rim, the Nusselt distribution is observed

to gradually grow towards the SS in blade IN01D (B). On blade AC06D, on the other hand, the rim-cavity pattern (peak of T_{aw}, rise and fall of $Nu_{c_{r,ax}}$) is repeated twice as the flow overcomes the central island. The shaped surface of blade AC07T is seen to promote a central area of low Nusselt over the tip, while the adiabatic wall temperature shows a generally decreasing trend from the tip PS to SS (C).

At 60% $c_{r,ax}$, as the flow approaches the PS of the squealer tips (right to left in the figure) the Nusselt number increases by 100%, suddenly dropping in close proximity to the rim (E). The local increase of T_{aw}, in this case, amounts to 20% of the average value for both IN01D and AC06D. Over the PS part of the IN01D cavity a low Nusselt number distribution is shown (B), increasing progressively up to a value of 200% $\overline{Nu_{c_{r,ax}}}$ in proximity of the tip PS (T). In blade AC06D the merged central island is seen to promote a local rim-cavity pattern before the Nusselt increases up to 250% $\overline{Nu_{c_{r,ax}}}$ at the blade SS (T). The sharp PS edge of the carved profile acts as a squealer rim at this location, with the tight clearance value contributing to rise the local Nusselt peak up to 320% of the average level and the local T_{aw} up to 140% $\overline{T_{aw}}$ (E).

At 85% of the rotor axial chord, a local increase of Nusselt is detected before the flow is ingested at the pressure side of tips IN01D and AC07T, with peaks of 200% and 320% $\overline{Nu_{c_{r,ax}}}$ respectively (E). The larger clearance generated by the rear rim aperture of blade AC06D, conversely, limits the peak to 120% $\overline{Nu_{c_{r,ax}}}$ (H). A gradual increase of Nusselt number is detected from the PS to the SS of the squealer tips, before a fast drop and rise over the SS rim. A local Nu minimum (F) is shown in the near-pressure side region for blade AC07T, due to the low velocity near-casing stream shown in Figure 5. A progressive rise is then observed towards the PS, as the TLV overhangs the tip surface (L). A near-SS maximum is visualized in the blade passage for the three tips (I), due to the TLV vortical motion. As expected, this maximum presents a larger peripheral distance from the squealer tips in comparison to blade AC07T, where the TLV core has been shown to travel closer alongside the blade SS. Traveling further towards the center of the channel, both T_{aw} and $Nu_{c_{r,ax}}$ are subject to a significant decrease between -20% and -40% $\Delta\varphi_r$.

Conclusions

The heat transfer field at the casing of three different blade tip geometries was investigated with the aid of time-resolved experimental data and steady numerical computations performed in the rotor domain. Good agreement was observed between the measured and predicted heat flux distributions.

The aerodynamic and thermal contributions to the casing thermal load were assessed by computing the adiabatic wall temperature and Nusselt number distributions.

T_{aw} shows a steep increase in those over-tip regions where the angular momentum of the flow is incremented by the blade tip load. For the squealer profiles, the most significant peaks are observed over the front pressure side rims (E) and in the direct bypass areas (G), where the ingested flow experiences the most significant tangential acceleration. For blade AC07T, similarly, the global maximum of T_{aw} is registered in the region of highest flow turning between 50 an 70% of the axial chord. In this case, a cold near-casing flow structure, entering the gap at the front SS, is seen to locally decrease the casing thermal load at 60% $c_{r,ax}$. In the rear part of the three profiles, the TLV core separates the high T_{aw} region, where the leakage fluid is conveyed towards the casing, from the low-temperature area above the blade passage.

A simplified model was introduced to predict the pitchwise-average T_{aw} in the over-tip and over-passage regions based on the near-casing work exchange mechanisms for the three profiles. While a good matching is achieved between T_{aw} and T_{mod} over the front part of the tips, the model could only partially replicate the temperature rise due to the tip leakage stream in the last 40% of $c_{r,ax}$. This limitation might be ascribed to the three dimensional nature of the flow in this region, not entirely representable by a 2D flow analysis performed at the midgap plane.

The casing Nusselt is observed to rise at the leading edge of the three profiles, where the flow ingested in the gap is driven towards the external casing. Similarly, high convection stripes are detected alongside the PS rims of the squealer geometries and from 40% $c_{r,ax}$ at the PS of blade AC07T. Additionally, blades IN01D and AC06D show high Nu avenues along the SS rim, between 50% $c_{r,ax}$ and the initiation of the direct flow bypass mechanism, taking place at 70%$c_{r,ax}$ for the former and 60%$c_{r,ax}$ for the latter. The TLV is observed to significantly increment the convection levels upstream of the vortex core, where the fluid impinges on the external casing and locally modifies the boundary layer status.

A simplified model was designed to predict the axial distribution of pitchwise-average casing $Nu_{c_{r,ax}}$, based on turbulent convection and impingement heat

transfer correlations. The modeled Nusselt number follows closely the computed trends over the rotor passage and over the first 50%$c_{r,ax}$ of the over-tip region. A negative offset of about 30% is observed in the model compared to the computed distribution. As for the thermal model, significant limitations are observed in the evaluation of TLV impact on the casing convection mechanism over the aft part of the tips.

The fluctuations of heat transfer coefficient and adiabatic wall temperature are shown to generate up to 25% of the time-mean heat flux over the aft part of blade AC07T. For the squealer profiles the unsteady contribution amounts to about 15% of the global thermal load. The maximum contribution is observed, for all the profiles, between 75% and 85% $c_{r,ax}$.

Nomenclature

C	=	Rotor Chord [m]
HPT	=	High Pressure Turbine
P	=	Pressure [Pa]
PS	=	Pressure Side
PLA	=	Phase-Locked Average
RANS	=	Reynolds-Averaged Navier-Stokes
Re	=	Reynolds Number
SS	=	Suction Side
Q	=	Heat flux [W/m^2]
T	=	Temperature [K]
y^+	=	Non-dimensional first cell size
Δx	=	Axial distance from rotor tip leading edge normalized by rotor axial chord [%]

Subscripts

0	=	total quantity
1	=	turbine inlet
2	=	stator-rotor plane
ax	=	axial
r	=	rotor

References

[1] R. S. Bunker, Axial Turbine Blade Tips: Function, Design, and Durability, Journal of Propulsion and Power 22 (2) (2006) 271–285. doi:10.2514/1.11818.
URL https://doi.org/10.2514/1.11818

[2] M. D. Polanka, D. A. Hoying, M. Meininger, C. D. MacArthur, Turbine Tip and Shroud Heat Transfer and LoadingPart A: Parameter Effects Including Reynolds Number, Pressure Ratio, and Gas-to-Metal Temperature Ratio, J. Turbomach 125 (1) (2003) 97–106. doi:10.1115/1.1515338.
URL http://dx.doi.org/10.1115/1.1515338

[3] K. Chana, B. Haller, Novel turbine rotor shroud film-cooling design and validation: Part 1, in: ASME Turbo Expo 2009: Power for Land, Sea, and Air, American Society of Mechanical Engineers, 2009, pp. 955–967.

[4] M. K. Chyu, Heat transfer near turbine nozzle endwall, Annals of the New York Academy of Sciences 934 (1) (2001) 27–36.

[5] B. Glezer, Thermal-mechanical design factors affecting turbine blade tip clearance, Turbine Blade Tip Design and Tip Clearance Treatment (von Karman Institute for Fluid Dynamics Lecture Series), T. Arts, ed., von Karman Institute for Fluid Dynamics, Rhode-St-Genese, Belgium.

[6] A. Yamamoto, Endwall flow/loss mechanisms in a linear turbine cascade with blade tip clearance, Journal of Turbomachinery 111 (3) (1989) 264–275.

[7] F. Heyes, Jg, hodson, hp, and dailey, gm, 1992,the effect of blade tip geometry on the tip leakage flow in axial turbine cascades,, ASME J. Turbomach 114 (3) 643–651.

[8] J. P. Bindon, G. Morphis, The Development of Axial Turbine Leakage Loss for Two Profiled Tip Geometries Using Linear Cascade Data, J. Turbomach 114 (1) (1992) 198–203. doi:10.1115/1.2927985.
URL http://dx.doi.org/10.1115/1.2927985

[9] H. Cho, D. Rhee, J. Choi, Heat/mass transfer characteristics on turbine shroud with blade tip clearance, Annals of the New York Academy of Sciences 934 (1) (2001) 281–288.

[10] S. Krishnababu, P. Newton, W. Dawes, G. D. Lock, H. Hodson, J. Hannis, C. Whitney, Aerothermal investigations of tip leakage flow in axial flow turbinespart i: effect of tip geometry and tip clearance gap, Journal of Turbomachinery 131 (1) (2009) 011006.

[11] S. Krishnababu, W. Dawes, H. Hodson, G. D. Lock, J. Hannis, C. Whitney, Aerothermal investigations of tip leakage flow in axial flow turbinespart ii: Effect of relative casing motion, Journal of Turbomachinery 131 (1) (2009) 011007.

[12] J. Tallman, B. Lakshminarayana, Numerical simulation of tip leakage flows in axial flow turbines, with emphasis on flow physics: part iieffect of outer casing relative motion, Journal of Turbomachinery 123 (2) (2001) 324–333.

[13] J. D. Coull, N. R. Atkins, The influence of boundary conditions on tip leakage flow, Journal of Turbomachinery 137 (6) (2015) 061005.

[14] M. Dunn, Phase and time-resolved measurements of unsteady heat transfer and pressure in a full-stage rotating turbine, in: ASME 1989 International Gas Turbine and Aeroengine Congress and Exposition, American Society of Mechanical Engineers, 1989, pp. V004T08A014–V004T08A014.

[15] G. Guenette, A. Epstein, R. Norton, Y. Cao, Time resolved measurements of a turbine rotor stationary tip casing pressure and heat transfer field, in: 21st Joint Propulsion Conference, 1985, p. 1220.

[16] S. Thorpe, S. Yoshino, R. Ainsworth, N. Harvey, An investigation of the heat transfer and static pressure field on the over-tip casing of a shroudless transonic turbine rotor at engine representative flow conditions.(i). time-mean results, International Journal of Heat and Fluid Flow 25 (2004) 933–944.

[17] S. J. Thorpe, R. J. Miller, S. Yoshino, R. W. Ainsworth, N. W. Harvey, The effect of work processes on the casing heat transfer of a transonic turbine, Journal of Turbomachinery 129 (1) (2007) 84–91.

[18] H. Hodson, T. Hynes, E. Greitzer, C. Tan, A physical interpretation of stagnation pressure and enthalpy changes in unsteady flow, in: ASME Turbo Expo 2009: Power for Land, Sea, and Air, American Society of Mechanical Engineers, 2009, pp. 773–784.

[19] S. Thorpe, S. Yoshino, R. Ainsworth, N. Harvey, An investigation of the heat transfer and static pressure on the over-tip casing wall of an axial turbine operating at engine representative flow conditions.(ii). time-resolved results, International journal of heat and fluid flow 25 (6) (2004) 945–960.

[20] T. Hofer, T. Arts, Aerodynamic Investigation of the Tip Leakage Flow for Blades With Different Tip Squealer Geometries at Transonic Conditions, ASME Paper No. GT2009-59909, 2009. doi:10.1115/GT2009-59909.
URL http://dx.doi.org/10.1115/GT2009-59909

[21] F. J. G. Heyes, H. P. Hodson, G. M. Dailey, The Effect of Blade Tip Geometry on the Tip Leakage Flow in Axial Turbine Cascades, J. Turbomach 114 (3) (1992) 643–651. doi:10.1115/1.2929188.
URL http://dx.doi.org/10.1115/1.2929188

[22] V. Shyam, A. Ameri, Comparison of Various Supersonic Turbine Tip Designs to Minimize Aerodynamic Loss and Tip Heating (2011) 887–895doi:10.1115/GT2011-46390.
URL http://dx.doi.org/10.1115/GT2011-46390

[23] J. S. Kwak, J. Ahn, J.-C. Han, C. P. Lee, R. S. Bunker, R. Boyle, R. Gaugler, Heat Transfer Coefficients on the Squealer Tip and Near-Tip Regions of a Gas Turbine Blade With Single or Double Squealer, J. Turbomach 125 (4) (2003) 778–787. doi:10.1115/1.1626684.
URL http://dx.doi.org/10.1115/1.1626684

[24] Q. Zhang, L. He, Tip-Shaping for HP Turbine Blade Aerothermal Performance Management, J. Turbomach 135 (5) (2013) 051025. doi:10.1115/1.4007896.
URL http://dx.doi.org/10.1115/1.4007896

[25] C. De Maesschalck, S. Lavagnoli, G. Paniagua, T. Verstraete, R. Olive, P. Picot, Heterogeneous Optimization Strategies for Carved and Squealer-Like Turbine Blade Tips, J. Turbomach 138 (12) (2016) 121011. doi:10.1115/1.4033975.
URL http://dx.doi.org/10.1115/1.4033975

[26] V. Andreoli, S. Lavagnoli, G. Paniagua, V. Fernandez Villace, Robust model of a transient wind tunnel for off-design aerothermal testing of turbomachinery, Measurement 82 (2016) 323–333. doi:10.1016/j.measurement.2015.12.032.
URL http://www.sciencedirect.com/science/article/pii/S0263224115006922

[27] B. Cernat, M. Pátỳ, C. De Maesschalck, S. Lavagnoli, Experimental and numerical investigation of optimized blade tip shapes: Part iturbine rainbow rotor testing and cfd methods, in: ASME Turbo Expo 2018: Turbomachinery Technical Conference and Exposition, American Society of Mechanical Engineers, 2018, pp. V05BT13A012–V05BT13A012.

[28] C. Sieverding, T. Arts, The vki compression tube annular cascade facility ct3, in: ASME 1992 International Gas Turbine and Aeroengine Congress and Exposition, American Society of Mechanical Engineers, 1992, pp. V005T16A001–V005T16A001.

[29] C. De Maesschalck, S. Lavagnoli, G. Paniagua, Blade Tip Carving Effects on the Aerothermal Performance of a Transonic Turbine, J. Turbomach 137 (2) (2014) 021005. doi:10.1115/1.4028326.
URL http://dx.doi.org/10.1115/1.4028326

[30] V. Iliopoulou, R. Dnos, N. Billiard, T. Arts, Time-Averaged and Time-Resolved Heat Flux Measurements on a Turbine Stator Blade Using Two-Layered Thin-Film Gauges, J. Turbomach 126 (4) (2004) 570–577. doi:10.1115/1.1791647.
URL http://dx.doi.org/10.1115/1.1791647

[31] M. Collins, K. Chana, T. Povey, Improved methodologies for time-resolved heat transfer measurements, demonstrated on an unshrouded transonic turbine casing, Journal of Turbomachinery 138 (11) (2016) 111007.

[32] B. Cernat, M. Paty, C. De Maesschalck, S. Lavagnoli, Experimental and numerical investigation of optimized blade tip shapes part ii: Tip flow analysis and loss mechanisms, in: ASME Turbo Expo: Turbomachinery Technical Conference and Exposition, American Society of Mechanical Engineers, GT2018-76567 - 2018, pp. –.

[33] A. M. Anderson, R. J. Moffat, The adiabatic heat transfer coefficient and the superposition kernel function: Part 1data for arrays of flatpacks for different flow conditions, Journal of Electronic Packaging 114 (1) (1992) 14–21.

[34] V. Pinilla, J. Solano, G. Paniagua, R. Anthony, Adiabatic wall temperature evaluation in a high speed turbine, Journal of Heat Transfer 134 (9) (2012) 091601.

[35] V. KolÅ, Vortex identification: New requirements and limitations, International Journal of Heat and Fluid Flow 28 (4) (2007) 638–652. doi:10.1016/j.ijheatfluidflow.2007.03.004.
URL http://www.sciencedirect.com/science/article/pii/S0142727X07000343

[36] S. J. Thorpe, S. Yoshino, R. W. Ainsworth, N. W. Harvey, An investigation of the heat transfer and static pressure on the over-tip casing wall of an axial turbine operating at engine representative flow conditions. (II). Time-resolved results, International Journal of Heat and Fluid Flow 25 (6) (2004) 945–960. doi:10.1016/j.ijheatfluidflow.2004.02.028.
URL http://www.sciencedirect.com/science/article/pii/S0142727X04000414

[37] D. E. Metzger, Spot cooling and heating of surfaces with high velocity impinging air jets. part 1. slot jets on plane surfaces, Tech. rep., STANFORD UNIV CA DEPT OF MECHANICAL ENGINEERING (1962).

SHAPE OPTIMIZATION

Aero-Elastic Tailoring of Composite Turbomachinery Blades through Gradient-Based Optimization

Tom De Bruyn

Turbomachinery and Propulsion Department, von Karman Institute for Fluid Dynamics, Belgium, tom.de.bruyn@vki.ac.be

Supervisor: Tom Verstraete

Associate Professor, Turbomachinery and Propulsion Department, von Karman Institute for Fluid Dynamics, Belgium, tom.verstraete@vki.ac.be

Visiting Professor, Department of Flow, heat and combustion mechanics, Ghent University, Belgium, tjvrstra.verstraete@ugent.be

Abstract

In order to increase the efficiency of gas turbine engines, new designs feature very high by-pass ratio's and highly optimized fan geometries. Supporting this evolution, the von Karman Institute's turbo machinery optimization framework 'CADO' is extended to include the vibrational (flutter) constraints limiting the stable operating range and to optimize fiber distribution in composite blades.

Keywords: turbomachinery, aero-elasticity, composite tailoring, optimization

1. Introduction

Vibrational effects, be it self-induced (flutter) or forced response to an external periodic excitation (e.g. due to struts or adjacent blade rows), strongly affect the operating range and life time (through high-cycle fatigue) of turbomachinery components. Despite shape optimization gradually becoming commonplace in the aerodynamic design of these machines, so far little effort has been undertaken to include these constraints in the optimization process.

2. planned research

In order take the aforementioned effects into account, without incurring the high computational penalty of unsteady simulation, a harmonic method is used to derive a system of steady-flow-like equations [1]. At the base of these methods is the representation of the unsteadiness as set of disturbances with a fundamental frequency and corresponding Fourier series. Only a limited set of frequencies, reflecting the vibrational modes of the system and possible external excitations, must thus be considered, greatly reducing computational cost while still capturing the dominating vibrational effects.

This harmonic method is combined with the addition to CADO of fluid-structure interaction (FSI). To model the aero-alastic interaction, aerodynamic loads and blade deformations are exchanged between the solid and fluid domains.

Particularly promising in this context is the increasing use of composite vanes and blades. By changing the internal structure, their deformation response to static and dynamic loads can be tailored allowing for a greatly increased operating range[2]. Including this tailoring in the optimization process directly is a necessity to compute novel blade shapes combining high aerodynamic efficiency with increased flutter stability and operating range.

As fan blades are most prone to flutter but also offer the best outlook on improved fuel efficiency, they are the central focus of this research project.

References

[1] K. C. Hall, J.P. Thomas and W. Clark, Computation of Unsteady Nonlinear flows in Cascades Using a Harmonic Balance Technique, AIAA Journal 40 (5) (2002) 879–886.

[2] C. Reiber and M. Blocher, Potential of Aeroelastic Tailoring to Improve Flutter Stability of Turbomachinery Compressor Blades, in: Proceedings of 12th European Conference on Turbomachinery Fluid dynamics & Thermodynamics ETC12, Stockholm, 2017.

Multipoint Optimization of an Axial Turbine Cascade using a Hybrid Algorithm

Arnaud Châtel

Turbomachinery and Propulsion Department, von Karman Institute for Fluid Dynamics, Belgium, arnaud.chatel@vki.ac.be

Supervisor: Tom Verstraete

Associate Professor, Turbomachinery and Propulsion Department, von Karman Institute for Fluid Dynamics, Belgium, tom.verstraete@vki.ac.be

University Supervisor: Grégory Coussement

Professor, Fluids-Machines Unit, University of Mons, Belgium, gregory.coussement@umons.ac.be

Abstract

This paper presents a constrained multipoint optimization of the LS89 turbine cascade. The objective of the optimization consists in minimizing the entropy losses generated inside the cascade over a predefined operating range. The operating range is bounded by two operating points respectively characterized by a downstream isentropic Mach number of 0.9 and 1.01. During the optimization, two aerodynamic constraints are imposed in order to conserve the same performance as the original cascade. The optimization is performed using a hybrid algorithm which combines efficiently a classical evolutionary algorithm with a gradient-based method. The hybridization process between both methods is based on the Lamarckian approach which consists in incorporating directly the gradient method inside the loop of the evolutionary algorithm. First, the better performance of the proposed hybrid method compared to the performance of a classical evolutionary algorithm is demonstrated. Then, the methodology is applied on a turbomachinery application in order to minimize the losses in the LS89. The optimization process allows to find a new blade profile which reduces the entropy losses over the entire operating range by at least 9.5 %.

Keywords: aerodynamic optimization, hybrid algorithm, evolutionary algorithm, gradient-based method, turbine cascade

1. Introduction

Nowadays, the design of turbomachinery components makes extensive use of optimization methods as they have proven to significantly improve the product quality. Accordingly, they are increasingly used for more elaborate and complex problems. Especially a trend to richer design spaces, propelled by significant advances in production techniques, requires optimization algorithms to work in and explore larger design spaces. Due to the so-called curse of dimensionality [12], these design tasks can be time consuming and require large computational resources. Therefore, it is currently essential to improve the methodology and the performance of optimization processes themselves.

Several techniques are currently used in numerical optimization and they can be distinguished depending on the order of the derivative of the objective function needed during the optimization process [23]. The zero order methods, also called gradient-free, use only the value of the objective function while gradient-based methods require additionally the gradients of the objective function with respect to the design parameters [24]. These two families of optimization algorithms have their respective advantages and drawbacks. First, the gradient-free methods generally used in the field of aerodynamic shape optimization are evolutionary algorithms, which tend

to mimic the biological evolution process described by Darwin. This kind of algorithms uses a population of individuals which evolves over the search space during the optimization through different mechanisms (e.g. mutation, crossover, selection). These methods allow to globally explore the design space and enable to identify the region where the global minimum is located. However, the major weakness of evolutionary algorithms lies in their poor convergence performance as the exact localization of the global minimum can require many iterations especially in large design spaces. The second family of optimization algorithms use the gradients of the objective function in order to concentrate the optimum search in a certain direction [11]. These methods are well-known to be less affected by the curse of dimensionality and tend to converge more rapidly. However, they only perform a local exploration of the design space and are prone to be trapped in local optima.

In this context, coupling an evolutionary algorithm and a gradient-based method can be an effective way in order to overcome their respective limitations. Indeed, hybrid algorithms which combine both methods benefit from their respective strengths; namely the global exploration capacity of the evolutionary algorithms and the fast convergence of the gradient-based methods. Several hybrid approaches combining both methods have already been developed in order to address discrete and continuous optimization problems and reference [7] presents a review of different hybridization methods. The hybridization approach commonly used for continuous optimizations is based on the Lamarckian evolution [29; 6; 7; 8], which directly incorporates the gradient-based method inside the loop of the evolutionary algorithm. This approach has already been applied on aerodynamic shape optimization of external flows [25; 26; 27; 28]. Moreover, this kind of hybrid algorithms has also been used in order to optimize the shape of a turbine cascade in [20]. The hybrid algorithm proposed in this work efficiently combines the Differential Evolution [4] and the steepest descent method [10; 11].

In the present work, we propose to improve the performance of the hybrid optimization algorithm described in [20]. The updated algorithm is then used in order to optimize the geometry of a turbine cascade. The objective of the shape optimization is to minimize the entropy generated in the cascade over a certain operating range while maintaining the performance of the baseline cascade.

This paper is structured as follows: in the first section the proposed hybrid algorithm is described and validated on two benchmark problems specially designed to assess the performance of the optimization methods. The second section presents the multipoint constrained optimization and the results obtained with the hybrid algorithm. In the last section, the optimized and baseline cascades are compared in order to understand the mechanisms behind the improved performance.

2. Hybrid optimization algorithm

The hybrid optimization algorithm used in this work combines a gradient-free method and a gradient-based method in order to benefit from their respective strength. The gradient-free method allows to explore the complete design space while the gradient-based algorithm is used to improve the most promising designs in order to accelerate the convergence of the evolutionary algorithm. The proposed methodology combines a classical Differential Evolution algorithm [4] as gradient-free method and the steepest descent method [10; 11]. The hybridization process between these two methods is illustrated in Fig. 1 and the basic principle of the hybrid algorithm is extensively described in [20].

The hybrid algorithm presented in [20] has been slightly modified in order to improve its convergence performance. In the method described in [20], at each iteration of the DE algorithm, the most promising individuals newly generated by the reproduction process are chosen to be locally improved by only one iteration of the steepest descent. As demonstrated on benchmark problems in the cited paper, the local improvements performed with the gradient-based method allow to significantly accelerate the convergence of the gradient-free method. However, in order to still improve the performance of the method, two modifications of the hybrid algorithm have been implemented. First, additionally to the most promising individuals generated by the last reproduction process, the best design obtained during the previous iterations of the algorithm is also selected for a gradient optimization. Therefore, if the best individuals remains the same during some iterations of the hybrid method, it will be locally improved several times by the gradient optimizer. This individual can be even optimized until the gradient method converges to an

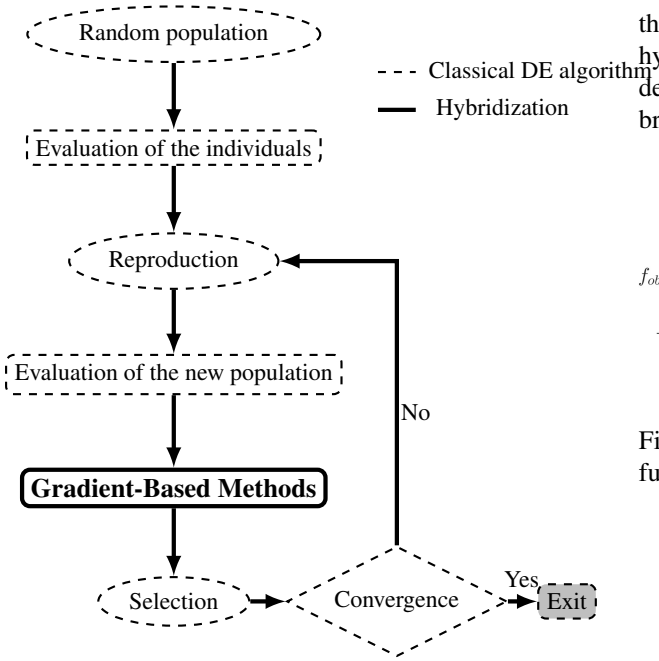

Figure 1: Hybrid Algorithm combining the DE algorithm and the steepest descent method.

optimum which could be just local. Since the individual has been improved several times by the gradient algorithm, the localization of a more global optimum can take many iterations of the hybrid method. In order to limit the risk of being trapped in this local optimum during many iterations, a second change has been made to the initial hybrid method. The number of gradient-based iterations is not fixed anymore and is dynamically increased when the best design remains the same during a certain number of generations. In the following section, the performance of the new hybrid algorithm is assessed on two analytical functions.

2.1. *Validation on analytical functions*

In this section, the proposed hybrid algorithm is tested on the Rastrigin and Rosenbrock functions respectively expressed by Eqs. 1 and 2 [19]. These two functions, presented in Fig. 2, are benchmark problems specifically designed to assess optimization methods. Indeed, as can be seen in Fig. 2, the Rastrigin function is highly multimodal, which makes the localization of the global minimum really challenging. In contrast, the Rosenbrock is unimodal, however the only minimum is located inside a flat valley, which deteriorates the performance of optimization methods. The value of both functions at the global minimum is equal to zero. The proposed hybrid method is tested on the Rastrigin function described by 5 and 10 parameters and on the Rosenbrock function computed with 2 and 10 parameters.

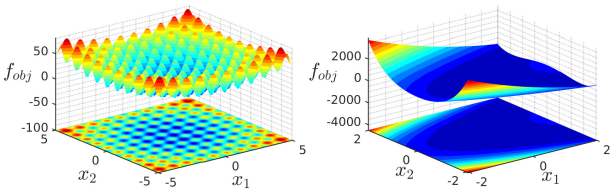

Figure 2: Rastrigin function (left) and Rosenbrock function (right) defined 2 parameters [19]

$$f_{Rastrigin} = 10 + \sum_{i=1}^{N_{Param}} [x_i^2 - 10 \times cos(2\pi x_i)] \quad (1)$$

$$f_{Rosenbrock} = \sum_{i=1}^{N_{Param}-1} [100 \times (x_{i+1} - x_i^2)^2 + (1 - x_i)^2] \quad (2)$$

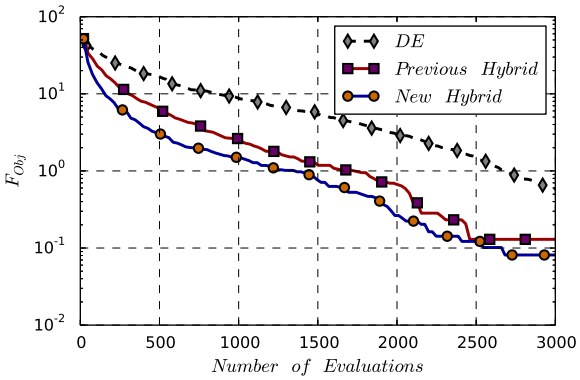

Figure 3: Comparison of the convergence performance of the DE algorithm and the hybrid methods in terms of number of evaluations for the Rastrigin function defined with 5 parameters.

Figures 3, 4, 5 and 6 compare the convergence rate of the proposed method with the performance of the DE algorithm and with the performance of the hybrid method described in [20] for the two analytical functions. Since in engineering optimization the evaluation of an objective involves generally complex and advanced computation methods (e.g. CFD, FEM), the performance of the optimization methods

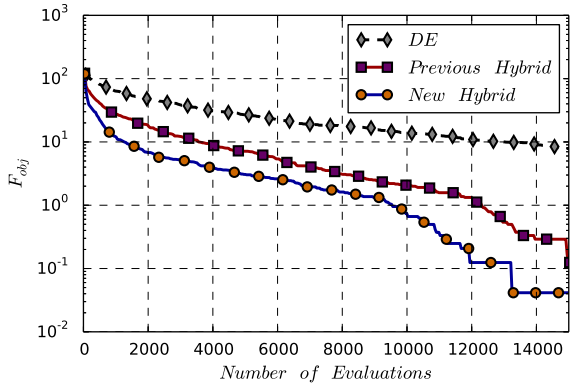

Figure 4: Comparison of the convergence performance of the DE algorithm and the hybrid methods in terms of number of evaluations for the Rastrigin function defined with 10 parameters.

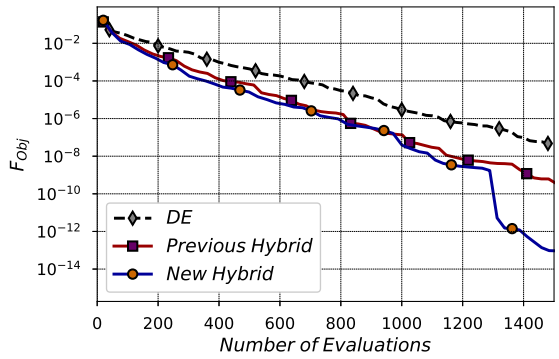

Figure 5: Comparison of the convergence performance of the DE algorithm and the hybrid methods in terms of number of evaluations for the Rosenbrock function defined with 2 parameters.

are assessed in terms of the number of evaluations needed to locate the global minimum. Indeed, in aerodynamic optimization where CFD is used, the reduction of the number of evaluations is essential in order to reduce the global computational cost of the complete optimization process. Moreover, in the hybrid methods, the gradients of the objective function with respect to the design variables have to be computed for certain individuals which are locally improved by the gradient method. The gradient can be computed at a similar computational cost as the evaluation of the objective function using an adjoint solver [9]. Therefore, a gradient computation is represented with one evaluation unit which represents the computational cost of the objective function.

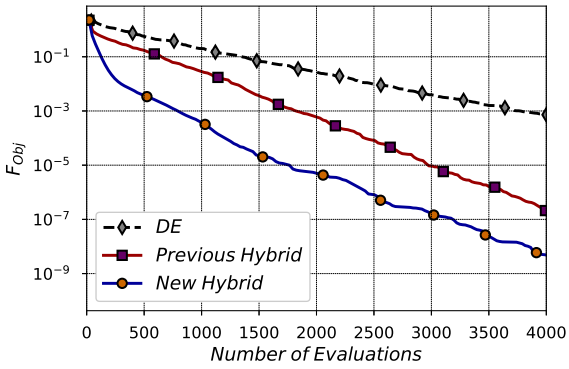

Figure 6: Comparison of the convergence performance of the DE algorithm and the hybrid methods in terms of number of evaluations for the Rosenbrock function defined with 10 parameters.

Figures 3, 4, 5 and 6 demonstrate that the improvements implemented in the hybrid method allow to accelerate the convergence towards the global minimum and that the computational cost of the optimizations is reduced. Moreover, as shown when comparing the results for different number of design variables, the benefit of the new method is larger when the number of parameters increases. Therefore the improved algorithm can be used in order to explore larger design spaces.

3. LS89 Optimization

The proposed optimization algorithm is used in order to optimize the geometry of the well known LS89 turbine cascade. The cascade is made of highly loaded blades characterized by a flow turning of approximately 75°[5]. The objective of the shape optimization presented in the paper consists in minimizing the losses generated in the cascade.

During the optimization process, the evaluation of the objective and the computation of the gradients are performed using a complete process chain of tools developed at the von Karman Institute. The chain of tools is illustrated in Fig. 7. First, the geometry of the cascade is constructed using the value of the optimization parameters. The full parametrization methodology is illustrated in Fig. 8 and is extensively presented in [20; 17]. In order to generate the turbine geometry, a blade camber line is defined with a second order

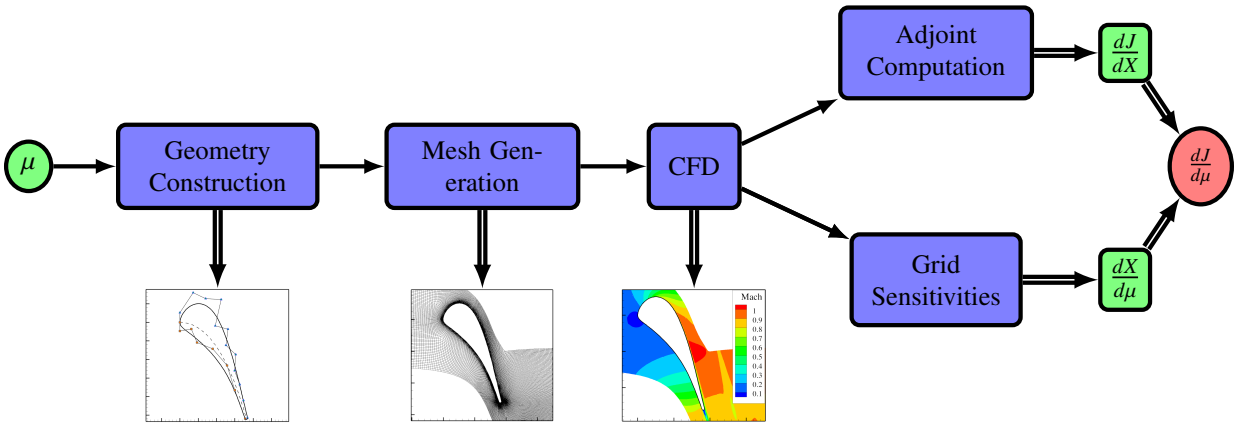

Figure 7: Evaluation of the performance parameters

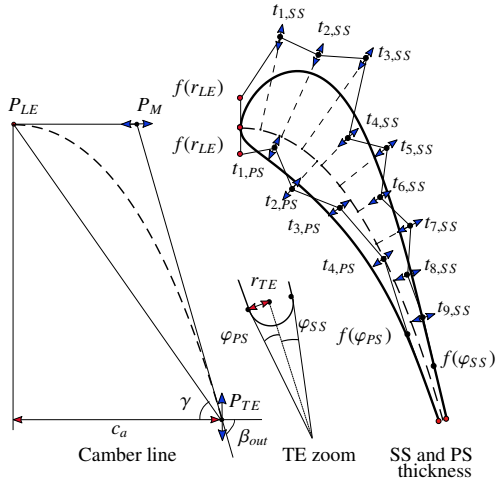

Figure 8: Parametrization of the axial turbine cascade

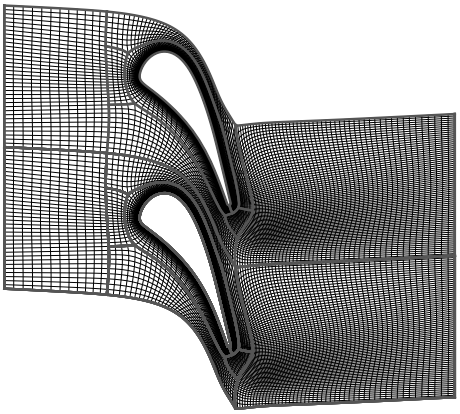

Figure 9: Structured mesh automatically generated during the optimization process(coarsened for visualization)

Bézier curve represented in the left part of Fig. 8. The three control points P_{LE}, P_M and P_{TE} are obtained using the axial chord c_a, the stagger angle γ and the outlet metal angle β_{out}. Then, the blade PS and SS are constructed separately with B-Splines curves. As presented in the right part of Fig. 8, the control points of the PS and SS B-Splines are located in a direction normal to the camber line at a distance t_i. At the LE, the first control points of the SS and PS are located in order to ensure a G2 continuity between the two curves. The exact position of these points is computed using the radius of curvature r_{LE}. At the TE, the last controls points of the SS and PS are localized using the two angles φ_{PS} and φ_{SS}. At the trailing edge, the profile of the blades is closed using a circular arc defined with the radius of the TE r_{TE}. Finally the linear cascade is constructed by imposing the solidity σ of the blades which allows to compute the pitch between two successive blades. During the optimization process, the axial chord is maintained in order to preserve the axial dimension of the original cascade and the TE radius is fixed for manufacturing purposes. Therefore, 19 geometric parameters μ are used during the optimization and they are listed in Table 1.

Then, as a second step of the evaluation chain, a structured mesh represented in Fig. 9 is automatically generated using one O-grid block and 6 H-grid blocks [1]. In order to evaluate the objective function, the RANS equations are numerically solved using the Spalart-Allmaras turbulence model. The numerical simulations are performed with the in-house CFD solver detailed in [18]. If the gradients of the performance parameters (objective function or con-

Table 1: Parameters used in the optimization

Index	Symbol	Index	Symbol	Index	Symbol
1	γ	8	$t_{6,SS}$	14	$t_{4,PS}$
2	β_{out}	9	$t_{7,SS}$	16	r_{LE}
3	$t_{1,SS}$	10	$t_{8,SS}$	17	φ_{SS}
4	$t_{2,SS}$	11	$t_{9,SS}$	18	φ_{PS}
5	$t_{3,SS}$	12	$t_{1,PS}$	19	σ
6	$t_{4,SS}$	13	$t_{2,PS}$		
7	$t_{5,SS}$	14	$t_{3,PS}$		

straints) J with respect to the design variables μ are needed, they are computed using the following relation:

$$\frac{dJ}{d\mu} = \frac{dJ}{dX}\frac{dX}{d\mu}. \tag{3}$$

Where:

- $\frac{dJ}{dX}$ represents the derivative of the performance parameters J with respect to the grid coordinates X. This first term is computed using the discrete adjoint solver extensively described and validated in [18].

- $\frac{dX}{d\mu}$ represents the derivative of the grid coordinates X with respect to the design variables μ. In order to compute this second term the in-house mesh generator has been differentiated using the AD tool called ADOL-C [22].

References [2; 1] provide a detailed description of the complete methodology and a validation of the gradients computed in the case of the LS89 application. The next section presents the results of the optimization of the same cascade performed with single operating point and the drawbacks of the profiles thus obtained at off-design conditions.

3.1. Single-Point optimization

In [20], a single-point optimization of the LS89 cascade is presented at an operating point characterized by a downstream isentropic Mach number of 0.9. The objective of the optimization was to minimize the entropy generated in the cascade while maintaining at least the flow turning of the original blades. The optimized cascade presented in the cited paper allows to reduce the entropy losses by a factor of 21% compared to the baseline. Table 2 summarizes the results of the single-point optimization compared to the LS89 original design.

Table 2: Results of the single-point optimization

		LS89	Opt	Variation
Entropy Production	$[\frac{Pa}{\frac{kg}{m^3}}]$	826.7	731	-21.3 %
Outlet flow angle	[°]	74.89	74.89	+0 %
Mass-flow	[kg/s]	0.008	0.011	+37.5 %

The flow in the optimized and LS89 cascades has been simulated using the CFD solver for off-design conditions defined in terms of outlet isentropic Mach number $M_{isen,2}$. The evolution of the total pressure losses generated in both cascades on the operating range are summarized in Fig. 10. The figure illustrates that, while for the considered downstream Mach number in the optimization the losses are strongly reduced, for higher outlet isentropic Mach number the losses significantly exceed the ones of the LS89. For this reason, the next section presents a multipoint hybrid optimization of the cascade performed in order to minimize the losses over the entire operating range comprised between $M_{isen,2} = 0.9$ and $M_{isen,2} = 1.01$.

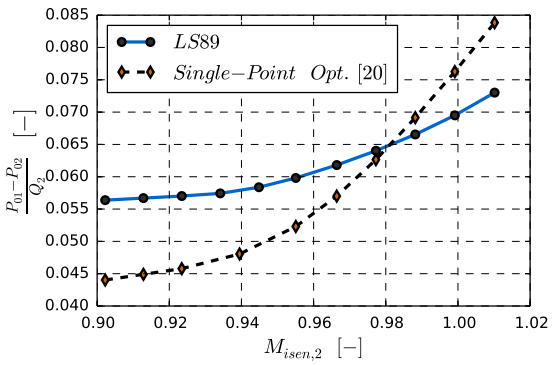

Figure 10: Evolution of the total pressure losses for different operating points in the LS89 cascade and in the cascade optimized for a single operating point.

3.2. Multi-Point optimization

The objective of the multipoint optimization is to minimize the entropy generated in three different operating points OP1, OP2 and OP3 characterized respectively by $M_{isen,2} = 0.9$, $M_{isen,2} = 0.955$ and $M_{isen,2} = 1.01$. The conditions at the inlet and at the

outlet of the computational domain for the different operating points are summarized in Table 3.

Table 3: Definition of the three operating point conditions

		OP1	OP2	OP3
Inlet	P_0	147 500 Pa	147 500 Pa	147 500 Pa
	T_0	420 °K	420 °K	420 °K
	α_{in}	0 °	0 °	0 °
Outlet	P	87 000 Pa	82 050 Pa	77 000 Pa

The constrained multipoint optimization can be expressed as follows:

Minimize:

$$\overline{J_{obj}} = \frac{1}{3} \times (J_{obj,OP1} + J_{obj,OP2} + J_{obj,OP3}) \quad (4)$$

with,

$$J_{obj} = S_2 - S_1 \quad (5)$$

Subject to:

$$J_{cstr,1} = \frac{\alpha_{2,OP3}}{\alpha_{2,OP3,ref}} \geq 1 \quad (6)$$

$$J_{cstr,2} = \frac{\dot{m}_{2,OP3}}{\dot{m}_{2,OP3,ref}} - 1 \leq 0.001. \quad (7)$$

The objective function (4) is a weighted sum of the entropy generated in the cascade for the three operating points. The entropy generated in the cascade J is computed with the mass-flow averaged entropy at the inlet and outlet of the computational domain S_1 and S_2. The first constraint (6) on the outlet flow angle is imposed in order to achieve at least the same flow turning than the original blades. The imposition of this constraint is essential, otherwise the optimization would reduce the entropy generation by unloading the blades. As shown in Table 2, the single-point optimization of the LS89 leads to a large increase of the mass-flow per passage (+37.5 %) in the optimized cascade. In order to avoid such an increase of the mass-flow, a second aerodynamic constraint (7) is applied on the mass-flow. The constraint imposes that the mass-flow per passage in the optimized cascade is at most the same than in the baseline taking into account a tolerance of 0.1 %. Since during the gradient-based optimizations the gradients of the aerodynamic constraints are required, the constraints are computed only at the OP3 which allows to limit the computational effort when computing the gradient values. The aerodynamic constraints are imposed in the last OP of the operating range because it represents the point where the constraints satisfaction is the most challenging. In the hybrid method, these non-linear constraints are efficiently handled by means of the projected gradient method [20]. The next section presents the results of the multipoint optimization.

3.3. Results of the optimization

Figures 11, 12 and 13 present the history of the hybrid optimization respectively in terms of objective function, outlet flow angle constraint and mass-flow constraint. These figures represent the performance of the best individual at each iteration of the hybrid optimization. The red areas depicted in the plots are the zones where the aerodynamic constraints are not satisfied. As can be visualized in the different figures, the hybrid optimization is trapped in a local minimum between the iterations 9 and 25. Indeed, no further improvement of the best individual is feasible with the gradient-based method during this period. Due to the combination of the global exploration capacity and the local refinements, the hybrid optimizer could get out of this local minimum and could find new promising areas of the design space to explore. Moreover, it can be noticed in Fig. 11 that the largest reduction of the losses appears in the third operating point characterized by the higher downstream isentropic Mach number (OP3). Finally, the optimized design presented in the next section of the paper is obtained at the iteration 54.

The total pressure losses generated in the optimized cascade on the complete operating range have been computed and compared, in Fig. 14, to the losses generated in the LS89 and in the cascade previously optimized in [20] for a single operating point. First it can be seen that the losses are higher in the operating range comprises between $M_{isen,2} = 0.9$ and $M_{isen,2} = 0.95$ compared to the losses obtained in the cascade previously optimized for the operating point OP1. However, in the newly optimized cascade the losses are reduced over the complete operating range. On the opposite to the behaviour of the *Single-Point Opt.* curve, the curve describing the evolution of the losses in the newly optimized turbine demonstrates that the reduction of the losses is larger when the outlet Mach number increases.

Table 4 summarizes the variations of the flow quantities obtained in the new design of the cascade with respect to the same quantities computed in the LS89. The constraint on the outlet flow angle is respected and the flow turning generated by the blades has been slightly increased (+1.3%) for the three operating points. The constraint imposed on the mass-flow is just active for OP3. The second constraint is handled with high accuracy because of the projected gradient method implemented in the gradient-based method. This method, extensively described in [20], allows to modify a design such that a non-linear constraint is just satisfied. In the hybrid method, this is used only if a design does not respect a constraint during the local improvement performed with the gradient-based method.

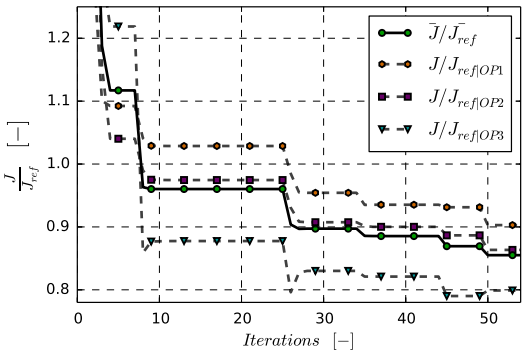

Figure 11: Evolution of the objective function for the different operating points during the hybrid optimization

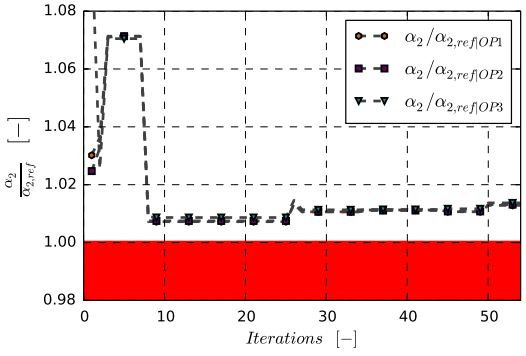

Figure 12: Evolution of the outlet flow angle for the different operating points during the hybrid optimization

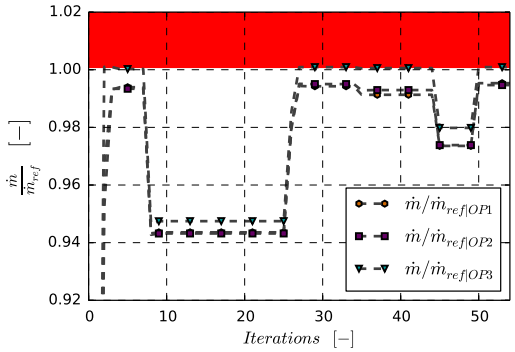

Figure 13: Evolution of the massflow for the different operating points during the hybrid optimization

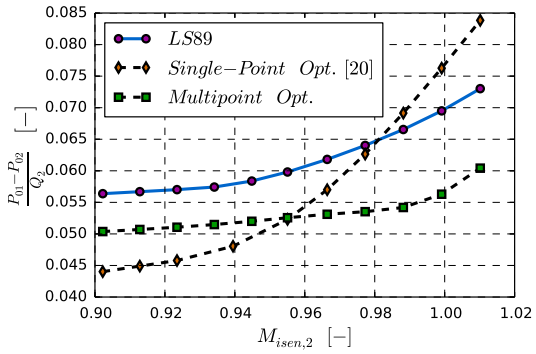

Figure 14: Evolution of the total pressure losses for different operating points

4. Comparison of the profiles

This section compares the newly optimized and the LS89 cascades in terms of geometry, isentropic Mach number distribution, total pressure loss coefficient, boundary layers, base pressure and shock losses.

Geometries of the cascades:. The profiles of the two cascades are compared in Fig. 15. As shown in the left plot, the pitch between the blades has been slightly

Table 4: Results of the multipoint optimization

	OP1	OP2	OP3
Entropy Production	-9.5%	-13.5%	-20.7%
Outlet flow angle	+1.3%	+1.3%	+1.4%
Mass-flow	-0.5%	-0.5%	+0.1%
Total Pressure losses	-10.6%	-12.1%	-17.3%

increased from 0.057 to 0.061. Since the chords of the two different profiles are approximately the same, the blade solidity has been decreased from 1.12 to 1.03. The major difference between the two blade profiles lies in the curvature of the suction and pressure sides. The curvatures of the suction side of both profiles are compared in Fig. 16.

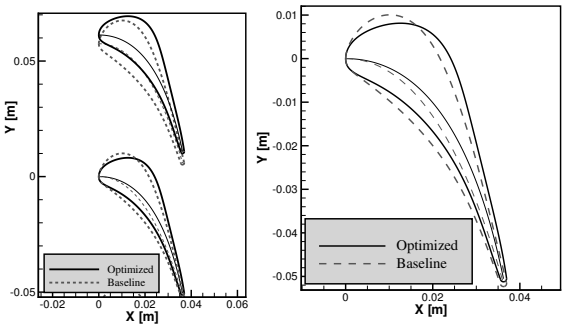

Figure 15: Comparison of the LS89 (baseline) and optimized cascade. Left: Comparison of the cascade geometries. Right: Comparison of the blade profiles

Isentropic Mach number and loading:. Figure 16 compares the evolutions of the isentropic Mach number measured along the suction and pressure sides of both blade profiles. Since the curvature of the optimized suction side has been largely modified, the distributions of the loading in both cascades are very different. As is illustrated in Fig. 16, the loading is more shifted to the rear part of the blades compared to the LS89 profiles. From the comparison of the suction side curvatures presented in the same figure, four regions can be identified:

- From $X = 0m$ to $X = 0.004m$: In the first part of the suction side, the curvature of the optimized blades is larger and therefore the aerodynamic loading has increased in this small region.

- From $X = 0.004m$ to $X = 0.016m$: In this second region, the curvature of the suction side has been significantly reduced compared to the LS89 blades. This reduction leads to a strong reduction of the loading in this part of the blades.

- From $X = 0.016m$ to $X = 0.028m$: Then, the curvature of the optimized suction side becomes larger resulting in a steep increase of the flow turning in this region. Due to the steep acceleration of the flow, a larger supersonic region appears on the suction side of the optimized blades compared to the supersonic pocket attached to the LS89 blades.

- From $X = 0.028m$ to $X = 0.037m$: Finally in this last part, the curvature of the optimized blade and consequently the loading of the blades are slightly reduced as compared to the baseline.

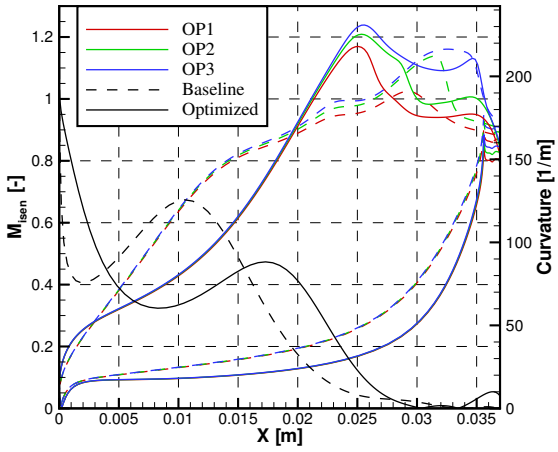

Figure 16: Comparison of the isentropic Mach number distribution along the optimized and baseline cascades and comparison of the curvature of the suction sides (black lines)

Entropy generation and total pressure loss coefficient:. The entropy generations in both cascades are compared for the three OP in Figs. 17, 18 and 19. Since the losses can be quantified using the total pressure loss coefficient, Fig. 20 compares the evolution of this coefficient in a plane downstream (located at $X = 1.5 \times c_a$) of the optimized and LS89 blades for the three different operating points. It can be seen from the plots that the total pressure losses increase from OP1 to OP3 in the wake regions downstream of both cascades, as expected. However, the comparisons between the losses downstream of the cascades demonstrate that the losses are reduced in the wake regions of the optimized cascade for all the operating points.

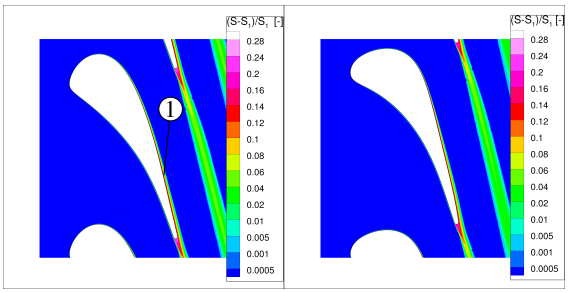

Figure 17: Comparison of the entropy generation in the optimized (right) and baseline (left) cascades at the OP1

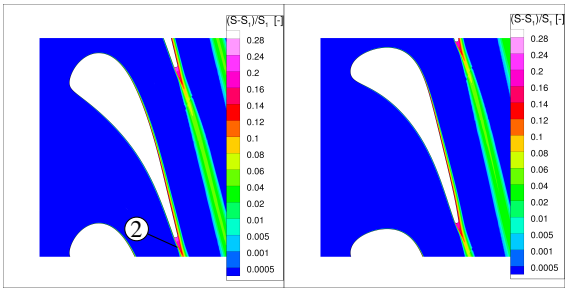

Figure 18: Comparison of the entropy generation in the optimized (right) and baseline (left) cascades at the OP2

Profile Losses:. In turbine cascades, two major terms contribute to the global profile losses: the boundary layer losses and the entropy generated in the trailing region of the blades [16]. The generation of losses in the boundary layers is illustrated by the ① in Fig. 17 while the entropy generated in the TE regions is pointed by the ② in Fig. 18. Figure 21 illustrates the boundary layer profiles measured along the suction side of the LS89 and optimized blades just before the trailing edge. As can be seen in the figures, the boundary layers obtained along the two profiles are very similar for all the operating conditions. The profile losses generated inside the boundary layers of the two cascades can be then considered as comparable to slightly worse. Therefore, the reduction of the entropy generation computed in the optimized cascade does not come from the boundary layer term.

At transonic operating conditions, Xu and Denton conclude in [15] that approximately 70% of the losses are generated downstream of the turbine blades. The losses are created, in the trailing edge region, by the mixing process between the boundary

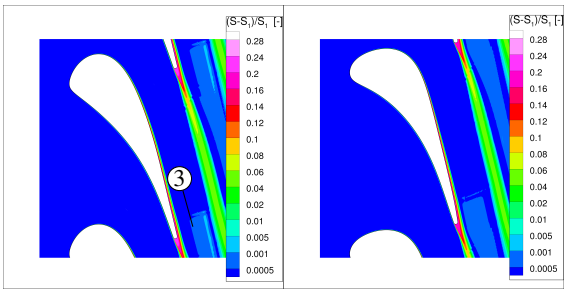

Figure 19: Comparison of the entropy generation in the optimized (right) and baseline (left) cascades at the OP3

layers coming simultaneously from the suction and pressure sides. The process has already been studied in numerous papers [15; 13; 14] and it has been shown that the dissipation occurring in this region is usually linked to the static pressure measured at the trailing edge of the blades, also called base pressure. Indeed, high base pressure values are well-known to be characteristic of low entropy generation in the trailing region. Figure 22 compares the base pressures obtained by RANS simulations along the trailing edges of the LS89 and optimized blades for the three different operating points. First, it can be noticed that the base pressure decreases from OP1 to OP3 for both cascades which means that more losses are generated downstream of the turbines when the downstream isentropic Mach number increases. This allows to explain why the total pressure loss coefficient increases in the wake region of both cascades when passing from OP1 to OP3 (Fig.20). Then, it can be clearly seen in Fig. 22 that the base pressures are smaller (-6%) along the trailing edges of the optimized blade profiles. Therefore, it can be concluded that the decrease of entropy generation measured in the optimized cascade is partly due to a the reduction of the mixing losses produced in the trailing region of the blades.

However, the base pressures presented in the figures are computed by solving the steady state RANS equations while the vortex shedding process is inherently unsteady and therefore the results can be inaccurate. Therefore, a validation of the optimization results by means of more advance CFD methods (e.g URANS, LES) or by experiments is still needed.

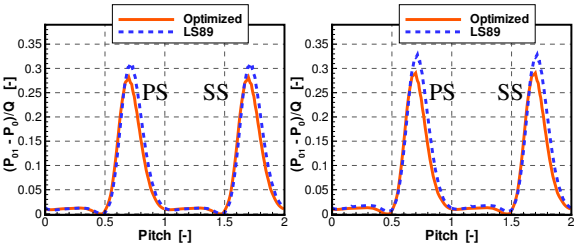

(a) OP1 (b) OP2

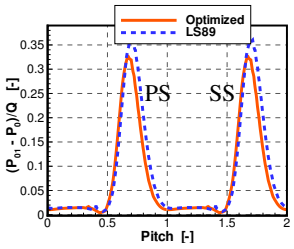

(c) OP3

Figure 20: Total pressure loss coefficient in a plane downstream of the blades ($\frac{X}{c_a} = 1.5$) for the three operating points

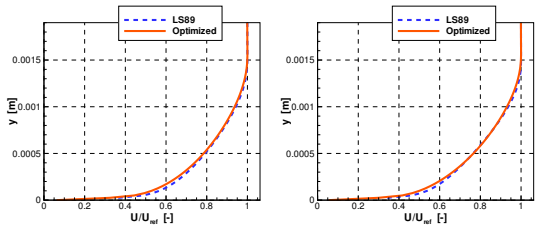

(a) OP1 (b) OP2

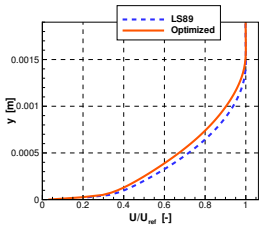

(c) OP3

Figure 21: Comparisons of the boundary layer profiles at 0.97 of the suction sides for the baseline and the optimized cascade

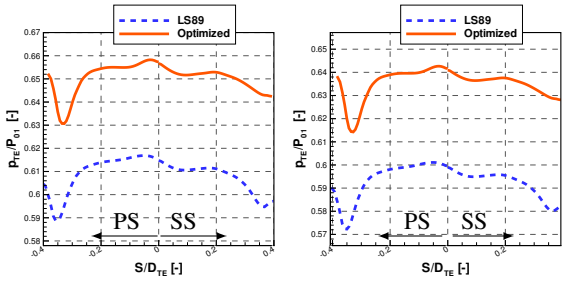

(a) OP1 (b) OP2

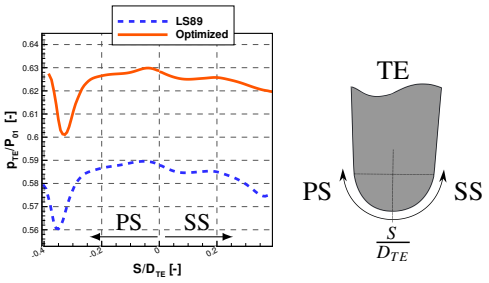

(c) OP3

Figure 22: Comparisons of the base pressure obtained along the trailing edge for the three operating points

Shock Losses:. In transonic cascades, another source of losses comes from the entropy generated in the shock waves [16]. The entropy generated by the shock wave is illustrated by the ③ in Fig. 19. Figure 23 compares the evolution of the total pressure loss coefficient in the passage between two successive blades and measured in the plane $X = 1.5 \times c_a$. These plots allow to visualize the losses generated in a passage, which are mainly dominated by the shock losses. Moreover the Mach number distributions in both turbines cascades are compared for the three operating points in Figs. 24, 25 and 26. As can be seen in Fig. 24, there are no shock waves in the turbines for the low Mach number case (OP1), therefore the passage losses are similar. For the other operating conditions, when the Mach number increases, shock waves appear on the suction-side of both turbines and can be distinguished in Figs. 25 and 26. The comparison presented in Fig. 23 demonstrates that the passage losses are smaller in the optimized turbine. This is due to the optimized curvature of the suction-side, which causes a large deceleration of the flow in the supersonic pocket before the normal shock. This deceleration of the flow can be clearly observed in Figs. 25 and 26. Therefore, the intensity of the normal shocks is weaker in the optimized cascade, resulting in lower passage losses. This allows to explain the larger reduction of the losses at the OP2 (-13.5 %) and the OP3 (-20.7 %). Indeed, at low Mach number (OP1), only the dissipation process occurring in the trailing

regions of the blades is reduced. On the contrary, for OP2 and OP3, the generation of entropy is reduced in the trailing edge regions but also in the passage between two successive blades.

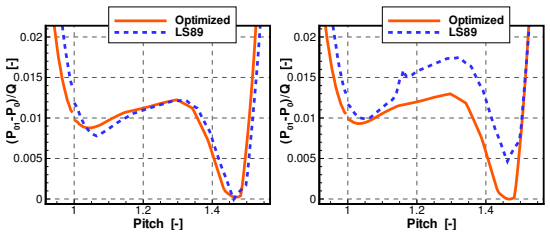

(a) OP1 (b) OP2

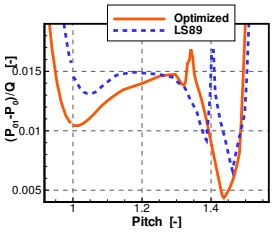

(c) OP3

Figure 23: Comparisons of the total pressure losses in the passage for the three operating points

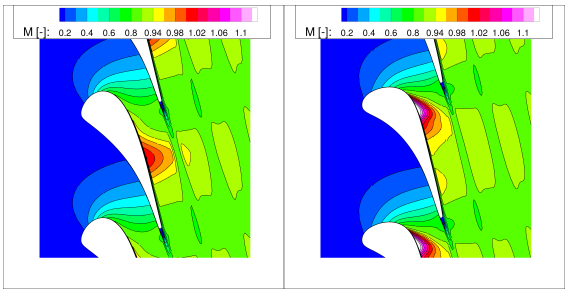

Figure 24: Comparison of the Mach number distributions in the optimized (right) and baseline (left) cascades at the OP1

Conclusions

This paper presents a constrained multipoint optimization of the LS89 turbine cascade. The optimization is performed using a hybrid algorithm which combines a classical evolutionary algorithm and a gradient-based method. The hybridization process between the two methods is based on the Lamarckian evolution and was extensively presented in a previous paper [20]. In this optimization method, the

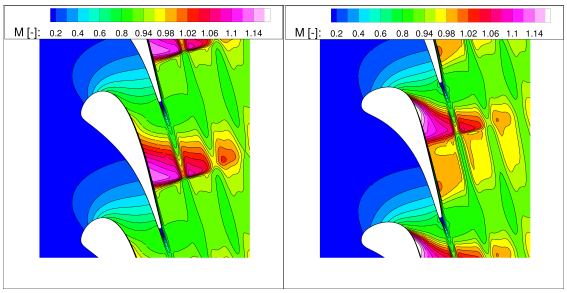

Figure 25: Comparison of the Mach number distributions in the optimized (right) and baseline (left) cascades at the OP2

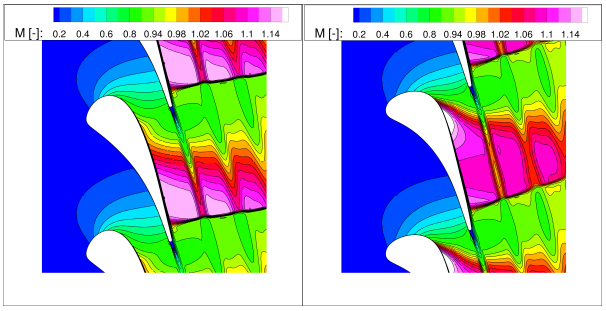

Figure 26: Comparison of the Mach number distributions in the optimized (right) and baseline (left) cascades at the OP3

evolutionary algorithm allows to globally explore the design space while the gradient searches accelerate the convergence of the gradient-free method. In the present paper, the hybrid method described in [20] has been modified in order to improve its convergence performance.

In the first part of the paper, the effectiveness of the proposed method is demonstrated on two benchmark problems especially designed to assess the performance of optimization algorithms. Then, the algorithm is used in order to optimize the shape of an axial turbine cascade. The objective of the optimization consists in minimizing the entropy losses generated in three operating points OP1, OP2 and OP3 respectively characterized by a downstream isentropic Mach number of 0.9, 0.95 and 1.01. During the optimization process, two aerodynamic constraints are imposed on the outlet flow angle and on the mass-flow in order to conserve the performance of the original turbine cascade.

The optimization results in a new design of the turbine blades which allows to reduce the entropy losses on the entire operating range by at least 9.5%. Moreover,

in the optimized turbine, the reduction of the losses increases over the operating range from OP1 (-9.5%) to OP3 (-20.7%). The major differences between the baseline cascade and the optimized lie in the curvatures of the suction and pressure sides which modify significantly the distribution of the aerodynamic loading along the blades. On all the operating range, the comparison of the flows in both cascades demonstrates that the decrease of the losses measured in the optimized turbine is partly due to a reduction of the entropy generated in the trailing edge region downstream of the blades. At higher Mach numbers, additionally to this improvement, the shock losses generated in the passage also decrease, which allows to explain the larger reduction of the entropy in this part of the operating range.

Acknowledgments

This work has been performed in the context of the MOTOR project (http://motor-project.eu/) funded by the European Union Horizon 2020 Framework Programme for Research and Innovation under Grant Agreement No. 678727. Therefore, the authors would like to thanks the European Union for funding the MOTOR project.

References

[1] I. S. Torreguitart, T. Verstraete, L. Mueller, Optimization of the ls89 axial turbine profile using a cad and adjoint based aproach, in: 12th European Conference on Turbomachinery Fluid dynamics & Thermodynamics, Stockholm, Sweden, 2017.

[2] I. S. Torreguitart, T. Verstraete, L. Mueller, Cad kernel and grid generation algorithmic differentiation for turbomachinery adjoint optimization, in: 7th European Congress on Computational Methods and Applied Sciences and Engineering, Hersonissos, Crete, Greece, 2016.

[3] T. Verstraete, Cado: A computer aided design and optimization tool for turbomachinery applications, in: 2nd Conf. On Engineering Optimization, Lisbon, Portugal, 2010.

[4] K. Price, N. Storn, Differential evolution, in: Dr. Dobb's Journal, Vol. 16, 1997, pp. 18–24.

[5] T. Arts, M. L. de Rouvroit, A. Rutherfort, Aero-thermal investigation of a highly loaded transonic linear turbine guide vane cascade. a test case for inviscid and viscous flow computations., Tech. Rep. 174, von Karman Institute for Fluid Dynamics (September 1990).

[6] W. E. Hart, N. Krasnogor, J. E. Smith, Recent Advances in Memetic Algorithms, Springer, 2005.

[7] T. El-Mihoub, A. Hopgood, L. Nolle, A. Battersby, Hybrid genetic algorithms: A review, in: Engineering Letters, 13:2, 2006.

[8] V. Kelner, F. Capitanescu, O. L. eonard, L. Wehenkel, A hybrid optimization technique coupling an evolutionary and a local search algorithm, Journal of Computational and Applied Mathematics (215) (2008) 448–456.

[9] A. Jameson, Aerodyninamic design via control theory, Journal of Scientific Computing 3 (1988) 233–260.

[10] G. Vanderplaats, Numerical Optimization Techniques for Enginnering Design, McGraw-Hill, New-York, 1984.

[11] J. Nocedal, S.J.Wright, Numerical Optimization, Springer, 2006.

[12] S. Chen, J. Montgomery, Measuring the curse of dimensionality and its effects on particle swarn optimization and differential evolution, Applied Intelligence 42 (2015) 514–526.

[13] C. Sieverding, H. Richard, J. Desse, Turbine blade trailing edge flow characteristics at high subsonic outlet mach number, Journal of Turbomachinery (2003) 298–309.

[14] C. Sieverding, M. Stanislas, J. Snoeck, The base pressure problem in transonic turbine cascade, Journal of Engineering for Power (1980) 711–718.

[15] L. Xu, J. Denton, The base pressure and loss of a family of four turbine blades, Journal of Turbomachinery (1988) 9–17.

[16] J. Denton, Loss mechanisms in turbomachines, in: ASME 1993 International Gas Turbine and Aeroengine Congress and Exposition, American Society of Mechanical Engineers.

[17] S. Pierret, Designing turbomachinery blades by means of the function approximation concept based on artificial neural networks, genetic algorithm and navier-stokes equations, Ph.D. thesis, Faculté Polytechnique de Mons (1999).

[18] L. Mueller, T. Verstraete, Cad integrated multipoint adjoint-based optimization of a turbocharger radial turbine, Int. J. Turbomach. Propuls. Power.

[19] M. Molga, Test functions for optimization needs (2005).

[20] A. Châtel, T. Verstraete, G. Coussement, L. Mueller, Single-point optimization of the ls89 turbine cascade using a hybrid algorithm, in: ASME Turbo Expo 2018, Oslo, Norway, 2018.

[21] I. S. Torreguitart, T. Verstraete, L. Mueller, Cad and adjoint based multipoint optimization of an axial turbine profile, in: In International Conference on Evolutionary and Deterministic Methods for Design Optimization and Control with Applications to Industrial and Societal Problems., 2017.

[22] A. Walther, A. Griewank, A package for the automatic differentiation of algorithms written in c/c+., uRL https://projects. coin-or. org/ADOL-C.

[23] T. Verstraete, Multidisciplinary Turbomachinery Component Optimization Considering Performance, Stress, and Internal Heat Transfer, Ph.D. thesis, Universiteit Gent (June 2008).

[24] T.Verstraete, Introduction to optimization and multidisciplinary design, in: VKI Lecture Series on Introduction to Optimization and Multidisciplinary Deesign, Brussels, Belgium, 2016.

[25] A. Vincini, D. Quagliarella, Airfoil and wing design through hybrid optimization strategies, AIAA Journal 37 (5) (1999) 634–641.

[26] O. Chernukhin, D. Zingg, Multimodality and global optimization in aerodynamic design, AIAA Journal 51 (6) (2013) 1342–1354.

[27] I. Kampolis, K. Giannakoglou, A multilevel approach to single- and multiobjective aerodynamic optimization, Comput. Methods Appl. Mech. Eng. (2008) 2963–2975.

[28] F. Muyl, L. Dumas, V. Herbert, Hybrid method for aerodynamic shape optimization in automative industry, Computers & Fluids (2004) 849–858.

[29] D. Whitley, S. Gordon, K. Mathias, Lamarckian evolution, the baldwin effect and function optimization, in: Springer-Verlag (Ed.), Parallel Problem Solving from Nature - PPSN III vol.886, Lecture Notes in Computer Science, 1994, pp. 6–15.

A Topological Adjoint Method for the Optimization of Stirling Engine Regenerators

Maria Faruoli

Environmental and Applied Fluid Dynamics Department, von Karman Institute for Fluid Dynamics, Belgium, School of Engineering, University of Basilicata, Italy, maria.faruoli@vki.ac.be

Supervisors: Jeroen van Beeck and Lilla Kapa Koloszár

Full Professor, Environmental and Applied Fluid Dynamics Department, von Karman Institute for Fluid Dynamics, Belgium, vanbeeck@vki.ac.be

Research Engineer, Environmental and Applied Fluid Dynamics Department, von Karman Institute for Fluid Dynamics, Belgium, koloszar@vki.ac.be

University Supervisors: Annarita Viggiano and Vinicio Magi

Associate Professor, School of Engineering, University of Basilicata, Italy, annarita.viggiano@unibas.it

Professor, School of Engineering, University of Basilicata, Italy, vinicio.magi@unibas.it

Abstract

This work aims to develop a numerical model for simulating a Stirling engine regenerator as porous media in the most accurate way, considering the flow as incompressible, both in laminar and turbulent cases. This model represents the initial configuration for the regenerator performance optimization process, based on a topological adjoint method. To this end, a tool has been developed by extending its capabilities to cases with thermal dependencies and is described in this work.

Keywords: Topological optimization, Adjoint method, Stirling Engine, Regenerator, Porous media

1. Introduction

In the last two centuries, the Stirling engine has been considered an interesting alternative to the classic steam engines or to the internal combustion engines. Indeed, it is characterized by high reliability and safety, but its specific power is lower than the other engines. The Stirling engines are external combustion engines, so almost all kinds of heat source can be used. They use compressible fluids as working fluids, therefore air is often used. The Stirling engines applications range from heating/cooling systems to mechanical propulsion and electric generation systems. The design of a Stirling engine is mostly related to two main aspects:

- Thermodynamic design, consisting in the sizing of the heat exchanger and the regenerator;
- Context design, consisting in combining the choice of the working conditions (e.g. the working fluid) and the proposed application.

Specifically, this work focuses on the thermodynamic design of the regenerator, since its efficiency is proved to be directly related to the efficiency of the engine [1] . The regenerator is a heat exchanger, placed between the hot and the cold streams, whose role is to store the thermal heat absorbed from the heat flux and to release it to the cold stream, in order to increase the thermal efficiency of the cycle [2]. Different types of regenerator exist. Among the others, the most used is the stoked woven wire regenerator type, composed of metallic wires organized in ordered structures, generally kept at a fixed temperature. The performances of this component are analysed in terms of friction coefficient and thermal efficiency, in order to assess both the pressure losses and the performance as a heat exchanger of the wire netting configuration. Indeed, an

increase of the pressure loss leads to a reduction of the power that can be produced. The thermal performance of the regenerator is studied by analysing the interaction between the flow and the wires surfaces. In order to perform the study of the thermo-physical phenomena characterizing the flow along the regenerator, it is possible to use Computational Fluid Dynamics (CFD). By using this strategy, several studies are performed. An example is given by the work of Costa et al. [3], which analyses the pressure drop in a wire stacked regenerator type and its thermal efficiency in terms of Nusselt number [4]. Moreover, the same authors carried out the modelling of the same configuration as porous media [5].

The process of optimization of the Stirling regenarator focuses on the reduction of the pressure losses and the increase of the thermal efficiency of the component. In Bello et al [6], a parametric analysis of a stacked wire regenerator is performed, evaluating different configurations. Instead, this work focuses on the possibility of using a topological optimization process based on a continuos adjoint method as optimization tool, using the optimal configuration in [6] as initial configuration.

Among the different techniques, the adjoint strategy represents an efficient approach to the optimization problems when a large number of design variables is involved. It is based on the computation of a sensitivity map in the domain, representing how to change the design variables to get the optimal configuration and leading to automatic modifications of geometry.

The technique is already used for aerodynamic applications and in OpenFOAM environment [7] a solver that implements the method, developed by Othmer [8], already exists, but it does not allow to optimize cases with thermal dependencies and thermal objective functions. The equations that drive the methods including the thermal phenomena have been derived and then implemented in OpenFOAM, by considering the pressure losses and the net thermal power dissipated in the domain as objectives of the optimization process. The choice of the topological approach requires the definition of a numerical model that represents the geometry under investigation as porous media, able to reproduce the same results obtained in the reference cases, before starting with the optimization process itself.

In this work, at first the topological adjoint optimization method with thermal constraints is described, and a simple example of application is shown in Section 2. Besides this, the model of the Stirling engine regenerator as porous media, working under different flow conditions is described in Section 3 and the results obtained by means of this model are compared with those obtained by using a more classical CFD technique in Section 4.

2. Topological adjoint optimization

2.1. Method Formulation

A constrained single-objective optimization problem in the field of fluid dynamics can be mathematically expressed as

$$\begin{aligned} &\textit{minimize } J = J(\xi_i, \mathbf{v}, p, T) \\ &\textit{subject to } \mathscr{R}(\xi_i, \mathbf{v}, p, T) = 0 \,, \end{aligned} \tag{1}$$

where ξ_i represents the design variables; $\mathbf{v}$, p and T are the flow velocity vector, pressure and temperature, respectively; $\mathscr{R}$ represents the residual form of the Navier-Stokes equations, referred to as primal system. The function J is called objective function and represents the physical quantity to be optimized.

In the present work a topological optimization tool previously developed is considered, thus the solid to be optimised is modelled as porous media. The design variable considered is the fluid volume fraction, ε, in each cell of the domain and it is expressed as

$$\varepsilon = \frac{volume\ of\ fluid}{total\ volume}. \tag{2}$$

Hence, a solid region is represented by a value $\varepsilon = 0$ while a fully fluid one is defined by $\varepsilon = 1$. The optimization process modifies the material distribution in the domain by introducing or removing porous zones, thus the fluid volume fraction for each cell is modified during the optimization process. The flow dependence on the porosity field is represented by the Darcy term in the momentum equation and by the definitions of the thermal properties for a porous media in the thermal equation. The fluid volume fraction is considered as the design variable in the topological optimization process.

The method is based on the computation of a sensitivity map in the domain, that defines the direction of the design variables modification in order to obtain the optimal configuration. Modifications of the design towards the optimal configuration are obtained by updating the design variable in each cell through a steepest descent method that uses the value of sensitivity. The value of sensitivity is related to both the primal flow variables (velocity, pressure, temperature)

and the adjoint flow variables (adjoint velocity, adjoint pressure, adjoint temperature), introduced in the formulation of the method, and solved by means of a system of equations derived from the definition of the method, referred to as adjoint system.

In the original formulation, the adjoint equations for the continuity and the momentum are considered [8]. In this work, an energy equation is introduced both in the Navier-Stokes system (also referred to as primal system) and in the adjoint system. The equations considered are:

- Primal system:

$$\nabla \cdot \mathbf{v} = 0 \tag{3}$$

$$\mathbf{v} \cdot \nabla \mathbf{v} - \nabla \cdot (\nu \nabla \mathbf{v}) + \nabla p + \alpha(\epsilon)\mathbf{v} = 0 \tag{4}$$

$$(\rho c)_m \mathbf{v} \cdot \nabla T - \nabla \cdot [k_m(\epsilon)\nabla T] = 0 \tag{5}$$

- Adjoint system:

$$\nabla \cdot \mathbf{u} = \frac{\partial J_\Omega}{\partial p} \tag{6}$$

$$\begin{aligned} -\nabla \mathbf{u} \cdot \mathbf{v} - (\mathbf{v} \cdot \nabla)\mathbf{u} + \alpha \mathbf{u} - \nabla(2\nu D(\mathbf{u})) + \nabla q \\ -(\rho c)_m \varphi \nabla T = -\frac{\partial J_\Omega}{\partial \mathbf{v}} \end{aligned} \tag{7}$$

$$-(\rho c)_m \mathbf{v} \cdot \nabla \varphi - \nabla \cdot (k_m \nabla \varphi) = -\frac{\partial J_\Omega}{\partial T} \tag{8}$$

In the equations above $D(\mathbf{v}) = \frac{1}{2}(\nabla \mathbf{v} + (\nabla \mathbf{v})^T)$, ν is the kinematic viscosity of the fluid, α the inverse permeability, ρ represents the density, c the heat capacity for the solid, c_p the heat capacity with constant pressure for the fluid, k the thermal conductivity, and the subscripts *s, f, m* refer to the fully solid, the fully fluid and the mixture zones, respectively. The term J_Ω represents the volume contributions of the objective function. Finally, $\mathbf{u}$ is the adjoint velocity, q the adjoint pressure, and φ the adjoint temperature.

In order to numerically solve the adjoint equations, boundary conditions for the adjoint variables need to be imposed. Such conditions are derived and summirized in Table 1. J_Γ indicates the surface contributions of the cost function.

The results, which will be shown in the following subsection, are obtained considering the net thermal power in the domain, computed as

Table 1: Boundary conditions for adjoint variables.

	u	q	φ
Inlet	$u_t = 0$; $u_n = \frac{\partial J_\Gamma}{\partial p}$	zeroGradient	0
Walls	(0 0 0)	zeroGradient	0
Outlet	$u_t = -\frac{1}{v_n}\frac{\partial J_\Gamma}{\partial v_t}$	$u \cdot v + v_n u_n + \frac{\partial J_\Gamma}{\partial v_n}$	$-\frac{1}{(\rho c_p)_m v_n}\frac{\partial J_\Gamma}{\partial T}$

$$J := \int_\Gamma (\rho c)_m T \mathbf{v} \cdot \mathbf{n} d\Gamma. \tag{9}$$

It is possible to notice that this objective does not involve any volume contributions, thus the dependence of the method on the objective function is present only in the boundary conditions definition. This represents one of the advantage of the method: it is not necessary to modify the implementation of the equations but only to change the boundary conditions in order to change the objective function if only surface contributions are present in the cost function definition.

In order to control the pressure losses in the domain, a multi-objective approach should be used, by considering as objective

$$J = w_p J_p + w_{th} J_{th} \tag{10}$$

where J_p represents the pressure loss minimization, J_{th} the net thermal power minimization, and w_p and w_{th} are the weights assigned to the different cost functions.

The topological adjoint optimization method is implemented developing a solver based on the routine described in Fig. 1.

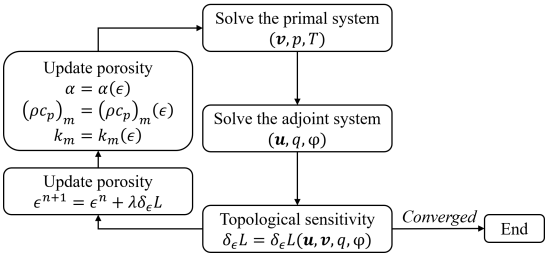

Figure 1: Algorithm implemented for the adjoint method with thermal constraints.

2.2. Test case

The capability of the solver has been tested considering a channel with a sudden enlargement. A 2D domain is considered for the numerical analysis. A uniform velocity (v= 0.5m/s) and temperature profile (T_{in} = 293K) are imposed at the inlet section.

The velocity magnitude is chosen in order to maintain the flow within the laminar regime (Re=350). A difference of temperature is introduced by heating and cooling the bottom and the top walls, respectively, for $^3/_4$ of their length. More specifically, the temperatures 243 K and 343 K are imposed on the top and on the bottom wall, respectively, while the remaining walls are considered as adiabatic. A schematic representation of the thermal boundary conditions is reported in Fig. 2. The simulations are carried out over a structured computational grid of 83200 hexahedral cells. The configuration is initially considered as fully liquid.

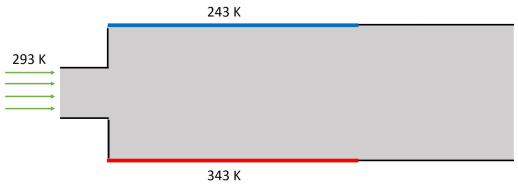

Figure 2: Thermal boundary conditions.

The velocity and temperature distribution of the original topology are shown in Fig. 3 and Fig. 4, respectively.



Figure 3: Velocity distribution with the original configuration.



Figure 4: Temperature distribution with the original configuration.

The materials for the solid and the liquid phases are defined by means of density, specific heat and thermal conductivity. Air and steel are selected as fluid and solid materials, respectively, and their properties are considered as constant, referring to a temperature of 300 K and are summarised in Table 2.

In Fig. 5, Fig. 6 and Fig. 7, the results obtained with the optimization process in terms of solid fraction distribution, velocity and temperature are shown.

Table 2: Thermal properties of the solid and fluid material.

			Steel	Air
Density	ρ	[kg/m^3]	7800	1.17
Specific Heat	c_p	[J/kgK]	460	1004.9
Thermal conductivity	k	[W/mK]	17	0.026

In Table 3 the values of the objective function for the original and optimized configuration are reported. A reduction of the value is observed, thus a higher value of thermal power is dissipated inside the domain, leading to a lower temperature on the outlet section (from 293 K to 279 K). By observing the modification of the topology, two main solid regions are introduced, one in proximity of the hot wall, in order to dissipate the higher temperature in the domain, due to the high thermal conductivity of the solid material. The region in proximity of the outlet instead is responsible for carrying a lower temperature towards the outlet section and reducing the net power on the outlet section.

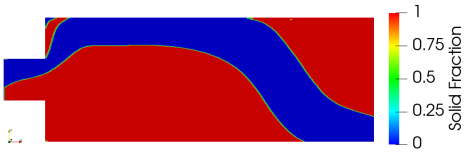

Figure 5: Solid fraction distribution in optimized configuration - Minimize net power.

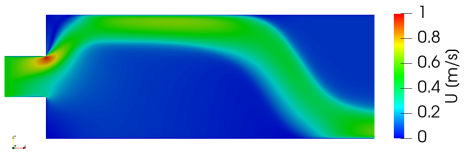

Figure 6: Velocity distribution in optimized configuration - Minimize net power.

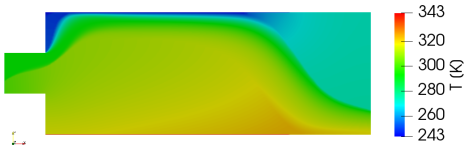

Figure 7: Temperature distribution in optimized configuration - Minimize net power.

Table 3: Evolution of the objective function - Minimization of thermal power.

J_{init}[W/m^2]	J_{opt}[W/m^2]
0.00035	-0.39695

Instead, by considering the objective function with opposite sign, a maximization of the net thermal power dissipated in the domain is obtained. Indeed, by computing the values of the objective function after the optimization, it results to be higher as reported in Table 4. The new topology obtained (Fig. 8) shows a symmetric distribution with respect to the previous case. In this case, a consequent decrease of the temperature on the outlet section is obtained with respect to the original configuration (Fig. 10). In this case the presence of solid material in proximity of the cold wall results in a higher release of thermal power in the domain, transmitted towards the outlet by the solid material close to the outlet section.

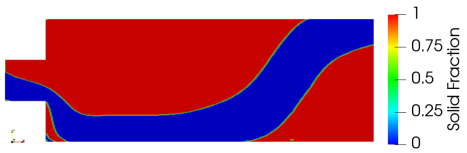

Figure 8: Solid fraction distribution in optimized configuration - Maximize net power.

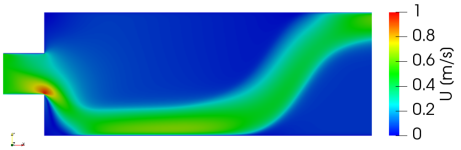

Figure 9: Velocity distribution in optimized configuration - Maximize net power.

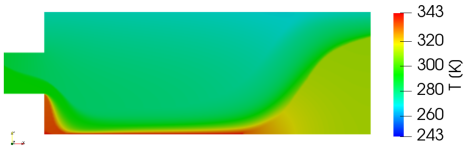

Figure 10: Temperature distribution in optimized configuration - Maximize net power.

Table 4: Evolution of the objective function - Maximization of thermal power.

J_{init}[W/m^2]	J_{opt}[W/m^2]
0.00035	0.42276

In both cases, by observing the velocity field in the optimized geometry (Fig. 6 and Fig. 9), it is possible to notice a significant increase of the velocity magnitude in the domain, that results in a consequent increase of the pressure drop between inlet and outlet, due also to the reduction of the outlet section area.

3. Stirling engine regenerator modelling

The regenerator is generally composed by matrices of wires netting stacked next, or on top, of each other. The configuration studied in this work is a misaligned wires distribution that is also employed by Bello et al. [6] as optimal configuration in their study. The domain considered is 3D, consisting of a parallelepiped with a cross-section of 1 mm $\times$ 1 mm and a total length of 5 mm. The wire matrix is placed 2 mm downstream the inlet section, and it has a length, L, of 0.922 mm. The wire matrix is characterized by the definition of the porosity, π_v, and of the hydraulic diameter, d_h (Table 5). The fluid domain used for the standard numerical computation is shown in Fig. 11.

Table 5: Geometrical properties of the regenerator matrix.

L	d_h	π_v
0.922 m	0.172 mm	0.641

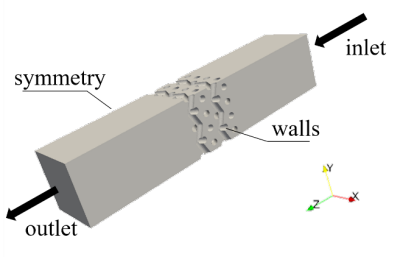

Figure 11: Computational domain and definition of the boundaries.

The numerical modeling of the flow in the regenerator is performed by solving the RANS equations with

both commercial and open-souce codes [9], leading to the same results. In [6] and [9], two different configurations are studied: in the first, the flow is considered as incompressible and no thermal phenomena are involved; in the second, the flow is considered as compressible and the thermal exchange between flow and wires is taken into account. The compressibility effects result to be not negligible above a $Re \approx 500$, as shown in [9], leading to a non monotonic behaviour of the c_f as a function of Re, with increasing pressure losses along the domain, not observed in incompressible cases. Despite this, in this work the flow is always considered as incompressible, because the equations of the adjoint method implemented in the solver can be applied only with incompressible flow hypothesis. Since in this case thermal performances are as important as the aerodynamic ones, the thermal phenomena are always considered in the simulations. Therefore, the temperature distribution is solved by employing the energy equation. The objective of this work is to reproduce the results in [9] with a numerical model that represents the regenerator as porous media. The development of an accurate model is necessary as a preliminary step for the following optimization process, that will use the results of this model as initial condition. Eq. 3, Eq. 4 and Eq. 5 are used in RANS simulations.

The flow is studied as a steady state system, according with the literature. It is reported that, in the experiments with oscillating flow the friction coefficients are estimated to be 30% higher than the theoretical value for the unidirectional flow [6]. Being aware of this, the steady state is an accepted simplification of the problem in numerical studies and the results are analysed by considering the necessary correction.

The wires net is considered as fully solid zone, thus with a value of solid fraction equal to 1. With this strategy no interaction between walls and fluid is modelled, and, as consequence, no boundary layer is generated. For this reason, an artificial layer characterized by an intermediate value of solid fraction is introduced, in order to reproduce the pressure distribution in the domain. The initial solid fraction distribution is represented in Fig. 12, where the values imposed for the fluid volume fraction are reported. The intermediate solid fraction value is chosen by performing a parametric analysis in order to tune the model.

The Reynolds number is calculated by considering the relation in Eq. 11:

$$Re = \frac{\rho v_{max} d_h}{\mu} \tag{11}$$

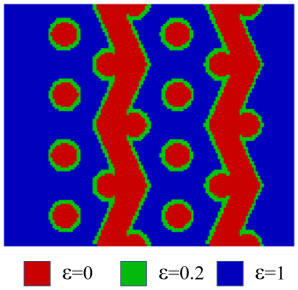

Figure 12: Fluid fraction distribution in a slice of the domain z=0.5 mm.

where $v_{max} = v_{in}/\pi_v$ with v_{in} the inlet velocity, and μ is the dynamic viscosity.

Both laminar and turbulent cases are analysed. The definition of laminar and turbulent flow is not directly related to the Reynolds number as in a pipe but a transition between the two regimes is observed at Re equal to about 500. Above this value, the flow is considered fully turbulent and the numerical modelling of the turbulence is necessary to accurately reproduce the phenomena in the regenerator. About the turbulence modelling, if the medium's inverse permeability is high enough, it can be assumed that the turbulence in it has no effect. For this reason, the turbulence model is modified to suppress the effect of turbulence in the medium when the solid fraction is higher than 50 %.

For the temperature modelling, the absence of interfaces results in significant differences in the temperature field distribution with respect to the literature results at a first attempt. In order to solve this issue, the heat transfer between the wires and the fluid is modelled introducing an heat sink located in the porous zone, using the correlation derived by Ushakov [10]. It consists in an expression of the Nusselt number, Nu, reported in Eq. 12:

$$Nu = 7.55\frac{P}{D} - 20\left(\frac{P}{D}\right)^{-3} + \frac{3.67}{90(\frac{P}{D})^2} Pe^{(0.19\frac{P}{D}+0.56)} \tag{12}$$

where $Pe = Re \cdot Pr$, with $Pr = \frac{\mu c_p}{k}$. The parameter P/D is the pitch-to-diameter ratio, equal to 2.5 in the geometry under investigation. From the Nu, the local heat transfer, h_e, and the total local heat transfer, U, are calculated with the relations in Eq. 13 and Eq. 14:

$$h_e = \frac{Nu \cdot k}{D_h} \tag{13}$$

$$U = \frac{1}{\frac{1}{h_e} + R}. \tag{14}$$

Finally, the volumetric heat sink, S_{HX} is computed taking in to account the total surface, A_{ex}, and the volume, V_{ex}, of the wire matrix, as reported in Eq. 15.

$$S_{HX} = \frac{UA_{ex}(T - Twires)}{V_{ex}F_{HX}} \tag{15}$$

In Eq. 15, the T_{wires} is fixed at 300 K, and the correction factor, F_{HX}, has been set to a value of 0.52.

For the velocity, the boundary condition imposes a uniform profile along the inlet section. For the pressure a fixed pressure value on the outlet section (i.e. the atmospheric pressure) is imposed. The regenerator working phase studied in this paper represents the heat absorption of the wires from the hot stream. Indeed, the wires are kept at a fixed temperature ($T_{wall} = 300K$) lower than the inlet temperature of the flow ($T_{in} = 500K$), used as boundary condition. Corrections are introduced in the velocity and temperature field in correspondence of the wires, where the velocity is forced to 0 and the temperature to a value of 300 K, in order to reproduce the working conditions of the component.

A k-ϵ turbulence model is used for the simulations, so it is necessary to define the initial conditions for the turbulent kinetic energy and the turbulent dissipation rate. A turbulence intensity of 5% is considered, and the hydraulic diameter is used as characteristic length in the computations.

The results are reported in terms of friction coefficient, in order to represent the pressure losses, and of average temperature at the outlet section. The friction coefficient is computed as

$$c_f = \frac{\Delta p}{\frac{rho}{2}\frac{L}{d_h}u_{max}^2}, \tag{16}$$

where $\Delta p = p_{out} - p_{in}$.

4. Results

Several simulations were performed, spanning a range of Reynolds numbers from approximately 5 to 1000.

In Figure 13, the friction coefficient is reported versus the Reynolds number. Specifically, in the graph three different series of data are reported: in the first the wires are considered as walls and the flow is modelled as compressible; in the second the incompressibility hypothesis is assumed, whereas the wires are again modeled as walls; in the last the wires are considered as porous zones and the flow is considered as incompressible. It is possible to notice that the behaviour of the friction coefficient is not always decreasing in the compressible case, but it starts to rise when Re is higher than 600, whereas in the other two cases it always decreases with increasing Re. This is justified considering that above this limit, the compressibility effects are more evident, leading to a change in the behaviour of the flow. Before the limit, all the results follow the same trend, after it, the incompressible case and the porous case are mismatching with the compressible one, but are in good agreement between each other. In Figure 14, the velocity field obtained by using the compressible flow and the porous media simulations at Re=45 are compared, showing a good correspondence between the two models also in the distribution of the velocity field.

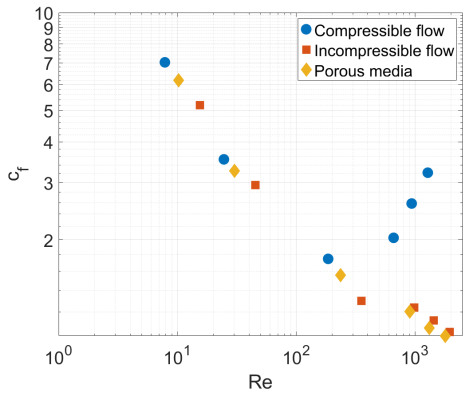

Figure 13: Friction coefficient as a function of Re.

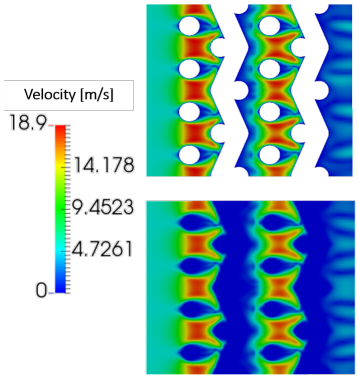

Figure 14: Comparison of velocity fields in the case of compressible flow and porous media simulation - Re=45.

As regards the temperature distribution, the thermal distribution, Fig 15 shows the average temperature at the outlet section as a function of the Reynolds number. It is possible to observe that a good agreement between the standard simulations and the porous media model is obtained, within laminar regime. In the three cases considered indeed the values obtained follow the same trend. The turbulent cases results for the porous media simulations are not reported here, because further analyses are required in order to obtain a satisfying correspondence between the two different approaches.

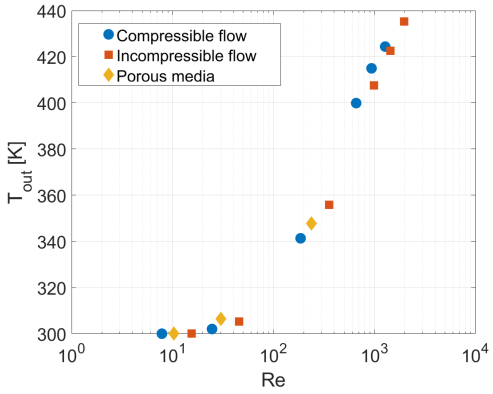

Figure 15: Average temperature at the outlet section as a function of Re.

The porous model with the current setup can properly reproduce the behaviour of the flow in the regenerator, both from the aerodynamic point of view and the thermal point of view, in case of laminar regime. In the next step, the model will be used as initial configuration in the optimization process. About the turbulent regime, further investigation will be performed in order to define a numerical model that can reproduce not only the pressure and the velocity evolution in the domain but also the temperature distribution. Moreover, the implemented solver capabilities have to be extended to manage cases where the flow is in a turbulent regime. To do this, while considering valid the hypothesis of "frozen turbulence" [8; 11], the effect of turbulence on the energy equation will be introduced by considering the effect of a turbulent Prandtl number, Pr_t, introducing Eq. 17 for the flow temperature and Eq. 18 for the adjoint temperature:

$$\mathbf{v} \cdot \nabla T - \nabla \cdot [(K_m + K_t)\nabla T] = 0 \qquad (17)$$

$$-\mathbf{v} \cdot \nabla \varphi - \nabla \cdot [(K_m + K_t)\nabla \varphi] = -\frac{\partial J_\Omega}{\partial T} \qquad (18)$$

where K_m represent the thermal diffusivity of the material computed as $K_m = k_m/(\rho c_p)_m$ and K_t is the turbulent thermal diffusivity, defined as $K_t = \nu_t/Pr_t$.

5. Conclusions

The regenerator design represents a crucial phase in the study of Stirling engine performance and, thus, in the optimization of its performance. The topological adjoint optimization method can be a valid tool for optimizing the component. The method has been described and implemented in OpenFOAM environment, extending the existing formulation to cases with thermal dependencies. The potential of the method has been shown by using a simple test case.

Then, an existing regenerator configuration composed by wires net has been simulated as porous media. The implementation of the model has been described and the results obtained show a good agreement with the reference results, considering both the friction coefficient and the temperature distribution in the domain within laminar regime. Instead, for turbulent cases further investigations are required.

Once the model will be defined it will be used as initial configuration for an optimization process aimed to obtain a new wire net configuration characterized by better performance both in terms of pressure losses and thermal efficiency.

References

[1] W. R. Martini, Stirling engine design manual., Tech. Rep. DOE/NASA/3194-1, US Department of Energy, Office of Conservation and Solar Applications, Division of Transportation Energy Conservation. (1978).

[2] S. K. Andersen, H. Carlsen, P. G. Thomsen, Numerical study on optimal Stirling engine regenerator matrix designs taking into account the effects of matrix temperature oscillations, Energy Conversion and Management 47 (7-8) (2006) 894–908. doi:10.1016/j.enconman.2005.06.006.

[3] S. Costa, H. Barrutia, J. A. Esnaola, M. Tutar, Numerical study of the pressure drop phenomena in wound woven wire matrix of a Stirling regenerator, Energy Conversion and Management 67 (2013) 57–65. doi:10.1016/j.enconman.2012.10.014.

[4] S. Costa, H. Barrutia, J. A. Esnaola, M. Tutar, Numerical study of the heat transfer in wound woven wire matrix of a Stirling regenerator, Energy Conversion and Management 79 (2014) 255–264. doi:10.1016/j.enconman.2013.11.055.

[5] S. Costa, I. Barreno, M. Tutar, J. Esnaola, H. Barrutia, The thermal non-equilibrium porous media modelling for CFD study of woven wire matrix of a Stirling regenerator, Energy Conversion and Management 89 (2015) 473–483. doi:10.1016/j.enconman.2014.10.019.

[6] F. Bello, A. Viggiano, E. Fanelli, V. Magi, A CFD Analysis of the Air Flow through the Matrix Regenerator of Stirling

Engines, in: ISEC Conference Proceedings, 2014, pp. p. 58–71.

[7] Openfoam and the openfoam foundation, https://openfoam.org/, accessed: 2019-12-04.

[8] C. Othmer, A continuous adjoint formulation for the computation of topological and surface sensitivities of ducted flows, International Journal for Numerical Methods in Fluids 58 (8) (2008) 861–877. doi:10.1002/fld.1770.

[9] V. A. M. V. Faruoli, M., An investigation of thermo-fluid dynamic performance of a Stirling engine regenerator by means of OpenFOAM, Modelling, Measurement and Control B 87 (3) (2018) 151–158. doi:10.18280/mmc_b.870306.

[10] P. A. Ushakov, Problems of heat transfer in cores of fast breeder reactor, heat transfer and hydrodynamics of single-phase flow in rod bundles, Izd. Nauka.

[11] C. Hinterberger, M. Olesen, Industrial application of continuous adjoint flow solvers for the optimization of automotive exhaust systems, in: CFD & Optimization, Antalya, Turkey, 2011.

Trained RANS by Means of an Adjoint Method

Giacomo Alessi

Environmental and Applied Fluid Dynamics Department, von Karman Institute for Fluid Dynamics, Belgium, giacomo.alessi@vki.ac.be

Supervisor: Jeroen van Beeck

Deand of the faculty and Full Professor, Environmental and Applied Fluid Dynamics Department, von Karman Institute for Fluid Dynamics, Belgium, vanbeeck@vki.ac.be

Supervisor: Tom Verstraete

Associate Professor, Turbomachinery and Propulsion Department, von Karman Institute for Fluid Dynamics, Belgium, tom.verstraete@vki.ac.be

University Supervisor: Bert Blocken

Part-Time Full Professor, Civil Engineering Department, Leuven University, Belgium, bert.blocken@bwk.kuleuven.be

Abstract

The pressure loss reduction inside the u-bends of internal cooling channels is of crucial importance to increase the performance of cooling systems of gas turbines. The correct prediction of the flow field is therefore fundamental to drive numerical optimization to a real improvement of a design. For this purpose, different numerical approaches can be used to study the fluid dynamics characteristics and the performance of the design. In particular, in the present work the Reynolds Averaged Navier-Stokes and Large Eddy Simulation approach are compared for an internal aerodynamic application and validated against experiments. Finally, it is proposed the solution of an inverse problem, using the adjoint method, to improve the comparison and validation of the numerical solutions obtained.

Keywords: U-bend design, adjoint optimization, RANS, LES, validation against experiments.

1. Introduction

Nowadays, the use of numerical tools to assist design development is of common practice. Thanks to the continuous growth of the computational resources and the increased accuracy of numerical simulation models, it is possible to compare different design prototypes and investigate the influence of several parameters with the aim to improve their performance. However, due to the designs complexity, many different parameters are usually coupled and their effect on the design could be difficult to assess. As a consequence, in the past decades it has been performed a large development of computational routines that autonomously maximize the design performance, i.e. the so-called optimization algorithms. The resulting optimum configuration can be validated through a comparison with experiments avoiding a costly and very time-consuming experimental campaign, as limited to one or two experiments only. As a consequence, numerical optimization followed by an experimental validation is of common practice during the design stage.

The described approach has been followed by Verstraete et al. [1; 2] in the study of the U-bend design. The different optimized U-bend designs found in literature, included the one of reference [1; 3; 4], highlight a common aspect: the minimization of the pressure drop is obtained through the reduction of the separated flow region along the internal side of the bend. As a consequence, the correct evaluation of the flow field characteristics is of crucial importance to maximize the design performance. However, the comparison with the experiments shows that the use of an incompressible Reynolds Averaged Navier-Stokes (RANS)

solver based on a two-equation turbulence model is not able to fully capture the flow characteristics in the present geometry. On the other hand, the use of high-fidelity simulations allows to obtain a more reliable evaluation of the flow field. In the present paper, Large Eddy Simulations (LES) are used to characterize the flow field and are validated against experiments [2]. A comparison with the RANS simulation results is also carried out in order to underline the different flow fields obtained with the two approaches.

The RANS approach is nowadays of common use in combination with different optimization strategies. Indeed, the integration of a LES simulation in an optimization cycle can be problematic from different point of views, e.g. computational resources and time required. Nevertheless, the use of LES would considerably improve the flow field evaluation and could allow a further improvement of the design. In the present paper, a way to combine the point of strength of the two computational strategies is proposed.

2. The U-bend test case

Cooling systems of gas turbines, in most of the cases, use air bled from the high pressure compressor, leading to a penalty in thermodynamic efficiency. A design of the internal cooling passages for minimal pressure losses would improve the global efficiency of the gas turbine. The U-bends that connect consecutive passages are amongst the largest contributors to the pressure losses in the cooling system and deserve special attention during the design phase. Hence, its design can be considered separated from the rest of the internal cooling structure. The considered design and flow configuration has received particular attention both from research groups and industries, thus various approaches and optimization strategies have been applied to it [5; 6; 7].

The present work refers in particular to the optimized design obtained in Verstraete et al. [1] by means of a metamodel assisted differential evolution algorithm. The initial design, Figure 1 (top), features a circular U-bend of square section (hydraulic diameter $D_h = 0.075\ m$). The optimal shape is shown in Figure 1 (bottom). The numerical domains include the U-bend geometries illustrated in Figure 1 and a straight channel, long $8D_h$, connected to each side of the bend. The geometrical details of the two numerical configurations can be found in Verstraete et al. [1].

The numerical domain consists in a scaled version of the experimental one, obtained shortening the legs

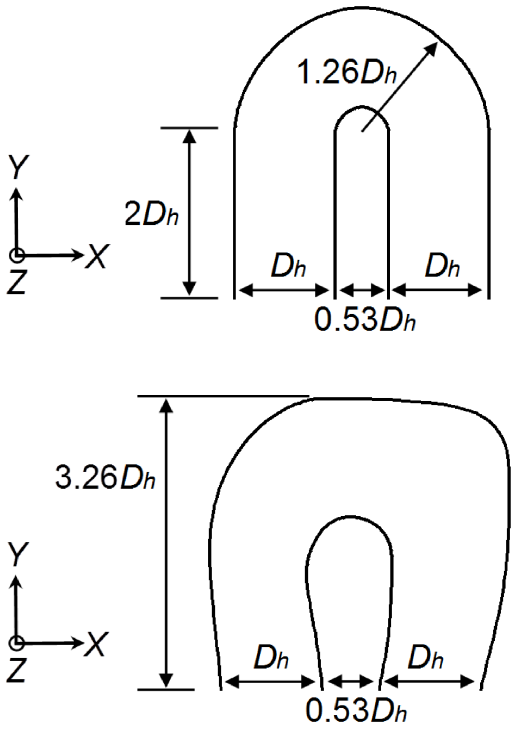

Figure 1: U-bend geometries: standard (top) and optimized (bottom).

of the bend [1; 2]. A RANS simulation of the experimental configuration has been initially carried out, considering a uniform inlet velocity, U_0=8.4 m/s, and a turbulence intensity of T.I.=5%. The velocity field and the turbulent quantities obtained have been sampled at the location corresponding to the inlet of the numerical configuration and used as boundary conditions for it. A zero pressure boundary condition has been applied to the outlet and a no-slip condition to the walls. The simulations have been performed using a structured grid with 342x50x50 cells with local refinements in the regions of high curvature. The maximum y_+ value does not exceed 2.2. A mesh convergence study has been performed with finer meshes with a maximum y_+ value of 0.9; since no variation of the results has been observed, the coarser mesh has been used.

The simpleFoam and pimpleFoam solver from OpenFoam [8] have been used for the RANS and LES simulations, respectively. The Launder-Sharma low-Reynolds $k-\epsilon$ turbulence model has been used in the RANS simulations. The Wall-Adapting Local Eddy-viscosity (WALE) model has been chosen for the LES simulations with a filter width related to the

local grid cell size, i.e. the cube root of cell volume in the present case. The averaging of the flow quantities has been started after 15 flow-through (ft) and carried out for 15 ft, sampling at each time step of the simulation. The Courant-Friederichs-Levy (CFL) number has been kept below unity. The computations require approximately 2 days on 40 cores for the LES simulations and one hour on 16 cores for the RANS ones.

3. Validation of the numerical results

The numerical results obtained with the RANS and LES approach have been validated against the experimental results of Coletti et al. [2] for both the standard and optimized U-bend. The flow field obtained numerically has been compared to the PIV measurements in order to understand if the numerical simulations are able to catch the physics under consideration. In particular, the normalized velocity field, $\underline{U}^\star$ (Eq. 1), is compared.

$$\underline{U}^\star = \underline{U}/U_0. \tag{1}$$

The flow field characteristics for the standard U-bend obtained with the different techniques are shown in Figure 2, Figure 3 and Figure 4, i.e. the velocity field and its surface streamlines at the middle plane, z/D_h=0.5.

In the standard U-bend the flow accelerates approaching the bend, it reaches the maximum velocity around the inner wall while it decelerates along the outer wall. The acceleration continues after the bend, reaching the outer-wall due to the section restrictions caused by the recirculation bubble. The separation and the consequent recirculation region is formed as a result of the adverse pressure gradient on the inner wall caused by the bend curvature. Figure 2 highlights the complex nature of the recirculation region that seems to end in a source point. The recirculation region extends for a length of about $1.6D_h$.

An overall validity of the flow characteristics is obtained with the RANS simulation. Nevertheless, the turbulence model used is not expected to give a reliable representation of complex vortex structures. In fact, the flow starts to separate before the end of the bend forming a classical separation bubble ending with a reattachment point (Figure 3). Its length, $1.3D_h$, and its height are underestimated. This causes a lower acceleration toward the outer-wall in comparison with the PIV visualization.

The use of a time-dependent simulation solving the motion of the large eddies of the flow (LES), could give a better insight to the flow characteristics and offer a more reliable comparison with the experiments especially when the flow separates and hence exhibit inherently an unsteadiness. Differently from the RANS results, the LES simulation is able to catch the feature of the recirculation region, showing as well a termination in a source point (Figure 4) and a length of the separation region of $1.7D_h$. Moreover, the magnitude of the normalized velocity is in agreement with the experimental one.

The optimized geometry presents a wider cross section in comparison to the standard U-bend, thus the normalized velocities are lower in comparison to the ones in the standard geometry, as highlighted from a section at the symmetry plane (Figure 5, Figure 6 and Figure 7). The PIV measurement, Figure 5, shows an initial acceleration around the inner-wall approaching the bend. The increment of the radius of curvature of the inner and outer-wall results in a smaller separation region than the one present in the standard geometry. The separation bubble is also much shorter and the flow reattaches before the end of the bend. Due to the particular configuration of the outer-wall given by the optimizer, the flow passing over the separation region does not display an acceleration and avoids the impinging on the outer-wall shown in standard geometry. The LES simulation, Figure 7, confirms the experimental observations: both the velocity field and its streamline features are in agreement with the experimental ones. On the other hand, the RANS approach fails in the characterization of the separation region, that is largely underestimated (Figure 6).

The RANS evaluations highlighted its unreliability in the prediction of the correct flow field inside the bend. Nevertheless, the optimization strategy used in combination with a RANS approach allowed to reach an improved design with a gain in pressure drop of 33.3%. The improvement in pressure drop has been also confirmed from the experimental tests (36.5±3 % [2]). As a consequence, a first optimization with RANS is meaningful since an improved design has been obtained at a low computational cost. However, the use of the LES approach has shown that a recirculation bubble is still present inside the optimal geometry. Therefore, further improvements of the design are possible and can be obtained only using a LES approach.

4. Trained RANS

The introduction of LES simulations in an optimization routine could be extremely expensive, even

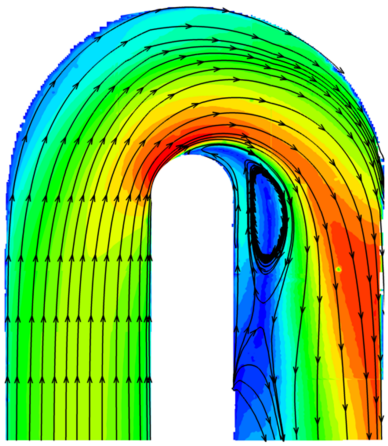

Figure 2: Normalized velocity field and its surface streamlines in the standard U-bend at z/$\mathbf{D_h}$=0.5: PIV measurement [2].

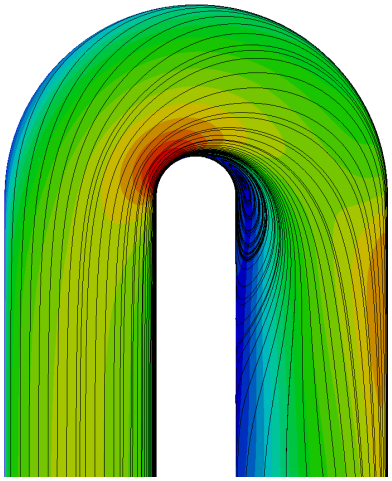

Figure 3: Normalized velocity field and its surface streamlines in the standard U-bend at z/$\mathbf{D_h}$=0.5: RANS simulation.

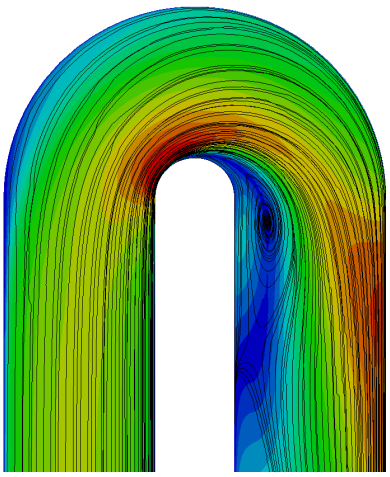

Figure 4: Normalized velocity field and its surface streamlines in the standard U-bend at z/$\mathbf{D_h}$=0.5: LES simulation.

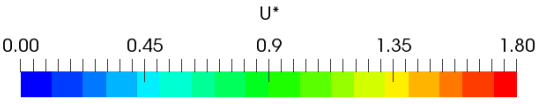

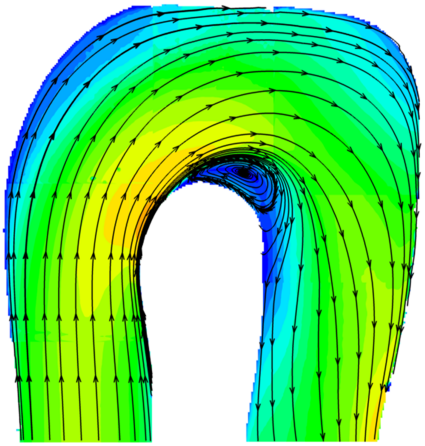

Figure 5: Normalized velocity field and its surface streamlines in the optimized U-bend at z/$\mathbf{D_h}$=0.5: PIV measurement [2].

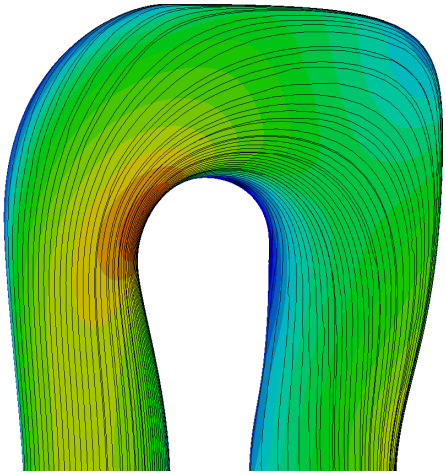

Figure 6: Normalized velocity field and its surface streamlines in the optimized U-bend at z/$\mathbf{D_h}$=0.5: RANS simulation.

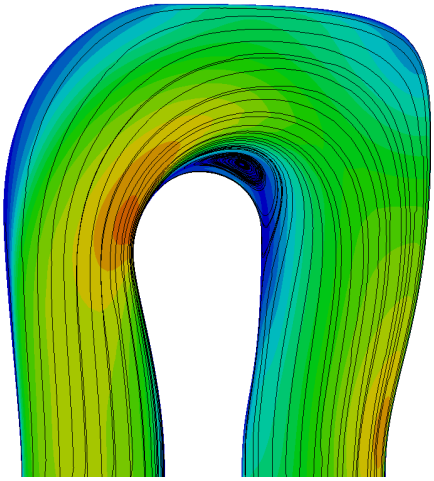

Figure 7: Normalized velocity field and its surface streamlines in the optimized U-bend at z/$\mathbf{D_h}$=0.5: LES simulation.

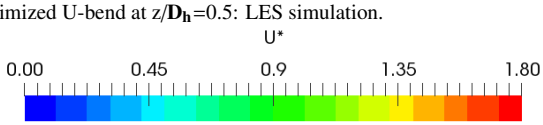

prohibitive depending on the optimization strategy used. As an example, the approach suggested by Verstraete et al. [1] would require a LES evaluation for each population member, i.e. 65, at the first step of the optimization in order to create the design of experiments (DOE). The different simulations can be run simultaneously but the computational demand is high. An optimization strategy that certainly minimize the computational cost required to obtain an improved geometry is a first order optimization strategy that use the adjoint method to calculate the gradient of the cost function. However, the use of LES in combination with an adjoint strategy can be problematic. Indeed, the adjoint solution travel backward in time requiring the necessity to store many intermediate solutions (checkpoint strategy [9]), thus increasing considerably the computational time and storage requirements needed. On the other hand, when applied in combination with a RANS simulation, the use of the adjoint approach is more straightforward. As a consequence, in order to further improve the optimized design obtained by Verstraete et al. [1], there is the necessity to satisfy two different requirements: on one hand there is the necessity to use a LES approach to correctly represent the flow field, on the other hand the use of RANS connected with an adjoint method for shape optimization is more advantageous.

A way to fulfil both requirements is to mimic the behaviour of a LES approach with a RANS simulation. The training of the RANS simulation requires the solution of an inverse problem where the aim is to obtain with a RANS simulation a velocity field (V_i) as close as possible to the average mean velocity obtained with a LES simulation ($\overline{V}_i$), i.e. the aim is to minimize the quadratic difference between the two velocity fields (Eq. 2).

$$min\left(V_i - \overline{V}_i\right)^2 \tag{2}$$

The turbulent viscosity, ν_t, can be used as design variable for the solution of the inverse problem. Following the loop in Figure 8, a frozen turbulence approach will be used in the solution of the Navier-Stokes equations, meaning that no turbulence model will be used as the turbulent viscosity is adapted according to the gradient of cost function to minimize. The solution of the adjoint equations follows the RANS evaluation. When both systems of equations have been solved, it is possible to evaluate a volumetric sensitivity that will indicate how to modify the turbulent viscosity in each cell of the domain in order to minimize the cost function. The turbulent viscosity can be then updated thanks to the use of an optimizer, e.g steepest descent algorithm in the present work. However, a simple steepest descent algorithm does not prevent the attainment of not-physical values of turbulent viscosity, such as negative values. As a consequence, a constrained steepest descent algorithm has been used in the present work (Eq. 3).

$$\nu_t^{T+1} = \nu_t^T + \gamma\left\{\min\left[\max\left(\nu_t^T + \lambda S, \nu_t^{min}\right), \nu_t^{max}\right] - \nu_t^T\right\} \tag{3}$$

Where the superscripts T and $T+1$ refer to two different iterations, λ defines the step size of the design variable modifications. Negative turbulent viscosity values are avoided imposing $\nu_t^{min} = 0$, while the enforcing of a maximum limit (ν_t^{max}) avoids a divergent solution. The relaxation factor γ is used to help the solution convergence.

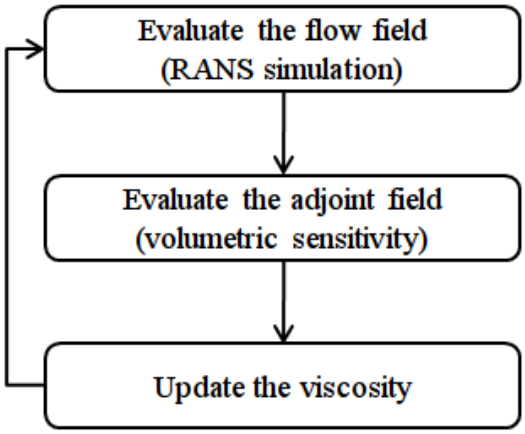

Figure 8: LES-based optimization loop.

The loop in Figure 8 has been solved following a one-step approach [10]. The optimal turbulent viscosity distribution is reached when a convergent cost function is attained. The resulting velocity field obtained from the solution of the inverse problem proposed is shown in Figure 9, in particular the normalized velocity field and its surface streamlines at the middle plane. The surface streamlines highlight the formation of a recirculation bubble in the internal bend region, recovering the correct fluid structures inside the bend. A comparison between Figure 7 and Figure 9 shows an agreement between the solution obtained with a LES evaluation and the one coming from the inverse problem solution. Approaching the internal bend, a slight higher velocity is reached in the trained RANS solution in comparison with the LES solution. The high velocity region is also spread in a

bigger area. On the other hand, a slower velocity region spread in a bigger area is present in the outer side of the bend.

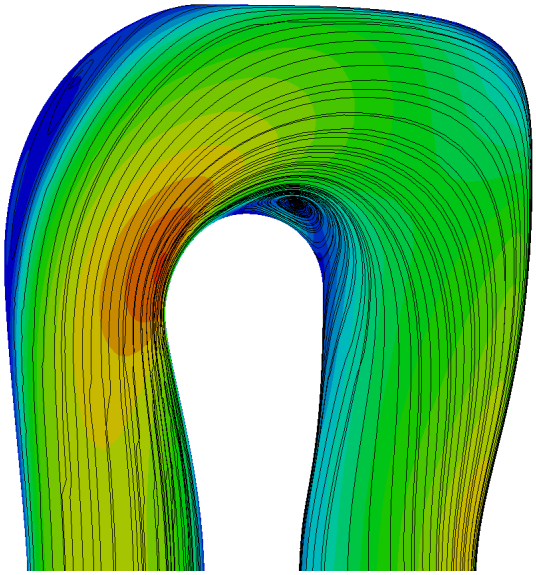

Figure 9: Normalized velocity field and its surface streamlines in the trained RANS optimized U-bend at $z/\mathbf{D_h}$=0.5.

5. Conclusion

The characterization of the flow field inside a U-bend has been shown in the present work, comparing RANS and LES to the experimental data available in literature. In particular, two geometries have been compared and validated: a standard U-bend and one modified by an optimization routine with the aim to reduce the pressure drop in it. The characterization gave an insight of the flow field inside curved channels and an understanding of the mechanisms that brought to an optimized design. The validation of the numerical study regards qualitative comparisons, I.e. a comparison of the velocity fields and its streamlines at the middle section of the bend. The latter are indeed of paramount importance, being able to identify the region of major losses inside the bend.

The validation study confirmed the inability of the RANS model to catch the complex vortex structures present in the given geometries. The separation regions evaluated with the RANS approach show indeed a different behaviour than the ones observed in the experiments. Nevertheless, an overall validity of the flow field characteristics is obtained. On the other hand, the LES simulation provided an accurate prediction in terms of flow field visualizations. The results obtained highlighted the creation of separation regions in agreement with the experiments in both geometries.

The validation study showed that the use of LES for numerical optimization could bring to more reliable results and to further improvements of the design. At this purpose, in order to take advantage from both techniques, the solution of an inverse problem using the adjoint methodology is proposed. Starting from a RANS simulation, it is aimed to obtain a velocity field that represents the average one coming from a LES solution. The result obtained by training the RANS solution shows that the proposed approach is able to overcome the limitations of the original RANS solution, as a separation region in agreement with the experimental one is obtained. This solution can be then used as starting point for an adjoint shape optimization routine to further improve the design.

Acknowledgments

This work was supported by the Fonds Wetenschappelijk Onderzoek Vlaanderen - FWO.

References

[1] T. Verstraete, F. Coletti, T. Vanderwielen, J. Bulle, T. Arts, Optimization of a u-bend for minimal pressure loss in internal cooling channels-part I: Numerical method, Journal of Turbomachinery 135 (2013) 051015.

[2] F. Coletti, T. Verstraete, T. Vanderwielen, J. Bulle, T. Arts, Optimization of a u-bend for minimal pressure loss in internal cooling channels-part II: Experimental validation, Journal of Turbomachinery 135 (2013) 051016.

[3] K. Elsayed, J. Miranda, C. Lacor, Minimization of the pressure loss in internal cooling channels using the adjoint method, 1st Aviation Engineering Innovations Conference paper AEIC-2015-000.

[4] G. Alessi, L. Koloszar, T. Verstraete, J. P. A. J. van Beeck, Node-based adjoint surface optimization of u-bend duct for pressure loss reduction, Evolutionary and Deterministic Methods for Design Optimization and Control With Applications to Industrial and Societal Problems. Computational Methods in Applied Sciences 49 (2018) 61–75.

[5] T. Verstraete, J. Li, Multi-objective optimization of a u-bend for minimal pressure loss and maximal heat transfer performance in internal cooling channels, ASME Turbo Expo 3A: Heat Transfer.

[6] S. Zehner, H. Steinbruck, S. Neumann, B. Weigand, The ice formation method: A natural approach to optimize turbomachinery components, International Journal of Design & Nature 3(4) (2009) 259–272.

[7] H. Namgoong, C. Son, P. Ireland, U-bend shaped turbine blade cooling passage optimization, 12th AIAA/ISSMO Multidisciplinary Analysis and Optimization Conference 3 (2008) 1439–1447.

[8] OpenFOAM, https://www.openfoam.com/.
[9] J. Goit, J. Meyers, Optimal control of wind farm power extraction in large eddy simulations, 32nd ASME Wind Energy Symposium, AIAA Journal DOI:10.2514/6.2014-0709.
[10] N. Gauger, E. Ozkaya, Single-step one-shot aerodynamic shape optimization, International Series of Numerical Mathematics 158 (2009) 191–204.

Turbocharger Design and Optimization by Adjoint Method Coupled with CHT Analysis

Alberto Racca

Turbomachinery and Propulsion Department, von Karman Institute for Fluid Dynamics, Belgium, alberto.racca@vki.ac.be

Supervisor: Tom Verstraete

Associate Professor, Turbomachinery and Propulsion Department, von Karman Institute for Fluid Dynamics, Belgium, tom.verstraete@vki.ac.be

University Supervisor: Lorenzo Casalino

Professor, Mechanical and Aerospace Engineering Department, Politecnico di Torino, Italy, lorenzo.casalino@polito.it

Abstract

This paper addresses the problem of multidisciplinary adjoint optimization methods for turbocharger Variable Geometry Turbine components with focus on thermal aspects. A Conjugate Heat Transfer procedure based on a loose coupling between a fluid and solid solver is introduced as a means to predict the heat transfer and temperature in the rotor. Consequently, as this method will be used to optimize the rotor in a gradient based framework, the adjoint method to the loose coupling procedure is presented to allow for an efficient computation of the objective function gradient.

Keywords: Adjoint methods, Conjugate Heat Transfer, Turbocharger optimization, Variable Geometry Turbine

1. Introduction

Multidisciplinary optimization methods are routinely applied in product development processes in the automotive industry as they provide system experts with a comprehensive view of the design opportunities about critical technologies operating in complex macro-systems, like internal combustion engines. The mutual interactions among different components included in a closed-loop environment and collaborating to the project targets of a new engine family pose significant challenges to designers, demanded to balance each technology performance with expected lifecycle, cost targets and packaging constraints. Moreover, prediction accuracy is demanded both at design and off-design conditions, further increasing the level of complexity in determining the so-called "right-sized" technical specifications. In such framework, concurrent engineering approaches have grown in the last decade with the aim of transitioning from workflows of serial mono-discipline evaluations to integrated strategies with simultaneous consideration of mutual influences among the different analysis fields involved in the problem under investigation. Such new design approach is demonstrating to be suitable to satisfy the demand of more accurate models predictions, minimization of prototyping and verification tests and finally to cope with the severe time constraints in product development cycle and roll-out.

The significant evolution in the market request that industry is currently facing, together with the legislators' demand for more aggressive emissions reductions, offers new challenges to the research community. The need of further advances in multidisciplinary design optimization techniques is reported in NASA 2040 roadmap [1], which highlights optimization methods as one of nine core technical work areas in the context of integrated multiscale modelling frameworks for the success in efficient design, manufacturing and certification of future aerospace systems. Enhanced modelling capabilities are also reflected in the requirements of the modern

automotive sector and, in particular, turbocharger technologies represent a peculiar field of investigation because of their fundamental role in the achievement of the engine targets and the interdisciplinary footprint necessary in their design cycle.

The state-of-the-art approach to turbocharger design and optimization is represented by extensive use of genetic algorithms as reported by Lotz et al. [2], describing the development process with respect to specific driving cycles characterized by key operative conditions and approached by the use of 3D-CFD and constraints for structural integrity. Wöhr et al. [3] showed a multi-disciplinary and multi-objective optimization workflow driven by evolutionary algorithms for aerodynamics, mechanical durability and manufacturability evaluations, combining both metamodels and high-fidelity 3D-CFD and CSM analyses and using native features in the CAD platform to guarantee conformity in the data exchange process between the different simulation environments. Similar strategies are reported by Ioannou et al. [4] for aerodynamic optimization of a high pressure turbine wheel and by Hildebrandt et al. [5] for a coupled aerodynamic and structural optimization of a compressor impeller, both based on gradient-free methods.

The wide popularity gained in industry by gradient-free methods is due to their generality and relative simplicity in implementation. Nevertheless, the new performance goals demanded to the turbocharging business require more detailed geometry investigations and full-scale system optimizations capable of capturing the propagation of the effect of local design modifications at global machine level, replacing processes with serial design of single subcomponents. Such holistic view is not easily achievable by gradient-free methods which suffer from the so-called "curse of dimensionality". A feasible approach to richer design spaces is therefore offered by gradient-based methods, and in particular adjoint methods, a convenient means of calculating the gradients of the cost function, discussed in the present work.

While adjoint methods represent an opportunity for efficient system-level optimizations, their introduction in production processes is still at an early stage, mainly because of the need to access the solvers source codes and the higher maturity demanded to their intrinsic stability properties, like in presence of limit cycle oscillations. Major advancements have been recently done in the field, as discussed in [6], opening this design technology to a wider range of applications.

An industrial consideration of adjoint methods for problems of internal and external aerodynamics in the aerospace sector is offered in [7]-[8], but their declination to multidisciplinary frameworks still represents an open field of research. Indeed, the exploitation of the time saving offered by such computationally less expensive optimization technique in favor of more comprehensive problem evaluations is a fundamental attribute for a future larger diffusion of the method.

In light of this objective, the present project is devoted to the development aspects of turbocharger components with application to the design and optimization of Variable Geometry Turbines (VGT) by multidisciplinary adjoint methods, as discussed in section 4, expanding the outreach of the original Conjugate Heat Transfer (CHT) analysis [9].

2. The Variable Geometry Turbine test case

The Variable Geometry Turbine (VGT) in automotive turbochargers is an established technology in the diesel sector, while it is gaining wide popularity in modern gasoline applications adopting a Miller cycle -based lean combustion system [10].

The main advantage of a VGT in comparison to a standard wastegate turbine is related to the wider operative range at high efficiencies since the machine is capable of managing the entire flow exhausted by the combustion chambers with no need of any bypass channel. Additionally, it can adjust the rotor inlet flow tangential component by means of inlet guide vanes. Therefore, more enthalpy is available for the extraction of power at the turbine wheel and near-optimal conditions are achievable according to Euler's equation. This is reflected in faster accelerations of the compressor and higher boosting targets realized by the turbocharger, finally disclosing more opportunities in the refinement of the calibration of the selected combustion package. In the specific case of a Miller cycle, Christmann et al. [11] showed that eventually the VGT technology might offer the boosting capability necessary to design an architecture for higher Miller rate values, thus leading to further improvements in fuel consumption.

VGT turbines, shown in Figure 1, mainly consist of three elements:

- A volute collecting the entire mass flow from the combustion chambers, except the rate ded-

icated to recirculation towards the intake manifold through the short-route system. The volute may be single channel or double channel.

- A set of vanes arranged in a cartridge that adapt the flow incidence angle at rotor leading edge and the expansion ratio through the turbine by controlled rotation around their pivots (from which the name "Variable Geometry" Turbine derives).

- A rotor, typically a radial or mixed-flow impeller, for the extraction of power made available to the compressor.



Figure 1: Variable Geometry Turbine components: volute fluid domain, vanes, rotor. Courtesy of General Motors

In contrast to aeronautical applications, the typical duty cycles for passenger car applications span the entire turbine map, from very low mass flow rates and pressure ratios in urban conditions up to peak power. Statistical approaches have been refined in order to synthesize the information in key operative conditions, resulting in requirements stretching the machine design over a wide range of vanes positions. Moreover, this turbine arrangement presents clearances between vanes-shroud and rotor-housing in the order of few hundreds of microns, whilst the typical thermal operative range spans from ambient temperature up to 1050C in gasoline applications, this without the possibility of rotor cooling. Such scenario clearly demonstrates the challenges in performance requirements and durability the designer is confronted with during the product development process.

In summary, a production-intent turbine design has to fulfill efficiency and permeability targets, structural integrity to centrifugal and fluid-induced stresses, robustness to vibrations, creep resistance and minimized thermal deformations, along with cost, mass and packaging constraints. Therefore, it is indeed recognized that a design based on experts' intuition alone would be highly challenging; consequently, multidisciplinary optimization methods play a fundamental role in this product development cycle.

To this end, the present work addresses the problem by means of the in-house multidisciplinary design and optimization (MDO) platform "CADO" developed at von Karman Institute [12], with specific reference to the gradient-based framework presented in [13]-[14]. The aim of the project is to expand the existing aerodynamic and structural mechanic evaluation capabilities with new features dedicated to thermal considerations introduced during the optimization process by the Conjugate Heat Transfer analysis.

A comprehensive review of heat transfer phenomena in turbochargers is reported in [15]. Nowadays, heat transfer effects are not directly implemented in design optimization processes because of their significant computational overhead, whilst replaced by safety margins based on experimental experience or by integration of reduced order models. Full 3D investigations are usually limited to verifications performed a posteriori on the geometry returned by the optimization system. Therefore, a reconsideration of the procedure is demanded for the realization of more sophisticated design proposals.

The new connections among the design disciplines offered by the CHT method are synthesized in Figure 2. Aerodynamic and structural mechanic aspects (maximum allowed stresses) are treated separately as reported in [16] and [17] and both contribute to the definition of the cost function. This assumption is acceptable in the case of a radial turbine rotor because of the negligible deformations induced by the fluid load on the structure (in the worst-case scenario, in the range of 5% compared to the contribution of the centrifugal stresses). Such simplification would be no longer valid in case of a complete treatment of the fluid-structure interactions for High Cycle Fatigue purposes, which is out of scope in the present work.

The role of CHT in this representation is twofold:

– On one side, the previous assumption of adia-

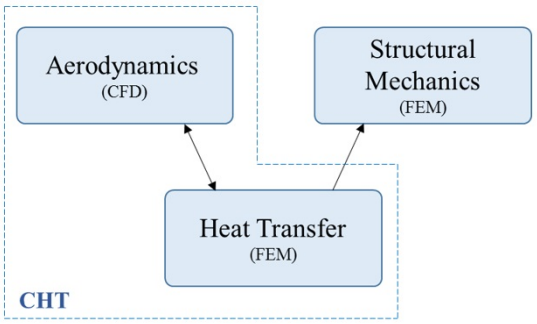

Figure 2: Schematic representation of problem framework with CHT closure between involved disciplines

batic walls is replaced by the computation of heat fluxes exchanged between the fluid and solid domains. The adopted coupling approach discussed in section 3 focuses on the VGT vanes region - responsible for the largest extraction of enthalpy from the exhaust gases - and the rotor, which represents the sensible element in the structure. The higher accuracy offered by the iterative calls to the CFD and heat transfer solvers improves the prediction of the turbine efficiency, avoids any overestimation of the choking mass flow rate and satisfies the request of more precise identification of temperature constraints at the inlet of the aftertreatment system.

– On the other side, the thermal field prediction into the rotor allows the optimization of the geometry avoiding local hot spots that could be detrimental in terms of Yield strength decay and creep formation. This is possible while overcoming the too restrictive assumption of a constant temperature distribution in the solid domain equal to the fluid temperature at the inlet of the turbine volute. Finally, the information is transferred to the structural solver for blade lifetime estimations.

This synergic approach to aerodynamic and thermo-mechanical optimization would be less suited for a gradient-free method because of the combination of the higher computational effort induced by the CHT analysis and the large number of iterations required to reach a satisfactory solution. The adjoint-based MDO system previously introduced overcomes this limitation thanks to the reduced number of loops required to identify the final geometry, as demonstrated in [18], in which gradient-free and gradient-based frameworks are compared in the optimization of a radial turbine wheel.

At the time of writing the present paper, only few publications were available in the literature about CHT introduced in an adjoint-based optimization framework ([19]-[20]), only one adopting a discrete adjoint formulation [21] and none treating a test case with radial impellers and their complex three-dimensional flow field. Therefore, the current research project is aimed at covering critical gaps in the design of radial Variable Geometry Turbines with the aim of creating a framework suitable for industrial application.
The remaining portion of the document describes the CHT coupling previously highlighted with focus on the turbine rotor region. A review of the implementations in the existing primal solvers is reported in section 3, while section 4 is devoted to the discussion of the adjoint formulation developed for the optimization problem in place.

3. CHT implementation in primal solver

The CHT analysis implemented in the current work follows the soft-coupling approach proposed by Verdicchio et al. [22], in which a fluid and a solid solver are sequentially called in an iterative process with mutual exchange of boundary conditions till reaching the convergence of the temperature at the interface. The advantage of this strategy is related to the possibility of adopting specialized numerical methods for the solution of each domain, increasing the robustness of the convergence of the analysis, and to the partial decoupling of the two fields, which present very different characteristic time scales.

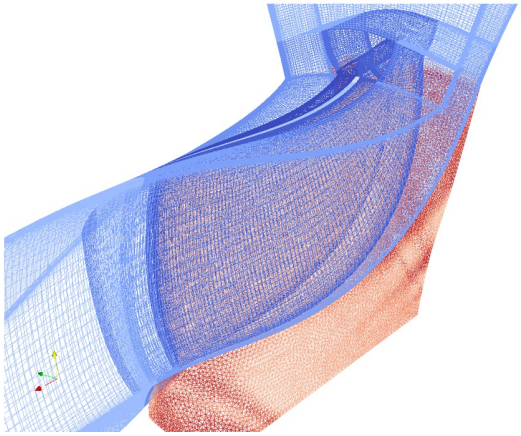

Figure 3: Radial turbine wheel: fluid and solid sector-meshes

The domain under investigation is shown in Figure 3, where a structured multi-block fluid mesh and an unstructured solid mesh have to be interfaced to allow the computation of heat fluxes.
In order to do so, following the discussion reported in [23], a distance-weighted interpolation technique is chosen because of the flexibility offered in establishing an interface between non-matching FEM and FVM meshes. In particular, the effectiveness of the method is demonstrated at the blade hub fillet, a region modelled in the solid domain but not accounted in the fluid one. Few minor modifications are applied to the original method in order to improve the accuracy and computational effort:

a) The surfaces of the rotor in the FEM mesh are distinguished in separate parts as reported in Figure 4 (e.g. blade pressure side, suction side, tip, hub, etc.). Similarly, all the block boundaries in the FVM mesh classified as "viscous walls" are labelled according to their corresponding region in the turbine rotor (e.g. blade pressure side, suction side, tip, hub, etc.). Therefore, a direct reference between the sub-regions of the two domains is established and the heat transfer is confined to regions actually in close contact. This implementation avoids any erroneous transfer of information in areas characterized by very thin walls, for instance at high blade spans close to the tip, where the solid portion of the blade at suction side might have been influenced by the fluid domain at the pressure side.
b) The original method requires the definition of a search radius, to which the search for neighboring nodes or cells is restricted for the interpolation of temperature or heat flux values. Defining the search radius value for a full, non-homogeneous domain bears the risk of intercepting too many or no samples at all for the exchange of information. Instead, with the current method, once a new geometry is created, a mapping of the mutual distances in each cell-node couple is performed for each turbine region defined above. After that, for each cell or node, the closest n neighbors (respectively nodes or cells) are selected for the distance-weighted interpolation function. While n is defined by the user, the new approach offers a stricter control over the information transfer process.

The communication established between fluid and solid domains allows the implementation of a CHT strategy according to the "heat transfer coefficient Forward Flux Back" (hFFB) method presented in [23].

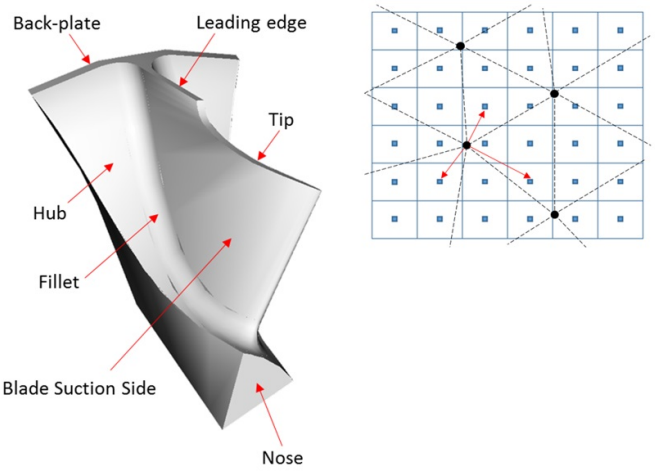

Figure 4: Turbine rotor sub-regions, example of FVM-FEM meshes nodes identification

The attractiveness of this partitioned method is due to the superior stability of the coupling scheme as discussed in [24]. The boundary conditions are repeated here for convenience:

$$q^i_{FW} = \tilde{h}(T^i_{FW} - T^i_{fl}) \quad (1)$$

$$q^i_{SW} = \tilde{h}(T^i_{SW} - T^i_{fl}) \quad (2)$$

$$q^{i+1}_{FW} = q^i_{SW} \quad (3)$$

where T_{fl} is a "virtual" fluid temperature in the thermal boundary layer.

The coupling method evolves according to this schedule:

1. At first, a fluid flow calculation is performed and values of q_{FW} and T_{FW} are extracted at the boundaries in common with the solid domain.
2. A "virtual" convective heat transfer coefficient $\tilde{h}$ is imposed and, through inversion of equation (1), T_{fl} is calculated.
3. $\tilde{h}$ and T_{fl} are imposed as boundary conditions to the FEM heat transfer model as reported below and the solid analysis is run till convergence
4. The heat fluxes at solid wall boundaries are evaluated through equation (2) and returned as boundary conditions to the next NS calculation. Such implementation follows the weak formulation approach discussed in [18] with the conversion of the heat flux into temperatures in the layers of ghost cells assuming a Thin Shear Layer

approach, constant pressure in wall normal direction and sign reversal for the velocity components in order to respect the no-slip condition.

The workflow is iteratively repeated till reaching the continuity of temperatures and heat fluxes between the two domains (Figure 5).

A FEM steady heat transfer solver was implemented according to [25] in order to calculate the energy balance in the solid region.

$$-k_s \nabla T = h(T - T_{fl}) \tag{4}$$

Once integrated over the reference domain, equation (4) can be reformulated in the discrete system form

$$A\mathbf{T} = \mathbf{b} \tag{5}$$

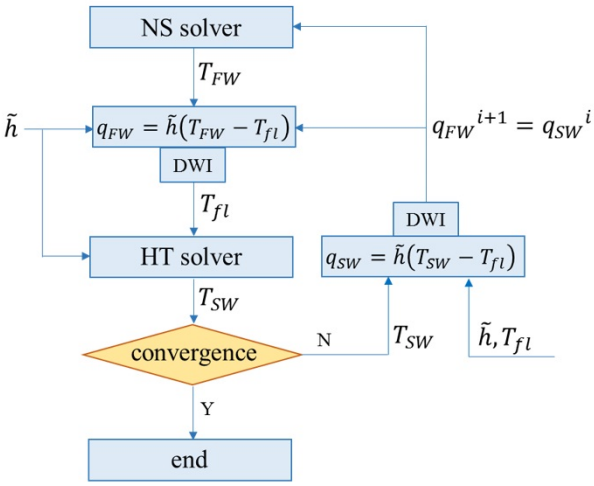

Figure 5: Conjugate Heat Transfer analysis workflow implemented in primal solver

with
$A = [K_{cond} + K_{conv}] \in R^{n,n}$ is the sparse stiffness matrix comprising conduction and convection contributions. The name "stiffness" is inherited from the classical FEM theory applied to structural-mechanics problems

$\mathbf{T} \in R^n$ is the vector of unknown solid temperatures

$\mathbf{b} = \tilde{h}T_{fl} \in R^n$ is the convective load from the fluid in contact with the solid surfaces

Therefore, the convective boundary condition from the hFFB method is implicitly applied to the system of equations (5) by implementation of the K_{conv} matrix at LHS and the b vector at RHS.

The system of equations (5) is solved by a conjugate gradient method. Once the temperature in the solid domain is determined, the heat flux towards the surrounding fluid is calculated through equation (2) and returned to the NS solver as described before.

4. Multidisciplinary adjoint method

The CHT analysis is introduced in an adjoint optimization framework with CAD-based parametrization as described in [17], which allows the two domains (solid and fluid) to evolve consistently according to the geometrical information contained in the CAD master-platform. Therefore, all the new thermal requirements are correctly reflected in the geometries under investigation, satisfying the problem in a multidisciplinary fashion. The grid sensitivity with respect to the CAD parameters follows the implementations discussed in [16] and [18], whilst the sensitivity of the cost function with respect to the grid points coordinates is discussed in this session. Finally, using the chain rule, the sensitivities of the cost function with respect to the CAD parameters are computed. A schematic representation of the optimization workflow is reported in Figure 6, recalling the optimization strategy presented in [18] and replacing the CFD primal and adjoint solvers with the combined CHT solvers in primal and adjoint modes. The new single objective function encloses performance-related contributes (e.g. efficiency) and one term specific for the CHT constraint with a penalty factor. Structural mechanic additions are accounted as well even if not explicitly reported in the chart.

The critical parameter for the problem under consideration is the maximum temperature in the material, whose value has to be treated during the optimization problem in order to avoid local hot spots promoting creep in the turbine rotor. Since the maximum temperature is a scalar value, following the indications reported in [16], a p-norm function is adopted to define the new contribution to the cost function related to the CHT analysis in the form of

$$J_{CHT} = \sqrt[p]{\frac{\int T^p dV}{\int dV}} \tag{6}$$

with $p \to \infty$

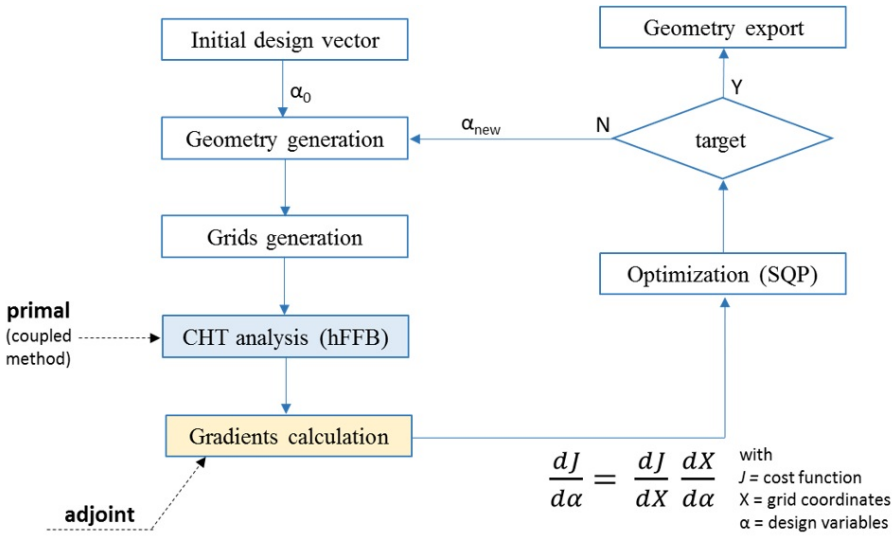

Figure 6: Simplified multidisciplinary optimization workflow

The gradients of the cost function are computed by an adjoint approach as summarized in Figure 6. The selection of the discrete adjoint method is driven by considerations of consistency with respect to the primal solver, code maintenance aspects and the availability of Algorithmic Differentiation (AD) techniques. The latter is implemented using the Operator-Overloading AD tool CoDiPack [26].

The interdisciplinary aspects introduced by a CHT problem do not allow treating separately the analyses as in [17]: therefore, a coupling approach is adopted in the present work.

Martins et al. [27] presented a "strong coupling" technique applicable to multidisciplinary problems in which cross-discipline Jacobian terms are evaluated in order to explicitly account for the mutual interactions between solid and fluid domains at the boundaries. Such cross-discipline contributions to the global Jacobian matrix are represented by very sparse sub-matrices with only few non-zero terms referred to the cells or nodes at the solid-fluid interface. The advantages shown by this method are related to the implicit exchange of boundary conditions between the domains, the exact calculation of the gradients and the direct computation of the adjoint vector by, for instance, the Lagged-Coupled Adjoint technique. Nevertheless, the actual implementation of the method is very involved, especially in the framework of a continuously growing modular multidisciplinary platform for more comprehensive problem evaluations. Therefore, as anticipated with the description of the primal solver, the present work focuses on the adoption of a "loose coupling" approach, as described below.

Following the iterative method applied to the primal solver (ref. Figure 5), the multidisciplinary adjoint framework is similarly structured as reported in Figure 7. The hFFB method is applied to the exchange of information between fluid and solid with convergence at the nth iteration. At each solvers call, the NS computation is executed first and the intermediate solution stored on hard drive, followed by the solid analysis whose information is stored in a tape. Tape positions are saved at each iteration in order to allow later recovery. Once the primal convergence is reached, the new cost function contribute J_{CHT} is finally computed.

The adjoint computation walks through the entire chain in reverse mode. The process is introduced by seeding the input $\overline{J_{CHT}} = 1$ (upper bar notation is used to denote adjoint variables) such that

$$\overline{T} = \frac{dJ_{CHT}}{dT}\overline{J_{CHT}} = \frac{dJ_{CHT}}{dT} \tag{7}$$

The FEM linear solver is not differentiated but, as discussed in [14] and [16], a new linear system solve is formulated, with the adjoint temperature vector (7) appearing at RHS as

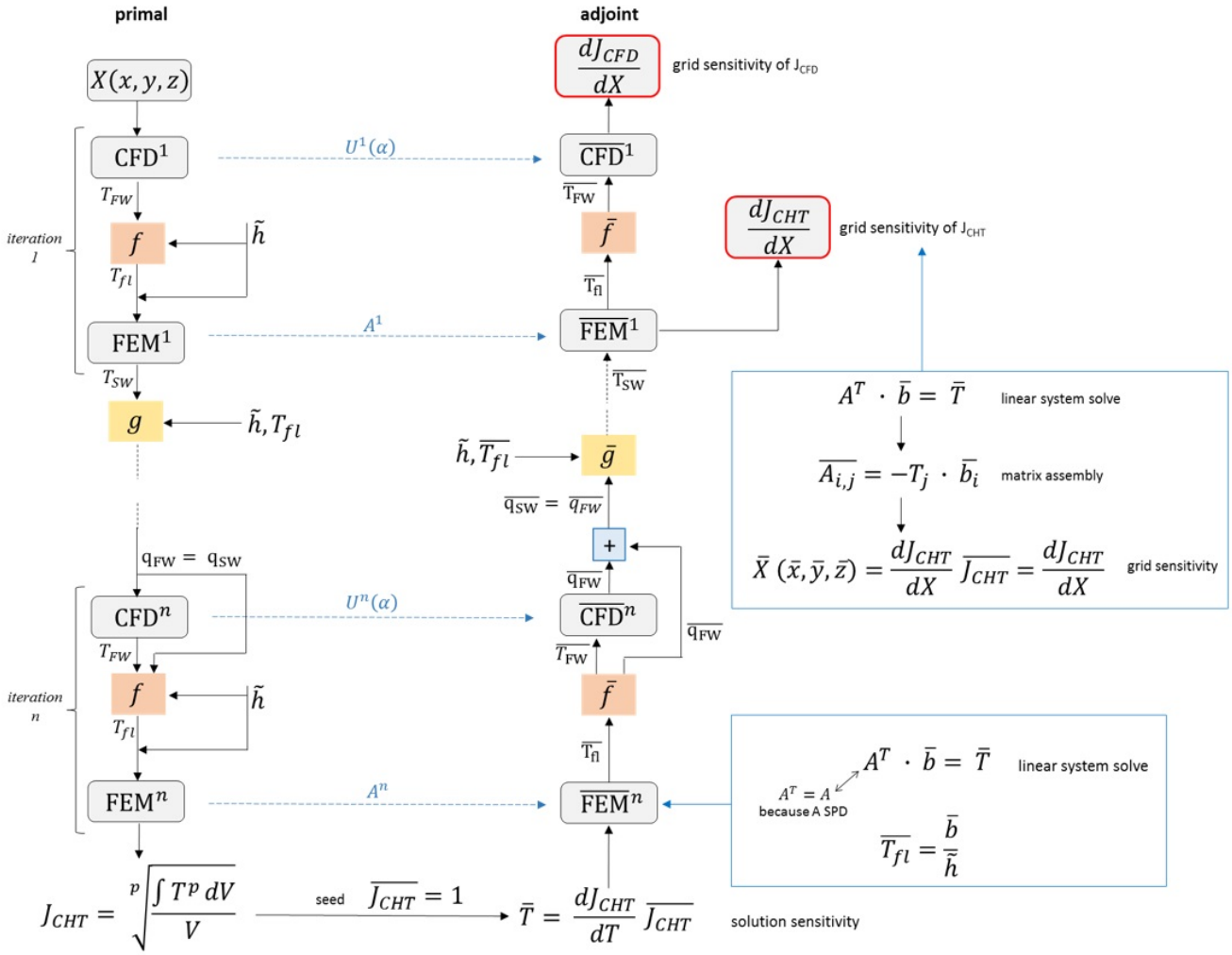

Figure 7: Workflow for cost function grid sensitivity

$$A^T \overline{b} = \overline{T} \tag{8}$$

with $A^T = A$ recovered from the primal solver because symmetric positive definite.

The system solution results in the adjoint vector $\overline{b}$, finally plugged in the calculation of the adjoint virtual fluid temperature in the thermal boundary layer

$$\overline{T_{fl}} = \frac{\overline{b}}{\overline{\tilde{h}}} \tag{9}$$

invoking the same virtual heat transfer coefficient imposed in the primal computations.

As next step, $\overline{T_{fl}}$ and $\tilde{h}$ are introduced as input of $\overline{f}$ in Figure 7, which is the differentiation of equation (1). The resulting adjoint wall temperature is introduced as boundary condition to the adjoint CFD computation, returning the adjoint heat flux at the solid walls. This wall heat flux needs to be accumulated with the wall heat flux computed by the differentiation of (1). This adjoint heat flux is then finally passed on as boundary condition for the next adjoint solid FEM solution.

The process is repeated in reverse order up to iteration one, which presents a bifurcation just after the adjoint FEM solution. On one side, the $\overline{T_{fl}}$ is propagated to the $\overline{f}$ and finally the adjoint CFD computation is followed by grid sensitivity of the

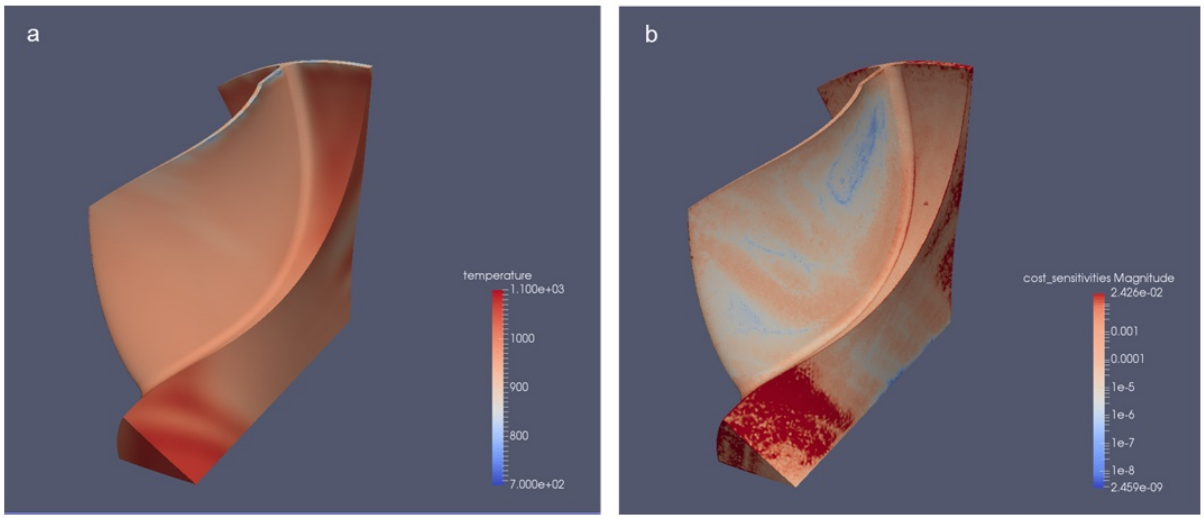

Figure 8: Solid temperature distribution (a) and grid sensitivity of the cost function J_{CHT} (b)

CFD portion of the cost function J_{CFD} as discussed in [18]. On the other side, $\overline{b}$ from the adjoint FEM solution at iteration one is followed by the assembly of $\overline{A}$ matrix, as shown in Figure 7; finally, the two are plugged into the algorithmically differentiated assembly of the couple *(A,b)*, resulting in the vector $\overline{X}(\overline{x}, \overline{y}, \overline{z})$. Therefore, the grid sensitivity of the cost function contribution J_{CHT} is achieved.

Figure 8 is a representative view of the temperature distribution in the solid domain and the grid sensitivity of the relative cost function J_{CHT} from equation (6). The picture shows a blade view from suction side with localized spots of lower temperatures towards the tip, in a region experiencing severe flow detachment and recirculation vortices. The same "signature" is also present in the grid sensitivity plot, reporting a limited area with low magnitude in correspondence of the portion of blade affected by the recirculation bubble.
At the time of writing, Figure 8 is considered as a work-in-progress result because generated from an uncomplete CHT loop; updates will follow.

The cost of computing the gradients in the FEM solver is approximately 1.3 times the cost of the primal solver, while the cost of each adjoint CFD solution is roughly 0.7 times the runtime of a primal solution as in [18].

For sake of clarity, the computation of the adjoint variables at iteration *i* is reported in detail in Figure 9.

5. Conclusion

A multidisciplinary adjoint framework for thermal optimization of turbomachinery components is presented with focus on Variable Geometry Turbines for automotive applications. A Conjugate Heat Transfer analysis driven by the partitioned "heat transfer coefficient Forward Flux Back" method is developed in order to compute heat fluxes between a solid and its surrounding fluid, interfaced by a distance weighted interpolation technique. The primal solver results in a p-norm function emulating the maximum temperature in the solid domain and representing the new contribute to the cost function. A discrete adjoint method with loose coupling technique is selected for the computation of the grid sensitivities of the cost function and its implementation is demonstrated in a modular framework open to integration of further scientific disciplines.

Future work is related to the extension of the method to more complex arrangements including rotor-stator interactions and the lightening of the computational effort for a complete iterative solution. Additionally, the stability of the method will be further investigated in order to address an optimization framework suitable for industrial applications.

Acknowledgments

The authors would like to acknowledge General Motors Global Propulsion Systems - Torino for the

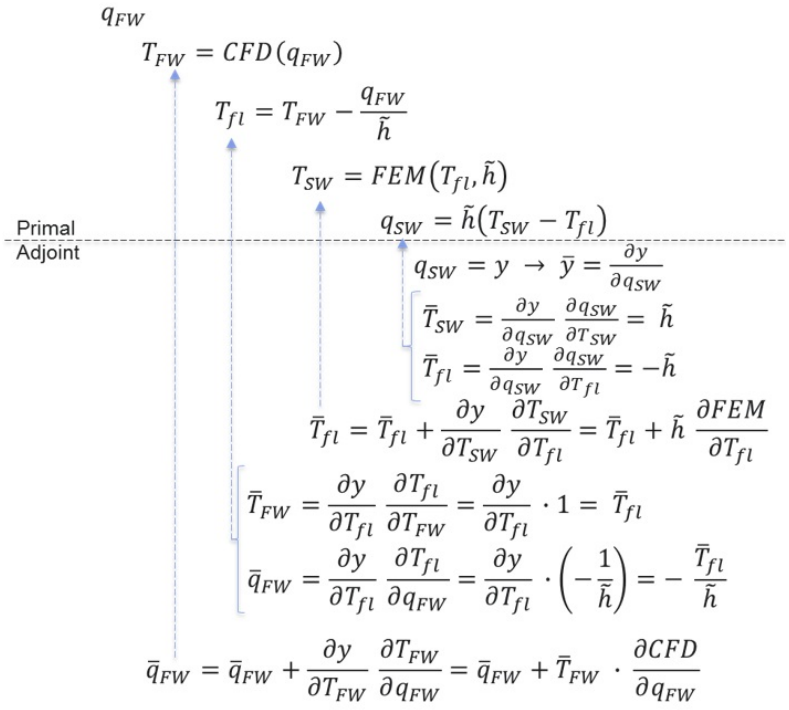

Figure 9: Computation of adjoint variables for iteration *i*

support to the present research project under the grant of the GM Industrial PhD Program.

References

[1] X. Liu, D. Furrer, J. Kosters, J. Holmes, "Vision 2040: A Roadmap for Integrated, Multiscale Modeling and Simulation of Materials and Systems", NASA/CR-2018-219771

[2] R.D. Lotz, D.N. Andrews, J.P. McHenry, D. VanSaun, J.P. Watson, "Further development of a high-efficiency compressor stage suited to post Euro VI emissions and fuel economy legislation", BorgWarner Turbo Systems USA, in The 13th International Conference on Turbochargers and Turbocharging, pp. 139-151, London, UK (2018)

[3] M. Wöhr, M. Schneid, T. Palenschat, A. Dillmann, M. Müller, "Automated turbocharger compressor development at Daimler Trucks", Daimler AG Mercedes-Benz Research & Development India, in The 13th International Conference on Turbochargers and Turbocharging, pp. 153-165, London, UK (2018)

[4] E. Ioannou, A.W. Costall, U. Khairuddin, P. Ramasamy, E. Haigh, "Turbocharger turbine aerodynamic optimization for reduced fuel consumption and CO2 emissions from heavy-duty diesel engines: Experimental validation and flow field analysis", Imperial College London & Caterpillar UK, in The 13th International Conference on Turbochargers and Turbocharging, pp. 373-388, London, UK (2018)

[5] T. Hildebrandt, P. Thiel, H. Suganuma, "Multidisziplinäre und multikriterielle Kennfeld Optimierung eines Turboladerverdichters für Motorsport Anwendungen", NUMECA Ingenieurbüro & Toyota Motorsport GmbH, in 23rd Supercharging Conference, pp. 355-371 , Dresden, Germany (2018)

[6] S. Xu, D. Radford, M. Meyer, J.D. Mueller, "Stabilisation of discrete steady adjoint solvers", Journal of Computational Physics, Volume 299, pp.175-195, 2015

[7] M. Meyer, "Introduction to optimization and multidisciplinary design", Rolls Royce Deutschland, in von Karman Institute for Fluid Dynamics Lecture Series 2018-04, Sint-Genesius-Rode, Belgium (2018)

[8] J.C. Vassberg, A. Jameson, "Industrial Application of Aerodynamic Shape Optimization", Boeing Commercial Airplanes USA and Texas A&M University USA, in von Karman Institute for Fluid Dynamics Lecture Series 2018-04, Sint-Genesius-Rode, Belgium (2018)

[9] T.L. Perelman, "On conjugated problems of heat transfer", International Journal of Heat and Mass Transfer, Volume 3, Issue 4, pp.293-303, 1961

[10] L. Pohorelsky, A. Vondrak, N. Turner, N. Luard, B. Cooper, A. Lane, R. Osborne, "The coupling of Advanced Gasoline Combustion and a fast-transient Boost System to produce a Low CO2 vehicle Concept", Honeywell & Jaguar Land Rover & Ricardo, in 23rd Supercharging Conference, pp. 397-421, Dresden, Germany (2018)

[11] R. Christmann, M. Gugau, S. Weiske, "Gasoline

VGT - a new trend for gasoline Miller engines?", Borg-Warner Turbo Systems Germany, in The 13th International Conference on Turbochargers and Turbocharging, pp. 563-576, London, UK (2018)

[12] T. Verstraete, "CADO: a computer aided design and optimization tool for turbomachinery applications", in 2nd International Conference on Engineering Optimization, pp. 6-9, Lisbon, Portugal (2010)

[13] L. Mueller, T. Verstraete, "CAD Integrated Multipoint Adjoint-Based Optimization of a Turbocharger Radial Turbine", International Journal of Turbomachinery, Propulsion and Power 2017, 2(3), 14

[14] M. Schwalbach, T. Verstraete, N.R. Gauger, "Adjoint Optimization of Turbomachinery Components Under Mechanical Constraints", in The 8th VKI PhD Symposium, von Karman Institute for Fluid Dynamics, Sint-Genesius-Rode, Belgium (2017)

[15] A. Romagnoli, A. Manivannan, S. Rajoo, M.S. Chiong, A. Feneley, A. Pesiridis, R.F. Martinez-Botas, "A review of heat transfer in turbochargers", Renewable and Sustainable Energy Reviews, Volume 79, pp. 1442-1460, 2017

[16] T. Verstraete, L. Mueller, J.D. Mueller, "CAD-Based Adjoint Optimization of the Stresses in a Radial Turbine", in ASME Turbo Expo 2017, Paper No. GT2017-65005, Volume 2C, Charlotte, USA (2017)

[17] M. Schwalbach, L. Mueller, T. Verstraete, N.R. Gauger, "CAD-Based Adjoint Multidisciplinary Optimization of a Radial Turbine under Structural Constraints", in Proceedings of 2018 Global Power and Propulsion Forum, Paper No. GPPS-NA-2018-133, Montreal, Canada (2018)

[18] L. Mueller, "Adjoint-Based Optimization of Turbomachinery Applied to Axial and Radial Turbines", PhD Thesis, von Karman Institute for Fluid Dynamics, Université Libre de Bruxelles (2019)

[19] K.T. Gkaragkounis, E.M. Papoutsis-Kiachagias, K.C. Giannakoglou, "The continuous adjoint method for shape optimization in Conjugate Heat Transfer problems with turbulent incompressible flows", Applied Thermal Engineering, Volume 140, pp. 351-362, 2018

[20] S.A. Mousavi, "Constrained Aerodynamic and Heat Transfer Optimization of Gas Turbine Blades Using an Adjoint Approach", PhD Thesis, McGill University, Montreal, Canada (2012)

[21] O. Burghardt, T. Albring, N.R. Gauger, "Computation of accurate adjoint-based gradients for optimization in conjugate heat transfer problems", in 6th European Conference on Computational Mechanics, 7th European Conference on Computational Fluid Dynamics, Glasgow (2018)

[22] J.A. Verdicchio, J.W. Chew, N.J. Hills, "Coupled Fluid/Solid Heat Transfer Computation for Turbine Discs", in ASME Turbo Expo 2001, Volume 3, Paper No. 2001-GT-0205, New Orleans, USA (2001)

[23] T. Verstraete, "Multidisciplinary Turbomachinery Component Optimization Considering Performance, Stress, and Internal Heat Transfer", PhD Thesis, von Karman Institute for Fluid Dynamics, Universiteit Gent (2008)

[24] T. Verstraete, S. Scholl, "Stability analysis of partitioned methods for predicting conjugate heat transfer", International Journal of Heat and Mass Transfer, Volume 101, pp.852-869, 2016

[25] K.J. Bathe, M.R. Khoshgoftaar, "Finite element formulation and solution of nonlinear heat transfer", Nuclear Engineering and Design, Volume 51, Issue 3, pp.389-401, 1979

[26] M. Sagebaum, T. Albring, N.R. Gauger, "High-Performance Derivative Computations using CoDiPack", arXiv preprint arXiv:1709.07229, 2017

[27] J.R.R.A. Martins, J.J. Alonso, J.J. Reuther, "A Coupled-Adjoint Sensitivity Analysis Method for High-Fidelity Aero-Structural Design", Optimization and Engineering, Volume 6, Issue 1, pp.33-62, 2005